Author:
Vallack, Hazel L

Title:
Physical and biogeochemical drivers of Modern carbonate diagenesis in intertidal sediments of Abu Dhabi

Author:
Vallack, Hazel L

Title:
Physical and biogeochemical drivers of Modern carbonate diagenesis in intertidal sediments of Abu Dhabi

Physical and biogeochemical drivers of Modern carbonate diagenesis in intertidal sediments of Abu Dhabi

Hazel Vallack

A dissertation submitted to the University of Bristol in accordance with the requirements for award of the degree of Doctor of Philosophy in the Faculty of Science.

School of Geographical Sciences

June 2021

Word count: 79,478

Summary

Authigenic carbonates are common early-diagenetic features of sedimentary rocks and have been linked directly to the global carbon, sulphur, and iron cycles. However, physical, chemical, and biological drivers of authigenic carbonate formation remain contentious. The sea floor of the modern Arabian Gulf is characterised by extensive areas of recently-lithified carbonate sediments, with firmgrounds and hardgrounds cemented by acicular aragonite and high Mg-calcite cements. This study presents the first comprehensive analysis of biologically-influenced aragonite mineralisation resulting in subsurface firmground formation within the sediment column in two contrasting shallow coastal lagoons in Abu Dhabi with varying degrees of restriction and hydrodynamic complexity. Physical and chemical characteristics of shallow sediment cores and firmground samples, corresponding porewater chemistry, and microbial community composition (*via* 16S SSU rRNA gene sequencing) were analysed to achieve a mechanistic understanding of the drivers of firmground formation.

Evidence suggests firmground formation is linked to the redox boundary and driven by increased porewater *p*H generated as a by-product of microbial respiratory processes. Archaeal Marine Benthic Group D (*Thermoprofundales*) in association with known sulphate-reducing bacteria and rare archaeal taxa are likely involved in sulphate reduction which, in conjunction with pyrite formation, could drive aragonite supersaturation. Additionally, Fe/Mn-oxide reduction may drive increased *p*H and precipitation of carbonate cements to form the firmground. Preliminary modelling results suggest that firmground formation may also be favoured in warmer summer months over winter months, particularly in the upper 20 cm of sediment in the lower-to-middle intertidal zone, as temperature is a key thermodynamic control on carbonate precipitation. These findings have implications for interpreting the role of biological processes in hardground formation in the geologic record. Additionally, these results help unravel the complex role microbes play in biogeochemical cycles within the coastal marine subsurface environment and provide constraints for reactive transport models of early diagenesis.

Acknowledgments

Firstly, I would like to express my heartfelt gratitude to Fiona Whitaker and Sarah Greene for their support, patience, and guidance throughout the project. It was a pleasure to work alongside such inspiring researchers and all-round lovely people.

I would also like to extend my sincere thanks to Stephen Lokier, Annette Lokier, Gordon Coy, Mohammad Alsuwaidi, Flavia Fiorini, and Prasanth Thiyagarajan for their support when conducting fieldwork in Abu Dhabi. In addition, I am grateful to Tom Kibblewhite and Adam McAleer for their valuable support in preparing for the field.

I am also extremely grateful to the co-authors who provided me with valuable discussion, feedback, inspiration, and data. I extend a special thanks to Stephen Lokier for teaching me everything I know about microscopy, Victoria Petryshyn for the invaluable discussion and feedback on geobiology, Bradley Stevenson and Emily Junkins for the amplification and analysis of the 16 SSU rRNA, Chelsea Pederson for analysing the cement mineralogy and isotopic signature of the Yas sediments, and Hilary Corlett for the CT-scans, XRD data and numerous enlightening discussions.

I am extremely grateful for the level of support and training I was provided by the technical staff at the University of Bristol. Specifically, I would like to thank Fotis Sgouridis, Ioanna Petropoulou, Simon Cobb, and Rowan Dejardin from the School of Geographical Sciences, and Stuart Kearns and Adam McAleer from the School of Earth Sciences. In addition, I thank Stuart Bellamy for his guidance when preparing risk assessments for field and laboratory work, and Dan Lunt for providing valuable support to the PGR cohort.

I would like to thank all the wonderful people that I have met at Bristol University for making my time here so enjoyable, and offer a special thanks to Markus Adloff, Cara Mazetti, Harry Bregazzi, Ciaran Hagan, Beatriz Olivas and Thomas Turpin-Jelfs. They quickly became my closest friends, and I am extremely grateful for their friendship and support over the years. In addition, Markus has provided me with valuable academic support, and I thank him for his patience, kindness, and apparently unlimited knowledge.

I would also like to thank my amazing parents and wonderful husband Alex. I would not have been able to do this without their unwavering love and support and for that I am incredibly lucky. And last, but not least, I would like to thank the little baby I have been growing alongside this thesis, for reminding me there is more to life than carbonate diagenesis!

Covid-19 impact statement

Covid has impacted my work in several ways. Firstly, with no laboratory access throughout much of 2020, some analyses were not able to be completed. Namely, microprobe analysis to quantitatively determine cement and grain mineralogy throughout the sediment profiles at Yas Lagoon and at the Qantur Lagoon Tidal creek sub-sites. Furthermore, our collaborators who analyse the DNA at Oklahoma University were involved in Covid-19 research, which meant none of the samples from the 2019 field campaign were analysed for their DNA. This impacted the thesis structure and required a new chapter to be developed at relatively short notice. Lastly, my primary supervisor got Covid in March 2020 had has suffered from extreme exhaustion associated with long covid ever since. This significantly reduced the amount of discussion time for the project, as well as increasing the time for feedback.

Author’s declaration

I declare that the work in this dissertation was carried out in accordance with the requirements of the University's *Regulations and Code of Practice for Research Degree Programmes* and that it has not been submitted for any other academic award. Except where indicated by specific reference in the text, the work is the candidate's own work. Work done in collaboration with, or with the assistance of, others, is indicated as such. Any views expressed in the dissertation are those of the author.

SIGNED: .... DATE: .02/06/2021.....

Table of contents

List of tables

Appendices

List of figures

Appendices

1. General introduction

1.1 Introduction

Marine carbonate sediments provide a crucial archive of Earth's history spanning over three billion years (Ahm *et al*., 2018). Analysis of the geochemical compositions of carbonate sediments and sedimentary rock has provided some of the most extensive records of past environmental and climatic conditions which have been applied to answering numerous questions regarding Earth's surface evolution (Caley *et al*., 2021), including the reconstruction of the global carbon cycle (Mayer, 1991), the oxygenation of the atmosphere (Broeker, 1970), past ocean temperature (Schrag *et al*., 1995), and past seawater composition (Viezer and Hoefs, 1976; Viezer *et al*., 1999).

Marine carbonates provide potential palaeoproxy archives for the environment within which they formed. However, carbonate minerals are reactive, and thus sediments are susceptible to post-depositional diagenesis which in some cases can eradicate or mask the original chemical signal (Banner and Hanson, 1980; Schrag *et al*., 1995). Hence authigenic minerals are typically rejected for use in paleoclimate studies as palaeoproxy archives aim to reconstruct primary environmental signals. However, diagenesis can happen any time between deposition and metamorphism (Flügel, 1982); the earlier and shallower, the more the secondary alterations derive from primary environmental inputs and characteristics. Understanding how diagenesis affects carbonate sediments is therefore vital to correctly interpret signals preserved in these archives (Fantle and Ridgewell, 2020).

Secondary (authigenic) carbonate features are dependent on several primary environmental characteristics such as the particulate inputs, dissolved species, marine anoxic conditions, and redox conditions, and can thus provide valuable insights into the history of the post-depositional setting, porewater characteristics, and temperature (Zhang *et al*., 2019). Some authigenic carbonates preserve a host-sediment signal and can provide insight into palaeoenvironmental conditions *via* geochemical analysis (Plet *et al*., 2016). Rare earth elements (REEs) in authigenic carbonates from methane seeps have been interpreted as tracers for fluid composition during early diagenesis (Himmler *et al*., 2010) and the isotopic signature of carbonates have been used to infer microbial metabolic origin (Mavromatis *et al*., 2012). However, direct interpretation of these palaeo-proxies remains challenging as a comprehensive understanding of the primary drivers of authigenic carbonate precipitation is limited.

Marine diagenesis is widespread and abundant in shallow-water carbonate settings, and ranges from precipitation of calcite cements and concretions to microporosity development and dolomitisation (Ahm *et al*., 2018; Ge *et al*., 2020). The formation and burial of marine calcium carbonate ($CaCO_3$) accounts for ~80% of total carbon removal from Earth's surface and ~10% of global modern marine

carbonates are precipitated authigenically (Sun and Turchyn, 2014). Furthering our understanding of modern authigenic carbonate formations will aid the identification and interpretation of similar features in the geologic record, potentially contribute to the construction of a global carbon isotopic mass balance and the reconstructions of past atmospheric oxygen concentrations (Schrag *et al*., 2013), and inform the application of authigenic carbonate geochemical properties as palaeoproxy archives.

1.1.1 Background

Authigenesis describes a process whereby minerals are formed *in situ* during sedimentation *via* precipitation and/or recrystallization and are not transported from elsewhere (allogenic). Authigenic carbonates are common early-diagenetic features of sedimentary rocks and have been linked directly to the global carbon, sulphur, and iron cycles. Authigenic carbonates occur throughout the geological record with a range of morphologies and sizes and are suggested to form *in situ* within the top few metres of sediment during early diagenesis (Sun and Turchyn, 2014; Plet *et al*., 2016) or at deeper depths during late-stage diagenesis (e.g., calcite and aragonite veins) (Coggon *et al*., 2010). Authigenic carbonates can take the form of pore-lining cements, laterally-extensive layers as firmgrounds and hardgrounds, or have spheroid morphologies forming concretions and nodules (Coleman 1993, Marshall and Pirrie 2013). Chemical, physical, and biological controls within the sediment and the surrounding porewater affect the mineralogical, chemical, and isotopic compositions of carbonates, resulting in the precipitation of authigenic minerals with differing characteristics (Coleman 1993). Authigenic carbonates typically consist of calcite, aragonite (the less stable polymorph), iron carbonates (siderite), magnesium rich carbonates (dolomite), manganese carbonates (thodochrosite) and mixed phase (ankerite) (Marshall and Pirrie, 2013).

Diagenesis is the post-depositional alteration of sediments/sedimentary rocks and can impact all particles that accumulate on the sea floor through a combination of physical, biological, and chemical processes (Schultz and Zabel, 2006). Diagenesis can begin at the sea floor (syngenetic or eogenetic alteration), can continue throughout deep burial (mesogenetic) and throughout subsequent uplift (telogenetic) (James and Choquette, 1989; Moore, 1989).

Carbonate diagenetic alterations occur through a variety of different processes:

1. Cementation: when primary or secondary pore space becomes filled with newly precipitated minerals.
2. Dissolution: when water-rock interactions occur with waters that are undersaturated with respect to a given carbonate phase, causing the unstable minerals to become leached from the solid.
3. Recrystalisation: a change in crystal size or shape, but no change to mineralogy.
4. Neomorphism: a change in mineralogy whereby one metastable polymorph is replaced by another more stable polymorph, e.g., aragonite or high Mg-calcite (HMC) being replaced by

calcite. Neomorphism occurs via replacement, stabilisation, and dissolution and re-precipitation reactions (Hu and Burdige, 2008).

From the start of the Archean to the end of the Paleoproterozoic there was substantial carbonate mineral precipitation within marine sediments or at the sediment-water interface in the form of calcite, dolomite, aragonite crystal fans, stromatolites, and cements (Higgins *et al*., 2009; Bergmann *et al*., 2013). This ubiquity began to decline throughout the remaining Proterozoic until the Phanerozoic when authigenic mineral deposits appear to become very rare (Bergmann *et al*., 2013). Since the evolution of $CaCO_3$ producing organisms by the end of the Precambrian (Grotzinger and Knoll, 1995), carbonate marine sediments have consisted primarily of skeletally derived $CaCO_3$ (Higgins *et al*., 2009). These periods have been interrupted by brief intervals of authigenic carbonate precipitation, associated with periods of widespread marine anoxia and mass extinction events (Phelps *et al*., 2015, Greene *et al*., 2012). Despite an apparent change in temporal frequency through time, authigenic carbonate concretions are still observed in modern day sediments (Loyd and Berelson, 2016) and are considered examples of processes which occur and have occurred ubiquitously since before the beginning of the Phanerozoic (Coleman, 1993).

Marine diagenesis is widespread and abundant in warm shallow-water carbonate settings (e.g., Florida Bay, the Bahamas, and the Persian/Arabian Gulf) and within the sediments of coastal areas, specifically the eastern margins of ocean basins where primary production is high, and hence there is a high delivery of organic carbon to the sediment-water interface (Sun and Turchyn, 2014). Authigenic carbonates are also common in active and passive continental margins (Mavromatis *et al*., 2014) which are associated with methane cold seeps (Peckmann *et al*., 2001; Naehr *et al*., 2007) as well as mud volcanoes and pockmarks (Gontharet *et al*., 2007). In contrast, dissolution is more prominent in pelagic sediments due to low primary production in the open ocean. The spatial variability in the dissolution and precipitation of $CaCO_3$ is governed by the flux of organic matter (OM) to the sediment-water interface, the dissolved inorganic carbon (DIC) reservoir, the solubility of carbonate minerals and the strength and metabolisms involved in the microbially mediated degradation of organic matter (Schultz and Zabel, 2006; Bergmann *et al*., 2013).

1.1.2 Drivers of early-marine diagenesis

The extent that diagenetic alterations impact primary chemical, textural, and isotopic signatures of carbonate sediments depend on several inter-related factors (Ahm *et al*., 2018): (i) the chemical composition of the diagenetic fluid (i.e., meteoric or seawater derived, salinity) (Folk, 1974; Sheikholeslami and Ong, 2003); (ii) gross seawater chemistry (that has varied secularly through time); (iii) chemical alterations to the diagenetic fluid by macro/microbiology (specifically affecting pH and alkalinity) (Kristensen, 2000); (iv) solute transport mechanisms (advection or diffusion); (v) marine

energy regime (Shinn, 1969); (vi) the reactivity of the carbonate mineral through time (dependent on grain size, reactive surface area, and impacted by other kinetic factors); (vii) pressure and temperature (climate, depth of burial and/or depth of overlying water) (Burton and Walter, 1987); (viii) organic matter (OM) delivery (Arndt *et al*., 2013) and sedimentation rate. However, the relative importance of different chemical, physical, and biological drivers, and the extent to which drivers are local, regional, or global are still poorly understood.

Whilst the impacts of hydrothermal and burial diagenesis are often identified through qualitative metrics (i.e., petrogrpahy), the impact of shallow water early marine diagenesis on chemical proxies has attracted less attention. The effects may be harder to identify as they undergo subtle, but substantial changes in even the most diagenetically resistant chemical proxies (Higgins *et al*., 2018). The mechanism of solute transport (diffusive versus advective) is a key determinant in diagenetic/authigenic systems. Fluid-buffered systems occur where diagenesis is dominated by the chemistry of the fluid and is common in settings governed by advective fluid flow. In shallow-water carbonate systems this can occur via hydrodynamic processes such as wave action, tidal pumping, evaporative reflux and mixing with meteoric waters (Ahm *et al*., 2018). In contrast, sediment-buffered diagenesis is largely controlled by the sediment chemistry, and most common in diffusion dominated settings (Ahm *et al*., 2018).

Critically, the breakdown of OM throughout the sediment column acts as the engine behind microbial respiratory pathways. Since their evolution *c*.3.5 billion years ago, microbial metabolic processes have modified the speciation of almost all elements on the Earth's surface (Falkowski *et al*., 2008). Their versatile metabolisms drive subsurface biogeochemical cycles of elements such as carbon, hydrogen, nitrogen, phosphorous, sulphur, iron, and manganese, as well as altering alkalinity and *p*H. The resulting water-rock interactions drive diagenesis which is reflected in the porewater chemistry, sediment mineralogy and pore structure (Fantle *et al*., 2020) (Fig. 1).

Respiratory processes are dominated by the electron acceptors that yield the greatest change in free energy per mol of organic carbon oxidised by dissimilatory bacteria and archaea (Claypool and Kaplan, 1974; Burdige, 2006). The sequence of oxic respiration, followed by nitrate, manganese oxides, iron oxides, sulphate and finally methanogenesis and/or the anaerobic oxidation of methane (AOM) (Froelich, 1979) continues until all the available electron acceptors have been utilised or until all the organic matter has been degraded (Fig. 1). The consumption of electron acceptors is balanced by the production of reduced species such as NH_4^+, Mn^{2+}, Fe^{2+}, HS^- and CH_4 which under specific thermodynamic conditions may be abiotically reoxidized, although catalysed microbiologically (Schultz and Zabel, 2006).

These reactions can have a profound effect on the carbonate chemistry of pore waters by producing DIC and changing DIC speciation (Moore *et al*., 2004; Sivan *et al*., 2007) which can alter the saturation state and promote carbonate dissolution and/or precipitation (Hu and Burdige, 2007). The precipitation of authigenic carbonate is generally attributed to a few metabolic pathways which either produce alkalinity (Coleman and Raiswell, 1993) or drive a net increase in *p*H such as organoclastic sulphate reduction in conjunction with pyrite precipitation (Boudreau and Canfield, 1993; Plet *et al*., 2016), ammonification (Krause *et al*., 2018), Mn and Fe cycling, and AOM (Soetaert *et al*., 2007) (Fig. 1B). Whilst aerobic respiration (Hu and Burdige, 2008), Fe and Mn oxidation (Soetaert *et al*. 2007) and sulphate reduction in environments without sufficient Fe to remove excess H_2S (Ben-Yaakov, 1973) are associated with dissolution (Fig. 1B). Microbes can also promote the precipitation of carbonate minerals *via* biologically-induced mineralization, whereby microbes act as catalysts or nucleation sites by providing a charged surface, e.g extracellular polymeric substances (EPS) (Weiner and Dove, 2003; Dupraz *et al*., 2009; Al Disi *et al*., 2019; Lyu *et al*., 2020).

Whilst thermodynamics (e.g., local mineral saturation state) is the first order control on carbonate precipitation or dissolution (Higgins *et al*., 2009), kinetic factors are also important as they may inhibit or accelerate reactions, determine reaction rates, and in some cases determine minerology (aragonite, HMC or calcite) (Burton and Walter, 1987). Kinetic factors such as temperature (Burton and Walter, 1987) and porewater geochemistry (e.g., high Mg/Ca ratios and high sulphate concentrations) can favour aragonite precipitation over calcite (Zhang and Dawe 2000; Crockford *et al*., 2014). The presence of seed crystals may increase precipitation reaction rates (Xyla *et al*., 1991) and in some cases dissolution may become self-limiting as minor ions released during early stages of mineral dissolution adsorb onto mineral surface, preventing further dissolution (Eisenlohr *et al*., 1999).

Physical process may also drive mineral precipitation. A hiatus in sedimentation has been suggested to be a critical formation requirement for carbonate concretions (Coleman and Raiswell 1993; Lash and Blood (2004) and cemented sea-floor hardgrounds (Shinn, 1969), with the suspension of burial allowing the zone of carbonate precipitation to be located at a constant depth below the sediment surface for a period long enough to allow cementation to occur. Similarly, progressive cementation downwards from the sediment-water interface can impact the downward diffusion of ions from overlying supersaturated seawaters, with the lower limit of cementation reached when pores become clogged and impermeable, a process also affected by grain size (Shinn, 1969). Another important factor is the energy conditions of the environment. High energy environments experiencing a large amount of sediment remobilisation will not maintain sediment within the zone of precipitation long enough to develop a carbonate surface/structure (Shinn, 1969).

This study focusses on the formation of marine firmgrounds and hardgrounds, though terminology in the literature can often be inconsistent (see discussion in Christ *et al*., 2015 and Ge *et al*., 2020a).

Firmgrounds are described as 'firm, dewatered, compacted sediment', and hardgrounds as 'hard, synsedimentary marine lithified sea floors' which can vary from incipiently to fully lithified (Christ *et al*., 2015). The term 'discontinuity surface' (Clari *et al*., 1995; Hillgärtner, 1998) is applied to all lithified surfaces in a stratigraphic section resulting from a hiatus in sedimentation, as is often used interchangeably with the term 'hardground'. Within the context of this study, both firmgrounds and hardgrounds describe laterally continuous (over scales ranging from 1 m to many km), semi-to-fully lithified surfaces forming *in situ* within the shallow subsurface sediment (typically 10 – 20 cm depth), sometimes referred to as 'sub-hardgrounds' (Molenaar and Zijlstra, 1997) and 'concretionary sub-hardgrounds' (Ge *et al*., 2020a). We follow the definition of 'concretionary sub-hardgrounds' of Ge *et al*. (2020a) and refer to partially-lithified (incipient sub-hardgrounds) as firmgrounds.

A conventional interpretation of these features is that they reflect low rates of, or a hiatus in sedimentation which typically results in inorganic cementation at, or near the sediment water interface (Kennedy and Garrison, 1975; Wilkinson *et al*., 1985). Hardgrounds typically form at, or near to the sediment-water interface in tropical/sub-tropical shallow-water environments over geologically short timescales of 10 – 10,000 years (McLaughlin *et al*., 2008; Christ *et al*., 2015). Formation is thought to be driven primarily by bottom water carbonate supersaturation and seawater circulation (Christ *et al*., 2015); low sedimentation rate or hiatuses in sedimentation (Strasser, 2015); and elevated hydrodynamic levels (Dravis, 1979; Lighty, 1985). Hardgrounds, such as those in coastal Abu Dhabi are often associated with maximum flooding surfaces of different sea level cycles; marine regressions and transgressions (Paul and Lokier, 2017). However, processes involving microbial activity may also be important in driving the precipitation of "abiogenic" cements (Kandianis *et al*., 2008) with processes such as organoclastic sulphate reduction being suggested as drivers of subsurface cementation in coastal Abu Dhabi (Lokier and Steuber, 2009; Get *et al*., 2020a; Chapter 3).

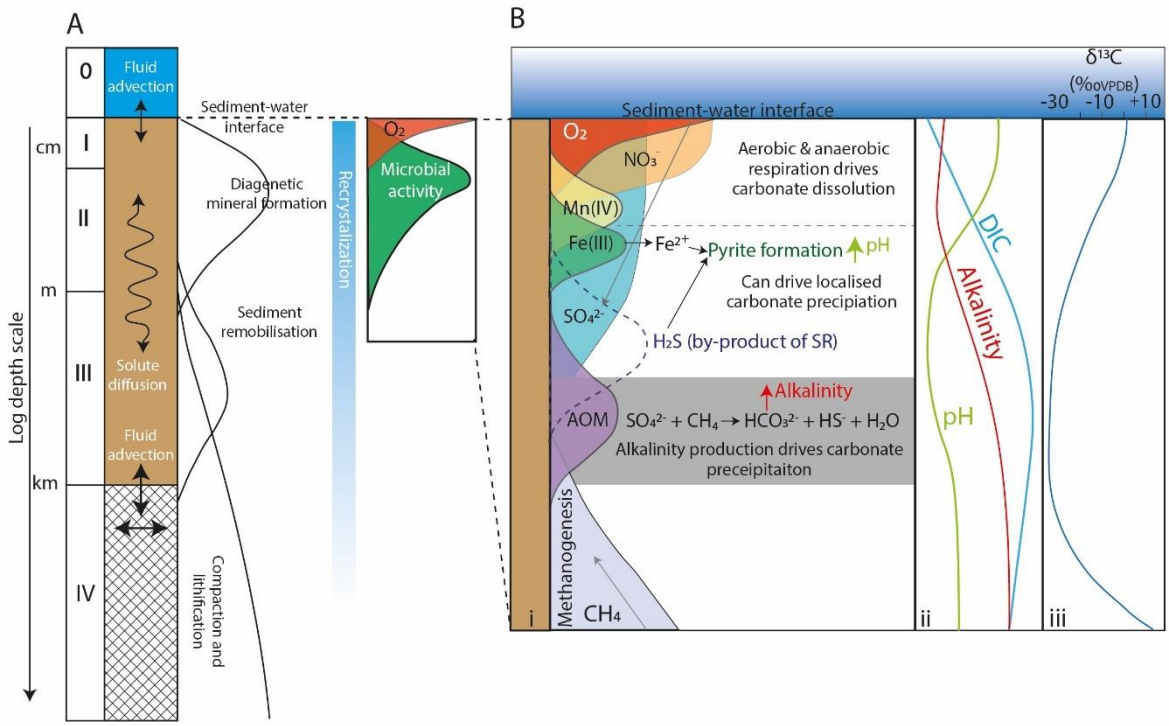

Figure 1.1. (**A**) Major diagenetic zones during depositional and burial zone 0: deposition; I: aerobic early diagenesis; II: anaerobic early diagenesis; III: abiotic sediment redistribution; and IV: lithification. (**B**) Simplified porewater chemical profile; (**i**): indicating idealised zones of oxic respiration, nitrate reduction, Mn and Fe-oxide reduction, sulphate reduction (SR), anaerobic oxidation of methane (AOM) and methanogenesis, highlighting those which promote dissolution, and those that favour authigenic carbonate precipitation and their relative impact on (**i**): relative porewater DIC, alkalinity, and pH and (**ii**): isotopic composition of DIC ($\delta^{13}C$) Adapted from Fantle *et al*. (2020).

1.1.3 Quantifying early marine diagenesis

The study of shallow-marine carbonate diagenesis spans several scientific disciplines which apply different approaches to investigating authigenic carbonate formation. One body of research takes a mechanistic approach to precipitation of layered marine carbonates from a biogeochemical perspective. These studies address issues of meta-stable carbonate phases (Morse *et al*., 1997; Drupp *et al*., 2016), microbially-mediated stromatolite formation (Visscher *et al* 1998; 2000; Reid *et al*., 2000; Petryshyn *et al.*, 2012; Frantz *et al*., 2015) and carbonate precipitation in microbial mats (Chafetz and Buczynski, 1992; Baumgartner *et al*., 2006; Dupraz *et al*., 2009). Some attention is specifically paid to the formation of authigenic firm/hardgrounds and concretions in relation to microbial respiratory processes (Coleman, 1993; Aghib *et al*., 1991; Raiswell and Fisher, 2004; Kandianis *et al*., 2008; Loyd and Berelson, 2016; Plet *et al*., 2016, Greene *et al*., 2012), however these often focus on deep sea localities. Limited process-based examples exist for modern aragonitic cemented firm/hardgrounds (McKenzie and Bernoulli, 1982; Ge *et al*., 2020a), and any assessment of microbial drivers is often limited.

Another approach focuses on products of shallow water precipitation, such as authigenic firm/hardgrounds and associated petrophysical characteristics, cement geochemistry, and isotopic composition (Christ *et al*., 2015 and references therein) with complementary studies of ancient deposits from deep sea (Lash and Blood, 2004; Gaines and Vorhies, 2016). However, diagenetic overprinting during burial makes it difficult to identify the primary causal factors in firm/hardground formation (Christ *et al*., 2015). Problems of overprinting can be circumvented by examining recent deposits, and there is a long history of work describing submarine lithification in the Arabian/Persian Gulf (hereafter referred to as 'the Gulf') (Evans *et al*., 1964; Shinn, 1969; Taylor and Illings, 1969; Khalaf *et al*., 1987; Paul and Lokier, 2017).

Coastal Abu Dhabi of the United Arab Emirates (UAE) provides one of the best and most accessible modern examples of coastal sabkha (salt flat) environments and acts as a rare recent analogue of ancient epeiric settings (Lokier *et al*., 2015; Lokier and Fiorini, 2016). Ancient epeiric shelf successions are common in the sedimentary record and provide globally important areas of carbonate sediment deposits (Bádenas and Aurell, 2008). Whilst the importance of the Gulf as an analogue for arid zone carbonate sedimentation has long been recognized, studies of shallow carbonate diagenesis in the modern are heavily biased towards Florida Bay and the Bahamas. The Gulf is characterised by carbonate sediment production, redistribution, accumulation, and diagenetic alteration (Kenig *et al*., 1990; Alsharhan and Kendall, 2003). Within the lower intertidal sediments, several authigenic carbonate surfaces occur at shallow depth (10s of cm below the sediment surface) displaying a variety of morphologies from firm/hardgrounds to beach-rock and other concretionary features (Ge *et al*., 2020a). Radiocarbon ages suggest sea floor lithification initiated in the Middle to Late Holocene (~9000 yBP) and that the active lithification continues in the modern (Lokier and Steuber, 2009; Ge *et al*., 2020a). Ge *et al*. (2020a) suggest the precipitation of aragonite cemented firmgrounds in Abu Dhabi's coastal sediments is driven by aragonite supersaturated seawater, tide-induced water circulation, evaporation, and microbial activity. However, they acknowledge that the level of research they present is likely insufficient to truly capture the complexity of firmground formation in the intertidal zone (ITZ) (Ge *et al*., 2020a). Although many studies invoke microbial metabolic processes as drivers of cementation and dissolution, uncertainty remains as to the respiratory processes responsible, and how physiochemical characteristics affect microbial community structure on different spaciotemporal scales.

Despite the extensive study of hardgrounds like those in Abu Dhabi, the physical, biological, and chemical processes and interactions that facilitate their precipitation remains elusive (Christ *et al*., 2015; Paul and Lokier, 2017). Since the seminal papers of the late 1960s describing submarine lithification of Holocene carbonate sediments in the Gulf (e.g., Evans *et al*., 1964; Shinn, 1969), there has been a step-change in both our understanding of biogeochemical processes that may drive changes

in the carbonate system, and in the toolbox of techniques that can be employed to unravel these processes.

1.2 Aims and objectives

The overarching aim of the thesis is to develop a mechanistic understanding of modern authigenic carbonate firmground formation in coastal Abu Dhabi. This interdisciplinary study addresses three significant knowledge gaps: (i) there is a need for rigorous processed-based assessments of factors affecting marine sediment diagenesis prior to subsequent meteoric diagenetic overprinting (Christ *et al*., 2015). (ii) There is a lack of field studies investigating the role of microbes in the formation of shallow marine calcite and specifically aragonitic early diagenetic firm/hardgrounds, which go beyond inference of the role of microbes in descriptions of early diagenesis. (iii) The need for further investigation into how the hydrodynamic complexity of the intertidal zone may impact diagenesis on diel, tidal, and seasonal timescales. In defining possible drivers of firmground formation, this work provides a starting point from which to investigate local, regional, and global controls on modern firmground formation, and aids in interpretation of these features in the geologic record.

1.3 Thesis structure

The thesis is structured as a collection of papers**. Chapter 1** provides a general introduction to the topic and outlines the aims and objectives of the thesis. **Chapter 2** provides details of methodology development; **Section 2.1** is a manuscript proposing an updated methodology for the application of Rhizon porewater samplers in shallow marine environments to minimise the amount of degassing compared with traditional methods. **Section 2.2** details a comparative study investigating the differences in two common software packages used to calculate thermodynamics of the marine carbonate system (PHREEQC and CO2SYS) to determine which model is best suited to describing surface seawater, sediment porewater, and groundwater geochemical properties from coastal Abu Dhabi. A detailed methodology and site description is described within each chapter along with information concerning author contributions.

Chapter 3 is a presented as a manuscript that details the biogeochemical drivers of modern carbonate firmground formation in Yas Lagoon, Abu Dhabi. This chapter presents the first comprehensive analysis of biologically-influenced aragonite mineralisation resulting in firmground formation within the sediment column in a shallow coastal lagoon in Abu Dhabi. The study analysed the physical and chemical characteristics of shallow sediment cores and firmground samples, corresponding porewater chemistry, and microbial community composition (*via* 16S SSU rRNA gene sequencing) to achieve a mechanistic understanding of the drivers of firmground formation. Evidence points to the potential involvement of archaeal Marine Benthic Group D (*Thermoprofundales*) in association with known sulphate-reducing bacteria and rare archaeal taxa in the few cm below the firmground. These groups are likely involved in sulphate reduction which, in conjunction with pyrite precipitation, could drive aragonite supersaturation.

Additionally, Fe/Mn-oxide reduction may drive increased *p*H and precipitation of carbonate cements to form the firmground.

Chapter 4 combines long- and short-term logger data (temperature, salinity, and water depth) with surface water chemical analyses to investigate temporal variations in surface water chemistry in two contrasting sites on the Abu Dhabi coast. Carbonate and evaporite sediments have been well-studied in the region, and we understand that these precipitates are strongly influenced by water chemistry. Thus, coastal Abu Dhabi provides an ideal location to explore temporal changes in surface water chemistry in the ITZ and investigate what impact this may have on diagenesis. We find that variability in the surface facies of inter- to supra-tidal zones are likely related to annual tide levels, which are controlled by both astronomical and seasonal forcing. The magnitude of peak salinity within the lower ITZ is largely a function of the magnitude of previous sea level highs, as higher tides reach the back of ITZ and flush out salts concentrated by evaporation. Daytime flooding across the microbial mats may promote the precipitation of carbonate minerals as photosynthesis removes carbon dioxide (CO_2). As the tide falls, supersaturated seawater from the microbial mats flows back down the ITZ and may promoted carbonate mineral precipitation in the lower ITZ.

Chapter 5 investigates whether the mechanistic model of firmground formation developed in Chapter 3 at Yas Lagoon is applicable to the more hydrodynamically complex environment surrounding a tidal creek in nearby Qantur Lagoon (hydrodynamics detailed in Chapter 4). Like Chapter 3, Chapter 5 combines analysis of porewater chemistry with physical and chemical characteristics of shallow sediment cores and firmground samples and microbial community composition (*via* 16S SSU rRNA gene sequencing) to investigate physical, chemical, and biological drivers of firmground formation. However, unlike Chapter 3, Chapter 5 compares the drivers of firmground formation at four contrasting sub-sites to determine whether the same processes that drive cementation in Yas lagoon are causing firmground formation in Qantur lagoon, and to ascertain which drivers of authigenic carbonate formation may be locally or regionally important.

Chapter 6 preliminarily explores a key question highlighted by the previous chapters: what role (if any) does seasonality play in driving subsurface cementation in the ITZ of coastal Abu Dhabi? Most carbonate platforms, including those in Abu Dhabi, are situated in arid climates where field work is typically biased towards cooler months. Thus, porewater chemistry samples obtained in winter may not be reflective of processes happening within the warmer summer months due to temporal variation in climate and coastal hydrodynamics on both regional and local scales. Chapter 6 applies a 1D reaction transport model to predict the impact of *in situ* porewater temperature change over seasonal timescales on porewater saturation state, finding that subsurface cementation may be favoured in summer over winter. This chapter ends by describing potential future research directions to better

explore the question of what role long-term temperature change has on authigenic carbonate precipitation at a global scale in the geologic past, and what impact, if any, this has on the global carbon cycle.

Chapter 7 provides a general discussion which synthesises the main findings from Chapters 3, 4, 5, and 6 and identifies possible implications of the findings of the study, along with possible directions for future research.

2. Method development

2.1 An updated methodology for the application of Rhizon porewater samplers *in situ* for shallow marine sediments

i. Abstract

Rhizon porewater samplers, initially designed for use in soil and agricultural science, are increasingly being applied to studying saturated sediments in marine settings. Crucial differences between terrestrial soils and marine sediments (such as the carbonate system biogeochemistry) prohibit a ready transfer of technical developments between fields, necessitating comprehensive analysis of Rhizon applications in marine settings. Rhizons provide a wide range of benefits compared to alternative methods of porewater recovery such as being non-destructive and providing high resolution sample recovery whist incurring minimal exposure to the air, however one of the main disadvantages is associated with degassing. We suggest that this is exacerbated by the 'traditional' methods, involving porewater recovery from excavated cores, and instead suggest that extraction of porewaters *in situ* provides reduced degassing and captures *in situ* carbonate chemistry more faithfully. We provide an updated methodology for the extraction of *in situ* porewaters from the upper ~1 m of sediment which is particularly applicable when sampling from relatively accessible sites. However, some method suggestions, such as maintaining a quasistatic force through the vacuum, are likely also beneficial and applicable when extracting porewaters from deeper or less accessible cores.

2.1.1 Introduction

For over 50 years interstitial waters, or porewaters, have been analysed for their water chemistry to shed light on an array of processes in a range of environments by measuring properties such as alkalinity, *p*H, dissolved inorganic carbon (DIC), dissolved organic carbon (DOC), redox state (Eh), salinity (SEC), and dissolved species (Berner *et al.,* 1970). To achieve this, porewater samples should be extracted from the sediment without contamination from the ambient atmosphere which would alter aspects of the porewater chemistry (Shotbolt, 2009). A range of methods have been employed to achieve this including the classical *ex situ* methods of "whole round" squeezing (Emerson *et al.* 1980; Schrum *et al.,* 2012), flushing out the sample with gas (Reeburgh, 1976) and centrifugation (Steiner at al., 2018) and *in situ* methods which rely on suction filtration by vacuum (Seeberg-Elverfeldt *et al.,* 2005; Dickens *et al.,* 2007) and dialysis (Hesslein, 1976).

Whilst no single method available produces optimal results for all chemical variables of interest, there have been a multitude of studies investigating the advantages and disadvantages of using the various methods for a variety of applications. Whole round squeezing is typically used onboard ocean drilling cruises for deep sea cores and provides reasonable sample recovery even from deep, highly compacted

sediments (Saffer *et al*., 2010). Near-surface porewaters are sometimes pushed out using compressed gas or extracted via centrifugation (Pohlman *et al.,* 2008). However, these methods have some practical limitations due to the destruction of the sediment core, low spatial resolution and relatively high labour and time costs. Furthermore, it has been suggested that squeezing (and other *ex situ* methods) may produce artefacts such as: nitrate contamination originating from filter papers and/or the pressure-related lysis of microbial cells (Bollinger *et al.,* 1992; Schrum *et al.,* 2012); oxygen contamination, degassing of methane or carbon dioxide during extraction (de lange *et al.,* 1992; Seeberg-Elverfeldt *et al.,* 2005); and temperature effects (Bischoff *et al.,* 1970).

These limitations led to alternative methods of marine porewater recovery being trialled, with recent attention given to assessing one of the latest developments in *in situ* porewater extraction using suction filtration by vacuum v*ia* Rhizon porewater samplers (Rhizons) (obtained from Rhizosphere, Wageningen, The Netherlands) (Seeberg-Elverfeldt *et al.,* 2005). Rhizons are made of an inert polymer with a hydrophilic porous tip (length 5 or 10 cm) attached to a thin polymer tube stabilised with a wire made of stainless steel, carbon fibre or nylon (depending on the application), with a diameter of approximately 2.4 mm. The Rhizon is attached to an evacuated vial, peristaltic pump or syringe that, when placed under vacuum, pulls water through the filter tip and into the syringe from the sediment. Rhizons offer a suite of benefits over alternative methods, they are: 1) inexpensive and disposable; 2) non-destructive: when coring the sediment profile and structure is maintained; 3) they can collect high resolution samples (typically 2 – 3 cm resolutions *in situ* and from cores (Seeberg-Elverfeldt *et al.,* 2005)); 4) the microfiltration membrane (0.12 μm and 0.18 μm) provides instant filtration by removing microbial and particulate matter (Knight, 1998); 5) they are made of an inert material meaning there is no ion exchange or adsorption with the sample; 6) they have a low dead volume (~0.5 ml); 7) cause minimal mechanical disturbance of the sediment due to small diameter of porous tip; 8) they negate the use of an anaerobic chamber as samples do not come into contact with the atmosphere (Shotbolt, 2010; Steiner *et al.,* 2018); 9) multiple samples can be collected simultaneously, and 10) it has been suggested they can be rinsed and reused (see recommended procedure for rinsing in Steiner *et al.,* (2018)) (however there are also reports of membranes becoming clogged if reused in fine grained sediments/clays (Falcon-Suarez *et al.,* 2014)).

Rhizon soil moisture samplers were initially designed for use in soil and agricultural science, studying unsaturated terrestrial soil properties *in situ* (Meijboom and Van Noordwijk, 1991; Seeberg-Elverfeldt *et al.,* 2005; Di Bonito, 2008). For many years they have also been used in saturated soils for a range of applications such as assessing methane and DOC concentrations in paddy fields (Ma and Lu*,* 2010); transition metal bioavailability and ecotoxicity in soils (Knight *et al*, 1998; Tye *et al.,* 2003; Tiensing *et al.,* 2001; Murtaza *et al.,* 2011) and soil pH, [DOC] and ^{14}C compositions (Bhupinderpal-Singh, 2005; Sigfusson *et al.,* 2006). More recently they have been employed to investigate saturated sediments in

a range of environments including the lacustrine sediment porewaters in a microcosm lab experiments (Song *et al.,* 2003) and the first application to an international discovery drilling programme core (IODP) by Dickens *et al.* (2007). This has been followed by studies on estuarine sediments (Shotbolt, 2010), and marine sediments (Steiner at al., 2018; Coffin *et al.,* 2013; Xu *et al.,* 2018). Crucial differences between terrestrial soils and marine sediments (e.g., carbonate system biogeochemistry which is particularly sensitive to effect of degassing CO_2) prohibit a ready transfer of technical developments and knowledge between fields, necessitating comprehensive analysis of Rhizon applications in marine settings.

Over the last decade, the number of studies investigating biogeochemical processes in marine sediments has increased. Sediments and their porewaters, particularly in the top 10s of centimetres below the sediment-water interface, host a vast array of biogeochemical reactions which in turn have a profound effect on nutrient and elemental cycling within the ocean. Recent research has focused on the microbially mediated biogeochemical reactions within the sediment, which affect nutrient cycling and fluxes (Song *et al.,* 2003), microbially mediated degradation of organic matter (Arndt *et al*., 2013; Reimers *et al*., 2013; Asaoka *et al*., 2020), and authigenic carbon sequestration and dissolution (Hu and Burdige, 2008). Most marine sediment studies using Rhizons have focused on deep sea drilling cores (e.g., Dickens *et al.* 2007), and the standard practice for porewater extraction by this method is based upon this relatively extensive literature. However, there are also several examples where porewaters have been extracted with Rhizons that have been inserted into push cores from accessible sites (Shotbolt, 2010; Steiner *et al.,* 2018) following the 'traditional' method described by Seeberg-Elverfeldt *et al.* (2005) and Dickens *et al.* (2007).

There is however a lack of literature dealing with the best approach when inserting Rhizons directly in the sediment of shallow/accessible marine environments (henceforth referred to as '*in situ*') and the potential advantages or disadvantages associated with doing so. In the seminal paper applying Rhizons to marine porewaters, Seeberg-Elverfeldt *et al.* (2005) introduce a Rhizon *in situ* sampler (RISS) designed for long term deployment and *in situ* sampling with a benthic chamber. The same authors have briefly discussed using Rhizons directly in the field however, to our knowledge, there have been no studies detailing variability in measured porewater parameters from samples collected by Rhizons *in situ* and Rhizons inserted into an extracted core.

This paper aims to address this gap in literature by comparing high vertical resolution (~2 cm) porewater chemistry profiles obtained from Rhizons applied *in situ* versus from the core in a shallow marine setting. We propose that the methods employed for porewater extraction from deep sea sediment cores using Rhizons is not necessarily the best approach when working in shallow marine environments (including those accessible with scuba) when analysing porewater chemistry in the top

metre of sediment. In general, we suggest that more complete porewater profiles producing more accurate data can be obtained when inserting Rhizons directly into the sediment instead of into an extracted core, as this typically provides larger sample volumes (enabling more types of analysis to be carried out) and results in reduced degassing.

2.1.2 Methodology

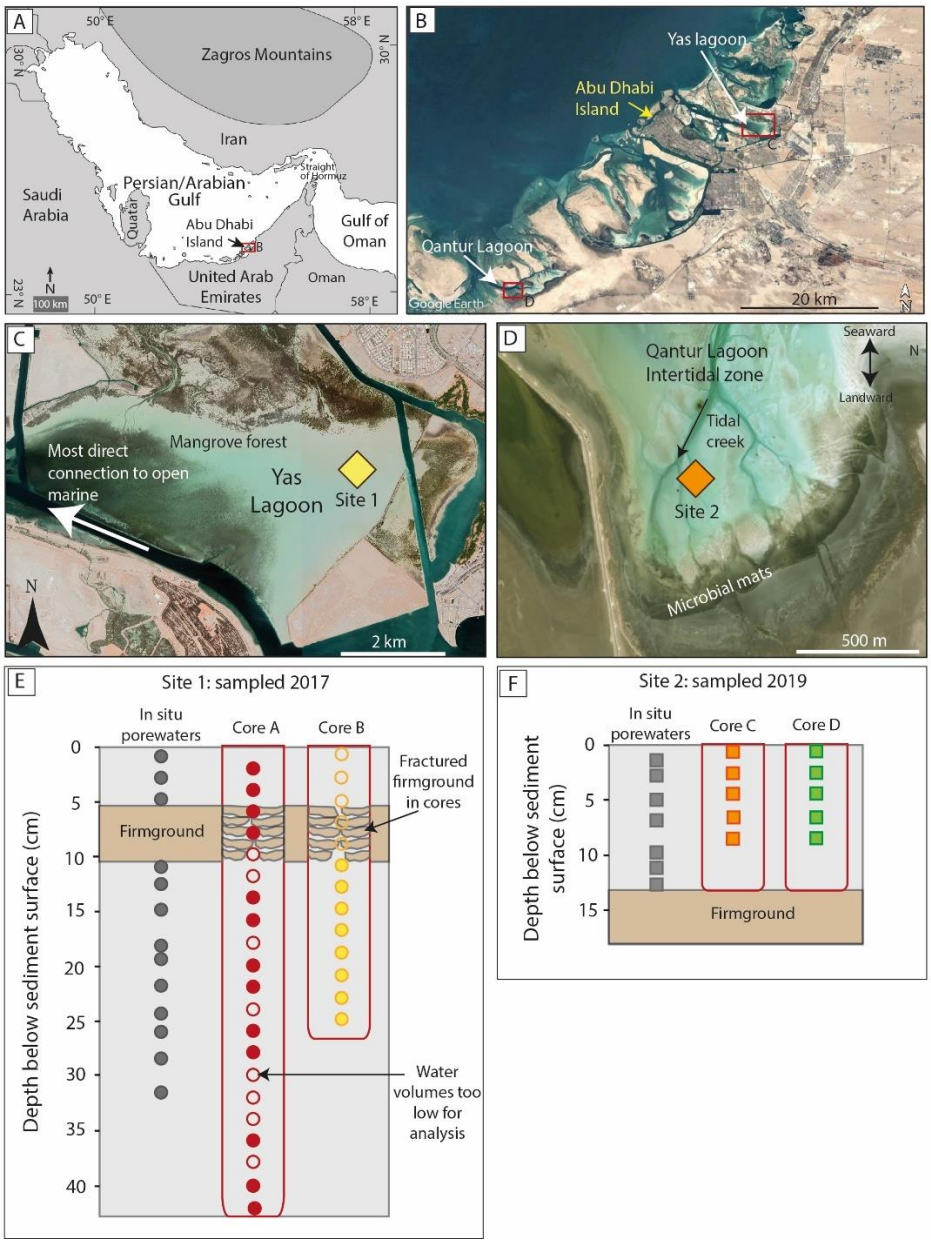

Figure 2.1. (A) Study area on the southern shore of the Gulf, adapted from Lokier *et al*. (2013). (B) Satellite image of coastal Abu Dhabi showing location of the Yas lagoon (Site 1) and Qantur lagoon (Site 2) study sites. (C) Location 1: Yas Lagoon field site and (D) Location 2: Qantur Lagoon field site. (E and F) Schematic illustrating porewater collection depths from *in situ* sediment and cores from; (E) Location 1: circles represent water samples obtained for analysis with hollow circles when porewater volumes were too low to permit analysis; and (F) Location 2 (note porewater recovery of cores took place in the lab).

2.1.2.1 Sample collection

Porewaters were collected from cores and *in situ* sediments in coastal Abu Dhabi over two field campaigns. The first location (Site 1, Fig. 2.1), Yas Lagoon, was sampled in October 2017 as part of a wider study investigating subsurface authigenic firmground formation (*in situ* porewaters only are used in Chapter 3) and is the primary focus of this study. The second location in Qantur Lagoon (Site 2, Fig. 2.1) was sampled in January 2019, as part of a wider study detailed in Chapter 5 (where *in situ* porewaters and porewaters from Core C are described as Site D)and describes additional methodological procedures adapted for the 2019 field campaign, though is discussed in less detail.

Two adjacent sediment cores (A and B) of ~30-40 cm length and *in situ* porewater samples were collected from the intertidal Yas Lagoon within an area of 1 m^2 (depths reported below sediment surface) (Fig. 2.1E). At Site 1, porewater samples were collected *in situ* at 1.5-3.0 cm vertical resolution, up to 31.5 cm sediment depth (n=13), and at 2 cm resolution from two cores (Core A = 42 cm depth, n = 21; and Core B = 25 cm depth, n=11) (Fig. 2.1E). At Site 2, one suite of *in situ* porewaters was collected at 1.5-2.0 cm vertical resolution and compared with two short sediment cores which were unable to penetrate the firmground at 13 cm (Cores C and D, both reaching 8.5 cm dept, sampled at 2 cm vertical resolution, n=5) (Fig. 2.1F). In all cases porewater samples were extracted and filtered using 5 cm long Rhizon CSS pore-water samplers (pore diameter 0.12-0.18 µm), with 0.5 and 1.0 m extension tubing when applied *in situ*.

Short sediment cores (8 cm diameter) were extracted using PVC piping pre-drilled with 2.8 mm holes at 2 cm intervals to later insert the Rhizons. The holes were covered with electrical tape during core extraction and transportation. In the laboratory, cores were drained of any water overlying the sediments (Steiner *et al.,* 2018), and held vertically as Rhizons were inserted (Fig. 2.2A). The room was air conditioned with an ambient temperature of 21 °C (similar to the *in situ* temperature). The syringes attached to the Rhizons were held open with the standard size wooden stoppers (as sold by Rhizosphere® ~9 cm length) for Core A and B (2017), creating a vacuum (Fig. 2A). During the 2019 field campaign (Site 2) porewater sample extraction followed the same methods as the *in situ* and core samples obtained in 2017, except in both cases the wooden stopper size was sequentially increased, aiming to reduce the amount of degassing by minimising the force exerted by the vacuum and maintaining a more constant flow rate throughout porewater recovery (Fig. 2.2C).

Dry Rhizons were inserted into sediment (both *in situ* and core, 2017 and 2019 field campaigns). Standard practice as described by Seeberg-Elverfeldt *et al.* (2005) suggests soaking the Rhizons porous tips in deionised water for 30 minutes until fully saturated before inserting into the sediment as this increases the efficiency of porewater recovery. This is because once wetted the microporous tip is only permeable to liquids which facilitates use in saturated and unsaturated soil (Shotbolt, 2010). Steiner

et al., 2018 found the largest disparities occurred when measuring gases in dry vs wet (wet being soaked in double distilled water for 24 hours), reporting higher levels of degassing (CO_2) when the Rhizon was inserted dry. On the other hand, there is evidence that if the sample is intended for analysing isotopes (as it was in this case) it is better to insert the filter tip dry, because even if the first few ml of water is discarded, contamination from the soaking fluid can impact isotope analysis (Miller *et al.,* 2014). Whilst pre-soaking Rhizons is not a problem when working in a controlled laboratory environment, it can pose several problems when working in the field. It is both time consuming and impractical to carry around soaking Rhizons and increases the risk of sample contamination. A test was conducted on fully saturated sediment which produced a negligible difference in the speed at which porewaters filled the syringe compared with those that had been pre-soaked. The first ~0.5 ml of liquid and any gas from the head space was expelled from the syringe which effectively flushes the Rhizon and tubing with sample whilst saturating the porous tip simultaneously (Seeberg-Elverfeldt *et al.,* 2005; Dickens *et al.,* 2007).

2.1.2.2 Porewater chemical analysis

In the laboratory, *in situ* samples were immediately aliquoted for later analysis (~6 hours after collection). Due to the time constraints of returning cores to the lab, inserting the Rhizons, and waiting for adequate water volumes to permit analysis, Core A porewaters were aliquoted for analysis <18 hours after collection and analysed 24 hours after collection, whereas those from Core B were stored within sealed plastic syringes at 4°C and in the dark for ~2 weeks prior to analysis, to determine if the speed at which samples were analysed had significant implications for the water chemistry results (Table 1). Lithification prevented the *in situ* insertion of Rhizons within the firmground at Site 1 (~6-11 cm depth) (Fig. 1E). In contrast, the mechanical force exerted during coring fractured the firmground in Core A and B, allowing porewater extraction from the firmground zone. At Site 2 (2019) *in situ* porewaters were aliquoted in the field immediately after collection (typically <30 minutes) into 4 ml pre-prepared glass vials (completely filled with no headspace) for analysis sensitive to degassing (*p*H, alkalinity, and Eh) and into pre-evacuated glass Wheaton vials with a butyl rubber septa seal (for CH_4). *p*h, alkalinity, redox potential (Eh), and specific electrical conductivity (SEC) (converted to salinity (‰) with the equation from Williams, 1986) were analysed within 24 hours of collection whereas samples extracted from Cores C and D were aliquoted ~12 hours after collection and stored in the dark at 4 °C prior to analysis 3 days after collection (Table 1).

In both 2017 and 2019 field seasons, porewater *p*H, SEC and Eh were measured within 6 hours of collection using a HQ40d Hach multi-meter and probes, with accuracies of ±0.02, ±0.5%, and ±0.05% respectively. Bicarbonate alkalinity was determined in triplicate by Gran titration (Sass and Ben-Yaakov, 1977) using 0.0005 M or 0.001 M HCl acid with 0.6% coefficient of variance (CV). Aliquots were

returned to the UK where samples were gravimetrically diluted for major ion analysis. Cations (Na^+, Mg^{2+}, Ca^{2+}, K^+, Sr^{2+}) were analysed by inductively coupled plasma atomic emission spectroscopy (ICP-OES; Agilent series 710 ICP-OES). Major anions (Cl^- and SO_4^{2-}) were measured isocratically by ion chromatography (Dionex™ ICS-5000+). Ion analyses had <1.25% CV based on multiple injections. The ion balance error (IBE) was -2.5 ±2.0% (n=55). Partial pressure of CO_2 (pCO_2), CO_3^{2-} activity, and saturation indices ($\log(IAP/K_{sp})$) of aragonite and calcite (SI_{arag} and SI_{calc}) were calculated using CO2SYS (Pelletier *et al*., 2007) (see methods discussion in Chapter 2.2). Uncertainties in pCO_2, CO_3^{2-} activity, SI_{arag}/ SI_{calc} were 0.002%, ±0.02 log units, and ±0.03 log units respectively. Headspace CH_4 concentration was analysed using the Carlo Erba HRGC5300 gas chromatograph (GC) following the method of Hornibrook and Bowes (2007) and calibrated against speciality gas standards (BOC, Guildford, UK) with CV mostly <2% based on multiple injections. Because of possible gas leakage during analysis, values are only considered minima and are reported as negligible when CH_4 was <1.6 ppm.

Figure 2.2. (A) 'Traditional' application of Rhizons into a pre-drilled core, and (B) *in situ* application of Rhizons, both using standard sized wooded stoppers to create a vacuum with the syringe (Oct. 2017). (C) *In situ* application of Rhizons using wooden stopper with sequentially increasing sizes; note the smaller stopper that had been used (arrow).

Table 2.1. Duration between sample collection, aliquoting and analysis (*p*H, Alkalinity, Eh, salinity) for the core and *in situ* samples collected in 2017 and 2019, and where data is used elsewhere in the thesis.

Sample type	**Location and date sampled**	**Duration from collection to aliquoting**	**Duration from collection to analysis**	**Chapter and site name throughout thesis**
2017 *in situ*	Yas Lagoon, Oct. 2017	6 hours	24 hours	Chapter 3
Core A	Yas Lagoon, Oct. 2017	<18 hours	24 hours	n/a
Core B	Yas Lagoon, Oct. 2017	2 weeks	2 weeks	n/a
2019 *in situ*	Qantur Lagoon, Jan. 2019	~30 minutes	<24 hours	Chapter 5: Site D *in situ*

Core C	Qantur Lagoon, Jan. 2019	12 hours	3 days	n/a
Core D	Qantur Lagoon, Jan. 2019	12 hours	3 days	Chapter 5: Site D, Core D1

2.1.3 Results

Fig. 3 shows the porewater profiles obtained by applying the Rhizons *in situ* compared with insertion into cores (A and B). Samples collected *in situ* and from Core A were analysed within 24 hours whereas porewaters from Core B were left in the plastic syringes for ~2 weeks before analysis. Salinity of the *in situ* porewaters increases with increased depth below the sediment surface in a broadly linear trend (Fig. 2.3A). Core A displayed a similar linear trend but with lower salinities and Core B displayed a more varied profile. There are numerous missing data points from the core samples as porewater volumes were often insufficient for analysis.

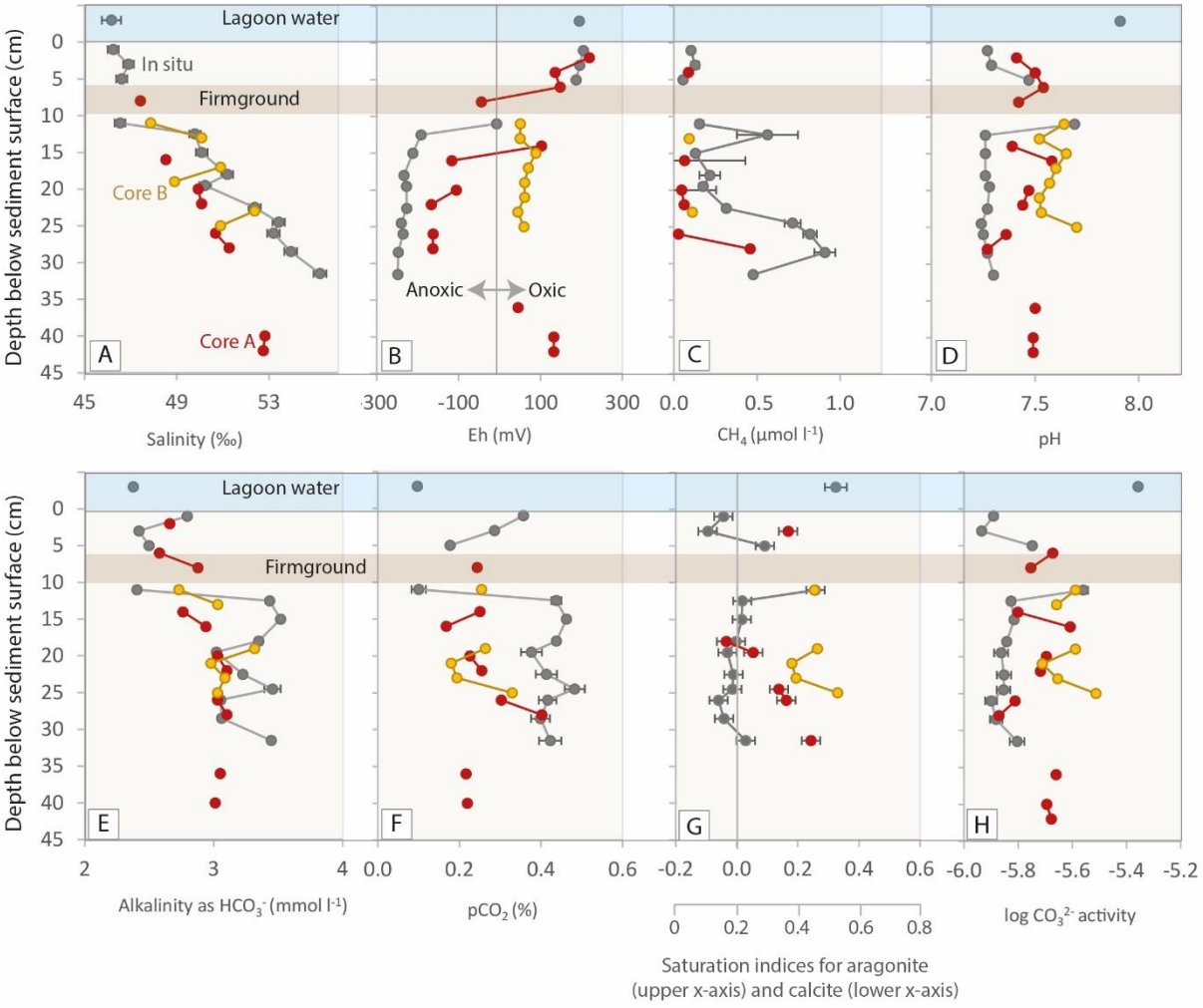

Figure 2.3. Site 1 lagoon seawater (upper panels, blue background) and porewater chemical profiles (lower panels, light grey background) from samples extracted with Rhizon porewater samplers applied *in situ* (grey) and extracted from Core A (red) and Core B (yellow). Figure displays (A) salinity; (B) redox potential (Eh); (C) methane (CH_4) concentrations; (D) *p*H; (E) alkalinity; (F) partial pressure of CO_2 (pCO_2)

(%); (G) mineral saturation indices (SI) for aragonite (upper x-axis) and calcite (lower x-axis) ($\log(IAP/K_{sp})$); and (H) log activity of carbonate ions (CO_3^-).

The redox potential (Eh) profile obtained from the *in situ* samples indicates porewaters are anoxic below ~12.5 cm, which is consistent with the smell of H_2S from sediments below the firmground (Fig. 2.3B). Whilst some samples below the firmground in Core A also appear anoxic (negative Eh), they typically have a higher Eh than their *in situ* counterparts. In contrast, porewaters obtained from Core B appear oxic throughout the sediment column (Fig. 2.3B). Methane was present within more samples and in higher concentrations in the *in situ* samples compared with the core samples, however analytical limitations (see methods) may be responsible for this discrepancy (Fig. 2.3C).

*p*h is typically lower from porewaters obtained *in situ* than those from the cores, with Core B displaying higher *p*H values than Core A (Fig. 2.3D) whereas alkalinity and $pCO_{2(aq)}$ from porewaters extracted *in situ* tend to be higher than those from the cores (Fig. 2.3E, F). Calcite and aragonite saturation indices (SI) reflect changes in the carbonate ion activity (Fig. 2.3G, H) which is largely controlled by *p*H, and thus *in situ* porewaters have the lowest carbonate mineral SI followed by Core A and the highest values from Core B.

In contrast to the 2017 samples (Fig. 2.3), those obtained in 2019 (from core and *in situ*) were more similar to one another and although *p*H (and thus mineral SI) was slightly higher in the core samples, there was not a systematic deviation between the core and the *in situ* samples (Fig. 2.4). In this case the vacuum was kept low and maintained more constant throughout sampling by using wooden stoppers with gradually increasing sizes. However, at this location, the cores were unable to penetrate the firmground (~13 cm below the surface), and thus only the upper half of the profile is shown.

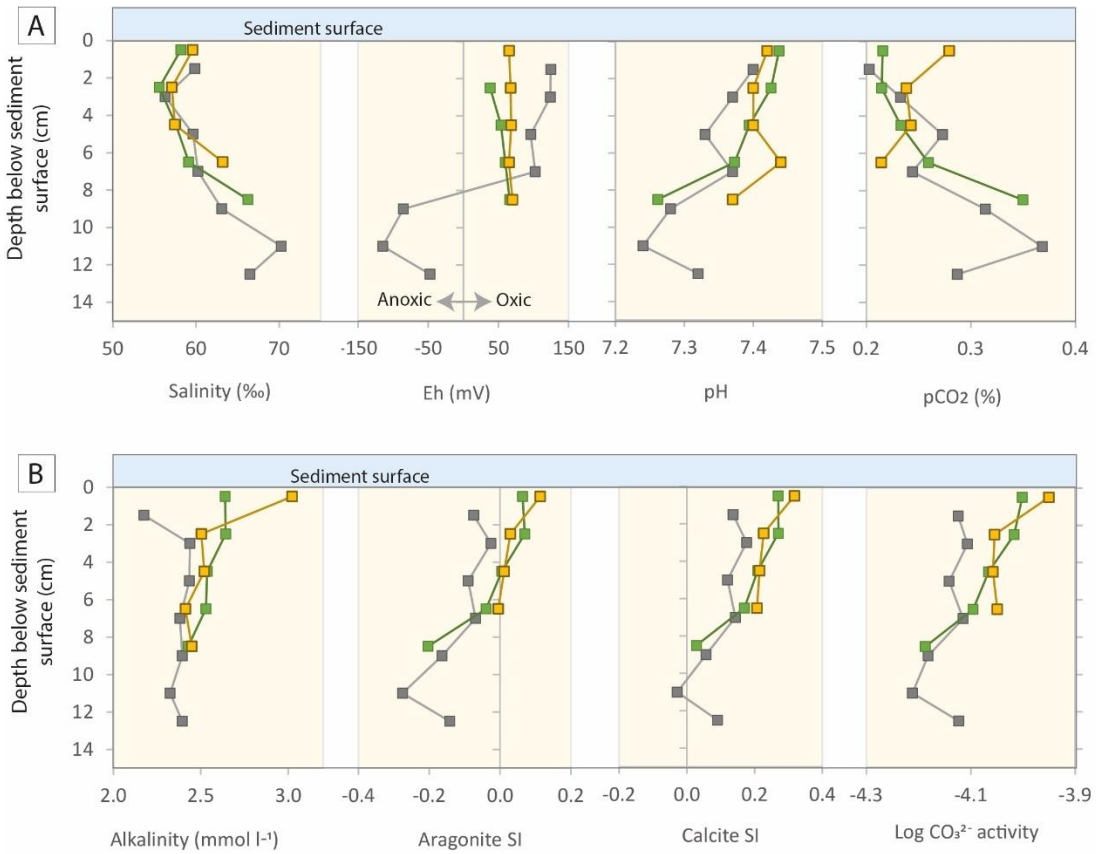

Figure 2.4. Site 2 porewater chemistry, with sample obtained with Rhizon porewater samplers applied *in situ* (grey) and from Core C (yellow) and Core D (green). Figure displays (A) salinity (‰); B) Redox potential (Eh); (C) *p*H; (D) partial pressure of CO_2 (pCO_2) (%); (E) Alkalinity; (F) saturation indices (SI) for aragonite; (G) calcite SI; and (H) log activity of carbonate ions (CO_3^{2-}).

2.1.3 Discussion

Most of the discussion will focus on the causes for differences in water chemistry between *in situ* and core porewater samples from Site 1 (2017). Additional discussion regarding amended methods applied to the samples from Site 2 (2019) is discussed, though in less detail.

2.1.3.1 Degassing

Porewaters obtained from the Site 1 cores display higher Eh, *p*H, carbonate ion activity and mineral saturation indices, and lower pCO_2, CH_4 and alkalinity than those collected *in situ*. These discrepancies suggest that samples obtained from the cores have undergone more degassing (of CO_2 and CH_4) than those collected *in situ*, and that Core B (where samples remained in the plastic syringes for 2 weeks prior to analysis) lost the more gas compared to Core A. Accurately measuring porewater *p*H and alkalinity is particularly vital when interpreting the marine carbonate system. If CO_2 is lost from solution *via* degassing, then *p*H and carbonate mineral activity increases which can trigger inorganic $CaCO_3$ precipitation when abundant calcite seed crystals are available, thereby decreasing alkalinity (Schrum *et al.,* 2012).

Degassing likely occurs when using Rhizons (*in situ* or from the core) for several reasons. Firstly, the force of the vacuum created inside the syringe pulls water through the filter to occupy the low-pressure headspace (Schrum *et al.,* 2012). As water molecules are pulled through the filter the flow is disturbed, causing minute bubbles of entrained gas to coalesce (Schrum *et al.,* 2012). As water flows through the pores, it is broken into small droplets which provide a large surface-to-volume ratio, thus enhancing the effect of the vacuum resulting in the degassing of fluids (Chambers *et al.,* 1998). Schrum *et al.* (2012) compared Rhizons inserted into cores with the squeezing method and found that degassing CO_2 resulted in consistently lower alkalinity and DIC concentrations from the Rhizons, as they induced more degassing than the traditional squeezing method. Steiner *et al*. (2018) support this, by concluding that Rhizons and centrifugation result in the preferential degassing of $^{12}CO_2$, resulting in elevated measurements of $\delta^{13}C$. Whilst some degree of degassing when porewaters are collected with Rhizons may be unavoidable, our results suggest that degassing may be minimalised when Rhizons are inserted directly into the sediment column rather than into extracted cores.

One reason the core samples may be impacted more by degassing than *in situ* samples, is that they typically spent a longer time under vacuum (taking >6 hours to extract <30 ml) compared to those obtained *in situ* (>50 ml in 0.5 hours). *In situ* sampling entrains porewater from a larger lateral reservoir providing a higher sample volume in much less time, reducing both the time it takes to obtain the samples, and the time between sample extraction and aliquoting. However, this may not be the case in more fine-grained sediment; this study was conducted in fine to medium grained sandy sediments dominated by calcium carbonate and quartz, which have been suggested to yield preferentially to Rhizons than clay rich sediment (Steiner *et al*., 2018). The unique characteristics of clay particles may cause clay-rich sediments to yield water preferentially via centrifugation over Rhizons, due to the strong resistance of clay particles to suction. This may cause elevated levels of CO_2 degassing in porewaters collected with Rhizons from clay rich sediments.

The second cause of degassing is associated with the strength of the pressure gradient imparted onto the sample by the vacuum. By pulling the syringe fully open, a strong pressure gradient causes a force to act on the liquid, breaking surface tension and allowing gases to escape. This is reduced by maintaining a quasistatic change in pressure (Schroeder, 2000), which is suggested to result is reduced degassing of water samples during collection. Gases are also potentially lost during storage in the plastic syringes (e.g., Core B, Site 1), suggesting that prompt analysis (specifically for carbonate chemistry) is important. In the 2019 field campaign (Site 2), the size of the wooden stopper was gradually increased to keep the pressure gradient to a minimum (e.g., Fig. 2.2C). This technique was applied to both *in situ* and core samples, which tended to be more similar to one another than Site 1 samples (2017) (Fig. 2.4). At Site 2, *in situ* samples were aliquoted in the field immediately after collection to further reduce the risk of degassing during transit to the laboratory.

Another cause of degassing specific to the Site 1 samples, was the subsurface firmground at 6-10 cm below the surface. *In situ* porewater extraction made it possible to obtain samples from above and below the firmground whilst not disturbing the sediment, thus providing a fairly complete porewater profile. In contrast, coring caused the firmground to break apart within the core, disturbing a layer that was potentially acting as a barrier to fluid (and gas) exchange. This is likely to have contributed to the less well-defined vertical changes observed above and below the firmground compared with the *in situ* samples. The firmground at Site 2 was more well-lithified than at Site 1 and was unable to be penetrated by the core. In this case *in situ* sampling was the only way to sample the porewater below the firmground.

2.1.3.2 Vertical mixing

It is possible that there was some vertical advection of porewaters through the core during Rhizon extraction, as often there would be several syringes with minimal water recovery, adjacent to a very full syringe a few centimetres above or below. This implies there may have been some mixing between porewaters from different depths which could affect the porewater chemistry results and inhibits analysis where yield was low. This is supported by (Steiner *et al*. (2018) who found Rhizons would preferentially remove water from above when overlying bottom water was retained in the core, however it could also reflect random localised spatial heterogeneity in permeability adjacent to the Rhizon. Alternatively, a variable porewater yield throughout the core could represent localised spatial heterogeneity in permeability throughout the sediment column. The presence of burrows (which can remain invisible to the naked eye even after the sediment has been extruded) may account for part of this effect as water will be preferentially extracted from the most permeable reservoir (Seeberg-Elverfeldt *et al.,* 2005). This may also occur within *in situ* samples, as it is not possible to determine if the Rhizon has been inserted into a pre-existing vertical burrow or a pocket of porewater that may not be representative of the mean porewater chemistry at a given depth. In comparison centrifugation can also obtain high resolution samples (>1 cm) (Steiner at al., 2018) with the added advantage of being able to obtain porewaters from the whole sample, as opposed to preferentially sampling the most accessible pool (Steiner at al., 2018). When comparing Rhizons against centrifugation, Steiner *et al.* (2018) found $\delta^{13}C_{DIC}$ to be systematically more negative in centrifuged porewaters compared with those extracted with Rhizons which is consistent with the theory of Rhizon-induced degassing as suggested by Schrum *et al.* (2012).

2.1.3.3 Other benefits of in situ Rhizon application

Rhizon porewater extraction from the cores was at times limited by the positioning of the pre-drilled holes. Rhizon insertion could be obstructed by highly consolidated sediments; sharp/gravelly layers and by larger fragments such as shells or pebbles. In certain cases, a stick of similar diameter could be used to create space through the hole before the fragile Rhizon porous tip was inserted. However, in

several instances this was not adequate resulting in gaps in the pore water chemistry profile. Although this problem still arose doing *in situ* sampling in the field, there was more lateral flexibility to sample a few cm to the left or right to insert the Rhizon successfully.

2.1.4 Conclusions

Rhizons provide a wide range of benefits compared to alternative methods of porewater recovery; they allow high resolution porewater sampling that is cost effective, non-destructive, and provides instant filtration. However, no single method is perfect, and Rhizons are associated with two main disadvantages over whole round squeezing and centrifugation; (i) they are likely to preferentially draw water from the largest pore network, which may not be representative of the entire pore-network; and (ii) degassing is likely more pronounced in Rhizons as minute bubbles of entrained gas to coalesce when passing through the porous tip. Further investigation into variations in the carbonate chemistry when comparing whole round squeezing and centrifugation with *in situ* porewater extraction with Rhizon would be valuable. Although the impacts of using dry verses wet Rhizon tips on degassing was not evaluated in this study, we are confident that the rate of water recovery is not hampered by inserting dry Rhizons into the sandy saturated marine sediments.

We suggest that degassing can be minimised in several ways by refining the 'traditional' method of pore water extraction from sediment cores.

1. Inserting Rhizons directly into the sediment (*in situ*) rather than the core provides larger sample volumes in shorter time (increasing the flow rate from ~0.08 ml min^{-1} to ~ 1.6 ml min^{-1}). This reduces the amount of time samples spend under vacuum and within plastic syringes and enables fast analysis of chemical properties sensitive to degassing. *In situ* sampling is recommended when sampling shallow sediment cores from relatively accessible sites.
2. Gradually increasing the size of the wooden stoppers used to create the vacuum in the syringe maintains a low and constant (quasistatic) force exerted by the vacuum as the water is being extracted, reducing bubbling and degassing in the tubes and syringe headspace. This method may provide benefits for porewater extraction from both *in situ* sites and sediment cores.
3. *In situ* application allows a greater degree of flexibility to avoid obstacles (e.g., large shells, or in this case firmgrounds) that may prevent successful porewater recovery from the core.
4. Some porewater analysis (alkalinity, pH, dissolved oxygen, redox potential [Eh] and CH_4) are vulnerable to degassing and/or ambient air contamination and should be processed as soon as possible, ideally <24 hours after sample collection. Whilst preservation of the filtered sample in the refrigerator helps minimise the risk of chemical changes due to biological processes, samples should be warmed back up to approximate *in situ* temperatures prior to analysis.

2.2 Comparing PHREEQC and CO2SYS for modelling the carbonate chemistry in Abu Dhabi coastal waters

2.2.1 Introduction

Thermodynamics (local gradients in calcium carbonate saturation state) is the first order control on carbonate precipitation or dissolution (Higgins *et al*., 2009), with kinetic factors determining reaction rate. The saturation state can be described by the ratio between the ion activity product and the solubility product for a given mineral and is often expressed on a logarithmic scale called the saturation index (SI) (Appelo and Postma, 1994) and is defined by the equation:

$$IAP = (\gamma Ca^{2})(\gamma CO_3^{2-})$$

$$K_{sp(CaCO3)} = [CO_3^{2-}]_{sat}[Ca^{2+}]_{sat}$$

$$SI = \log(IAP/K_{sp})$$

Where IAP = ion activity product, γCa^{2+} and γCO_3^{2-} are the behaviours of Ca^{2+} and CO_3^{2-} in seawater (*in-situ* concentrations) (Garrels *et al*. 1961; Barker and Ridgwell, 2012) and K_{sp} is a constant for the thermodynamic solubility of calcite (at a given temperature, pressure, and salinity). Surface oceans are supersaturated with respect to both calcite and aragonite, though their solubilities increase with decreasing temperature and increasing pressure (depth). When the solution is at equilibrium for a given carbonate mineral SI = 0, with positive values denoting supersaturation, favouring precipitation and negative values indicating undersaturation, favouring dissolution.

To investigate drivers of marine carbonate precipitation numerically we must be able to accurately represent the marine carbonate system. The thermodynamic equilibrium of the marine carbonate system is well-constrained for seawater, allowing any two carbonate system variables to be used to calculate the other unknown carbonate variables (at a given temperature, pressure, salinity, and nutrient concentration) (Orr *et al*., 2015) and multiple publicly available software packages are available to perform these calculations. However, subtle variations, predominantly in the equilibrium constants (Orr *et al*., 2015), mean different packages may produce different results. The solution speciation of seawater is notoriously complex (Naviaux *et al*., 2019) and the difference between model outputs becomes greater with increased departure from 'normal' surface seawater conditions (i.e., with increased ionic strength, very high (or low) temperatures and/or with reducing conditions).

This chapter section aims to investigate the differences in output of carbonate system variables calculated with several commonly used thermodynamic model software packages and to determine which is most suitable when modelling carbonate system variables for coastal Abu Dhabi seawaters, porewaters, and continental brines. We compare CO2SYS which is widely used for modelling modern

seawater (Naviaux *et al*., 2019) and several PHREEQC databases, including Pitzer which is considered the best model for solutions with high ionic strength (Harvie and Wear, 1980; Clegg and Whitfield, 1991).

2.2.2 The carbonate system solvers CO2SYS and PHREEQC

Lewis and Wallace (1998) developed CO2SYS for the computation of carbonate variables in response to the stark contrast in the computed output of pre-existing models. Since then, numerous versions of CO2SYS and other software packages have been developed; for a detailed account of the different packages available, a comprehensive assessment of the differences between them, and the causes of these differences see Orr *et al*. (2015). CO2SYS allows the user to select pH scales and constants; the constants K_1 and K_2 from Lueker *et al*. (2000) are considered best practice (though there are other options in CO2SYS). However, these constants were constructed for waters with salinity between 19-43 psu and temperatures between 2-35 °C. For waters outside these ranges, there are no recommended K_1 and K_2 constants in CO2SYS (Orr *et al*., 2015).

CO2SYS requires the input of salinity (psu or g/kg), temperature (°C) and pressure (dbars), and at least two carbonate system variables including total alkalinity (TA) (µmol/kgSW), total CO_2 (µmol/kgSW), *p*H (on chosen scale), fCO_2 (µatm) and pCO_2 (µatm). Total Si and P (µmol/kgSW) are optional. CO2SYS is available in a range of packages including two variants in Excel spreadsheets (Pierrot *et al*., 2006; Pelletier *et al*., 2007) and the most recent in MATLAB (van Hueven *et al*., 2011). Orr *et al*. (2015) found near-identical results between the Excel and MATLAB variants, and thus we will be using the Excel version for simplicity, referred to as 'CO2SYS' henceforth.

The US Geological Survey (USGS) model PHREEQC is a one-dimensional computer program for speciation, batch-reaction, one-dimensional transport, and inverse geochemical calculations (Parkhurst and Appelo, 2013). PHREEQC requires the input of dissolved major ion concentrations, pH, alkalinity, and temperature and has several built-in databases available with different methods for calculating the thermodynamics. One such database is the Specific Interaction Theory (SIT); a classical thermodynamic model based upon Debye-Hückel extended law (Salhi *et al*., 2019). Unlike some databases, silica is included in SIT and ion pairs are considered so that the activity is calculated by simultaneously solving mass balance and mass action law equations (Salhi *et al*., 2019).

In (semi)arid areas evaporation leads to increased ionic strength of solutions. Strong non ideality of electrolyte solutions complicates calculations of carbonate system variables such as minerals SI (Salhi *et al*., 2019). The Pitzer model (Pitzer, 1973; Pitzer and Mayorga, 1973), implemented in the computer programme PHREEQC (Parkhurst and Appelo, 2013), has generally been considered to provide the best model for solutions with high ionic strength, including brines (Harvie and Wear, 1984; Clegg and Whitfield, 1991), however it is also over-parameterised and lacks parameters for several elements,

such as silica (Garthe and Plyasunov, 1997). In the Pitzer model, ion pairs are not considered as it is primarily designed for entirely dissociated strong electrolytes, however acid-base reactions are included (Salhi *et al*., 2019). For a comprehensive overview of the Pitzer and SIT databases, please refer to Salhi *et al*. (2019).

2.2.3 Methodology

A sub-set of water samples (n=23) collected from coastal Abu Dhabi in October 2017 and January 2019 have been selected to cover the full range of salinities observed throughout both field campaigns. These waters will be used to compare how the output of calculated carbon system variables (CO_3^{2-} activity, aragonite saturation indices (SI_{arag}), and the partial pressure of CO_2 (pCO_2)) varies between software packages CO2SYS, PHREEQC-Pitzer (Pitzer hereafter), PHRREQC-SIT (SIT hereafter) and the default PHREEQC database (PHREEQC-default hereafter). The Pitzer, SIT, and PHREEQC-default databases were implemented in PHREEQC version 3.5.0-14000 using the pitzer.dat, sit.dat and phreeqc.dat databases respectively (Parkurst and Appelo, 2013). Uncertainties in pCO_2, CO_3^{2-} activity, and SI_{arag}/SI_{calc} were calculated for three representative water samples over a range of salinities: low (35‰), medium (105‰) and high (223‰), for Pitzer, SIT, PHREEQC-default, and CO2SYS (Table 2.2.1). Uncertainties in CO2SYS are generated by the software and include uncertainties associated with constants. PHREEQC uncertainties do not include those within the model (e.g., constants) and were calculated as the total fractional error using the equation:

$$\sum fe = \sqrt{fe_1^2 + fe_2^2 + fe_3^2 + \cdots fe_n^2}$$

Table 2.2. Uncertainties in pCO_2, CO_3^{2-} activity, and SI_{arag}/SI_{calc} modelled with PHREEQC (Pitzer, SIT and the default database) and CO2SYS, for low, medium, and high salinity surface and porewaters.

	Pitzer			**SIT and PHREEQC-default**			**CO2SYS**		
Salinity:	Low	Medium	High	Low	Medium	High	Low	Medium	High
***p*CO₂ (%)**	±0.004	±0.004	±0.134	±0.004	±0.004	±0.110	±0.002	±0.01	±913
CO_3^{2-} activity (log units)	±0.017	±0.018	±0.021	±0.017	±0.018	±0.021	±0.02	±0.02	±0.02
SI_{arag}/SI_{calc} (log units)	±0.018	±0.018	±0.021	±0.018	±0.018	±0.022	±0.03	±0.03	±0.03

Whilst variability in both aragonite and calcite saturation are important, aragonite (the less stable polymorph) is of particular interest throughout the rest of the study, and so will be the primary focus when discussing carbonate mineral SI. Additionally, porewater profiles from Yas Lagoon (Chapter 3) and Qantur Lagoon (Chapter 5) are presented to demonstrate the variability of the different models and the implication this has for interpreting the carbonate chemistry.

CO2SYS only considers the empirically determined values for seawater association constants, however there are no recommended constants when solutions exceed 43 psu (Orr *et al*., 2015). On the other hand, PHREEQC adjusts thermodynamic parameters from freshwater experiments using the ionic strength and interaction corrections and can thus be applied to a variety of water compositions (Pitzer, 1973; Millero and Pierrot, 1998). However, both SIT and Phreeqc-default were not intended for brines with salinity in excess of seawater (Hain *et al*., 2015) and Pitzer produces inaccurate results for modern seawater (Hain *et al*., 2015). The Abu Dhabi coastal waters cover a range of salinities from near-normal seawater (~35‰ ≈ 53 mS cm^{-1}) to brines (>200‰ ≈ >220 mS cm^{-1}).

Surface waters, porewaters, and groundwaters were collected using Rhizon porewater samplers, and applied *in situ* for porewater extraction (see Methods section 2.1 for details). *p*H, temperature, and specific electrical conductance (SEC) were measured using a HQ40d Hach multi-meter and probes, with accuracies of ±0.02, ±0.2 °C and ±0.05% respectively. Bicarbonate alkalinity was determined in triplicate by Gran titration (Sass and Ben-Yaakov, 1977) using 0.0005 M or 0.001 M HCl acid with 0.6% coefficient of variance (CV). Aliquots were returned to the UK where samples were gravimetrically diluted for major ion analysis. Cations (Na^+, Mg^{2+}, Ca^{2+}, K^+, Sr^{2+}) were analysed by inductively coupled plasma atomic emission spectroscopy (ICP-OES; Agilent series 710 ICP-OES) and major anions (Cl^- and SO_4^{2-}) were measured isocratically by ion chromatography (Dionex™ ICS-5000+). All measured ions had CV <2%.

Whilst SEC was measured directly, it was not possible to accurately convert SEC to practical salinity units (psu) (PSS-78, Lewis and Perkin, 1981) as the calculations are only valid for salinities <42 (~62 SEC). Other methods for converting between SEC and salinity are available (Williams, 1986), but only for conductivities <100 mS cm^{-1} owing to the non-linear relationship between SEC and salinity at high ionic strength. However, as many water samples involved in this study have conductivities over this threshold, we present salinity as total dissolved solids (TDS) in parts per thousand (‰) calculated as the sum of grams per litre of major anions (Cl^- and SO_4^{2-}), cations (Na^+, Mg^{2+}, Ca^{2+}, K^+ and Sr^{2+}) and bicarbonate alkalinity (Fig. 2.5).

2.2.4 Results

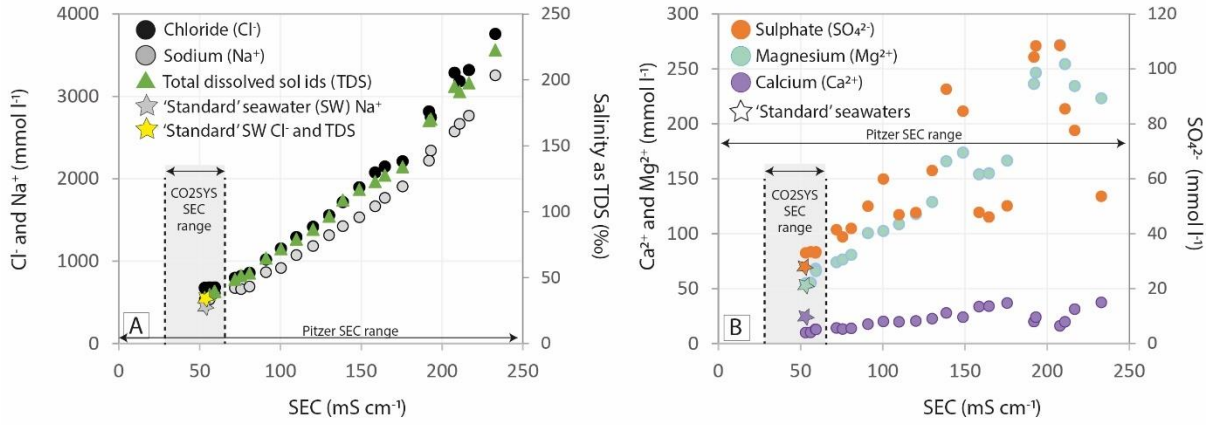

Figure 2.5. (**A**) The relationship between conservative ions Cl^- and Na^+, total dissolved solids (TDS), and specific electrical conductivity (SEC); and (**B**) the relationship between SO_4^{2-}, Mg^{2+}, and Ca^{2+} with SEC. Stars show relationships for 'standard seawater' from (Nordstrom *et al.*, 1979). Shaded area shows the range of conductivities (30-65 mS cm^{-1} ≈ 19-43 psu) for which the K_1 and K_2 constants (Lueker *et al.*, 2000) applied in CO2SYS were constructed. In theory PHREEQC can cover the entire range of salinities.

Model comparisons

The PHREEQC default database (phreeqc.dat) produced near identical results for the Abu Dhabi waters as PHREEQC-SIT, and thus only SIT results are presented in Figs. 2.6 and 2.7. Both PHREEQC databases (Pitzer and SIT) produce relatively similar aragonite saturation indices (SI_{arag}) compared to CO2SYS. However, Pitzer gives slightly lower SI_{arag} compared to the SIT database for salinities 35-72‰ (Fig. 2.6.A, B), and higher SI_{arag} for salinities ~79-222‰ (Fig. 2.6.A). In contrast, CO2SYS gives SI_{arag} ~0.11 log units higher than Pitzer and ~0.07 log units higher than SIT for salinities ≤54‰ (Fig. 2.6.A). However, at salinities >65‰, CO2SYS produces SI_{arag} lower than Pitzer, with the difference in SI_{arag} (ΔSI_{arag}) between CO2SYS and Pitzer growing with increasing salinity (Fig. 2.7.A). At the highest salinity (222‰), Pitzer provides the highest SI_{arag} (-0.37), with SIT twice as low and CO2SYS ~24 times lower (Fig. 2.6.A).

There is a large offset in the carbonate ion (CO_3^{2-}) activity between PHREEQC models and CO2SYS, with CO2SYS being systematically higher for all but the most saline sample (Fig. 2.6.C, D). For salinities between 35-135‰, CO_3^{2-} activity is ~1.70 log units higher in CO2SYS than PHREEQC databases (Fig. 2.6.C, D). The difference between CO_3^{2-} activity in CO2SYS and Pitzer (ΔCO_3^{2-}) becomes increasingly large between 35-87‰, and then remains high though decreases slightly with increasing salinity, bar the most saline sample which is slightly higher in Pitzer than in CO2SYS and SIT (Fig. 2.7.C, D).

pCO_2 was fairly similar for CO2SYS and both PHREEQC models for salinities <100‰ (Fig. 2.6.E, F), however for salinities >100‰, CO2SYS outputs for pCO_2 are significantly larger than those calculated by PHREEQC and grow increasingly large with increasing salinity (Fig. 2.6.E). For salinities <72‰, Pitzer calculates the highest pCO_2 values, followed by SIT and CO2SYS (Fig. 2.6.F). However, at 79‰, Pitzer

and CO2SYS calculate near identical pCO_2 outputs, whereas SIT was lower. At salinities >80‰, CO2SYS produces the highest pCO_2, with values increasing with increased salinity (Fig. 2.6.E, 2.7.E) and the difference between Pitzer and SIT pCO_2 outputs also increase with increasing salinity (Fig. 2.7.F). pCO_2 of the most saline porewaters and groundwaters calculated with CO2SYS were exceptionally high (90-19,000%) and cannot be reflective of real conditions.

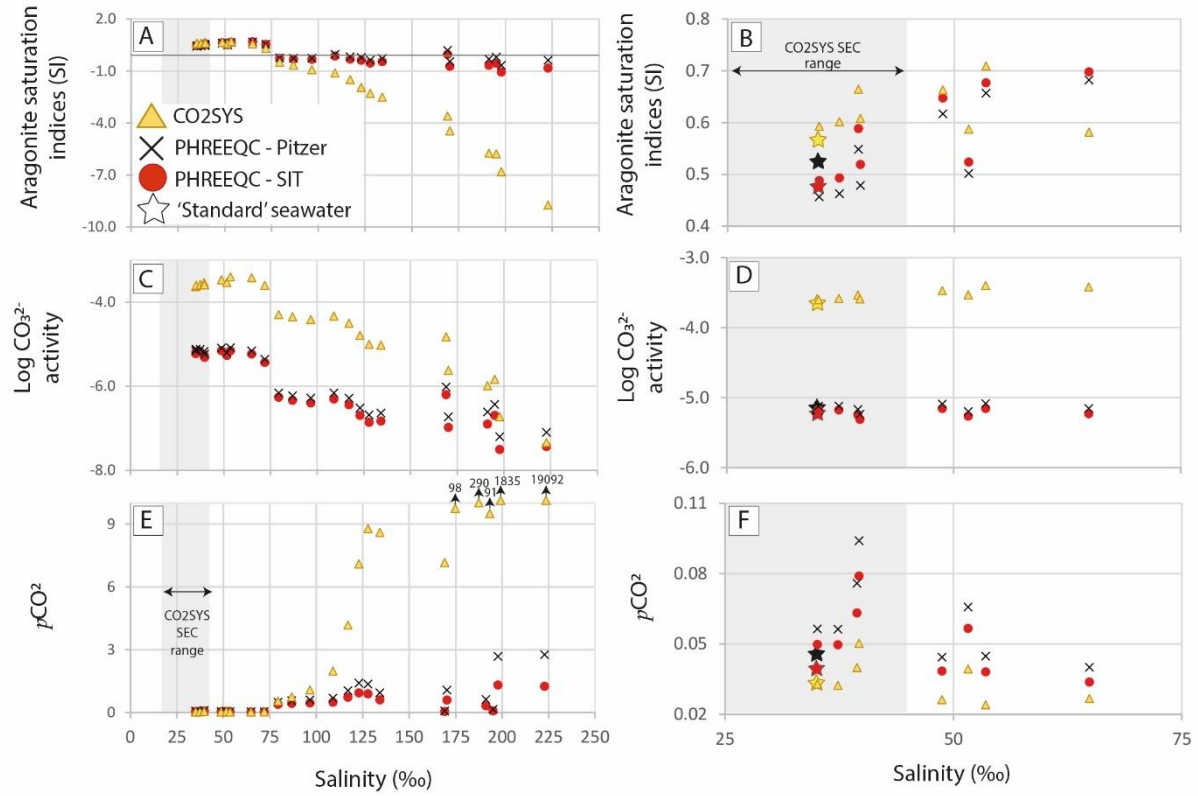

Figure 2.6. Carbonate chemistry output for seawaters, porewaters, and groundwaters of varying salinities from coastal Abu Dhabi modelled using CO2SYS (yellow triangles), PHREEQC-Pitzer model (black crosses) and PHREEQC-SIT model (red circles), for their aragonite mineral saturation indices (SI_{arag}) (log(IAP/K_{sp}) (**A** and **B**); log carbonate ion (CO_3^{2-}) activity (**C** and **D**) and partial pressure of CO_2 (pCO_2) (**E** and **F**). **A**, **C**, **E** show the full subset of data used, and **B**, **D**, **F** show a zoomed-in portion of the figures **A**, **C** and **E** for the low salinity waters (<65‰). Stars show relationships for 'standard seawater' from (Nordstrom *et al.*, 1979). Shaded area shows the range of conductivities (19-43 psu) for which the K_1 and K_2 (Lueker *et al.*, 2000) applied in CO2SYS were constructed. In theory PHREEQC can cover the entire range of salinities. For raw water chemistries see Table A, Appendix A.

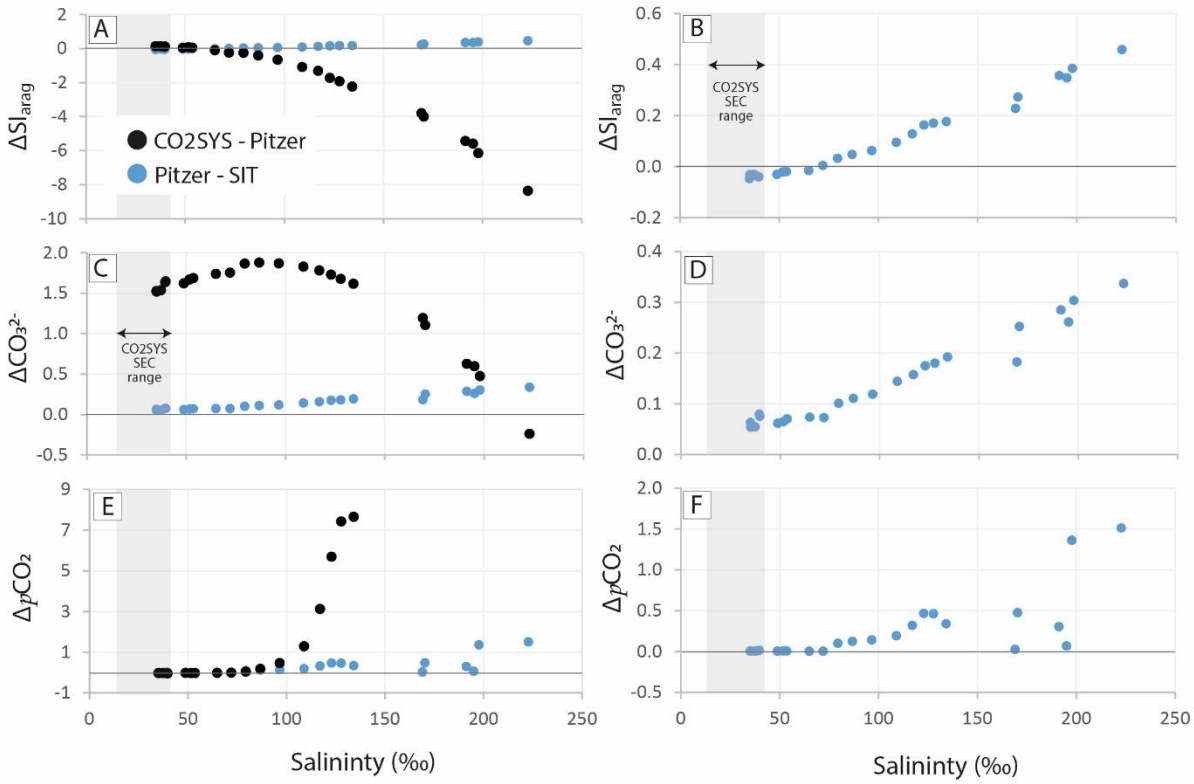

Figure 2.7. The difference (Δ) in SI_{arag}, CO_3^{2-}, and pCO_2 output between CO2SYS and Pitzer (black) and Pitzer and SIT (blue) software packages: (**A, B**) ΔSI_{arag}; (**C, D**) ΔCO_3^{2-}, and (**E, F**) ΔpCO_2. Shaded area shows the range of conductivities (19-43 psu) for which the K_1 and K_2 constants from Lueker *et al*. (2000) applied in CO2SYS were constructed. In theory PHREEQC can cover the entire range of salinities.

Variations in model output for porewater chemical profiles

In Yas Lagoon (Chapter 3), porewater salinity is relatively low (<56‰) (Fig. 2.8.A). Aragonite appears predominantly undersaturated with the PHREEQC models, with SIT more undersaturated than Pitzer. In contrast, CO2SYS produces SI_{arag} predominately at equilibrium. SIT produces calcite saturation indices (SI_{calac}) close to equilibrium, whereas Pitzer and CO2SYS produces similar results to one another suggesting calcite supersaturation. CO_3^{2-} activity is near identical in Pitzer and SIT, though CO2SYS is larger, offset by ~1.8 log units and pCO_2 is lowest in CO2SYS, followed by SIT and Pitzer (Fig. 2.8.A).

In Qantur Lagoon (Site C, Chapter 5), porewaters in the upper 6 cm are <56‰ and salinity increases with depth to peak at 28.5 cm (107‰) (Fig. 2.8.B). In the upper 6 cm CO2SYS produces higher SI_{arag} and SI_{caalc} that SIT and Pitzer, however below 6 cm Pitzer produces the highest SI_{arag} and SI_{caalc} followed by an offset with SIT and CO2SYS that increases with depth. CO_3^{2-} activity is near identical in Pitzer and SIT, though CO2SYS is larger, offset by ~1.8 log units. pCO_2 is lowest in CO2SYS compared to PHREEQC models in the upper 6 cm, though becomes increasingly larger than pCO_2 values calculated with PHREEQC with depth (Fig. 2.8.B).

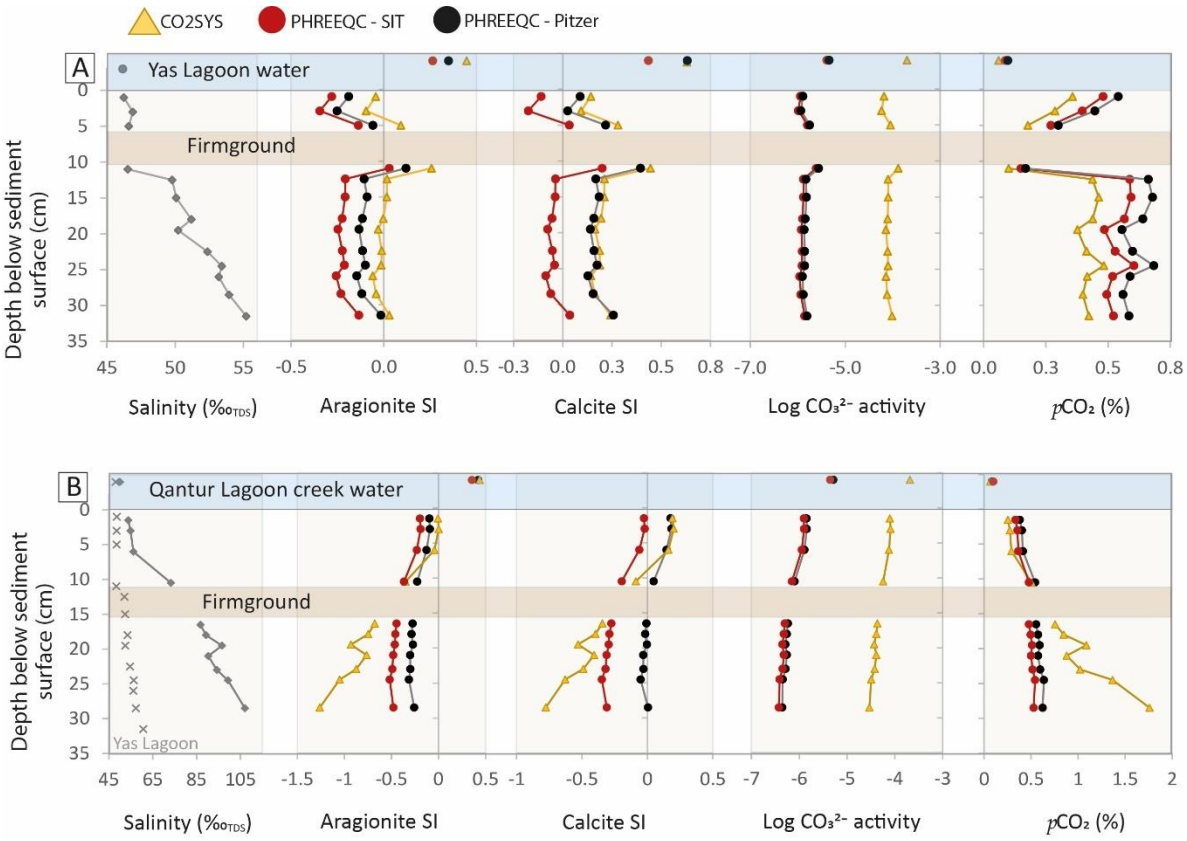

Figure 2.8. Salinity and porewater carbonate chemistry (aragonite and calcite saturation indices (SI) [log(IAP/Ksp); activity of carbonate ions (CO3-); and the partial pressure of carbon dioxide [pCO2] modelled with CO2SYS (yellow triangles); SIT (black circles) and Pitzer (red circles), for: (**A**) Yas Lagoon (Chapter 3) and (**B**) Site C from Qantur Lagoon Tidal Creek (QLTC) (Chapter 5). For raw water chemistries see Appendix B, Table B5 (Yas Lagoon) and Appendix D, Table D3 (QLTC).

2.2.5 Discussion

Pitzer versus SIT

Pitzer and SIT produce similar results for SI_{arag} (±0.05 log units) for salinities <90‰, however the two PHREEQC databases produce increasingly different results for SI_{arag}, CO_3^2 activity, and pCO_2 with increased salinity (Fig. 2.7.B). Similar results were found by Grenthe and Plyasunov (1997), who considered SIT and Pitzer to be equivalent up to 3-4 M (≈90-120‰), however our results suggest that at the upper limit of their threshold, significant differences are apparent. Sahli *et al*., (2019) found that Pitzer produced better results when computing the activities of calcium, magnesium, and sulphate than the SIT model for concentrated brine solutions, as the hydration of ions is not correctly considered in SIT. However, Sahli *et al*. also found that SIT produced better results for the activities of sodium and chloride and found both models to provide equivalent results for computing carbonate activity. However, Sahli *et al*., (2019) did not consider solutions with such high ionic strength as the Abu Dhabi coastal waters. At salinities >90‰ Pitzer produces increasingly large values for major carbonate system

parameters which is likely to be more accurate as Pitzer was designed to incorporate brines whereas SIT was not (Hain *et al*., 2015).

CO2SYS verses PHREEQC

CO2SYS calculates Abu Dhabi coastal waters to be more supersaturated with respect to aragonite than Pitzer (and SIT) resulting from higher carbonate ion activities and lower pCO_2 values calculated in CO2SYS for salinities <~56‰. There is a large, and systematic offset in CO_3^{2-} activity between PHREEQC models and CO2SYS for all but the highest salinity waters (Fig. 2.6.C), whereas pCO_2 values calculated in CO2SYS become exponentially larger for salinities >100‰.

Naviaux *et al*. (2019) found that the difference in carbonate speciation between CO2SYS and PHREEQC-default (which gave near identical results to SIT for all Abu Dhabi waters tested) had significant implications for calculating carbonate mineral SI. They found that the PHREEQC-default typically underestimated mineral SI compared to CO2SYS and so implemented several updates to the database by removing individual carbon system ion pairing reactions and calculating total HCO_3^- and CO_3^{2-} using the empirical pK values (pK is the negative logarithm of the association constant K; with pKs based on concentrations, meaning their updated version calculated concentrations of solution species, rather than activities) (Naviaux *et al*., 2019). Hain *et al*., (2015) also found that Pitzer produced inaccurate results for modern seawaters, which would suggest that CO2SYS is more reliable for the lower salinity waters from coastal Abu Dhabi. However, Naviaux *et al*. (2019) only investigated seawater-like solutions and makes no comment as to the best practice for modelling brines.

Typically, seawater speciation is calculated using a 'top down' or 'bottom up' approach (Naviaux *et al*., 2019). The 'top down' approach is used in CO2SYS, and only considers the empirically determined values for seawater association constants. This approach had been demonstrated to provide the best estimates of modern seawater chemistry but is not applicable to variable solution compositions (e.g., past ocean conditions or modern waters that deviate significantly from seawater) (Naviaux *et al*., 2019). In contrast, the 'bottom up' approach, employed in PHREEQC uses the ionic strength and interaction corrections to adjust thermodynamic parameters from freshwater experiments, and can thus be applied to a variety of water compositions (Pitzer, 1973; Millero and Pierrot, 1998). This would suggest that at relatively low salinity (<~56‰), CO2SYS provides a more accurate model for calculating SI_{arag} in the Abu Dhabi coastal waters. However, CO_3^{2-} activity calculated with CO2SYS and PHREEQC become increasingly similar with increasing salinity (Fig. 2.7.C) whilst SI_{arag} becomes increasing dissimilar (Fig. 2.7.A) suggesting calculated CO_3^{2-} activity is the not the primary driver in the differences in SI_{arag} calculated from CO2SYS versus PHREEQC. Thus, the large discrepancy in SI_{arag} is more likely related to the exceptionally high pCO_2 values calculated by CO2SYS for the most saline waters. Such non-sensical

pCO_2 values highlight that CO2SYS is not appropriate for computing thermodynamics in highly saline waters, and thus should not be applied to waters that deviate significantly from seawater.

Naviaux *et al*. (2019) applied an updated version of the MyAMI code (Hain *et al*., 2015) which uses the Pitzer equations to calculate changes in seawater association constants relative to empirically determined values (Naviaux *et al*., 2019). MyAMI was employed to calculate equilibrium constants for specific seawater compositions, which were then incorporated into CO2SYS to calculate mineral saturation state (Naviaux *et al*., 2019). Future work investigating the application of MyAMI for highly saline solutions would be valuable.

Comparison of CO2SYS and PHREEQC in Abu Dhabi porewaters

The porewater profiles (Fig. 2.8) demonstrate how the variability between models may impact interpretations of the carbonate system. In Yas Lagoon, an aragonitic firmground is thought to be actively forming at ~6-11 cm (Chapter 3). Thus, the increased degree of saturation displayed in CO2SYS is likely more accurate than the aragonite undersaturation calculated in PHREEQC. Salinity in Yas Lagoon was low (<56%) for most of the samples, and therefore supports the use of CO2SYS for samples with low salinity. In contrast the porewaters from QLTC (Chapter 5) are more saline (54-107‰), and the relationship between models is more variable. CO2SYS produces higher SI_{arag} and SI_{caalc} estimates for salinities 54-56‰ (1.5-6.0 cm depth), however below 6 cm, differences between CO2SYS and PHREEQC increase with salinity (and thus depth), as CO2SYS produces increasingly negative SI_{arag} and SI_{caalc} values. In contrast, below the firmground at QLTC (Chapter 5) Pitzer produces porewater SI_{caalc} estimates around equilibrium. This supports sedimentary evidence that suggests transformations of aragonite to calcite below the firmground, and thus suggests Pitzer is more appropriate for modelling highly saline solutions (>56‰).

2.2.6 Conclusions

Porewaters and brines involved in this study have complicated chemical compositions, thus the current Pitzer model may not have enough parameters to account for all ion-interactions within it. This may have particularly significant implications for ions found in low concentration such as CO_3^{2-}; which directly relates to the SI_{arag}. CO2SYS is more able to accurately calculate carbonate speciation than PHREEQC for seawater-like solutions, and thus throughout this project, for open seawaters, surface waters, and porewater profiles where salinity is ≤56‰, CO2SYS will be applied to calculate the carbonate mineral SI, CO_3^2 activity, and pCO_2.

However, the K_1 and K_2 constants employed in CO2SYS are not recommended for salinity >43 psu and our results suggest that the benefits of CO2SYS over PHREEQC may only be suitable for salinities ≤56‰. Above this threshold the application of CO2SYS is limited and becomes increasingly erroneous with

increasing salinity. Thus, for Abu Dhabi coastal waters with salinity is >56‰, PHREEQC-Pitzer will be used.

This analysis highlights the limitations of applying the most common thermodynamic models to waters that deviate significantly from modern seawater compositions. Future work investigating the application of MyAMI (Hain *et al*., 2015) to calculating the equilibrium constants for brines would be a valuable next step, though further amendments (*sensu* Naviaux *et al*., 2019) may need to be implemented to account for the complexity of modelling brine geochemistry.

3. Biogeochemical drivers of modern subsurface carbonate firmground formation: Yas Lagoon: Abu Dhabi

i. Authors

Hazel Vallack[1], Sarah E. Greene[2], Emily N. Junkins[3], Stephen W. Lokier[4], Chelsea L. Pederson[5]; Victoria A. Petryshyn[6], Bradley S. Stevenson[3], Fiona Whitaker[7]

1: School of Geographical Sciences, University of Bristol

2: School of Geography, Earth and Environmental Sciences, University of Birmingham

3: Department of Microbiology and Plant Biology, University of Oklahoma

4: School of Ocean Sciences, Bangor University

5: Institute for Geology, Mineralogy and Geophysics, Ruhr-Universität, Bochum

6: Environmental Studies Program, University of Southern California, Los Angeles

7: School of Earth Sciences, University of Bristol

ii. Author contributions

Porewater chemical analysis, grain size analysis, scanning electron analysis (SEM), microscopy, data analysis, writing, and interpretation were conducted by H. Vallack with interpretive support from S. Greene, F. Whitaker, and V. Petryshyn. DNA extraction and analysis were performed by E. Junkins and B. Stevenson, and interpretation and analysis of the data by H. Vallack. Cement mineralogy was determined *via* electron backscattered diffraction (EBSD), performed by C. Pederson. Field work was conducted by H. Vallack, S. Greene, S. Lokier, F. Whitaker, with support from Prasanth Thiyagarajan.

iii. Abstract

Authigenic carbonates are common early-diagenetic features of sedimentary rocks and have been linked directly to the global carbon, sulphur, and iron cycles. However, physical, chemical, and biological drivers of authigenic carbonate formation remain contentious. This study presents the first comprehensive analysis of biologically-influenced aragonite mineralisation resulting in subsurface firmground formation within the sediment column in a shallow coastal lagoon in Abu Dhabi. Physical and chemical characteristics of shallow sediment cores and firmground samples, corresponding porewater chemistry, and microbial community composition (*via* 16S SSU rRNA gene sequencing) were analysed to achieve a mechanistic understanding of the drivers of firmground formation. Most porewaters were supersaturated with respect to calcite and at equilibrium with respect to aragonite, however, immediately below the firmground, increased saturation indices occurred in a narrow (<2 cm) interval of elevated porewater *p*H and low bicarbonate alkalinity. Porewaters above the firmground were oxic, whilst those below showed sulphate depletion and an abundance of archaeal Marine Benthic Group D (*Thermoprofundales*) in association with known sulphate-reducing bacteria

and rare archaeal taxa in the few cm below the firmground. These groups are likely involved in sulphate reduction which, in conjunction with pyrite formation, could drive aragonite supersaturation. Additionally, Fe/Mn-oxide reduction may drive increased pH and precipitation of carbonate cements to form the firmground. These findings have implications for interpreting the role of biological processes in hardground formation in the geologic record. Additionally, these results help unravel the complex role microbes play in biogeochemical cycles within the coastal marine subsurface environment and provide constraints for reactive transport models of early diagenesis.

3.1 Introduction

Authigenic carbonates occur throughout the geological record with a range of morphologies and sizes and are suggested to form *in situ* within the top few metres of sediment during early diagenesis (Sun and Turchyn, 2014; Plet *et al*., 2016). Authigenic carbonates can form laterally-extensive layers as firmgrounds and hardgrounds, or have spheroid morphologies forming concretions and nodules, and have been linked to the carbon, sulphur, and iron cycles (Coleman, 1993; Marshall and Pirrie, 2013). This study focuses on the formation of marine firmgrounds and hardgrounds, though terminology in the literature can be inconsistent (see discussion in Christ *et al*., 2015 and Ge *et al*., 2020a). We follow the definition of 'concretionary sub-hardgrounds' of Ge *et al*. (2020a) and refer to partially-lithified (incipient sub-hardgrounds) as firmgrounds.

An estimated 10% of global modern marine carbonate deposits are precipitated authigenically (Sun and Turchyn, 2014). In the past, authigenic carbonate deposits played an even larger role in the global carbon cycle, particularly during periods of widespread marine anoxia (Higgins *et al*., 2009) when they would have been a substantial carbon sink (Schrag *et al*., 2013). Carbonate concretions also preserve a host-sediment signal and can provide insight into palaeoenvironmental conditions *via* geochemical analysis (Plet *et al*., 2016).

Environmental drivers that can influence precipitation include temperature, salinity, sedimentation rate, dissolved species (e.g., carbonate ion activity (CO_3^{2-}), pH (H^+), and Mg/Ca ratio), redox conditions, sediment characteristics, macro- and microbiology, and the quantity and reactivity of organic matter (OM). The breakdown of OM in the sediment column is the engine behind microbial respiratory pathways, the by-products of which (e.g. CO_2) can alter chemical conditions and promote carbonate dissolution or precipitation (Bergmann *et al*., 2013; Soetaert *et al*., 2007). A hiatus in sedimentation (Lash and Blood, 2004) or reduction in sediment remobilisation associated with low energy conditions (Shinn, 1969) are also suggested as mechanisms maintaining the zone of carbonate precipitation at a constant depth below the sediment surface long enough to permit cementation. Cementation can also impact the downward diffusion of ions from overlying seawaters, with the lower limit of cementation reached when pore throats become occluded and permeability is reduced, a process also affected by

grain size and sorting (Shinn, 1969). Hillgärtner (1998) describes discontinuity surfaces within an ancient shallow-marine carbonate platform including inter- to supra-tidal hardgrounds resulting from rapid and substantial environmental changes in relative sea level, accumulation rate, energy regime and sediment type.

Despite the extensive study of hardgrounds like those in Abu Dhabi, the physical, biological, and chemical processes and interactions that facilitate their precipitation remain poorly understood (Christ *et al*., 2015; Paul and Lokier, 2017). Since the seminal papers of the late 1960s describing submarine lithification of Holocene carbonate sediments in the Gulf (e.g., Evans *et al*., 1964; Shinn, 1969), there has been a step-change in both our understanding of biogeochemical processes that may drive changes in the carbonate system, and in the toolbox of techniques that can be employed to unravel these processes. Studies focused on geochemical and textural evidence have investigated ancient authigenic carbonates (e.g. Lash and Blood, 2004), however these are likely impacted by significant diagenetic overprinting, making it difficult to identify the primary drivers for firm/hardground formation. Christ *et al*. (2015) aimed to synthesize geochemical and textural evidence of hardgrounds using a process-based framework to assess environmental controls on the petrography, mineralogy, and geochemistry of carbonate hardgrounds from the Phanerozoic. They concluded that environmental controls on hardground formation are variable and complex, but generally hardgrounds are most prevalent in tropical/sub-tropical shallow-water environments, with their formation driven by bottom water carbonate supersaturation and seawater circulation. In contrast, more rare authigenic carbonates forming in non-tropical settings are more likely to be driven by anaerobic oxidation of methane (AOM), while deep-water hardgrounds are likely linked to hiatuses in sedimentation and current-driven circulation (Christ *et al*., 2015).

A second body of literature takes a mechanistic approach to precipitation of layered marine carbonates from a biogeochemical perspective. These studies address issues of meta-stable carbonate phases (Drupp *et al*., 2016), microbially-mediated stromatolite formation (Reid *et al*., 2000; Petryshyn *et al*, 2012), and carbonate precipitation in microbial mats (Dupraz *et al*., 2009). Specific attention is paid to the formation of authigenic firm/hardgrounds and concretions in relation to microbial respiratory processes (Greene *et al*., 2012; Loyd and Berelson, 2016; Plet *et al*., 2016), however these are often in deep-sea localities. Few process-based studies exist of modern aragonitic cemented firm/hardgrounds (Ge *et al*., 2020a), and any assessment of microbial drivers is often limited.

This interdisciplinary study targets two significant knowledge gaps: (i) there is a need for process-based assessments of factors affecting marine sediment lithification prior to any diagenetic overprinting (Christ *et al*., 2015), and (ii) whilst microbes are often implicated in descriptions of early diagenesis, few studies have investigated the role of microbes in the formation of shallow marine

firm/hardgrounds. This study presents the first comprehensive description and analysis of shallow marine microbially-influenced aragonite firmground formation. We analysed the sediment and firmground physical and chemical characteristics, the porewater chemistry, and the sedimentary microbial community composition in a coastal lagoon in Abu Dhabi, UAE. In defining possible drivers of firmground formation, this work provides a starting point from which to investigate local, regional and global controls on modern firmground formation, and aids in interpretation of these features in the geologic record.

3.2 Depositional setting of the study area

The southern shore of the Arabian Gulf represents a rare recent analogue for ancient low-angle carbonate-evaporate ramp systems (Lokier and Fiorini, 2016). The shallow Gulf (maximum depth ~35 m) has high salinity (45-46‰) (Lokier and Steuber, 2009) owing to high evaporation and relative restriction (and, locally, the discharge from desalinisation plants, Hashim and Hajjaj, 2005).

Diurnal variations in air temperature are 2-26 °C and summer daytime temperatures exceed 50 °C, while winter nights reach lows of 7 °C (Lokier and Fiorini, 2016). The area is arid, with a mean monthly rainfall of up to 15.4 mm (Abu Dhabi airport, 1982–2019), falling during rare high-intensity events, typically between February and March (Raafat, 2007). Average monthly rainfall is <0.2 mm (May to October) and relative humidity ranges from 75% in winter to 93% in summer months (Abu Dhabi airport, 2003–2019, National Centre of Meteorology, UAE, 2020). Solar insolation is high, but evaporation is limited by the humidity (Lokier and Steuber, 2009), with a potential mean annual evaporation of 2.75 m (Bottomley, 1996).

The study site is located ~15 km east of Abu Dhabi Island (Fig. 3.1A, B), within the intertidal zone of a semi-restricted inner lagoon with mangrove forest (*Avicennia marina*) along the northern limit (Fig. 3.1C). The area experiences semi-diurnal tides of 1-2 m amplitude (Paul and Lokier, 2017). A network of tidal channels dissects the lagoon and island complex, some of which have been dredged, increasing the connectivity and exchange of water between the Gulf and the previously restricted lagoons. Dredged channels near the study sites reveal a 7-12 cm thick older hardground, which likely extends beneath our site at a depth of 1-2 m and is thought to correspond to an extensive hardground described by Paul and Lokier (2017) ~65 km SW of our study site that formed during the marine transgression ~4.6-1.5 kya BP.

Within the lower intertidal sediments, a number of surfaces occur at shallow depth (10's of cm below the sediment surface) displaying a variety of morphologies from firm/hardgrounds to beach-rock and other concretionary features (Ge *et al*., 2020a). Radiocarbon ages of gastropod and bivalve shells

cemented within the hardground suggest lithification initiated in the Holocene (<268 yBP) and that lithification is still active (Lokier and Steuber, 2009; Ge *et al*., 2020a).

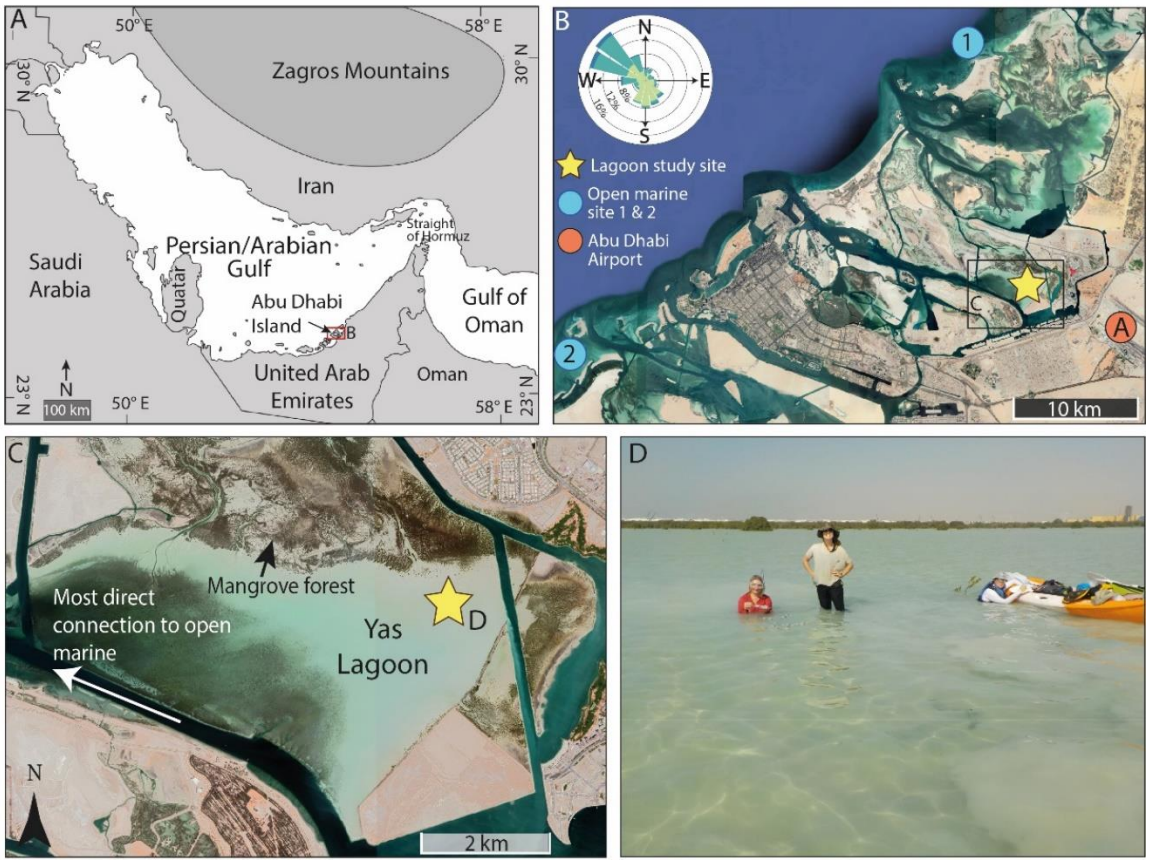

Figure 3.1. (**A**) Study area on southern shore of the Gulf, adapted from Lokier *et al*. (2013). (**B**) Satellite image of coastal Abu Dhabi showing location of the Yas lagoon study site (star), two offshore 'open marine' sites (1 and 2) and meteorological station (with rain gauge) at Abu Dhabi Airport (A). Wind rose (pale green <4 m/s, dark green 4-10 m/s and blue 10-14 m/s), numbered rings represent frequency (%), adapted from Paul *et al*. (2021). (**C**) Yas lagoon field site (star). (**D**) Field photograph at water depth ~40 cm. Satellite images (B and C) obtained 31/03/2020 by © Maxal Technologies 2020.

3.3 Methods

3.3.1 Sampling and characterisation of cores, sediments, and firmgrounds

Three adjacent sediment cores (A, B, and C) of 40-60 cm length, firmground specimens, and *in situ* porewater samples were collected within an area of 1 m^2 in October 2017 (depths reported below sediment surface). Cores were stored upright, with all samples kept in the dark at 4°C prior to subsampling. Cores A and B were split longitudinally and subsampled under sterile conditions for grain size analysis, X-ray diffraction (XRD), scanning electron microscope (SEM), thin section preparation, OM content, and SSU rRNA gene identification. Core A (42 cm) was subsampled <24 hours from collection for grainsize analysis (n=18), and rRNA (n=23), while rRNA samples were taken from Core B (32 cm) <3 days after collection (n=16). Comparison with hand samples showed that, although manual

coring penetrated the firmground at ~5-11 cm depth, this led to some co-mingling of fragmented firmground with unconsolidated sediments immediately above and below the firmground. For subsamples of grainsize and rRNA, where these elements cannot be separated, this is referred to as the 'firmground zone'. Grainsize was determined using a Malvern Mastersizer 2000 particle size analyser following the method described by Lokier *et al*. (2013) after wet sieving the >1 mm grain size fraction. Thin sections of unconsolidated sediment (n=9) and firmground specimens (n=1) were impregnated with blue epoxy resin, and half stained with Alizarin Red S to differentiate calcite/aragonite from dolomite.

Sediments (Cores A and B) and firmground samples were examined using standard light microscopy with a polarizing microscope and a FEI Phillips Quanta 200 MK2 SEM. For SEM analysis, firmgrounds were freshly broken and rinsed with deionised water to dissolve any halite precipitated after sampling, then coated with a gold-palladium mixture. SEM Energy-dispersive X-ray spectroscopy (EDS) provided a semi-quantitative insight into mineralogy. Crystallographic orientation for a central part of a firmground specimen from Core A (Fig. 3.2G) was determined on a thin section with a 10 nm carbon coating using electron backscattered diffraction (EBSD; Nordlys detector by OXFORD Instruments) following the methods of Pederson *et al*. (2020). The field-emission scanning electron microscope (FESEM, Merlin Gemini II by ZEISS) was operated in high-resolution mode, with a beam energy of 20 kV, a sample current of 164 pA, a working distance of 25.3 mm, and a tilt angle of 70°. The data was collected and analyzed using the software packages AZtec and Channel 5 (Oxford Instruments). Identified Kicuchi patterns were used to create carbonate mineralogy maps of the peloid grains and encasing cements. The maps were generated with a step size of 2.83 μm.

Core B was sub-sampled at 2 cm resolution for bulk $\delta^{13}C$ and $\delta^{18}O$ analysis (n=18), using ~120 μg of sample powder using a Gasbench II equipped with a GC autosampler and coupled to a ThermoFinnigan MAT253 mass spectrometer (Thermo Fischer Scientific) following the methods of Pederson *et al*. (2019b). $\delta^{13}C$ and $\delta^{18}O$ values are presented in per mil (‰) relative to the Vienna Pee Dee Belemnite (VPDB) standard, with an average standard error of ±0.02‰ and ±0.07‰ respectively. From Core A, total carbon (TC) (n=17) and total nitrogen (TN) (n=17) were measured on untreated homogenised aliquots and total organic carbon (TOC) (n=17) on decarbonated aliquots following Yamamuro and Kayanne, (1995). Samples were run in duplicate on a Thermo Scientific FlashSmart Elemental Analyser, with a relative analytical precision (CV) of 0.16%, 3.90%, and 1.75% respectively.

3.3.2 Porewater sampling and analysis

Porewater samples were collected at 1.5-3 cm vertical resolution, up to 31.5 cm sediment depth (n=15). Samples were extracted and filtered using 5 cm long Rhizon CSS pore-water samplers (pore diameter 0.12-0.18 μm) following a method adapted from Dickens *et al.* (2007) and applied *in situ*. Lithification

prevented insertion of Rhizons within the firmground (~6-10 cm depth). Surface samples of open marine and lagoon water (Fig. 1) were also collected with Rhizons, and bottom waters at open marine sites (~5.5 m in 6 m water depth) were sampled using a Van Dorn horizontal open water sampler, stored in glass bottles and filtered through Rhizons within 6 hours of collection.

Porewater pH, specific electric conductivity (SEC) and redox potential (Eh) were measured within 6 hours of collection using a HQ40d Hach multi-meter and probes, with accuracies of ±0.02, ±0.5%, and ±0.05% respectively. Bicarbonate alkalinity was determined in triplicate by Gran titration (Sass and Ben-Yaakov, 1977) using 0.0005 M or 0.001 M HCl acid with 0.6% CV. Aliquots were returned to the UK where samples were gravimetrically diluted for major ion analysis. Cations (Na^+, Mg^{2+}, Ca^{2+}, K^+, Sr^{2+}, and total dissolved Fe and Mn) were analysed by inductively coupled plasma atomic emission spectroscopy (ICP-OES; Agilent series 710 ICP-OES). Major anions (Cl^- and SO_4^{2-}) were measured isocratically by ion chromatography (Dionex™ ICS-5000+). Ion analyses had <1.25% CV based on multiple injections, except for Mn^{2+} (9% CV) which was present at concentrations <0.7 µmol. Fe and Mn were only analysed for the upper 12.5 cm. Phosphate (PO_4^{3-}) and ammonium (NH^{4+}) were analysed photometrically on a Gallery Plus Discrete Analyzer with <5% CV. The ion balance error (IBE) was -5.9 ±0.4% (n=17). Partial pressure of CO_2 (pCO_2), CO_3^{2-} activity, and saturation indices ($\log(IAP/K_{sp})$) of aragonite and calcite (SI_{arag} and SI_{calc}) were calculated using CO2SYS (Pelletier *et al*., 2007) (see methods discussion in Chapter 2.2). Uncertainties in pCO_2, CO_3^{2-} activity, SI_{arag}/ SI_{calc} were 0.002%, ±0.02 log units, and ±0.03 log units respectively. The concentration of major ions largely varies as a function of salinity, thus molar ratios are plotted using sodium (Na^+) as a conservative tracer for evaporation and/or mixing between surface seawater and continental groundwater endmembers. Raw concentrations of major ions are provided in Appendix B, Supplementary Tables B4 and B5.

Porewater total dissolved organic carbon (DOC) (1.8% CV) was analysed using a Shimadzu TOC-L Total Organic Carbon analyser, with simultaneous total determination of nitrogen (TN) *via* Kemi-luminescence using a non-infrared detector (TN: 0.40% CV). Headspace CH_4 concentration was analysed using the Carlo Erba HRGC5300 gas chromatograph (GC) following the method of Hornibrook and Bowes (2007) and calibrated against speciality gas standards (BOC, Guildford, UK) with CV mostly <2% based on multiple injections. Because of possible gas leakage during analysis, values are only considered minima and are reported as negligible when CH_4 was <1.6 ppm.

3.3.3 DNA analysis of microbes

Microbial community composition was inferred *via* 16S SSU rRNA (small subunit ribosomal ribonucleic acid) amplification and sequencing. SSU rRNA is the smaller of the two major RNA components within the ribosome. The 16S rRNA gene encodes the small subunit ribosomal RNA molecules of ribosomes, which convert genetic messages to functional cell components by translating messenger RNA (mRNA)

to proteins (Byrne et al., 2018). The 16S rRNA gene thus serves as molecular target for methods exploring microbial community membership and acts as a proxy for bacterial and archaeal communities. However, the identification of 16S rRNA genes does not provide evidence of active community structure.

To determine microbial community composition *via* 16S SSU rRNA amplification and sequencing, cores were sampled at 2 cm intervals in Core A (n=23), and at 2 cm intervals in triplicate in Core B (n=16). The firmground specimen was sampled 1, 3 and 5 cm from the upper surface (Fig. 3.2F). Approximately 0.25-0.50 mg of sediment was collected from the most pristine centre of the core, transferred to a DNA/RNA Shield Lysis Tube (Zymo Research) containing 1 mL of DNA/RNA Shield and ultra-high density BashingBeads (0.5 mm and 0.1 mm) for homogenization. These were shaken vigorously for one minute and stored at ambient temperature until received in the lab. Samples were stored at -20 °C until used, thawed and homogenized again for 45 s using a BeadBeater-8 (BioSpec Products Inc., Bartlesville, OK) at the maximum rate. Total DNA and RNA from each sample was then extract and purified according to manufacturer's protocol (Zymo *Quick*-DNA Miniprep kit; Zymo Research). The following methods were previously described by Junkins and Stevenson, (2020).

A conserved region of the SSU rRNA gene of most Bacteria, Archaea, and Eukarya was amplified using primers 515F-Y and 926R (Parada *et al*., 2016) *via* the following PCR protocol: initial denaturation at 94˚C for 2 min, followed by 30 cycles of denaturation at 94˚C for 45 s, annealing at 50˚C for 45 s, and extension at 68˚C for 90 s, with a final extension at 68˚C for 5 min. These primers produced two amplicons, a ~400 bp fragment for bacteria and archaea, and a 600 bp fragment for eukaryotes. The forward primer 515F-Y (5'-GTA AAA CGA CGG CCA G CCG TGY CAG CMG CCG CGG TAA-3') contains the M13 tag (underlined) fused to the 5' end of the forward primer (Kraus *et al*., 2018). The reverse primer 926R (5'-CCG YCA ATT YMT TTR AGT TT-3') was unmodified from Parada *et al*. (2016). Each PCR contained 5 PRIME HOT master mix (1X; 5 PRIME Inc., Gaithersburg, MD), 0.2 µM of each primer, and 3.0 µL of extracted DNA at a final volume of 50 µL. The amplified fragments were purified using Sera-Mag magnetic beads (GE) with the AmPureXP (Beckman Coulter) protocol at a final concentration of 1.8x v/v. After purification, 3 µL of each PCR product, 1x 5 PRIME HOT master mix (Quantabio, Massachusetts, USA), 0.2µM of the 926R primer, and 0.2 µM of a specific 12 bp oligonucleotide was used in a separate barcoding PCR (6 cycles) in 50 µL reactions to attach a unique barcode to amplicons of each library. The same thermocycler protocol was used as above but only run for 6 cycles. The now barcoded amplicons were purified using Sera-Mag (GE) beads with the AmPureXP (Beckman Coulter) protocol to a final volume of 40 µL, quantified using the QuBit HS DS DNA assay kit (Thermo Fisher Scientific Inc., Waltham, MA), and pooled in equimolar amounts. The pooled, barcoded amplicon libraries were then concentrated to a final volume of 40 µL (209 ng/ µL) with an Amicon-Ultra filter (Millipore, Burlington, MA, USA) following manufacturer's protocol. The combined amplicon libraries

were denatured according to Miseq library preparations protocol (Illumina, San Diego, CA, USA). The sample was loaded at a concentration of 10 pM and sequenced using 2x250 paired-end strategy on the Miseq (Illumina San Diego, CA, USA) platform for 251 cycles.

Resulting sequences were trimmed and merged using PEAR v 0.9.5 (Zhang *et al*., 2014). Barcodes from merged SSU rRNA amplicon sequences were removed and sequences were demultiplexed using QIIME v 1.9.1 (Caporaso *et al*., 2010). Demultiplexed reads were quality filtered (MaxEE=1) and clustered into OTUs using the UPARSE algorithm (Edgar, 2013) in USEARCH v 8.1 (Edgar, 2010). Chimeras were removed via USEARCH and the Gold database (Edgar, 2010). Taxonomy was assigned using the UCLUST algorithm (Edgar, 2010) and SILVA v 123 database (Quast *et al*., 2013; Yilmaz *et al*., 2014). The final dataset included a total of over 950,000 reads with an average of 14,000 reads per sample (±3200 reads).

3.3.4 Data availability

Sequence data has been deposited at NCBI's Sequence Read Archive (SRA) database under accession number PRJNA684433.

3.4 Results

3.4.1 Sedimentology

3.4.1.1 Sediment and firmground physical characteristics

Through much of the profile, sediment was dominated by very fine to medium sand-sized (20-65 wt%) and silt-sized (20-50 wt%) grains, with typically <5% clay-sized grains and variable amounts of coarse sand grains and components >2 mm (Fig. S1). The high proportion (38 wt%) of the >2 mm fraction at the base of the profile (46-42 cm) reflected a gastropod-rich bioclastic layer. Sediments fined upwards from the base of the core to 32 cm depth, above which there was a more subtle coarsening upward to the base of the firmground (11 cm depth). The >2 mm fraction increased from 5 wt% at 15 cm to 39% at 12-8 cm reflecting associated cementation. Above the firmground (≤5 cm) the sediment was predominantly (60–65 wt%) very fine to medium sand and pervasively bioturbated.

Aside from the basal gastropod layer, the sediment dominantly consisted of peloids (80-90%), with subsidiary ooids (5-10%), bioclasts (2-8%) and quartz (3-6 %). Peloids were 120–320 µm in length, and 70–240 µm in width, and often pervasively bored. Ooids (90–230 µm diameter) exhibited 5–20 µm thick micritised rims (e.g. Fig. 3.2E). The biogenic component consisted of complete smaller bioclasts, dominantly benthic foraminifera (e.g. *Quinqueloculina* and *Trochammina)* and ostracods, and larger complete and fragmented bioclasts including gastropods and fragments of bivalves and rare bryozoans.

Whilst individual clast size and composition varied slightly throughout the profile, the degree of cementation varied markedly. Thin sections showed cement rims surrounding grains with an average thickness of 10–30 μm within the firmground and <22 μm in unconsolidated sediment, but no obvious trend with depth (Fig. 3.2 and 3.3). EBSD identified firmground cements as aragonite (Fig. 3.2K and L). Qualitative EDS data suggested microscystalline cements coating unconsolidated sediments immediately above (e.g. 0-2 cm, Fig. 3.2B, C and D) and below (e.g. at 20-22 cm Fig. 3.2N, O and P) the firmground contain 1.1-7.5 wt% Mg^{2+}, whilst the platy firmground cements contained no detectable Mg^{2+}.

In the shallowest 2 cm, some peloid borings were fringed by microcrystalline equant crystals. The rare (<5%) composite grains were cemented with an equigranular microcrystalline aggregate which consists of randomly orientated acicular crystals (3.49 wt% Mg^{2+}) with pointed terminations and lengths <4 μm (Fig. 3.2C), and small amounts of rhombic crystals (length 2 μm, 7.50 wt% Mg^{2+}) (Fig. 3.2D). Carbonate grains were surrounded by a thin (0-10 μm), locally intermittent layer of isopachous microcrystalline cement. Cement type changed at 4-6 cm depth, with more abundant cemented aggregate clusters of ~4 grains surrounded by microcrystalline cement (1.43 wt% Mg^{2+}) and, more rarely, slightly thicker (5-22 μm) rims of isopachous bladed crystals (Fig. 3.2E).

The 6 cm thick firmground (5–11 cm depth) was semi-lithified, dominated by the same fine sand that comprised overlying and underlying sediment, and lacked sedimentary structures. The upper surface of the firmground was planar and cementation declined gradually towards the base, which was more irregular than the upper surface (Fig. 3.2F). The firmground contained localised dark patches (~2 cm) (Fig. 2G) that could be anoxic, and iron-stained borings ~3 mm in diameter (Fig. 3.2F). Grains were typically surrounded by a relatively thin (10-30 μm) isopachous fringe of small rectangular well-defined aragonite platy crystals with an average individual crystal length of 5–10 μm (Fig 3.2. H - I). Pyrite framboids (~10 μm) were fairly common. (Fig. S3.E). Rare hexagonal crystals were also observed (9.4 wt% Mg^{2+} *via* EDS) (Fig. S3.H), as well as larger (~30 μm) radial crystal bundles (Fig. S3.D). Most grains demonstrated a high degree of neomorphism and micritisation. Acicular and fibrous crystals predominantly occurred in the most restricted inter- and intra-granular pore space and were rarer in larger, better-connected pores within the firmground, with lower abundance in the overlying and underlying sediments.

The degree of sediment cementation was found to generally increase with depth. Unconsolidated sediments beneath the firmground (at 12-14 cm) showed a higher degree of neomorphism (destructive micritic envelops) and cementation (constructive micritic envelopes) than those overlying the firmground (4-6 cm) (Fig. 3.3). The sediments below the firmground had a relatively thin (6-20 μm) isopachous fringe of microcrystalline crystals, with rare acicular crystals in inter-granular pore spaces.

Micritisation was also slightly greater compared to just above the firmground (~30% of grains cemented together below *versus* ~15% above). From 22-24 cm, 60% of the grains were cemented together, forming aggregates typically 250-500 µm in diameter, comprising ~15–25 grains (Fig. 3.3). Microcrystalline cements resembled those above the firmground, with predominantly acicular crystals <4 µm (Fig. 3.2N, O and P). At 44-47 cm, the aggregates were larger (400–2000 µm), typically comprising 10–30+ grains, with micritised rims similar to those at 22–24 cm.

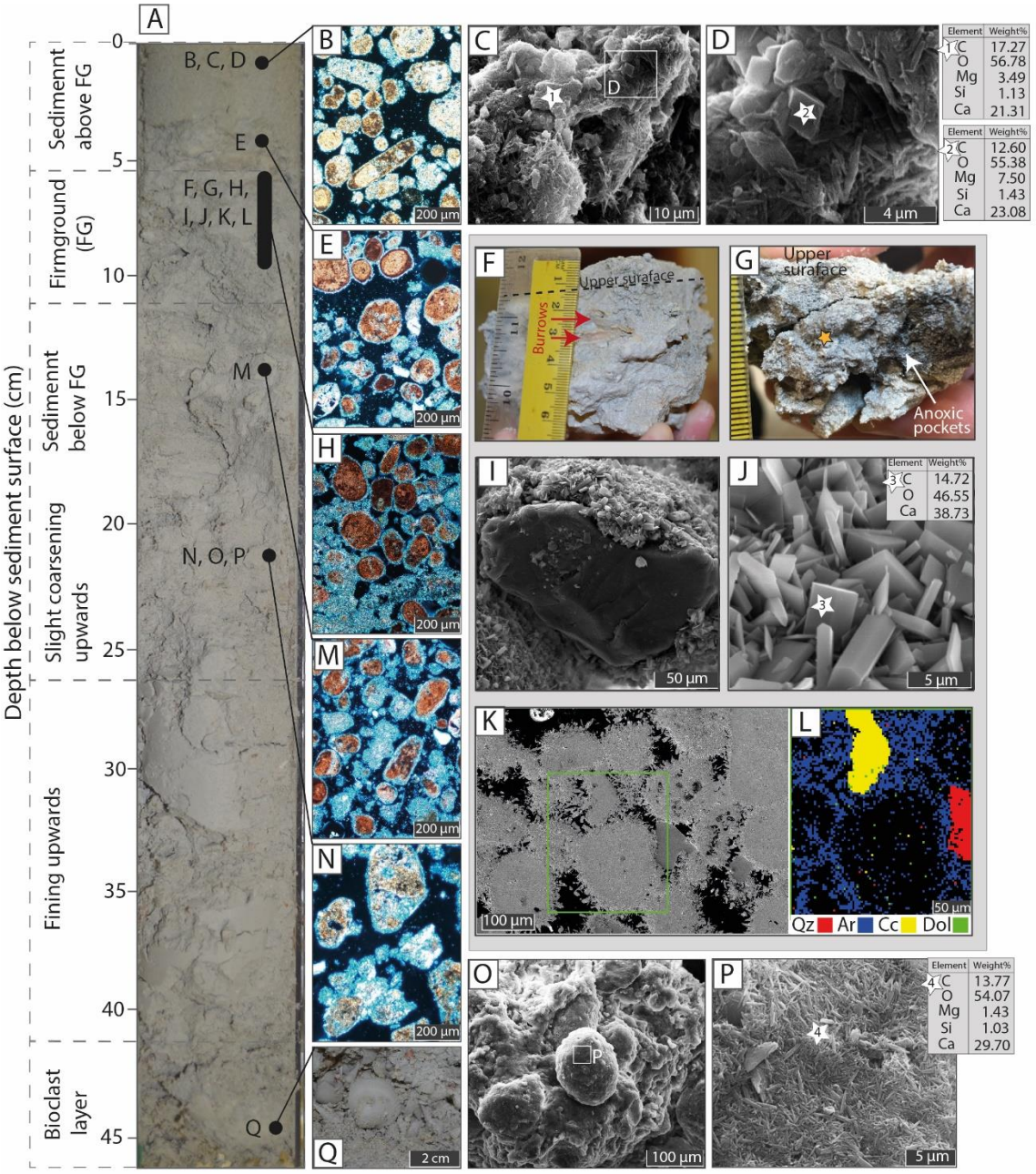

Figure 3.2. (**A**) Photograph of Core A. This section photomicrographs (**B**, **E, H**, **M** and **N**) taken in cross polarised light. All are unconsolidated sediment samples, except for **H** (firmground hand specimen) where porosity is black. Images illustrate 1) increased crystal rim thickness in and around the firmground; 2) increased percentage of grains in clusters downcore; 3) increased neomorphism downcore. SEM images **C** and close-up **D** show micritic cements at 0-2 cm, containing Mg^{2+} (EDS results

from the white stars displayed in Tables 1 and 2); (**F**) Hand specimen showing full thickness of firmground (typically 4-6 cm) with iron-stained burrows (red arrows) and sites sampled for 16S-rRNA (yellow stars); (**G**) upper 3 cm of firmground from Core A with the lower, most poorly lithified 1-2 cm disaggregated and missing, location of EBSD mineralogy map (star), and localised dark anoxic pockets (white arrow). **I** and **J** show SEM images of firmground sample (from Core A) dominated by well-defined platy cements with less common acicular/fibrous needles at random orientation (no detectable Mg^{2+} in EDS - Table 3). **K** shows the SEM image of the firmground from the centre of Core A (star in Fig. 2G) used to produce the mineralogy map (**L**) ***via*** EBSD, showing platy cements of aragonite (blue), calcite (yellow), quartz (red) and minor dolomite (green). SEM images **O** and **P** from 21 cm show the typical micritic cements covering unconsolidated sediments below the firmground, with EDS data (star and Table 4); (**Q**) Photograph of coarse grained bioclastic layer at base of core dominated by gastropods and bivalves at 44 cm (Core A).

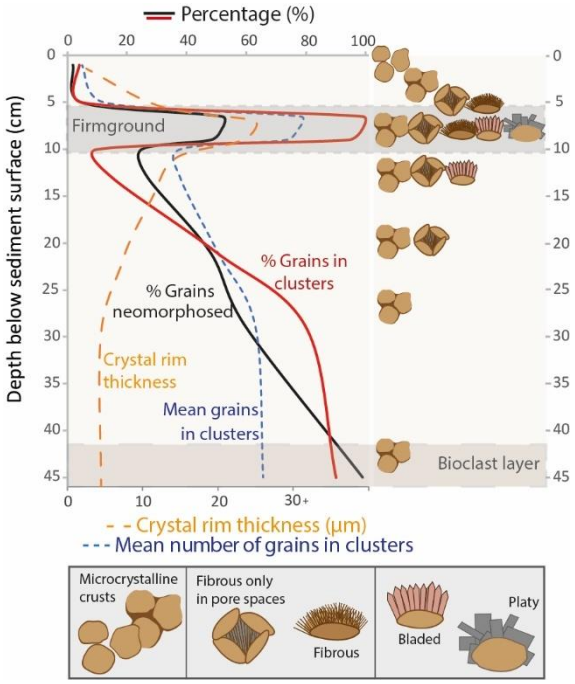

Figure 3.3. Sediment profile of; crystal rim thickness and mean number of grains in clusters (lower X-axis); and the percentage of grains in clusters or neomorphosed (upper X-axis). Right tab illustrates changing crystal morphologies through the profile, from microcrystalline crusts, to fibrous crystals only in inter- and intra-granular pore-spaces, fringed fibrous cements, bladed and platy crystals.

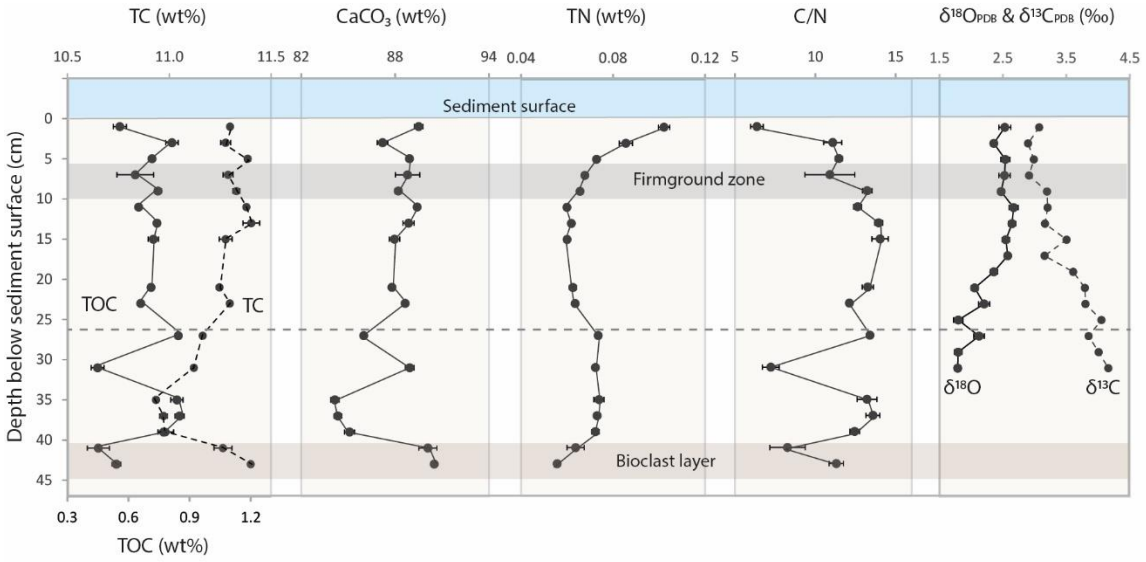

Figure 3.4. Sediment profiles showing the wt% of total carbon (TC) (dashed line, upper x-axis) and total organic carbon (TOC) (solid line, lower x-axis); $CaCO_3$ (wt%); Total nitrogen (TN) (wt%); the ratio of TOC/TN (C/N); and Core B bulk sediment $\delta^{18}O_{PDB}$ (‰) (solid line) and $\delta^{13}C_{PDB}$ (‰) (dashed line) relative to VPDB. Horizontal dashed line at 26 cm distinguishes change from grain size fining upwards (below) to a slight coarsening upwards trend (above).

3.4.1.2 Sediment organic composition

Total organic carbon (TOC) made up 4-8% of sediment total carbon (TC) throughout the profile, and broadly showed an opposing trend to the carbonate fraction (Fig. 4). From 26-40 cm, most samples had slightly higher TOC than the shallower sediment and carbonate content was fairly stable from 0-35 cm and then decreased from ~88% to ~84% until the bioclast layer, which increased to 91% (Fig. 3.4). Sediment total nitrogen (TN) was highest (0.10%) at the surface and decreased with depth to the base of the firmground, below which values were fairly constant (av.=0.07±0.01%, n=12), though slightly lower in the bioclast layer (Fig. 3.4). In the upper 26 cm this was broadly mirrored by TOC/TN (C/N), which increased from 6.4 at the surface to 14.0 at 13 cm (Fig. 3.4). C/N ratios remained >10 for much of the profile, with markedly low values at 31 and 44 cm, reflecting the decline in TOC.

3.4.1.3 Sediment isotopic composition

Carbonate carbon isotopic composition ($\delta^{13}C$) for the upper 30 cm ranged from 2.9-4.2‰ (av.=3.4±0.4‰ n=17), while oxygen isotope values varied from 1.8-2.7‰ (av.=2.4±0.3‰, n=17) (Fig. 3.4). The samples above and within the firmground zone showed no significant trend with depth. However, below the firmground (11-31 cm) there was a strong negative correlation between $\delta^{13}C$ and $\delta^{18}O$ (R^2 0.93, $p<0.0001$, n=11) (Fig. 3.5), with $\delta^{18}O$ decreasing and $\delta^{13}C$ increasing with depth ($\delta^{13}C$: R^2 0.85, $p<0.001$; $\delta^{18}O$: R^2 0.87, $p<0.001$).

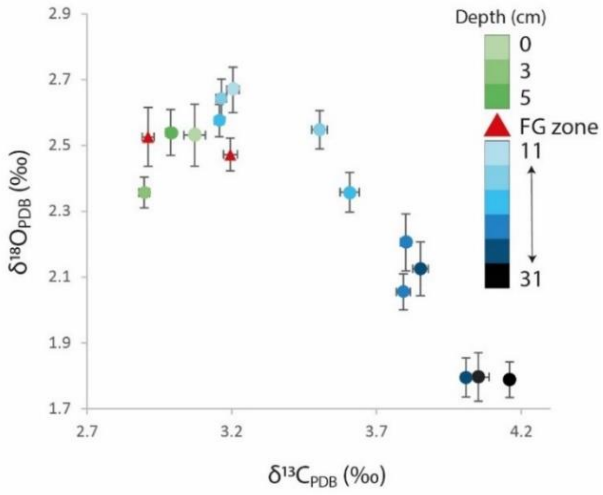

Figure 3.5. Cross plot showing relationship between bulk sediment $\delta^{13}C$ and $\delta^{18}O$ coloured by depth. Sediment above the firmground is green, unconsolidated sediment within the firmground zone is red and sediment below the firmground is blue.

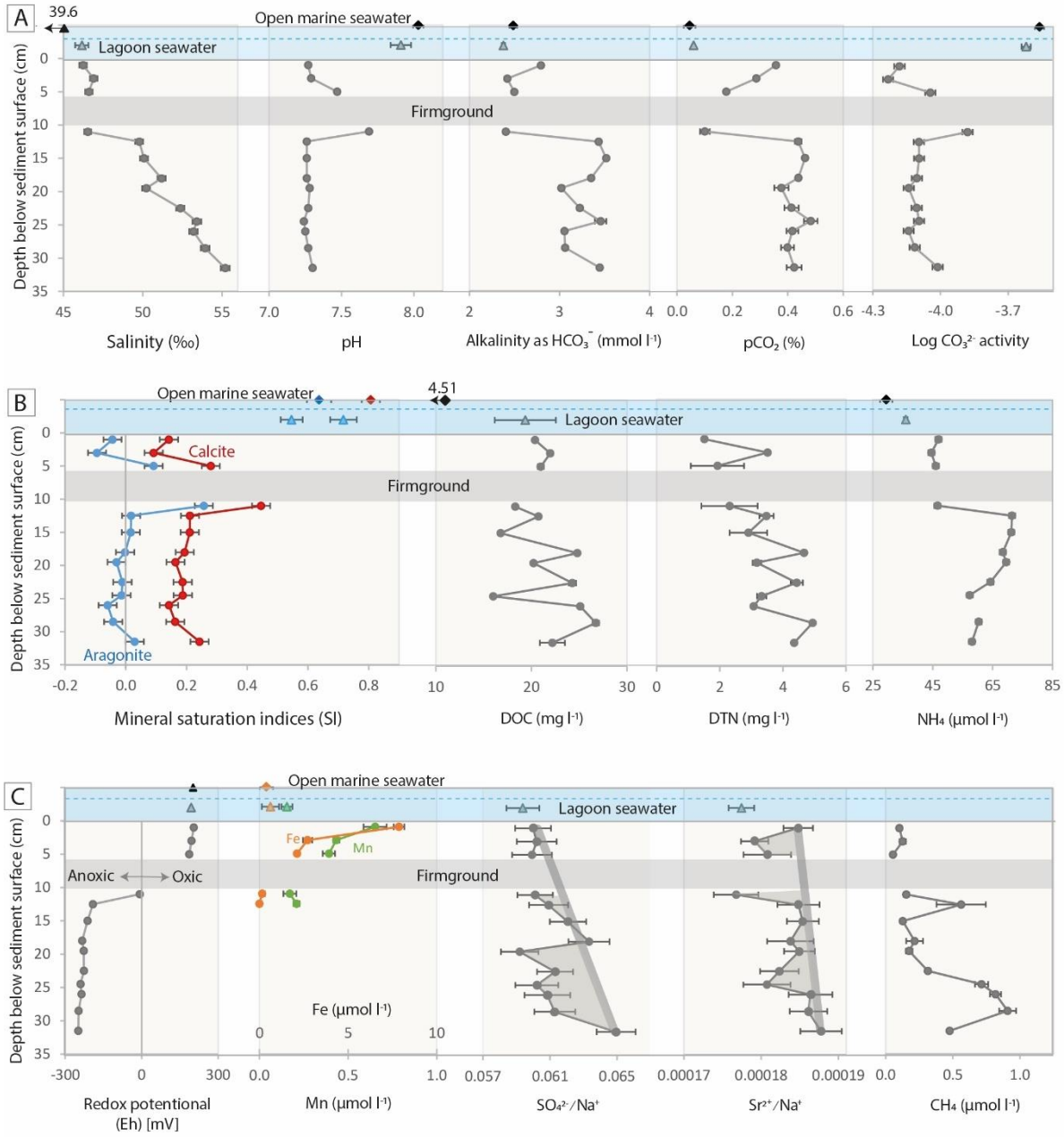

Figure 3.6. *In situ* porewater chemistry, with open marine (diamond) and lagoon surface seawater (triangle) in the upper blue panels. (**A**) salinity and carbonate chemistry (pH, bicarbonate alkalinity, *p*CO2(%), and the log activity of CO_3^-). (**B**) saturation indices (SI) for aragonite (blue) and calcite (red), dissolved organic carbon (DOC), dissolved total nitrogen (DTN) and ammonium (NH_4^+). (**C**) redox potential (Eh), manganese (green) and iron (orange) [Mn and Fe not measured below 12.5 cm], sulphate (SO_4^{2-}) and strontium (Sr^+) relative to sodium (Na^{2+}) (conservative tracer), and minimum methane concentrations. Raw concentrations of major ions are presented in Appendix B, Tables B4 and B5.

3.4.2 Water chemistry

3.4.2.1 Lagoon and coastal seawater

Open marine, lagoonal, and porewater chemistries are displayed in Fig. 3.6. Salinity in the lagoon was ~7‰ higher than the two open marine samples (Fig. 3.6A) and increased from 45.9 to 46.5‰ over 1.5 hours during the falling tide. The shallow lagoon water had a slightly lower pH (7.9) and bicarbonate alkalinity than that of the open marine (pH 8.0) (Fig. 3.6A). All surface waters were near atmospheric pCO_2 and supersaturated with respect to both aragonite and calcite (Fig. 3.6B). At this pCO_2 and at the surface temp of 32.5°C, lagoon waters had the potential to precipitate 116±6 µmol aragonite/kg water (196±5 µmol calcite/kg) to reach equilibrium, compared to 154±9 µmol aragonite/kg water (243±10 µmol/kg calcite) for open marine sites (at surface water temperature of 31°C). All lagoon and open marine seawaters were oxic, with an Eh of av.=199.2±4.2 mV (n=3) but dissolved total iron (Fe) in the lagoon water (0.62±0.49 µmol l^{-1} Fe) was almost twice that of the open marine (Fig. 3.6C).

3.4.2.2 Porewaters overlying the firmground

Shallow porewater salinity resembled that of the overlying lagoon, but the pH was markedly lower (7.27-7.45 *versus* 7.9). Bicarbonate alkalinity at 1 cm was higher than both the lagoon and the porewater at 3–5 cm depth (Fig. 3.6A). Porewaters had significantly lower SI values compared to lagoon waters; porewaters were calcite supersaturated and aragonite was undersaturated at 1-3 cm and became aragonite supersaturated just above the firmground (Fig. 3.6B). Sr^{2+}/Na^{+} indicate porewaters at 1 cm were enriched in Sr^{2+} (0.111 mmol l^{-1} Sr^{2+}) relative to overlying lagoon water (0.100 mmol l^{-1} Sr^{2+}), and from 3-5 cm there was a marked reduction in Sr^{2+}/Na^{+} (Fig. 3.6C) (av.= 0.108 mmol l^{-1} Sr^{2+}). Ca^{2+} and Mg^{2+} concentrations ranged from 12.4-13.0 mmol l^{-1} and 64.8-65.6 mmol l^{-1} respectively and Mg:Ca increased from 5.1 (1 cm) to av.=5.19 ±0.1 (3-5 cm) (Table B4).

Porewater DOC values were similar to those of the overlying lagoon water and showed no significant change with depth. Dissolved total nitrogen (DTN) varied from 1.51-3.52 mg l^{-1} with a peak at 3 cm (Fig. 3.6B). Porewaters above the firmground remained oxic (positive Eh), with redox potentials similar to the overlying lagoon water, and significantly elevated Mn and Fe at 1 cm depth, which declined sharply with depth. Sulphate concentrations above the firmground (37.2 mmol l^{-1}) were similar to the overlying Lagoon water (36.2 mmol l^{-1}) and sulphate depletion (SO_4^{2-}/Na^{+}) and CH_4 were negligible (Fig. 3.6C).

3.4.2.3 Porewaters below the firmground

Salinity increased with depth below the firmground to a maximum of 55‰ (31.5 cm), ~9‰ higher than lagoon water. The highest porewater pH (7.69) was measured immediately below the firmground (11 cm depth), below which values dropped sharply (Fig. 3.6A). Immediately below the firmground (11 cm), bicarbonate alkalinity was low (similar to above the firmground) but increased with depth from 12.5-

31.5 cm. Below the firmground (11 cm) increased pH drives increased carbonate saturation states despite the low bicarbonate alkalinity, resulting in supersaturation with respect to aragonite, capable of precipitating 34±7 µmol/l to equilibrium (at 23°C) (Fig. 3.6B). Beneath this, porewaters were generally at aragonite equilibrium and calcite supersaturation. Sr^{2+} (0.107 mmol l^{-1}) appeared depleted beneath the firmground (11 cm) and at 22.5-24.5 cm (Fig. 3.6C) (av.= 0.125 mmol l^{-1}). From 12.5-31.5 cm Ca^{2+} and Mg^{2+} concentrations ranged from 13.6-15.3 mmol l^{-1} and 71.6-81.1 mmol l^{-1} respectively and Mg:Ca ranged from 5.20-5.32 (Table B4).

Dissolved TN was variable but increased with depth below the firmground, with a maximum of 4.9 mg l^{-1} at 28.5 cm (Fig. 3.6B). Immediately below the firmground, redox potential declined sharply at 12.5 cm depth, then continued to fall more subtly. Mn and Fe concentrations beneath the firmground were ~5% of those above the firmground but were not measured below 12.5 cm (Fig. 3.6C). SO_4^{2-}/Na^+ showed a negative deviation from the mixing trend within the sediment column, that was most marked at 22.5-28.5 cm (where SO_4^{2-} concentrations ranged from 42.5-44.9 mmol l^{-1}) (Table B4), corresponding with the porewater from 22.5 cm that smelled particularly strongly of H_2S (Fig. 3.6C). This was mirrored by likely peaks (see Methods) in CH_4 concentration at 13 cm and 24.5–28.5 cm that were superimposed on an apparent overall increase with depth (Fig. 3.6C).

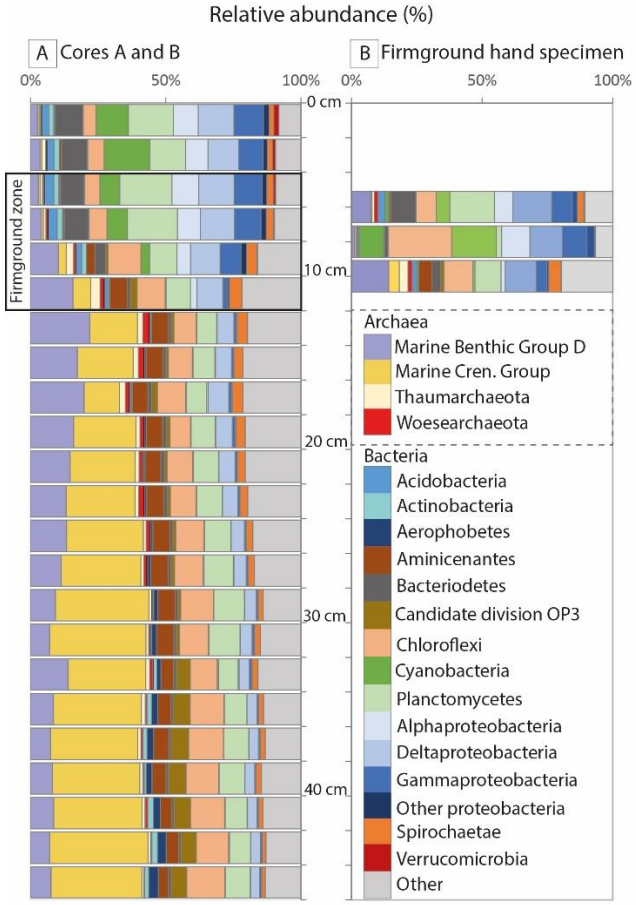

Figure 3.7. Relative abundance of 16S SSU rRNA gene sequences for common communities from (**A**) 0–31 cm (Core B based on triplicate analyses) and 32–45 cm (Core A no replicates) [The two cores have

been combined as triplicate sampling in Core B provides a more robust data set, however Core A sampled below 31 cm]. (**B**) Firmground hand specimen. See supplemental Fig. S4 for full 16S SSU rRNA gene relative abundance profiles of all cores and Fig. S5 and S6 for rare archaeal taxa and *Deltaproteobacteria* respectively, presented at a higher taxonomic level.

3.4.3 Microbial communities

Cores A and B displayed a high degree of similarity in the relative abundance of identified operational taxonomic units (OTUs) and have therefore been combined in Fig. 3.7 (0-31 cm from Core B based on triplicate analyses and 32–45 cm from Core A with no replicates: original data from each core in Fig. S4). Unless specified, all figures <30 cm are mean of triplicate analyses from Core B. Within the Yas lagoon cores, 24/41 bacteria phyla and 5/9 archaeal phyla had a relative abundance >1%. Using 16S SSU rRNA gene diversity as a proxy for bacterial and archaeal communities, there were distinct changes in community composition in the sediments above the firmground compared to below. Above the firmground, bacteria accounted for >90% of the relative abundance of total identified OTUs, but <60% below the firmground as archaea became more prevalent.

3.4.3.1 Microbial communities above the firmground

Sediment overlying the firmground was dominated by photosynthetic and heterotrophic facultatively anaerobic microbes belonging to the Phylum *Proteobacteria*, and in decreasing relative abundance *Cyanobacteria*, *Planctomycetes*, *Bacteroidetes, Chloroflexi (Anaerolineae)*, and *Acidobacterias* (Fig. 3.7A). The *Bacteroidetes* and *Cyanobacteria* only comprised a significant proportion (>1.5%) of the community above the base of the firmground, with the highest relative abundances at 1 cm (10.2%) and 3 cm (16.9%) respectively. *Alpha-* and *Gammaproteobacteria* were also most abundant in the upper 7 cm av.=9.0±0.8%, and av.=9.6±1.6% (n=4) respectively. Members of the *Deltaproteobacteria* phyla also occurred above the base of the firmground, specifically members of the *Desulfobacteraceae* (av.=4.7±0.4%, n=5), *Sandaracinaceae* (1.7±0.6%, n=5), *Desulfobulbaceae* (1.2±0.2% n=5), and Sh765b-TzT-29, at their maximum relative abundance of 2.9% (5 cm; core A), 1.8% (6 cm in the firmground specimen) and 2.6% (9 cm; Core B). *Planctomycetes* were at their highest relative abundance in the upper 7 cm (av.=16.9±2.7%, n=4), but were also present below that (av.=9.3±1.4%, 9–31 cm, n=2).

Archaea comprised <9% of the total community above the firmground but increased with depth. Among the archaea, most abundant were; (i) an uncultured archaeon belonging to the family Marine Benthic Group D (MGB-D), recently named *Thermoprofundales* (Zhou *et al*., 2019), of the Thermoplasmata class and *Euryarchaeota* phylum, and (ii) an uncultured group belonging to the phylum *Bathyarchaeota* (Pan *et al*., 2020), previously named the Miscellaneous Crenarchaeotal Group (MCG). Above the firmground *Bathyarchaeota* were near-negligible (<1%) and the relative abundance of MBG-D was ~3%. However, the MBG-D increased to 16.9% and 3.9% and at the top of the

firmground (~7 cm) in Core A and B respectively. There was a strong positive correlation between relative abundance of these two groups (R^2 0.97, P<0 .01, n=4) in the upper 8 cm where they made up 65% of total archaea.

3.4.3.2 Microbial communities within and below the firmground

The communities observed from the upper and lower surfaces of the firmground resembled the sediment above and below the firmground respectively (Fig. 3.7B). The upper surface contained an abundance of *Planctomycetes* (17.0%), *Deltaproteobacteria* (14.9%), *Bacteroidetes* (9.5%), *Gammaproteobacteria* (7.9%), and archaeal group MBG-D (7.4%). Here archaea accounted for 10.3% of OTUs. However, in the central part of the firmground there was a distinctly higher abundance of *Chloroflexi* (24.2%), *Cyanobacteria* (17.1%), and *Acidobacteria* (9.4%), with a near absence of the *Spirochaetae* and archaea (<2.5%).

In contrast, at the base of the firmground (10 cm), archaea were abundant (23.5%), predominantly MBG-D (14.2%), with other archaea groups (not MBG-D and *Bathyarchaeota*) accounting for 6.5%, such as Group C3 (*Thaumarchaeota*) (2.4%) (Fig. 7B). The most abundant bacteria were members of the *Deltaprotreobacteria* (12.0%), including members of the *Desulfobacterales* such as SEEP-SRB1 (1.3%) and the Sva0081 sediment group (2.2%) and the only notable presence of a known methanogen, *Methanomicrobia* (0.22%).

Below the firmground archaea increased in abundance relative to bacteria, accounting for av.=42.7±2.0% (n=17) of OTUs below 12 cm (Fig. 3.7A). Several groups were most abundant within the firmground zone, and specifically within the few centimetres of sediment underlying the firmground (~11–15 cm depth). The MBG-D was the most abundant group at 13 cm (22.0%), along with archaeal groups at 11 cm belonging to the *Thaumarchaeota* phylum, predominantly Group C3 (1.7%) and Marine Benthic Group B (*Lokiarchaeota*) (1.2%); and *Woesearchaeota,* which were the most abundant at 13 cm (2.3%). Similarly, some bacteria were most abundant within this zone, such as members of the sulphate reducing bacterial families *Desulfarculaceae* and *Syntrophobacteraceae* around 13 cm (at 2.7% and 1.7% respectively), which were also present at depth.

Below ~13 cm the relative abundance of MBG-D decreased with depth, which positively correlated (R^2>0.94, P<0.001, in Cores A, n=16 and B, n=9) with the relative abundance of members of the *Bathyarchaeota* (max. of 36.4%, 43 cm, Core A). MBG-D and the *Bathyarchaeota* accounted for 80% of archaea immediately below the firmground, increasing to 96.7% at 44 cm (Core A). The relative abundance of the MBG-D showed a strong positive correlation with Lokiarchaeota (MBG-B) below 13 cm (R^2≥0.90, p <0.0001, in Cores A, n=17 and B, n=10). In Core A, *Woesearchaeota* were most abundant at 19 cm (3.3%). The relative abundance of some bacterial groups also increased with depth, such as

Dehalococcoidia (*Chloroflexi*) (max. of 9.6% at 45 cm) and *Aerophobetes* that are <1% above 25 cm but reached 3.6% at 45 cm.

3.5 Discussion

In Yas lagoon a firmground occurs at ~5–11 cm below the sediment surface, where grains are partially cemented by well-defined platy aragonite crystals. The degree of cementation decreases with depth in the firmground from a well-defined upper surface, which is a common trait of marine firmgrounds (Bathurst, 1980). Beneath this firmground, porewaters are anoxic (negative Eh) whilst in the overlying sediment oxic conditions are maintained by a combination of diffusion, bioturbation, and bio-irrigation. One key question is whether the firmground develops at the redox boundary, or whether redox zonation is controlled by the firmground acting as a barrier to fluid exchange. Oxic sediments above the firmground host abundant bacterial communities, whilst the anoxic sediments below support a relatively high abundance of archaeal groups and sulphur reducing microorganisms (SRM). The thermodynamic effects of metabolic pathways on porewater pH and alkalinity are well documented (e.g., Soetaert *et al*., 2007), and include the direct impact of metabolic reactions, and indirect effects involving the products of dissimilatory transformations (Table 3.1). These reactions can have a profound effect on the carbonate chemistry by producing or removing DIC and changing DIC speciation (Moore *et al*., 2004; Sivan *et al*., 2007), which can alter the saturation state and promote carbonate dissolution or precipitation (Hu and Burdige, 2007; Pederson *et al*., 2019a). Microorganisms can also promote precipitation of carbonate minerals *via* biologically-induced mineralization, whereby cells or extracellular polymeric substances (EPS) act as catalysts or nucleation sites by providing a charged surface onto which ions can bind (Dupraz *et al*., 2009). EPS may also inhibit precipitation by binding Ca^{2+}, whereas the degradation of EPS by various heterotrophic bacteria may subsequently release Ca^{2+}, promoting carbonate precipitation (Dupraz *et al*., 2013).

Biogeochemical processes within the sediment link directly to the quality and quantity of OM settling on the sediment surface (Thamdrup and Canfield, 1996) though may also be linked to *in situ* OM production, light gradients, and redox gradients (Hochard *et al*., 2010). Particulate OM is transported through the sediment column *via* burial, bioturbation and bioirrigation, controlling OM availability in different microbial respiratory zones (Burdige, 2006). Transport of reactive solutes depends on the porosity and permeability of the sediment. In deep-water systems, diffusion dominates solute fluxes between the sediment and the overlying water, but wave and tidal-influenced fluxes and the effect of burrowing (Bertics and Ziebis, 2009) are likely more important in the shallow Yas Lagoon. Exposure at low tide will further affect advective transport, and in coastal settings the effects of groundwater discharge from the adjacent continent may be significant. With an estimated permeability based on similar near-shore sandy sediments (median grainsize ~0.2 mm) of 10^{-11} to 10^{-10} m^2 (Wilson *et al*. 2008),

rates of advection are likely more than two orders of magnitude greater than those of diffusion (Huettel *et al*., 2003).

3.5.1 Evidence of active subsurface firmground formation *via* aragonite precipitation

Thermodynamics is the first order control on carbonate precipitation or dissolution (Higgins *et al*., 2009), with kinetic factors determining reaction rate. Porewater pH and carbonate alkalinity control how much DIC is present as carbonate ions, which can combine with available cations (e.g. Ca^{2+}) to form carbonate minerals (Dupraz *et al*., 2009). Though porewater SI_{arag} and SI_{calc} are lower than the overlying lagoon water, both peaking in supersaturation just below the firmground. This local peak is driven not by increased alkalinity, but rather is coincident with a decrease in HCO_3^- (11 cm depth, Fig. 3.6). Porewater alkalinity is controlled by the balance between sources (dissolution, microbial respiration) and sinks (calcite precipitation) (Berner *et al*., 1970). We interpret this alkalinity nadir below the firmground as the result of active carbonate formation. Notably, porewater pH peaks above and below the firmground, suggesting that the driver for cementation is a biogeochemical process which increases pH, rather than one that simply increases DIC.

Platy aragonite crystals are only observed within the firmground, in accordance with aragonite supersaturation at 11 cm. In contrast, unconsolidated sediments above and below the firmground host porewaters at aragonite equilibrium or slightly undersaturated with respect to aragonite and are commonly coated by microcrystalline cements. This typically occurs on an underlying destructive micrite envelope formed by deformation of the grain surface *via* the activity of boring microorganisms and subsequent infilling (Ge *et al*., 2020b). Grains surfaces may be colonised by microbes which from biofilms acting to bind grain fragments and form constructive micrite envelopes (Perry, 1999; Ge *et al*., 2020b). These microcrystalline cements can then initiate firmground formation by providing nuclei for platy or needle-like aragonitic cements (Ge *et al*., 2020b). Mg^{2+} was only detected *via* EDS within the micritic cements, and not within the platy aragonite crystals that cement the firmground, suggesting calcite mineralogy.

Where porewaters are undersaturated or near aragonite equilibrium (as above and below the zone of firmground formation in Yas Lagoon), we would typically expect to see the stabilisation of aragonite to calcite *via* dissolution-reprecipitation processes (Hu and Burdige, 2007). The orthorhombic aragonite lattice preferentially incorporates cations with relatively large ionic radii such as Sr^{2+} and Ba^{2+} (Cubillas *et al*., 2005; Pederson *et al*., 2020), producing aragonite Sr:Ca ratios approximately five times those of calcite (Joseph *et al*., 2013). Aragonite-calcite transformation would therefore increase porewater Sr^{2+}. Using Na^+ as a conservative tracer for mixing, there are notable minima in Sr^{2+} above and immediately below the firmground where we propose aragonite is precipitating, and surprisingly between 22.5–24.5 cm, associated with higher levels of sulphate depletion (Fig. 3.6).

Though carbonate precipitation requires supersaturation, the prevalence of aragonite over calcite within the firmground also likely reflects kinetic controls (Morse and Mackenzie, 1990). Porewater phosphate concentrations are below the threshold suggested to impact aragonite growth rate (Tadier *et al*., 2017), and high porewater Mg:Ca favours the precipitation of aragonite over calcite (Folk, 1974). The porewaters also have high sulphate concentrations (3.5-5 times those suggested by Bots *et al*., 2011), which can lower the Mg:Ca threshold required to destabilise calcite in favour of aragonite (Bots *et al*., 2011). Additionally, the presence of EPS, as observed on some of the platy aragonite crystals (Fig S3.G), may affect crystal morphology and polymorphism by release of DOC into solution, which is suggested to favour calcite (Tourney and Ngwenya, 2009).

3.5.2 Potential metabolic drivers of firmground formation

The shallow sediments in Yas lagoon host a range of phylogenetically diverse, metabolically active bacterial and archaeal communities with distinct vertical trends in relative abundance. Porewater chemistry (Fig. 3.6) and 16S SSU rRNA gene signatures (Fig. 3.7) suggest changes in community composition and metabolic activity over centimetre-scales, creating geochemical zonation. Respiratory processes involved in OM degradation are dominated by electron acceptors that yield the greatest change in free energy per mol of organic carbon oxidised (Burdige, 2006). The sequence of oxic respiration, followed by nitrate, manganese oxides, iron oxides, sulphate and finally AOM and methanogenesis (Burdige, 2006) continues until either all available electron acceptors have been utilised or all OM has been degraded. The consumption of electron acceptors is balanced by the production of reduced species such as NH_4^+, Mn^{2+}, Fe^{2+}, HS^- and CH_4, which under specific thermodynamic conditions may be abiotically reoxidized, although catalysed microbiologically (Table 1). Authigenic carbonate precipitation is generally attributed to a few metabolic pathways which either produce alkalinity (Coleman and Raiswell, 1993) or drive a net pH increase, such as organoclastic sulphate reduction in conjunction with pyrite formation (Plet *et al*., 2016), Mn and Fe cycling, and AOM (Soetaert *et al*., 2007).

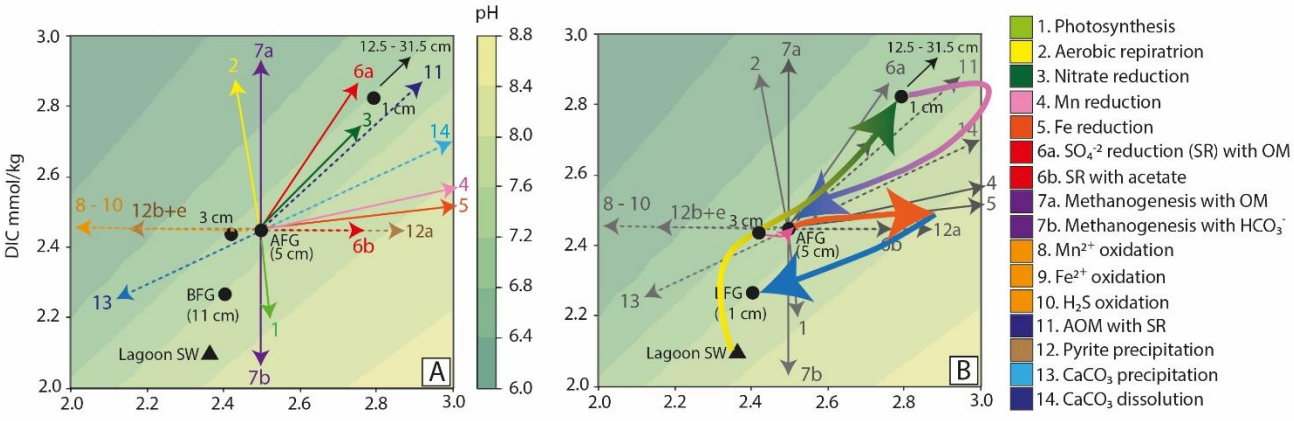

Figure 3.8. (**A**) Potential effect of different respiratory metabolisms on alkalinity, DIC and pH. Numbers proceeding metabolisms relate to equations in Table 1. Solid arrows represent primary reactions and dashed arrows represent secondary reactions. Arrows denote direction of ΔDIC/ΔALK, and not magnitude of relative change, refer to Table 1 for magnitude of change. The porewater sample above the firmground (AFG) is used as a central point to determine which pathways could result in the ΔDIC, ΔALK, and ΔpH observed between this point and the porewater sample immediately below the firmground (BFG). (**B**) Coloured arrows indicate potential metabolic pathways involved in altering the porewater chemistry in the upper 11 cm of the profile. pH contours were calculated based on varying DIC and ALK for the mean porewater chemistry from 3 cm and 5 cm. For a version plotting SI_{arag} contours and scaled vectors, refer to Appendix B, Fig. S7.

Table 3.1. Microbial metabolic reactions: ΔALK and ΔDIC indicate change in alkalinity/DIC per mol of organic carbon oxidised to CO_2 (based on Loyd *et al*., 2012) (Eq. 1-6a). pH indicates the pH midpoint, below which the reaction results in a pH increase and above which results in a pH decrease (based on Soetaert *et al*., 2007).

	Primary reactions	Stoichiometry	ΔDIC	ΔALK	ΔALK/ ΔDIC	*p*H
1.	Photosynthesis	$122\mathbf{CO_2} + 138\mathbf{H_2O} + 16\mathbf{NO_3^-} + 0.5\mathbf{HPO_4^{2-}} + 0.5\mathbf{H_2PO_4^-} + 1.5\mathbf{H^+} \rightarrow (CH_2O)_{106}(NH_3)_{16}H_3PO_4 + 138\mathbf{O_2} + 16\mathbf{HCO_3^-}$	-106	+17.5	-0.09	+
2.	Aerobic respiration	$(CH_2O)_{106}(NH_3)_{16}H_3PO_4 + 138\mathbf{O_2} + 16\mathbf{HCO_3^-} \rightarrow 16\mathbf{NO_3^-} + 0.5\mathbf{HPO_4^{2-}} + 0.5\mathbf{H_2PO_4^-} + 122\mathbf{CO_2} + 138\mathbf{H_2O} + 1.5\mathbf{H^+}$	+106	-17.5	-0.17	5.2
3.	Nitrate reduction	$(CH_2O)_{106}(NH_3)_{16}H_3PO_4 + 94.4\mathbf{NO_3^-} + 92.9\mathbf{H^+} \rightarrow 55.2\mathbf{N_2} + 0.5\mathbf{HPO_4^{2-}} + 0.5\mathbf{H_2PO_4^-} + 106\mathbf{CO_2} + 177.2\mathbf{H_2O}$	+106	+93.4	+0.89	6.8 – 7.0
4.	Mn-oxide reduction	$(CH_2O)_{106}(NH_3)_{16}H_3PO_4 + 212\mathbf{MnO_{2\,(s)}} + 318\mathbf{CO_2} + 106\mathbf{H_2O} + 13.5\mathbf{H^+} \rightarrow 15\mathbf{NH_4^+} + 0.5\mathbf{HPO_4^{2-}} + 0.5\mathbf{H_2PO_4^-} + 424\mathbf{HCO_3^-} + 212\mathbf{Mn^{2+}}$	+106	+438	+4.13	+
5.	Fe-oxide reduction	$(CH_2O)_{106}(NH_3)_{16}H_3PO_4 + 424\mathbf{Fe(OH)_{3\,(s)}} + 742\mathbf{CO_2} + 13.5\mathbf{H^+} \rightarrow 15\mathbf{NH_4^+} + 0.5\mathbf{HPO_4^{2-}} + 0.5\mathbf{H_2PO_4^-} + 848\mathbf{HCO_3^-} + 424\mathbf{Fe^{2+}} + 318\mathbf{H_2O}$	+106	+862	+8.13	+
6.	Sulphate reduction (SR)	a) $(CH_2O)_{106}(NH_3)_{16}H_3PO_4 + 53\mathbf{SO_4^{2-}} + 13.5\mathbf{H^+} \rightarrow 15\mathbf{NH_4^+} + 0.5\mathbf{HPO_4^{2-}} + 0.5\mathbf{H_2PO_4^-} + 53\mathbf{CO_2} + 53\mathbf{HCO_3^-} + 53\mathbf{HS^-} + 53\mathbf{H_2O}$ b) $CH_3COO^- + SO_4^{2-} \rightarrow 2HCO_3^- + HS^-$	+106 0	+67 +2	+0.63	6.7
7.	Methanogenesis	a) $8\ C_{106}H_{175}O_{42} + 330\mathbf{H_2O} \rightarrow 333\mathbf{CO_2} + 515\mathbf{CH_4}$ b) $2HCO_3^- + 4H_2 \rightarrow CH_4 + CO_3^{2-} + 3H_2O$	+1 -1	0 0		5.6
Reoxidation reactions						
8.	Mn^{2+} oxidation	$Mn^{2+} + 0.5O_2 + 2H_2O \rightarrow 2MnO_{2\,(s)} + 2H^+$	0	-2		-
9.	Fe^{2+} oxidation	$4\ Fe^{2+} + 4H_2O + O_2 \rightarrow + 2Fe_2O_{3\,(s)} + 8H^+$	0	-8		-
10.	H_2S oxidation	$H_2S + 2O_2 \rightarrow SO_4^{2-} + 2H^+$	0	-2		-
11.	AOM with SR	a) $CH_4 + 2H_2O \rightarrow CO_2 + 4H_2$ b) $SO_4^{2-} + 4H_2 + H^+ \rightarrow HS^- + 4H_2O$ c) Net: $CH_4 + SO_4^{2-} \rightarrow HCO_3^- + HS^- + H_2O$	+1	+1	+1	7.9
Precipitation/ dissolution reactions						
12.	Pyrite precipitation	a) $2Fe(OH)_{3\,(s)} + 5H^+ + HS^- \rightarrow 2Fe^{2+} + S^0{}_{(s)} + 6H_2O$ b) $Fe^{2+} + HS^- + S^0{}_{(s)} \rightarrow FeS_{2\,(s)} + H^+$ c) $FeS_{(s)} + H_2S \rightarrow FeS_{2\,(s)} + H_2$	0 0 0	+5 -1 0		+ +
	Iron sulphide precipitation	d) $FeOOH_{(s)} + 1.5H_2S \rightarrow FeS_{(s)} + 2H_2O + 0.5S^0{}_{(s)}$ e) $Fe^{2+} + H_2S \rightarrow FeS_{(s)} + 2H^+$	0 0	0 -2		+ -
13.	$CaCO_3$ precipitation	$CO_3^{2-} + Ca^{2+} \rightarrow CaCO_{3\,(s)}$	-1	-2		-
14.	$CaCO_3$ dissolution	$CaCO_{3\,(s)} \rightarrow CO_3^{2-} + Ca^{2+}$	+1	+2	+2	+

Metabolic reactions from Loyd *et al*., (2012) [2, 3, 4, 5, 6a, 7b, 11c, 12a and b]; Fantle and Ridgwell, (2020) [6b]; Bergmann *et al*., (2013) [7a, 9 and 10]; Cui *et al*., (2015) [11a and b]; and Soetaert *et al*., (2007) [8, 12c, d, e, 13 and 14]. Primary redox reactions are balanced with approximate marine organic matter stoichiometry using the Redfield ratio (Redfield *et al*., 1963). ALK = $2(CO_3^{2-}) + HCO_3^- + OH^- + HPO_4^{2-} - H^+$. + pH tends to very high pH values, and – *p*H tend towards very low pH values. Equilibrium pH values for reactions 2-11 and 12c-14 are from Soetaert *et al*., (2007) and are calculate based on a pH of 8.2, T of 25°C, salinity 35‰, 1 atm pressure and Redfield stoichiometry. The stoichiometry of organic matter and/or reactant species may have significant implications on ΔDIC:ΔALK, hence these reactions only provide a guide to the potential implications for ΔDIC, ΔALK and pH for given metabolic processes.

3.5.2.1 Microbial metabolic processes above the firmground

The influx of labile OM and oxygen through diffusion, bioturbation, and bioirrigation likely result in a complex spatial mosaic of oxidising and reducing conditions, or 'subsurface microniches' (Bertics and Ziebis, 2009) in the sediment overlying the firmground, which is not fully represented in our 2D profile (Fig. 3.6). Abundant bacterial phyla above the firmground include *Proteobacteria*, *Cyanobacteria*, *Planctymycetes* and *Bacteriodetes*, which are associated with a diverse range of environments including mangroves (Andreote *et al*., 2012) and hypersaline lakes (Weigold *et al*., 2016). Cyanobacteria typically obtain energy *via* oxygenic photosynthesis (Fernandez-Gomez *et al*., 2013), which consumes CO_2 and produces alkalinity (Dupraz *et al*., 2009). This may promote carbonate precipitation close to the sediment surface during the daytime (Eq. 1). In contrast, aerobic respiration produces CO_2, which dissociates to produce H^+, which lowers pH and promotes carbonate dissolution at pH >5.2 (Eq. 2 and 14) (Soetaert *et al*, 2007). Denitrification produces CO_2 and OH^-. However, the net impact on porewater pH and alkalinity depends on the starting pH, and at ~7.26 in Yas lagoon, likely has a negligible impact on carbonate mineral SI (Eq. 3). A combination of aerobic respiration and nitrate reduction could drive changes in porewater DIC, alkalinity, and pH from the overlying lagoon water to the porewater at 1 cm depth (Fig. 3.8). To shift the porewater chemistry from 1 to 3 cm (Fig. 3.8b), a process that increases alkalinity relative to DIC is required (e.g., Mn or Fe-oxide reduction), followed by carbonate precipitation (Eq. 13). However dissolved Mn and Fe concentrations are low, and future work analysing the solid phase would be valuable. Furthermore, this is at odds with a reduction in mineral SI (Fig. 3.6), but perhaps the equilibration with calcite reflects local conditions that overcome kinetic barriers for calcite precipitation.

The decomposition of OM with Fe and Mn (hydr)oxides monotonically trend towards a higher pH, with the impact of Fe reduction twice that of Mn (Eq. 4 and 5). However, this is often balanced by the remineralisation of reduced species which lowers pH (Eq. 8 and 9), predominantly with O_2 (Eq. 9) but less with NO_3^- and Mn-oxides (Soetaert *et al*., 2007). Metal-oxidizing and metal-reducing bacteria may not be equally abundant in all environments (Weber *et al*., 2006), therefore pH may increase or decrease depending on which metabolic process is dominant. *Chloroflexi* and *Planctymycetes* have been linked to metal oxide reduction (Wang *et al*., 2020) and are relatively abundant within the upper 2 cm where Fe and Mn are also abundant, along with a small increase in alkalinity at 1 cm (Fig. 3.6). The contradiction between apparent oxic porewaters and microbiology associated with reducing conditions may result from Rhizons preferentially sampling porewater from the most well-connected pores. In contrast, the 16-SSU rRNA gene data may reflect the complexity of anoxic microniches associated with smaller pores or burrows (Bertics and Ziebis, 2009).

Deltaproteobacteria have been linked to metal oxide-reduction (Wang *et al*., 2020). Jörgensen *et al*. (2012) found correlations between the *Deltaproteobacteria* order Sh765b-TzT-29 and Mn^{2+}. Sh765b-

TzT-29 is most abundant at 5-9 cm within the Yas lagoon sediments and firmground, possibly suggesting their involvement in the Mn^{2+} cycle above and within the firmground. Additionally, *Deltaproteobacteria and Gammaproteobacteria* in the upper 10 cm of sediment/firmground could play an active role in the S cycle (Oni *et al*., 2015). The presence of these microbial populations in conjunction with dissolved Mn/Fe suggests that reduction of Mn and Fe-oxides and SO_4^{-2} may drive both carbonate precipitation on the upper firmground surface and changes in DIC, alkalinity and pH within the upper ~10 cm (Fig. 3.8).

3.5.2.2 Microbial activity within the firmground

Microbial communities in the upper 1 cm of firmground closely resemble the overlying sediment. However, *Chloroflexi* (predominantly *Anaerolineae*) are particularly abundant within the central firmground hand specimen and the unconsolidated sediment from the firmground zone. Known *Anaerolineae* are anaerobic, mesophilic chemolithoheterotrophs or chemoorganoheterotrophs with a multicellular filamentous morphology (Yamada and Sekigughi, 2009). Culture experiments by Yamada and Sekigughi, (2009) suggest *Anaerolineae* show no relation to dissimilatory sulphate or nitrate reduction. The second most abundant taxa within the central firmground were members of the *Cyanobacteria*. An EPS-like substance was observed around some of the platy aragonite crystals (Fig S3.G), which may indicate that EPS and *Cyanobacteria* filaments provide a charged surface for crystal nucleation and/or aid in binding the sediments together, though this warrants further investigation. EPS have the capacity to bind large quantities of Ca^{2+}, which has an inhibitory effect on carbonate precipitation (Braissant *et al*., 2007; Pace *et al*., 2018). However, the heterotrophic degradation of EPS (e.g., by SRM) could release Ca^{2+}, allowing for carbonate nucleation (Dupraz *et al*., 2013).

Members of the *Desulfobacteracea* and *Desulfobulbaceae* were also observed above the base of the firmground. These taxa are known to be predominantly mesophilic SRM, many of which oxidise organic substrates incompletely to acetate (Kuever, 2014). Previously SRM were considered strict anaerobes, however some species can thrive in oxic conditions (Camacho, 2009). Some *Desulfobacteracea* may also be capable of nitrogen fixation (Almstrand *et al*., 2016). One member of the *Desulfobacteracea* genus, the Sva0081 sediment group, is most abundant in the upper and lower firmground surfaces. It is suggested to be an important H_2 scavenger in marine sediments, which is important to ensure anaerobic degradation remains energetically favourable (Dyksma *et al*., 2018). Additionally, a small increase in SRM (SEEP-SR1) along with increased archaea occur on the lower 1 cm of firmground. Archaeal Group C3 represents an uncultured class of the *Thaumarcheota* phylum that has been described as rare but active in muddy sediments (Agogué *et al*.,2015). Some members can oxidize ammonia aerobically, providing the first example of nitrification in the archaea (Könneke *et al*., 2005). However, it remains unknown if this trait extends to all members (Brochier-Armanet *et al*., 2012).

3.5.2.3 Microbial metabolic processes below the firmground

Geochemical data (Fig. 3.8) indicates that aragonite precipitation on the lower firmground surface may be influenced by several microbial metabolisms, including sulphate reduction coupled to pyrite formation, AOM and methanogenesis. Here we discuss the evidence for each of these metabolisms, or for a combination of these metabolisms, as drivers of firmground formation.

Sulphate reduction and pyrite formation

In most marine systems, porewater sulphate concentrations are dependent on downwards transport from overlying seawater (Sivan *et al*., 2007), but porewater sulphate increases with depth in Yas Lagoon. This more saline water at the base of the profile likely represent either leakage of continental brines confined beneath the deeper Holocene hardground (Wood *et al*., 2002), or density-driven reflux of evaporated brines from more restricted areas at the back of the lagoon that flow laterally at shallow depth over the top of the hardground (McKenzie *et al*., 1980). This advection of sulphate-rich fluids would support sulphate reduction (SR) as the dominant microbial respiratory pathway beneath the firmground.

Two of the most frequently cited metabolic processes promoting carbonate precipitation involve SR. Organoclastic SR (Eq. 6) involves the degradation of OM in anoxic sediments by SRM and increases carbonate alkalinity, theoretically favouring carbonate precipitation (Loyd and Berelson, 2016). However, SR also produces H_2S, which freely dissociates under normal porewater pH, typically lowering the pH to ~6.9 (Higgins *et al*., 2009). Organoclastic SR has been suggested to only promote carbonate precipitation if SR rates are high (Zhang, 2020), if electron donors are acetate (Eq. 6b), formate, or hydrogen (which do not produce H^+) (Fantle and Ridgwell, 2020), or if excess H_2S is efficiently removed from solution by iron-sulphide (pyrite) precipitation which increases pH and supersaturation (Ben-Yaakov, 1973).

The SO_4^{2-}/Na^+ indicates potential SR immediately above and below the firmground, and more significantly at ~20-29 cm. The SO_4^{2-} depletion underlying the firmground (11-13 cm) may be related to peaks in the relative abundance of SRMs belonging to the families *Desulfarculaceae* and *Syntrophobacteraceae* (Sun *et al*., 2010; Kuever, 2014). Additionally, *Thermoprofundales* (MBG-D) and *Bathyarchaeota* have also been suggested to have the genetic potential for SR.

A SR promotion of carbonate precipitation in Yas Lagoon would require removal of H_2S. The formation of pyrite framboids within the firmground (Fig S3.E) likely enhances carbonate formation by removing some H_2S and increasing pH. Reactions which drive an increase in alkalinity relative to DIC typically increase pH (e.g. $\Delta ALK/\Delta DIC > 1$, Table 1) (Loyd *et al*., 2012) as in pyrite formation and Mn/Fe-oxide reduction (Fig. 3.8). It is possible that the reduction of iron(III)oxide-hydroxide, followed by pyrite

formation (Eq. 12a+b), and then carbonate precipitation (Eq. 13), could account for change in DIC, alkalinity and pH observed in porewaters above and below the firmground (Fig. 3.8b). While there is evidence of dissolved Mn and Fe above the firmground, further investigation into sedimentary Mn and Fe would be required to determine if these processes could be responsible for driving an increase in pH below the firmground.

Anaerobic Oxidation of Methane

Observed sulphate depletion coincides with peaks in CH_4 at 12-13 cm and 24-29 cm, suggesting SR coupled to anaerobic oxidation of methane (AOM) (Eq. 8) may drive subsurface lithification (downward growth) of the firmground by increasing porewater pH below the firmground. AOM produces bicarbonate (Hoehler *et al*., 1994) and has been invoked as the dominant metabolic driver of carbonate precipitation involving SR. AOM coupled to SR is linked to the formation of authigenic carbonate nodules and concretions (Loyd and Berelson, 2016) and authigenic carbonate precipitates in a wide range of modern marine environments including methane seeps (Joseph *et al*., 2013), deep ocean sediments (Raiswell and Fisher, 2004), continental shelf sediment (Loyd and Berelson, 2016), and shallow water settings (Jørgensen, 1992), though to our knowledge not previously from a shallow subtidal (or supratidal) setting.

AOM promotes electron transfer between methane and a terminal electron acceptor (TEA) such as sulphate (Moore *et al*., 2004) and is microbially mediated by a syntrophic microbial consortium within anoxic sediments (Hoehler *et al*., 1994). AOM requires a consortium of predominantly SRM and anaerobic methanotrophs (ANME), which are polygenic relatives of methanogenic archaea (Cui *et al*., 2015). Despite the presence of SRM within the Yas Lagoon sediments, no known ANME sequences occur. However, recent studies suggest there may be potential genes for methane metabolisms within some other archaeal phyla (Evans *et al*., 2015), so this process cannot be fully ruled out. The degradation of OM produces DIC with characteristic $\delta^{13}C$ signatures (Irwin *et al*., 1977). DIC $\delta^{13}C$ values of porewaters are recorded in authigenic carbonate $\delta^{13}C$ signatures, with low (<-50‰) $\delta^{13}C$ values produced by AOM (Mavromatis *et al*., 2014). However, as the cements in Yas Lagoon constitute a minor fraction of the sedimentary carbonate volumetrically, the isotopic signatures obtained in this study may represent the bulk sediment consisting primarily of skeletal material and seawater-derived carbonate (Claypool and Kaplan, 1974). Future work obtaining cements $\delta^{13}C$ signature separate from the allochems $\delta^{13}C$ signature would be valuable.

Assuming equilibrium and electron neutrality, AOM converges towards pH 7.9 (at 25°C, salinity 35‰, 1 atm and Redfield stoichiometry) (Soetaert *et al*., 2007); which could counteract the drop in pH associated with calcite precipitation in Yas Lagoon. However, AOM (and organoclastic SR) also

produces DIC (Fig. 3.8), and therefore would drive ΔDIC relative to ΔALK in the opposite direction to that observed between porewaters above and below the firmground (Fig. 3.8b). Instead, this change in porewater chemistry requires a metabolic process that increases alkalinity greater than DIC, such as Fe reduction combined with pyrite formation (Eq. 12a+b). Alternatively, a process that decreases DIC without altering alkalinity such as methanogenesis with bicarbonate, (Eq. 7b) which in conjunction with carbonate precipitation could drive the changes in porewater chemistry above *versus* below the firmground (Fig. 3.8a).

Methanogenesis

Recent studies of mangrove and intertidal sediments suggest MBG-D possess genes potentially capable of encoding the Wood–Ljundahl (WL) pathway, which would allow them to produce methyl coenzyme M reductase (MCR) (Zhou *et al*., 2019), the principle enzyme for methanogenesis observed in all known methanogens (Ciu *et al*., 2015). MBG-D show a strong positive correlation with *Lokiarchaeota* (MBG-B) below the firmground, supporting the findings of Zhou *et al* (2019) that the two groups display non-random co-occurrence patterns. Lokiarchaeota are anaerobic mixotrophic acetogens or homoacetogens (Orsi *et al*., 2020). They possess the WL pathway, though lack the gene for methyl-co-M reductase (for methanogenesis). To our knowledge MBG-D, *Lokiarchaeota* and *Bathyarchaeota* have not previously been connected to carbonate precipitation.

Bathyarchaeota are the most abundant phylum below the firmground, but their role in methanogenesis/methanotrophy remains contentious (Biddle, 2006; Kubo *et al*., 2012). A recent study on two near complete *Bathyarchaeota* genomes has detailed the first evidence for potential methane metabolisms outside the *Euryarchaeota* (Evans *et al*., 2015). This included many genes associated with the WL pathway and, most importantly, divergent homologs of genes that encode MCR. Although this suggests that *Bathyarchaeota* could utilize diverse methyl compounds, including the potential for methylotrophic methanogenesis, Evans *et al*. (2015) found no evidence for AOM.

Bathyarchaeaota appear to increase in a broadly linear trend with depth and show neither a change in community structure around the firmground nor any correlation with methane or SR. Similar results were found by Kubo *et al*. (2012), who also noted the high relative abundance of *Bathyarchaeaota* compared to other archaea in low energy anoxic environments characterised by low rates of microbial respiration and deeper (≥10 cm) sulphate depletion. The dominant control on community composition for certain sub-groups is suggested to be pH (Pan *et al*., 2019), however in Yas Lagoon pH remains near-constant below the firmground. In Yas lagoon *Bathyarchaeaota* may increase in abundance with depth due to a potential specialisation for the degradation of recalcitrant OM (Wang *et al*., 2020).

3.5.2.4 Isotopic evidence

The isotopic signature of authigenic carbonates is commonly used to infer metabolic origin (Irwin *et al*., 1977). However, the isotopic values for the Yas Lagoon profile do not require any microbial activity ($\delta^{13}C$ +2.9‰ to +4.2‰ and $\delta^{18}O$: +1.8‰ to +2.7‰) and are within the range for oxidised carbon present in carbonate ions $(CO_3^{2-})_{aq}$ and in $CaCO_3$ that precipitates out of solution at equilibrium with modern ocean surface waters ($\delta^{13}C$ +2‰ to +4‰) (Sharp, 2007) and nearby Qatar seawater $\delta^{18}O$ (1-8‰) (Rivers *et al*., 2019). Similar results were described in two hardground samples (dated ≤268 yBP) from a coastal Abu Dhabi sabkha by Paul and Lokier (2017), with $\delta^{13}C$ values 2.6-4.3‰ and $\delta^{18}O$ values from 1.5-2.8‰. However, the isotopic signature from the firmground sediment zone may reflect the fact that aragonite cements constitute only a minor fraction of the bulk sample. Future work targeting the cement crystal rims for isotopic analysis via secondary ion mass spectrometry (SIMS) would provide targeted analysis of cement isotopic signature and a valuable insight into metabolic drivers, with mid-range $\delta^{13}C$ (~-25‰) values indicative of organic-derived carbon (e.g. sulphate reduction) (Irwin *et al*., 1977), and lighter values (<-50‰) indicative of AOM (Mavromatis *et al*., 2014).

3.5.3 Feedbacks

As in most shallow tropical environments, Yas lagoon waters are substantially supersaturated with respect to calcite and aragonite. With the addition of surficial daytime photosynthetic activity by microphytobenthos, cementation of the sediment surface would be expected. Lack of significant surface cementation may reflect the mobility of surface sediments and/or mixing *via* bioturbation/bioirrigation. A stable substrate may be required for cementation at the surface (Shinn, 1969), but may also impact the microbial community composition. Within a temperate, shallow subtidal sand flat, Böer *et al*. (2009) found that disturbance by hydrodynamic forces led to lower species richness (i.e. fewer OTUs) inhabiting the upper 5-10 cm of sediment. This disturbance would favour microbial communities able to tolerate occasional resuspension, physical abrasion from mobilized sediment, grazing, and respond to rapid fluctuations in O_2 and nutrients.

This multi-disciplinary study suggests that a combination of physical, biological and chemical factors drive shallow (5-11 cm) subsurface firmground formation in Yas lagoon. Although EPS was not quantified, it may be important for initiating subsurface sediment binding and/or providing a charged surface for carbonate crystal nucleation (Shiraishi *et al*., 2020). Mn/Fe-oxide reduction may be responsible for initially driving an increase in pH, pushing pore-fluids from equilibrium to aragonite supersaturation, and promoting crystal formation. The firmground may form at the redox boundary - an area often associated with high microbial diversities (Bertics and Zeibis, 2010), heightened biogeochemical activity (Alego and Li, 2020) and likely less impact from flushing of oxygenated waters. Additionally, anoxic micro-niches associated with burrows and/or faecal pellets may support diverse

communities with a range of metabolisms, even within the oxygenated zone (Bertics and Zeibis, 2010). As the firmground develops, it stabilises the sedimentary environment. This may favour slow growing anaerobes, which could lead to an increasing pH below the firmground, promoting cementation on the lower firmground surface. Thus, positive feedbacks enhance firmground development by increasing subsurface sediment stability. Furthermore, the supply of ions at the base of the profile may favour firmground development. Without this supply of ions, pore-occluding cements may reduce downwards diffusion of Ca^{2+} and key ions for microbial respiratory processes from overlying lagoon water causing cementation to become self-limiting (Fig. 3.9).

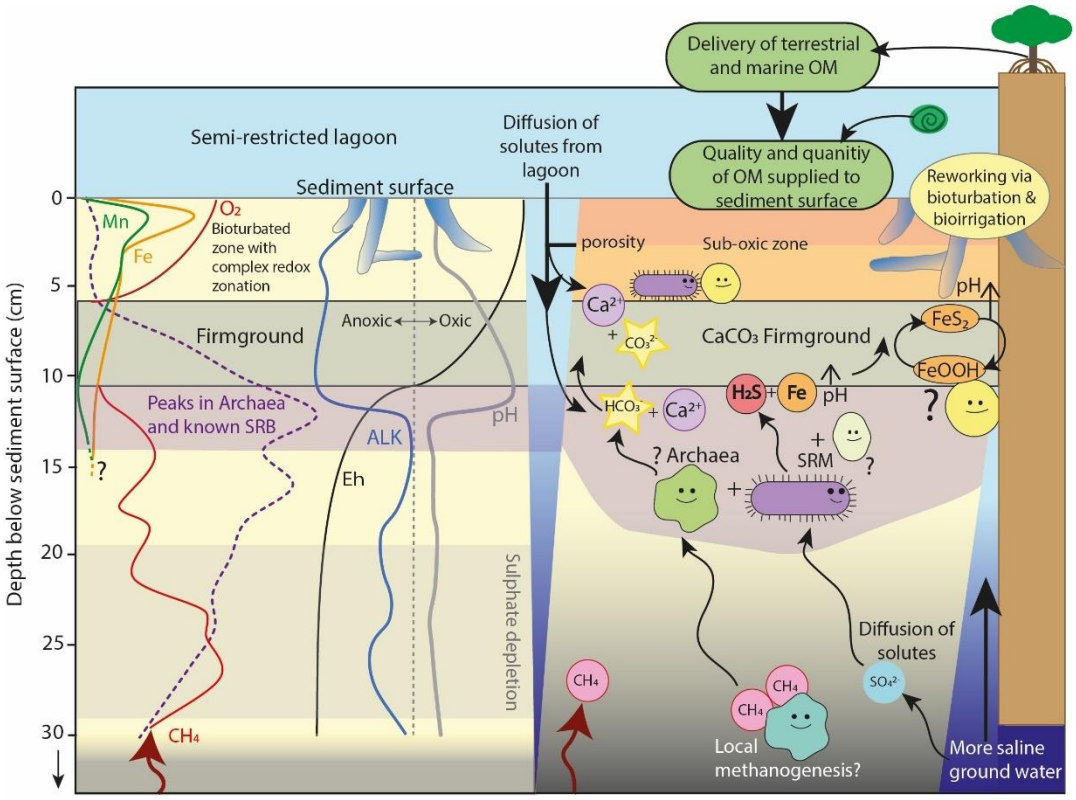

Figure 3.9. Schematic figure of potential microbial metabolic drivers of firmground formation in Yas lagoon, including the likely role of iron cycling and/or pyrite precipitation combined with sulphate reduction mediated by sulphate reducing microbes (SRM) and possibly archaea such as MBG-D.

3.5.4 Wider implications

Within the geologic record hardgrounds are often assumed to form at the sediment-water interface and are used to distinguish hiatuses in sedimentation and/or changes in sea level, acting as stratigraphic indicators (Christ *et al*., 2015). However, this study shows that cementation may rely on processes operating beneath the surface, within the shallow sediment column. Continued cementation may lead to formation of concretionary sub-hardgrounds (Ge *et al*., 2020a) that may subsequently become exposed by winnowing of overlying sediment or could be buried by continued sediment accumulation without any exposure. Further investigation into potential biosignatures of

hardgrounds formed by biologically-influenced subsurface precipitation could identify distinguishing features to avoid their erroneous identification as 'classic' hiatal hardgrounds.

Authigenic carbonates have been identified as important indicators of palaeoenvironmental conditions (Plet *et al*., 2016), but direct interpretation of these palaeo-proxies is challenging without a comprehensive understanding of the drivers of precipitation. Additionally, authigenic carbonates forms part of the global carbon cycle. Modern environments characterised by a diffusive CH_4 flux, DIC production and authigenic carbonate accumulation *via* AOM and SR have implications for ocean acidification and CO_2 sequestration (Akam *et al*., 2020). The inclusion of these pathways into coastal and geological carbon models requires reference to detailed porewater biogeochemical analysis (Akam *et al*., 2020).

Hardgrounds form barriers or baffles to fluid flow (Manchini *et al*., 2004), generating important permeability anisotropy that tends to increase with burial. Their lateral continuity and spatial variations thus have important implications for effective utilisation of both groundwater and hydrocarbon resources (Agar and Geiger, 2015). Reactive transport models have been increasingly applied to understand and predict changes in depositional properties that result from early diagenesis and infer reservoir properties (Whitaker and Frazer, 2018). However, to confidently apply such process-based models, there is a need for evaluation with reference to hydrological and biogeochemical data from modern environments such as Yas Lagoon.

3.6 Conclusions

This study presents the first comprehensive analysis of physical, chemical, and biological drivers of modern firmground formation within shallow intertidal lagoonal sediments. Despite extensive literature on hiatal-hardground and carbonate concretion/nodule formation, investigation into the microbial drivers of biologically influenced carbonate mineralisation of firmgrounds is limited. Far fewer studies investigate processes in areas with a low CH_4 diffusive flux. This study addresses some of these knowledge gaps by interpreting modern firmground formation in relation to biogeochemical processes within the sediment and porewater. This work concludes:

1. Active firmground formation occurs *via* precipitation of platy aragonite on the lower surface of the firmground. Positive feedbacks operate whereby the firmground forms a redox boundary, promoting cementation, and porosity occlusion limits oxygen exchange.
2. In the shallow, predominantly oxic sediment above the firmground, bacteria utilizing aerobic respiration dominate the microbial community, as well as those possibly associated with the degradation of metal oxides and organoclastic sulphate reduction. These microbes do not appear to follow a classic depth profile relating to sequential utilisation of available terminal

electron acceptors, but instead likely form a complex network governed by the distribution of burrows.

3. Below the firmground an increase in both the relative abundance of archaea and bacterial groups associated with the degradation of recalcitrant organic matter occurs.
4. The increase in pH that drives cementation at the base of the firmground is likely the by-product of a combination of microbial processes, with sulphate reduction and pyrite formation possibly acting as key drivers, with potential contribution from localised AOM.
5. Molecular data indicate an importance of archaeal groups such as MBG-B, suggesting previously unknown metabolic functionality, with potential involvement in SR and/or cycling of Mn/Fe.
6. Positive feedbacks may operate, with cements stabilising the substrate and limiting the depth of bioturbation. Stability of environmental conditions below the firmground may promote microniches and support development of slow growing anaerobic communities, that in turn promote firmground formation by increasing pH.

This study contributes information on the composition and distribution of bacterial and archaeal communities in an intertidal coastal sub-tropical lagoon alongside porewater chemical profiles. This provides valuable insight into the potential metabolic roles that microbial communities play on biogeochemical cycles within coastal lagoon sedimentary ecosystems. This is important for advancing our understanding of the carbon cycle and specifically carbon sequestration *via* authigenic carbonate precipitation. A better understanding of the drivers of firmground formation in modern settings will aid the interpretation of similar features in the geologic record. Future work investigating these processes in other coastal environments and at different spatial and temporal scales would be valuable to help assess local, regional, and global controls on carbonate firmground formation.

4. Hydrodynamic and geochemical complexity of the intertidal zone: Abu Dhabi

i. Authors

Hazel Vallack[1], Gordon Coy[2], Sarah E. Greene[3], Stephen W. Lokier[4], Gemma Tong[5], Fiona Whitaker[5]

1: School of Geographical Sciences, University of Bristol, England
2: Karachaganak Petroleum Operating PB, Kazakhstan
3: School of Geography, Earth and Environmental Sciences, University of Birmingham, England
4: School of Ocean Sciences, Bangor University, England
5: School of Earth Sciences, University of Bristol, England

ii. Author contributions

Porewater chemical analysis, data analysis, writing, and interpretation were conducted by H. Vallack with interpretive support from S. Greene, F. Whitaker, and G. Coy. Inland surface waters were sampled and analysed by G. Tong under the supervision of F. Whitaker. Field work was conducted by H. Vallack, S. Greene, S. Lokier, F. Whitaker, and Gordon Coy and logger data was processes by H. Vallack, G. Coy, F. Whitaker. The long-term loggers were collected by Mohammad Alsuwaidi and Prasanth Thiyagarajan.

iii. Abstract

Hydrodynamic variability, the changes in seawater and porewater chemistry driven by tidal, wave, and current-driven circulation, produces a dynamic intertidal environment which has important implications for nutrient cycling and carbon storage. In coastal Abu Dhabi, hydrodynamic variability has been implicated in the development of microbial mats, the precipitation and redistribution of sediments, and mediating biogeochemical processes in the subsurface that have been invoked as drivers of dissolution, micritisation, and cementation. Carbonate and evaporite sediments have been well-studied in the region, and we understand that these precipitates are strongly influenced by water chemistry, however explicit linkages with intertidal zone hydrodynamic data are surprisingly rare and we do not understand how hydrodynamic variability impacts sediment over seasonal to annual timescales. Thus, coastal Abu Dhabi provides an ideal location to explore temporal changes in surface water chemistry and temperature driven by hydrodynamic variability in the intertidal zone and investigate what impact this may have on diagenesis. To assess the hydrodynamic complexity of Abu Dhabi's intertidal zone, a combination of long- and short-term logger data (temperature, salinity, and water depth) has been combined with surface water sample analysis to investigate the role of hydrodynamics in driving diagenesis at two contrasting sites on the Abu Dhabi coast. We propose new definitions of the lower, middle, and upper intertidal zone boundaries based on annual tidal limits and

surface facies and find that the microbial mats inhabit an environmental niche flooded ~2-15% of the time annually. As the flood tide flows over the mats, photosynthesis consumes CO_2 which increases pH and promotes the precipitation of aragonite in the middle and lower intertidal zones as supersaturated seawater drains off the back of the microbial mats mat with the ebb tide. This effect is likely enhanced during the summer months and spring tide periods, when the increased water level can travel further across the intertidal zone and over the microbial mats.

4.1 Introduction

Identifying pathways and exchange of dissolved species across the supratidal-intertidal-subtidal zones is important for developing our understanding of carbon and nutrient fluxes in the coastal environment (Bouillon *et al*., 2007). Despite covering <2% of the total ocean area, coastal habitats (mangroves, tidal flats, and seagrasses) account for ~50% of the total carbon sequestered in ocean sediments (Duarte *et al*., 2005), with microphytobenthos inhabiting the sediment surface accounting for >50% of total primary productivity in coastal ecosystems (Cahoon, 1999). The intertidal zone (ITZ) is a highly dynamic environment that comprises the area of coastline within range of the highest and lowest annual tides (under normal meteorological conditions) and represents the transition from terrestrial to marine ecosystems (Bishop-Tailor *et al*., 2019; Oueslati *et al*., 2019). ITZs typically receive significant inputs of terrestrially-derived nutrients and allochthonous carbon, which drives *in situ* primary production (e.g., by microphytobenthos, microalgae and seagrass) providing important areas for nutrient cycling (Billerbeck *et al*., 2006) and carbon storage (Bianchi, 2007; Lee *et al*., 2011; Mcleod *et al*., 2011).

Hydrodynamic variability describes the changes in seawater and porewater chemistry driven by tidal, wave, and current driven circulation (Christ *et al*., 2015). In the ITZ, this produces a dynamic environmental gradient from permanently to occasionally immersed sediment which is reflected by a strong coastal habitat zonation by elevation (Bearup and Blasius, 2017; Bishop-Tailor *et al*., 2019). In (sub)tropical low latitude ITZs, the combination of restricted shallow water circulation and arid climate (where high evaporation rates cannot be balanced by low meteoric input) produce shallow water systems prone to high salinities (Rivers *et al*., 2019). Such environmental conditions are typically expressed in the sedimentary record as associations of shallow water carbonate and marine evaporite deposits (Warren, 2016). A classic example of such environments is the southern coast of the Persian/Arabian Gulf (hereafter referred to as the Gulf) where the ITZ is characterised by the production of carbonate and evaporite (gypsum, anhydrite, and halite) sediment, redistribution, and accumulation (Kenig *et al*., 1990; Alsharhan and Kendall, 2003). Coastal hydrodynamics control the development of microbial mats (Court *et al*., 2017) and influence the shallow alteration of sediments *via* dissolution, micritisation and cementation. These subsurface processes depend on fluid exchange not only with overlying seawater but also adjacent groundwaters.

The extremely arid climate of the Gulf produces surface water salinities in the ITZ ranging from near-normal seawater to locally reaching halite saturation (Lokier *et al*., 2017; *Rivers et al*., 2019; Chapter 3,). The southern side of the Gulf acts as a rare recent analogue of ancient epeiric settings (Lokier *et al*., 2015; Lokier and Fiorini, 2016). Ancient epeiric shelf successions are common in the sedimentary record and provide globally important areas of carbonate sediment deposits (Bádenas and Aurell, 2008). The Gulf coast of Abu Dhabi also provides one of the best and most accessible modern examples of coastal sabkha (salt flat) environments and has frequently been employed as an analogue for the Tertiary and Mesozoic subsurface rocks of the Arabian Gulf, Mesozoic carbonates from the Middle East, Europe, and the Gulf of Mexico and Paleozoic carbonates from Europe, Asia, and the Western USA (Alsharham and Kendall, 2003). Sedimentological research in the region has focussed on the geomorphology and geologic history (Evans *et al*., 1964; Shinn, 1969; Lokier and Steuber, 2009; Lokier, 2012; Lokier *et al*., 2013), deposition of carbonate and evaporite facies (Kendal and Alsharhan, 2012; Lokier *et al*., 2013), early marine diagenesis (Paul and Lokier, 2017; Ge *et al*., 2020a; Chapter 3) and dolomitization within the sabkha (Kinsman, 1968; Hsu and Schneider, 1973; McKenzie *et al*., 1980; Patterson and Kinsman, 1982) and more recently, the potential role of microbial communities in dolomite formation (Bontognali *et al*., 2010; Bontognali *et al*., 2012; Sadooni and Strohmenger, 2013; Geske *et al*., 2015).

In coastal Abu Dhabi, hydrodynamic variability and seawater chemistry control the development, extent, and distribution of microbial mats, and together with biogeochemical processes, have been invoked as drivers of dissolution, micritisation, and cementation within the shallow marine settings. The microbial mats form in the upper portion of the ITZ on the Abu Dhabi coast (Lokier *et al*., 2017) and comprise microbial communities that work together to fix inorganic carbon into biomass either photosynthetically or chemosynthetically (Rich and Maier, 2015). The seaward margin of the mat is limited by the activity of grazing fauna and the landward margin is controlled by the lack of regular tidal inundation, resulting in desiccation (Lokier *et al*., 2017). Coastal hydrodynamics have also been suggested to promote cementation within the shallow marine settings, with firmground and hardground formations linked to tide-induced circulation of aragonite-supersaturated seawater, evaporation, and microbial activity (Christ *et al*., 2015; Ge *et al*., 2020a; Chapter 3). However, such processes may also influence the shallow sediment porewater system, with implications for dissolution and the generation of micritic textures, providing a precursor to microporosity development (≤10 µm pore spaces) (Moshier, 1989; Kaczmarek *et al*., 2015). Successful reservoir characterisation and fluid flow simulations rely on the accurate predictions of the distribution of microporosity (Harland *et al*., 2015), as well as predictions of the lateral continuity and spatial variations of hardgrounds which may form barriers or baffles to fluid flow (Manchini *et al*., 2004). Understanding the role of coastal hydrodynamics and seawater chemistry plays in driving shallow marine dissolution and cementation

may therefore have important implications for the effective utilisation of both groundwater and hydrocarbon resources (Agar and Geiger, 2015).

Whilst studies on the microbial mats and physical and diagenetic characteristics of sediments of the southern Gulf are abundant, and in many cases are linked to hydrodynamics processes, less attention has been paid to specifically understand the hydrodynamic complexity of this coastal environment, and how it changes temporally. Any prior studies tend to be focused on the groundwater geochemistry of the supratidal sabkha (Hsu and Schnider, 1973; Patterson and Kinsman, 1977; McKenzie *et al*., 1980; Sanford and Wood, 2001; Wood *et al*., 2002). Sabkha groundwater salinities range from 70 – 356‰ and have variable chemical characteristic which suggest complex origins and alterations due to mixing, evaporation, and diagenetic precipitation, dissolution and/or replacement processes (Evans *et al*., 1969). Wood *et al*. (2002) proposed an ascending brine model to explain the sources of solutes and flux of water within the sabkha, with >95% of solutes originating from ascending brines of continental origin. They suggest that ~90% of the fluid is recharged by rainfall and ~10% is from lateral and ascending groundwater flow, with almost 100% of water lost through evaporation. Hence the source of water and solutes is different.

In contrast, Rivers *et al*. (2019) investigated the variability in the geochemistry of Qatar coastal subtidal sea and pond waters and the effect this may have on sediment carbonate chemistry and diagenesis. They found that aragonite precipitation was driven by initial evaporation (up to ~90 psu), however further evaporation resulted in aragonite dissolution, followed by gypsum and halite precipitation (Rivers *et al*., 2019). Whilst Rivers *et al*. (2019) focused on seaward (and ponds) areas, Whitaker *et al*. (2014) characterised water chemistry throughout the Holocene siliciclastic-dominated sabkha of the upper ITZ and supratidal zone (STZ) in Qatar and found that the precipitation of diagenetic gypsum in the middle sabkha was driven by water table evaporation. Calcium and sulphate depleted porewaters then refluxed downwards into the underlying Eocene aquifer. Whitaker *et al*. (2014) suggest evaporative pumping of brackish groundwaters is an important source of solutes in the upper sabkha of Qatar, whereas seawater recharges the lower sabkha.

Variation in sediment texture within coastal sedimentary systems is frequently conceptualised in 3D box models, supplemented by 2D mapping of the sediment surface using statistical algorithms applied to satellite images (Kaczmarek *et al*., 2010; Bishop-Taylor, *et al*., 2019). Sediment characteristics may also be viewed in vertical cross-section in response to temporal changes in sediment production, supply, erosion, and thus accumulation, applying time as the third dimension (Rankey, 2002). However, coastal hydrological systems tend to be presented in 2D, predominantly oriented perpendicular to coast (e.g., Whitaker *et al*., 2014), with rare examples giving a third dimension of time (e.g., Waska *et al*., 2019). In contrast, porewater analysis is presented in 1D (Burdige *et al*., 2008; Chapter 3), 2D (Nickerson and Thibobeau, 1985; Beck *et al*., 2017) and 3D (with time as the third dimension) (Beck *et*

al., 2009; Waska *et al*., 2019) and although variations in submarine groundwater discharge have been studied at a range of scales (Bratton, 2010), the spatial and temporal complexity of the ITZ surface water chemistry is rarely linked to the nature of sediment and porewaters. The complexity of lateral and vertical fluid flow combined with variations in microtopography have important chemical implications for surface waters and subsurface porewater chemistries, which ultimately impact water-rock reactions and diagenesis. For example, Xiao *et al*. (2013) applied 3D reaction transport models to demonstrate how brine pools give complex spatial variations in pore water chemistry resulting from refluxing brines, without considering the additional complexity that results from tide effects.

Carbonate and evaporite sediments have been well-studied in the coastal Abu Dhabi region, and these precipitates are strongly influenced by water chemistry, though explicit linkages with ITZ hydrodynamic data are surprisingly rare. Thus, coastal Abu Dhabi provides an ideal location to explore temporal changes in surface water chemistry in the ITZ and offers the opportunity to better constrain the influence of hydrodynamics on sediment production/accumulation as well as to investigate what impact this may have on diagenesis in the shallow pore waters. This study aims to assess the changes in surface water chemistry across two transects on the Abu Dhabi coast from offshore open marine settings, through the ITZ with microbial mats, and into the upper ITZ/STZ. A better understanding of how the surface water chemistry of the ITZ changes on diel, tidal, and seasonal timescales will allow sedimentological and microbiological research to be contextualised within this dynamic environment. The overarching aim is to develop an understanding of the hydrodynamic controls on surface water chemistry and temperature within the intertidal zone, and to address the following questions:

a. How does the chemistry of the flood tide change as the tidal front progresses inland, and what impact may this have on shallow diagenesis in the carbonate-dominated sediments?
b. How does seawater chemistry of the ITZ differ in areas which are drained by shallow tidal creeks from those without creeks?
c. How does creek water chemistry change with the tide, and how might the timing of high/low tide with day/night affect this?
d. What role, if any, do the microbial mats play in altering surface/porewater chemistry of ITZ sediment down-dip (seaward) of them, and what effect may this have on shallow carbonate diagenesis in the ITZ?

4.2 Depositional and regional climate of the study area

The Gulf is a shallow epicontinental sea (mean depth of 35 m) comprised of a low-angle carbonate-evaporite ramp system that progresses offshore from a supratidal evaporite sabkha, through a complex and laterally extensive intertidal zone and into a carbonate-dominated subtidal environment

(Evans *et al*., 1964; 1969; Lokier and Steuber, 2008). This topography is complicated by a complex of barrier islands and offshore shoals.

The sabkha is typically divided into the inner (more proximal) and outer (more distal) sabkha (Evans *et al*., 2011), describing the fully supratidal zone and the zone of marine influence respectively (Court *et al*., 2017) (Fig. 4.1.A, B, C). The spatial occurrence of different surface facies across the intertidal-supratidal zone is controlled by duration of tidal flooding, dependent on the local slope angle (Court *et al*., 2017). The shallow sub-tidal sediments predominantly consist of fine to medium-grained carbonates with abundant skeletal grains in the bioturbated lower-intertidal sediments, which continue to be an area of active carbonate precipitation and sedimentation (Evans *et al*., 1964; Lokier *et al*., 2013; Lokier and Fiorini, 2016). The intertidal sediments are bioturbated and typically poorly sorted, locally well-sorted and silt-dominated, whereas sediments underlying the microbial mats in the middle to upper ITZ are fine-grained and well-sorted with abundant silt-grade material (Lokier *et al*., 2013). The abundance of evaporites (e.g., anhydrite, gypsum, and halite) increases inland, from the upper intertidal and supratidal zones (Lokier *et al*., 2013). More detail on ITZ and STZ sedimentology is given in the site description section below.

The Gulf is almost entirely landlocked, with the only connection to the Arabian Sea being the 50 km wide Strait of Hormuz and experiences a semi-diurnal micro-tidal regime (amplitude 1 - 2 m) (Paul and Lokier, 2017). As a result of this restriction, the shallow Gulf has high salinities (45‰ – 46‰) relative to the nearby Indian Ocean (Lokier and Steuber, 2009) and high Mg/Ca ratios (Wood *et al*., 2002; Rivers *et al*., 2019) owing to high evaporation and relative restriction if the Gulf. The dominant north-westerly Shamal wind in the Gulf can produce strong winds (≤15.4 m/s) (Paul *et al*., 2021) and storm surges (Lokier and Steuber, 2009). The UAE experiences an extremely arid climate, with mean annual rainfall of 72 mm, the majority of which falls in short-lived torrential rainstorms, typically between February and March (Raafat, 2007). Annual air temperatures typically range from 7°C during winter nights to 50°C in summer days (Lokier and Fiorini, 2016). The warm shallow Gulf results in high humidity, reaching 100% in summer months.

4.3 Site descriptions

This field study combines water chemical analysis from sites mostly within the lower to upper ITZ of Qantur Lagoon with additional data from offshore sites both west and east of Abu Dhabi island, and from groundwater samples obtained from three boreholes (Fig. 1C, F). The offshore sites (1-OS and 2-OS) are located 2.0 km and 2.7 km offshore respectively in water depths ~5.5 m (Fig. 4.1.A). Offshore sediments are dominated by fine-grained to muddy carbonate sediments (Evans, 1966; Uchupi *et al*., 1996) with large areas of the sea floor composed of lithified carbonate sediments (Shinn, 1969).

Qantur Lagoon runs parallel to the coast extending from ~40-52 km southwest of Abu Dhabi Island. It is connected to the Gulf by a branch of the Khawr Qantur channel and is protected from the open marine conditions by three barrier islands (area of largest island ~5 km^2) (Fig. 4.1.A). Site 3 is in the centre of Qantur Lagoon (Site 3-QL) (Fig. 4.1.C, D, E). The Site 3-QL transect runs 1.04 km perpendicular to the coast, starts in the eastern tip of a small branch of the Khawr Qantur channel and extends to the landward edge of the microbial mat belt (~48 km from Abu Dhabi Island) (Fig. 4.1.D). At Site 3-QL, surface temperature was recorded across the ITZ over several days (5^{th}-12^{th} Jan. 2019, Fig. 4.1.D) and channel water temperature, salinity, and water level were recorded over ~1 year, 9 months (Jan. 2019-Oct. 2020). Surface water samples were also collected across the flood tide (7^{th} Jan. 2019) (Fig. 4.1.E).

In contrast, Site 4 is in the western part of the Lagoon (Site 4-QL) (~2 km west of the Site 3-QL transect) (Fig. 4.1.F), in an area drained by a tidal creek network (Site 4-QL-TC) that connects the Khawr Qantur channel to the ITZ. The Site 4-QL transect extends ~0.9 km landwards with two sub-sites in the microbial mat belt (Sites 4-QL-MM1 and 4-QL-MM2) and one site in the upper intertidal zone (Site 4-QL-UI) (Fig. 4.1.F). Creek water samples were collected during ebb and flood tides and surface waters were collected from the microbial mats and upper ITZ site. Additionally, three groundwater samples from below the underlying (basal) hardground were obtained from two boreholes situated ~0.3 km west of the tidal creek (BH1 and BH2) and one situated 2 km further inland (BH3) (Fig. 4.1.C, F). Table 4.1 provides a summary of site names, locations and dates sampled and Table 4.2 provides details of loggers deployed in the area as part of this study.

For a detailed description of surface sedimentary facies along transects approximate to the ones presented here at Site 3-QL and Site 4-QL, please refer to 'Transect 2' in Court *et al*. (2017) and 'Transect 9' in Lokier *et al*., (2013) respectively (locations in Fig. 4.1.C). Court *et al*. (2017) describes several distinct laterally continuous facies belts relating to their elevation above the present-day sea level from 'Transect 2' (Site 3-QL here) spanning the intertidal-supratidal zone:

1. The ITZ transitions from predominantly subaqueous unconsolidated muddy carbonate sediments with no surficial microbial mats offshore through three periodically flooded distinct surface microbial mat morphologies (spongey, leathery, and pustular). The ITZ and can be subdivided into three zones:
    i. The lower ITZ is characterised by light grey muddy carbonate sediments of unlithified packstone to moderately well-sorted unlithified grainstone (Fig. 4.2.B) and underlain by a variably cemented marine hardground (referred to here as the basal hardground) (Lokier *et al*., 2013; Court *et al*., 2017). The upper few centimetres are highly bioturbated with evidence of gastropod trails on the sediment surface and openings to decapod burrows. Beneath the sediment surface, there is a complex network of burrows, with dark grey organic-rich linings. Vegetation is absent in the area aside from a very few sparse

mangrove trees at Site 4-QL. The transition between the lower to middle ITZ is marked by a shift to fine-grained unlithified packstone to grainstone with a discontinuous surficial spongey microbial mat made up of pink and green-coloured microbial communities on the seaward edge (~5 mm thick), which become darker and increase in thickness inland (~1.4 cm tick) (Court *et al*., 2017) (Fig. 4.2.D).

ii. The middle ITZ is characterised by predominantly black-coloured, laterally continuous leathery microbial mats that forms a near continuous belt (117-320 m wide) parallel to the shoreline and marking the transition between middle and upper ITZs (Lokier and Steuber, 2008; Court *et al*., 2017; Lokier *et al*., 2017) (Fig. 4.2.C). The microbial mats have an average thickness of 8 cm (range 0.5 – 23 cm) (Court *et al*., 2017) forming polygonal structures ~20 -30 cm in diameter (Fig. 4.2.E) and are suggested to flood at high tide for a few hours most days (except during lowest neap tides) (Lokier *et al*., 2017).

iii. The upper ITZ is characterised by a pustular, dark-coloured microbial mat morphology that ranges from 0.1 – 1.6 cm thick becoming increasingly discontinuous as it progresses inland (Fig. 4.2.F, G). Pustular mats are underlain by brown, fine- to coarse- grained unlithified gypsum rudstone with fine grained carbonate and siliciclastic material with mm- cm scale lenticular gypsum crystals (Court *et al*., 2017).

2. The STZ is characterised by an assemblage of evaporite minerals (anhydrite, gypsum, and halite) that comprise an increasing fraction of the sediment with distance from the sea (up to 72% of sediments) (Lokier *et al*., 2013). The STZ can be further subdivided into three zones (Court *et al*., 2017):

   i. The lower STZ (landward of the pustular microbial mats) is a largely featureless zone that is only inundated during storm surges. Here surface sediments comprise silt to fine sand grade material with lenticular gypsum crystals (mm- to cm-scale) (Fig. 4.2.H).

   ii. The middle STZ is characterised by a 0.1-1.3 cm thick halite crust overlying dark brown silt and fine sand with mm-scale gypsum crystals (Fig. 4.2.I).

   iii. The upper STZ is characterised by a long-lived halite crust frequently overlain by fine-grained, carbonate-dominated aeolian sediments (Fig. 4.2.J, K)

The transect at Site 3-QL spans from the lower ITZ to the middle STZ. At Site 4, the tidal creek (Site 4-QL-TC) is situated in the lower ITZ (Fig. 4.3.A, B) and Site 4-QL-MM1 is located at the seaward edge of the microbial mat belt where the surface is covered in a 3 – 4 cm thick polygonal microbial mat and had no significant surface water pooling (Fig. 4.3.C). Site 4-QL-MM2 is in the centre of the microbial mats belt in a relative topographic low forming a semi-closed pool (maximum water depth 6 cm) (Fig. 4.3.D, F) and Site 4-QL-IU is located at the transitions between the pustular microbial mats and the featureless zone (Fig. 4.3.E). At Site 3-QL the landward limit of the microbial mats denotes the

boundary between intertidal and supratidal settings (Court *et al*., 2017) whereas at Site 4-QL, the zone landward of the microbial mats is described as a muddy tidal flat that is only inundated during spring tides (Lokier *et al*., 2013).

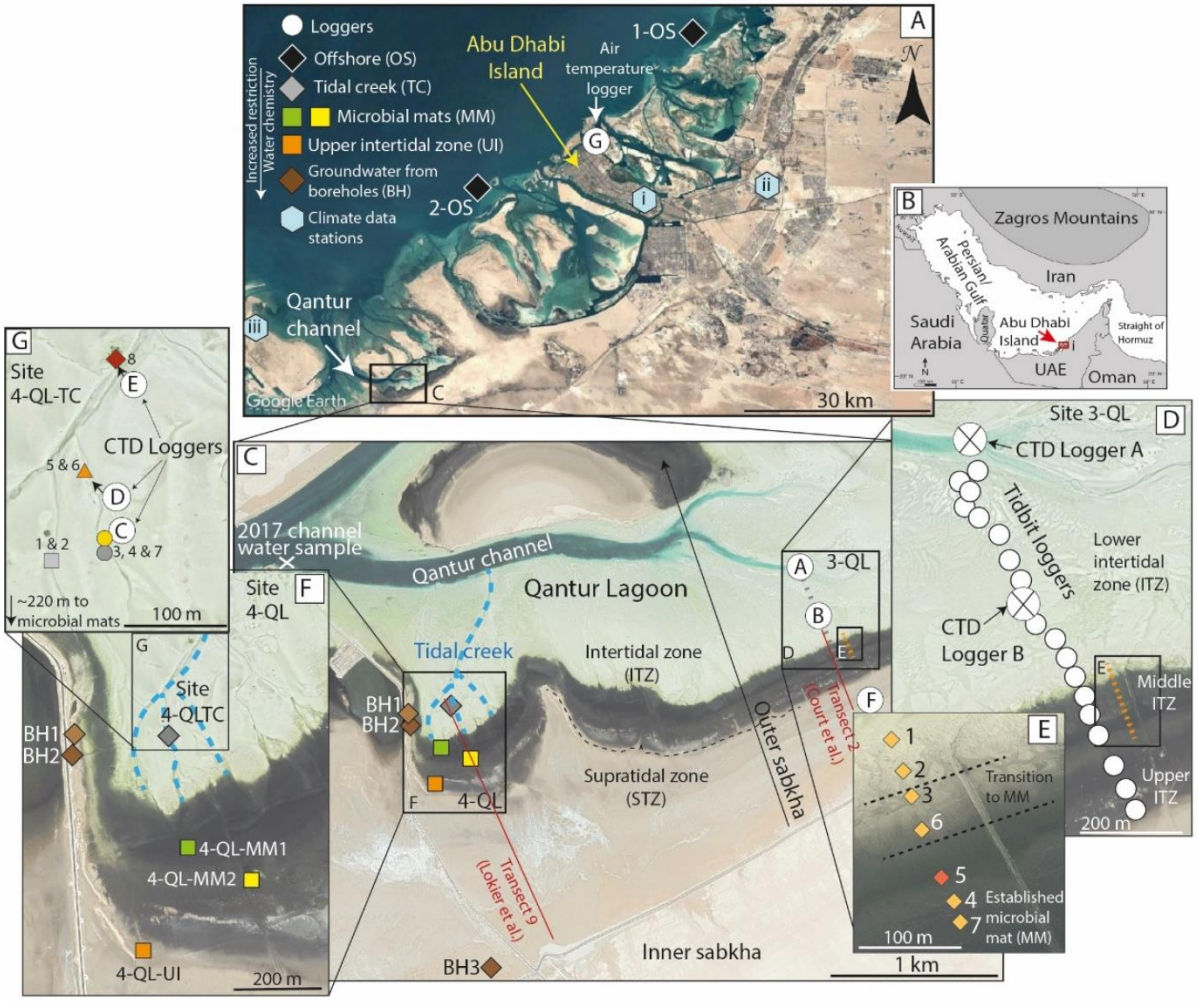

Figure 4.1. (**A**) Coastal Abu Dhabi (with regional location shown in (**B**) adapted from Lokier *et al*. (2013)) highlighting locations of offshore seawater samples (1-OS and 2-OS) (black diamonds); climate data stations (i) Abu Dhabi International airport, (ii) Abu Dhabi Bateen airport, and (iii) Abu Al Abyad meteorological station; and air temperature Logger G. (**C**) The study area surrounding Qantur lagoon, highlighting the location of CTD-Diver Loggers A and B, and a barometric logger (Logger F), the location of Sites 3-QL, 4-QL, surface water samples (site 4-QL -MM-1, -MM-2, -UI) and borehole locations (Boreholes 1, 2, and 3) (brown diamonds) and the Qantur channel water samples from 2017 (white cross). (**D**) Site 3-QL illustrating the location of CTD Logger A within Qantur channel, CTD Logger B within the lower intertidal zone, and the TidbiT temperature logger transect (small white circles). (**E**) Surface waters sampled during the flood tide across the middle intertidal zone (water samples collected from locations with orange diamonds, and *in situ* measurements from locations with red diamonds). (**F**) Sampling locations at Site 4-QL, with the tidal creek (4-QL-TC; grey diamond), microbial mat surface waters sites 4-QL-MM1 (green square), 4-QL-MM2 (yellow square), upper intertidal zone site 4-QL-UI1 (orange square), and Boreholes 1 and 2 (brown diamonds). (**G**) Sampling locations surrounding the tidal creek; highlighting the four locations of creek water samples collected on the 16th Jan. 2019 (small, numbered shapes); the locations of creek water samples collected on the 24th Oct. 2017 (grey circle) and Loggers C, D and E (white circles).

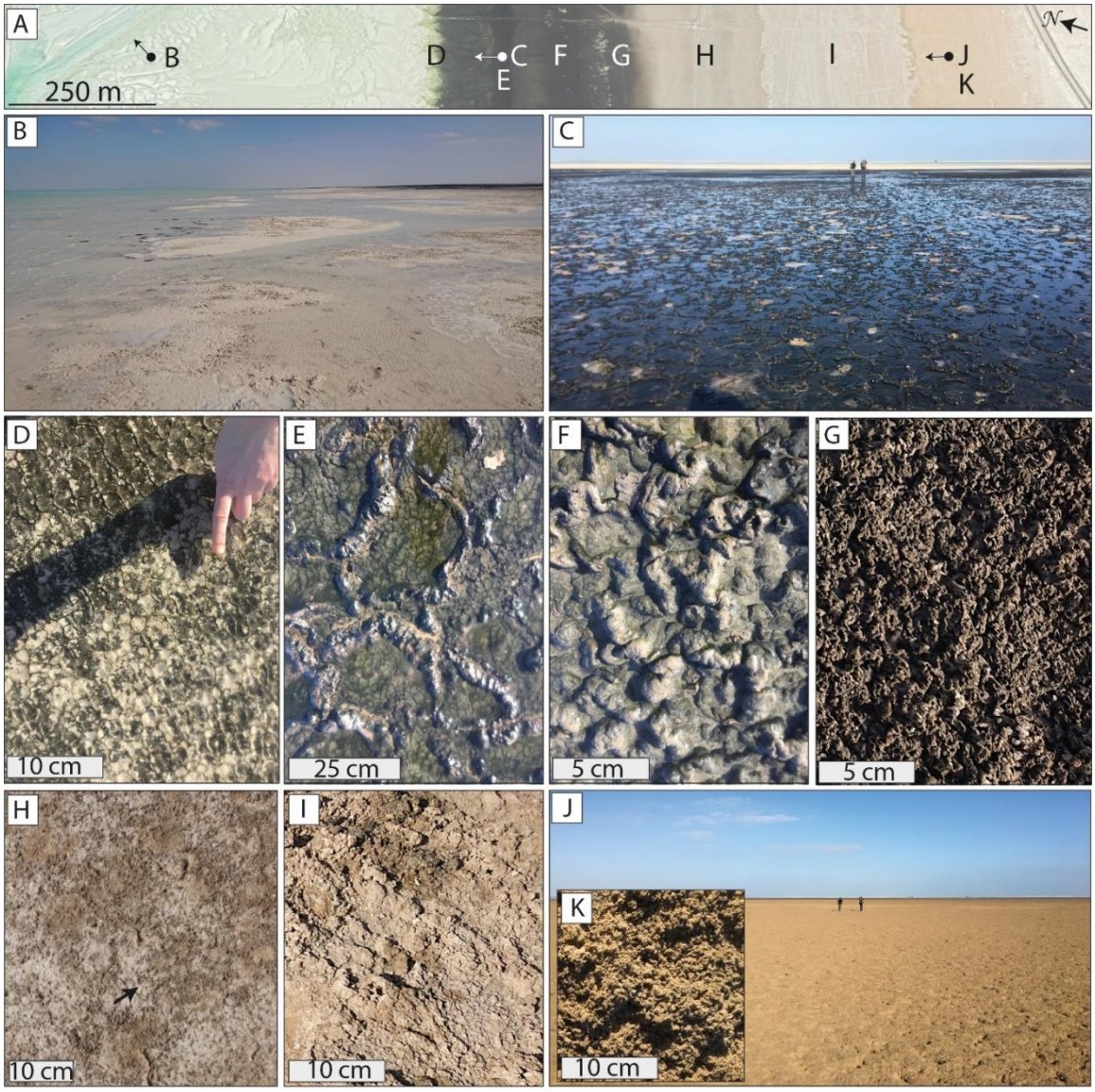

Figure 4.2. (**A**) Satellite image of the surface facies across the lower ITZ to STZ transect at Site 3-QL showing locations of photographs (**B**) to (**K**), with arrows denoting the direction the photograph was taken where relevant. (**B**) to (**K**) show surface facies as described by Court *et al*. (2017). (**B**) View parallel to the shoreline showing the muddy carbonate sediments of the Lower ITZ. (**C**) Microbial mats looking seaward at very low tide. (**D**) to (**G**) display varying microbial mat surface morphologies from the seaward (**D**) to landward margins of the mat zone (**G**); (**D**) small cm-scale polygons, referred to as 'spongey mats'; (**E**) polygonal mat structures from the central part of the mat zone with mm-scale (width) micro-polygonal cracks populating the interior of the polygons ('leathery mats'); (**F**) microbial divots and pustules (transition from leathery to pustular mats); and (**G**) the landward margin of the microbial mats, dominated by pustules: photo F shows a continuous mat, which become increasingly discontinuous further inland with increased desiccation. (**H**) the brown sediment of the 'featureless zone' with discontinuous mm-thick halite crust (arrow) (image from Court *et al*., 2017). (**I**) The 'ephemeral halite zone' with a surface halite crust 0.1-1.3 cm thick and anhydrite crust. (**J**) The 'long-lived halite zone' looking seaward with a close-up of the sediment surface (**K**) showing a halite crust 0.5-2.0 cm thick, covered with soft sediment and pock marks caused by rain.

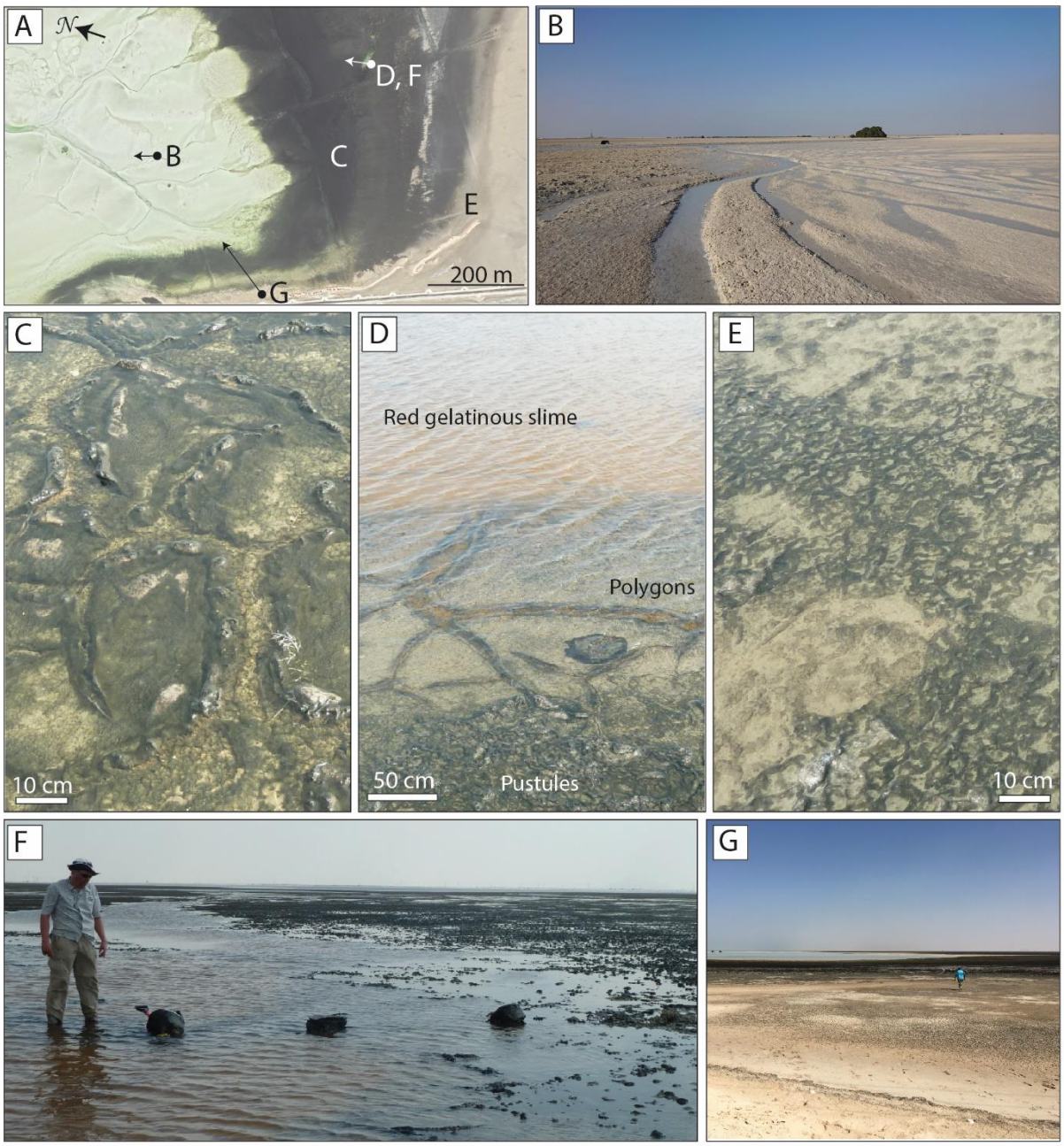

Figure 4.3. (**A**) Satellite image of the surface facies across the lower ITZ to supratidal transect at Site 4-QL showing locations of photographs (**B**) to (**G**), with arrows denoting the direction the photograph was taken where relevant. (**B**) Site 4-QL surface facies with the tidal creek in the lower ITZ looking seaward (apparent contrast in sediment colour west to east of creek are due to low light level). (**C**) Surface morphology of microbial mat polygons at MM-1; (**D**) microbial mats at site MM-2 showing pustular microbial mast in the shallow foreground which transitions into microbial mat polygons and then to red gelatinous slime within the deepest parts of the pond. (**E**) Thin pustulous microbial mats of the upper intertidal zone (site 4-QL-UI), which are easily ripped and transported by the wind during exposure at low tides; and (**F**) the semi enclosed pond at site MM-2 looking seaward. (**G**) View looking seawater from the supratidal zone, across the microbial mats to the flooded lower ITZ.

Table 4.1. Summary of field site names and locations, with the dates sampled for water chemistry samples, and corresponding tidal phase.

Site #	Coastal zone	Sample type	Site name	GPS	Date sampled	Nearest spring/neap tide
1	Offshore (OS)	Surface and bottom water chemistry	1-OS	24°38'19.62"N 54°30'53.16"E	18/10/2017	19th Oct: Spring
2	Offshore (OS)		2-OS	24°25'54.18"N 54°12'35.22"E	22/10/2017	19th Oct: Spring
3	Intertidal transect – central Qantur lagoon (QL)	Flood tide surface water chemistry transect	3-QL	24° 9'20.02"N 54° 7'1.29"E to 24° 9'13.23"N 54° 7'4.47"E	07/01/2019	6th Jan: Spring
4	Intertidal transect – western Qantur lagoon (QL)	Flood tide chemistry of tidal creek (Lower intertidal)	4-QL-TC	24° 8'57.21"N 54° 5'9.92"E	24/10/2017 16/01/2019	28th Oct: Neap 14th Jan: Neap
		Ebb tide chemistry of tidal creek (Lower intertidal)		24° 8'57.54"N 54° 5'10.07"E	16/01/2019	14th Jan: Neap
		Microbial mat surface water chemistry (Middle to upper intertidal)	4-QL-MM1	24° 8'44.08"N 54° 5'11.40"E	06/02/2014	6th Feb: Neap
			4-QL-MM2	24° 8'43.71"N 54° 5'17.41"E	06/02/2014	6th Feb: Neap
		Upper intertidal zone surface water chemistry	4-QL-UI	24° 8'36.92"N 54° 5'6.64"E	05/02/2014	6th Feb: Neap
5	Groundwater from boreholes (GW)	Ground water chemistry from three boreholes	BH1 BH2 BH3	1: 24° 8'55.89"N 54° 4'58.72"E 2: 24° 8'55.70"N 54° 4'58.43"E 3: 24° 8'53.75"N 54° 4'59.25"E	15/01/2019	14th Jan: Neap

Table 4.2. Summary of Logger deployment.

Logger	Type	Coastal zone and site name	Duration logging	GPS	Date deployed	Date collected
A	CTD-diver	Intertidal: 3-QL	1 yr, 9.3 months	24° 9'37.98"N 54° 6'50.94"E	05th Jan. 2019	19th Oct. 2020
B	CTD-diver	Intertidal: 3-QL	~31 hrs	24° 9'23.7"N 54° 6'58.92"E	05th Jan. 2019	06th Jan. 2019
C	CTD-diver	Intertidal: 4-QLTC	~20 hrs	24° 9'5.70"N 54° 5'10.57"E	15th Jan. 2019	16th Jan. 2019
D	CTD-diver	Intertidal: 4-QLTC	2 hrs	24° 8'57.31"N 54° 5'10.33"E	16th Jan. 2019	16th Jan. 2019
E	CTD-diver	Intertidal: 4-QLTC	3 hr 45 mins	24° 9'5.46"N 54° 5'10.68"E	16th Jan. 2019	16th Jan. 2019
F	Barometric logger	Supratidal	~ 3 days	24° 8'59.58"N 54° 7'11.82"E	12th Jan. 2019	15th Jan. 2019
G	TidbitT v2	Coastal Abu Dhabi	~8 months	24° 30'47.06"N 54° 23'25.27"E	16th May. 2019	11th Jan. 2019
TidbiT transect	TidbitT v2	Intertidal: 3-QL	~7 days	24° 9'37.98"N 54° 6'50.94"E to 24° 9'8.58"N 54° 7'7.14"E	05th Jan. 2019	12th Jan. 2019
H	CTD-diver	Boreholes	~3 hours	See Table 1	15th Jan. 2019	15th Jan. 2019

4.4 Methods

Samples for this study were obtained as part of three field campaigns in February 2014, October 2017, and January 2019. Surface water chemistry was assessed by combining water sampling and analysis with *in situ* records of salinity, temperature, and water depth recorded with CTD-Diver loggers (obtained from ©2020 Eijkelkamp Soil and Water). Furthermore, HOBO TidbiT v2 temperature loggers were deployed at the sediment surface at Site 3-QL, a HOBO-Diver was deployed at the sediment surface as a barometric logger (Logger F, Fig. 4.1.A) from 12th – 15th Jan. 2019 to record local air pressure, and a TidbiT v2 temperature logger was deployed in the shade (Logger G, Fig. 4.1.A) to record local air temperature from 16th May 2018 – 11th Jan. 2019.

4.4.1 Data loggers

CTD-Diver loggers (©2020 Eijkelkamp Soil and Water) were deployed to compare record variations in temperature, specific electrical conductivity (SEC), and pressure (water level) with accuracies of ±0.1 °C, ±1% and ±0.5 cm H_2O respectively. Logger locations and deployment dates are detailed in Table 4.2 and locations are marked in Figure 4.1. From the lower intertidal zone at Site 3-QL, one long-term CTD-Diver (Logger A) was deployed within the tidal channel (7th Jan. 2019 – 20th Oct. 2020) and a second short-term logger (Logger B) was located at the sediment surface (5th – 6th Jan. 2019) (Fig. 4.1.D). Three short-term (<2 days) CTD-Divers were installed at Site 4-QL-TC; Logger C was situated on the bank of

tidal creek, ~1.15 m elevation above Logger A; and Logger D and E were within the creek, ~90 m and 250 m seaward of Logger C respectively and ~0.75 m and 0.55 m elevation above Logger A respectively (Fig. 4.1.G).

Pressure (mbar) was converted to water level by subtracting the barometric pressure under the assumption that 1 cm of H_2O = 1 mbar. Local atmospheric pressure was recorded with a HOBO-Diver (12^{th} – 15^{th} Jan. 2019) (Logger F, Fig. 4.1.A) and used to correct Logger B. Loggers A, C, D, and E, were corrected with mean monthly air pressure from Abu Dhabi International airport (Location (i), Fig. 4.1.A) (Jan. 2019 – Oct. 2020) accessed from ©World Weather Online (2021). The tidal range describes the daily maximum water level minus the minimum daily water level.

All water levels are reported relative to the local datum established during this study at the base of the tidal channel at Site 3-QL (Logger A, Fig. 4.1.C). Logger A lost its protective end cap *in situ*, which may be responsible for a decline in conductivity readings around September 2019. This data has therefore been disregarded. Furthermore, when water level was <4-7 cm in the channel, the SEC logger briefly stops recording, suggesting that the logger may become exposed to the air. When these periods of logger exposure coincide with near-mid-day solar radiation, temperature also peaks, suggesting there is a localised warming effect on the dark coloured exposed logger. These peak temperatures have also been disregarded.

Conductivity was converted to salinity using the relationship between SEC and total dissolved solids in parts per thousand (TDS_{ppt}). For waters within SEC <80 mS, the equation from Williams, (1986) ($S = 0.4665x^{1.0878}$, R^2 0.99, where S = salinity and x = SEC) was applied, however, the equation is only valid ≤100 mS. Therefore, seawaters with SEC >80 mS were converted to TDS using an equation developed from Abu Dhabi surface and porewaters samples collected from the 2019 field campaign. Total dissolved solids were calculated as the sum of milliequivalents per litre of major anions (Cl^- and SO_4^{2-}), cations (Na^+, Mg^{2+}, Ca^{2+}, K^+ and Sr^{2+}) and bicarbonate alkalinity (HCO_3^-). Samples with an ion balance error (IBE) <-5 or >+5 were removed, and as were samples with SEC >175 mS, as above this threshold the relationship between SEC and TDS became non-linear. The linear regression model was used to convert SEC logger data to salinity as TDS_{ppt} ($y = 0.8711x - 14.9$, where x = SEC and y = TDS (R^2 0.99, n = 106)) for SEC 80-175 mS.

A set of HOBO TidbiT v2 temperature loggers were deployed at the sediment surface across a ~1 km transect at Site 3-QL (5^{th} - 12^{th} Jan. 2019). The loggers record the onset of tidal inundation, which when calibrated against the water depth in the channel (Logger A), provides the surface elevation of the transect relative to Logger A (to the nearest 5 m). On the 6^{th} of January coastal Abu Dhabi experience a relatively small spring tide (tidal range 1.64 m), moving towards a neap tide on the 14^{th} (tidal range 1.25 m), and a large spring tide on the 21^{st} of January 2019 (tidal range 1.85 m).

4.4.2 Additional climate data

The lunar calendar (2014, 2017, and 2019) for Abu Dhabi was accessed via ©tides4frishing (2021). Mean monthly solar radiation (1982-2020) for Abu Al Abyad station (Location (iii), Fig. 4.1A) was obtained from the National Centre of Meteorology, Ministry of Presidential Affairs, UAE (2021). Mean, minimum and maximum daily air temperature records for January 2019 to October 2020 were obtained for Abu Dhabi Bateen airport (Location (ii), Fig. 4.1.A) from ©Meteostat (2021). Daily solar radiation was also estimated based on the latitude and date, using the online calculator provided by pveducation (Bowden and Honsberg, 2021). Climatological data including hourly air temperature, windspeed, wind direction, weather descriptions, precipitation, humidity, cloud cover, heat index and air pressure was purchased from ©WorldWeatherOnline (2021) for Abu Dhabi Bateen airport (Location (ii), Fig. 4.1.A).

4.4.3 Water sample collection and analysis

4.4.3.1 Sample collection

The open marine surface seawater samples were collected in 2017 (Fig. 4.1.A, Site 1-OS and 2-OS), using 5 cm long Rhizon CSS pore-water samplers (pore diameter 0.12 µm - 0.18 µm, providing instant filtration). Bottom water samples from the open marine sites were collected in a Van Dorn horizontal open water sampler, <1 m above the sediment-water interface (~5.5 m water depth), stored in glass bottles and filtered through Rhizons on return to the lab. Water samples were also collected using Rhizons at Site 3-QL (7th Jan. 2019) over ~2 hours following a small spring tide on the 6th January, as the tidal front progressed landward across the ITZ over a ~250 m transect (Fig. 4.1.E).

At Site 4-QL, situated in the western side of Qantur lagoon, surface waters were collected with Rhizons from a shallow tidal creek that crossed the ITZ seaward of the microbial mats throughout the day during two field campaigns (Site 4-QL-TC). The first batch was collected over 5 hours, predominantly during a mid-phase tide on 24th October 2017 between a large spring tide (19th) and a neap tide on the (28th), and the second batch was collected over ~6 hours on 16th January 2019 following a neap tide (14th), from several locations within the creek (Fig. 4.1.G). Inland surface water samples were also collected from the microbial mats (middle to upper ITZ) and the upper ITZ edge of the mats (Sites 4-QL- MM1, -MM2, -UI respectively) between the 5-6th February 2014 and filtered through 0.22 µm Millex filters. The inland surface waters were sampled around a neap tide (6th Feb.). The 5th had the first and largest high tide at 05:50 (1.9 m), low tide at 12:20 (0.7 m), and the second high tide at 17:57 (1.6 m). The 6th had the largest high tide at 06:30 (1.9 m), low tide at 13:30 (0.7 m) and the second high tide at 18:55 (1.4 m).

4.4.3.2 Water chemistry analysis

During all three field campaigns, porewater *p*H, specific electric conductivity (SEC), redox potential (Eh) and dissolved oxygen (DO) were measured within 6 hours of collection using a HQ40d Hach multi-meter and attachable probes, with accuracies of ±0.02 pH units, ±0.5%, ±0.05% and ±0.01% respectively. Bicarbonate alkalinity was determined in triplicate by Gran titration (Sass and Ben-Yaakov, 1977) with a mean relative analytical precision coefficient of variance (CV) of 0.6%. Aliquots were filtered and returned to the UK for further analysis.

All water samples were gravimetrically diluted for major cation analysis (Na^+, Mg^{2+}, Ca^{2+}, K^+) and analysed via inductively coupled plasma atomic emission spectroscopy (ICP-OES; Agilent series 710 ICP-OES). Major anions (Cl^- and SO_4^{2-}) from 2014 were analysed via colorimetric analysis (UV-VIS) on a Discrete analyser and major anions from 2017 and 2019 were measured isocratically on a DIONEX ion chromatograph (Dionex™ ICS-5000+). All ion analysis had a CV of <1.25% based on multiple injections. The mean ion balance error (IBE) was -0.8±2.5% (n = 26). Major ions were not measured for the 2017 tidal creek water samples (Site 4-QL-TC) and were therefore estimated based on the conductivity when modelling carbonate chemistry in PHREEQC (*p*H and alkalinity were measured for 2017 tidal creek samples).

Given the range of surface water salinities (~35-80 ‰) both CO2SYS (Pelletier *et al.*, 2007) and the USGS aqueous geochemical model PHREEQC version 3.5.0 (Parkhurst and Appelo, 2013) using the Pitzer database (Pitzer, 1973; Pitzer and Mayorga, 1973), were applied to calculate the partial pressure of CO_2 (pCO_2) and saturation indices ($\log(IAP/K_{sp})$) of aragonite (SI_{arag}) and calcite (SI_{calc}) (see methods discussion in Chapter 2.2). PHREEQC was also applied to calculate dolomite, gypsum, and halite saturation index (SI_{dol}, SI_{gyp}, SI_{hal} respectively) using the Pitzer database. Uncertainties for the carbonate variable and saturation indices calculated in CO2SYS and PHREEQC are presented in Table 4.3. As surface water *p*H was sometimes measured in the field and sometimes measured in the lab, PHREEQC was used to normalise *p*H to the estimated ocean surface temperature for offshore Sites 1-OS and 2-OS (30 °C) and to measured and predicted *in situ* creek temperatures (Fig. 5.13.B), and *p*H and SI are reported based on these calculations.

Table 4.3. Uncertainties in variables modelled with PHREEQC using the Pitzer database and CO2SYS.

	PHREEQC-Pitzer	**CO2SYS**
pCO_2 **(%)**	±0.019%	±0.002%
CO_3^{2-} **activity**	±0.023 log units	±0.02 log units
SI_{arag}/SI_{calc}	±0.019 log units	±0.03 log units
$SI_{dol}/SI_{dolDiss}$	±0.038 log units	n/a
SI_{hal}	±0.008 log units	n/a
SI_{gyp}/SI_{anhy}	±0.007 log units	n/a

4.5 Results

4.5.1 Defining intertidal zones

Abu Dhabi experiences a semi-diurnal tide with one daily high tide larger than the other. The relative difference between daily maximum and minimum water levels (tidal range) varies from 1.43 m (neap periods) to 1.79 m (spring periods) and with more variable water levels during daily high tides than low tides. The broad ITZ (average 1 km) reflects the low angle of sediment surface. For the following analysis we use the highest and lowest daily water levels in the channel recorded by Logger A. Distance travelled inland across the ITZ is also given relative to Logger A and calculated with the elevation profile generated with the TidbiT temperature loggers and extended with surface elevations from Court *et al*. (2017) for distances >850 m (Fig. 4.4).

Defining spring tide periods from the date of the full and new moons ±1 day, during 2019 spring periods the daily tidal ranges were ~10% higher than the annual mean daily tidal range (Table 4.4) and would have travelled an average of ~85 m higher up the shoreface at high spring tides (av. = 905 m, sd. range = 720 – 1110 m), and exposed an additional ~5 m during spring low tides (av.= 10 m, sd. range = 0-15 m) compared to the 2019 mean (Fig. 4.5).

In contrast, during 2019 neap periods (defined from the date of the first and third quarter moons ±1 day), the daily tidal range was ~12% lower than the annual 2019 mean daily tidal range (Table 4.4) and would have reached an average of ~145 m lower down the shoreface at high neap tides (av. = 680 m, sd. range = 615 - 885 m), and exposed ~4 m less during neap low tides (av.= 20 m, sd. range = 10-25 m) compared to the 2019 mean (Fig. 4.5).

To assess the range of annual hydrodynamic variations in temperature, salinity, and water level within the tidal channel, a subset of data was examined in more detail for a one-month period in winter (20th Jan. – 20th Feb. 2019) and summer (20th Jul. – 19th Aug. 2019). The specific focus of this analysis was to compare the effect of spring, neap, and mid-phase tides (± 1 day) (Fig. 4.7 and 4.8; Table 4.5 and 4.6). The summer month had slightly higher mean water levels and maximum daily water levels than annual

spring tides, and the winter month had the lowest mean and maximum daily water levels of the investigated time periods (Table 4.4). Both are discussed in greater detail in section 4.5.2.1.

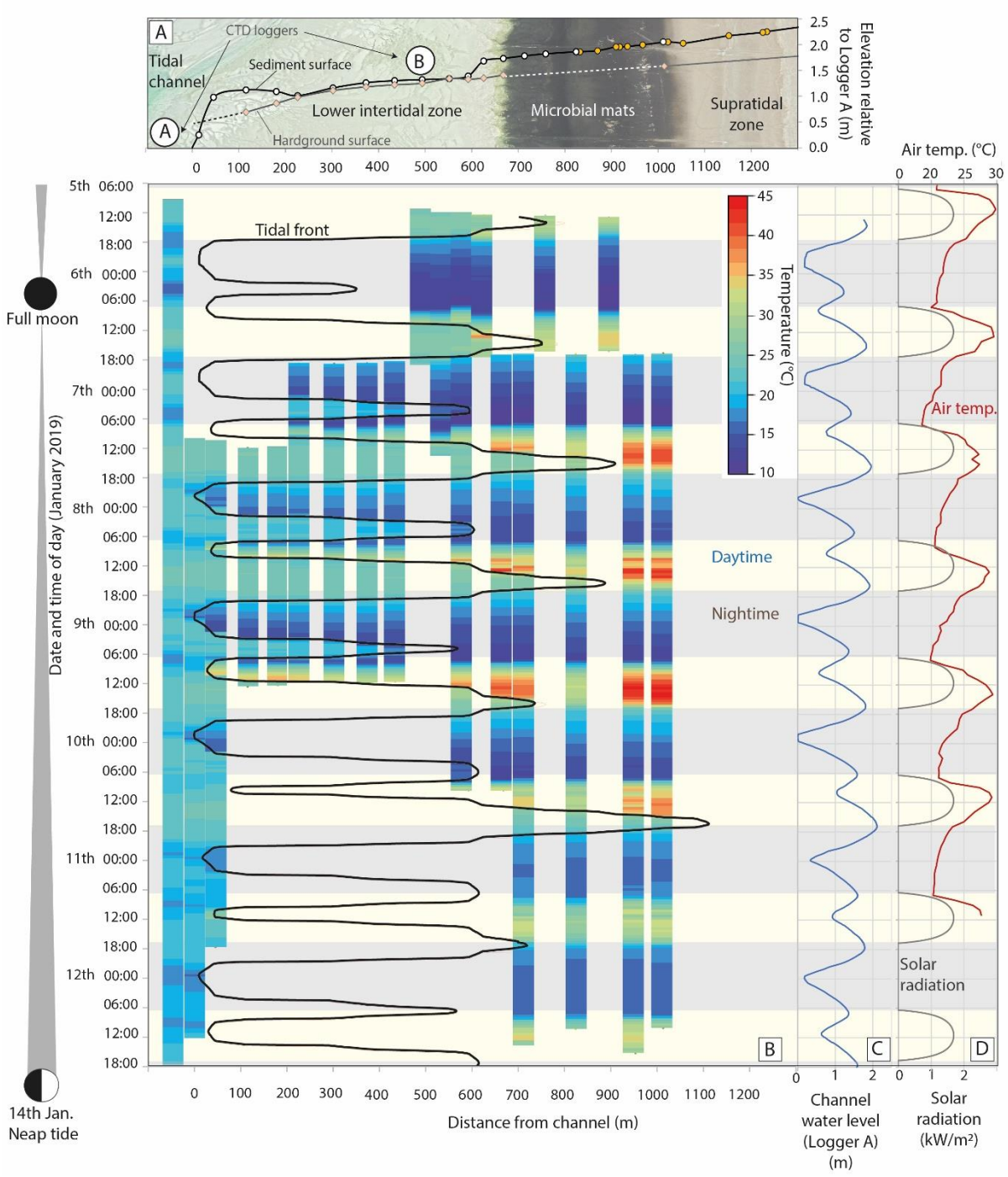

Figure 4.4. (**A**) Location of the TidbiT temperature logger transect at Site 3-QL (white points) with the elevation of the sediment surface relative to Logger A in the tidal channel. The transect was extended landward with surface elevations from Court *et al*. (2017) (yellow points) and highlights the location of Loggers A and B. Pink diamonds show the depth of the basal hardground. Surface elevation was calculated for this study by relating the timing of flooding (recorded by changes in temperature) relative to water level in the channel. (**B**) Coloured bars represent surface temperatures recorded across the transect by the TidbiT temperature loggers (5th – 12th Jan. 2019), with the black line denoting the location of the tidal front. (**C**) Water level recorded in the channel (Logger A); and (**D**) air

temperature (red line) recorded near the coast on Abu Dhabi Island (Logger G, Fig. 1A) and predicted solar radiation for 24° latitude, though this does not account for cloud effects (grey line, accessed from pveducation, 2021).

Table 4.4. Mean, daily maximum, and daily minimum water level in the channel. All water levels are relative to the local datum (Logger A).

	Number of days per period	Mean water level	Maximum daily water level	Minimum daily water level	Mean daily tidal range
Full long-term logging period: Jan 2019 – Oct 2020	635	1.17 ±0.49 m	1.87 ±0.20 m (range 1.28-2.50 m)	0.26 ±0.26 m (range 0-0.99 m)	1.62 ±0.27 m
One calendar year: 2019 ***Jan – Dec 2019***	365	1.15 ±0.48 m	1.84 ±0.20 m (range 1.28-2.50 m)	0.23 ±0.18 m (range 0-0.78 m)	1.62 ±0.25 m
Winter example period: 20th Jan – 20th Feb 2019	16	1.01 ±0.49 m	1.73 ±0.17 m (range 1.42-2.08 m)	0.09 ±0.09 m (range 0-0.42 m)	1.64 ±0.20 m
Summer example period: 20th Jul – 19th Aug 2019	16	1.25 ±0.48 m	1.99 ±0.14 m (range 1.67-2.16 m)	0.27 ±0.21 m (range 0-0.69 m)	1.72 ±0.30 m
2019 Spring tides: ***Full and new moon ±1 day***	60	1.17 ±0.52 m	1.95 ±0.16 m (range 1.59-2.25 m)	0.16 ±0.16 m (range 0.01-1.06 m)	1.78 ±0.22 m
2019 Neap tides: ***Half moon ±1 day***	70	1.05 ±0.59 m	1.74 ±0.17 m (range 1.28-2.20 m)	0.31 ±0.15 m (range 0.02-0.65 m)	1.46 ±0.19 m

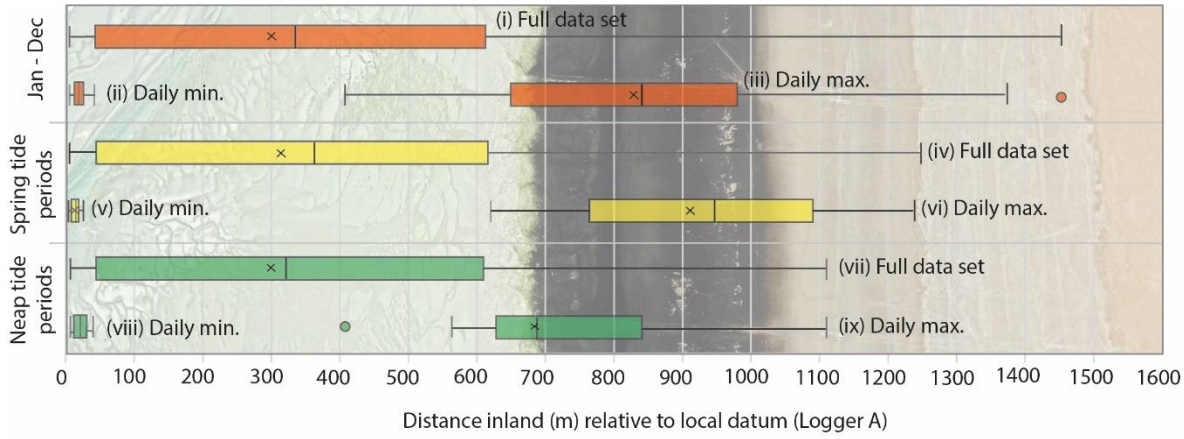

Figure 4.5. Site 3-QL ITZ tidal ranges as distance travelled inland by the tide relative to the CTD-diver (Logger A) within the tidal channel and the elevation profile presented in Fig. 4.4. Box plots represent a one-year period (Jan – Dec. 2019: orange) with the full data set (i), the daily minimum water level (ii), and daily maximum water level (iii); spring tide periods in 2019 (yellow) (iv), the daily spring minimum water level (v) and daily spring maximum water level (vi); and neap tide periods in 2019 (green) (vii) with the neap daily minimum water level (vii) and the neap daily maximum water level (ix).

4.5.2 Long-term climate variability and CTD-Diver records from the tidal channel at Site 3-QL

Mean windspeed at Abu Dhabi Bateen airport over the long-term logging period was 4.4 ±1.3 m s^{-1} (range 1.7 – 10.0 m s^{-1}), predominantly from the WNW to NW (the "Shamal") (Fig. 4.6.Ai). The summer example period experienced average wind speeds of 4.3±0.8 m s^{-1}, with a dominant WNW direction and the winter example period 4.5 ±1.7 m s^{-1}, with a dominant NW direction (Fig. 4.6.Aii, iii). Mean daily atmospheric pressure varies throughout the year and was significantly higher during the winter period (1018 ±2 mbar) than the summer period (996±2 mbar) (Fig. 4.6.B) (Abu Dhabi Bateen airport) (location (i), Fig. 4.1.A).

Mean monthly solar radiation (1982-2020) for Abu Al Abyad station (Location (iii), Fig. 4.1.A) was typically lowest in December and January and highest in May and June (Fig. 4.6.C). During the long-term logging period (18th Jan. 2019 - 19th Oct. 2020), December to April were the cloudiest months and June to September were the clearest (Fig. 4.6.C). Air temperature at Abu Dhabi Bateen Airport (Location (i), Fig. 4.1.A) ranged from 12.8-47.0 °C during the long-term logging period (Fig. 4.6.D). In winter months (Jan.-Feb. 2019 and Dec. 2019-Feb. 2020) mean air temperature (21.4 ±2.0 °C) was ~14.5 °C lower than in summer months (Jun.-Aug. 2019 and 2020) (35.9 ±2.3 °C) (Fig. 4.6.D).

During the long-term logging period, water temperature at the base of the channel ranged from 12.5-41.6 °C (Fig. 4.6.E) (av.= 27.8 ±5.4 °C), in winter months mean water temperature (20.9 ±2.6 °C) was 12.4 °C lower than in summer months (33.3 ±1.8 °C) (Fig. 4.6.E). Channel water level appeared slightly lower during January to May and were slightly higher June to December. Mean water level in the channel over the long-term logging period was 1.17 ±0.48 m, compared to 1.08 ±0.49 m in winter months and 1.28 ±0.48 m in summer months (Fig. 4.6.F).

Salinity (TDS) (recorded Jan.-Sep. 2019) ranged from 34.4 – 81.5‰ (av. = 60.6 ±6.3‰) (Fig. 4.6.G). Salinity displayed an overall increasing trend from January to August, and typically displayed an inverse relationship with water level, although on the 9th, 19th and 23rd of February and 7th March, salinity was particularly low (34.4 – 44.6‰) even when water level was high. Based on a mean offshore salinity of 37.9 ±2.1 ‰ (n=4), mean channel water salinity in winter months (53.7 ±4.9‰) (Jan. – Feb. 2019) was ~42% higher than offshore, whereas mean channel water salinity in summer months (65.0 ±4.5‰) (Jun.-Aug. 2019) (Fig. 4.6.G) was ~72% higher than offshore.

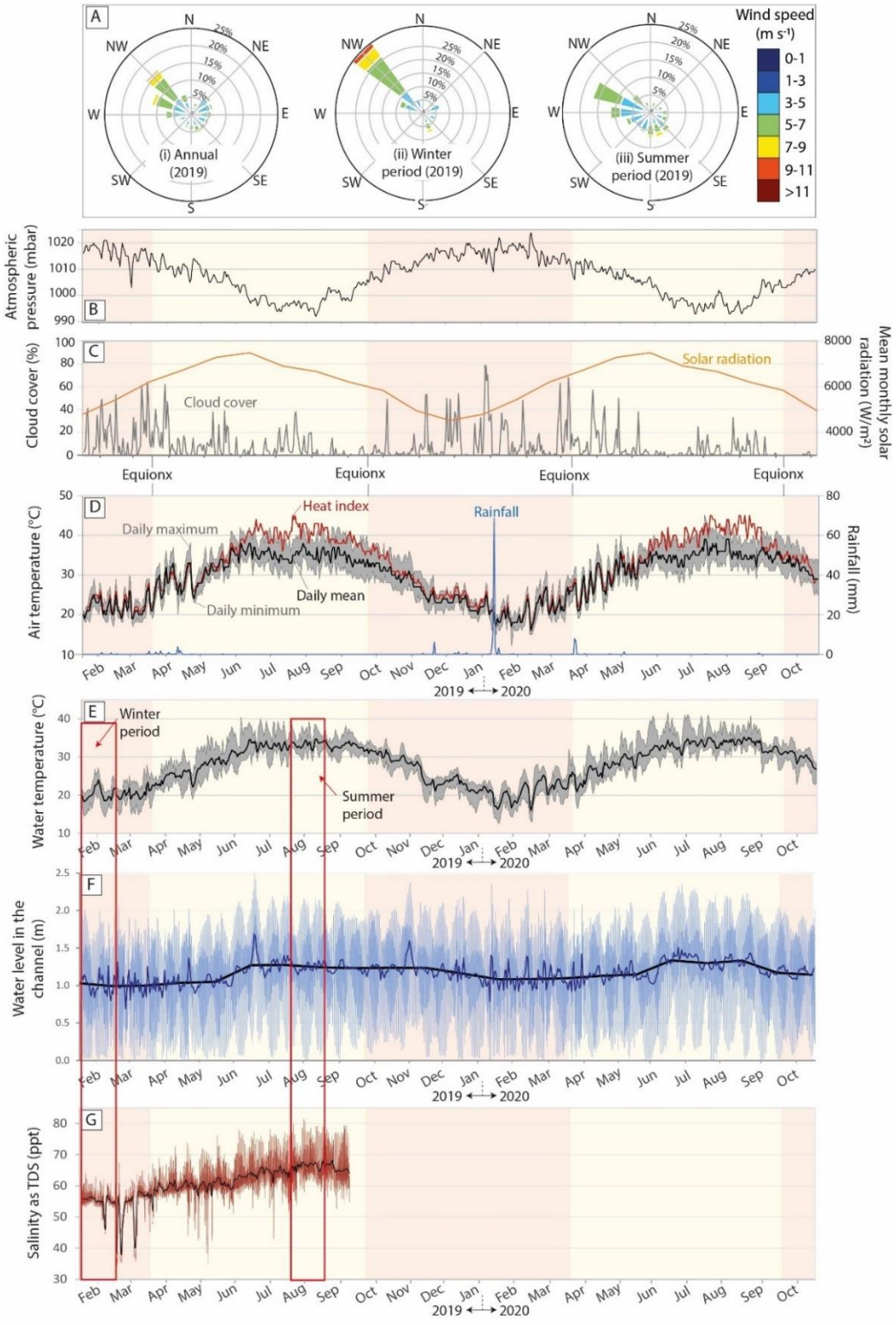

Figure 4.6. (**A**) Wind roses showing the dominant wind directions from the NW and WNW during (**i**) Jan.-De. 2019; (**ii**) the winter example period (20th Jan. - 20th Feb.); and (**iii**) the summer example period (20th Jul. – 19th Aug.). (**B-D**) show climate data corresponding with the full logging period (Jan. 2019 – Oct. 2020) predominantly from Abu Dhabi Bateen airport (location (i), Fig. 1A) for (**B**) atmospheric pressure (mbar); (**C**) cloud cover (grey) and mean monthly solar radiation at Abu Al Abyad meteorological station (National Centre of Meteorology, 2021); and (**D**) air temperature and rainfall. (**E-G**) present long-term CTD-diver data from the tidal channel at Site 3-QL (Logger A, location in Fig. 4.1.A) showing; (**E**) channel water temperature daily range (grey) with daily mean (black line); (**F**) water level in the tidal channel (blue) with a daily running mean (dark blue) and a monthly running mean

(black); and (**G**) salinity (red) with daily mean (black). Red boxes (D-E) highlight the month-long winter and summer periods compared in greater detail in Fig. 7 and 8, respectively.

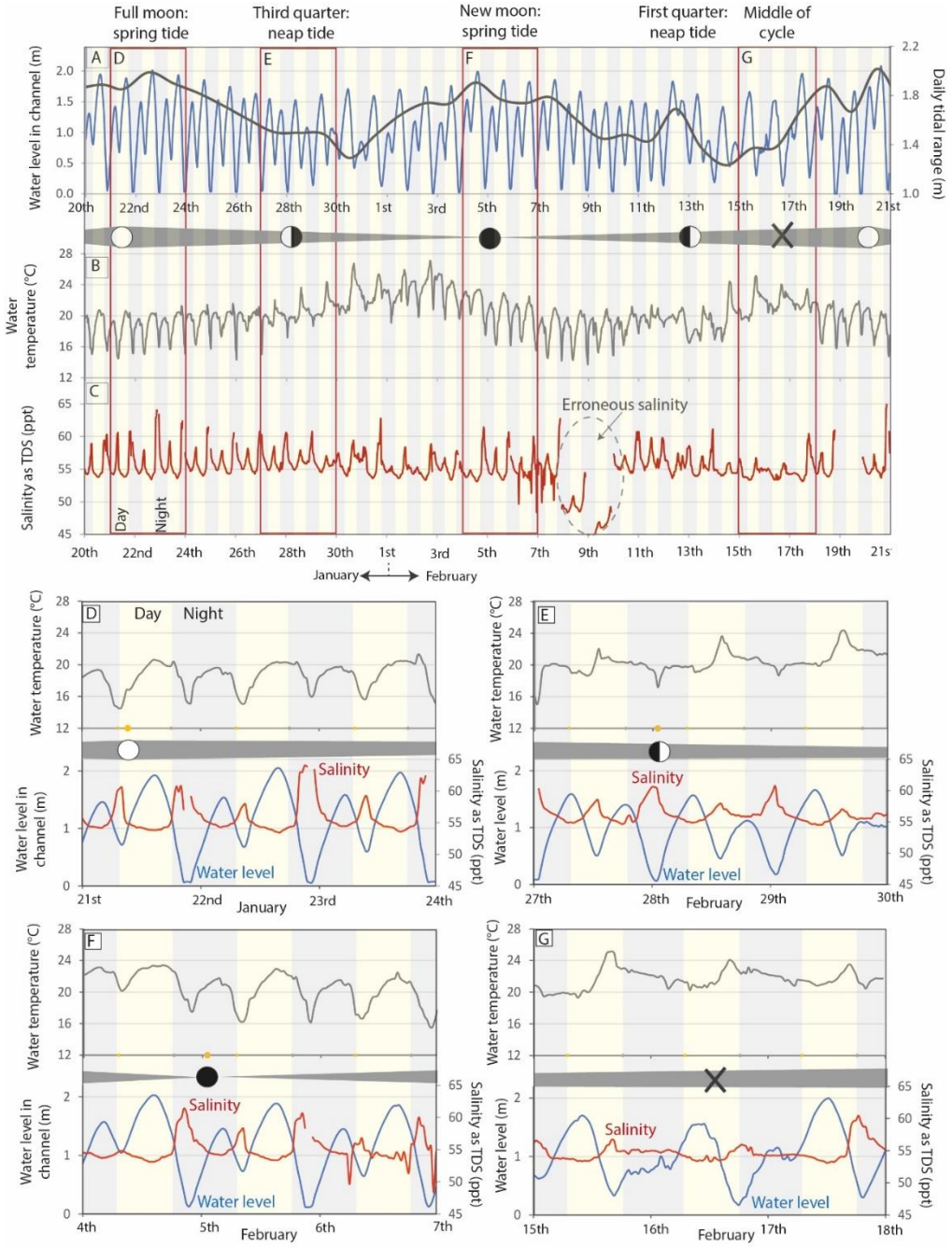

Figure 4.7. Winter 2019 (20th Jan. - 20th Feb.) long-term CTD-Diver data from the tidal channel showing; (**A**) water level in the channel (blue) and the daily tidal range (grey), with the moon-phases illustrated below and red boxes highlighting the areas detailed in the following figures. (**B**) Water temperature and (**C**) salinity (red) and the tidal coefficient (grey). **D** to **F** illustrate record changes in temperature (grey line, upper panel); water level in the channel (blue line lower panel) and salinity (red line lower panel) during different moon phases. (**D**) 21st – 23rd January, throughout a spring tide surrounding a full moon; (**E**) 27th - 30th February throughout a neap tide surrounding a third quarter moon; (**F**) 4th – 6th February throughout a spring tide surrounding a new moon, and (**G**) 15th – 17th February throughout a mid-way tide half-way between a first-quarter moon and a full moon.

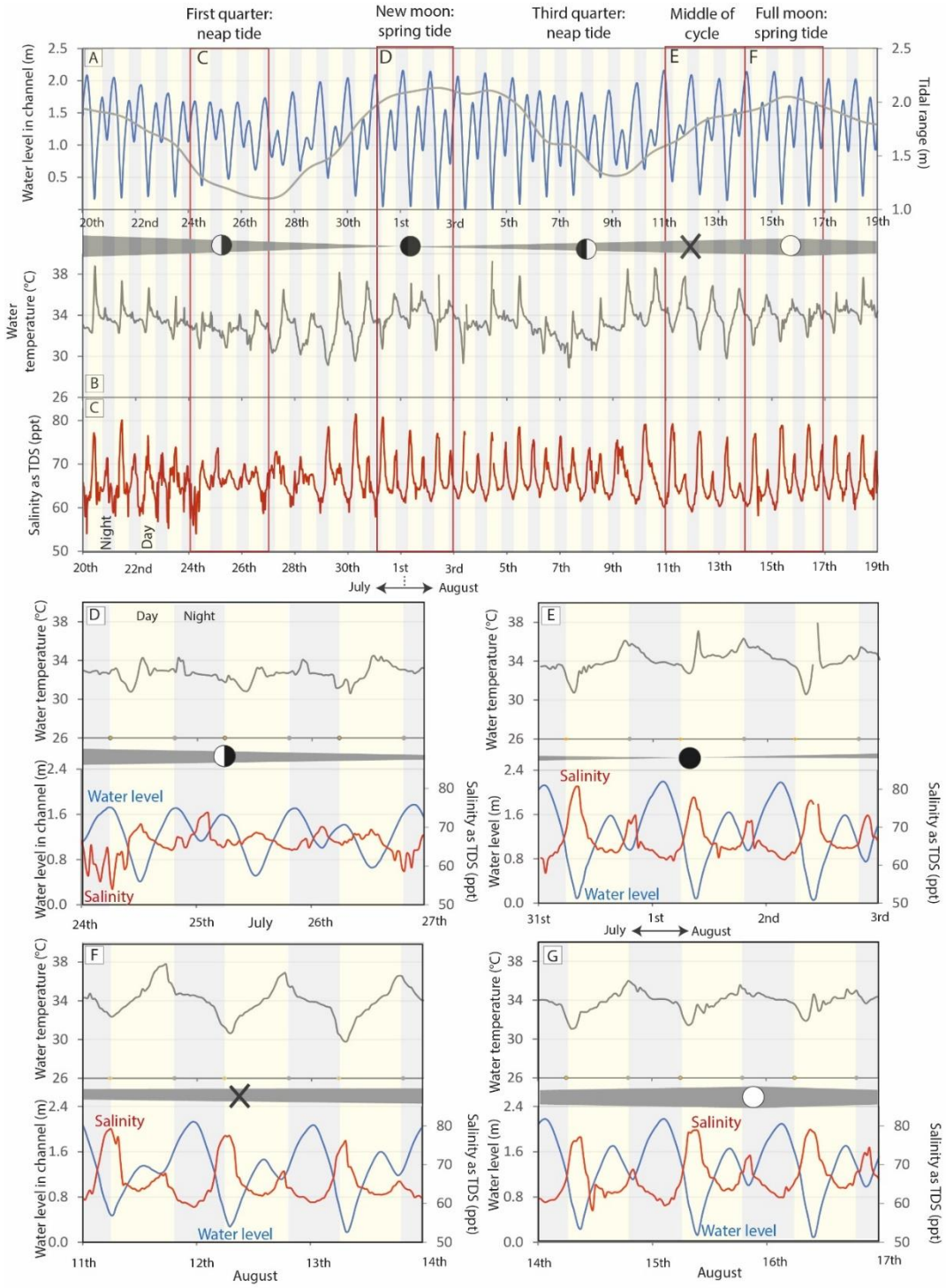

Figure 4.8. Summer 2019 (20th Jul. – 19th Aug.) long-term CTD-Diver data from the tidal channel showing; (**A**) water level in the channel (blue) and the tidal range (grey) with the moon-phases illustrated below and red boxes highlighting the areas detailed in the following figures. (**B**) Water temperature and (**C**) salinity (red) and the tidal coefficient (grey). **D** to **G** illustrate record changes in temperature (grey line, upper panel); water level in the channel (blue line lower panel) and salinity (red line lower panel) during different moon phases; (**D**) 24th – 27th July throughout a neap tide surrounding a first-quarter moon; (**E**) 31st July – 3rd August, throughout a spring tide surrounding a new moon; (**F**) 11th – 14th August throughout mid-way tide half-way between a third-quarter moon and a full moon and (**G**) 14th – 17th of August throughout a spring tide surrounding a full moon.

Table 4.5. Variability in channel water temperature, salinity, and water level during different moon-phase analysis periods within the month-long winter period (20th Jan.- 20th Feb. 2019)

Moon phase	Analysis period	Water temp.	Daily tidal range	Daily peak water level	Dist. travelled inland by peak water level	Mean high tide salinity	Mean low tide salinity
Winter month period	20th Jan-20th Feb	13.8-27.1 °C	1.64 ±0.20 m (range: 1.23 – 2.01 m)	1.73 ±0.17 m (range 1.42-2.08 m)	~1090 m	53.8±0.9‰ (range: 45.0-56.6‰)	57.6 ±2.8‰ (range: 46.9-63.9‰)
Spring tide: Full moon 21st Jan.	21st – 23rd Jan.	14.5-21.3 °C	1.84 ±0.10 m (range: 1.72-1.96 m)	1.94 ±0.05 m (range: 1.88-2.01 m)	~980 m	54.1 ±0.4‰ (range: 53.6-54.5‰)	60.1 ±2.1‰ (range: 59.1-63.9‰)
Neap tide: half-moon 28th Jan.	27th – 30th Jan.	15.0-24.4 °C	1.49 ±0.01 m (range: 1.48-1.50 m)	1.57 ±0.04 m (range: 1.55-1.62 m)	~620 m	54.9 ±0.5‰ (range: 54.5-55.8‰)	59.1 ±1.4‰ (range: 57.9-60.7‰)
Spring tide: new moon 5th Feb.	4th – 6th Feb.	15.5-23.4 °C	1.80 ±0.07 m (range: 1.74-1.90 m)	1.89 ±0.07 m (range: 1.82-1.99 m)	~965 m	53.7 ±0.4‰ (range: 53.1-54.1‰)	57.2 ±2.1‰ (range: 54.8-60.7‰)
Neap tide: First quarter moon 13th Feb.	12th – 14th Feb.	16.5-24.4 °C	1.35 ±0.24 m (range: 1.13-1.69 m)	1.62 ±0.17 m (range: 1.42-1.83 m)	~755 m	54.9 ±0.5‰ (range: 54.3-55.8‰)	59.1 ±1.4‰ (range: 57.1-60.7‰)
Mid phase tide	15th-18th Feb.	19.3-25.1°C	1.48 ±0.15 m (rang: 1.37-1.69 m)	1.71 ±0.18 m (range: 1.52-1.95 m)	~905 m	53.8 ±0.6‰ (range: 53.1-54.8‰)	56.1 ±1.4‰ (range: 54.4-58.7‰)

Table 4.6. Variability in channel water temperature, salinity, and water level during different moon-phase analysis periods within the month-long summer period (20th Jul. – 19th Aug. 2019)

Moon phase	Analysis period	Water temperature	Mean daily tidal range (m)	Daily maximum channel water level	Dist. travelled inland by peak water level	Mean high tide salinity	Mean low tide salinity
Summer month period	20th Jul. – 19th Aug.	28.9-39.2°C	1.72 ±0.30 m	1.99 ±0.14 m (range 1.67-2.16 m)	~1145 m	62.9±3.0‰ (range: 55.3-74.0‰)	73.0±3.8‰ (range: 65.4-81.2‰)
Neap tide: half-moon 25th Jul.	24th - 26th Jul.	30.6-37.9 °C	1.20 ±0.07 m (range: 1.11-1.30 m)	1.72 ±0.04 m (range: 1.68-1.77 m)	~705 m	62.4 ±4.7‰ (range: 54.0-66.3‰)	70.4 ±1.7‰ (range: 68.6-73.0‰)
Spring tide: new moon 1st Aug.	31st Jul-2nd Aug.	30.6-37.9 °C	2.06 ±0.04 m (range: 2.01-2.10 m)	2.13 ±0.03 (range 2.09-2.15 m)	~1140 m	62.2 ±2.5‰ (range: 57.9-64.6‰)	74.8 ±3.3‰ (range: 71.6-80.5‰)
Neap tide: 8th Aug.	7th – 9th Aug.	30.6-37.5 °C	1.42 ±0.12 m (range: 1.33-1.59 m)	1.87 ±0.07 (range 1.81-1.96 m)	~910 m	65.0 ±4.6‰ (range: 61.7-74.0‰)	69.6 ±1.8‰ (range: 66.6-72.6‰)
Mid-phase tide	11th-13th Aug.	29.8-37.8 °C	1.78 ±0.10 m (range: 1.65 -1.88 m)	1.85 ±0.3 m (range: 1.42-2.09 m)	~1100 m	61.5 ±1.7‰ (range: 59.1-63.9‰)	71.1 ±5.5‰ (range: 65.5-79.2‰)
Spring tide: full moon 16th Jul.	14th-16th Aug.	31.1-36.0 °C	1.99 ±0.05 m (range: 1.94-2.05 m)	2.11 ±0.04 m (range: 2.05-2.14 m)	~1130 m	61.9 ±01.8‰ (range: 59.5-63.9‰)	75.1 ±4.1‰ (range: 68.7-79.0‰)

4.5.2.1 Summer and winter channel water level variability during spring and neap tide periods

During the winter example period (20th Jan. - 20th Feb. 2019), the mean daily tidal range during spring tides (1.82 ±0.09m) was ~10% (0.28m) more than the average daily tidal range for this period (1.64 ±0.20 m) and ~20% (0.40 m) larger than the mean daily tidal range during neap tides (1.42 ±0.19 m) (Fig. 4.7.A; Table 4.5). During winter spring tide periods, mean daily peak water level in the channel (1.92 m) was ~17% (0.33 m) higher than during neap tide periods (1.59 m) (Fig. 4.7.D, E, F; Table. 4.5). Thus, the tide would have travelled ~890 m inland of the datum (Logger A) during springs to reach the pustular mats of the upper ITZ and ~615 m during neaps to reach the spongey mats of the lower ITZ zone (Fig. 4.4.A). During the mid-tide phase (15th-18th Feb.) the water level in the channel displayed a less smooth tidal cycle, with less well-defined second high tides (Fig. 4.7.G). During this period daily maximum water levels (1.71 ±0.18 m) suggest the tide would have travelled ~720 m inland, reaching the leathery mat of the middle ITZ (Fig. 4.4.A).

During the summer period (20th Jul. – 19th Aug.), the mean daily tidal range during spring tides (2.03 ±0.05 m) was ~15% (0.29 m) more than the summer period mean tidal range (1.72 ±0.30 m) and ~35% (0.72 m) higher than the mean daily tidal range during neap tides (1.31 ±0.15 m) (Fig. 4.8.A; Table 4.6). Mean daily peak water levels during summer spring tides (2.12 ±0.04 m) were ~15% (0.32 m) higher than during summer neaps (1.80 ±0.10 m) and the tide would have travelled ~1120 m inland to the lower supratidal zone and ~730 m inland to the leathery mats of the middle ITZ, respectively (Fig. 4.4.A).

4.5.2.2 Relationship between channel water level, salinity, and temperature in winter and summer

Daily high and low tide water levels in the channel had a strong inverse relationship with the corresponding channel water salinity during the summer period (20th Jul.-19th Aug., R^2 0.83, $p<0.0001$, n=124) and a slightly weaker inverse relationship during the winter period, (20th Jan.-20th Feb., R^2 0.60 $p<0.0001$, n=110 excluding 6 outliers) (Fig. 4.9.A). The relationship between water level in the channel (relative to local datum) and salinity was heteroskedastic in summer and winter (variance is systematically related to values with a larger variance at high salinity and lower channel water levels). Average daily salinity minima (Jan. – Sept. 2019) was 54.9 ±5.6‰, with the lowest values corresponding with the highest water levels. In the summer period, mean channel water salinity during high tide was similar during spring tides (62.2 ±2.0 ‰) and neap tide periods (64.7 ±3.1 ‰) (Fig. 4.8.D, E, G; Table 4.6). Similarly, mean channel water salinity during high tides in the winter period were similar during spring (53.9 ±0.4 ‰) and neap tide periods (54.8 ±0.6 ‰) (Fig. 4.7.D, E, F; Table 4.5), and both spring and neap low tide salinities were ~9‰ lower in the winter period than the summer period.

During the summer period, channel water salinity at low tide ranged from 65.4-81.2‰ (av.=73.0±3.8‰, n=31) (Fig. 4.9.B) and had a positive correlation with the height of the previous high tide (R^2 0.65, $p<0.0001$, n=31), whereas there was no significant relationship during winter (Fig. 4.9.B). In the

summer period, spring tides produced large tidal ranges, and peak water levels in the channel (≤2.15 m) (Table 4.6) which were followed by relatively high salinities at low tide (av.=74.2 ±2.9‰) (Fig. 4.8.E, G). In contrast summer neap tides had lower tidal ranges and peak water levels (≤1.96 m) (Table 4.6) which were followed by slightly lower channel water salinities during low tide (av.= 70.9 ±2.6 ‰) (Fig. 4.8.D). In the winter period, mean low tide salinities were 58.4 ±2.6‰ following spring high tides (Fig. 4.7.D, F, Table 4.5) and 58.0 ±1.9‰ following neap high tides (Fig. 4.7.E). Low tide channel water salinities measured following winter springs high tides were ~54% higher than the mean offshore seawaters (measured winter 2017) whereas low tide salinities following summer springs high tides were ~95% high than offshore seawater salinity (winter 2017).

4.5.2.3 The effect of summer solar radiation on low tide salinity and temperature

The role of evaporation driven by solar radiation during periods of low tide exposure across the ITZ in determining low tide salinity and temperature was investigated for the summer period (Fig. 4.10). A daytime falling tide (following high tide 1) may leave behind the most surficial salt and brine on the surface of the ITZ due to higher rates of evaporation and the channel water during the following low tide (low tide 1) may have higher temperatures (Fig. 4.10.A). The next high tide (high tide 2) may be able to dissolve more salt and/or mix with more surface brine, and therefore supply more saline water to the tidal channel at low tide (low tide 2) (Fig. 4.10.A). If this was the case, then the more saline low tides may be associated with the second-to-last (penultimate) high tides that peak in the daytime.

There was no significant correlation between channel water temperature at low tide and the time of the previous high tide from ~01:00 to midday (R^2 0.14, p=0.06, n=28) (Fig. 4.10.B). In contrast, when the previous high tide occurred between ~midday and midnight there was a strong negative correlation with water temperature (R^2 0.87, p<0.0001, n=33), with particularly strong correlation during daylight hours (12:00-18:00: R^2 0.92, p<0.0001, n=21) (Fig. 4.10.B).

Channel water salinity at low tide was negatively correlated with the timing of the second-to-last (penultimate) high tide, when the penultimate high tide occurred between ~04:00-09:00 (R^2 0.59, p<0.001, n=18) (Fig. 4.10.C). However, channel water salinity at low tide had a positive correlation with the timing of the penultimate high tide, when high tide occurred between 09:00 and 04:00 (R^2 = 0.62, p<0.06001, n=45) (Fig. 4.10.C).

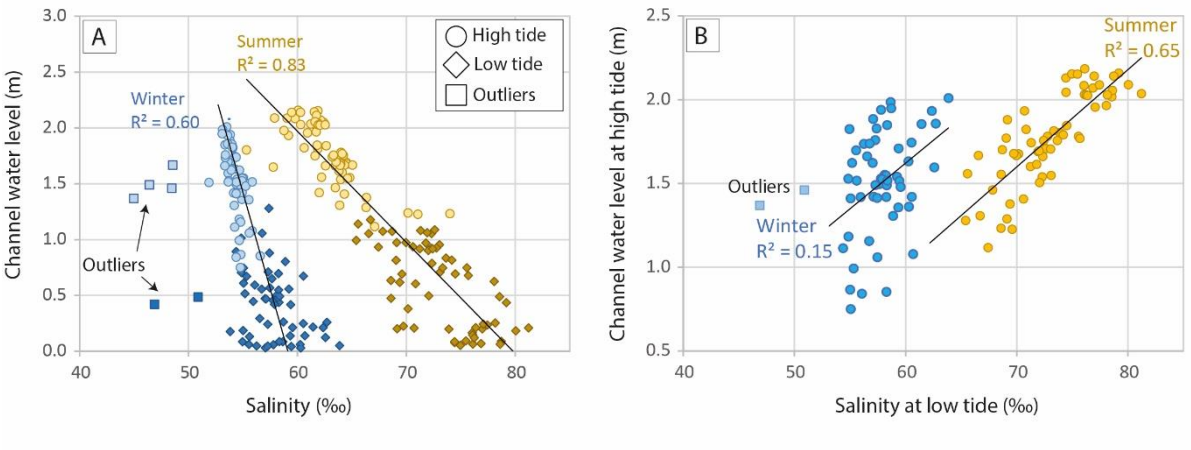

Figure 4.9. (**A**) Daily maximum and minimum channel water level against salinity (TDS) for winter (blue) and summer (yellow). Circles indicate high tide values and diamonds indicate low tide values. Squares represent winter outliers. (**B**) Daily maximum channel water level (high tide) against the following low tide salinity for winter (blue), winter outliers (blue squares), and summer (yellow).

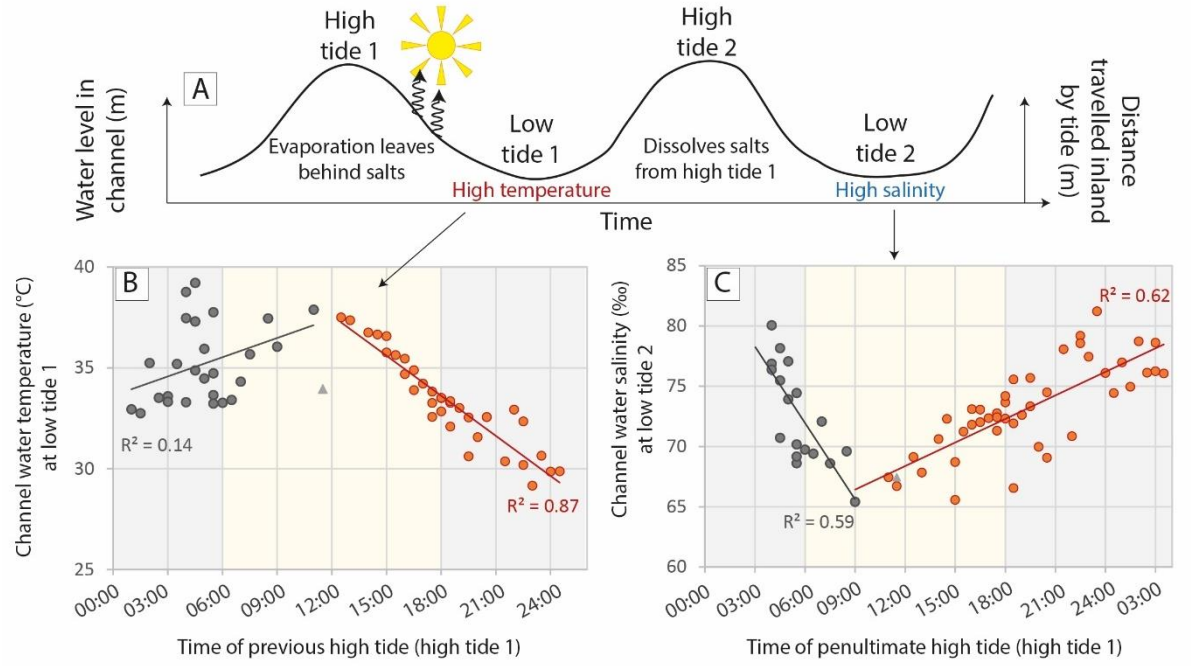

Figure 4.10. (**A**) Conceptual model for the effect of daytime heating as the ebb tide flows across the ITZ, and the subsequent effect on low tide temperature and low tide salinity. Graphs show the effect of summer (20th Jul. – 20th Aug.) daytime and night-time flooding (solar radiation) across the intertidal zone. (**A**) Low tide 1 temperature against the time of the previous high tide (high tide 1); (**B**) low tide 2 salinity against the timing of the penultimate high tide (high tide 1).

4.5.3 Variations in surface water chemistry as the flood tide travels across the ITZ (Site 3-QL)

The hydrodynamic complexity of the flood tide, and the potential impact on diagenesis, was investigated at Site 3-QL on January 6th-7th, 2019. This combined data from a surface CTD-Diver (Logger

B) (Fig. 4.11) situated at the sediment surface in the lower ITZ (location highlighted in Fig. 4.1D and 4.11) over 8 hours (09:50 – 17:50, 6th Jan. 2019) and water samples collected as the flood tide travelled across the middle ITZ (13:30 – 16:00, 7th Jan. 2019). Samples were both from the shallow tidal front (water depth 1- 3 cm) and 75-140 m behind the tidal front (14 – 50 cm water depth) (Fig. 4.12). The neap tide (6th Jan.) meant that only the highest daily tide (being sampled) reached Logger B at 10:50 on the 6th, and the middle ITZ around midday on 7th.

Logger B had an elevation of ~+1.30 m relative to the local datum (Logger A) and recorded a maximum water level of 0.58 m over the 8-hour study period. When the tidal front reached Logger B at ~10:50, salinity was 3.7‰ higher (55.6‰) than at the same time at Logger A (51.9‰), and then decreased to 45.4‰ at 11:56 (Fig. 4.11.B). This was followed by a rapid increase in salinity to 54.1‰ at 12:16, which then remained fairly stable (53.7 ±0.4‰) until 14:26 when salinity dropped to 52.8 ±0.5‰ until 16:40, when the tide began to recede. Logger B also recorded a decrease in temperature as it was first submerged by the flood tide to a minimum of 21.9 °C at 12:10 (Fig. 4.11.C). This was then followed by a gradual increase to 24.8 °C at 15:50 followed by a slight decrease as the tide begins to recede.

On the 7th January, the deepest water samples (14 – 50 cm water depth) from the middle ITZ had salinities (52 ±1‰, n=3) that were the same as high tide salinity in the channel (Logger A). However, salinity at the shallow tidal front was up to ~2 times higher (at 1 – 3 cm water depth, salinity ranged from 63-99‰) (Fig. 4.12.C). Similarly, at 13:38 and 15:05, *p*H of the deeper water samples resembled offshore seawaters (8.07 ±0.01, n=2), however *p*H of the deeper waters behind the tidal front increased as the flood tide moved further inland, with the highest *p*H (8.21) at 15:34 (14 cm) (Fig. 4.12.D). In contrast, *p*H of the shallow tidal front remained fairly constant (8.13-8.16) (Fig. 4.12.D). Alkalinity of the shallow waters decreased as the tidal front moved inland from 2.53 to 2.44 mmol l^{-1}, whereas the highest alkalinity was from the deepest water sample at 15:05 (2.62 mmol l^{-1}), which was ~4% higher than the mean offshore alkalinity (Fig. 4.12.E).

Comparison between the carbonate chemistries of shallow tidal front seawaters (with high salinity) and deep flood tide/offshore seawaters (with relatively low salinity) using thermodynamic models was complicated as the low salinity samples are best suited to modelling in CO2SYS, whereas high salinity samples are best suited to modelling in PHREEQC (see methods Chapter 2.2). CO2SYS will be used to model the offshore seawaters, but for ease of comparison both shallow and deep surface waters will be compared using PHREEQC (unless specified otherwise). Both CO2SYS and PHREEQC outputs are presented in Fig. 4.12.

The partial pressure of CO_2 (pCO_2) of the offshore seawaters at Sites 1-OS and 2-OS (0.05 ±0.01%, n=4) were at approximate equilibrium with the atmosphere (pCO_2 ~0.04 %) (Fig. 4.12.O). Modelling in PHREEQC suggests the deeper surface waters have a higher pCO_2 relative to the shallow tidal front

waters and offshore seawaters (Fig. 4.12.G). However, when using CO2SYS for modelling pCO_2 of the offshore seawaters and the deeper flood tide waters and PHREEQC for the shallow waters (Fig. 4.12.G, O), all flood tide surface waters pCO_2 appear within range offshore seawater and at approximate equilibrium with the atmosphere.

PHREEQC calculations indicate that all surface waters were supersaturated with aragonite, calcite, and disordered dolomite (Fig. 4.12.H, I, K); waters at the shallow tidal front had the highest degree of supersaturation, and this increased as the tide moved inland. The tidal front mineral SI was 0.12-0.28 log units higher than the deeper water behind it for SI_{arag} and SI_{calc} and 0.28-0.62 log units higher for SI_{dol}. The shallow tidal front remained more supersaturated with respect to aragonite and calcite when CO2SYS was applied to calculate the mineral SI of the deeper waters (Fig. 4.12.P, Q).

All surface waters remained undersaturated with respect to gypsum, and halite (calculated in PHREEQC) though the degree of undersaturation was lower in the shallow tidal front waters and became increasingly less negative as the tide moved inland (Fig. 4.12.L, M). Using K as a conservative tracer for evaporation and/or mineral dissolution, the shallow tidal front waters have lower Na/K and Ca/K ratios than the deeper waters (Fig. 4.12.J, N).

Dissolved oxygen (DO) in the surface water of the flood tide was highest at 15:05 (~40 cm water depth, overlying the leathery microbial mats) (sample 3), although all measurements were within the range of the offshore seawaters, and no data was obtained for high tide (15:40) (Fig 4.12.F). Ammonium (NH_4^+) at the shallow tidal front at 13:28 resembled the offshore sites (29.4±2.0 µmol l^{-1}, n=4) and then decreased by ~30% as the tide moved inland (Fig. 4.12.R). In comparison the deeper water behind the front had >15% more NH_4^+ than the offshore sites.

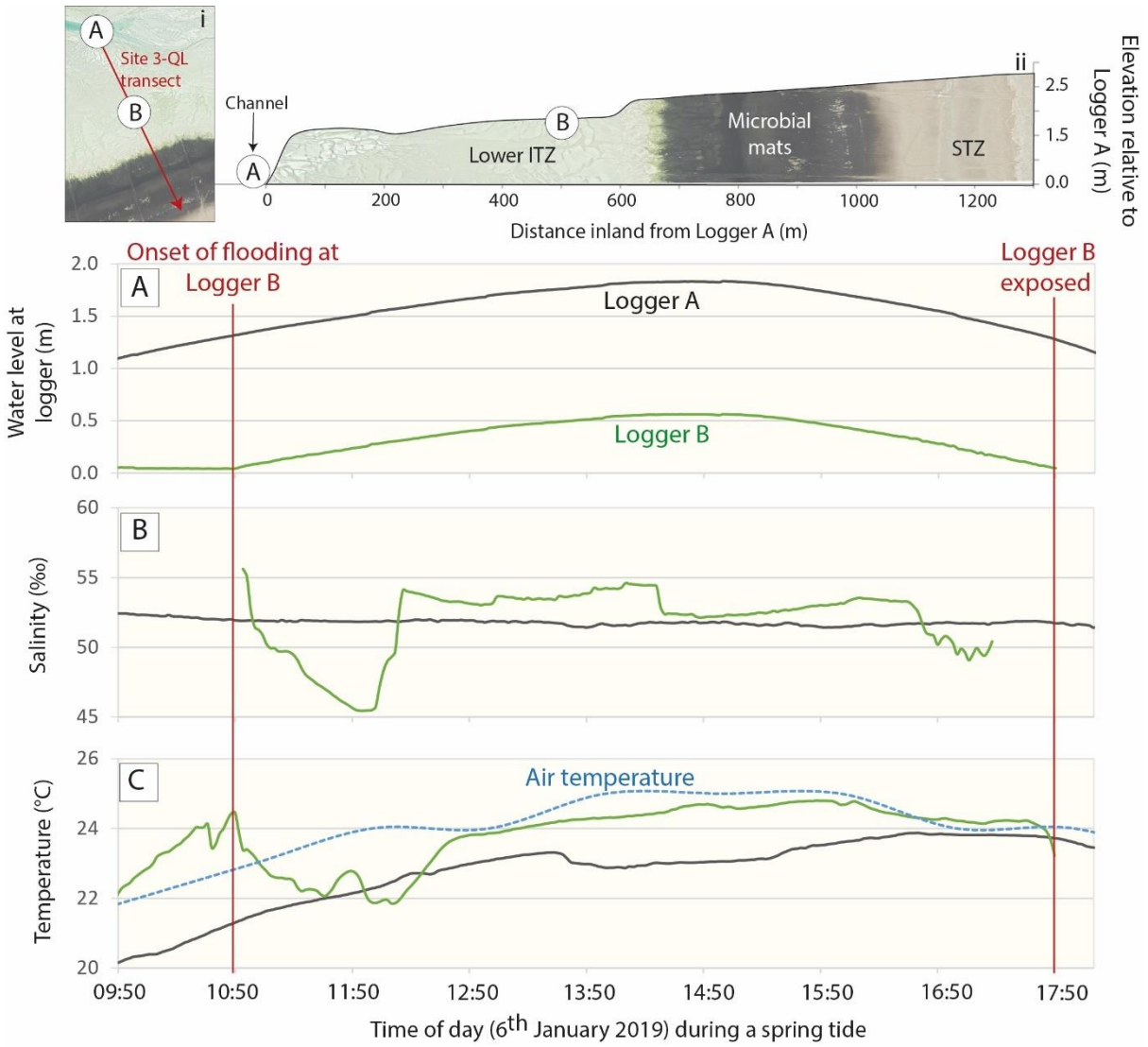

Figure 4.11. Records from CTD-Diver Logger A within the tidal channel (grey) and Logger B (green) from the lower ITZ at site 3-QL. Logger B is 1.30 m elevation above Logger A. Figures show (**A**) water level, (**B**) salinity (TDS) and (**C**) logger recorded temperatures and air temperature at Abu Dhabi Bateen airport (dashed blue) (6th Jan. 2019, 09:50 – 18:00). (i) and (ii) show location of Loggers A and B relative to the Site 3-QL transect.

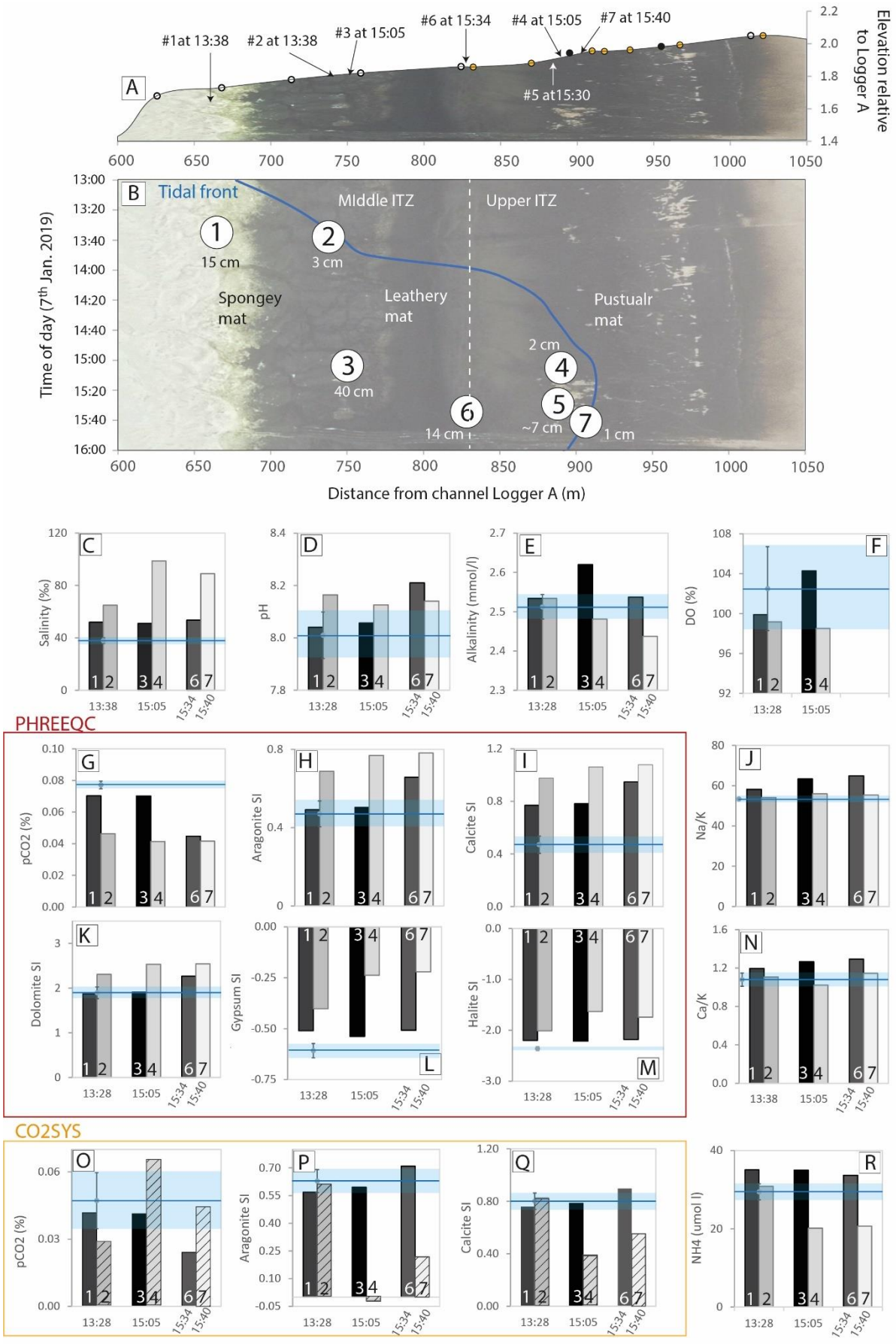

Figure 4.12. Surface water samples from flood tide across the middle ITZ at Site 3-QL (7th Jan. 2019). (**A**) locations of water samples 1-9 with distance and elevation relative to Logger A in the tidal channel.

(**B**) Location of water samples in time and space relative to the tidal front (blue line). **C - Q** display the water chemistries of samples collected as the flood tide progressed across the ITZ. The degree of shading on the bars represents the water depth, with the first bar of each pair being the deeper water (7-50 cm water depth) located ~75-140 m behind the shallow tidal front (< 3 cm water depth, second bar per pair); water depths of each sample provided in (**B**). The blue horizontal line and shaded blue area represents the mean and standard deviation of water chemistry from offshore sites 1 and 2. Bar charts illustrate the variability in flood tide seawater chemistry in (**C**) salinity (as TDS); (**D**) pH; (**E**) alkalinity; (**F**) dissolved oxygen (DO) (%). (**G-I** and **K-M**) Display carbonate chemistry modelled using PHREEQC (with seawater carbonate chemistry mean and standard deviations from CO2SYS in orange): (**G**) pCO_2 (%), (**H**) aragonite SI; (**I**) calcite SI. (**J**) Cl/K; (**K**) dolomite SI; (**L**) Gypsum SI; and (**M**) halite SI. (**N**) Ca/K. (**O-Q**) Display carbonate chemistry modelled using CO2SYS, though the salinities of the shallow waters were out of the range for CO2SYS (see methods, Chapter 2.2) (hashed bars out of salinity range): (**O**) pCO_2 (%), (**P**) aragonite SI; (**Q**) calcite SI. (**R**) ammonium (NH_4^+). For raw water chemistry data, see Appendix C, Table C1

4.5.4 Variability in tidal creek water chemistry during the ebb and flood tides (Site 4-QL)

4.5.4.1 Temperature, salinity, and water level surrounding the tidal creek

Site 4-QL was ~3 km closer to the entrance of Qantur Lagoon than Site 3-QL, however data from Logger A (Site 3-QL) is used for comparison. On the day when creek water samples were collected at Site 4-QL (11:15 – 17:30, 16th Jan. 2019), Logger A (Site 3-QL) recorded the largest daily high tide (1.66 m) in the channel at 10:00 and low tide (0.66 m) at 16:05 (Fig. 4.13.A) following a neap tide on the 14th Jan. Three loggers (C, D, and E) recorded changes in salinity, temperature, and water level surrounding the tidal creek at Site 4-QL (04:50 – 17:30, 16th Jan. 2019) with elevation relative to Logger A (Site 3-QL) of ~1.15 m, 0.75 m, and 0.55 m respectively. Logger C recorded a peak water level of 0.50 m at 09:52 and became exposed at 13:11. Logger D recorded a low water level throughout sampling (2.3±1.7 cm from 15:30 – 17:30) with flow maintained by drainage from the upper ITZ, and Logger E reached a minimum of 11.5 cm at 16:08 (Fig. 4.13.A).

Logger C recorded the highest salinities at the onset of the first flood tide (56‰ at 06:00) and just before becoming exposed with the ebb tide (57‰ at 13:05) and remained fairly constant (51 ±0.4‰) between 07:15 and 12:50. In contrast salinity at logger E increased throughout low tide reaching a maximum of 63‰ at 17:20 (Fig. 4.13.B).

Air temperature at Abu Dhabi Bateen airport (16th Jan.) increased from 21-27 °C from ~05:00 to 14:00 and Site 3-QL channel water temperature (Logger A) remained fairly constant at 21.5 ±0.3 °C from 04:50-12:00, and then increased to peak at 26.7 °C at 16:25 (Fig. 4.13.C). Logger C was coolest at night-time before the tide came in (14.6 °C at 06:01), warmed throughout the day and increased more rapidly as the ebb tide brought warmer water from updip before peaking with exposure (30.1°C at 13:23). In

contrast Logger D and E did not become exposed and peaked at low tide at 27.4 °C and 28.5 °C respectively.

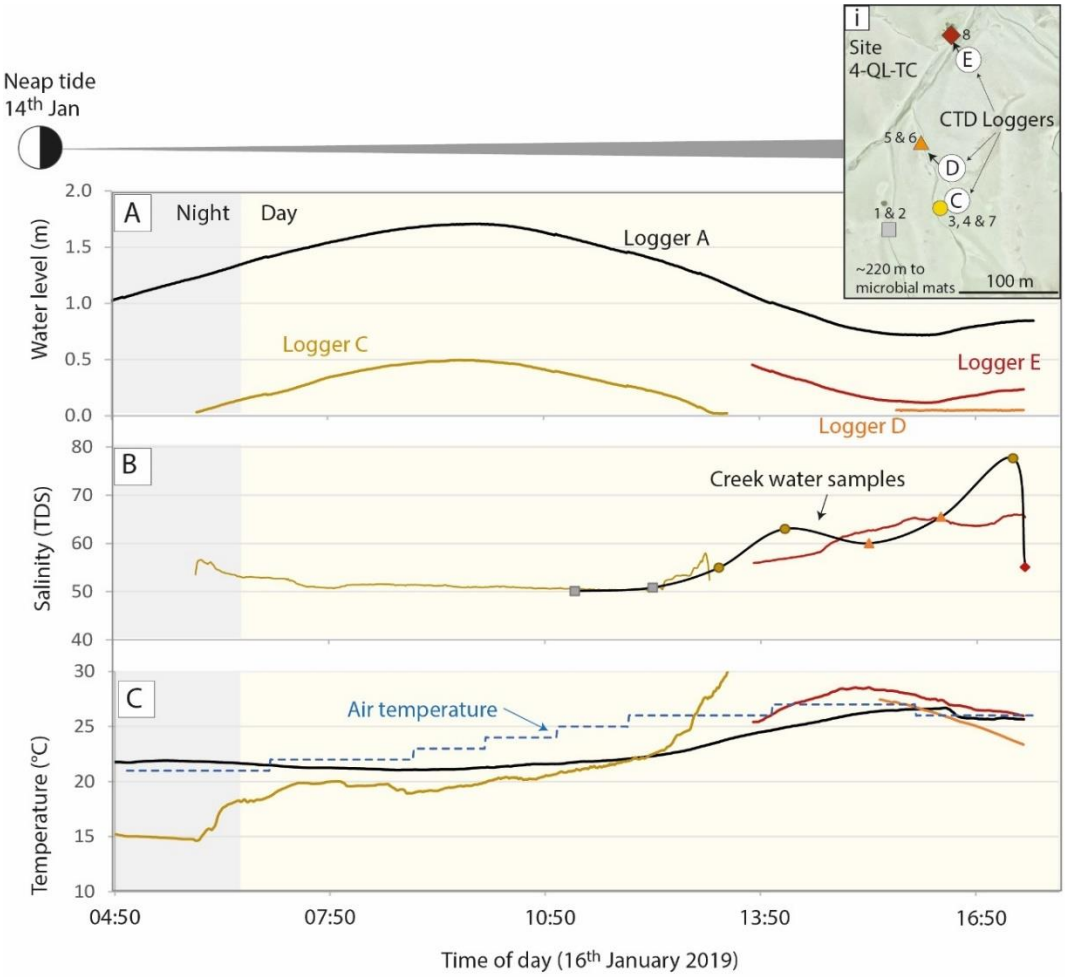

Figure 4.13. Records from CTD-Diver Logger A (grey, site 3-QL), and from three locations at site 4-QL; (1) Logger C (yellow: situated at the sediment surface ~10 m east of creek site 4-TC with a surface elevation 1.15 m above Logger A (12.5 cm higher than the sediment surface in the adjacent creek), (2) D (orange: within the creek ~ 90 m seaward of logger B, and 0.75 m above Logger A) and (3) E (red: within the creek ~250 m seaward of logger B, and 0.55 m above Logger A) (relative locations in (i)). Figure shows (**A**) water level, (**B**) logger recorded salinity, and creek water sample salinity as total dissolved solids (TDS) and (**C**) logger recorded temperatures and air temperature at Abu Dhabi Bateen airport (dashed blue). (i) Shows locations of loggers and creek water samples at Site 4-QL-TC.

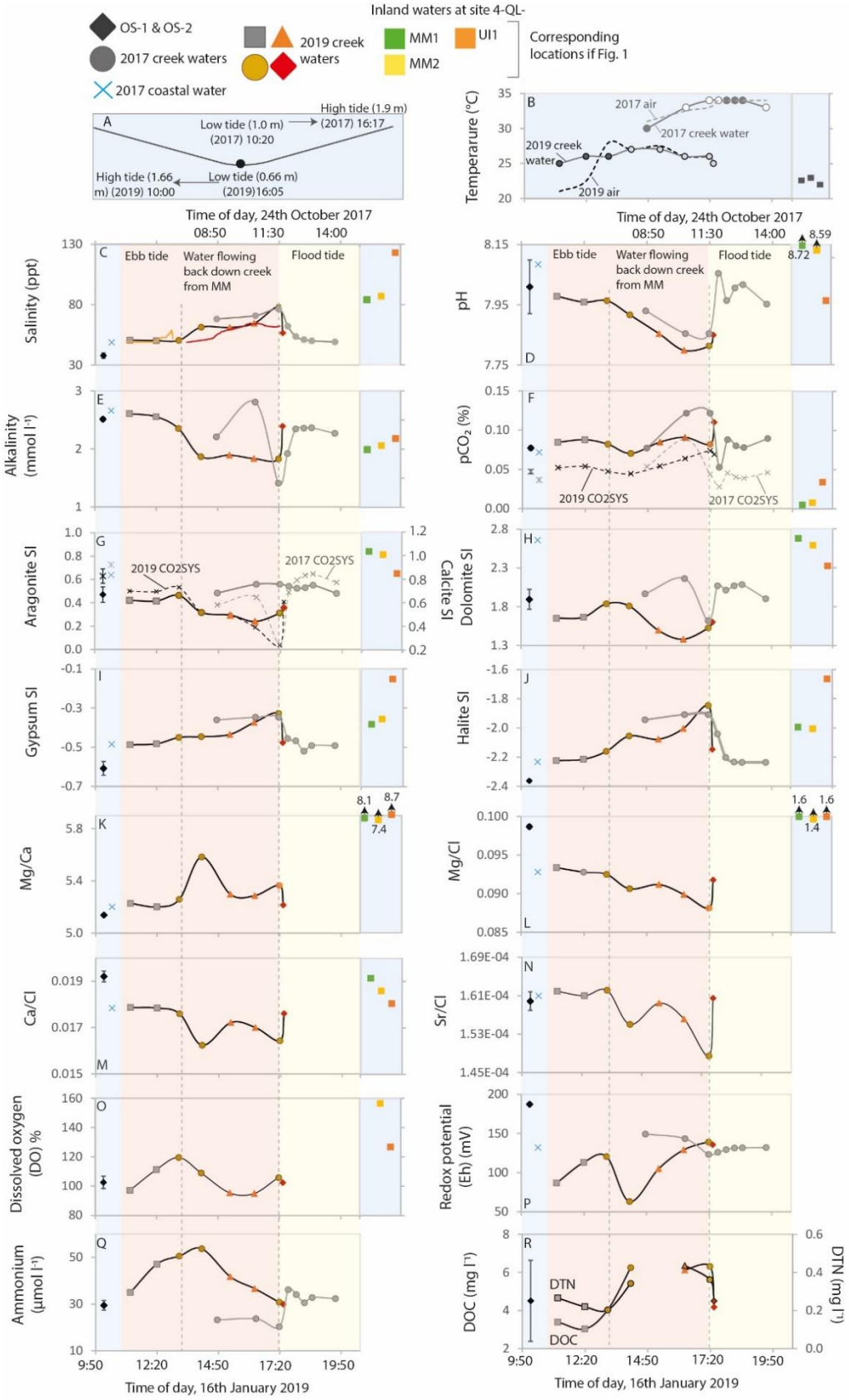

Figure 4.14. Variations in creek water chemistry throughout an ebb tide (2019) (black line) and a transition from ebb to flood tide in 2017 (grey line). Coloured shapes refer to sampling locations in Fig. 4.1. Upper and lower x-axis gives times of day in 2017 and 2019, respectively. First blue panel contains offshore sites (1-OS and 2-OS) (location in Fig. 4.1A) and the near the mouth of Qantar channel (Fig. 4.1C). The red and yellow panel indicate samples obtained in the ebb and flood tide respectively, and

the last blue panel displays inland surface waters from the middle to upper ITZ. (A) Times of high and low tide at the coast (2017) and in the channel at site 3-QL (2019). (B) *In situ* water temperatures (solid circles) and estimated *in situ* temperatures (hollow circles) for the creek and inland water samples. (C) salinity (TDS) with Logger C salinity (yellow line) and Logger E salinity (red line); (D) *p*H; (E) alkalinity as HCO_3^-; (F) $pCO_{2(aq)}$ (%) [~0.04% = atmospheric pCO_2 (%)]; (G) Aragonite saturation indices (SI) (left x-axis) and calcite SI (right x-axis); (H) dolomite SI; (I) gypsum SI; (J) halite SI; (K) Mg/Ca; (L) Mg depletion using Cl as a conservative tracer for mixing (Mg/Cl); (M) Ca depletion (Ca/Cl); (N) Sr depletion (Sr/Cl); (P) dissolved oxygen (DO) (%) and (O) Redox potential (Eh) [note: Eh measurements appear less accurate in oxic waters, and this may account for the disparity wit DO]. (Q) Ammonium (NH_4^+) and (R) dissolved organic carbon (DOC) (left x-axis, solid line) and dissolved total nitrogen (DTN) (right x-axis, dashed line). For raw water chemistry data, see Appendix C, Table C2.

Table 4.7. Groundwater chemistry from the three boreholes (BH).

BH	Salinity (‰)	Temp. (°C)	*p*H	Alkalinity (mmol/l)	SI_{arag}	SI_{calc}	SI_{dol}	SI_{gyp}	SI_{hal}
1	198	29.9	6.25	2.05	-0.64	-0.34	-2.23	-0.14	
2	170	30.3	6.68	2.22	-0.43	-0.13	0.33	-0.15	-1.10
3	223	32.1	6.29	2.48	-0.34	-0.40	0.26	-0.20	-0.71
	***p*CO2 (%)**	**Mg/Ca**	**Ca/Cl**	**Sr/Cl**	**DO (%)**	**Redox potential (Eh)**	**NH_4 (µmol/l)**	**DOC (mg/l)**	**DTN (mg/L)**
1	3.12	7.46	0.0095	0.00010	44	79	14.6	4.8	2.6
2	1.26	10.24	0.0098	0.00013	89	94	15.3	5.9	1.9
3	3.40	5.94	0.0010	0.00014	83		8.5	4.9	1.2

4.5.4.2 Water chemical analysis during ebb and flood flow in the tidal creek

Water samples from the tidal creek (Site 4-QL-TC) were collected during two separate periods: over an ebb tide (16th Jan. 2019) two days after a neap tide, and also over the transition from ebb to flood tide (24th Oct. 2017) between a spring tide (19th Oct.) and a neap tide (28th Oct.). Although no tide logger was installed in Qantur channel during creek water sampling in October 2017, low tide at 10:20 (1.0 m) and high tide at 16:17 (1.9 m) (Fig. 4.14.A) were reported for coastal Abu Dhabi. Similarly, the inland surface waters (sampled 5-6th Feb. 2014), were sampled around a neap tide (6th Feb.) between high tide (05:50: 1.9 m) and low tide at (12:20: 0.7 m) (5th). The inland surface waters at site MM-1, MM-2 and UI-1 had *in situ* temperatures of 22.6 °C, 23 °C and 22 °C respectively (Fig. 4.14.B). Dissolved organic carbon (DOC) and total nitrogen (DTN) were only analysed for the 2019 samples, and problems with major ion analysis for the 2017 samples means ion ratios are only presented for 2019 and 2014 samples.

Salinity

In October 2017, offshore seawaters (Sites 1-OS and 2-OS) had salinities of 37.9 ±2.1‰ (n=4) and the salinity from near the mouth of Qantar channel (location in Fig. 4.1.C) was 48.7‰ (1 hour before high tide). In January 2019, offshore seawater was not sampled, however the best approximation near the

mouth of Qantar channel was collected as the flood tide travelled across the lower ITZ at Site 3-QL (51% at Location 1, Fig. 4.1.E). During the winter period (20th Jan. – 20th Feb. 2019) the long term CTD-Diver at Site 3-QL (Logger A) recorded a mean daily salinity minimum of 53.1 ±2.3‰ in association with high tide in the tidal channel.

During low tide periods the tidal creek continued to run, being fed by the microbial mats ~200 m inland, where the creek terminated. In 2019, salinity of the creek water samples increased during the ebb tide and continued to increase to a maximum of 78‰ before rapidly decreasing to 55‰ as the flood tide flowed back up the creek (~1 hour 20 mins after low tide in the channel at Site 3-QL). In 2017, salinity in the tidal creek also increased throughout the latter half of the ebb tide and peaked at 11:27 (76‰) 1 hour and 7 mins after low tide at the coast (Fig. 4.14.C). Salinity then decreased during the flood tide to 49‰ at 13:45 which closely resembled the coastal water sample near the mouth of Qantar channel (location in Fig. 4.1.C), though was >10‰ higher than offshore seawaters. The range of creek water salinity was similar during both field campaigns. Waters overlying the microbial mats (site 4-Ql-MM1 and -MM2) ranged from 84-87‰, whereas the surface water from the upper intertidal zone (site 4-QL-UI; 123‰) was over twice as saline as high tide salinity in the channel at Site 3-QL (Fig. 4.14.C) and groundwaters were highly saline (170-223‰) (Table 4.7).

Carbonate chemistry: pH, alkalinity and pCO_2

Within the tidal creek in 2019, between ~11:15-13:15 *p*H (7.97 ±0.01, n=4) resembled offshore seawater *p*H (8.01 ±0.09, n=4), and then declined to ~7.80 between 16:20 and 17:20 before increasing slightly (7.85) as the ebb tide began to flow back up the channel (Fig. 4.14.D). In 2017, creek water *p*H also declined through the ebb tide to a nadir of 7.96 at 12:10, and then increased to 8.02 by 12:50 with the onset of the flood tide flowing back up the creek (Fig. 4.14.D). Surface water *p*H from the microbial mats (Sites 4-QL-MM1 and MM2) was high compared to all other samples (*p*H 8.72 and 8.62 respectively) whereas surface water *p*H further inland (site 4-QL-UI) (7.99) resembled the 2017 offshore seawaters (Fig. 4.14.D). Groundwaters had significantly lower pH values than surface waters (6.25-6.28) (Table 4.7).

At 11:15 and 12:20 (16th Jan. 2019), alkalinity within the creek (2.58 ±0.03 mmol l^{-1}) resembled off-shore seawater alkalinity (2.51 ±0.03 mmol l^{-1}), but then decreased by ~30% throughout the first half of the ebb tide with the input of higher salinity waters from the upper ITZ reaching the upper creek zone. Alkalinity then remained low (1.85 ±0.03 mmol l^{-1}, n=4) from 14:10-17:20 before increasing to 2.39 mmol l^{-1} with the onset of the flood tide at 17:30 (Fig. 4.14.E). In 2017, alkalinity increased during the ebb tide, peaking at 10:30 (2.81 mmol l^{-1}) but decreased to 1.41 mmol l^{-1} for the final sample before the tidal creek filled with incoming seawater (Fig. 4.14.E). Alkalinity then increased and remained relatively stable at 2.33 ±0.04 mmol l^{-1} (n=4) between 12:09 and 13:40, through decreased slightly. In

contrast alkalinity from the middle ITZ microbial mats (Site 4-QL-MM1 and MM2) and upper ITZ mats (Site 4-QL-UI) had alkalinities 14-20% lower than offshore seawater, though increased with distance inland (Fig. 4.14.E), and groundwater alkalinity (2.05-2.48 mmol l l^{-1}) was within range of creek water alkalinity (Table 4.7).

The first three samples from 2019 and the latter four samples from 2017 were within the salinity range for the application of CO2SYS (see methods in Chapter 2.2). However, most creek waters were close to the threshold (~56‰), and thus for simplicity only PHREEQC results will be discussed for pCO_2, SI_{arag} and SI_{calc}, though both sets of results are presented in Fig. 4.14.F and 4.14.G. CO2SYS will only be used for describing the offshore seawaters.

In 2019, creek water pCO_2 was typically slightly higher than the offshore seawaters (0.05 ±0.01%, n=4) (Fig. 4.14.F). There was a subtle decrease in pCO_2 during the first half of the flood tide, followed by a slight increase in the latter half of the ebb tide, and a more significant increase to 0.11% with the onset of the flood tide at 17:30 (Fig. 4.14.F). In 2017, pCO_2 increased from 0.08-0.12% throughout the latter half of the ebb tide and then decreased with the onset of the flood tide to 0.05% at 11:50, before increasing to values that resemble the offshore seawater pCO_2 for the remainder of the flood tide (Fig. 4.14.F). Inland surface waters from the microbial mats (MM1 andMM2) had low pCO_2 (0.002 – 0.008% respectively), which increased slightly at the upper intertidal zone (0.03%) and groundwaters had significantly higher pCO_2 values than surface waters, ranging from 1.26-3.40% (Table 4.7).

Mineral saturation state

During the first half of the ebb tide (2019) creek water supersaturation with respect to aragonite, calcite, and dolomite (SI_{arag}, SI_{calc}, and SI_{dol} respectively) resembled the offshore seawaters. Carbonate mineral supersaturation in the creek then decreased throughout the latter half of the ebb tide to remain below seawater saturation. Towards the end of the ebb tide and at the onset of the flood tide (17:30) carbonate mineral SI increased slightly, though remained below seawater mineral SI (Fig. 4.14.G, H). In contrast, creek water samples in 2017 were more supersaturated with respect to calcite, aragonite, and dolomite, with a slight increase throughout the latter half of the ebb tide and slight decrease throughout the flood tide. The inland surface waters were more supersaturated with respect to calcite, aragonite, and dolomite, with MM-1 the most supersaturated, followed by MM-2 and UI-1 (Fig. 4.14.G, H). Groundwaters were calcite and aragonite undersaturated, and samples from Boreholes 2 and 3 were supersaturated with respect to dolomite whilst groundwaters from Borehole 1 were dolomite undersaturated.

Gypsum and halite (calculated in PHREEQC) remained undersaturated in the offshore seawater, creek waters, and inland surface waters, with variability largely reflecting salinity (Fig. 4.14.I, J). The least gypsum and halite undersaturated waters were from the most inland surface water sample (-0.2 and

-1.7 respectively) (Site 4-QL-UI), and the creek waters were the least undersaturated during peak backflow from updip (17:30 in 2019, and ~11:30 in 2017), prior to the onset of the flood tide in the creek (Fig. 4.14.I, J).

Mg/Ca ratios in the creek were slightly higher than seawater Mg/Ca during periods of relative high-water level in the creek (first half of the ebb tide, and the onset of the flood tide). However, Mg/Ca increased as the water starts to flow back down the creek (2019) but remained considerably lower than values from the inland surface waters (>7) (Fig. 4.14.K). Using Cl as a conservative tracer for mixing between seawater and groundwater and evaporation, Mg and Ca appear slightly depleted in the creek waters relative to the offshore seawater (Fig. 4.14.L, M). In contrast, the inland surface waters are significantly enriched in Mg relative to seawater, and are slightly depleted in Ca relative to seawater, with the degree of Ca depletion increasing inland. Sr depletion (as Sr/Cl) suggests creek waters during the first half of the ebb tide and the onset of the flood tide have Sr/Cl roughly equal to seawater, however as the tide falls and waters flow down the creek from inland areas, Sr in the creek becomes depleted relative to offshore seawater (Fig. 4.14.N).

Redox potential and organic chemistry

Dissolved oxygen (DO) in the creek increased throughout the first half of the ebb tide to peak at ~13:15 (coincident with increasing solar radiation) and then decreased throughout the latter half of the ebb tide. The surface water from MM-2 had the highest DO values (~160%) (Fig. 4.14.O). DO was not measured for the 2017 samples, however redox potential (Eh) suggests the creek waters remain fairly constant throughout sampling, though decrease slightly before the onset of the flood tide before stabilising (Fig. 4.14.P). The disparity between trends in DO and Eh for the 2019 samples likely highlights problems with the Eh probe, which works less effectively in oxic then anoxic waters.

In 2019 ammonium (NH_4^+) increased through the first half of the ebb tide from 35.0 µmol l^{-1} (11:15), to peak at 53.7 µmol l^{-1}, coincident with the first increase in salinity and drop in alkalinity at (14:10) (Fig. 4.14Q). NH_4^+ then decreased throughout the latter half of the ebb tide and drainage from the upper ITZ, reaching values within range of the offshore seawaters as the tide flowed back in (Fig. 4.14Q). In 2017 creek water NH_4^+ was ~33% lower during the ebb tide than the flood tide (Fig. 4.14Q). During the ebb tide (2019) dissolved organic carbon (DOC) and total nitrogen (DTN) increased at 14:10, (6.15 and 0.34 mg l^{-1} respectively), appear to remain high throughout low tide and then decreased with the flood tide. Most creek DOC values were within the range of offshore seawater DOC (3.2 – 5.9 mg l^{-1}) (DTN not measured for offshore seawaters) (Fig. 4.14R).

4.6 Discussion

4.6.1 Defining the lower, middle, and upper intertidal zone boundaries

Definitions of intertidal zone (ITZ) boundaries are inconsistent throughout the literature. Uncertainty and ambiguity surrounding ITZ definitions are commonplace (Harris *et al*., 2014; Tagliapietra *et al*., 2009), and the lack of consistent definitions has inhibited estimations of the global extent of ITZs (Freiss *et al*., 2012), rates of global decline of ITZs, and in the application of coastal conservation and management strategies (Rog and Cook, 2017). The ITZ is commonly subdivided into lower, middle, and upper ITZ (e.g., by sedimentologists and ecologists), however such boundaries are equally poorly constrained. Here we consider two ways of interpreting the lower, middle, and upper limits of the ITZ; (i) using tidal limits, and (ii) using the proportion of time spent flooded per year. These boundaries will then be compared with the surface facies at Site 3-QL as described by Court *et al*. (2017).

The seaward limit of the ITZ is typically defined as the lowest water mark, which would normally be associated with spring lows (Oxford Dictionary of Geography, 2016), however as the channel at Site 3-QL becomes periodically exposed, the lower reaches of the transect are considered within the ITZ. Beyond the landward limit of the ITZ is the supratidal zone (STZ), which is described as the portion of tidal flat that lies above the mean spring high tide mark and is only inundated by exceptional tides and storms (Oxford Dictionary of Geography, 2016). This definition places the landward limit of the ITZ at Site 3-QL at 905 m inland from the channel (above which is flooded <4% of the time). However, Rog and Cook (2017) define the landward limit as the highest astronomical high tide (the highest water level under average meteorological conditions) which encompasses above average spring high tides. For Site 3-QL, we use the upper interquartile range of spring high tides (Jan. – Dec. 2019) to approximate the highest astronomic tide, which places the landward limit of the ITZ ~1090 m inland from the channel, within the featureless zone (Court *et al*., 2017), above which is flooded <1.5% of the time (Fig. 4.15.B).

The ITZ can be further divided into the lower, middle, and upper intertidal zones, terms which are often applied, though definitions of boundaries between these zones are rarely defined in the literature. Rog and Cook (2017) describe four key tide lines which are used to determine boundaries between land, sea, and intertidal zone: (i) astronomical high tide; (ii) mean spring tide high water mark; (iii) mean high water mark, and (iv) low water mark. If these tidal boundaries are applied to define the ITZ at Site 3-QL (Fig. 4.15.B), then the lower ITZ (mean low water level to mean high water level) stretches from ~15 – 825 m, the middle ITZ (mean high water to mean spring tide high water) from ~825-905 m and the upper ITZ (mean spring tide high water to astronomical high tide) from ~905-1090 m (Fig. 4.15.B). However, this classification system means the lower ITZ encompasses nearly the entire ITZ, with the middle and upper parts of the ITZ flooded <7% of the time. Furthermore, these boundaries do not align

with the surface facies defined by Court *et al*. (2017) (Fig. 4.15C), and is therefore rejected as an adequate way to subdivide the ITZ at Site 3-QL.

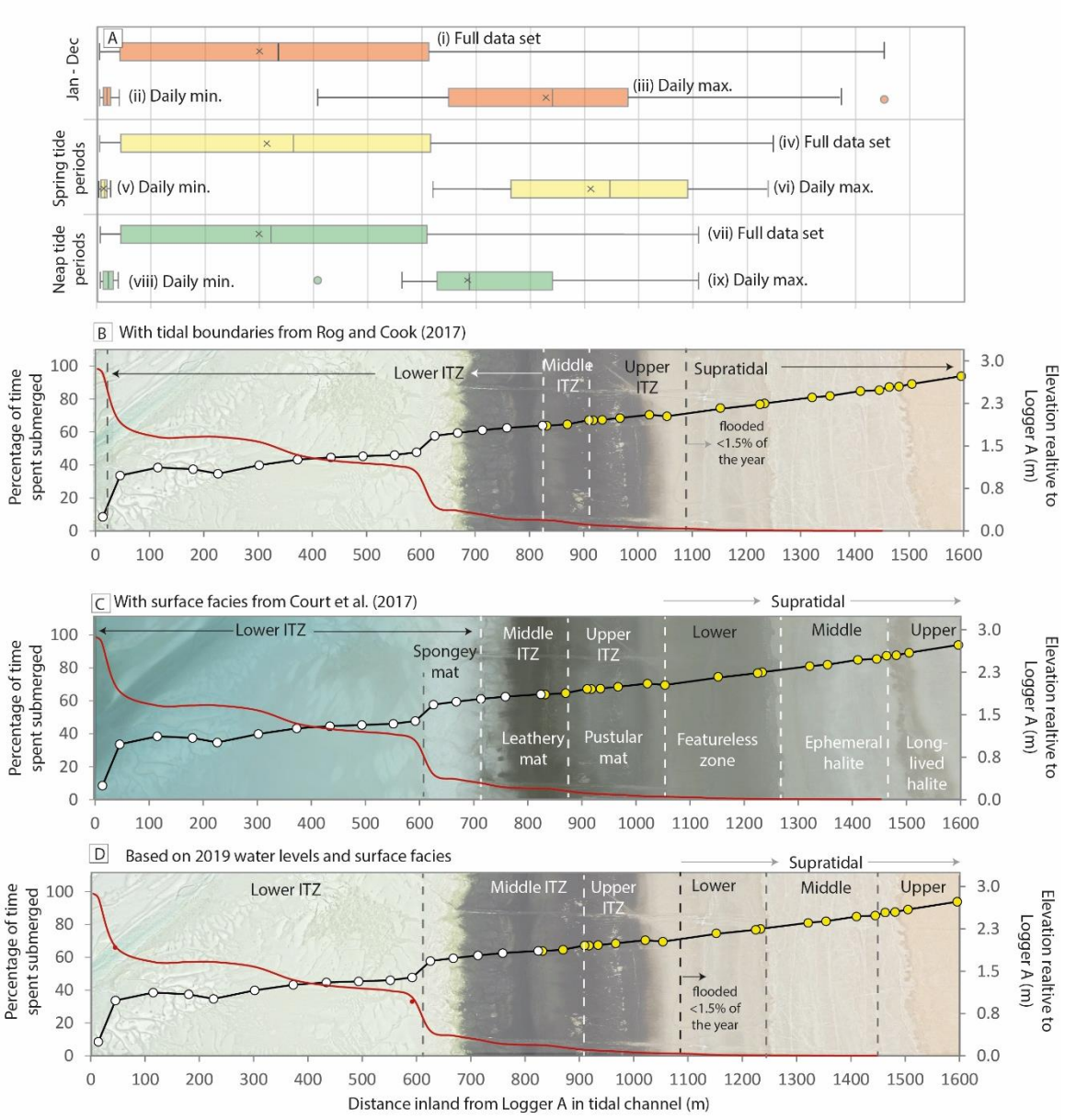

Figure 4.15. (**A**) Site 3-QL ITZ tidal ranges as distance travelled inland by the tide relative to the CTD-diver (Logger A) within the tidal channel and the elevation profile presented in Fig. 4.4. Box plots represent a one-year period (Jan – Dec. 2019: orange) with the full data set (i), the daily minimum water level (ii), and daily maximum water level (iii); spring tide periods in 2019 (yellow) (iv), the daily spring minimum water level (v) and daily spring maximum water level (vi); and neap tide periods in 2019 (green) (vii) with the neap daily minimum water level (vii) and the neap daily maximum water level (ix). (**B**) Dividing the ITZ by tide lines as suggested by Rog and Cook (2017); (**C**) dividing the ITZ by surface facies (from Court *et al*., 2017) (Google Earth image from 2014); and (**D**) suggested ITZ divisions based on 2019 water level, whilst accounting for surface facies where possible (B and D use Google Earth image from 2019).

The ITZ could also be subdivided into thirds (lower, middle, upper) based on time spent submerged per year. In this case we have defined the ITZ as the area flooded ≥4% of the time annually (above the mean spring high tide line in 2019) and the STZ as the area flooded <4% of the time annually. Of the ITZ (≤905 m from the channel), the lower ITZ (submerged >66% of the time) would have an upper limit of 45 m from the channel (corresponding to a channel water level of ≤0.97 m), the middle ITZ (submerged 33-66% of the time) would be between 45-590 m (water levels 0.97 -1.39 m) and the upper ITZ (submerged <33% of the time) would be between 590 - 905 m (corresponding to a water level of 1.39 – 1.95 m). This method also fails to accord with the boundaries described by Court *et al*. (2017) and places the boundary between lower and middle ITZ on the bank of the channel, compared to the seaward limit of the microbial mats. It also places the middle and upper ITZ within the middle of the microbial mat belt, whereas Court *et al*. (2017) had this boundary at the landward limit of the mats. This suggests that time spent submerged may also be an insufficient way to describe the ITZ at Site 3-QL. Our findings suggest that the microbial mats inhabit an environmental niche that is flooded ~2-15% of the time annually.

The middle, lower, and upper intertidal and supratidal zones of Site 3-QL have previously been described based on their surface facies (Court *et al*., 2017), however such zones have not previously been linked to water level monitoring data. Court *et al*., (2017) place the landward limit of the lower ITZ at the transition between spongey and leathery mat (~710 m from the channel), with the spongey mat at ~605-710 m and grainstone/packstone sediments <605 m. Our data thus suggest that the lower ITZ as described by Court *et al*., (2017) is flooded ~10-100% of the time, and the spongey mats ~10-25% of the time. The seaward margin of the spongey mat corresponds with the mean distance travelled inland by the upper quartile of annual water levels (Fig. 4.15.A (i)), whereas the landward limit occurs ~30 m landward of the mean daily maximum water levels during 2019 neap tides (Fig. 4.15.A (ix)). Based on the surface facies boundaries defined by Court *et al*., (2017), the leathery microbial mats of the middle ITZ (~710-875 m) are flooded ~5-10% of the time, and the pustular mats of the upper ITZ (~875-1055 m) are flooded ~2-5% of the time. The boundary between them lies between the mean distance travelled inland by annual daily maximum water levels (Fig. 4.15.A (iii)) and mean daily maximum water levels during spring tides (Fig. 4.15.A (vi)).

The lower supratidal, or 'featureless zone' (Court *et al*., 2017) (~1055-1280 m) is flooded 0.1-2% of the time, with the upper limits corresponding to the maximum water levels during spring tides (Fig. 4.15.A (iv)); the ephemeral halite zone (1280-1460 m) is flooded ≤0.1% of the time, with the upper limits defined by the maximum annual water levels (Fig. 4.15A (i)) and the upper STZ (>1460 m) was not flooded in 2019. This suggests that the middle and upper STZs are very rarely, if ever flooded by seawater, whereas the lower STZ may be flooded during rare storm periods (low atmospheric pressure) or spring high tides that correspond with strong onshore winds (Lokier *et al*., 2013).

Some of the surface facies boundaries described by Court *et al*., (2017) correspond with key tide levels from 2019, however others are less well matched. This may represent the variability between key tide boundaries between years or represent variability in the location of surface facie boundaries. The seaward limit of the dark coloured microbial mats appears to have shifted ~60 m seaward between the 2014 Google Earth imagery (used by Court *et al*. 2017; Fig. 4.15.C) and the 2019 images used here (Fig. 4.15.D), suggesting that the microbial mats may have migrated seaward over relatively short timescales. Earlier images suggest a fairly stable seaward margin of the dark coloured mast between 2010-2012, followed by a ~10 m landward migration of the mats in 2014 and then a 30-50 m seaward migration in 2019. However, no new images are available since 2019, and it is unclear if this apparent change is due to changes in light conditions and/or methods for image capture. Future work assessing whether the microbial mats have responded rapidly to recent sea level change would be interesting.

We suggest a slight variation on the zonal boundaries of the ITZ and STZ that applies the 2019 tide levels whilst considering some of the surface facies using the 2019 Google Earth imagery (Fig. 4.15.D). Here, the lower ITZ (0-615 m, flooded >20% of the time) has the landward limit defined by the upper quartile of annual water levels in the channel. The landward limit of the middle ITZ (615 – 905 m, flooded 4-20% of the time) is defined by the mean spring high tide and the landward limit of the upper ITZ (905 – 1090 m, flooded 1.5-4% of the time) is defined by the upper quartile of spring high tides. The lower STZ (featureless zone) spans from 1090 – 1235 m (flooded 0.2-1.5% of the time), with the upper limits defined by the distance travelled inland by the maximum spring high tide. The upper limits of the middle STZ (ephemeral halite) (1235 – 1450 m, flooded <0.2% of the time) corresponds with the maximum water level in 2019, and the upper supratidal zone (not flooded) (long-lived halite) is above the maximum 2019 water level. These definitions will be applied throughout the following discussion.

Spring and neap periods are not the only drivers of water level variability in the channel as the summer example period (20th Jul. – 19th Aug) had the highest mean water level and the winter example period (20th Jan. – 21st Feb.) had the lowest (Table 4.4). This suggests there is a strong seasonal driver of water level that is not just dependent on lunar phases. Whilst astronomical tides (e.g., springs and neaps) dominate water level variability in many areas, regions where these effects are smaller are likely to also be affected by other processes such as atmospheric forcing (Afshar-Kaveh *et al*., 2020) with semidiurnal tides responding to long-term changes such as seasonality (Woodworth *et al*., 2019).

Seasonal variability in mean sea level, sea level extremes, and tides can be caused by meteorological changes in air pressure and wind speed (Woodworth *et al*., 2019) as well as changes in ocean density due to temperature (thermosteric) and salinity (halosteric) variability (Vinogradov and Ponte, 2010) and in seasonal circulation changes, e.g., upwelling (Middleton, 2000). In the northern part of the Gulf, non-tidal sea level variability of 0.75 m was observed due to the combined effect of cross-shore winds

and low atmospheric pressure (Afshar-Kaveh *et al*., 2020), however the relative importance of air pressure and wind speed varies depending on location and timescale (Woodworth *et al*., 2019).

The 2019 summer period experienced the lowest air pressure (996±2 mbar) compared to the winter period (1018 ±2 mbar) (Fig. 4.6B), with similar results detailed by Afshar-Kaveh *et al*., (2020) who found that mean sea level pressure in the northern Gulf was lowest during summer (specifically Jul. – Aug.) and highest in the winter (specifically Jan. – Feb.) which corresponded with the sea-level in summer being 0.20-0.25 m higher than winter. One of the most important meteorological forcings on open ocean and coastal water level is air pressure (Woodworth *et al*., 2019). The sea surface responds to changes in atmospheric pressure and will rise in response to a drop in air pressure, theoretically by 1 cm for every 1 mbar (the inverse barometric effect (IB)), which could potentially result in a difference of 0.22 m between the 2019 summer and winter periods. Whilst this theoretical IB effect is rarely a reality in coastal areas (Goring, 1995) it could contribute towards the higher water levels (av.= 0.3 m higher) recorded at Site 3-QL in summer than in winter.

However, on shallow shelf areas, wind stress (the sheer force of wind on the ocean surface) may be even more significant than air pressure (Woodworth *et al*., 2019) as winds blowing over shallow water bodies can increase (wind set-up) or decrease (wind set-down) coastal water level (Afshar-Kaveh *et al*., 2020). The summer period experienced below average wind speeds (av. 4.3±0.8 m s^{-1}) (Fig. 4.6.A(iii)) suggesting that onshore wind was unlikely to be the primary cause of the higher water levels at Site 3-QL. The highest channel water levels in 2019 (2.50 m) was recorded on June 19th (2019) corresponding with a full moon spring tide, low atmospheric pressure (996 mbar) and above average wind speeds (7.50 m s^{-1}) blowing onshore from a NWN direction. This suggests that the combined effect of astronomical tides and seasonal meteorological variability (air pressure and wind speed) are responsible for promoting the highest channel water levels, which is most dominant in summer, though also may be significant during winter periods.

4.6.2 Long-term trends in channel water level, temperature, and salinity at Site 3-QL

We will use the long-term salinity, temperature, and water level data from the channel CTD-Diver (Logger A at Site 3-QL) to test the following conceptual model:

i. The lowest channel water salinity occurs at high tide and is the closest approximation of open marine conditions in the channel, though likely more saline owing to residual effects of the brines drained off the sabkha.
ii. As the flood tide progresses across the ITZ, surface salts (e.g., halite) are dissolved, and the tidal front becomes increasingly saline. As the tide falls, water drains back down the ITZ, so by the end of low tide, the water flowing back into the channel is the water that travelled the furthest inland, and hence has dissolved the most surface salts (e.g., Fig. 4.16). The salinity at

low tide is therefore proportional to the magnitude of the previous high tide. This would suggest that low tides following spring high tides would be the most saline, and low tides following neap high tides would be the least saline. This may also be impacted by seasonal variations in tidal range.

iii. Alternatively, channel water salinity may also be a function of evaporation (dependent on temperature, humidity, solar radiation, and wind). This would suggest that flooding during the daytime results in increased evaporation, which may cause the following high tide to dissolve more surface salts. Therefore, low tides following daytime high tides would be more saline than low tides following night-time high tides. This would also have a seasonal impact on salinity, with higher channel water salinities in summer compared to winter (e.g., Fig. 4.17).

iv. A final hypothesis is that channel water salinity may be related to groundwater discharge from beneath the buried hardground. This may vary seasonally if the confined aquifer head varies seasonally.

4.6.2.1 The relationship between channel water level and salinity

Channel water salinity had an inverse relationship with channel water level in both winter and summer periods (Fig. 4.9.A). The lowest channel water salinities were typically coincident with the highest channel water levels during each tidal cycle and represent the best approximation of open marine seawater salinity in the tidal channel. However, the minimum daily channel water salinity (Jan.-Sept. 2019) (54.9 ±5.6‰) is 17‰ higher than the salinity of offshore seawaters obtained in October 2017 (1-OS and 2-OS, av.= 37.9 ±2.1‰ (n=4)) and higher than other values reported for the Gulf (40-46‰) (Ge *et al*., 2020a; Rivers *et al*., 2019; Lokier and Steuber, 2009). This suggests that even at high tide, salinity in the tidal channel is elevated relative to offshore seawater, likely owing to the restriction relative to the Gulf (~10 km from the opening to open marine conditions) and due to the residual effects of the brines drained off the sabkha.

Channel water salinity during high tide was lowest in winter and ~9‰ higher in summer. On the 9th February, during a period of weak offshore winds, high tide salinities in the channel resembled offshore salinities reported in the Gulf (Rivers *et al*., 2019; Lokier and Steuber, 2009). This suggests that at times 'fresher' seawater (i.e., with chemistries similar to offshore seawater) enters the channel in winter which is less impacted by the discharge of residual brines from the ITZ. This may reflect reduced evaporation on the ITZ following winter high tides which leaves behind less surface salts to be dissolved by subsequent high tides. Furthermore, low channel water salinities may be favoured by offshore winds, which prevent the high tide from travelling as far inland.

The most landward portion of Abu Dhabi's coastal sabkha is characterised by evaporite minerals with surficial halite crusts and subsurface gypsum and anhydrite, which are transported seaward into the

microbial mats (Lokier and Steuber, 2008; Court *et al*., 2017). Behind the microbial mats there was a subtle topographic depression, where halite precipitates would form in footprints. It is therefore predicted that high tides that reach the microbial mats or beyond will dissolve these evaporites and produce increasingly saline low tide channel waters, with increased distance travelled inland by the previous high tide (hypothesis ii). During average meteorological conditions, channel water levels that reach maxima of 1.74-2.05 m are reflected in the flow of seawater into the dark coloured microbial mat zone (680-1020 m), and water levels >2.05 m travel past the mats and into the 'featureless zone' behind with an increasing prevalence of evaporites further inland (Lokier *et al*., 2013; Court *et al*., 2017).

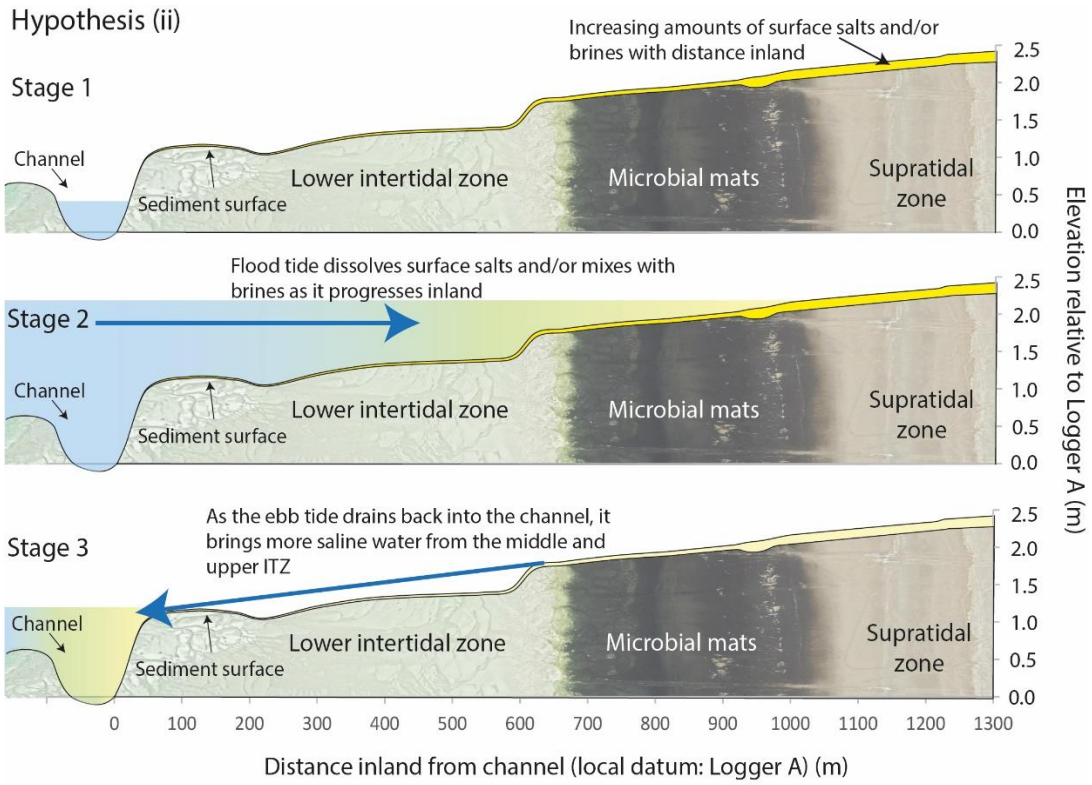

Figure 4.16. Conceptual model of hypothesis (ii): The salinity at low tide is proportional to the magnitude of the previous high tide. As the flood tide progresses across the intertidal zone, surface salts are dissolved, and the tidal front becomes increasingly saline. As the tide falls, water drains back down the intertidal zone, so by the end of low tide, the water flowing back into the channel is the water that travelled the furthest inland, and hence has dissolved the most surface salts.

Channel water salinity maxima occurred during the lowest channel water levels in summer and winter (Fig. 4.9.A), likely reflecting the final ebb tide waters that flowed back into the channel from the most landward part of the flooded ITZ. In summer, salinity at low tide was ~15‰ higher than in winter, and correlates positively with the height of the previous high tide, suggesting that high tides that travel the greatest distance inland dissolve the most surficial salt (Fig. 4.9.B).

One question is what effect subsequent high tides may have, and whether one high tide may dissolve more surface salts across the ITZ, leaving less to be dissolved by the following high tide which would result in a less saline low tide. To test this, we compared periods with successive high tides of similar magnitude, however the asymmetrical nature of the semi-diurnal tide means that there are rarely two consecutive high tides of similar magnitude. In the neap summer period, there were two consecutive high tides with water levels of 1.67 m at 19:00 on the 23rd July and 1.68 m at 05:30 on the 24th July, which would have travelled ~625 m inland reaching the microbial mat zone, and both with falling tides occurring during night-time hours. The latter had the highest channel water salinity at low tide (70.2‰ compared to 66.6‰) suggesting that the first high tide did not dissolve more of the surface salts.

The highest water level range occurs during spring tides, which were associated with most of the highest salinities at low tide, particularly in summer. Similarly, neap tides, which have the lowest tidal range, were associated with the lowest low tide salinities in summer, however the difference between neap and spring salinities at low tide were less pronounced in winter. Summer and winter spring tides had similar mean semi-diurnal tidal ranges (Tables 4.5 and 4.6), and similar peak channel water levels, however low tide salinities in the channel were >16‰ more saline in summer than in winter. Furthermore, the difference in low tide salinity between spring and neap periods was higher in summer (3.3‰) than in winter (0.4‰), suggesting that seasonal variations in evaporation across the intertidal zone plays an important role in governing temporal variations in channel water salinity.

4.6.2.2 The effect of solar insolation on channel water salinity and temperature

According to hypothesis (iii), one might expect that a daytime falling tide may leave behind the most surficial salt (e.g., halite) on the surface of the ITZ due to higher rates of evaporation particularly during peak solar radiation (e.g., during summer and between ~11:00-13:00) (e.g., Fig. 4.17, stage 1). Additionally, the sediment surface and the seawater will have been warmed (both as the ebb and flood tide progress across the ITZ), resulting in elevated temperatures in the channel during the following low tide (e.g., Fig. 4.17, stage 1 and 2).

Weak positive correlation between channel water temperature at low tide and the timing of the previous high tide from midnight to midday suggests that high tides in the morning have a minor impact on low tide channel water temperature, but generally high tides in the later morning produce low tides with higher temperatures (Fig. 4.10.A). However, there are several low tide temperatures >37 °C following high tides between 04:00 and 05:30 am when there would have been no solar heating of the tidal front as it travelled across the intertidal zone (Fig. 4.10.A). In these cases, low tides occurred between 10:30 and 12:00, suggesting solar heating throughout the latter stages of the ebb tide. In contrast there was strong negative correlation (R^2 0.84) between channel water temperature at low tide and the timing of the previous high tide from midday to midnight, suggesting

that low tides in the channel have the highest temperatures following high tides at midday, and low tide channel water temperature decreases following increasingly later high tides (Fig. 4.10.A).

If high tides leave behind more salt, or pools of evaporated brines in relative topographic depressions during periods corresponding with high solar radiation, then this may mean the following high tide can dissolve more salt/mix with surface brines, and therefore supply more saline water to the tidal channel at low tide (Fig. 4.17, stage 3 and 4). If this is the case, then the more saline low tides may be associated with the second-to-last (penultimate) high tides that peak in the daytime. Whilst there was positive correlation between low tide salinity and daytime penultimate high tides (after 9 am), the highest low tide salinities in the channel were associated with penultimate high tides between 03:00-06:00, which would be unaffected by evaporation (Fig. 4.10.B). This implies that although the timing of the penultimate high tide may impact low tide salinity, other more significant controls such as the distance travelled inland are likely to be important.

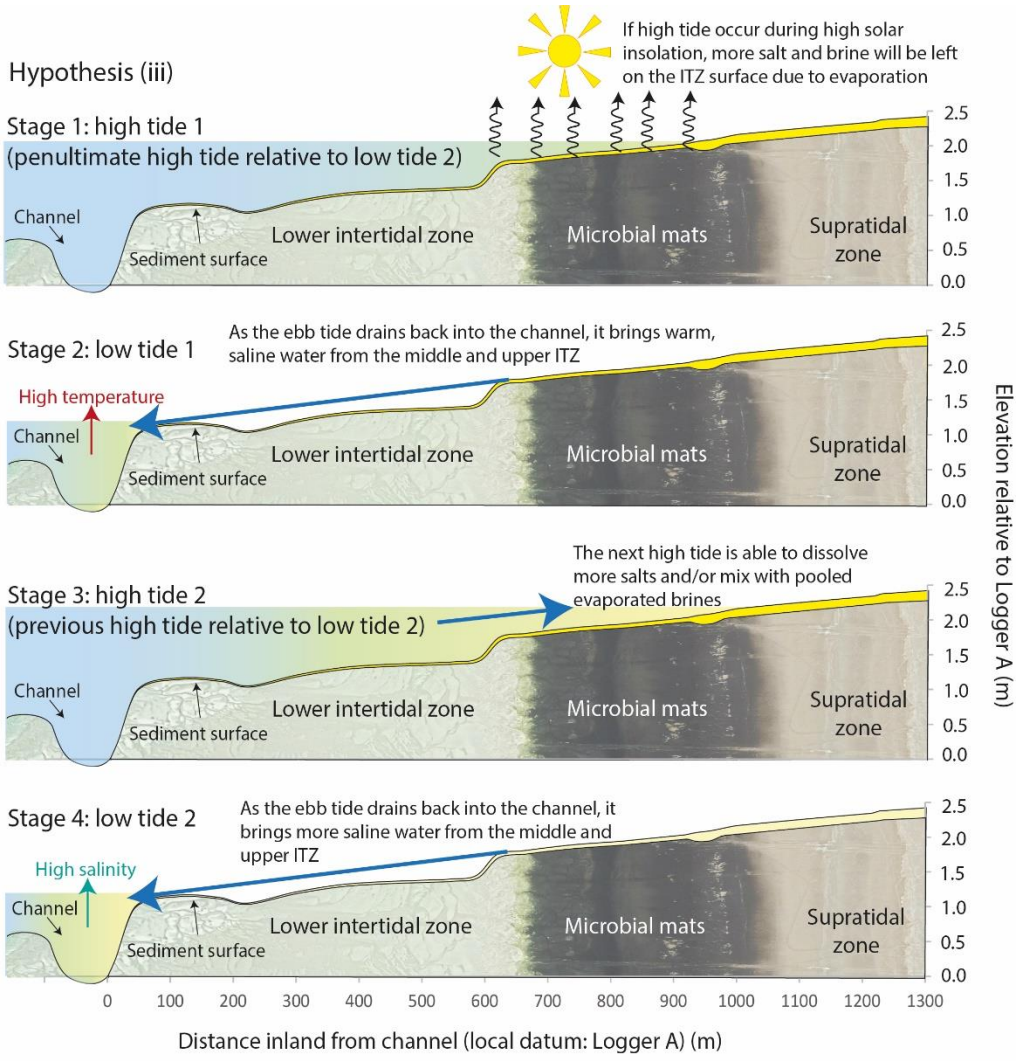

Figure 4.17. Conceptual model of hypothesis (iii): Low tide channel water salinity is a function of evaporation (dependent on temperature, humidity, solar radiation, and wind). Flooding during the

daytime (high tide 1) results in increased evaporation, which may cause the following low tide (low tide 1) to have high temperatures. The following high tide (high tide 2) is then able to dissolve more surface salts than normal, meaning the following low tide (low tide 2) is more saline than low tides following penultimate high tides during low solar radiation.

4.6.2.3 Discharge of continental brines as the source of increased channel water salinity at low tide

A final source for the increased channel water salinity at low tide may be the discharge of groundwaters from beneath the basal hardground (hypothesis iii). At high tide, the head difference below verses above the basal hardground may prevent the upwards leakage of continental brines. However, as the tide falls, the larger pressure difference may mean waters can discharge into the sediment column from below the basal hardground. Further inland in the coastal sabkha, Wood *et al*. (2002) document the leakage of continental brines and suggest these provide the primary source of solutes within the sabkha sediments. Sediment porosity will then control whether these denser brines flow laterally atop the basal hardground and downdip towards the channel. This effect may vary seasonally if the confined aquifer head varies seasonally, though this warrants further investigation. If the deeper brines are the source of high salinity waters (and not the seawater draining the back of the ITZ) then the solute balance may be different (Wood *et al*., 2002), however, solute concentrations were not measured in the channel waters at Site 3-QL. Future work investigating groundwater tracers in the low tide channel water, as well as employing loggers to assess the equivalent fresh-water head (to account for density effects) above verses below the basal hardground would be interesting. Observations in the field also suggest the buried mats may acta as a confining layer, though this warrants further investigation.

4.6.3 Changes in flood tide chemistry across the ITZ (Site 3-QL)

The hydrodynamic complexity of the flood tide, and the potential impact on diagenesis, were investigated at Site 3-QL by combining data from Logger B in the lower ITZ (6th Jan. 2019) with water samples collected as the flood tide travelled across the middle ITZ (7th Jan. 2019). Samples were both from the shallow tidal front (water depth 1- 3 cm) and 75-140 m behind the tidal front (14 – 50 cm water depth) (Fig. 4.11, 4.12). The high salinity seawater that first reached Logger B had likely dissolved surface salts as the tidal front travelled across the ITZ, increasing salinity by ~4‰ relative to water in the tidal channel at the same time (Logger A). However, salinity at Logger B then decreased to values below Logger A. This may suggest that the logger was unable to accurately measure salinity during low flow, however salinity only began to increase at a water depth of 0.28 m, which is substantially higher than the depth below which Logger A recorded erroneous salinity (4-7 cm). Another explanation for the low salinity recorded at Logger B is that ‘fresher’ (low salinity) seawater flows across the whole

area once the tide rises high enough that flow is not guided by the channel. This is supported by the salinity minima at Logger B (45.5‰) resembling the salinity measured at the mouth of Qantur Lagoon in 2017 (48.7‰), though warrants further investigation.

Temperature at Logger B initially increased with daytime solar insolation whilst the logger was exposed, before declining with the onset of the flood tide. The small increase in temperature at 11:50 could be driven by circulation from the back of the ITZ, suggesting there may be more complex 3D circulation patterns rather than the simple in and out of the flood and ebb tides. However, it is also possible that the increased temperature at 11:50 represents a short-lived sunny spell, and the continued warming from ~12:15 is likely the product of solar warming.

As the tidal front progresses inland at Site 3-QL, it passed over the lower ITZ which then transitioned into a microbial mat belt ~700 m landward of the tidal channel. Salinity was always higher at the shallow tidal front relative to the deeper water 75-140 m behind the front. Gypsum and halite remained undersaturated for all samples (Figs. 4.12.L, M) though appear to become less undersaturated as the tide floods the exposed ITZ, suggesting some dissolution of surface halite may occur. However, if the dissolution of halite were the primary driver of the increased salinity of the shallow tidal front (Fig. 4.12.C), then one would expect to see an increase in dissolved Na (relative to K), which is not observed (Fig. 4.12.J). Despite the limited data, this suggests that dissolution of surface salts alone in unlikely to be the primary source of increased salinity. Instead, the shallow tidal front salinity may increase as waters mix with evaporated surface waters trapped within the microbial mat topographic depressions and/or the discharge of shallow porewaters into the shallow tidal front. Additionally, sediment porespaces that were previously air filled at low tide, may get filled by the flood tide waters. This may push gases out into the tidal water (e.g., CO_2) into the shallow flood tide waters, but as the depth increases this effect will be greatly diluted. However, pCO_2 of the shallow tidal waters was also low, suggesting other processes may be affecting the pCO_2 of the shallow waters.

The pCO_2 (calculated with PHREEQC) of the shallow tidal front and the deeper (7 cm) water sample at 16:34 (sample 6) were lower than the deeper water samples and offshore seawater (Fig. 4.12.G). This likely reflects the consumption of CO_2 (and production of O_2) by the photosynthesising surficial microphytobenthos within the microbial mats within the shallow tidal front waters, which acts to increase the *p*H. Sub-tropical intertidal sand flats shift from a CO_2 sink (autotrophic system) during daytime emersion, to a CO_2 source (heterotrophic system) during immersion (e.g., samples 1 and 2, Fig. 12F) and night-time emersion (Lee *et al*., 2011).

However, if the low pCO_2 of the shallow tidal front was driven by photosynthetic activity, then one would expect to see elevated levels of O_2, which is not observed. Dissolved oxygen (DO) is highest in the deepest seawater samples (1 and 3), and though was not sampled for the locations overlying the

microbial mats, bubbles were observed escaping from the mats into the overlying seawater during the flood tide. However, all DO values from the flood tide were within the range of values obtained from the offshore seawaters. In contrast, ammonium appeared to decrease as the shallow tidal front progressed across the mats. This may reflect the activity of chemolithotrophs within the mat that fix inorganic carbon *via* redox reactions (e.g., the oxidation of ammonium) (Dupraz *et al*., 2009).

Alkalinity decreases as the tidal front progresses inland, suggesting there may be some daytime precipitation of carbonate minerals likely driven by the reduction in pCO_2 by photosynthetic activity in the shallow (≤3 cm) water body. This is supported by the increase in carbonate mineral SI throughout the flood tide (Fig. 12.H, I) and by a slight reduction in Ca/K in the shallow compared to the deep waters (Fig. 4.12.N). During night-time emersion, sediments may begin to release CO_2 (Lee *et al*., 2011) which would act to lower the *p*H and carbonate mineral SI of surface waters, potentially promoting the dissolution of carbonate minerals. As access restrictions meant that no samples were obtained during night-time flooding for this study, this warrants further investigation.

4.6.4 Creek water chemistry variability during ebb and flood tides (Site 4-QL)

In 2019 the creek water samples were collected two days after a neap tide, whereas in 2017 samples were collected between a spring and neap tide when both low and high tides were ~0.20 m higher than during 2019 sampling. The timing of the tides was also different during both sampling periods; in 2019, samples were collected throughout a daytime ebb tide, with midday peak solar radiation coincident with low creek water levels (0-30 cm water depth), and water flowing back down the creek from the back of the ITZ (Fig. 4.13, 4.14.A). This backflow of water from the microbial mats would therefore be expected to contain by-products reflecting the maximum biological response to solar radiation. In contrast the 2017 samples were collected throughout a morning ebb to flood tide transition, when midday solar radiation would have been coincident with slightly higher creek water levels, and with 'fresh' seawater travelling up the creek from Qantur channel. Seasonal differences may also drive variability in water chemistry between the two sampling periods; in 2017 the creek was sampled at the end of a particularly long summer, with peak daytime air temperatures at Abu Dhabi Bateen airport (34 °C) 7 °C higher than peak temperatures during January 2019 sampling (Fig. 4.13.C, 4.14.B).

Regardless of these expected differences, there were similarities between water chemistry during these two periods. Maximum and minimum creek water salinity were near identical during 2019 and 2017, with both periods displaying an increase in creek water salinity throughout the ebb tide, followed by a lower salinity throughout the flood tide when salinity resembled that from near the mouth of Qantar channel (2017) (~50 ‰) (Fig. 4.14.C). The increasingly saline water in the creek throughout the ebb tide is suggested to represent the backflow of waters from the microbial mats at the back of the

ITZ. Alternatively, as the water table falls, shallow porewaters may be discharged into the creek and porewaters may be impacted by the upwards advection of continental brines through local areas of high permeability.

On the 16th January 2019, high tide in the channel at Site 3-QL (1.66 m) would have travelled ~625 m inland reaching the seaward margin of microbial mats at Site 3-QL (Fig. 4.15.D), whereas on the 24th October, high tide at the coast (1.90 m) would have travelled ~880 m inland, reaching the pustular mats at Site 3-QL, which is likely to be similar at Site 4-QL. The salinity of microbial mat surface waters sampled in February 2014 (84-87‰) were similar to peak creek salinity in 2017 and 2019 (76 and 78‰), however the sample from the upper intertidal zone (Site 4-QL-U) was significantly higher (127 ‰) likely owing to reduced recharge from seawater, increased evaporation, and/or the input of continental brines from below. Peak creek salinity (Site 4-QL) was higher than peak channel water salinity at Site 3-QL during low tide in the winter period (57.6 ±2.8‰) reflecting the higher degree of restriction within the creek relative to the open marine conditions.

This suggests a model where creek water chemistry transitions from open marine-like chemistries during periods of relatively high creek water level and flood tide flow, to chemistries reflecting processes from the inland surface waters and microbial mats during low water levels and during the latter half of the ebb tide flow. The discharge of more saline porewaters may also contribute to increased salinity at low tide as porewaters may be impacted by the leakage and advection of continental brines.

Evaporation over the microbial mats drives increased salinity which may result in CO_2 degassing (Markham and Kobe, 1941). Similar results were described by Rivers *et al*., (2019), who noted that with increased evaporation, *p*H increased, and alkalinity decreased between salinities of ~60 – 90‰, which they attributed to aragonite precipitation driven by decreased CO_2 associated with the increased ionic strength. In contrast, the inland waters of the upper ITZ had high salinity (123 ‰), low *p*H (approximate to offshore) and a slightly higher alkalinity than the microbial mats surface waters. Rivers *et al*., (2019) found that when evaporation produced salinities >90‰, alkalinity increased due to increased ionic concentration, whereas pH decreased, likely resulting in the dissolution of carbonate minerals, which may also be occurring at Site 4-Ql-UI (Fig. 4.14. C, D, E). When using Cl as a tracer for evaporation, Ca/K suggests that the inland surface waters appear slightly Ca depleted, with the degree of deletion (relative to seawater) increasing inland, suggesting there may be some precipitation of $CaCO_3$.

Evaporation was not the only driver of chemical changes updip of (and within) the creek. Within the tidal creek in 2019, there was a distinct change in the organic water chemistry at ~13:15 -14:10 when DOC, DTN and NH_4^+ increased, and alkalinity, pCO_2 and redox potential (Eh) decreased (Fig. 4.14). This was likely driven by an increase in primary production within the microbial mats and/or within the

creek by microphytobenthos (photosynthetic diatoms, cyanobacteria, flagellates, and green algae), driven by increased midday solar radiation, the effects of which are enhanced by low water levels. Microphytobenthos inhabit the sediment surface of intertidal settings (Cahoon, 1999) and microbial mats (Dupraz *et al*., 2009) and produce extracellular polymeric substances (EPS) which form a stabilising biofilm on the sediment surface providing protection from erosion by storm and wave action (Consalvey *et al*., 2004). EPS provides a source of primary production which may result in increased dissolved organic components (e.g., DOC and DTN) and increased inorganic by-products of microbial metabolisms (e.g., NH_4^+, CO_2 and alkalinity – depending on the metabolisms) (Beck *et al*., 2008) within the creek as the ebb tide flows back downdip. Heterotrophic degradation of EPS could also release Ca^{2+} into the shallow porewaters, which may discharge into the creek at low tide allowing for carbonate nucleation (Dupraz *et al*., 2013).

The high dissolved oxygen concentrations (~160% at site MM-2) and extremely low pCO_2 in the microbial mat surface waters reflect photosynthesis which consumes CO_2, thereby driving an increase in *p*H and carbonate mineral saturation, producing significantly supersaturated surface waters with respect to aragonite, calcite, and dolomite (Fig. 4.14.G, H). Similar chemical changes are observed in other hypersaline microbial mats; daytime photosynthetic activity in the surface of the mat drives an increase in O_2 production, whilst consuming CO_2 and hence increasing *p*H (Ludwig *et al*., 2005). As pH has an order-of-magnitude impact on carbonate ion concentration this may drive the localised precipitation of carbonate minerals (Sun and Turchyn, 2014). Despite having high *p*H, low pCO_2 and high carbonate mineral SI, the surface waters from the microbial mat surface waters have alkalinities below seawater. This suggests that the increase in *p*H may drive an increase in carbonate mineral SI and therefore promote the precipitation of carbonate minerals, which results in decreased alkalinity by removing carbonate ions from solution.

As the tide recedes in the lower ITZ one would expect this CO_2 depleted, and mineral supersaturated water to flow back down the tidal creek. However, in 2017 and 2019, creek water *p*H decreases, and $pCO_{2(aq)}$ increases slightly throughout the latter half of the ebb tide, despite the high *p*H values (>8.5) and extremely low $pCO_{2(aq)}$ values (<0.02%) associated with the microbial mat surface waters. This suggests that continued precipitation of carbonate mineral may occur as the water flows back down the ITZ, which drive a decrease in alkalinity and *p*H within the creek. This is supported by the decreasing carbonate mineral SI (Fig. 4.14.G), and by strontium depletion (as Sr/Cl) using Cl as a conservative tracer. During the first half of the ebb tide and the onset of the flood tide (2019), Sr/Cl resembles offshore seawater (Fig. 4.14.N). The orthorhombic aragonite lattice preferentially incorporates cations with relatively large ionic radii such as Sr^{2+} and Ba^{2+} (Cubillas *et al*., 2005; Pederson *et al*, 2020), producing aragonite Sr/Ca ratios approximately five times those of calcite (Joseph *et al*., 2013). Throughout the latter half of the ebb tide, Sr/Cl decreases relative to seawater, suggesting aragonite

precipitation may be removing Sr from solution. Furthermore, Mg/Ca increased throughout the latter half of the ebb tide and high porewater Mg/Ca favour the precipitation of aragonite over calcite (Folk, 1974; De Choudens-Sánchez and González, 2009; Sun *et al*., 2015).

Whilst samples were not obtained during night-time ebb and flood tides in the creek, it is likely the chemistry of the ebb tide in the tidal creek would change considerably without the effect of photosynthesising mats on surface waters updip of the creek, which may promote dissolution of carbonate minerals. To determine if the backflow of surface waters from the microbial mats into the lower ITZ promotes net carbonate minerals production or dissolution requires further investigation.

4.6.5 Wider implications

4.6.5.1 Defining the ITZ

Definitions of ITZ boundaries are often inconsistent within the literature and there is a need for a robust approach to defining and comparing similar environments. This study highlights the limitations and complex nature of defining boundaries in a shallow carbonate ramp environment, though supports the combined use of water level data and sediment surface morphologies. Recently, satellite remote sensing has been applied to categorise ITZs based on duration of time flooded (Bishop-Taylor, 2019), however our knowledge, there are few examples of field-based studies investigating how water level changes across the ITZ over multiple seasons. Future work applying satellite remote sensing to low angle coastal environments may therefore benefit from the water level and ITZ classifications presented here to ground truth and test methodologies for defining coastal zones.

4.6.5.2 Inferring salinity from foraminifera

The subsurface distributions of benthic foraminifera are strongly influenced by salinity (Wu et al., 2015). This work highlights the spatiotemporal heterogeneity in salinity associated with channels and creek networks within costal ITZ environments. This may have implications for studies using foraminifera as salinity indicators or as palaeoproxies for salinity and thus channel/creek systems should be avoided for sampling as the range of salinity is likely not reflective of the wider environment.

4.6.5.3 The sub-surface flow of solutes

Considering ITZ hydrodynamics in 3D compared to 2D is important not only for establishing where the flow goes, but also for understanding the solute budget. This is particularly important for understanding the sedimentological evolution of carbonate ramp systems as a function of hydrodynamics and for workers in similar environments that may collect samples at one time of day/year.

Channels and creek networks provide an opportunity to understand the export of solutes from the ITZ system to the offshore environment. Our observations suggest that whilst the topographic depressions

in the microbial mats stay wet during low tide, the sediment surface seaward and landward of the mats becomes dry when exposed. This may be most significant seaward of the microbial mats where there are no sub-surface buried microbial mats to act as a confining layer. At low tide, the water level in the sediment will drop and shallow porewaters flow laterally towards the sea and/or creek network allowing oxygen-rich air to permeate the sediment (Fig. 4.18).

As the sea level rises, fresher (less-dense) seawater may flow laterally into sediments adjacent to the channel until the surrounding sediment surface is flooded by the incoming tide when most exchange will occur vertically. The influx of seawater to fill the voids displaces air from the partially saturated pore network, and drives a net flux of water, oxygen, and solutes into the upper part of the pore system. This work highlights there is likely a significant seasonal difference in the solute balance, with an increased ITZ salt budget in summer months. This is important for controlling the density of fluids and subsurface flow as a function of salinity which may promote a seasonality to carbonate diagenesis, however future work is needed to budget the mass of salts exchanged by this process.

As tide falls, lower water levels in and around the creeks reduce the head difference between the confined brines beneath the deeper basal hardground and the overlying porewaters in the recent sediment compared to within the surrounding ITZ sediment. This may promote the preferential leakage of continental brines into the creeks at low tide (Fig. 4.18.C).

4.6.5.4 The impacts of sub-surface later flow on diagenesis

Understanding the subsurface flow of solutes and the impact this has on sediment redox zonation has important implications for reactions driven by the advection of fluids such as carbonate diagenesis (calcite and aragonite precipitation/dissolution and potentially reflux dolomitisation). The lateral flow of water adjacent to creek and channel networks may preferentially favour carbonate precipitation and firmground formation by circulating supersaturated seawater within the shallow sediments and/or by influencing microbial communities by controlling the depth of the redox boundary. As the tide falls, shallow porewaters likely flow towards the nearest creek network following the steepest hydraulic gradient, meaning areas near creeks have the greatest lateral flux of porewaters (Fig. 4.18.B). The flood tide may then flush carbonate supersaturated and oxygenated seawater back into the sediment, potentially promoting firmground formation which may act to stabilise creeks over time (Fig. 4.18.D).

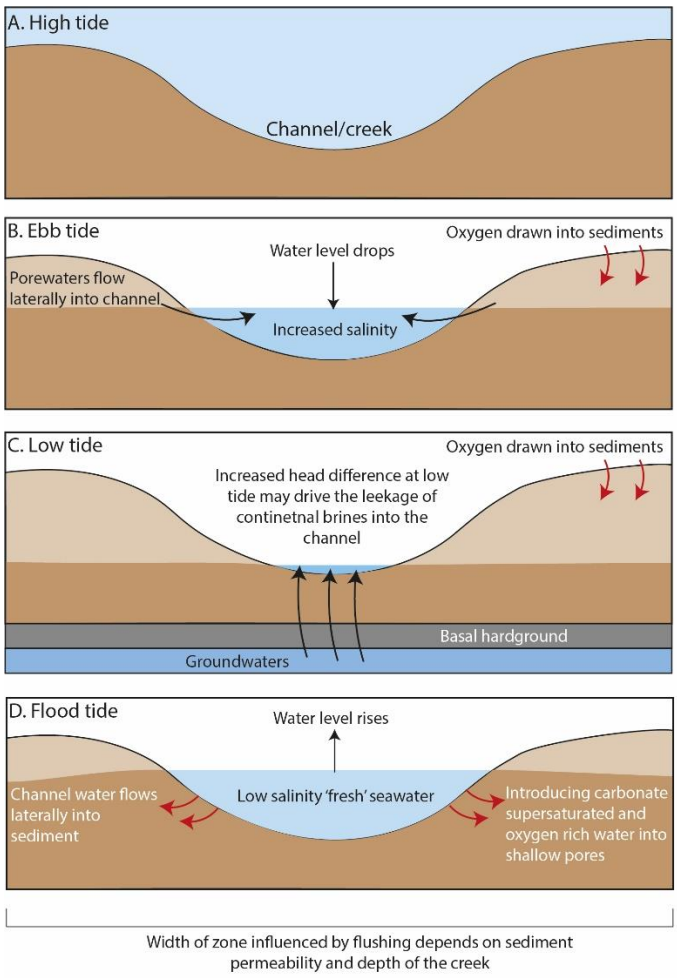

Figure 4.18. Schematic illustrating the potential later flow pathways of solutes surrounding a tidal creek during the transition from ebb to flood tide.

4.7 Conclusions

Carbonate and evaporite sediments have been well-studied in coastal Abu Dhabi and these precipitates are strongly influenced by water chemistry. However, the degree to which temporal variations in surface water chemistry drive diagenesis (e.g., dissolution, micritisation, and cementation) within the shallow marine settings has received less attention. This study investigates how the spatial occurrence of different surface facies across the intertidal-supratidal zone is controlled by duration of tidal flooding. Furthermore, it presents temporal changes in surface water chemistry in the intertidal zone (ITZ) over short (~1 day) and longer (>1 year) timescales and investigates what impact this may have on diagenesis. This work concludes:

1. Variability in surface facies observed across the ITZ are likely related to annual tide limits, with the lower, middle, and upper ITZ flooded >20%, 4-20% and 1.5-4% of the time per year, respectively. The microbial mats inhabit the middle to upper ITZ and reside in an environmental niche that is flooded ~2-15% of the time annually.

2. Landward of the microbial mats, the supratidal zone (STZ) (defined by the area above the upper quartile of spring high tide water levels) is flooded <1.5% of the time. The lower STZ is flooded 0.2-1.5% of the time during extreme and rare storm periods or spring high tides that correspond with strong onshore winds and/or low atmospheric pressure. The middle STZ is rarely flooded (<0.2% of the time), and the upper STZ is never flooded.
3. Whilst astronomical tides (e.g., springs and neaps) are largely responsible for variability in coastal water level, seasonal forcing such as low atmospheric pressure are likely responsible for a large proportion of the higher channel water levels measured in summer (av. =~0.30 m higher), than in winter.
4. In both summer and winter periods the magnitude of the maximum channel water salinity at low tide at Site 3-QL is largely a function of the magnitude of previous sea level highs, as higher tides reach the back of ITZ and flush out salts concentrated by evaporation.
5. Summer months experience higher channel water salinities than winter months at Site 3-QL due to higher summer water levels which travel further inland and dissolve more surface salts, and possibly due to increased evaporation across the ITZ in summer months leaving more surface salts behind compared to winter months.
6. Daytime flood tides travelling across the microbial mats of the middle ITZ increase in *p*H and mineral SI due to the consumption of CO_2 by surficial microphytobenthos, which promotes the precipitation of carbonate minerals.
7. Daytime ebb tides flowing back down the ITZ from the microbial mats of the middle to upper ITZ and may drive the precipitation of aragonite in the lower ITZ by supplying supersaturated seawater. This may be most significant surrounding tidal creek networks that preferentially drain waters from the upper ITZ to the lower ITZ.

This study suggests that the salinity and temperature of surface waters flowing over the ITZ vary significantly throughout the year. Whilst surface water chemistries of ebb and flood tide seawaters were only obtained during winter days, results suggest that the ITZ is an area of active carbonate precipitation, likely driven by the backflow of CO_2 depleted and carbonate mineral supersaturated seawaters from the microbial mats. Future work assessing the effect of night-time ebb and flood tides across the ITZ and the surface water chemistry at different times of the year (e.g., summer) would be valuable, and would help ascertain whether the surface waters of the ITZ promote net carbonate mineral dissolution or precipitation annually. Furthermore, further investigation is needed to determine to what degree shallow porewaters and surface waters are affected by the leakage of continental brines, and what role this plays on diagenesis in the ITZ. Nevertheless, this study demonstrates the hydrodynamic complexity of this carbonate depositional environment and highlights the importance of multi-seasonal sampling where possible.

5. Physical, chemical, and biological drivers of firmground formation surrounding Qantur Lagoon Tidal Creek, Abu Dhabi

i. Authors

Hazel Vallack[1], Hilary Corlett[2], Sarah E. Greene[3], Emily N. Junkins[4], Stephen W. Lokier[5], Victoria A. Petryshyn[6], Bradley S. Stevenson[4], Gemma Tong[7], Fiona Whitaker[7]

1: School of Geographical Sciences, University of Bristol
2: Department of Physical Sciences, MacEwan University
3: School of Geography, Earth and Environmental Sciences, University of Birmingham
4: Department of Microbiology and Plant Biology, University of Oklahoma
5: School of Ocean Sciences, Bangor University
6: Environmental Studies Program, University of Southern California, Los Angeles
7: School of Earth Sciences, University of Bristol

ii. Author contributions

Porewater chemical analysis, grain size analysis, scanning electron analysis (SEM), microscopy, data analysis, writing, and interpretation were conducted by H. Vallack with interpretive support from S. Greene, F. Whitaker, H. Corlett, and V. Petryshyn. X-ray diffraction (XRD) analysis was performed at the University of Alberta, financially supported by H. Corlett. Cores were CT-scanned in the School of Biological Sciences (Bristol University) by H. Corlett and F. Whitaker, with post-processing of the images by H. Corlett. DNA extraction and analysis were performed by E. Junkins and B. Stevenson, and interpretation and analysis of the data by H. Vallack. Inland surface waters were sampled and analysed by G. Tong under the supervision of F. Whitaker. Field work, sampling of sediment and porewaters, and analysis of porewater pH, alkalinity, Eh, and SEC was conducted by H. Vallack, S. Greene, S. Lokier, F. Whitaker, with support from and Gordon Coy (2019 field campaign) and Prasanth Thiyagarajan (2017 field campaign).

iii. Abstract

Marine firmgrounds and hardgrounds are common early-diagenetic features in modern and ancient carbonate successions and have been employed as stratigraphic indicators for the effective utilisation of both groundwater and hydrocarbon resources. Furthermore, hardgrounds that remain unaltered by subsequent meteoric diagenesis provide potential paleoseawater/paleoporewater chemical proxies, however direct interpretation of these palaeo-proxies remains challenging as the genesis of marine firmgrounds and hardgrounds remains poorly understood. Firmgrounds are typically assumed to form at the sediment-water interface *via* hydrodynamic forces, however recent work in coastal Abu Dhabi suggests they may be forming *via* the active precipitation or aragonite in the shallow subsurface driven by microbial processes operating within the sediment column. This study combines analysis of the

physical and chemical characteristics of shallow sediment cores and firmground samples, corresponding porewater chemistry, and microbial community composition (*via* 16S SSU rRNA gene sequencing) from an intertidal zone in coastal Abu Dhabi to investigate physical, chemical, and biological drivers of modern firmground formation. Firmgrounds were present at three out of four sub-sites surrounding a tidal creek, and evidence of early subsurface lithification was observed where firmgrounds were not present. A decrease in porewater alkalinity at the upper firmground surface of one sub-site (~7cm depth) suggests active subsurface lithification, and is concurrent with an increase in porewater *p*H, suggesting cementation may be linked to microbial metabolic processes associated with the redox boundary. In contrast <10 m away, firmgrounds at ~11-16 cm below the surface shows no evidence of active cementation highlighting the complex nature of diagenesis in the intertidal zone. Whilst abiotic processes cannot be ruled out, these findings provide evidence for a counter hypothesis to the classically held view of abiotic drivers of firmground formation which may have implications for interpreting the role of biological processes in hardground formation in the geologic record.

5.1 Introduction

Marine diagenesis is widespread and abundant in shallow-water carbonate settings (Moore and Wade, 2013). Abiotic and microbially mediated authigenic carbonate precipitation results in early-diagenetic features which are common in sedimentary rocks throughout the geological record (Hillgärtner, 1998; Christ *et al*., 2015). Such features include pore lining cements, laterally extensive firmground and hardground layers, or spheroid concretions and nodules (Marshall and Pirrie, 2013). They are suggested to form *in situ* (Sun and Turchyn 2014, Plet *et al*., 2016; Ge *et al*., 2020; Chapter 3) within the top few meters of sediment and have been linked directly to the global carbon, sulphur, and iron cycles (Schrag *et al*., 2013; Plet *et al*., 2016).

This study focuses on the formation of marine firmgrounds, though the terminology applied to such features can be inconsistent (see discussion in Christ *et al*., 2015 and Ge *et al*., 2020a). We follow the definition of 'concretionary sub-hardgrounds' Ge *et al*. (2020a) when describing hardgrounds and refer to partially-lithified (incipient sub-hardgrounds) as firmgrounds. Despite being abundant in modern and ancient carbonate successions (Hillgärtner, 1998), the genesis of marine firmgrounds and hardgrounds remains poorly understood.

Hardgrounds have been employed as stratigraphic indicators (Christ *et al*., 2015) and may form barriers or baffles to fluid flow (Manchini *et al*., 2004). Their lateral continuity and spatial variations thus have important implications for platform- and/or basin-wide correlation in sequence stratigraphy and for the effective utilisation of both groundwater and hydrocarbon resources (Agar and Geiger, 2015). Furthermore, owing to their relatively quick formation in equilibrium with seawater, hardgrounds that remain unaltered (e.g., by subsequent meteoric diagenesis) have been identified as potential

paleoseawater/paleoporewater chemical proxies using trace elements concentrations and isotopic ratios (Erhardt *et al*., 2020). Geochemical analysis of authigenic carbonates may also preserve a host-sediment signal (Plet *et al*., 2016), act as tracers of fluid composition during early diagenesis (Himmler *et al*., 2010), and be used to infer microbial origin (Mavromatis *et al*., 2012). However, direct interpretation of these palaeo-proxies remains challenging as a comprehensive understanding of the direct drivers of authigenic carbonate precipitation is limited.

The extent that diagenetic alterations impact primary chemical, textural, and isotopic signatures of carbonate sediments depend on several inter-related factors (Ahm *et al*., 2018): (i) the chemical composition of the diagenetic fluid (i.e., meteoric or seawater derived, salinity) (Folk, 1974; Sheikholeslami and Ong, 2003); (ii) gross seawater chemistry (that has varied secularly through time); (iii) chemical alterations to the diagenetic fluid by macro/microbiology (specifically affecting *p*H and alkalinity) (Kristensen, 2000); (iv) solute transport mechanisms (advection or diffusion); (v) marine energy regime (Shinn, 1969); (vi) the reactivity of the carbonate mineral through time (dependent on grain size, reactive surface area, and impacted by other kinetic factors); (vii) pressure and temperature (climate, depth of burial and/or depth of overlying water) (Burton and Walter, 1987); (viii) organic matter (OM) delivery (Arndt *et al*., 2013) and sedimentation rate. However, the relative importance of different chemical, physical, and biological drivers, and the extent to which drivers are local, regional, or global are still poorly understood.

Hillgärtner (1998) describes discontinuity surfaces within an ancient shallow-marine carbonate platform including subtidal firm- and hardgrounds and inter- to supra-tidal hardgrounds resulting from rapid and substantial environmental changes associated with changes in relative sea level, accumulation rate, energy regime and sediment type. Environmental controls on firm/hardground formation are thus variable and complex, however they typically form at, or near to the sediment-water interface in tropical/sub-tropical shallow-water environments over geologically short timescales of 10 – 10,000 years (McLaughlin *et al*., 2008; Christ *et al*., 2015). Formation is thought to be driven primarily by bottom water carbonate supersaturation and seawater circulation (Christ *et al*., 2015); low sedimentation rate or hiatus in sedimentation (Coleman and Raiswell 1993; Lash and Blood, 2004); and elevated hydrodynamic levels (Dravis, 1979; Lighty, 1985). Hardgrounds are associated with the maximum flooding surfaces of different sea level cycles (marine regressions and transgressions), which may be particularly important in some coastal areas (e.g., Abu Dhabi) where the sedimentary basin experienced rapid re-flooding in the Holocene (Lokier *et al*., 2015; Paul and Lokier, 2017). However, processes involving microbial activity may also be important in driving the precipitation of “abiogenic” cements (Kandianis *et al*., 2008) with processes such as organoclastic sulphate reduction being suggested as drivers of subsurface cementation in coastal Abu Dhabi (Lokier and Steuber, 2009; Ge *et al*., 2020a; Chapter 3),

The study of shallow-marine carbonate diagenesis has attracted attention from several fields. One body of research takes a mechanistic approach to precipitation of layered marine carbonates from a biogeochemical perspective. These studies address issues of meta-stable carbonate phases (Morse *et al*., 1997; Drupp *et al*., 2016), and the precipitation of carbonate minerals in microbial mats (Chafetz and Buczynski, 1992; Baumgartner *et al*., 2006; Dupraz *et al*., 2009). Some attention is specifically paid to the formation of authigenic firm/hardgrounds and concretions in relation to microbial respiratory processes (Coleman, 1993; Aghib *et al*., 1991; Raiswell and Fisher, 2004; Kandianis *et al*., 2008; Loyd and Berelson, 2016; Plet *et al*., 2016, Greene *et al*., 2012), however these often focus on deep sea localities. Limited process-based examples exist for modern aragonitic cemented firm/hardgrounds (McKenzie and Bernoulli, 1982; Ge *et al*., 2020a), and any assessment of microbial drivers is often limited.

Another approach focuses on products of shallow water precipitation, such as authigenic firm/hardgrounds and associated petrophysical characteristics, cement geochemistry, and isotopic composition (Christ *et al*., 2015) (and references therein) with complementary studies of ancient deposits from deep sea environments (Lash and Blood, 2004; Gaines and Vorhies, 2016; Liang *et al*., 2016). However, diagenetic overprinting during burial makes it difficult to identify the primary causal factors in firm/hardground formations (Christ *et al*., 2015). Problems of overprinting can be circumvented by examining Recent deposits, and there is a long history of work describing submarine lithification in the Arabian/Persian Gulf (Evans *et al*., 1964; Shinn, 1969; Taylor and Illing, 1969; Khalaf *et al*., 1987; Paul and Lokier, 2017; Ge *et al*., 2020a).

Whilst firm/hardgrounds are typically assumed to form at the sediment-water interface, recent work in Yas lagoon, Abu Dhabi, describes a firmground forming *via* the active precipitation of aragonite in the shallow subsurface driven by processes operating within the sediment column (Chapter 3). In Yas lagoon, increased aragonite and calcite saturation indices occur in a narrow (<2 cm) interval of elevated porewater *p*H and low bicarbonate alkalinity surrounding the firmground. Increased *p*H is likely the by-product of sulphate reduction possibly in conjunction with pyrite formation and suggests that firmground formation is linked to microbial processes. Continued cementation may lead to the development of concretionary sub-hardgrounds (Ge *et al*., 2020a) that may subsequently become exposed by winnowing of overlying sediments or could be buried by continued sediment accumulation without any exposure, which may result in the erroneous identification as 'classic' hiatal hardgrounds.

Although many studies invoke microbial metabolic processes as drivers of cementation and dissolution, uncertainty remains as to the respiratory processes responsible, and how physiochemical characteristics affect microbial community structure on different spaciotemporal scales. Ge *et al*. (2020a) suggest the precipitation of aragonite cemented firmgrounds is Abu Dhabi's coastal sediments

is driven by aragonite supersaturated seawater, tide-induced water circulation, evaporation, and microbial activity. However, they acknowledge that the level of research presented is likely insufficient to truly capture the complexity of firmground formation in the intertidal zone (ITZ) (Ge *et al*., 2020a). Previous work in the region has investigated the role microbes play in promoting the formation of non-stoichiometric dolomite (or very high Mg-calcite) (Bontognali *et al*., 2010) whereas studies detailing the role microbes play in driving firmground formation by aragonite precipitation are lacking (Ge *et al*., 2020a).

This interdisciplinary study addresses three significant knowledge gaps: (i) the need for rigorous processed-based assessments of factors affecting marine sediment diagenesis prior to subsequent meteoric diagenetic overprinting (Christ *et al*., 2015). (ii) The lack of field studies investigating the role of microbes in the formation of shallow marine, calcite and specifically aragonitic early diagenetic firm/hardgrounds, to go beyond inference of the role of microbes in descriptions of early diagenesis; and (iii) the need for further investigation into the complexity of firmground formation within the ITZ of coastal Abu Dhabi.

This study aims to investigate whether the mechanistic model of firmground formation developed for Yas Lagoon (Chapter 3) is applicable to the more hydrodynamically complex environment surrounding a tidal creek in nearby Qantur Lagoon (hydrodynamics detailed in Chapter 4). We combine analysis of porewater chemistry with physical and chemical characteristics of shallow sediment cores and firmground samples and microbial community composition (*via* 16S SSU rRNA gene sequencing) to investigate physical, chemical, and biological drivers of firmground formation. However, unlike Yas lagoon, here we compare the drivers of firmground formation at four contrasting sub-sites to ascertain which drivers of authigenic carbonate formation may be locally or regionally important, which will provide a basis for interpreting similar features in the geologic record. We aim to address the following questions:

a) Are firmgrounds actively forming in the subsurface?
b) What is driving the heterogeneous distribution of firmgrounds surrounding the tidal creek?
c) Is formation primarily driven by the circulation of supersaturated seawater, which may be dependent on sediment physical characteristics and hydrodynamics surrounding the creek?
d) Or are microbial metabolisms important for driving cementation? And if so, are these likely to be similar metabolic processes to those driving cementation in Yas lagoon?

5.2 Depositional setting of the study area and regional climate

The southern side of the Persian/Arabian Gulf (hereafter referred to as the Gulf) is a shallow epicontinental sea (mean depth of 35 m) and acts as a rare recent analogue of ancient low-angle carbonate-evaporate ramp systems (Lokier *et al*., 2015; Lokier and Fiorini, 2016). The shoreline trends in a northeast to southwest direction and is protected from the open marine conditions of the Gulf by several barrier islands. The coastal area is an extremely low ramp environment (0.4m/km) which progresses offshore from a supratidal evaporite sabkha, through a laterally extensive ITZ into a carbonate-dominated subtidal environment (Evans *et al*., 1964; 1969).

The shallow Gulf has high salinities (37‰ – 46‰) relative to the nearby Indian Ocean (Lokier and Steuber, 2009; Chapter 3) and high Mg/Ca ratios (Wood *et al*., 2002; Rivers *et al*., 2019) owing to high evaporation and relative restriction. Coastal Abu Dhabi experiences a semi-diurnal micro-tidal regime (amplitude 1 - 2 m) (Paul and Lokier, 2017) and the dominant north-westerly Shamal wind can produce gale force winds and storm surges (Lokier and Steuber, 2009). The UAE experiences an extremely arid climate, with mean annual rainfall of 72 mm, the majority of which falls in short-lived torrential rainstorms, typically between February and March (Raafat, 2007). Annual air temperatures range from 7°C during winter nights to 50°C in summer days (Lokier and Fiorini, 2016).

The study area is located on the southern shore of the Gulf, ~45 km southwest of Abu Dhabi Island (Fig. 5.1.A, B). The Qantur Lagoon Tidal Creek Site (QLTC) is situated in the middle ITZ of the eastern Qantur Lagoon (Fig. 5.1.C, D), downdip from the supratidal sabkha and centred around a small tributary tidal channel, with prior work on surface sediments in the area described by Lokier *et al*. (2013) and hydrodynamics of the creek described in Chapter 4 (Site 4-QL-TC). The tidal creek is located 1.25 km south (landward) of a branch of the Khawr Qantur channel, a wide channel (minimum width 4.4 km) connecting Qantur Lagoon to the Gulf (Fig. 5.1.C). Four sub-sites (A-D) were selected based on the heterogeneous distribution of subsurface firmgrounds within a short (<10 m) distance from the creek (Fig. 5.1.D, E). QLTC is ~180 m seaward of an extensive microbial mat belt locally reaching 10 cm in thickness, which form a near continuous belt av. 360 m wide, locally up to 700 m wide, running parallel to the shoreline and marking the transition between intertidal and supratidal settings (Lokier and Steuber, 2008; Lokier *et al*., 2017; Chapter 4). The seaward margin of the mat is limited by the activity of grazing fauna and the landward margin is controlled by the lack of regular tidal inundation, resulting is desiccation (Lokier *et al*., 2017). The microbial mats are flooded at high tide for a few hours most days (except during lowest neap tides) (Lokier *et al*., 2017) and inhabit an environmental niche flooded ~5-25% of the time annually (Chapter 4). As the tide recedes, waters pool within the microbial polygon structures which often reach halite saturation *via* evaporation (Lokier *et al*., 2017).

The floor of the Gulf is characterised by extensive areas of carbonate-dominated sediments that are lithified at shallow (cm-m) depth by acicular aragonite and high Mg-calcite (HMC) marine cements (Evans *et al*., 1964; Lokier and Fiorini, 2016; Ge *et al*.,2020). Calibrated radiocarbon ages suggest seafloor lithification began in the Middle to Late Holocene (~9000 yr BP) and continues to the present day (Ge *et al*., 2020a). Previous work by Paul and Lokier (2017), describes a diachronous hardground that is locally exposed in the lower ITZ and extends beneath the supratidal sabkha and the mid-intertidal lagoons (henceforth referred to as the basal hardground). The basal hardground is primarily composed of aragonitic bioclastic grains, originating from the ITZ and lithified with primary pore-filling aragonite, HMC (part originating from the dissolution of aragonite and re-precipitation) and dolomitic cements (Taylor and Illing, 1969; Paul and Lokier, 2017). Some secondary HMC and non-stoichiometric dolomite is also observed which is suggested to be the produce of microbially mediated recrystallisation. The basal hardground is overlain by prograding late Holocene carbonate, evaporite and microbial sediments with subordinate aeolian siliciclastics (Paul and Lokier, 2017). These hardgrounds were formed by changes in sea level, with an initial Early Holocene transgressive phase of cementation (7,184 – 6,869 yrs BP) overlain by a Late Holocene regressive phase (5,290-4570 yrs BP) (Paul and Lokier, 2017).

Furthermore, a variety of cemented surfaces are present in the upper 10's of cm of the ITZ sediment overlying the basal hardground that display a variety of morphologies from firm/hardgrounds and stacked cemented horizons to beach-rock and other concretionary features (Lokier and Steuber, 2009; Ge *et al*.,2020; Chapter 3). The present-day Abu Dhabi coastline is in a period of marine transgression (Lokier *et al*., 2018). Ge *et al*. (2020a) suggest the formation of shallow firmgrounds within Abu Dhabi's ITZ is driven by the influence of a rising sea level, with firmgrounds representing lithified transgressive lag deposits. As the sea level rises the active zone of lithification moves landwards, although active lithification may also occur at the sea floor, or below the surface at the redox boundary (Ge *et al*. 2020a). The cements described by Ge *et al*. (2020a) contain a less diverse range of mineralogies compared to the hardgrounds described by Paul and Lokier (2017), suggesting the firmgrounds represent the initial phase of early cementation prior to full lithification and hardground formation. Radiocarbon ages suggest lithification of shallow firmgrounds initiated in the Holocene (<268 yBP) and that the ITZ continues to be an area of active lithification (Lokier and Steuber, 2009; Ge *et al*., 2020a).

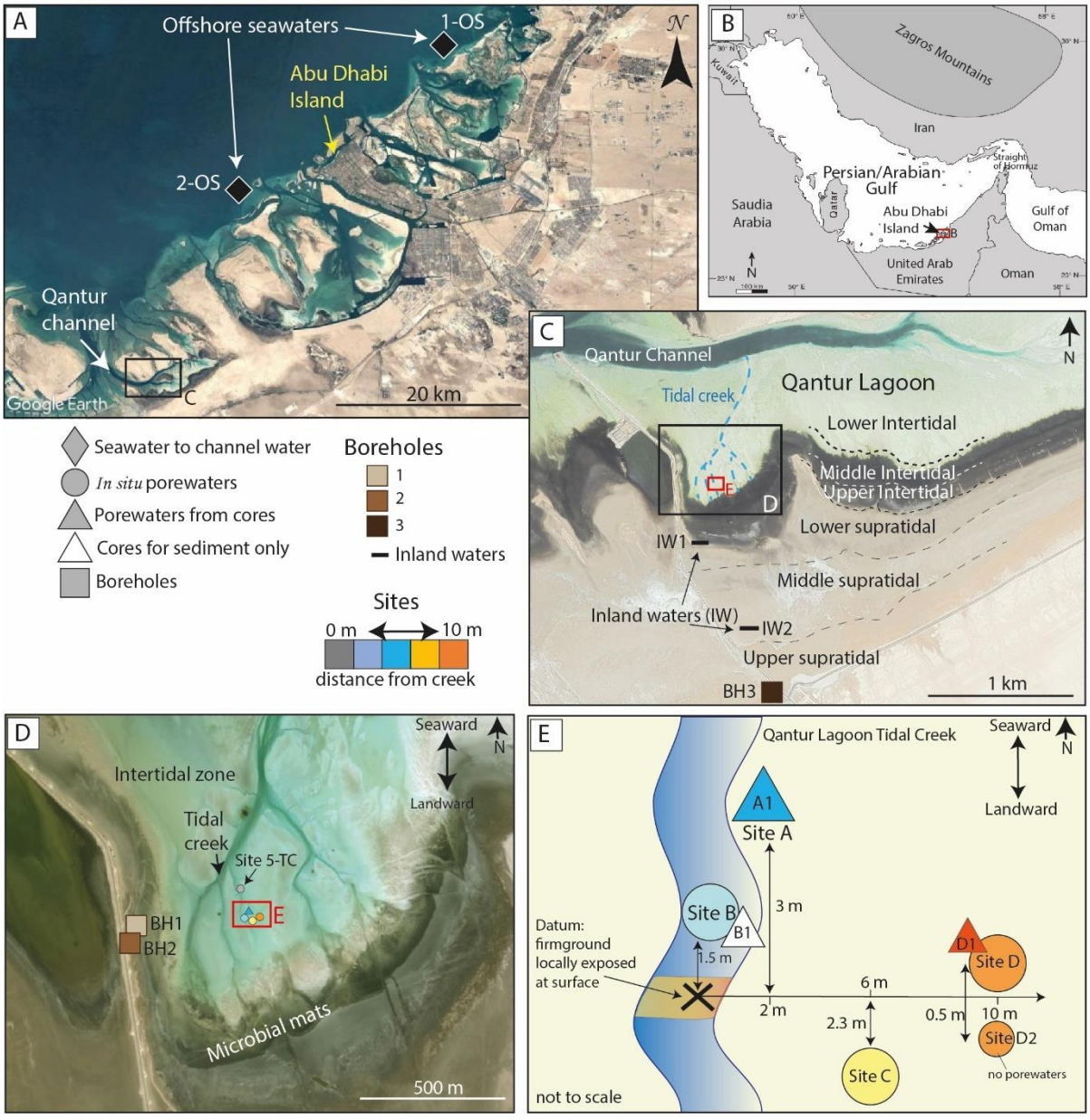

Figure 5.1. (**A**) Study area on the southern shore of the Gulf, with regional location in (**B**) adapted from Lokier *et al*. (2013). (**C**) Qantur lagoon showing location of the study site surrounding the tidal creek (red box), inland porewaters, Borehole 3 and intertidal to supratidal zones (Chapter 4). (**D**) Sample locations surrounding a tidal creek in the lower ITZ seaward of the microbial mat belt, and Boreholes 1 and 2. (**E**) Schematic of sub-sites A-D and their relative proximity to a datum (exposed firmground within the channel with coordinates 24° 8’57.18’’N 54° 5’10.03’’E). This site was chosen based on the heterogeneous distribution of subsurface firmgrounds within a relatively short distance from the creek.

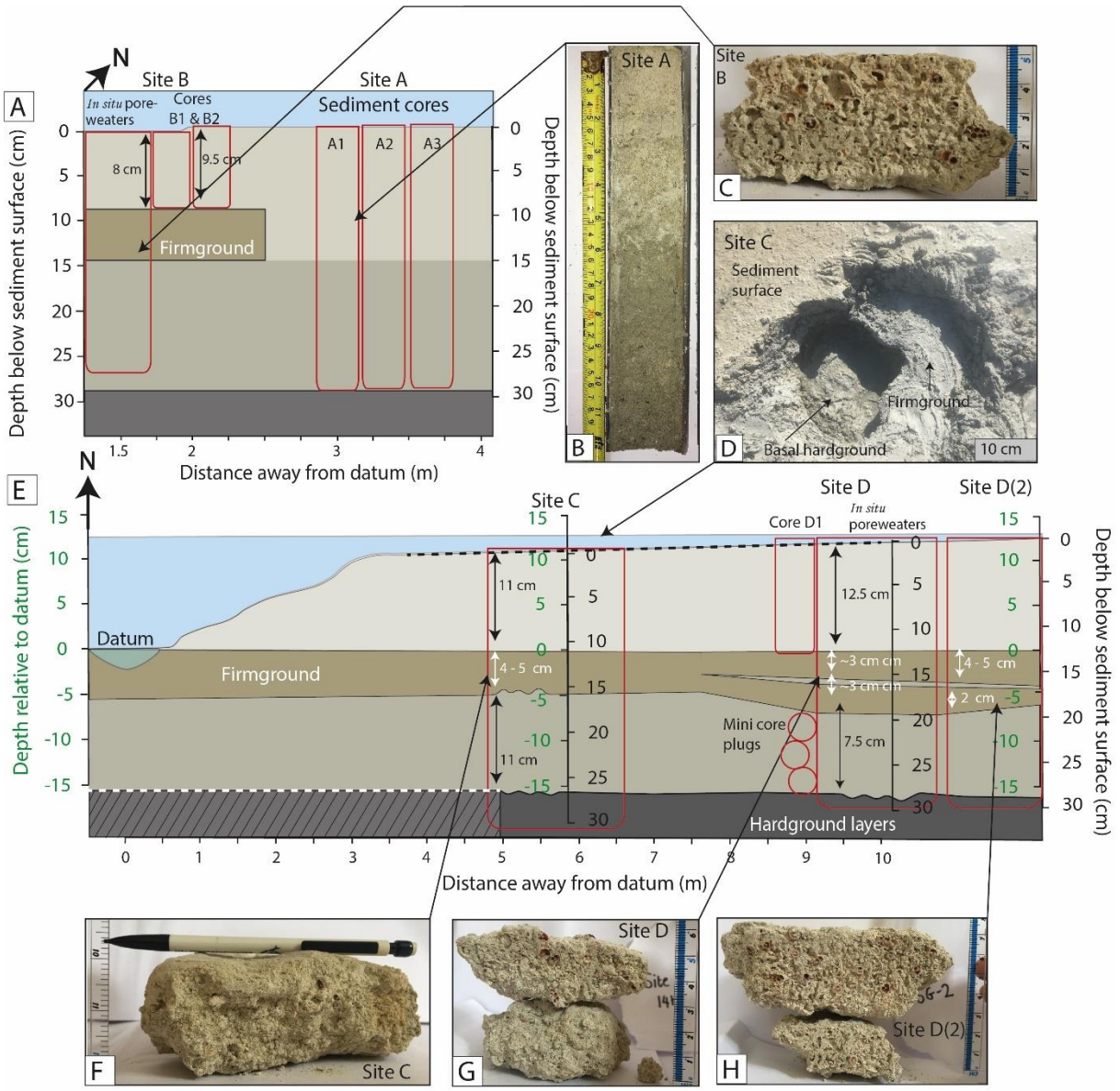

Figure 5.2. Schematic of sub-site transects with surface topography and depth below sediment surface (black right-hand y-axis) and sediment depth relative to an exposed firmground datum within the channel (green left-hand y-axis) (solid lines represent measured surface heights and sediment depths and dashed lines are inferred heights and depths). (**A**) Site A and B with sediment cores and *in situ* porewater extraction sites highlighted in red. (**B**) Photo of Core A1 from Site A with no firmground present but a distinct colour change at 15 cm. (**C**) Firmground at Site B, and (**D**) sample pit at Site D showing exposed firmground within the pit and the pit terminating on the deeper basal hardground. (**E**) Transect (~10 m) from the datum to Sites C and D, with sample pits, Core D1 and mini core plugs taken below the firmground (Site D) highlighted in red. (**F**) Firmground at Site C (~5 cm thick); (**G**) two stacked firmgrounds at Site D, each ~3 cm thick and (**H**) two stacked firmgrounds at a replicate pit (Site D2; 0.5 m south of the pit at Site D), where the upper firmground had increased in thickness (~4 cm) and the lower firmground had decreased (~2 cm).

5.3 Methods

The areas surrounding Qantur Lagoon Tidal Creek (QLTC) was selected for this study based on the presence and heterogeneous distribution of a subsurface firmground(s) in a more hydrodynamically

complex environment compared to Yas Lagoon (Chapter 3). Samples were collected over three field campaigns. Samples from offshore Sites 1 and 2 and QLTC Sites A and B were collected in October 2017 whereas samples from QLTC Sites C and D, Site 5-TC, and Boreholes 1, 2 and 3 were collected in January 2019. Site 5-TC was situated within the creek ~90 m seaward of the QLTC sub-sites and is used to assess porewater chemistry underlying the creek, in an area without apparent active firmground formation. The inland porewaters were collected in February 2014 from 0-32.5 cm (IW1) and 26.5 - 47.5 cm (IW2) (Locations in Fig. 5.1.C).

5.3.1 Sediment and firmground sampling and analysis

Sediment cores were collected using 8 cm diameter PVC piping. In 2017, sediment cores were collected at Site A (Core A1, A2, and A3: ~30 cm length) and Site B (Cores B1: 8 cm and B2: 9.5 cm length) along with a hand sample of the lithified sediment at ~8-13 cm extracted from the porewater pit at Site B (Fig. 5.2.A-C) (depths reported below sediment surface). Site A cores terminated on the basal hardground whereas cores from Site B only extracted sediment from above the firmground. In 2019, sediment samples from Site D were collected *via* core (D1) above the firmground, and mini core plugs (3 cm diameter) were inserted horizontally to sample sediment below the firmground (Fig. 5.2.E), sediments from within the creek at Site 5-TC were also collected by push core (~30 cm depth) (Fig. 5.3.H). Hand samples of lithified sediment were collected at ~11-16 cm from Site C (unconsolidated sediment samples from Site C were lost in transit) and at ~13-16 cm and 18-20 cm from Site D. A replicate pit was sampled 0.5 m south of Site D (pit D2) (Fig. 5.2.E) for firmground samples only (no sediment or porewaters). Cores were stored upright, with all samples kept in the dark at 4°C prior to subsampling. For a summary of which analysis were performed on each core, see Table 5.1.

Cores were split longitudinally and subsampled under sterile conditions for grain size analysis, X-ray diffraction (XRD), scanning electron microscopy (SEM), thin section preparation, and SSU rRNA gene identification. Grain size was analysed on Core B2 (n=3), and sediments from Site D (n=11) and Site 5-TC (n=14) using a Malvern Mastersizer 2000 particle size analyser following the method described by Lokier *et al*. (2013) after wet sieving the >1 mm grain size fraction. Thin sections of unconsolidated sediment and firmground specimens were impregnated with blue epoxy resin, and half stained with Alizarin Red S to differentiate calcite/aragonite from dolomite. Sediments and firmground samples were examined using standard light microscopy with a polarizing microscope and a FEI Phillips Quanta 200 MK2 SEM (2017 samples) and a Hitachi S3500N SEM with a Thermo Fisher EDS running NSS version 4.0 (2109 samples).

For SEM analysis, firmgrounds were freshly broken and rinsed with deionised water to dissolve any halite precipitated after sampling, then coated with a gold-palladium mixture (2017 samples) and carbon coating (2019 samples). SEM Energy-dispersive X-ray spectroscopy (EDS) provided a semi-

quantitative insight into cement and clast elemental composition. Bulk sediment mineralogy was determined on Core A3 (n=26) *via* powder x-ray diffraction (PXRD) on sediments using a Rigaku Ultima IV with radiation sourced form a Cobalt tube at 38 kV and 38 mA and wavelengths of 1.78900 ($K\alpha_1$ (100)), 1.79283 ($K\alpha_2$ (50)) and 1.62083 ($K\beta_1$). Sediment total iron (Fe) and manganese (Mn) were measured on a Thermo Scientific iCAP 6300 ICP-OES following the methods of Northdruft *et al*. (2014). Computed Tomography (CT) scans were performed on Core A3 using a Nikon XTH 225ST X-ray tomography scanner and images were analysed using 3D Slicer software.

Table 5.1. Summary of analysis performed on cores and sediment samples at each sub-site. Sediments from Site C were lost in transit.

Analysis	**Site A**			**Site B**		**Site D**
	Core A1	Core A2	Core A3	Core B1	Core B2	Core D1
Porewaters from core	X	X		X	X	X
Grain size					X	X
XRD			X			
DNA analysis	X				X	
Microscopy	X				X	X
CT scan			X			
Elemental analysis			X		X	

5.3.2 Porewater sampling and analysis

Porewater samples from 2017 and 2019 were extracted and filtered at 1.5-3 cm vertical resolution using 5 cm long Rhizon CSS pore-water samplers (pore diameter 0.12-0.18 µm) following a method adapted from Seeberg-Elverfeldt *et al*. (2005) and Dickens *et al.* (2007). Porewaters were obtained from Cores A2 and D1 back in the laboratory (~6 hours after collection) (24th Oct. 2017) whereas at Sites B, C, and D porewaters were extracted directly from the sediment, with Rhizons applied *in situ* (14th and 16th Jan. 2019) (methodology for Rhizon insertion into cores and *in situ* detailed in Chapter 2.1). Sampling from the core may be associated with increased degassing (Chapter 2.1). Partial lithification prevented insertion of Rhizons from ~8-13 cm at (Site B), 11-16 cm (Site C) and at both 13-16 cm and 18-20 cm (Site D).

Surface open marine seawater samples were also collected *via* Rhizon samplers to ensure immediate filtration and consistency with porewaters from Site 1-OS and 2-OS (18th and 22nd Oct. 2019 respectively) (Fig. 5.1.A, locations 1 and 2). Bottom water samples from the open marine sites were collected in a Van Dorn horizontal open water sampler, near the sediment-water interface at approximately 5.5 m water depth, stored in glass bottles and filtered through Rhizons on return to the lab. Porewaters from the inland sites (collected 5th Feb. 2014) were obtained from 1-3 cm sediment

slices centrifuged at 200 RPM for 30 minutes, porewaters were then filtered through 0.22 µm Millex filters. Groundwaters were collected from three boreholes (Boreholes 1, 2, and 3) (locations in Fig. 5.1.C, D) on 15th January 2019.

Porewater pH, specific electric conductivity (SEC) and redox potential (Eh) were measured within ~6 hours of collection (*in situ* samples) and ≤3 days of collection (for porewaters obtained from the cores) using a HQ40d Hach multi-meter and probes, with analytical accuracies of ±0.02 pH units, ±0.5%, and ±0.05% respectively. Bicarbonate alkalinity was determined in triplicate by Gran titration (Sass and Ben-Yaakov, 1977) using 0.0005 M or 0.001 M HCl acid with <2% coefficient of variance (CV). Aliquots were returned to the UK where samples were gravimetrically diluted for major ion analysis. Cations (Na^+, Mg^{2+}, Ca^{2+}, K^+, Sr^{2+}) were analysed by inductively coupled plasma atomic emission spectroscopy (ICP-OES; Agilent series 710 ICP-OES). Major anions from Site C and D (Cl^- and SO_4^{2-}) were measured isocratically by ion chromatography (Dionex™ ICS-5000+) and the 2017 samples (Site A, B, and open marine) were analysed photometrically on a Gallery Plus Discrete Analyzer. Ion analyses had <5% CV based on multiple injections.

Ammonium (NH^{4+}) was analysed photometrically on a Gallery Plus Discrete Analyzer with <5% CV for both 2017 and 2019 samples. The ion balance error (IBE) was -1.02 ±2.22 (n=66). Partial pressure of CO_2 (pCO_2), CO_3^{2-} activity, and saturation indices ($\log(IAP/K_{sp})$) of aragonite and calcite (SI_{arag} and SI_{calc}) were calculated using PHREEQ-C (Parkhurst and Appelo, 2013) with the Pitzer database (Pitzer, 1973; Pitzer and Mayorga, 1973). Uncertainties in pCO_2, CO_3^{2-} activity, SI_{arag}/ SI_{calc} were ±0.019%, ±0.023 log units, and ±0.019 log units respectively. pCO_2, CO_3^{2-} activity and SI_{arag}/SI_{calc}, and were also calculated with CO2SYS (Pelletier *et al.*, 2007) for comparison (discussed in Chapter 2.2) with errors of ±0.002%, ±0.02 log units, and ±0.03 log units respectively.

Porewater total dissolved organic carbon (DOC) (1.8% CV) was analysed using a Shimadzu TOC-L Total Organic Carbon analyser, with simultaneous total determination of nitrogen (TN) *via* Kemi-luminescence using a non-infrared detector (TN: 3.6% CV). Headspace CH_4 concentration were analysed using the Carlo Erba HRGC5300 gas chromatograph (GC) equipped with a Porapak® QS packed column and fitted with a NiO_2 catalyst methaniser and Flame Ionization Detector (FID) with H_2 at 30 ml min^{-1} and zero air at 400 ml min^{-1} as support gases. ~100 µl of headspace gas was injected through an injection port (at 125 °C) with a butyl rubber septa seal, following the methods of Hornibrook and Bowes (2007). Issues with equipment during methane analysis (2017 only) mean values are only considered minimums and are reported as negligible when sample headspace CH_4 was <1.6 ppm. For the 2019 samples, Wheaton *via*ls were first brought to atmospheric pressure by injecting argon and left upside down over night to equilibrate prior to analysis. 5 ml of headspace was collected by first injecting 5 ml of argon to avoid creating negative pressure during sampling. Headspace CH_4 concentration were analysed using an Agilent 7980A gas chromatograph equipped with a 1 mL valve-

injection loop, fitted with a Porapak Q 80-100 mesh, 2.5 m X 2.0 mm SS column, methanizer and flame ionization detector following the methods of Lamarche-Gagon *et al*. (2019). Samples from 2017 and 2019 were calibrated against speciality gas standards (BOC, Guildford, UK) with CV mostly <2% based on multiple injections.

5.3.3 Microbial 16 SSU gene sequencing

To investigate the potential role of microbiology in driving cementation surround QLTC, 16 SSU gene diversity was compared at Site A (no firmground) and Site B (firmground). To determine microbial community composition *via* 16S SSU rRNA amplification and sequencing, Cores A1 and B2 (collected on the same day) were sampled at 2 cm resolution. Approximately 0.25-0.50 mg was collected from the most pristine centre of the core, transferred to a DNA/RNA Shield Lysis Tube (Zymo Research) containing 1 mL of DNA/RNA Shield and ultra-high density BashingBeads (0.5 mm and 0.1 mm) for homogenization. These were shaken vigorously for one minute and stored at ambient temperature until received in the lab. Amplification and sequencing was performed on the same batch as the samples described in Chapter 3, and follow the methods described therein.

5.4 Results

5.4.1 Sediment physical and diagenetic characteristics

The upper few cm of the intertidal light grey muddy sediments of the QLTC sites are highly bioturbated with evidence of gastropod trails on the sediment surface and open decapod burrows. Beneath the sediment surface there is a complex network or burrows with a dark grey organic-rich lining, with vertical burrows typically reaching 5-10 cm depth (e.g., Fig. 5.3.H). Grain size was not analysed for Site A and C; however grain size analysis at Sites B, D, and 5-TC, suggest that above ~12 cm, sediment grain size is dominated by silt-sized (40 ±7%) and sand-sized grains (30 ±8%), with subordinate clay-sized grains (13 ±6%) and highly variable proportions of grains >2mm (15 ±8%) which is largely dominated by gastropods (Fig. 5.3.E, F, G). At Site 5-TC, sediment become coarser with depth between ~12-22 cm (Fig. 5.3.G). Below ~22 cm (Sites D and 5-TC) grain size is fairly homogeneous and typically slightly coarser than the overlying unconsolidated sediments, being predominantly sand (39 ±7%) and silt-sized particles (27 ±2%), with the >2 mm sized components variable (25 ±10%) and subordinate clay sized particles (5 ±1%) (Fig. 5.3.F, G).

Above 6 cm (Site A) and above the firmgrounds (Site B – D) sediments are a light grey to white peloidal bioclast packstone. From ~6-12 cm (Site A) and within the firmgrounds at Sites B-D, qualitative observations suggest the sediment contains more abundant gastropods compared with sediments above and below. Below the firmgrounds, sediments become dark grey and slightly more coarse-grained than sediments overlying the firmground. The non-biogenic component is dominated by

peloids (~80-90%), bioclasts (~4-12%) and quartz (~5-10%). Throughout the sediment profile peloids are pervasively bored. The biogenic component consists of complete smaller bioclasts, dominated by abundant and diverse benthic foraminifera (e.g. *Quinecquiloculina* and *Trochammina),* ostracods, and larger bioclasts including bivalves and abundant gastropods.

Most grains demonstrate a high degree of neomorphism and micritisation. Whilst microcrystalline cements are ubiquitous, fibrous and bladed crystals are most commonly associated with the firmgrounds but are also observed within intergranular pore spaces in some unconsolidated sediments. Firmgrounds are cemented by acicular, fibrous, and bladed crystals and abundant microcrystalline cements. Bladed crystals typically form cemented rims growing perpendicular to carbonate grains, most of which are pervasively bored. Pyrite framboids (~10 µm diameter) are common within firmgrounds (e.g., Fig. 5.9.L). Fibrous and bladed crystals predominantly occur in the most restricted inter- and intra-granular pore space and are rarer in larger pore networks within the firmground. Fibrous and bladed crystals are mostly absent in the overlying and underlying sediments, except for their rare occurrence in small pore spaces associated with aggregate clusters.

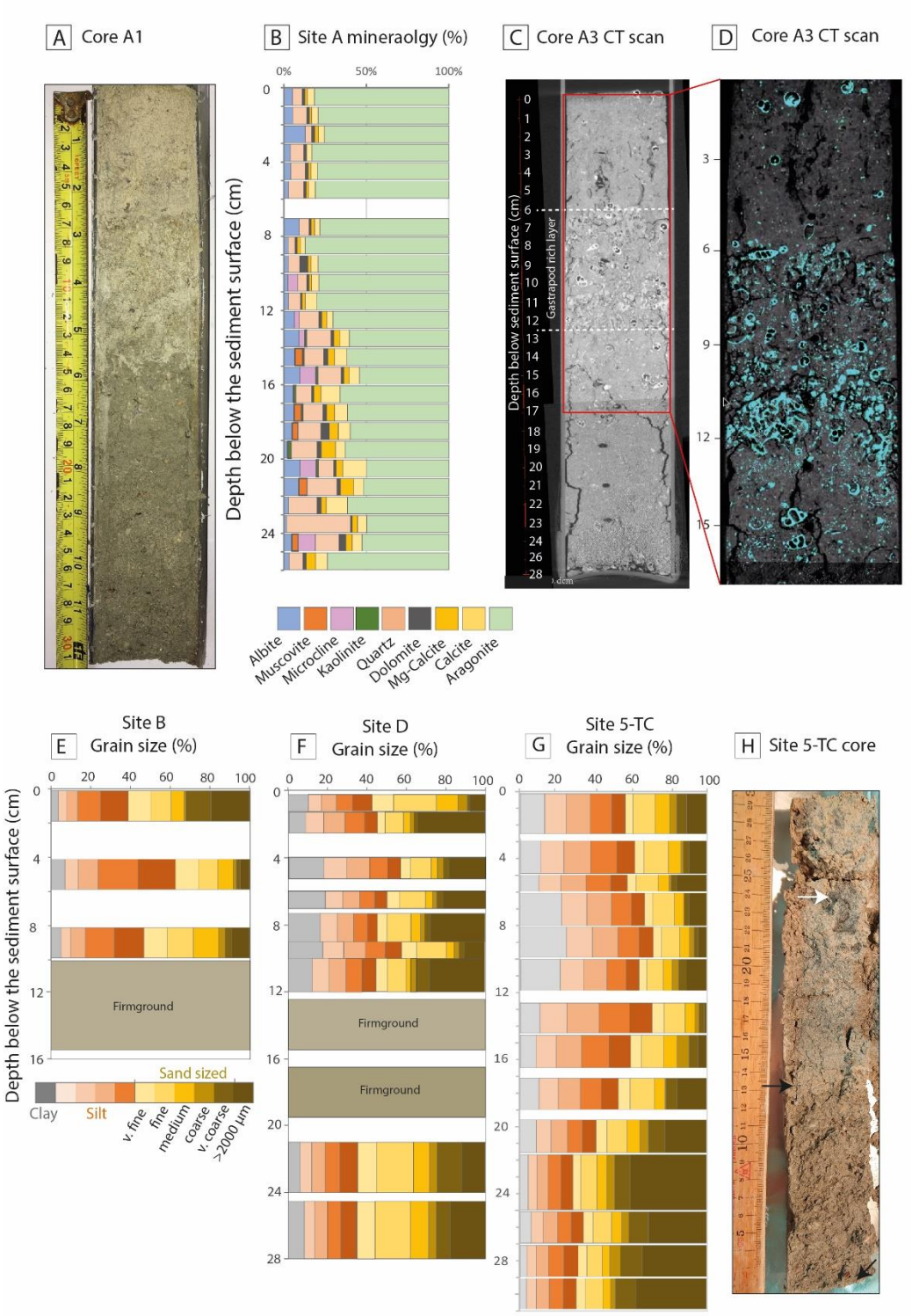

Figure 5.3. Top row: Site A (**A**) photograph of Core A1; (**B**) XRD mineralogy for Core A3; (**C**) CT-scan of Core A3, and (**D**) close-up of Core A3 CT-scan with cemented zones and gastropods highlighted in blue. Lower row: grain size at Sites B (**E**); Site D (**F**); and Site 5-TC (**G**). (**H**) Core photo from Site 5-TC showing colour change at ~17 cm depth (black arrow) and dark, anoxic burrows in the upper 10 cm (white arrow).

5.4.2 Site specific sedimentary results

5.4.2.1 Site A

Site A is located 3 m northeast of the datum, ~1 m east of the channel, with the sediment core terminating on the deeper basal hardground at 30.5 cm depth (Fig. 5.1.E, 5.2.A). Although no firmground was observed when coring, dissection of the core displays a distinct colour change in Core A1 at 15 cm (Fig. 5.3.A). CT-scan images of Core A3 display two slightly cemented horizons at ~6-8 cm and ~9.5-12.5 cm below the surface within a gastropod rich layer at ~6-12 cm (Fig. 5.3.D), and subsequent dissection of the cores found pieces of poorly lithified sediment. CT-scan analysis also suggests that burrows cease at 8 cm.

Aragonite is the most abundant mineral throughout the profile and remains fairly constant from 1- 12 cm (79.1 ±1.6% n=8), though peaks at 8 cm (87.1%). Below 12 cm, aragonite decreases with depth reaching a minimum of 49.7% at 23 cm. Total calcite remains low in the upper 11 cm (5.5 ±0.4% n=8) and increases with depth from 11 cm to peak at 21 cm (18.4%) before decreasing slightly. Calcite is typically ~50% more abundant than HMC, except at 20 and 23 cm where HMC peaks at 8.7% and 5.9% respectively (Fig. 5.3.B). Quartz is less abundant above (6.3 ±1.6% n=9) than below 12 cm (14.9 ±7.1, n=14), with an anomalous peak at 24 cm (39%). Dolomite remains low (<3%) throughout the profile except for peaks at 10 cm (5.1%), 19 cm (5.0%), and 25 cm (4.2%). Muscovite (mica) is present in low quantities (3.5-5%) in some samples from 15-25 cm, kaolinite (a silicate clay mineral) is present in low abundance from 14-21 cm, with a minimum relative abundance of 0.9% at 15 cm and a maximum of 2.2% at 20 cm. Microcline (feldspar) is present in a few samples below 11 cm and ranges from 3.1-10.2% (Fig. 5.3.B). Elemental analysis found total sedimentary Fe and Mn to be fairly stable in the upper 6 cm (4.9 ±0.2 ppm and 0.1±0.0 ppm respectively). Fe and Mn were ~50% lower at 7-12 cm, before increasing with depth to peak at 19 cm (8.2 ppm Fe and 0.2 ppm Mn), and then decreasing with depth [data not shown in figure].

Microcrystalline cements are present throughout the profile, with loose grains coated in thin cement rims with diameters of ~8±4 µm (e.g., Fig. 5.4.D). Subtle variations in the degree of cementation are observed through the profile, with cementation apparently decreasing slightly with depth. At the surface (0-2 cm) sediment is poorly sorted, with ~80% of grains cemented into aggregate clusters with diameter typically ranging from 250-1200 µm and containing 4 - >40 grains (Fig. 5.4.B, C). At 12-14 cm ~70% of grains are cemented into aggregates (aggregate clusters ranging from 225-885 µm in diameter and contain ~10->40 grains) (Fig. 5.4.E, F), with rare needle-like acicular crystals (5-10 µm long) within intergranular pore spaces (Fig. 5.4.G). At the base of the profile (26-29 cm) ~60% of grains are cemented into aggregate clusters (220-660 µm wide) with slightly thinner micrite rims than the shallower sediments (6±3 µm wide) and rare acicular crystals are present in small intergranular pore

spaces (~10 µm long) (Fig. 5.4.H, I, J). However, the coarse resolution of sediment microscopy analysis at Site A may have missed smaller scale variations in cementation, particularly within the sediment at ~6-12 cm.

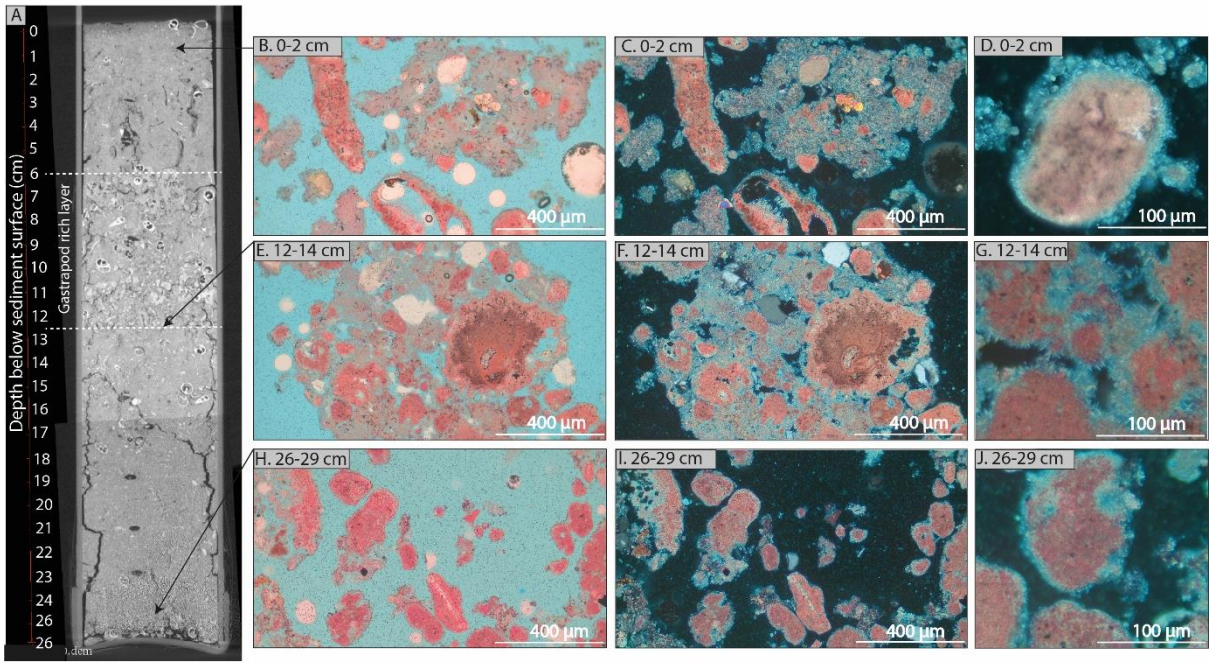

Figure 5.4. Site A: (**A**) CT scan of Core A3; and thin section photomicrographs of Core A1 at 0-2 cm (**B**. PPL, **C**. XPL and **D**. XPL); 12-14 cm (**E**. PPL, **F**. XPL and **G**. XPL); and 26-29 cm (**H**. PPL, **I**. XPL and **J**. XPL).

5.4.2.2 Site B

Sediments above the firmground

Site B was located within the channel, (1.5 m north of the datum) and exhibited a 5 cm thick firmground, covered by 8-9.5 cm of unconsolidated sediment (Fig. 5.1.E, 5.2.A). Grains throughout the profile are pervasively bored, making it difficult to recognise individual grains. Unconsolidated sediments above the firmground are coated in equigranular microcrystalline cements, though the cement rim thickness shows no significant trend with depth, with rims typically 5-15 µm diameter (Fig. 5.5, 5.6A-F, 5.7A). The percentage of grains cemented into aggregate clusters increases from ~30% at 0-2 cm to ~80% at 8.5-9 cm (Fig. 5.5.A, D, G; 5.7.A). The average width of cemented clusters also increases with depth from 105-500 µm at 0-2 cm, to 135-1260 µm at 4-6 cm and 120-1780 µm at 8-9.5 cm. At 4-6 cm and 8-9.5 cm some large clusters have small randomly orientated needles (10-35 µm long) forming on the outside of the grains and within the inter-granular pore spaces (e.g., Fig. 5.5.F). Some large biogenic chambers have equant crystals forming an isopachous fringe on the internal wall.

The percentage of sediment as $CaCO_3$ (Core B2) increases with depth from 79.0 ±0.3% at 0-2 cm to 82.1 ±1.3% at 6-8 cm, whereas total nitrogen (TN) and total organic carbon (TOC) decrease with depth

and the ratio of carbon to nitrogen (C/N) increases slightly with depth but remains between ~10-12 throughout the profile (Fig. 5.7.B).

The firmground

The firmground at Site B (~5 cm thick at 8-13 cm) consists of similar components as the overlying sediment, though with abundant gastropods. Within the firmground, cementation and sorting decrease, and grain size and porosity increase down profile from a predominantly planar upper surface to the slightly undulated lower side of the firmground (Fig. 5.2.C; 5.5.J-R).

Cement morphology varies throughout the firmground. Typically, grains with outer edges in small, poorly connected pore spaces (most abundant in the upper firmground) are surrounded by an isopachous fringe (5-25 µm) of acicular aragonite needles and bladed crystals with pointed and blunt terminations (Fig. 5.5.J-L and 5.6.G-J). In contrast, larger pores in the upper firmground are fringed by microcrystalline cements (6-12 µm diameter). Similarly, towards the base of the firmground, small fibrous crystals (5-10 µm long) are fairly common in the less well-connected inter-granular pore spaces. Abundant equigranular microcrystalline cements form around grains surfaces and are also present within pore spaces (Fig. 5.5.P, Q, R).

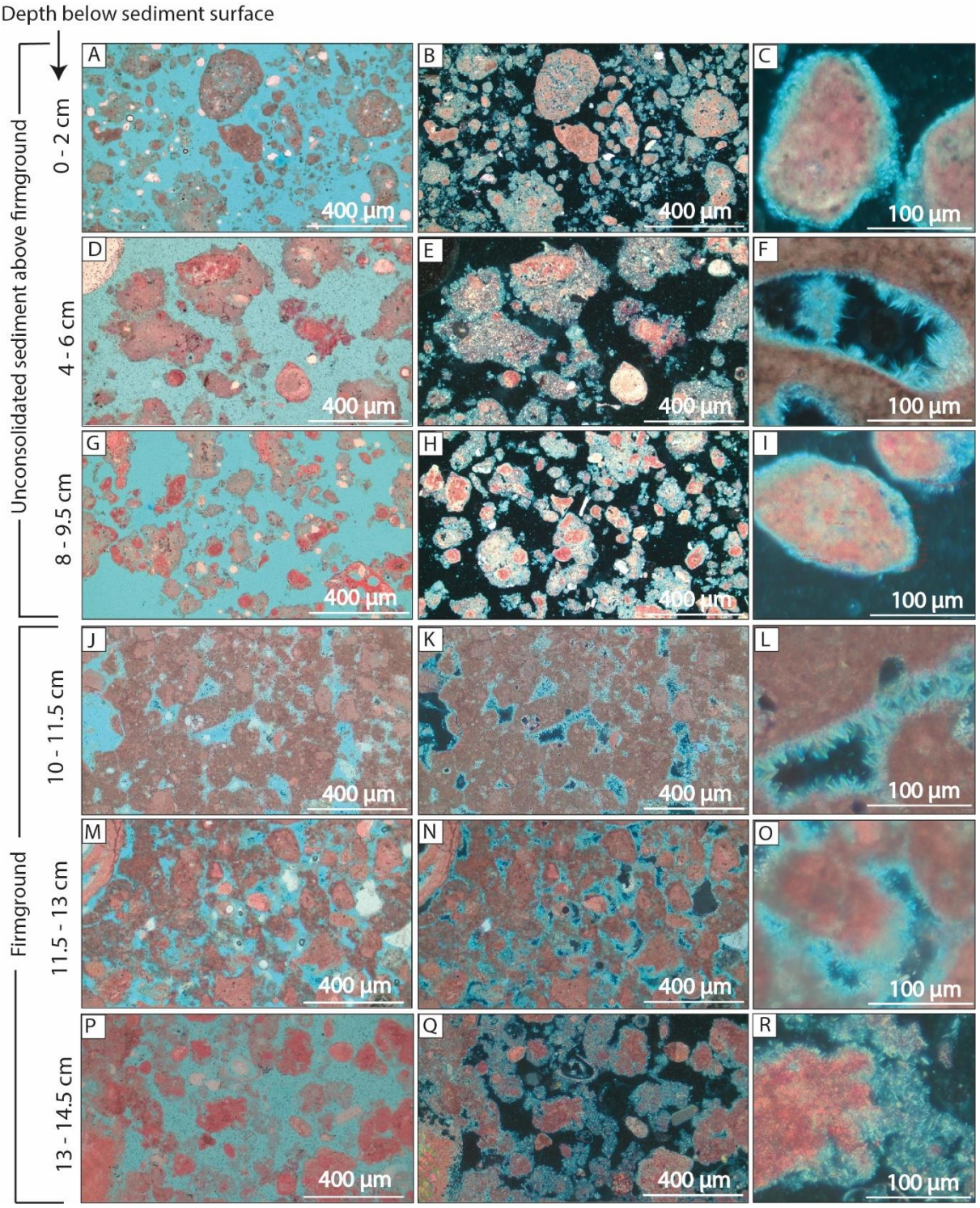

Figure 5.5. Site B photomicrographs in plain polarised light (PPL) (first column) and cross polarised light (XPL) (second and third columns) of unconsolidated sediment above the firmground from Core B2 at 0-2 cm (**A**, **B**, **C**); 4-6 cm (**D**, **E**, b) and 9-9.5 cm (**G**, **H**, **I**) and the upper (**J**, **K**, **L**), middle (**M**, **N**, **O**) and lower (**P**, **Q**, **R**) firmground. Images show an increase in cemented clusters downcore above the firmground, and grains predominantly coated in microcrystalline cements (**C**, **I**), with rare acicular crystals in biogenic chambers (**F**). Within the firmground (**J-R**) cementation and sorting decrease, and grain size and porosity increase down profile. Cements are a mixture of acicular aragonite needles and bladed crystals with pointed and blunt terminations (**L**) and microcrystalline cements (**R**).

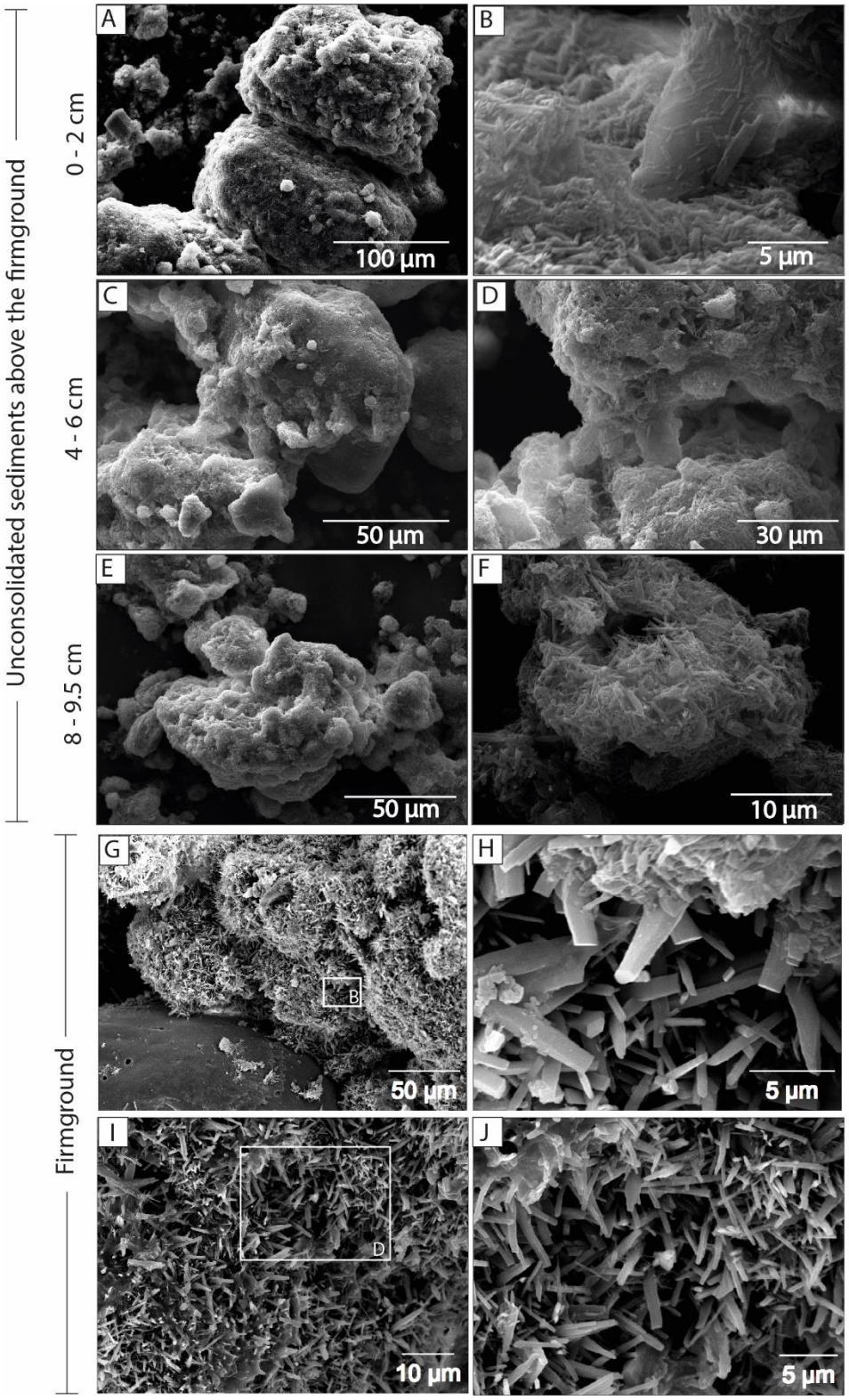

Figure 5.6. Site B SEM images from unconsolidated sediment above the firmground (Core B2) at 0-2 cm (**A** and **B**), 4-6 cm (**C** and **D**) and 8-9.5 cm (**E** and **F**) showing grains cemented with a microcrystalline aggregate. (**G**-**H**) show firmgrounds cemented with fibrous crystals with predominantly blunt terminations.

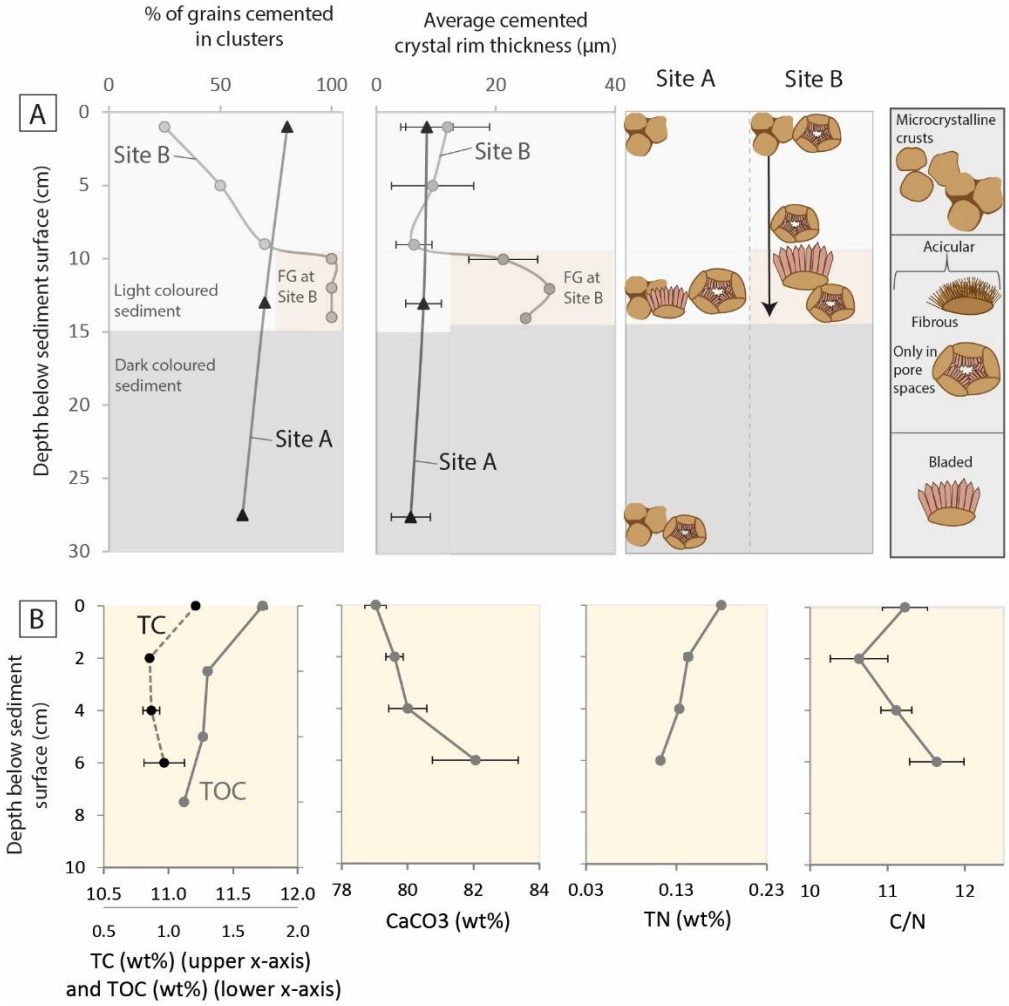

Figure 5.7. (**A**) Schematic illustrating variations in cementation at Sites A and B (Core A1 and B2 respectively), showing the percentage of grains cemented in clusters, average crystal rim thickness and the cement morphology. (**B**) Site B (Core B2) total carbon (TC) (black dashed line, upper x-axis) (wt%) and total organic carbon (TOC) (grey line, lower x-axis) (wt%); calcium carbonate content ($CaCO_3$) (wt%); total nitrogen (TN); the ratio of TOC/TN (C/N).

5.4.2.3 Site C

The sediment surface at Site C, (6 m east and 2.3 m south of datum) is 11 cm higher than the datum (Fig. 5.1.E). Here, 11 cm of light grey-white unconsolidated sediment overlies a firmground 3.2-5.0 cm thick (Fig. 5.2.D, E, F). The firmground has a predominantly planar upper surface with cementation decreasing from the surface towards the predominantly planar, slightly undulating base. Below the firmground, dark grey unconsolidated sediments extend down to the basal hardground at 28-29 cm that was unable to be penetrated by the core. Unconsolidated sediments were not analysed at this site.

Within the firmground, carbonate grains are pervasively bored and fringed with an isopachous fringe of well-defined bladed and fibrous crystals with predominantly blunt terminations (individual crystal length 5-20 µm) (Fig. 5.8) typically forming on top of a micritised rim (~5 µm diameter). Semi-

quantitative EDS analysis suggests fibrous and bladed crystals contain negligible Mg^{2+} and small amounts of Sr^{2+} (0.90-1.09 wt%) whilst microcrystalline rims contain small amounts of Mg^{2+} (0.55 wt%) and negligible Sr^{2+}. Non-carbonate grains do not have fibrous or bladed crystals growing perpendicular to the grain surface. Microcrystalline cements are also abundant, typically forming clusters within pore spaces (Fig. 5.8.H). EDS suggests microcrystalline cements contain 0-0.55 wt% Mg^{2+} and 0.46-0.79 wt% Sr^{2+} (Fig. 5.8.G).

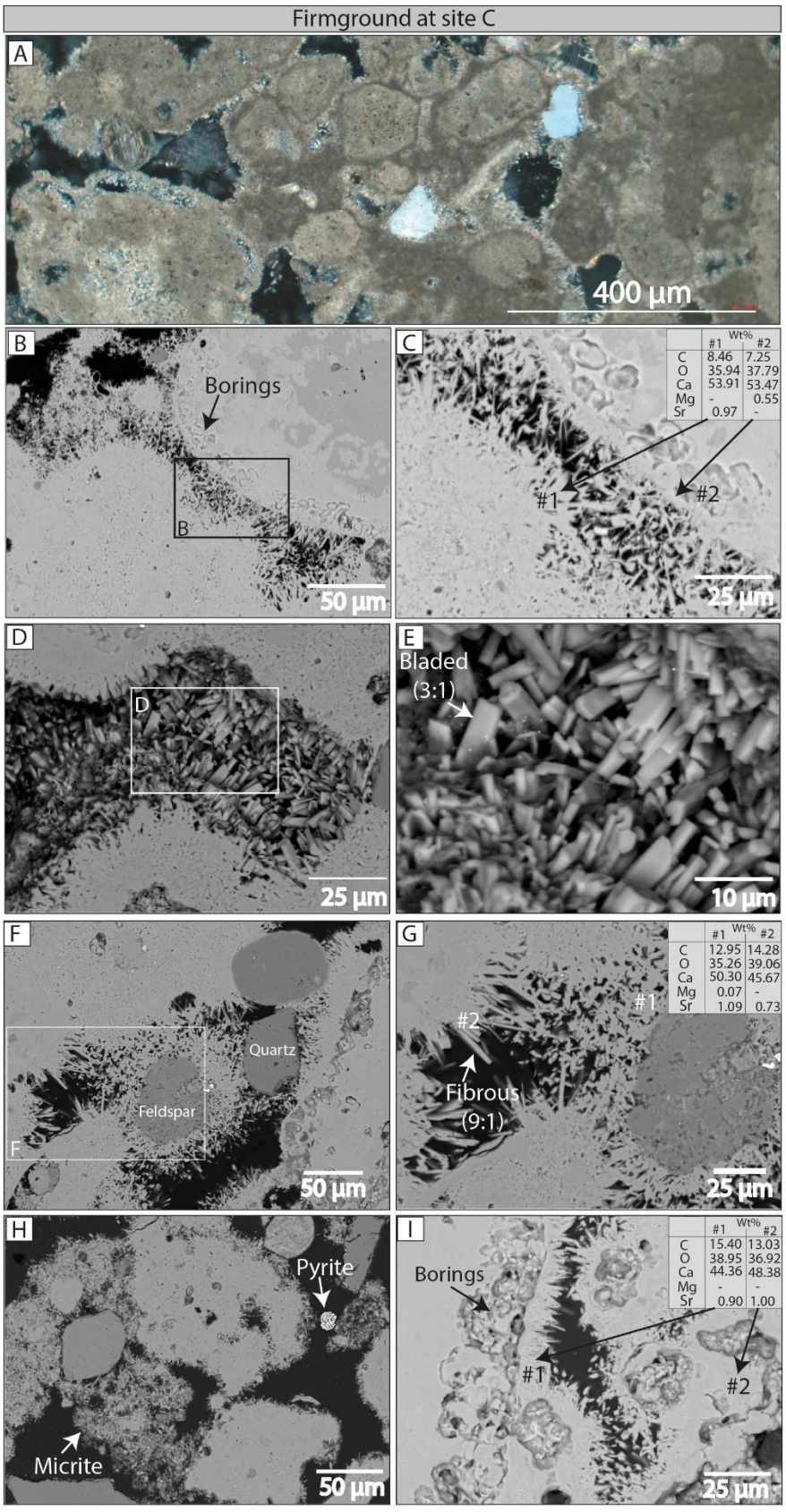

Figure 5.8. Site C firmground images. (**A**) Photomicrograph in cross polarised light showing predominantly peloidal grains with micritised rims (darker edges) and cemented with bladed and fibrous crystals. (**B**-**I**) SEM images of firmground cements from upper 1-2 cm (**B** – **G**) and lower 1-2 cm (**H** and **I**).

5.4.2.4 Site D

Site D is located 10 m east of the datum (Fig. 5.1.E). Here, the sediment surface is 11.5 cm higher than at the datum and ~12.5 cm of unconsolidated sediment overlays the firmground. Unlike the other Sites, Site D exhibits two firmground layers (Fig. 5.2.E, G, H), each ~3 cm thick. There was a small (<1 cm) gap of unconsolidated sediment separating the two firmground layers at ~17 cm. At Site D-2 (0.5 m south of Site D) the upper firmground was thicker (3.5-4.4 cm) and the lower firmground was thinner (2.2-2.9 cm) compared to the firmgrounds at Site D (Fig. 2.H).

Above the upper firmground (0 – 12.5 cm) unconsolidated grains are coated in randomly orientated microcrystalline crystals (<5 µm long) (Fig. 5.9). Within the firmgrounds, grains are predominantly cemented with an isopachous fringe of fibrous needles and bladed crystals (5-15 µm long) (Fig. 5.9.F-I) within which semi-quantitative EDS analysis identified no Mg^{2+} and Sr^{2+} present in low abundance (0.9 ±0.3 wt% n=5 spot analysis). Fibrous and bladed crystals typically form on top of a micritised envelope (width 5 ±3 µm) with 7.5 wt% Mg^{2+} and no Sr^{2+} detected *via* EDS (Fig. 5.9.F). An EPS-like substance is observed around some of the bladed crystals (Fig. 5.9.I). Abundant microcrystalline crystals are present within intergranular pore spaces (Fig. 5.9.J, M) containing 0.9 ±0.7 wt% Mg^{2+} and 0.4 ±0.3 wt% Sr^{2+} (n=11 spot analysis). Pyrite framboids (~10 µm diameter) are common, and in some cases form clusters in association with possible EPS (Fig. 5.9.L).

The upper firmground (~16-12.5 cm) is less well lithified than the lower firmground and transitions from light grey at the upper surface to dark grey at the base. The upper firmground consists of a peloidal packstone and grainstone and qualitative observations suggest sediments were finer grained than the lower firmground. Dark patches are also present that were absent in the lower firmground. The upper firmground consists of sand, shell fragments, with some bored holes and a few tubes. The lower firmground (17-20 cm) is well lithified, dark grey, and very coarse grained with some gastropods, shell fragments, tubes, and holes.

Below the lower firmground, dark grey unconsolidated sediments are present to the base of the profile and the upper surface of the basal hardground at ~29 cm. Grains are predominantly peloids, with abundant gastropods and some bivalves. Gastropods may be a different species to those higher up in the profile, though this warrants further investigation. Grain surfaces are heavily neomorphosed and coated in microcrystalline crystals (2-4 µm long) (Fig. 5.9.E). The base of the profile terminates on the upper surface of a well-cemented basal hardground consisting of bioclastic grainstone with abundant gastropods (29-32 cm) but was unable to be penetrated or sampled and thus the vertical extent is unknown.

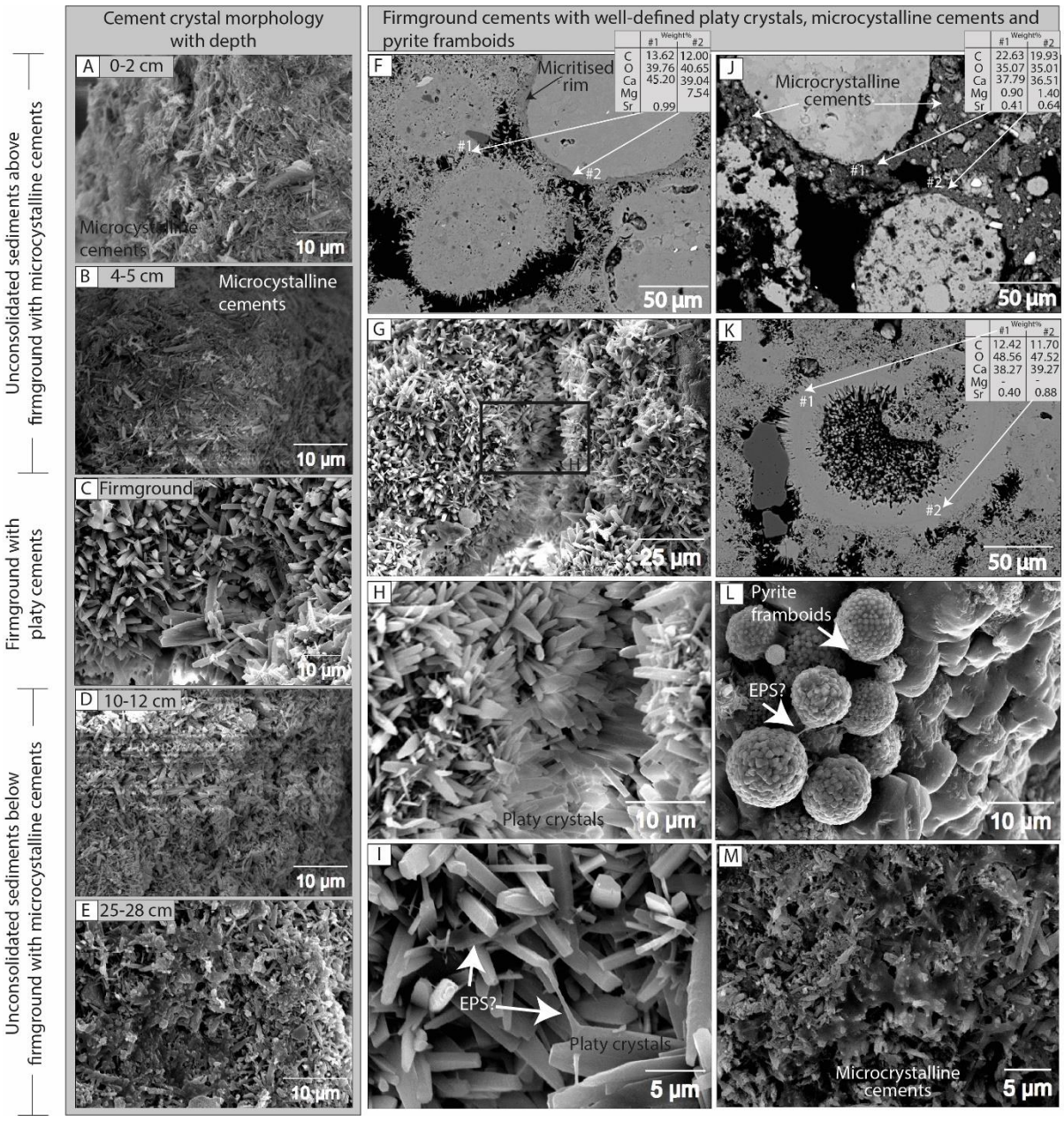

Figure 5.9. Site D SEM images of crystal morphologies. (**A**), (**B**) and (**C**) display microcrystalline cements coating unconsolidated sediments above the firmground at 0-2cm, 4-5 cm and 10-12 cm. (**D**) shows bladed and platy crystals present within the firmground; and (**E**) demonstrates a return to micrite cements below the firmground (25-28 cm). (**F**) Polished section of the lower firmground showing grains coasted in bladed and platy crystals. The dark micrite envelope contains Mg^{2+} and no detectable Sr^{2+} *via* EDS (#1), whereas bladed/play crystals contain Sr^{2+} and no apparent Mg^{2+} (#2). (**G**), (**H**), and (**I**) display images of platy/bladed crystals from the lower firmground with increasing magnification, with potential EPS highlighted in (**I**). (**J**) shows the intergranular micrite containing varied amounts of Mg^{2+} and Sr^{2+}. (**K**) Polished section of the upper firmground, showing a biogenic chamber (e.g., foraminifera) cemented on the internal and external wall with bladed aragonite, containing Sr^{2+} and no detectable Mg^{2+}. (**L**) shows pyrite framboids in association with potential EPS (highlighted by white arrows) and (**M**) displays the micrite cement within the lower firmground at high magnification.

5.4.3 Porewater Chemistry

Porewater chemistries from Sites A-D are contrast with possible endmembers (offshore seawater, creek waters from 2017 and 2019 (Chapter 4) and groundwaters from boreholes), as well as porewaters obtained from the creek (~85 m seaward of QLTC) (Site 5-TC; an area without an area of subsurface lithification), inland porewaters (~640 m and ~1455 m inland from QLTC), and where relevant, also against porewaters obtained from Yas Lagoon (Chapter 3).

5.4.3.1 Salinity and redox

Salinity, presented as total dissolved solids (TDS) in parts per thousand (‰), increases in a broadly linear trend with depth at all sites and appears to track towards the highly saline waters obtained from the nearby boreholes (170-223‰). Porewaters salinities in the upper ~7 cm of all sites are within the range of creek surface water salinities measured throughout the day in 2019 (57.3 ±9.4‰, n=9) (Fig. 5.10.A), though salinity at Site B (within the channel) is higher than the other sites and resembles salinities in the upper ~6 cm at channel Site 5-TC. Salinity at all sites converge at 7 cm (61.5±3.4‰, n=5), before becoming increasingly different with depth; salinity below 7 cm is highest within the creek (Site B) and decreases with distance from the creek channel. Inland surface waters are highly saline (>180‰) below 5 cm (Fig. 5.10.A).

Redox potential (Eh) was only analysed for the 2019 sites (C, D, 5-TC, and boreholes). Sites C and D are similar to one another; above the firmground there is a slight decline in Eh with depth from 1 to ~7 cm, though at Site D, Eh is lower than Site C by ~12%. Porewater at Sites C and D become anoxic above the firmground at ~8-9 cm (3-3.5 cm above the firmgrounds) and remain anoxic with depth (Fig. 5.10.A). Porewaters from Site 5-TC become anoxic at ~7 cm and boreholes appear to be oxic, though this may be due to aeration whilst pumping.

5.4.3.2 Carbonate chemistry

Porewater *p*H, alkalinity, and carbonate mineral SI are not noticeably different around the firmgrounds. *p*H is highest within the tidal creek surface waters, lowest in the boreholes and tends to display and overall decrease downcore (Fig. 5.10.A, B). Porewater *p*H at all sites is significantly lower than the average tidal creek *p*H on the day of sampling (7.89 ±0.7, n=8) (Fig. 5.10.A). *p*H is variable at all sites in the upper ~5 cm of porewaters (7.15-7.51 *p*H), however variability reduces around 6-7 cm (7.24-7.36 *p*H). Above the firmground at Site B, *p*H increases with depth, whereas at Sites C and D *p*H decreases towards the firmgrounds upper surface. Below 6 cm porewater *p*H declines with depth at all sites; *p*H is lowest at Site C, followed by Sites D and A. Unlike Yas lagoon, QLTC Sites C and D show no increase in *p*H surrounding the firmground (Fig. 5.10.A). Porewater *p*H is higher at all sites compared to the channel porewaters (Site 5-TC). The deepest inland porewaters have *p*H values approximate to

groundwaters from borehole 2 (6.72), whereas *p*H from Boreholes 1 and 3 were lower (6.29 and 6.34 respectively) (Fig. 5.10.A).

Porewater alkalinity at Sites A-D was mostly lower than Yas lagoon and Site 5-TC and higher than the inland porewaters (Fig. 5.10.A). Creek surface water alkalinity is typically lower than offshore seawater alkalinity, though variable (av.=2.16 ±0.34 mmol l^{-1}). At Site A, alkalinity increases between 2.5-4.5 cm (from 2.34-2.62 mmol l^{-1}) before decreasing with depth in a broadly linear trend. In contrast, alkalinity at Site B decreases with depth above the firmground, most significantly from 5.5-7 cm (2.36-1.95 mmol l^{-1}). Below the firmground alkalinity increases with depth to stabilise at 19-27 cm (2.23±0.01 mmol l^{-}) (Fig. 5.10.A). Alkalinity at Sites C and D peak at 3 cm (2.71 mmol l^{-1}) and 5 cm (2.44 mmol l^{-1}) respectively and then decrease with depth, though Site D increases slightly above the firmground at 12.5 cm (2.39 mmol l^{-1}). Alkalinity at Sites C and D remain fairly stable below the firmground at 2.31±0.01 mmol l^{-1} (16.5–28.5 cm, n=7) and 2.28 ±0.04 mmol l^{-1} (21 – 28.5 cm, n=4) respectively. The deepest porewaters at Sites A-D have alkalinities within the range of groundwaters samples, whereas the inland porewaters are significantly lower (Fig. 5.10.A).

Due to the relatively low salinities (<60 ‰) of some of the creek surface waters and shallow porewaters (above ~6 cm), the thermodynamic model CO2SYS may provide a more accurate representation of the carbonate chemistry than PHREEQC. However, below ~6 cm, the high salinities negate the application of CO2SYS (See methods in Chapter 2.2). For lower salinity waters (<56‰), CO2SYS produces slightly lower pCO_2 estimates and slightly higher carbonate mineral SI estimates than PHREEQC. For simplicity, only PHREEQC outputs are presented in Fig. 5.10, however, where the difference between model outputs has implications for the interpretation, both models will be discussed. Carbonate chemistry calculated with CO2SYS and PHREEQC is presented for Site C in Chapter 2.2 (Fig. 2.8B).

The partial pressure of CO_2 (*p*CO2) is lowest at Site A throughout much of the profile and increases in a broadly linear trend with depth to peak at 14.5 cm (0.40%), before becoming fairly stable from 16.5-29.0 cm (0.29 ±0.01%) (Fig. 5.10.B). In contrast pCO_2 at Site B decreases with depth towards the upper firmground surface (no data available for below the firmgroud). Sites C has the highest pCO_2 which increases with depth and peaks at 24.5 cm (0.69%). pCO_2 at Site D is variable above the firmground and increases with depth below the firmground to peak at 28.5 cm (0.55%) (Fig. 5.10.B). Inland porewater pCO_2 remains similar to creek water values in the upper 4.5 cm, though increases with depth (inland Site 1) and appears fairly stable below 28.5 cm, though peaks at 35.5 cm (0.77%). In contrast pCO_2 is significantly higher in the creek porewaters at Site 5-TC, and the highest pCO_2 is observed in Boreholes 1 and 3 (3.1 and 3.4% respectively) (Fig. 5.10.B).

All porewaters are less saturated with respect to aragonite and calcite than the local offshore seawater and tidal creek surface water (Fig. 5.10.B). All porewaters are supersaturated with respect to calcite, whereas only Site A is supersaturated with respect to aragonite (Fig. 5.10.B). At Site B, aragonite saturation indices (SI_{arag}) increase slightly above the upper firmground surface at 5 cm. PHREQQC suggests porewaters above the firmground at Site B remain aragonite understated, whereas CO2SYSY suggest they reach aragonite equilibrium at 6 cm. At Sites B-D, PHREEQC suggest porewaters remain undersaturated with respect to aragonite, however CO2SYS suggests Site C porewaters may remain at aragonite equilibrium from 1-6 cm. Below the firmground(s) at Site C and D, and below ~10 cm at Site 5-TC, porewaters remain aragonite undersaturated and at ~calcite equilibrium and remain fairly stable with depth.

5.4.3.3 Organic chemistry

Porewater dissolved organic carbon (DOC) was typically higher than offshore and tidal creek surface waters, and groundwaters, though was variable between sites and between field campaigns (2017 samples typically had higher DOC than 2019) (Fig. 5.10.C). Site A has the highest concentration of DOC, peaking at 16.5 cm (23.5 mg l^{-1}) which most closely resembles DOC concentrations within Yas Lagoon. DOC at Site B peaks at 22 cm (18.8 mg l^{-1}) and DOC at Sites C and D vary with depth, though peak at 10.5 cm (10.1 mg l^{-}) and 3 cm (10.0 mg l^{-}) respectively. DOC at Sites C and D resemble one another and resemble DOC concentrations within the tidal creek porewaters (Site 5-TC) which remained fairly constant with depth (av.=7.0±1.6, n=5) (Fig. 5.10.C).

Dissolved total nitrogen (DTN) was only measured for Sites C and D and displays no significant trend with depth, though peaks at 18 cm (1.4 mg l^{-1}) and in between the firmgrounds at 17 cm (1.8 mg l^{-1}) respectively (Fig. 5.10.C). Values closely resemble those from the tidal creek porewaters at Site 5-TC and are significantly lower than those from Yas Lagoon. Ammonium (NH_4^+) is lowest at the base of the profile at Site A and below the firmground at Site B, which most closely resemble creek porewaters at Site 5-TC. In contrast Site D has the highest NH_4^+ above the firmground, which closely resembled porewaters above the firmground in Yas Lagoon, though all porewaters from QLTC had significantly less NH_4^+ compared to porewaters below the firmground in Yas Lagoon (Fig. 5.10.C).

5.4.3.4 Sulphate depletion, strontium depletion, and dissolved methane

Sulphate depletion, using Cl^- as a conservative tracer for mixing between endmembers (seawater and groundwater) (SO_4^{2-}/Cl^-) suggests porewater beneath the firmground at Site B are the most sulphate depleted (relative to a mixing trend between overlying seawaters and groundwaters), followed by Site A (Fig. 5.10.C). SO_4^{2-}/Cl^- at Sites C and D fall within the possible range of values from mixing between endmembers. Strontium depletions (Sr^{2+}/Cl^-) suggests Sites A and B are the most depleted in Sr^{2+}

(relative to a mixing trend between overlying seawater and groundwater), whereas Sites C and D are within the range of values from mixing between endmembers.

Methane above the firmground was negligible at all sites (Fig. 5.10.C). Below ~15 cm methane increases slightly with depth though remains <0.44 µmol l^{-1} at all sites, other than at 15 cm (below the firmground) at Site B (0.67 µmol l^{-1}) which most closely resembles methane concentrations in Yas Lagoon.

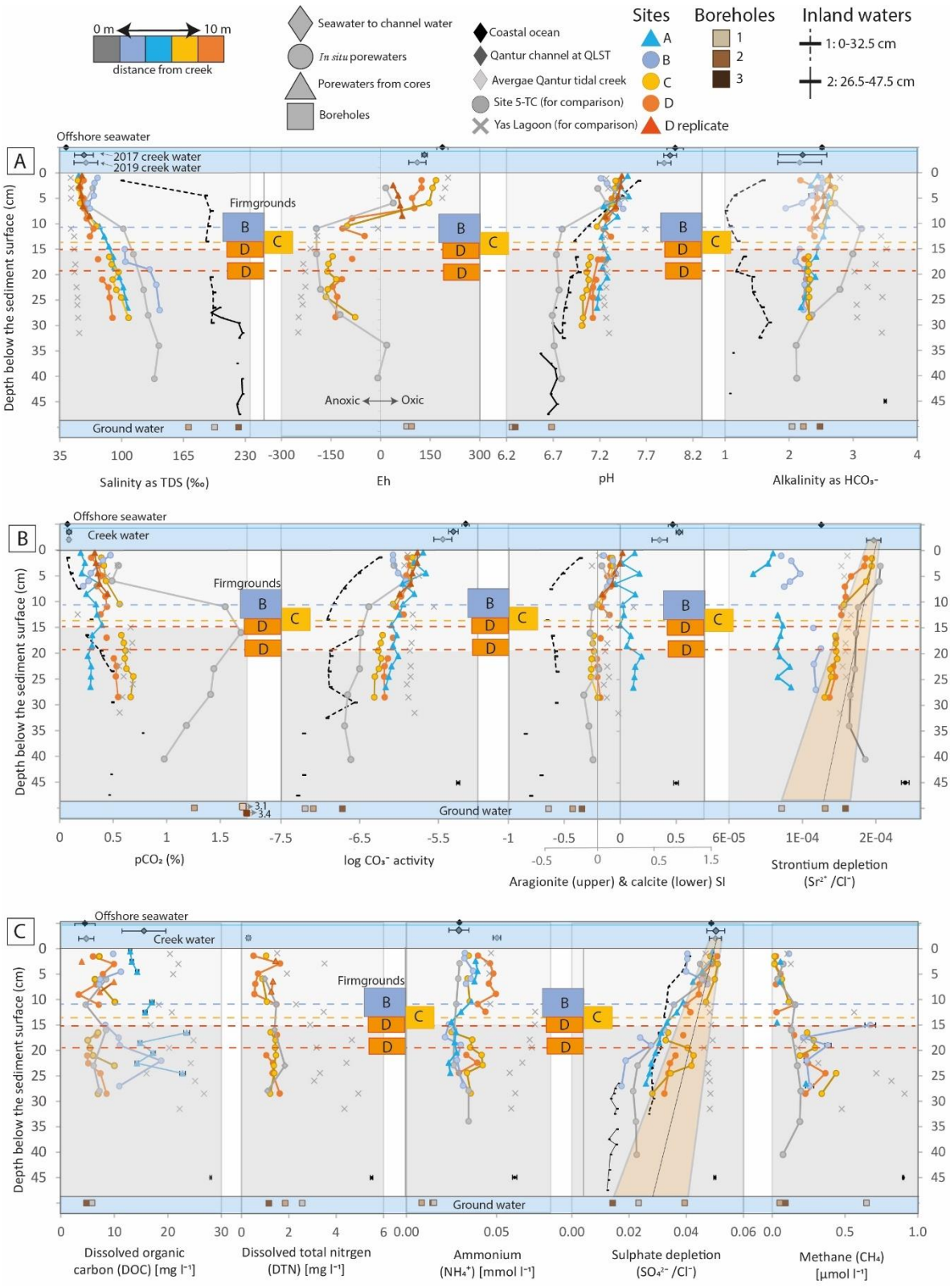

Figure 5.10 Porewater chemical profiles at Sites A-D alongside open marine waters (black diamond, upper blue panel); tidal creek surface waters sampled throughout the day on the 24th Oct. 2017 (middle diamond, upper blue panel) and on the 16th Jan. 2019 (lower diamond, upper blue panel) (discussed in detail within Chapter 4); and groundwaters from boreholes (lower blue panel). Additionally, porewaters from Yas Lagoon (Chapter 3), Site 5-TC, and inland waters (Site IW1 = Site 4-TC-UI in Chapter 4) are included for comparison. (**A**) salinity as total dissolved solids (TDS) in parts per thousand (‰); Redox potential (Eh) in milli volts (mV); pH, and alkalinity as HCO_3^- (mmol l^{-1}). (**B**) Porewater

carbonate chemistry calculated using PHREEQ-C: pCO_2(%); log carbonate activity (CO_3^{2-}); aragonite saturation indices (SI_{arag}) (upper x-axis) and calcite saturation indices (SI_{calc}) (lower x-axis) and strontium depletion as Sr^{2+}/Cl^-. (**C**) Dissolved organic carbon (DOC) (mg l^{-1}); dissolved total nitrogen (DTN) (mg l^{-1}); ammonium (mmol l^{-1}); sulphate depletion as SO_4^{2-}/Cl^-; and methane concentrations (µmol l^{-1}). Standard error is displayed in the lower right-hand corner of each figure, and when exceeded is displayed on the corresponding data point as error bars. Raw water chemistries are presented in Appendix D, Table D3.

5.4.4 Microbial communities

16S SSU rRNA gene signatures were analysed at Site A and B. Data is presented as the relative abundance of identified operational taxonomic units (OTUs). Taxa with a maximum value <1% relative abundance were summed to create the 'Other' group (Fig. 5.11). 16S SSU rRNA gene diversity is used as a proxy for active bacterial and archaeal communities within the sediment.

5.4.4.1 Site A

The microbial community structure of the upper 2 cm of sediment was very different from the rest of the profile and dominated by bacteria (>98%). Over 80% of the surface communities belong to three Phlya: *Cyanobacteria* (40.2%), *Chloroflexi*; predominantly the Class *Anaerolineae* (19.3%); and *Proteobacteria* (20.0%), containing an abundance of the Class *Alphaproteobacteria* (11.4%), and Order *Rhodospirillales* (4.3%). Furthermore, lower relative abundances of the Phylum *Bacteriodetes* (3.3%), *Planctomycetes* (2.5%) and *Actinobacteria* (1.9%) were present at 0-2 cm (Fig. 5.11.A).

Some bacterial communities were most abundant between 3-7 cm and then declined with depth, including the Classes *Deltaproteobacteria (Proteobacteria)* (13.2% at 5 cm)*, Planctomycetacia (Planctomycetes)* (5.4% at 3 cm*)*, and the Phyla Candidate division OP3 (4.0% at 7 cm*)* and *Bacteroidetes* (2.2% at 3 cm) (Fig. 5.11.A). The most abundant *Deltaproteobacteria* at 3 cm were members of the *Desulfobacterales* (8.4%; predominantly belonging to the Sva0081 sediment group; the SEEP-SRB-1 genus and an uncultured genus) and Sh765B-TzT-29 (1.3%) (Fig. 5.12.A). Similarly, some archaeal groups were also most abundant around this depth including an uncultured archaeon belonging to the family Marine Benthic Group D (MGB-D), recently named *Thermoprofundales* (Zhou *et al*., 2019) (av.=14.6 ±1.3%, n=4, 3-9 cm) which then declined in relative abundance to remain <5% from 19–31 cm (Fig. 5.13.A). Similarly, *Woesearchaeota* (previously named the Deep-Sea Hydrothermal Vent Euryarchaeota Group 6, or DHVEG-6) peaked in abundance at 3 cm (7.6%) before declining with depth to remain <1% from 17-31 cm (Fig. 13.A).

In contrast, a few bacterial Classes increase with depth, including *Aminicenantes, Phycispaerae (Planctomycetes), Actinomicrobia and Dehalococcoidia (Chloroflexi)* with maximum relative abundances at 19 cm (8.2%); 21-23 cm (6.2%); 31 cm (3.5%); and 23 cm (8.1%) respectively (Fig. 5.11.A). Additionally, some members of the *Deltaproteobacteria* class increased with depth (from ~0% at the

sediment surface), including *Syntrophobacter,* which were most abundant at 9-11 cm (3.5%) but decreased to <1% from 19-31 cm; the Sva0485 clade, which were most abundant at 19 cm (1.2%) before stabilising at 0.9 ±0.1% (n=6) from 21-31 cm; and *Desulfarculales*, which increased with depth and were most abundant at 19-21 cm (2.7%) but decreased to 1.4% at 31 cm (Fig. 5.12.A).

Additionally, the relative abundance of total archaea increased with depth from 23% at 3 cm to reach a maximum relative abundance of 47 ±1% between 26-30 cm (n=3) (Fig. 5.11.A). The most abundant archaeal Phylum was the *Bathyarchaeota* (Evans *et al*., 2015), previously Miscellaneous Crenarchaeotal group (MCG), which remained <2% in the upper 7 cm, but then increased in a broadly linear trend from 9 cm (~5%) to stabilise around 20-30 cm (37.6% ±2.7%, n=6) (Fig. 5.11.A). Members of the *Thaumarchaeota* Phylum were present in low abundance, predominantly members of Group C3 peaking in relative abundance at 12 cm (2.0%) and Marine Benthic Group B (MBG-B/*Lokiarchaeota*) which increased in relative abundance slightly with depth, but within a small range (av.=0.6% ±0.3% from 4-30 cm, n=14) (Fig. 5.13.A).

5.4.4.2 Site B

The upper 0-2 cm of sediment at Site B was dominated by bacteria (>98%) with abundant photosynthetic and heterotrophic facultatively anaerobic microbes belonging to the Phylum *Proteobacteria* (25.9%), of which the Classes *Alphaproteobacteria* (13.6%), *Betaproteobacteria* (6.1%) and *Deltaproteobacteria* (5.6%) were most abundant; *Cyanobacteria* (25.7%), *Bacteroidetes* (16.9%), predominantly the *Sphingobacteriia* Class (10.3%), *Planctomycetes* (13.2%); and *Chloroflexi* (6.5%), predominantly the *Anaerolineae* Class (5.43%) (Fig. 5.11.B).

Cyanobacteria decreased with depth below the surface to become negligible at 7 cm (Fig. 5.11.B). In contrast, *Chloroflexi* increased from the surface to peak in relative abundance at 5 cm (39.1%), containing an abundance of *Anaerolineae* (27.9 ±1.6%, n=2), and minor amounts of *Ardenticatena* (2.2 ±0.7%, n=2). *Anaerolineae* declined in relative abundance just above the firmground at 7 cm (6.6%) (Fig. 11.B). *Desulfobacterales* (*Delatproteobacteria)* peak in relative abundance at 3 cm (13.1%) and remained present to the base of the profile at 7cm (7.5%) where *Desulfarculales* also peak in relative abundance (1.7%) (Fig. 5.12.B).

In contrast *Planctomycetes* displayed the opposite trend*,* with the lowest values at 3-5 cm (av.=5.5 ±1.6%, n=2) which increased to 11.4% at 7 cm. *Acidobacteria* also increased towards the firmground, reaching a maximum relative abundance at 7 cm (2.3%) (Fig. 5.11.B). Archaea also increased from av.=4.3 ±1.9% at 0-5 cm (n=3) to 22.6% at 7 cm, dominated MGB-D (15.6%), and microbes belonging Phylum *Woesearchaeota* (4.5%) and *Thamarchaeota* (1.2%) (Fig. 5.13.B).

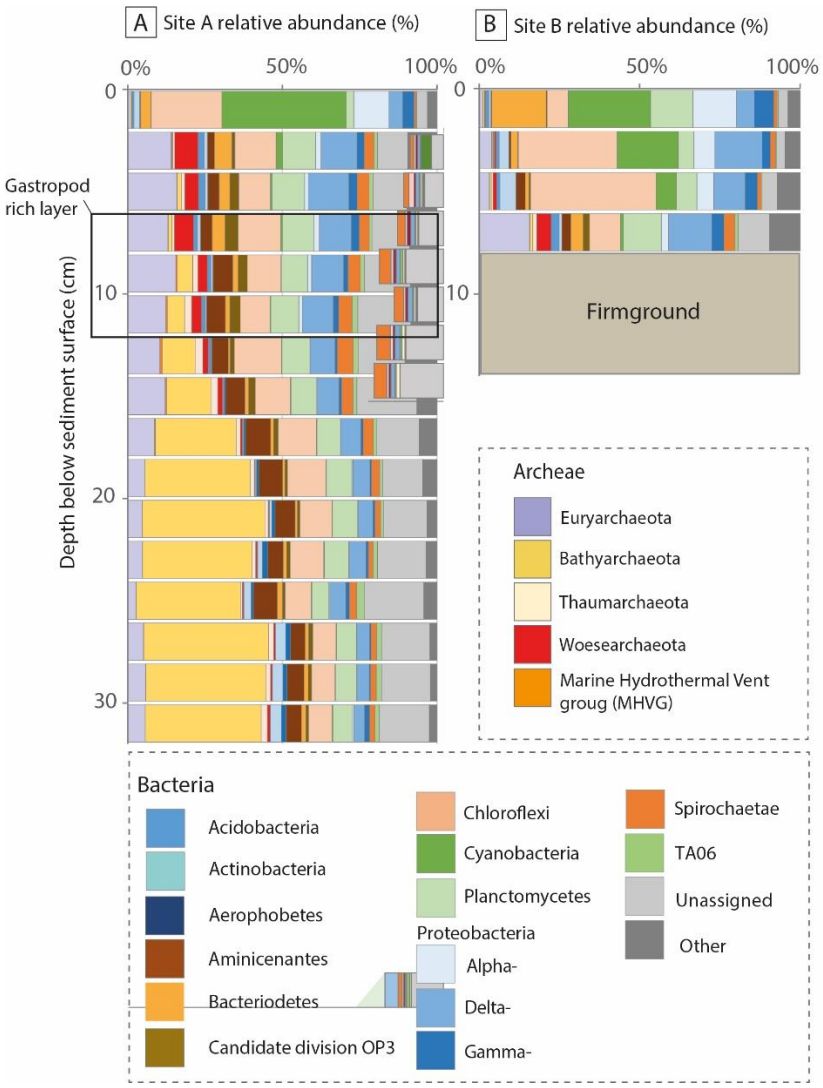

Figure 5.11. Relative abundance of 16S SSU rRNA gene sequences for common communities from (**A**) Site A and (**B**) Site B.

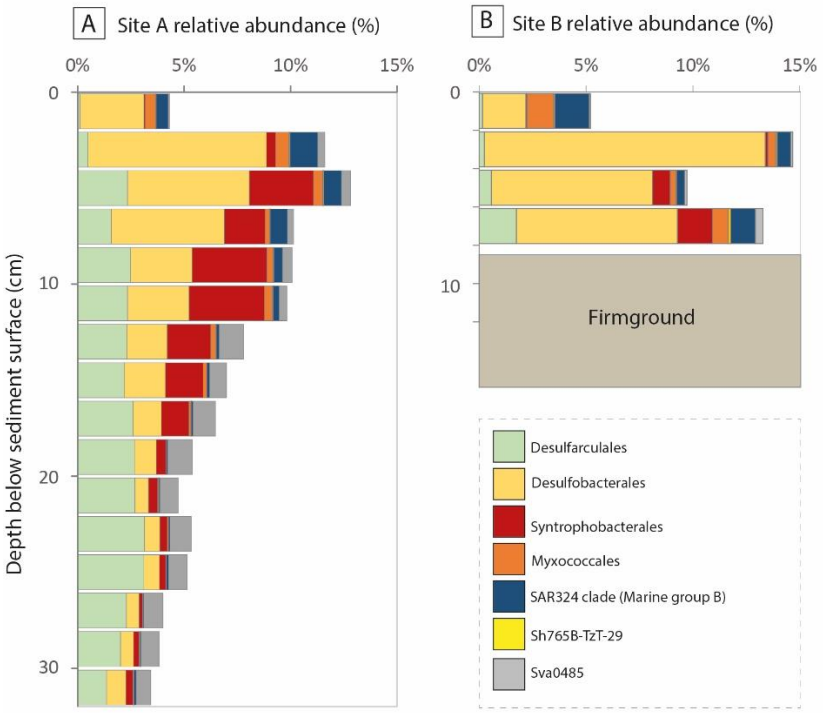

Figure 5.12. Relative abundance of 16S SSU rRNA gene sequences of known sulphate reducing bacteria (SRB) belonging to the Class *Deltaproteobacteria* at Sites A (**A**) and B (**B**).

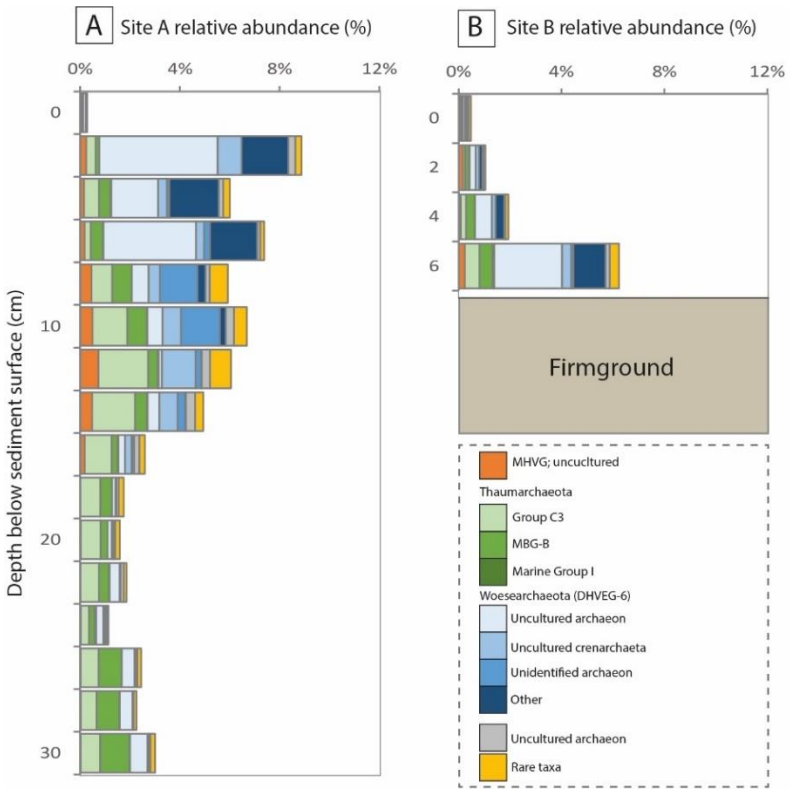

Figure 5.13. Relative abundance of 16S SSU rRNA gene sequences of minor archaea other than MBG-D and *Bathyarchaeota* at Sites A (**A**) and B (**B**).

5.5 Discussion

Within the shallow sediment (~30 cm depth) surrounding the tidal creek in Qantur Lagoon (QLTC), firmgrounds are absent from Site A, but present at Sites B, C, and D, indicating the heterogeneous nature of cementation over a relatively small distance (~10 m). The firmground at Site B and C is ~5 cm thick, whereas Site D exhibited two stacked firmgrounds, each ~3 cm thick. Unconsolidated sediments at all sites are coated in microcrystalline cements, with rare fibrous crystals in intergranular pore spaces and within biogenic chambers (e.g., foraminifera and gastropods). In contrast the firmgrounds are cemented by acicular, fibrous, and bladed crystals in association with pyrite framboids and abundant microcrystalline cements. Whilst firmground cement mineralogy was not quantitatively determined, semi-quantitative EDS analysis of the acicular, fibrous, and bladed pore filling crystals suggest aragonite mineralogy owing to the low Mg^{2+} content and presence of Sr^{2+}. The orthorhombic aragonite lattice preferentially incorporates cations with relatively large ionic radii such as Sr^{2+} (Cubillas *et al*., 2005; Pederson *et al*., 2020), which may reach 1-2% $SrCO_3$, whereas the incorporation of Mg^{2+} in aragonite is typically <1% $MgCO_3$ (Kinsman, 1964). Furthermore, Ge *et al*. (2020a) identified near identical acicular, fibrous, and bladed crystal morphologies as aragonite from concretionary features in nearby coastal lagoons in Abu Dhabi by combined EDS, microprobe, and Raman spectroscopy. However, Ge *et al*. (2020a) suggest that microcrystalline and micrite cements may be HMC, containing ~2 wt% Mg which is likely formed by direct precipitation from solution and should not be confused with detrital micrite (Ge *et al*. 2020a). Microcrystalline cements within the QLTC firmgrounds typically contain slightly higher Mg^{2+} (0.9 ±0.7 wt%) and slightly lower Sr^{2+} (0.4 ±0.3 wt%) than the acicular, bladed, and platy crystals, suggesting they are likely aragonite or HMC.

The first question to address is whether the firmgrounds at QLTC appear to be actively forming in the subsurface (as in Yas Lagoon, Chapter 3), or whether they may be older, and/or no longer actively forming, suggesting they may have formed closer to the sediment surface. The second question to address is what physical, chemical, and/or biological processes are responsible for driving cementation at QLTC. One option is that firmgrounds surrounding QLTC have formed by similar processes to those in Yas Lagoon (Chapter 3) but may have been forming over a longer period and/or may no longer be forming. In this case, cementation may have initiated in the subsurface by microbial processes which promote mineral precipitation by biologically-influenced mineralisation resulting from interactions between organisms and their environment. Alternatively, cementation at QLTC may be driven by abiotic cementation (Schrag *et al*., 2013) which may be associated with the physical properties of the sediment and/or localised variations in the hydrodynamic system (e.g., the circulation of supersaturated seawater and sea level rise).

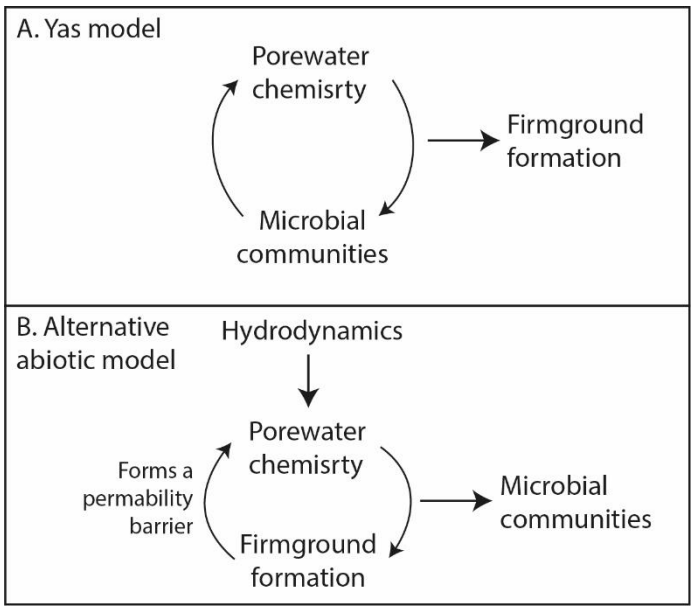

Figure 5.14. Simplified conceptual models describing potential primary drivers of firmground cementation at QLTC. (A) The 'Yas Lagoon' model, whereby microbial respiratory processes (dependent on the downward diffusion and/or upwards advection of dissolved species and organics) alters the porewater chemistry, which promotes firmground formation at (ore near to) the redox boundary. (B) An alternative abiotic model of firmground formation, whereby hydrodynamics (e.g., the circulation of supersaturated seawaters, potentially liked to the present marine transgressive phase) controls porewater chemistry and thus firmground formation. Firmgroud formation forms a permeability barrier which may have implications for the vertical zonation of certain microbial communities.

5.5.1 Are firmgrounds actively forming in the subsurface surrounding QLTC?

Firmgrounds are typically considered to form *via* abiotic processes occurring at, or near to, the sediment surface (Hillgärtner 1998; Schrag *et al*., 2013; Christ *et al*., 2015). However, recent work in coastal Abu Dhabi suggests cementation may also be occurring in the subsurface *via* microbial respiratory processes (Paul and Lokier, 2017; Ge *et al*., 2020a; Chapter 3). Evidence of active subsurface firmground formation at QLTC may therefore support the involvement of microbes in driving cementation. The Modern age of similar shallow firmground and hardground features near Qantur lagoon (<268 yBP) (Lokier and Steuber, 2009; Ge *et al*., 2020a) preclude the application of radiocarbon dating to distinguish the relative ages of the firmgrounds at the QLTC sites. However, evidence of active carbonate precipitation may include chemical signatures within porewaters (e.g., aragonite/calcite supersaturation, increased *p*H and/or alkalinity surrounding firmgrounds, strontium depletion (Chapter 3)), or be attainable based on year-on-year change, if a longer-term study were possible. Additionally, physical analysis of crystal morphologies may provide evidence of dissolution (or lack thereof). Alternatively, evidence of formation in the near surface oxic zone (e.g., marine borings and encrusting organisms) (Bathurst, 1971) would suggest firmgrounds may have been subsequently buried and thus may no longer be actively forming.

Whilst there is no firmground visible at Site A, cemented intervals are associated with the gastropod rich layer at ~6-12 cm, and fibrous crystals were observed within intergranular pore spaces (predominantly in the larger cemented clusters) at 12-14 cm (Fig. 5.4.F). This is just above the sediment colour change from light to dark grey at 15 cm (Fig. 2C), which corresponds with the lower surface of the firmground at Site C and the upper firmground at Site D (Fig. 5.2.E). Abundant aragonite in the upper 12 cm suggests that the precipitation of authigenic aragonite may be favoured here, whereas below 12 cm the abundance of aragonite decreases whilst calcite increases, possible indicating the increased replacement of aragonite by calcite with depth. It is possible that an aragonitic firmground will form within the gastropod rich layer (~6-12 cm) at Site A soon, and the larger cemented clusters are the precursor to the firmground. In this case the firmground would form at roughly the same depth as observed at Site B and thus supports the theory of subsurface cementation. Alternatively, the intergranular pore spaces of the cemented clusters may provide microniches for microbial communities (Bertics and Ziebis, 2009), which may promote different respiratory process (and chemical by-products) that promote the precipitation of localised acicular and fibrous aragonite crystals compared to the more well-connected pores.

Very early lithification appears to be favoured at two separate depths within the gastropod rich layer at Site A (6-8 cm and ~9.5-12.5 cm) suggesting that cementation may be driven by two separate subsurface processes, which may be synchronous or asynchronous. Unfortunately, the coarse resolution of microscopy analysis at Site A misses the section of interest (~5-12 cm), and thus further work analysing the morphology and mineralogy of cements within the semi-lithified sections from the two cemented horizons is required. Furthermore, future work investigating the laterally continuity of these early cemented layers would be valuable alongside targeted secondary ion mass spectrometry (SIMS) analysis of the cements to determine if the isotopic signature suggests the inclusion of carbonate sourced from the microbial degradation of OM (Irwin *et al*., 1977; Mavromatis *et al*., 2014).

Site A is the only site where porewaters are predominantly supersaturated with respect to aragonite. However, porewater samples from this site were obtained from the core (see Methods), which may have caused increased degassing of CO_2 relative to those sampled *in situ* (Site B-D). At Site A porewaters have a slightly higher *p*H and lower pCO_2 than other sites which would support degassing. It remains unclear if the degree of aragonite supersaturation observed at Site A is erroneous due to the sampling methodology, or if it reflects the true nature of the environment at the time of sampling, and future studies should aim to resample porewaters at this location.

Within the firmground at Site B cementation and sorting decrease and porosity and grain size increase from the upper surface towards the lower surface, suggesting the firmground may be cementing downward. However, the alkalinity nadir at ~7 cm (Site B) suggests active carbonate precipitation may

be occurring above the firmground. This is concurrent with a slight increase in porewater *p*H from 0 - 7 cm, suggesting that the driver for cementation is a biogeochemical process which increases porewater *p*H, rather than one that simply increases DIC. The aragonite saturation indices (SI) (calculated with CO2SYS) increase with depth to reach equilibrium at 6 cm though become slightly undersaturated at the upper firmgroud surface (7 cm) (no SI data available below the firmground) which suggests this would be an area of aragonite dissolution and calcite precipitation unless local conditions overcome kinetic barriers for calcite precipitation. Aragonite has Sr^{2+}/Ca^{2+} ratios approximately five times larger than calcite (Joseph *et al*., 2013). Aragonite-calcite transformation would therefore increase porewater Sr^{2+}. Using Cl^- as a conservative tracer for mixing between endmembers, Sr^{2+}/Cl^- at Site A and B suggest porewaters are Sr^{2+} depleted, particularly near the sediment surface, which would suggest aragonite precipitation, however issues with major cation analysis for 2017 samples may have artificially inflated this ratio, and further analysis of cations would be required to confirm the degree of Sr^{2+} depletion presented in Fig. 5.10B.

In contrast, Sites C and D show no significant increase in saturation indices, alkalinity, or *p*H surrounding the firmground. Instead, *p*H and alkalinity decrease in a broadly linear trend with depth, suggesting mixing between surface seawaters and groundwater (Fig. 5.10.A). No distinct variations were observed in cements morphology from the upper and lower firmground at Site D, however the upper firmground was less well-lithified than the lower. This may be a result of the upper firmground being younger than the lower. The observation of pyrite framboids in association with firmground cements (Sites C, and D) suggests they formed in anoxic conditions in the presence of H_2S. However, pyrite formation may have taken place after firmground formation and be the product of microbial processes occurring throughout the burial stage (Christ *et al*., 2015). Future work analysing the rare earth elemental composition could further support this, as the Ce anomaly is commonly employed to distinguish the oxic/anoxic conditions associated with carbonate formation (Haley *et al*., 2004; Wallace *et al*., 2017). Using Cl^- as a conservative tracer for mixing, porewater Sr^{2+}/Cl^- at Sites C and D fall within the mixing trend between creek surface waters and groundwaters, although groundwater values vary considerably. If Borehole 1, which was the closest to the QLTC sites is used as the endmember, then porewaters at Sites C and D appear to have more Sr^{2+} than expected by mixing, which would suggest aragonite-calcite transformations. However, if Borehole 3 is used as the endmember for Sites C and D, then porewaters appear to have lower Sr^{2+} than expected from mixing, which would suggest aragonite precipitation (Fig. 5.10.B).

Whilst Site B exhibits a small decrease in alkalinity approaching the upper surface of the firmgroud (possibly caused by the precipitation of carbonate minerals), no significant changes in carbonate chemistry are observed surrounding the firmground(s) at Sites C and D, or within the gastropod layer (Site A). In Yas Lagoon (Chapter 3), cementation was thought to be driven by an increase in *p*H

surrounding the firmground. Whilst an increase in *p*H is observed at the upper firmground surface at Site B, there is no significant increase in *p*H surrounding the firmgrounds or gastropod layer at the other sub-sites. This suggests that whilst subsurface cementation may be active at Site B, there is little evidence of active cementation at Sites C and D, and insufficient evidence to conclude active cementation at Site A.

Aside from Site A, porewaters at Site B, C, and D (Fig. 5.10.B) are predominantly undersaturated with respect to aragonite suggesting that these porewaters should promote aragonite dissolution and calcite precipitation. However, the observation of well-defined aragonitic crystals and sediments at these sites suggests otherwise. Similarly, Paul and Lokier (2017) identified the co-occurrence of acicular aragonite and dolomite cements in the Holocene hardground (thought to be the same surface at the basal hardground underlying the QLTC profiles). The co-occurrence of these minerals suggests the hardground has not undergone a significant phase of dissolution suggesting there may be unknown and ongoing processes that promote new phases of aragonite/HMC precipitation and/or prevent dissolution (Paul and Lokier 2017). This raises the question of why porewaters apparently undersaturated with respect to aragonite are not driving aragonite-calcite transformations?

One simple reason may be that model calculations for carbonate mineral saturation indices applied in PHREEQC and CO2SYS fail to accurately represent the complex ion pairings in such highly saline waters (as discussed in Chapter 2.2), and thus porewaters are more saturated than they appear. Alternatively, sampling at QLTC may only provide a temporal snapshot of the porewater chemistry that is not representative of annual variations, possibly owing to changes in *in situ* sediment temperatures (discussed further in Chapter 6), or seasonal variations in hydrodynamics and/or microbial respirations, though this warrants further investigation. Another reason for the contradiction between aragonite crystals morphologies (showing no evidence of dissolution) and porewater undersaturation may be that H^+, Ca^{2+}, CO_3^{2-}, and HCO_3^- species concentrations in the bulk solution (i.e., that sampled by the Rhizons) may not be the same as those at the mineral surface (controlling rates of dissolution/precipitation) (Eisenlohr *et al*., 1999). In future studies, a combined methodology involving extracting porewaters with Rhizons (*in situ*) plus replicate porewater samples obtained *via* centrifugation of an adjacent core, may help determine if preferential sampling from larger pore networks by Rhizons significantly impacts the porewater carbonate chemistry.

5.5.2 Microbial drivers: a Yas Lagoon-type model of subsurface firmground formation at QLTC

Whilst there is limited chemical evidence that firmgrounds at QLTC are actively forming as they appear to be in Yas Lagoon, it is possible the firmgrounds at QLTC formed *via* the same subsurface processes but over a longer period, and active cementation has since ceased. Previous work in coastal Abu Dhabi

suggests that firmgrounds may form at the redox boundary (Ge *et al*., 2020a; Chapter 3); an area often associated with high microbial diversities (Bertics and Ziebis, 2010), heightened biogeochemical activity (Alego and Li, 2020) and likely less impacted from flushing of oxygenated waters.

At Site C and D, Eh (redox potential) suggests the redox boundary is ~3-3.5 cm above the upper firmground surface suggesting that if formation is connected to the redox boundary (as in Yas Lagoon) then firmgrounds at Site C and D may have formed higher up in the sediment column prior to burial. This would suggest the more-lithified lower firmground at Site D formed prior to the less-lithified upper firmgroud. However, there is no evidence in the porewater chemistry to suggest that a new firmground may be forming at the current redox boundary at Sites C and D, though this warrants further investigation. Although redox potential was not measured at Sites A or B, it is likely to occur at roughly the same depth as Site C and D (~8-9 cm) which corresponds with the upper firmground surface at Site B suggesting the firmground may be younger at this location, and possibly still actively forming. Similarly, the cemented fragments within the gastropod layer at Site A (~6-12 cm) may represent the early stages of firmground development (though as porewaters were only obtained from the core and may have been affected by degassing, this cannot be corroborated with porewater chemical evidence). The CT-scan imagery suggests early lithification may be promoted at two depths, separated by a less cemented central zone, which would imply the involvement of two different microbial respiratory pathways if they are forming synchronously. In the upper ~5 cm of sediment, porewaters at Yas Lagoon appeared more oxic than QLTC Sites C and D (Fig. 5.10.A) which may reflect a higher degree of bioturbation within Yas Lagoon, possibly due to a more abundant and/or diverse macrofauna in the less saline environment. In contrast the porewaters below the firmgrounds at QLTC are less reducing than those in Yas lagoon, which may reflect a variable supply of organic matter and/or different respiratory processes between sites.

Microbes can promote the precipitation of carbonate minerals in two main ways; (i) *via* biologically-induced mineralization, by acting as catalysts or nucleation sites by providing a charged surface, e.g., extracellular polymeric substances (EPS) (Weiner and Dove, 2003; Dupraz *et al*., 2009; Al Disi *et al*., 2019; Lyu *et al*., 2020); or (ii) *via* biologically-influenced precipitation whereby microbial respiratory processes affect the porewater carbonate chemistry by producing DIC and changing DIC speciation (Moore *et al*., 2004; Sivan *et al*., 2007) which can alter the saturation state and promote carbonate dissolution/precipitation (Hu and Burdige, 2007). At QLTC, like Yas Lagoon, fibrous crystals and pyrite framboids are observed within the firmgrounds in relation to small amounts of possible EPS (e.g., Fig. 5.9L, I). Ge *et al*. (2020a) also identified organic films associated with individual crystals suggesting a link between microbial metabolic processes and early diagenesis. Whilst EPS has been suggested to promote hardground formation (Hillgärtner et al., 2001), it is unlikely to be the primary driver of cementation in QLTC, though warrants further investigation.

Microbial respiratory processes involved in the degradation of OM are dominated by the electron acceptors yielding the greatest change in free energy per mol of organic carbon oxidised by dissimilatory bacteria and archaea (Claypool and Kaplan, 1974; Burdige, 2006). The sequence of oxic respiration, followed by nitrate, manganese oxides, iron oxides, sulphate and finally methanogenesis and/or the anaerobic oxidation of methane (AOM) (Froelich, 1979) continues until all available electron acceptors have been utilised or all OM degraded. The consumption of electron acceptors is balanced by production of reduced species such as NH_4^+, Mn^{2+}, Fe^{2+}, HS^- and CH_4 which under specific thermodynamic conditions may be abiotically reoxidized, although catalysed microbiologically (Schultz and Zabel, 2006).

The decomposition of OM may release acids that act to lower the carbonate saturation state (Berner *et al*., 1978) of shallow sediments underlying carbonate supersaturated seawaters (Morse *et al*., 1985). However, microbially mediated changes in microenvironments can also promote carbonate precipitation from apparently undersaturated porewaters (Shiraishi *et al*., 2008; Konhauser and Riding, 2012). Precipitation of authigenic carbonate is generally attributed to a few metabolic pathways which produce alkalinity (Coleman *et al.*, 1993) or drive a net increase in *p*H, such as organoclastic sulphate reduction (SR) with pyrite formation (Boudreau and Canfield, 1993; Plet *et al*., 2015), ammonification (Krause *et al*., 2018), Mn and Fe cycling, and AOM (Soetaert *et al*., 2007). Whilst dissolution is associated with aerobic respiration (Hu and Burdige, 2008), Fe and Mn oxidation (Soetaert *et al*. 2007) and sulphate reduction (in low Fe environments) (Ben-Yaakov, 1973). Thus, precipitation and/or dissolution reactions in the subsurface are intimately linked to the microbial respiratory processes within the sediment column. In Yas Lagoon, subsurface cementation was thought to be driven primarily by SR in conjunction with pyrite formation, and possible localised AOM which caused increased porewater *p*H (Chapter 3). This was likely mediated by archaeal Marine Benthic Group D (*Thermoprofundales*) in association with known sulphate-reducing bacteria and rare archaeal taxa in the few cm below the firmground.

5.5.2.1 Microbial metabolisms in the upper 2 cm of sediment

Unlike Yas lagoon, the microbial communities in the surficial 0-2 cm at Site A (no firmground) and B (firmground) are distinct from the underlying sediment and dominated by aerobic and phototrophic bacteria belonging to the Phylum *Cyanobacteria*, *Chloroflexi*, and (predominantly alpha)-*Proteobacteria*. These communities resemble surface microbial mats communities from other hypersaline environments, which are often dominated by *Cyanobacteria*, *Alphaproteobacteria* and *Bacteroidetes* (Wong *et al*., 2016). In intertidal mudflats microphytobenthos (photosynthetic diatoms, cyanobacteria, flagellates, and green algae) (Underwood, 2001) produce biofilms (EPS) on the sediment surface during the daily tidal exposure which provides a substantial organic carbon source

for heterotrophic bacteria inhabiting the sediment column (Haynes *et al*., 2007). This may suggest that the QLTC sediments are exposed at low tide more frequently than those in Yas Lagoon, though water level monitoring in Yas Lagoon would be required to confirm this.

Site B has less abundant *Cyanobacteria* and *Chloroflexi* at the surface than Site A but a significant relative abundance (>5%) down to 4-6 cm. This may suggest the upper 0-6 cm of sediment at Site B are more well-mixed (e.g., by bioturbation) as cyanobacteria are predominantly a photosynthetic group of bacteria (Garcia-Pichel, 2009). In contrast below 0-2 cm at Site A *Cyanobacteria* are negligible, but archaea become abundant (23% at 2-4 cm) and increase with depth. This suggests a thin (≤2 cm), fairly stable layer of microbial mat-like bacteria inhabits the surface sediment layer at Site A. The presence of archaea close to the surface suggests oxygen is consumed at shallow depth and/or that the sediment sampled for DNA analysis may not have been affected by the flushing of oxygenated waters *via* bioturbation, or may reflect an organic rich burrow lining, which may provide a more reducing microinch (Bertics and Ziebis, 2009).

5.5.2.2 Microbial metabolisms in the shallow sediment (~2-10 cm)

Like Yas Lagoon, the upper ~10 cm of sediment host to a range of microbial communities, including abundant sulphate reducing microbes (SRM), and other communities potentially involved in the cycling of nitrogen (N) and metal oxides. At Site A, several bacterial Phyla involved in the cycling of N, metal oxides, and SO_4^{2-} peak in their relative abundance within the sediment at 2-4 cm including *Desulfobacteracaea* (*Deltaproteobacteria*) which are thought to play a key pole in acetolactic SR in marine sediments; Sh765b-TzT-29 which are suggested to be involved in the Mn^{2+} cycle (Jorgensesn *et al*., 2012); and *Planctomycetes,* predominantly *Planctomycetacia, which* are typically associated with a microalgae host (Bondoso *et al*., 2017) but have also been associated with the nitrogen cycle and metal oxide reducing metabolisms (Wang *et al*., 2020). Candidate division OP3 peak at 6-8 cm at Site A and are often found in anaerobic environments characterised by the redox cycling of heavy metals such as Fe, Mn, and/or sulphur cycling (Glöckner *et al*., 2010). This suggests sediment at 2-8 cm at Site A reflects the sub-oxic zone, which typically supports the highest abundance of bacterial diversity (Fenchal and Finlay, 2008) and may in part reflect reduced disturbance from hydrodynamic forces (Böer *et al*. 2009). At Site A porewater *p*H and alkalinity peak at 4.5 cm, which may result from the by-products from SR and/or Mn and Fe cycling. Sedimentary Fe was fairly abundant (~5 ppm) in the upper 0-6 cm (Site A) and porewater appear to become slightly sulphate depleted below 5 cm.

Site B exhibits a high abundance of *Chloroflexi* at 2-6 cm (max 39% at 4-6 cm), predominantly *Anaerolineae* which are associated with deeper anoxic layers of microbial mats in hypersaline environments (Wong *et al*., 2015) as well as with the degradation of recalcitrant OM (Oni *et al*., 2015) in deeper sedimentary layers (Monteverde *et al*., 2018; Qiao *et al*., 2018). The second most abundant

Chloroflexi belong to an uncultured organism within the class *Ardenticatenia. Ardenticatenia* represent a thermophilic, chemoheterotrophic group of bacteria, with one species isolated from iron-rich sediments from a coastal hydrothermal field that is suggested to grow with dissimilatory iron and nitrate reduction under anaerobic conditions (Kawaichi *et al*., 2013). They can utilise oxygen, nitrate, and ferric iron as TEAs, tolerate high salinity, and can grow at a range of temperature (Kawaichi *et al*., 2013). This may suggest that iron and/or nitrate reduction are important metabolic pathways at 2-6 cm at Site B, however future work assessing dissolve N species and dissolved- and solid-state Mn and Fe would be beneficial.

At Site B the mesophilic SR *Desulfobacterales* peak at 3 cm, most members oxidise OM to CO_2, whilst some perform incomplete oxidation to acetate (Keaver, 2014). They have been found to correlate with sulphate and decrease in abundance with depth (Wang *et al*., 2020). Archaea remain low (<6%) until above the upper firmground surface at 6-8 cm (22%) with peaks in MBG-B (15.5%) (Fig. 5.11), *Woesearchaeota* (4.5%) and *Thaumarchaeota,* (1.2%) (Fig. 5.13) in association with SRM such as *Desulfobacterales* and *Desulfarculales* (Fig. 5.12). Similar groups were found at the lower firmground surface in Yas Lagoon (Chapter 3). This would suggest that SR may be an important metabolic pathway on the upper firmgrounds surface, however this is not reflected in the porewater chemistry which shows a decrease in the degree of sulphate depletion from the sediment surface to the upper firmground. This could potentially be linked to the dissolution of gypsum ($CaSO_4$) which remain undersaturated throughout the profile, though this warrants further investigation.

At both Sites A and B, MBG-D and *Woesearchaeota* are the most abundant archaea populations at shallow depth (above ~10 cm). MBG-D have been suggested to possess a putative nitrate reductase gene, indicating the potential involvement in dissimilatory nitrate reduction to ammonia (NH_3) (Lazar *et al*., 2017) as well as putative genes for the first stages in assimilatory SR (sulphate to sulphite, though lack the later stages to reduce sulphite to sulphide) (Zhou *et al*., 2019). They also possess genes potentially capable of encoding the Wood–Ljundahl (WL) pathway which would allow them to produce the methyl coenzyme M reductase (MCR) (Zhou *et al*., 2019); the principal enzyme for methanogenesis observed in all known methanogens (Cui *et al*., 2015). Despite this potential, Lloyd *et al*., (2013) reported that the relative abundance of 16s SSU rRNA appears unrelated to the biogeochemical zones of SR and methanogenesis. *Woesearchaeota* are thought to be capable of carbon and hydrogen-based metabolisms under anoxic condition and may rely on symbiotic and/or fermentive-based lifestyles (Castelle *et al*., 2015).

At Site B the decrease in alkalinity from the sediment surface to the upper firmground surface may result from the removal of CO_3^{2-} from solution by $CaCO_3$ precipitation. This is supported by an increasing percentage a $CaCO_3$ in the sediment from 0 – 8 cm (Fig. 5.7.B), along with increases in the

percentage of grains cemented in aggregate clusters and an increase in the size of clusters with depth (Fig. 5.7.A). As porewater alkalinity decreases with depth, *p*H increases, which suggests that the driver of precipitation is a microbial process that increases *p*H, not just DIC, like Yas Lagoon. The presence of sulphate reducers and microbes potentially involved in Mn/Fe cycling suggest that these processes may be responsible for driving an increase in *p*H above the firmground. SR produces carbonate alkalinity, theoretically favouring carbonate precipitation (Loyd and Berelson, 2016). However, SR also produces H_2S which freely dissociates under normal porewater pH, typically lowering the *p*H to ~6.9 (Higgins *et al*., 2009). Carbonate precipitation is only favoured if excess H_2S is efficiently removed from solution by iron-sulphide (pyrite) formation which increases *p*H and carbonate supersaturation (Ben-Yaakov, 1973). The presence of pyrite framboids within the firmgrounds suggests this mechanism for the removal of H_2S is active within the QLTC sediments.

5.5.2.3 Microbial metabolisms below 10 cm

Microbial samples were not obtained below the firmground at Site B, however porewaters appear sulphate depleted and the porewater sample at 15 cm has the only significant concentration of CH_4 of all QLTC sites (Fig. 5.10.C). This suggests that SR is likely an important process below the firmground along with possible localised AOM, like in Yas Lagoon. Such processes likely contribute to promoting the precipitation of aragonite on the underside of the firmground by increasing *p*H (although H was not measured below the firmground at Site B) and by producing alkalinity.

At Site A, *Actinobacteria* increased with depth from 14-16 cm which is concurrent with the change in sediment colour at ~15 cm and a reduction in the abundance of aragonite (Fig. 5.3.A, B). Around this depth there are also peaks in the relative abundance of archaea *Thaumarchaeota* Group C3 (12-14 cm) and bacterial groups *Spirochaetae* (12-14 cm) and *Aminicentantes* (16-18 cm). *Aminicenantes* have not been isolated in pure culture, however a near complete genome of one member suggests it is an anaerobic organotroph, capable of utilising nitrate for fermenting carbohydrates and proteinaceous material (Kadnikov *et al*., 2019). At Site A *Aminicenantes* have a relative abundance >8% which represents an unusually large proportion of the community. Farag et al. (2014) analysed >1000 environmental 16 SSU datasets, of which *Aminicenantes* were present in ~30%, though with a low mean relative abundance (0.20%) and rarely exceeding 5%. They are typically most abundant in highly stressed environments such as hydrocarbon-impacted environments and hydrothermal vents (Farag *et al*., 2014; Kadnikov *et al*., 2019). This suggest that the deeper sediment (below ~15 cm) represents a more stressed environment with potentially less competition from other microbial communities.

Below ~16 cm the relative abundance of MBG-D continues to decline (after peaking in abundance at 16% at 4 cm) and *Woesearchaeota* are negligible (<1%). In contrast the relative abundance of Bathyarchaeota is <2% above 8 cm but increases with depth to remain fairly stable between 20-32cm

(av.=37.6 ±2.6%). *Bathyarchaeota* were also highly abundant (>10%) below 12 cm in Yas Lagoon and have been suggested to have the genetic potential for SR (Evans *et al*., 2015; Zhang *et al*., 2016) as well as the potential to utilize diverse methyl compounds, including the potential for methylotrophic methanogenesis, although showed no evidence for AOM (Evans *et al*., 2015). *Bathyarchaeaota* are suggested to be involved in the degradation of recalcitrant OM (Wang *et al*., 2020) and a high relative abundance of compared to other archaea has been observed in low energy anoxic environments characterised by low rates of microbial respiration and deeper (≥10 cm) sulphate depletion (Kubo *et al*. 2012). Similarly, *Dehalococcoidia* (*Chloroflexi*) increased with depth to peak at 18-20 cm and correlate with NH_4^+ (R^2 0.79 $p<0.001$, n=11) suggesting their involvement in the degradation of recalcitrant organic matter (Wang *et al*., 2020).

5.5.3 Alternative drivers of firmground formation at QLTC

Alternatively, firmground formation surrounding QLTC may be primarily driven by abiotic hydrodynamic processes which drive cementation at, or near to, the sediment surface. Lithification may subsequently impact porewater chemistry by acting as a permeability barrier and changing subsurface flow dynamics. This may control the downward diffusion of dissolved species, limit the vertical extent of bioturbation by burrowing macrofauna, and impact the vertical zonation of different microbial communities (Fig. 5.14.B). In the upper ~7 cm at Sites A-D, porewater salinity predominantly lies within the range of creek salinities measured in 2017 and 2019 (Fig. 5.10.A) suggesting porewater chemistry above the firmgrounds (or in the upper ~7 cm) is largely controlled by the downward diffusion of ions and nutrients from the overlying seawater, which supports a wide diversity of microbial communities (Fig. 5.11, 5.12, 5.13). Below the firmgrounds, water chemistry may be impacted by the leakage of groundwater (Chapter 4), which may provide a less habitable environment for many species, proving an environmental niche suited to microbes involved in the decomposition of recalcitrant OM (e.g., *Bathyarcheaota*) or those associated with stressed environments (e.g. *Aminicenantes*).

Several abiotic processes may be important for driving firmground formation at QLTC; (i) the circulation of supersaturated seawater, controlled by hydrodynamic processes in the ITZ; (ii) the lateral flow of brines sourced from updip *via* tidal pumping; and (iii) changes in relative sea-level associated with the current marine transgressive phase. The circulation of seawater and/or porewaters within the subsurface sediment is also intimately linked to the sediment physical characteristics such as grain size, sorting, minerology, porosity, and permeability.

5.5.3.1 Abiotic drivers of cementation

Hardgrounds are most prevalent in tropical/sub-tropical shallow-water environments, where their formation is typically driven by bottom water carbonate supersaturation and seawater circulation (Christ *et al*., 2015 and references therein). At QLTC, this may result from tidal pumping and circulation which flushes supersaturated seawaters into the uppermost porous sediments, potentially promoting cementation (Shinn, 1969; Christ *et al*., 2012) and removing fine grained sediments, reducing sediment accumulation, and further enhancing porewater circulation (Christ *et al*., 2015). If cementation is driven by the downwards diffusion of supersaturated seawater, then the lower limit is reached when pore throats become occluded, and permeability is reduced, which typically occurs in the upper few centimetres in muddy sediments (Shinn, 1969) though may be deeper in sandy sediments such as those at QLTC.

Physical sediment characteristics controlling permeability and fluid flow may also be important for promoting abiotic cementation in the subsurface. If porewater circulation is an important driver of cementation, then sediments with a higher permeability would favour cementation. Permeability (the ability to circulate porewaters) is largely depended on grain size, sorting, and porosity, with a higher permeability in more coarse-grained sand-sized sediments and a lower permeability in finer-grained mud-dominated sediments (Forster *et al*., 2003; Bourg and Ajo-Franklin, 2017). Qualitative observations suggest the cemented firmground intervals consist of more coarse-grained sediment than that overlying and underlying the firmgrounds, with a higher abundance of bioclasts, specifically gastropods. This layer may represent a transgressive lag deposit, and thus may have been preferentially cemented when closer to the sediment surface, prior to burial.

However, if the circulation of supersaturated seawater were the primary diver of lithification, one would expect to see more cementation closer to the sediment surface at QLTC. One possibility is that cementation did occur when sediments were near the sediment surface prior to burial, and that processes promoting surface cementation have since ceased.

Additionally, refluxing brines from the up-dip intertidal and supratidal zones may drive lateral porewater pumping (McKenzie *et al*., 1980). The increased porosity and permeability of the coarser gastropod-rich layer may have promoted the lateral flow of evaporated brines and/or chemically different porewaters from the up-dip, which may favour cementation and thus firmground formation. Carbonate precipitation is largely dependent on the supply of carbonate ions to the crystal surfaces, which is depended on temperature, fluid chemistry, microbial metabolic activity, and flow intensity (which determines the rate of fluid exchange at the site of precipitation) (Given and Wilkinson, 1985). The inland porewaters have high salinity (below 5 cm), low alkalinity, and fairly low *p*h (Fig. 5.10.A). If the lateral flow of these chemically different waters were reaching QLTC through the subsurface, then

we would expect to see some evidence of this in the porewater profiles, which is not observed. Furthermore, if lateral flow were important for promoting lithification, this process would quickly become self-limiting as pores become occluded with cement, and thus refluxing brines are not expected to be an important driver of cementation at QLTC.

Hardgrounds and firmgrounds forming in Abu Dhabi's shallow marine environment have previously been associated with transgressive or regressive surfaces (Paul and Lokier, 2017; Ge *et al*., 2020a). Ge *et al*. (2020a) analysed firmground physical and chemical characteristics across a transect in Qantur Lagoon 5 km NE from QLTC. Here the transect started at the landward edge of the microbial mats and extended 3 km seaward, perpendicular to the coast through the middle and lower ITZ. Firmgrounds in the upper ITZ were thin, patchy, and shallow, interpreted to represent the most recent and incomplete stages of lithification (Ge *et al*., 2020a). Moving seaward, firmgrounds increased in depth, thickness, and cementation and were interpreted as lithified transgressive lag deposits which form under the influence of rising tides, with the zone of active cementation (and firmground formation) stepping landward over time due to the current marine transgressive phase (Ge *et al*., 2020a). However, authigenic crystals were also observed in association with EPS, suggesting that microbial metabolic processes may be important for driving early lithification. The study of firmgrounds surround QLTC would benefit from an investigation into firmground cementation in the wider intertidal study area to investigate weather subsurface firmgrounds becomes covered by increasing less sediment inland, and/or if surface firmgrounds are observed to be actively forming in the upper ITZ. Furthermore, future work investigating porewater chemistry and sediment microbiology surrounding the firmgrounds described by Ge *et al*. (2020a) may provide a valuable comparison to the sub-sites at QLTC.

5.5.3.2 Kinetic factors promoting aragonite precipitation at QLTC

Whilst thermodynamics (e.g., local mineral saturation state) is the first order control on carbonate precipitation or dissolution (Higgins *et al*., 2009), kinetic factors are also important as they may inhibit or accelerate reactions, determine reaction rates, and in some cases determine minerology (aragonite, HMC or calcite) (Burton and Walter, 1987). QLTC porewater properties such as high Mg/Ca ratios, sulphate concentrations, and temperature may favour aragonite precipitation over calcite (Sun *et al*., 2015). Additionally, reaction rates can vary considerably with changes in brine geochemistry (Crockford *et al*., 2014) and dissolution may become self-limiting as minor ions released during early stages of mineral dissolution may adsorb onto mineral surface, preventing further dissolution (Eisenlohr *et al*., 1999).

Pioneering work by Plummer *et al*. (1978) described carbonate dissolution/precipitation rates as a function of the surface activities of species H^+, Ca^{2+}, CO_3^{2-}, and HCO_3^-. However, in many circumstances dissolution results in localised concentration gradients such that species concentrations in the bulk

solution may not be the same as those at the mineral surface (Eisenlohr *et al*., 1999). Experimental evidence by Eisenhlohr *et al*. (1999) (and references therein) suggests calcium carbonate dissolution rates are inhibited with increasing solution volume (V) to mineral surface area ratio (A) (V/A). Natural minerals contain impurities such as aluminosilicate nano-complexes which are released from the calcite matrix during dissolution and become irreversibly adsorbed onto the crystal surface where they act as inhibitors (Eisenhlohr *et al*., 1999). Furthermore, it has been suggested that the porewater concentrations of trace ions such as Sr^{2+} may also act to inhibit dissolution owing to interactions with the trace element and the mineral surface (Crockford *et al*., 2014).

The high salinity (ionic strength) of the QLTC porewaters (~45-140‰) may impact carbonate dissolution rates. Finneran and Morse (2009) investigated calcite dissolution kinetics in saline waters (NaCl ionic strength ~2.2-5.0 m) and found that dissolution rates decreased with increasing ionic strength possibly due to complex and ion specific processes affecting hydration mechanisms on the calcite mineral surface. Calcite dissolution rates increased with increasing pCO_2 and temperature, but their relative influences diminished at high ionic strength, however Finneran and Morse did not investigate if these effects may be similar for aragonite dissolution rates. In contrast, under experimental conditions (salinity 5-44‰), Zhong and Mucci (1989) found salinity had no noticeable kinetic effect on calcite precipitation rates, and a slight effect on the reaction rate of aragonite by causing precipitation rates to decrease when salinity increased from solutions with low (5-25‰) to the high (35-44‰) salinity ranges. However, this may be due to the comparatively low range of salinities analysed (which only encompasses the upper ~5 cm of the QLTC porewaters).

Variable calcite and aragonite precipitation rates over different seawater salinities (but at identical SI) are most likely due the kinetic effects of Mg/Ca, temperature, and pCO_2 (Zhong and Mucci, 1989). Increased porewater Mg/Ca molar ratios can lower the rate of/inhibit calcite precipitation (Zhang and Dave 2000) in favour aragonite precipitation (Folk, 1974; Pederson *et al*., 2019). In Mg^{2+} rich environments, calcite crystal growth can be inhibited as Mg^{2+} is incorporated in the crystal lattice it becomes absorbed on the calcite crystal surface, which reduces the thermodynamic stability (Berner 1975; Davies *et al*., 2000). However, this has a negligible effect on aragonite solubility (Bots *et al*., 2011), hence at typical ocean *p*H levels and at temperatures of 25°C and 40°C, Mg/Ca ratios >1 and >0.5 respectively favoured aragonite over calcite (Morse *et al*., 1997; Niedermayr *et al*., 2013) whereas other authors suggest a Mg/Ca ratio of 4 is required to induce aragonite precipitation over calcite (Mann *et al*., 1990). QLTC porewater Mg/Ca molar ratios range from 4.7-6.2, well above the threshold to favour aragonite. Furthermore, sulphate can act to inhibit calcite in favour of aragonite (Bots *et al*., 2011) as high sulphate concentrations can lower the Mg/Ca threshold required to destabilise calcite in favour of aragonite, e.g. at 10 mM SO_4^{2-} a Mg/Ca ratio of 0.9 favours aragonite over calcite (Bots *et al*., 2011). The precipitation rates of aragonite over calcite also increase with temperature (Burton and

Walter, 1987) which may cause a temporal variation in aragonite precipitation at QLTC, though this warrants further investigation (Chapter 6).

5.5.4 Limitations and future directions

Whilst this study contributes to the limited literature investigating potential microbial drivers of modern firmground formation, the level of research presented is insufficient to conclusively determine which physical, chemical, and/or biological processes are the primary drivers of cementation. However, it does provide evidence for an alternative hypothesis to the classic view that these features represent abiotic cementation in relation to hydrodynamic processes. Furthermore, this study highlights some key areas for future research that would aid in determining if microbial processes are responsible for driving subsurface cementation in Qantur Lagoon. Resampling of *in situ* porewaters from Sites A and B would be particularly helpful to ascertain if firmgrounds are actively forming at these sites. Only having porewaters from the core at Site A negates an accurate assessment of mineral SI. Similarly, *p*H was not obtained for samples below the firmground at Site B, which may indicate if similar processes are driving cementation as in Yas Lagoon.

Furthermore, a wider investigation into the spatial extent of firmground in the ITZ would also be valuable. Ge *et al*. (2020a) describe actively forming firmgrounds elsewhere in Qantur lagoon, but do not provide accompanying porewater or 16S SSU rRNA gene sequencing data. Applying methods for the porewater and microbial analysis detailed here for some of the firmgrounds detailed in Ge *et al*. (2020a) would be a logical step forward to further our understanding of physical, chemical, and biological drivers of cementation in coastal Abu Dhabi. Further investigation into the potential role that EPS plays in initiating subsurface lithification would also be valuable as EPS was observed in Yas lagoon, QLTC firmgrounds, and firmgrounds described by Ge *et al*. (2020a) in association with carbonate and pyrite minerals. Additionally, applications of some of the geochemical methods employed by Ge *et al*. (2020a) (Ramen microscopy, combined EDS and microprobe) to the firmgrounds and sediments at QLTC would be beneficial.

Analysis of firmground cement isotope chemistry would provide valuable clues as to potential drivers of cementation. Geochemical fingerprinting of SR and AOM can be detected *via* characteristic $\delta^{13}C$ signatures. Whilst many authigenic carbonates have light carbon isotopic signatures, reflecting carbon sourced from the microbially mediated decomposition of organic matter (Raiswell and Fisher, 2004), values span a very large range from <-50‰ to +3‰ $\delta^{13}C$ (Mavromatis *et al*., 2014; Mozley and Burns, 1993). The lowest values are associated with the incorporation of CH_4 from AOM (Mavromatis *et al*., 2014), mid-range (~-25‰) values are derived from organic-derived carbon (e.g., SR) (Irwin *et al*., 1977), and the heavier values reflecting addition of skeletal material, seawater carbonate, or residual carbonate produced *via* methanogenesis (Claypool and Kaplan, 1974; Botz *et al*., 1996; Sharp, 2017).

Secondary ion mass spectrometry (SIMS) would provide targeted analysis of cement isotopic signature and may help distinguish between carbonate cements forming *via* microbial processes with those that form *via* abiotic cementation, that would produce cements in approximate equilibrium with seawater ($\delta^{13}C$ +2‰ to +4‰) (Sharp, 2007).

Questions raised regarding the capabilities of PHREEQC and CO2SYS to accurately model carbonate saturation indices at such high ionic strengths (detailed in Chapter 2) also have important implication for this study. The observation of well-defined aragonite needles and platy crystals is at odds with apparently undersaturated porewaters with respect to aragonite; suggesting that these models may be unable to capture the true complexity of ion pairings in such saline and/or reducing conditions, and future work investigating the true nature of mineral saturation at QLTC would be valuable. Alternatively, field work undertaken in winter may not capture the true variability of porewater chemistry experienced throughout the year. If possible, future field campaigns in summer would provide an interesting comparison to the porewaters presented here (collected in winter) and would help ascertain whether there is a seasonality to firmground formation.

5.5.5 Wider implications

Ancient hardgrounds are often used as stratigraphic indicators as they are assumed to form at the sediment-water interface via abiotic process relating to hiatuses in sedimentation and/or changes in sea level (Christ *et al*., 2015). However, we suggest that processes within the sediment column may be driving early cementation of subsurface firmgrounds at QLTC, which may continue to cement over time becoming concretionary sub-hardgrounds (Ge et al., 2020a). Such features may contribute to the discussion surrounding shallow water limestone-marl alterations (Munnecke et al., 2001) which are assumed to be related to cyclic sedimentation associated with Milankovitch cycles, however processes within the present-day Abu Dhabi sediments provide an alternate hypothesis to the formation of similar features. Similarly, sub-hardgrounds may be erroneously identified as hiatal surfaces, and thus researchers should consider both abiotic and microbially driven models of firmground/hardground cementation before utilising hardgrounds as stratigraphic indicators.

Processes that produce layering within the sediment are important for understanding fluid flow. Observations of two early cemented horizons at Site A suggest that two firmgrounds may be forming synchronously at this site, and therefore similar processes may have formed the presumably older, double fimrground at Site D, and possibly the basal hardground below. If both cemented layers form synchronously, then their formation may alter fluid flow characteristics as increased cementation alters the sediments permeability. Progressive cementation of the upper firmground may eventually limit the downwards supply of ions from seawater, whilst the cementation of the lower firmground may limit the supply of ions via the upwards leakage of groundwaters from below. This may cause

cementation to eventually become self-limiting, resulting in the small amount of sediment in between the two cemented horizons remaining unlithified.

Understanding how early diagenesis contributes to permeability layering and anisotropy and the impacts this has on subsurface flow in the ITZ has implications for the effective utilisation of both groundwater and hydrocarbon resources (Agar and Geiger, 2015). Reactive transport models have been increasingly applied to understand and predict changes in depositional properties that result from early diagenesis and infer reservoir properties (Whitaker and Frazer, 2018), however such process-based models require assessment with reference to hydrological and biogeochemical data from modern environments such as Qantur Lagoon.

5.6 Conclusions

This study provides insights into the potential drivers for (sub)surface cementation in coastal Abu Dhabi. The firmgrounds documented at QLTC exemplify the highly complex nature of diagenesis in this dynamic depositional environment. The ITZ is exposed to high frequency, low-amplitude sea level variability over a range of spaciotemporal scales which may promote the precipitation of aragonite cements near the surface. Alternatively subsurface cementation may be promoted *via* metabolic processes involving the cycling of sulphate and metal oxides. We acknowledge the data presented is often incomplete, and likely fails to capture the true complexity of firmground formation in this dynamic environment. Nevertheless, we provide evidence to suggest that abiotic cementation at the surface and subsequent burial may not be an adequate mechanistic model of firmground formation at QLTC. Instead, we offer an alternative hypothesis and highlight the potential involvement of microbial processes in driving firmground formation with the following conclusions:

1. Whilst no firmground was detected at Site A, cemented intervals within the gastropod rich layer suggest that subsurface cementation may result in a firmground forming here in the future. However, potential issues of degassing during porewater extraction prevent corroboration with porewater carbonate chemistry.
2. The observation of two separate layers of early cementation at Site A may be the precursor to the double layer firmground at Site D and may suggest that both layers formed synchronously *via* different microbial metabolic processes.
3. Site B was the only sub-site at QLTC to show evidence of active cementation similar to that observed in Yas Lagoon, with decreasing alkalinity towards the upper firmground surface interpreted to represent the removal of CO_3^{2-} ions by $CaCO_3$ precipitation.
4. Sites C and D show no evidence of active cementation, suggesting that firmgrounds at these sites may be older and no longer actively forming.

5. A ‘Yas Lagoon’ model of firmground formation at QLTC would point to the primary diver of lithification being subsurface microbial process which specifically increase *p*H rather than just increasing DIC.
6. Lithification would thus be focussed at the redox boundary and may be linked to microbial respiratory processes involved in SR and Fe/Mn-oxide reduction. The formation of pyrite framboids within the firmgrounds provides a pathway for the effective removal of H_2S (by-product of SR), producing a chemical environment favourable to carbonate precipitation.
7. The surface 0-2 cm hosts a range of microbial communities typically associated with microbial mats that can produce EPS which provides a source of organic matter to the heterotrophic microbes within the sediment column.
8. Below ~15 cm there is an increase in communities associated with stressed environments and recalcitrant organic matter. This may be linked to the firmground which acts as a permeability barrier causing porewater chemistries below this depth to be more impacted by the leakage of continental brines than the downward diffusion of seawater.
9. However, limitations with data sets, and/or incomplete data sets for the sub-sites mean it is not possible to definitively determine if metabolic processes are the primary driver of cementation at QLTC.
10. Alternatively, the circulation of supersaturated seawater (relating to hydrodynamics controlled by the present marine transgressive phase) may have resulted in cementation at, or near to, the sediment surface which would suggest processes driving cementation may have since ceased at the QLTC sub-sites.

6. Temporal variability in authigenic carbonate diagenesis

i. Authors

Hazel Vallack[1], Gordon Coy[2], Sarah E. Greene[3], Stephen W. Lokier[4], Chai Pei Teoh[4], Fiona Whitaker[5]

1: School of Geographical Sciences, University of Bristol
2: Karachaganak Petroleum Operating PB, Kazakhstan
3: School of Geography, Earth and Environmental Sciences, University of Birmingham
4: School of Ocean Sciences, Bangor University
5: Department of Geology and Geophysics, Texas AandM University
6: School of Earth Sciences, University of Bristol

ii. Author contributions

Writing, porewater analysis, data analysis, modelling, and interpretations were performed by H. Vallack with interpretive support from S. Greene and F. Whitaker; sedimentary analysis (XRD and grains grain size analysis) were performed by C. Teoh at Texas AandM University. Field work, sampling of sediment and porewaters and analysis of porewater pH, alkalinity, Eh, and SEC was conducted by H. Vallack, S. Greene, S. Lokier, F. Whitaker and G. Coy.

iii. Abstract

The formation and burial of marine calcium carbonate accounts for ~80% of total carbon removal from Earth's surface and ~10% of global modern marine carbonates are precipitated authigenically. Whilst thermodynamics (e.g., local mineral saturation state) is the first order control on carbonate precipitation or dissolution, kinetic factors are also important as they may inhibit or accelerate reactions, determine reaction rates, and in some cases determine minerology. Temperature influences both the thermodynamics and kinetics of carbonate precipitation and has been identified as a driver of carbonate precipitation in subtropical seas (whitings) and is both directly and indirectly linked to seasonal carbonate precipitation and dissolution within temperate marine sediments. However, we do not understand how seasonal temperature variability affects shallow water carbonate diagenesis in subtropical carbonate platforms, where fieldwork is typically biased to cooler months. This Chapter aims to investigate if temperature thermodynamically promotes seasonally oscillating periods of carbonate precipitation and dissolution in an intertidal carbonate platform in coastal Abu Dhabi. The thermodynamic model PHREEQC is applied to model *in situ* porewater chemistries collected in winter at *in situ* sediment temperatures measured with subsurface temperature loggers in both winter and summer periods. Whilst thermodynamic predictions do not provide conclusive evidence of precipitation/dissolution, results suggest that carbonate precipitation is favoured in the upper ~20 cm of sediment in the lower intertidal zone in summer. This depth corresponds with the depth of

subsurface firmgrounds identified elsewhere in the lower intertidal zone and suggests a summer cyclicity to subsurface cementation.

6.1 Introduction

Marine carbonate sediments represent arguably the most important archives of Earth's climate and the evolution of the biosphere. Whilst most marine carbonate sediments are comprised of skeletally-derived calcium carbonate ($CaCO_3$), the warm saline waters of some shallow (sub)tropical seas can precipitate $CaCO_3$ crystals directly from seawater, forming non-skeletal carbonates such as carbonate mud (micrite) and ooids (Perkis *et al*., 2017; Harris *et al*., 2019). Carbonate sediments can also form *in situ* during sedimentation *via* precipitation and/or recrystallization (authigenesis) through both abiotic and microbially mediated processes (Schrag *et al*., 2103; Dupraz *et al*., 2009).

Marine diagenesis is widespread and abundant in modern and ancient settings, and ranges from the precipitation of pore-lining cements and concretionary features (e.g., firmgrounds, hardgrounds, beachrock, and concretions), to microporosity development and dolomitisation (Ahm *et al*., 2018; Ge *et al*., 2020). The spatial variability in the dissolution and precipitation of $CaCO_3$ is governed by the sedimentation rate (Arndt *et al*., 2013), flux of organic matter to the sediment-water interface (Arndt *et al*., 2013), bottom water redox conditions (Higgins *et al*., 2009), the dissolved inorganic carbon (DIC) reservoir, the solubility of carbonate minerals, and the strength of metabolisms involved in the microbially mediated degradation of organic matter (OM) (Schultz and Zabel, 2000; Bergmann *et al*., 2013), and many of these variables are indirectly or directly linked to temperature.

Local mineral saturation state is the first order control on carbonate precipitation or dissolution (Higgins *et al*., 2009), with kinetic factors determining reaction rate. The saturation state can be described by the ratio between the ion activity product and the solubility product for a given mineral and is often expressed on a logarithmic scale called the saturation index (SI) (Appelo and Postman, 1993) and is defined by the equation:

$$IAP = (\gamma Ca^{2})(\gamma CO_3^{2-})$$

$$K_{sp(CaCO3)} = [CO_3^{2-}]_{sat}[Ca^{2+}]_{sat}$$

$$SI = \log(IAP/K_{sp})$$

Where IAP = ion activity product, γCa^{2+} and γCO_3^{2-} are the behaviours of Ca^{2+} and CO_3^{2-} in seawater (*in-situ* concentrations) (Garrels *et al*. 1961; Barker and Ridgwell, 2012) and K_{sp} is a constant for the thermodynamic solubility of calcite at a given temperature, pressure, and salinity. Surface oceans are supersaturated with respect to both calcite and aragonite, though their solubilities increase with

decreasing temperature and increasing pressure (depth). When the solution is at equilibrium for a given carbonate mineral SI = 0, with positive values denoting supersaturation, favouring precipitation and negative values indicating undersaturation, favouring dissolution. Porewater chemistries become modified by microbial respiratory processes (Bergmann *et al*., 2013; Soetaert *et al*., 2007) which may promote carbonate precipitation (e.g., sulphate reduction in conjunction with pyrite formation or the anaerobic oxidation of methane (AOM)) or dissolution (e.g., aerobic respiration, iron (Fe) and manganese (Mn) oxidation) (Soetaert *et al*., 2007).

The predominance of metastable aragonite precipitation over the more-stable calcite phase has been a long-standing observation in marine environments, dubbed the 'calcite-aragonite problem' (Sun *et al*., 2015). Many different (though often interrelated) variable such as a solutions mineral saturation, temperature, *p*H, ionic composition (e.g., Mg and Sr) (Zhang and Dave 2000; Crockford *et al*., 2014), and the effects of microbial metabolisms (Soetaert *et al*., 2007) can inhibit or accelerate reactions, determine reaction rates, and impact the mineralogy of authigenic carbonate formation (Burton and Walter, 1987; Jones, 2017; Sun *et al*., 2015). Even though a reaction is thermodynamically favourable, reactions may not proceed if they are kinetically unfavourable. Whilst temperature is a key thermodynamic control on carbonate precipitation, it has also been identified as a key kinetic factor impacting the polymorphism of carbonate minerals (Burton and Walter, 1987) and driving the replacement of carbonate minerals by more stable polymorphs (Perdikouri *et al*., 2013; Milano and Nehrke, 2018).

Prior work has identified a seasonal cyclicity to the precipitation of aragonitic lime mud (whitings) in the Bahamas (Purkis *et al*., 2017), where the subtle seasonal (winter) environmental forcing is enough to increase the rate of production of lime mud by 70% in winter compared to summer. Whitings initiated within mixing fronts atop the Great Bahamans Bank when the temperature gradient exceeded 1 °C (Purkis *et al*., 2017). Furthermore, multi-annual cyclicity doubled the rate of lime mud production (2011-2019 compared to 2003-2010), coincident with a 10 cm sea level rise and a 1 °C warming of the Florida current (Purkis *et al*., 2017). Thus, the lime mud carbonate factory in the Bahamas is exceedingly sensitive to subtle environmental forcings. Similarly, temperature has been identified as a seasonal driver of diagenesis in marine sediments. Prior work in terrigenous muddy near-shore sediments in temperate locations has identified seasonal variations in carbonate mineral saturation state (and thus carbonate dissolution and precipitation) resulting from changes in temperature and primary productivity (Green and Aller, 1998). In late spring, porewater carbonate supersaturation was driven by increased dissolved inorganic carbon (DIC) production driven by higher temperatures and an increased supply of organic matter (OM) to subsurface heterotrophic microbial communities (Green and Aller, 1998). In contrast, during winter periods, porewaters were undersaturated with respect to calcite and aragonite, owing to lower rates of heterotrophic metabolisms (lower DIC production) and

the oxidation of reduced species (e.g., iron sulphides (FeS)) (Green and Aller, 1998). However, we do not understand how seasonal temperature variability affects shallow water carbonate diagenesis in the intertidal zone of subtropical carbonate platforms.

The intertidal zone (ITZ) is a highly dynamic environment that typically receives significant inputs of terrestrially derived nutrients and allochthonous carbon, which drives *in situ* primary production providing important areas for nutrient cycling (Billerbeck *et al*., 2006) and carbon storage (Bianchi, 2007; Lee *et al*., 2011; Mcleod *et al*., 2011). Despite covering <2% of the total ocean area, coastal habitats (mangroves, tidal flats, and seagrasses) account for ~50% of the total carbon sequestered in ocean sediments (Duarte *et al*., 2005), with microphytobenthos (MPB) inhabiting the sediment surface accounting for >50% of total primary productivity in coastal ecosystems (Cahoon, 1999).

In situ sediment temperature has been identified as the main driver for temporal (seasonal and diurnal) variations in benthic metabolisms within ITZs (Hanke and Glud, 2004; Hubas *et al*., 2006; Lee *et al*., 2011). MPB activity is predominantly driven by light (Parsons *et al*., 1984), however, factors such as temperature, erosion, nutrient availability, and sediment dynamics, and bioturbation also impact productivity (Hubas *et al*., 2006, and references therein). In temperate fine-sand intertidal sediments (France), bacterial activity contributed up to 88% of benthic community respiration (BCR) (compared to macro- and meio-faunal respiration), and both gross primary production and BCR were most influenced by temperature (Hubas *et al*., 2006). Sub(tropical) areas experience high light fluxes and relatively warm temperature year-round which should produce high rates of annual primary production. Nonetheless, Lee *et al*. (2011) found that in sub-tropical ITZ sand flats, maximum community primary production and BCR rates were highest in summer and lowest in winter and were positively correlated with air temperature.

The production of skeletal and non-skeletal $CaCO_3$ and the early modification (diagenesis) of $CaCO_3$ sediments produces 'carbonate factories', and carbonate platforms, typically in warm (sub)tropical low latitude shallow-water carbonate settings such as the Present-day Florida Bay, Bahama Banks, and Persian/Arabian Gulf. Such areas provide principal sites of preserved carbonate in the geologic record (Kiessling *et al*., 2003) and provide analogous to globally important carbonate reservoirs (Alsharham and Kendall, 2003). Whilst recent work has highlighted the important role that temperature can play in the production of non-skeletal $CaCO_3$ (e.g., in the Bahamas) (Purkis *et al*., 2017), we do not understand what impact temperature has on subsurface carbonate sediment diagenesis in similar environments. Most carbonate platforms are in hot climates, where fieldwork is biased towards cooler months meaning many field studies may fail to capture temporal variations in diagenesis. Evidence from temperate environments (e.g., Green and Aller, 1998) suggests there are three main ways temperature may drive carbonate precipitation/dissolution by altering mineral SI: (i) by altering carbonate mineral thermodynamics, (ii) by directly increasing the rates of microbial respiratory

processes (for autotrophs and heterotrophs) and by (iii) indirectly increasing heterotrophic metabolic rates by increasing the supply of OM from surface dwelling MPB. When heterotrophic metabolic activity rates are low, the oxidation of reduced minerals (e.g., FeS) may also contribute to decreasing mineral SI. This study aims the investigate how sediment *in situ* temperature varies on seasonal timescales at two sites in the intertidal zone (ITZ) of coastal Abu Dhabi (UAE), and to investigate the potential role this may have on carbonate mineral saturation, and thus on driving subsurface carbonate precipitation and dissolution. Whilst thermodynamic predictions do not provide evidence that dissolution or precipitation will occur, they suggest whether chemical conditions would promote such reactions.

The Abu Dhabi coast provides one of the best and most accessible modern examples of coastal sabkha (salt flat) environments and acts as a rare recent analogue of ancient epeiric settings (Lokier *et al*., 2015; Lokier and Fiorini, 2016). Ancient epeiric shelf successions are common in the sedimentary record and provide globally important areas of carbonate sediment deposits (Bádenas and Aurell, 2008). The Abu Dhabi coast is an area of active carbonate sediment production, alteration, redistribution, and accumulation (Kenig *et al*., 1990; Alsharhan and Kendall, 2003). Recent work (Ge *et al*., 2002a; Chapter 3 and 5) has identified aragonitic firmgrounds in the shallow subsurface (~0-20 cm below the sediment surface), presumed to be actively forming, but forming in predominantly aragonite undersaturated porewaters. An alternative explanation for this contradiction is that field work undertaken in winter may not capture the true variability of porewater chemistry experienced throughout the year. In warmer months, porewaters may become supersaturated with respect to aragonite at certain depths due to the combined effect of biogeochemical activities and increased *in situ* temperatures.

Here we test the hypothesis that increased *in situ* sediment temperature in summer may promote subsurface carbonate precipitation at specific depths (likely linked to microbial respiratory processes) by increasing carbonate mineral SI. This hypothesis is tested by using a 1D reaction transport model (PHREEQC) (Parkhurst and Appelo, 2013) to model shallow porewater chemistry profiles (~30 cm) (samples collected in winter) over a range of annual *in situ* temperatures measured with subsurface loggers (*in situ* for 1.25 years), with a focus on comparing a winter and summer period.

If subsurface authigenic carbonate formation is likely to be favoured in summer compared to winter months, this may have implications for understanding the global carbon cycle in the past. Authigenic carbonates account for ~10% of global modern marine carbonate deposits (Sun and Turchyn, 2014). However, in the past, authigenic carbonate deposits played an even larger role in the global carbon cycle, particularly during periods of widespread marine anoxia (Higgins *et al*., 2009) when they would have been a substantial carbon sink (Schrag *et al*., 2013). During the Phanerozoic, the spatial extent

and palaeogeographical distribution of carbonate platforms varied substantially due to plate tectonics, climate change, evolution of carbonate platform biota, and secular changes in ocean chemistry (Kiessling *et al*., 2003). Kiessling *et al*. (2003) speculate that plate tectonics reduced the tropical shelf areas in the icehouse tropics which forced carbonate-secreting organisms to higher latitudes where extensive carbonate platforms could develop. Higher latitudes experience a high seasonal temperature variability. If carbonate precipitation was thermodynamically favoured during summer months, but dissolution limited in winter (e.g., by kinetic inhibitors), then there may have been a net increase in authigenic carbonate formation, providing a potentially significant global carbon sink.

Furthermore, authigenic carbonate features such as hardgrounds have been identified as potential archives for reconstructing ancient seawater chemistries from trace elements concentrations and isotopic ratios (Erhardt *et al*., 2020), however it has been suggested that the temperature during precipitation and rate of mineral precipitation affects the distribution coefficient of trace elements into carbonate matrix (Lorens 1981) and that temperature may also cause carbonate oxygen isotopic ratios to vary (Swart, 2015). Therefore, understanding formation temperatures is important for accurate interpretation of these proxies. Clumped isotopes (Δ_{47}) are increasingly being applied to determine formation temperatures of carbonates, however in many cases the predicted temperatures are assumed to reflect mean annual temperatures. The Δ_{47} signature of palaeosol carbonates and biogenic carbonate have demonstrated a seasonal cyclicity to carbonate precipitation (Ghosh *et al*., 2006; Peters *et al*., 2013; Kelson *et al*., 2020), though seasonality is rarely considered when assessing chemical archives in shallow-water carbonate settings.

6.2 Depositional and regional climate of the study area

The shoreline of coastal Abu Dhabi of the United Arab Emirates (UAE) trends in a northeast to southwest direction and is protected from the open marine conditions of the Gulf by several barrier islands. The coastal area is an extremely low ramp environment (0.4m/km) which progresses offshore from a supratidal evaporite sabkha, through a laterally extensive intertidal zone (ITZ) into a carbonate-dominated subtidal environment (Evans *et al*., 1964; 1969). Coastal Abu Dhabi experiences a semi-diurnal micro-tidal regime (amplitude 1 - 2 m) (Paul and Lokier, 2017) and the dominant north-westerly Shamal wind can produce gale force winds and storm surges (Lokier and Steuber, 2009). The shallow Gulf has high salinities (45‰ – 46‰) relative to the nearby Indian Ocean (Lokier and Steuber, 2009) and high Mg/Ca ratios (Wood *et al*., 2002; Rivers *et al*., 2019) owing to high evaporation and relative restriction.

The UAE experiences an extremely arid climate, with mean annual rainfall of 72 mm, the majority of which falls in short-lived torrential rainstorms, typically between February and March (Raafat, 2007). Diurnal variations in air temperature are 2-26 °C and summer daytime temperatures exceed 50 °C,

while winter nights reach lows of 7 °C (Lokier and Fiorini, 2016). Solar insolation is high, but evaporation is limited by the humidity (Lokier and Steuber, 2009), giving a potential evaporation up to twice the annual rainfall (Bottomley, 1996). However actual evaporation measured in the sabkha (Sanford and Wood, 2001) is comparable to rainfall at 0.24 mm/day in September and March. Seawater temperature in the gulf is significantly higher in summer compared to winter, however more evaporation occurs in winter owing to higher wind speeds (Reynolds *et al*., 1983).

The spatial distribution of surface facies across the ITZ is controlled by duration of tidal flooding, dependent on the local slope angle (Court *et al*., 2017). The shallow sub-tidal sediments predominantly consist of fine to medium-grained carbonates with abundant skeletal grains in the bioturbated lower-intertidal sediments, which continue to be an area of active carbonate precipitation and sedimentation (Evans *et al*., 1964; Lokier *et al*., 2013; Lokier and Fiorini, 2016). The bioturbated intertidal sediment are typically poorly sorted, locally well-sorted and silt-dominated, whereas sediments underlaying the microbial mats in the middle to upper intertidal zones are fine-grained and well-sorted with abundant silt-grade material (Lokier *et al*., 2013). The abundance of evaporites (e.g., anhydrite, gypsum, and halite) increases inland moving from the upper intertidal and supratidal zones (Lokier *et al*., 2013).

This study combines sediment and water chemical analysis (collected in winter 2019 and representing a single period in time) from two contrasting sites in the middle and upper ITZ in Qantur Lagoon, Abu Dhabi, with *in situ* sediment temperature recorded at both sites for over one year (Fig. 6.1). Sites were selected that did not have subsurface firmgrounds that may alter the thermal conductivity of the sediment. Parts of the ITZ with thick, laminated microbial mats were also excluded due to the potential impact of their dark colour on surface albedo. Site 1 is located ~50 m seaward of the dark coloured microbial mats at the boundary between lower and middle ITZ and is flooded ~15% of the time (Fig. 6.1.C-E). Seaward of Site 1 sediments atop of the basal hardground thin offshore (Fig. 6.1.G).

Site 2 lies ~390 m inland in the upper intertidal zone at ~0.40 m elevation relative to Site 1, near the landward boundary of the pustular microbial mats (Court *et al*., 2017) and is flooded <2% of the time annually (Chapter 4). At Site 2 the sediment surface is covered in a relatively thin (0.1 – 1.6 cm thick) dark-brown pustular microbial mat which has a lower albedo compared to the light-coloured sandy sediments overlying Site 1 (Fig. 6.1.E, F). Previous work (Paul and Lokier, 2017) describes a diachronous hardground primarily composed of aragonitic bioclastic grains that is locally exposed in the lower ITZ and extends beneath the mid-intertidal lagoons and the supratidal sabkha and underlies Sites 1 and 2 at depths of ~33 cm and ~50 cm respectively (Chapter 4) (Fig. 6.1.G). Site 1 provides an analogue to the sites discussed at Qantur Lagoon Tidal Creek (QLTC) (Chapter 5), which are also within the ITZ, seaward of the microbial mats, and with ~30 cm of sediments overlying the basal hardground. The key differences between QLTC and Site 1, is that Site 1 is not close to a creek network, nor does it have (or

is yet to develop), a firmground. Whilst understanding the reasons for the lack of firmground at Site 1 was not the primary focus of the present study, we speculate that the local position within the Qantur Lagoon area may mean that sediment overlying the basal hardground at Site 1 may have been deposited more recently and/or may be more mobile. In the winter sampling period, porewaters immediately above the basal hardground felt noticeably warmer and the groundwaters collected from boreholes ranged in temperature from 29.9-32.1 °C (Chapter 4).

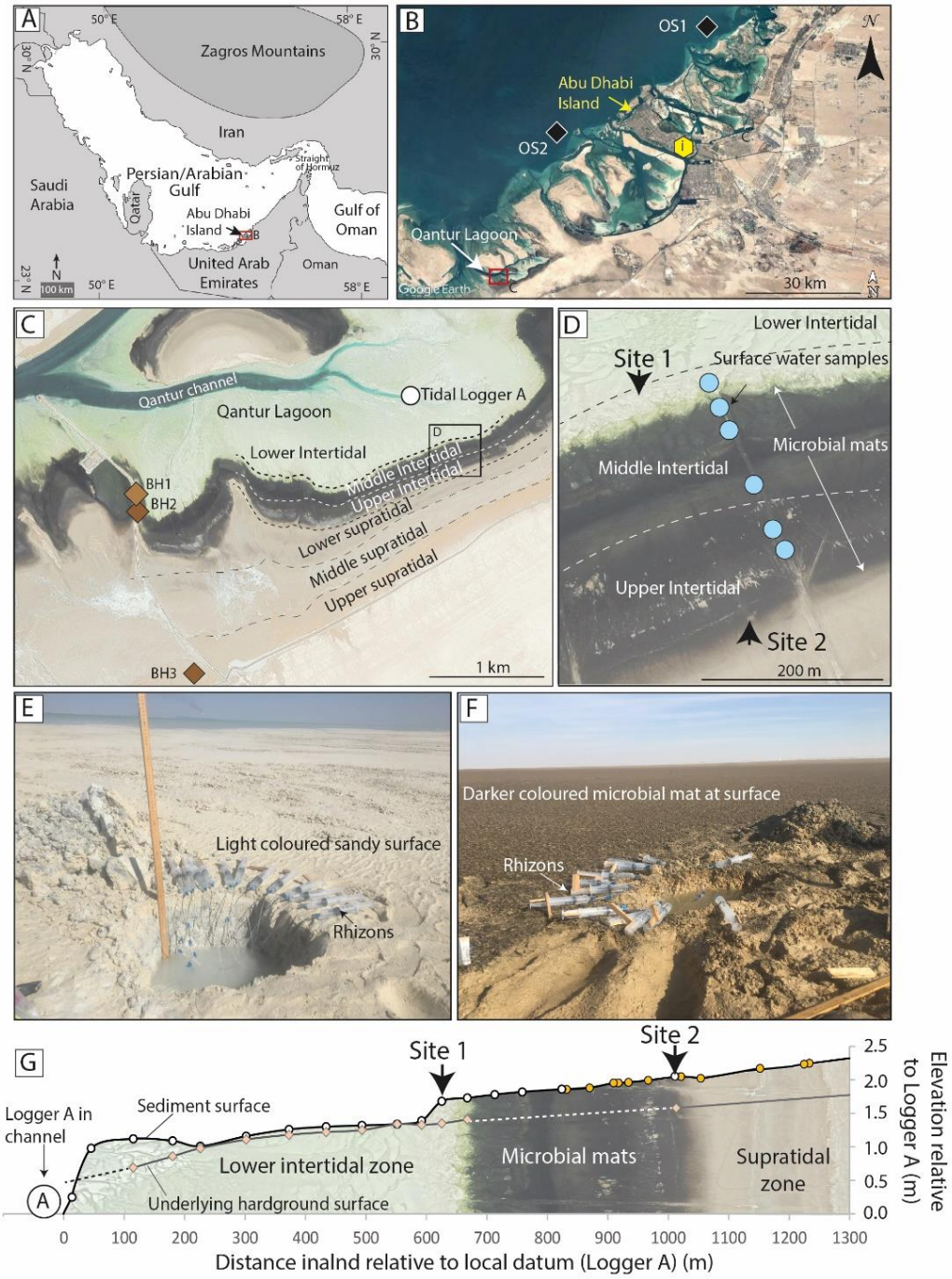

Figure 6.1. (**A**) Regional location of Abu Dhabi (adapted from Lokier *et al*. (2013)); (**B**) Coastal Abu Dhabi highlighting locations of offshore seawater samples (OS1 and OS2) (black diamonds), Abu Dhabi Bateen airport (i) and Qantur Lagoon study area (red box). (**C**) The study area surrounding Qantur lagoon, highlighting the location of Logger A, Boreholes 1, 2 and 3, and intertidal/supratidal zones (Chapter 4);

(**D**) Close-up of the lower to middle intertidal zones showing the location of Site 1, Site 2, and surface water samples (blue circles) collected Jan. 2019. (**E**) Photograph of the pit at Site 1 showing orange staining and dark mottles patches in the sandy sediments; and (**F**) photograph of Site 2 showing a pustular microbial mat surface morphology. Both (**E**) and (**F**) show porewater extraction from *in situ* sediments using Rhizon porewater samplers. (**G**) Locations and elevations of Site 1 and 2, and the depth of the underlying hardground relative to the local datum (Logger A). Topographic profile was constructed using the TidbiT temperature logger profile (white dots) and surface elevations from Court *et al*. (2017) (yellow points) (Chapter 4).

6.3 Methodology

6.3.1 Sediment sampling and analysis

Sediment cores were obtained from Site 1 (~33 cm long) and B (~36 cm long) using an 8 cm diameter PVC tubing. Cores were stored upright, with all samples kept in the dark at 4°C prior to subsampling (<3 days after collection). Cores were extruded, split longitudinally, and subsampled at 2 cm resolution under sterile conditions for grain size analysis and X-ray diffraction (XRD) (Site 1: n=16, Site 2: n=19) and depths are presented below the sediment surface. Grain size was determined on a Camsizer® P4 particle size and shape analyser following the methods of Andronico *et al*. (2009). Samples for XRD analyses were powdered using an agate mortar and pestle and analysed using a Rigaku Miniflex 6G using standard XRD techniques (Poppe *et al*., 2001). Quantification was done using the Relative Intensity Ratio method as described in Hubbard and Snyder (2013).

6.3.2 Porewater sampling and analysis

Porewater samples were collected at 2-4.5 cm vertical resolution from 0-33 cm at Site 1 (7th Jan. 2019) and from 5.5-47.5 cm at Site 2 (no porewater was recovered from the upper 0-5.5 cm at Site 2 as this was in the vadose zone) (6th Jan. 2019) (locations in Fig. 6.1.D). Porewaters were obtained from pits <30 cm away from the locations from which the cores were taken (Fig. 6.1.E, F) and extracted with Rhizon CSS pore-water samplers (pore diameter 0.12 μm - 0.18 μm, providing instant filtration) following the methods adapted from Dickens *et al.* (2007) but applied *in situ* (as described in Chapter 2.1). Samples were collected around a new moon and small spring tide (tidal range 1.65 m) on the 6th January 2019.

Offshore seawaters (collected Oct. 2017; Locations C and D, Fig. 6.1.B) and groundwaters from below the basal hardground from three boreholes (collected in Jan. 2019; Locations E, F and G, Fig. 6.1.C) were filtered through Rhizons following collection. Surface waters were collected using Rhizons as the flood tide progressed across a ~250 m transect in the middle to upper ITZ on the 7th of January 2019 (Blue circles in Fig. 6.1.D) over ~2 hours following a small spring tide on the 6th (also described as part of Site 3-QL in Chapter 4).

Porewaters were analysed within 12 hours of collection for *p*H, specific electric conductivity (SEC) and redox potential (Eh) using a HQ40d Hach multi-meter and probes, with accuracies of ±0.02 pH units, ±0.5%, and ±0.05% respectively. Bicarbonate alkalinity was determined in triplicate by Gran titration (Sass and Ben-Yaakov, 1977) using 0.0005 M or 0.001 M HCl acid with 0.6% coefficient of variance (CV). Aliquots were returned to the UK for analysis of major ions, methane (CH_4) concentrations, ammonium (NH_4), dissolved organic carbon (DOC) and dissolved total nitrogen (TN) following the methods described in Chapter 3.

6.3.3 Logger deployment

A suite of long-term TidbiT temperature loggers were deployed within the sediment, buried at depths of 5.5, 20, 28 and 39.5 cm at Site 1 and 3, 8, 18, 25, 39, and 45 cm Site 2 for 1 year and 3 months, from January 2019 to April 2020. Hourly air temperature records, weather records (air temperature, cloud cover, and heat index (combining temperature and relative humidity)) were obtained from Abu Dhabi Bateen airport (Location (i), Fig. 6.1.B) from ©WorldWeatherOnline (2021) from 2019-2020. Water level above the sediment surface at Sites 1 and 2 was calculated using a Long-term CTD-Diver Logger deployed in the tidal channel (Tidal Logger A (detailed in Chapter 4), deployed 5th Jan. 2019 – 19th Oct. 2020; Fig. 6.1.C) and the topography profile constructed with surface TidbiT temperature loggers, as discussed in Chapter 4. TidbiT temperature loggers were situated at the sediment surface of Site 1 (5th-6th January 2019) and at Site 2 (6th-8th January 2019), however they were not shielded from the sun and thus may have experienced a localised warming effect during daytime hours relative to the surrounding sediment.

6.3.4 Modelling

The partial pressure of CO_2 (pCO_2), carbonate (CO_3^{2-}) activity, and saturation indices (log(IAP/K_{sp})) of aragonite, calcite, dolomite, halite and gypsum (SI_{arag}, SI_{calc}, SI_{dol}, SI_{hal} and SI_{gyp}) were calculated using PHREEQC (Parkhurst and Appelo, 2013) with the Pitzer database (Pitzer, 1973; Pitzer and Mayorga, 1973) owing to the high salinity of the samples being modelling which preclude the application of many other models (Chapter 2.2). Uncertainties (presented in Table 6.1) do not include uncertainties within the model (e.g., constants) and were calculated as the total fractional error using the equation:

$$\sum fe = \sqrt{fe_1^2 + fe_2^2 + fe_3^2 + \cdots fe_n^2}$$

Table 6.1. Uncertainties in carbonate variable and saturation indices modelled with PHREEQC using the Pitzer database.

	pCO_2 (%)	CO_3^{2-} activity	SI_{arag}/SI_{calc}	$SI_{dol}/SI_{dolDiss}$	SI_{hal}	SI_{gyp}
PHREEQC-Pitzer	±0.019%	±0.023 log units	±0.019 log units	±0.038 log units	±0.008 log units	±0.007 log units

Water chemistries obtained in January 2019 were modelled at the *in situ* sediment temperatures recorded with a suite of TidbiT temperature loggers (±0.2 °C accuracy) during summer months (in 1 hour intervals) to determine what impact, if any, increased summer temperature may have on mineral SI. Temperature loggers were not installed during porewater sample collection in winter (6th-7th Jan. 2019), thus the water chemistry is adjusted to the *in situ* temperatures recorded on the 26th January 2019 at 11:00 (Site 1) and 24th January 2019 at 10:30 (Site 2) as these days had comparable air temperatures and both sites were not inundated with water during this time (Fig. 6.2.B). For field conditions during sediment and porewater sampling, see Fig. 6.2.A.

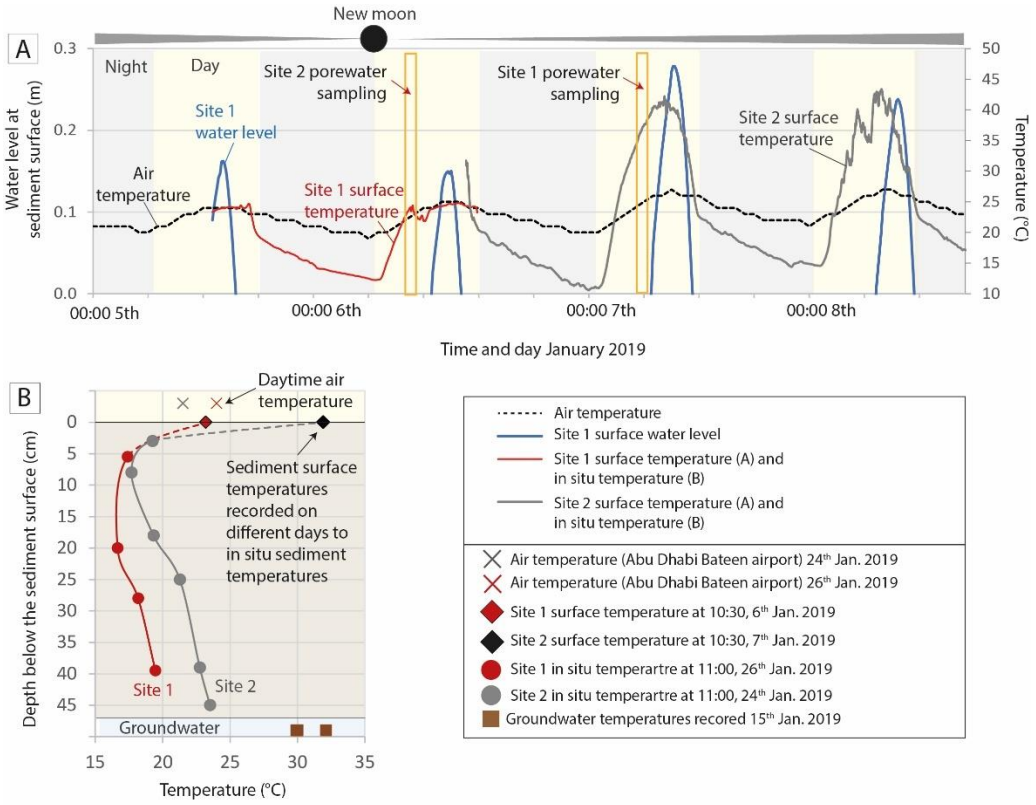

Figure 6.2. Sampling conditions during the days surrounding porewater extraction at Site 1 and 2. (**A**) Figure shows air temperature (Abu Dhabi Bateen Airport) (black dashed line); surface temperature at Site 1 (red line) and Site 2 (grey line); and water level at Site A (blue line). Site 1 was flooded once each day by the highest tides of the two diel asymmetrical tides, but Site 2 was not inundated with water

and there was no recorded cloud cover at Abu Dhabi Bateen Airport during this period. Surface temperature at Sites 1 and 2 were recorded with surface TidbiT temperature loggers, however these were not located in the shade and may have experienced a localised warming effect during daytime hours. (**B**) *In situ* sediment temperatures at Site 1 (26th Jan. 2019 at 11:00) and Site 2 (24th Jan. 2019 at 11:00) as the best approximation of *in situ* temperatures during sampling (circles), with the corresponding air temperatures recorded at Abu Dhabi Bateen Airport (crosses, yellow upper panel). Surface temperatures (diamonds) were recorded at on separate days at Site 1 (6th Jan. 2019 at 10:30) and Site 2 (7th Jan. 2019 at 10:30) and borehole temperatures (brown squares, lower blue panel) were recorded 15th January 2019.

6.4 Results

6.4.1 Sedimentology

At Site 1 the upper 1 cm of sediment has laterally discontinuous orange staining, which transitions into a laterally continuous orange band at 2-3 cm. Below this (3-11 cm) is a light grey peloidal packstone with orange iron (Fe) staining and from 11-31 cm is a beige to light grey with mottled dark grey peloidal packstone with bioclasts. The base of the profile (~33 cm) terminated on a well-lithified hardground with a planar upper surface (Fig. 6.3.A, B). The sediment mineralogy at Site 1 is fairly homogenous throughout the core, being predominantly aragonite (85±4%) with subordinate calcite (4±2%), quartz (3±3%), anhydrite (2±2%), and minor dolomite (0.4±0.8%, maximum 3% at 12 cm), plus ~5% halite which was likely an artefact from drying the cores (Fig. 6.3.C). Sediments consist almost entirely of fine to coarse sand sized particles and mean grainsize increases with depth from 0.15 mm at the sediment surface to peak at 18-20 cm (0.81 mm) and then remains fairly stable from 20-32 cm (0.49 mm) (Fig. 6.3.D, E).

At Site 2 the upper 0.5 cm of the sediment consist of a thin dark-coloured microbial mat. Below this (0.5-10.5 cm) is a brown gypsum mush with lenticular crystals ≤5 mm wide. From 10.5-23 cm the gypsum mush become grey with crystals ~5 mm wide and at 23-28 cm there is a black laminated buried microbial mat (Fig. 6.3.F, G, H). From 28-42 cm the buried microbial mat contains isolated gypsum crystals and gastropods with large fissures ≤7 cm wide filled with the grey intertidal sand from the base of the profile. From 42-49 cm is a peloidal bioclast packstone; grey intertidal sands have a strong H_2S odour and contain abundant gastropods with fragments of bivalves, peneroplis foraminifera and incipient gypsum (Fig. 6.3.F, G, H).

The upper 0-17 cm of sediment at Site 2 is predominantly gypsum (73.3 ±8.4%), with aragonite (10.8 ±6.0%), halite (7.4 ±3.0%), and subordinate calcite (3.6 ±3.1%), dolomite (3.3 ±1.5%), and quartz (1.5 ±1.2%). Dolomite peaks within the upper buried microbial mat at ~17-23 cm (9.8 ±1.4%) and towards the base of the microbial mat (10% at 34 cm) (Fig. 6.3H). Aragonite increases from ~18-22 cm, and from 22-36 cm sediment is predominantly aragonite (49.7 ±5.7%) with abundant halite (30.5 ±5.3%) and subordinate calcite (7.3 ±2.7%), dolomite (4.9 ±3.6%), and quartz (4.9 ±3.3%), plus minor anhydrite

at ~7 and 10 cm (4.1%) (Fig. 6.3.H). Mean grainsize at Site 2 remains fairly constant in the upper 0-27 cm (2.6 ±0.5 mm), peaks within the buried microbial mat at 29 cm (4.1 mm) and then decreases to the base of the profile (1.1 mm at 37 cm) (Fig. 6.3.I, J).

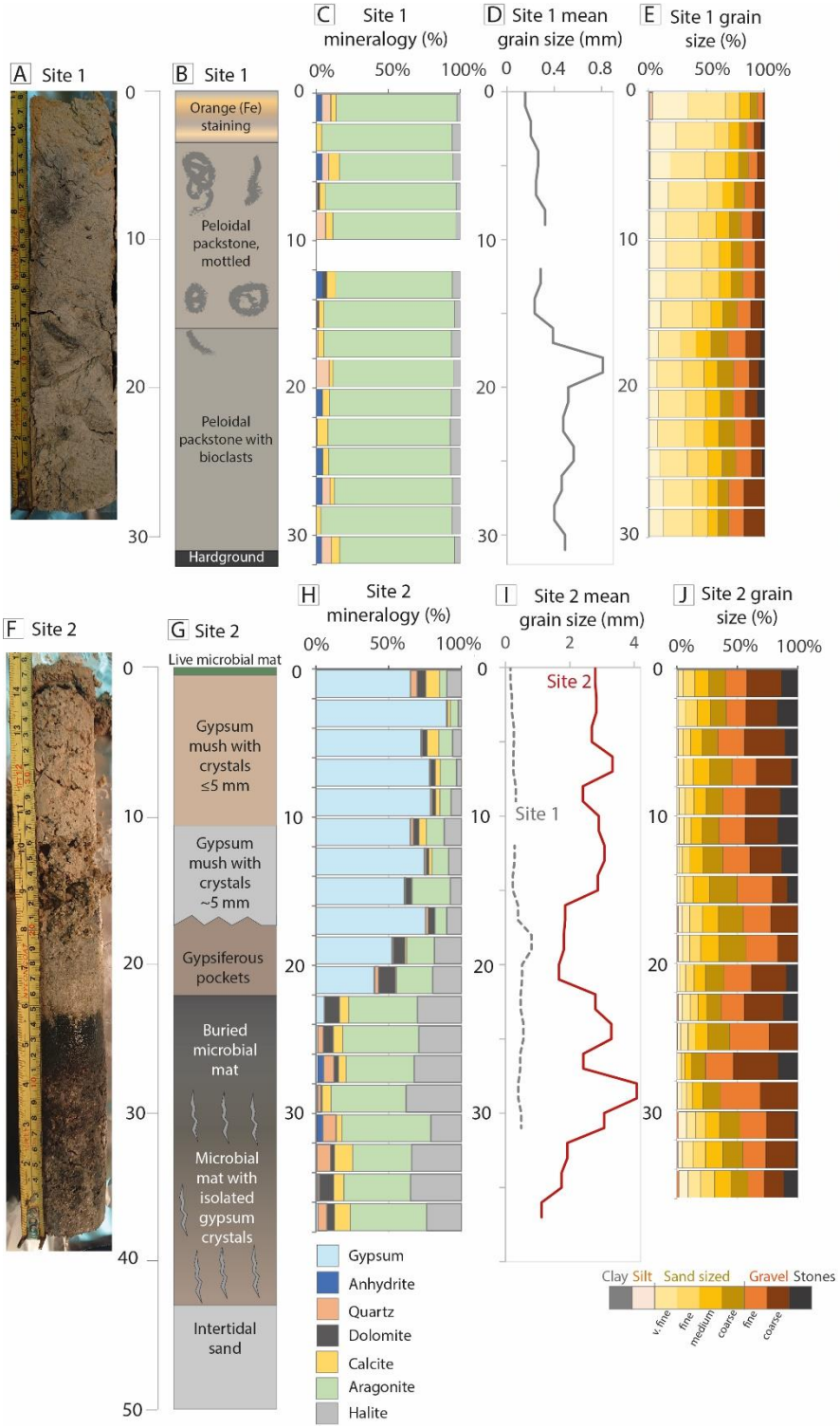

Figure 6.3. Sediment stratigraphy, mineralogy, and grain size for Site 1 (upper row) and Site 2 (lower row). Upper row, Site 1: (**A**) core photo and (**B**) interpreted sediment stratigraphy; (**C**) mineralogy from XRD; (**D**) mean grain size (mm) and (**E**) grain size relative distribution. Lower row Site B: (F) core photo and (**G**) sediment stratigraphy; (**H**) mineralogy; (**I**) mean grain size (mm) and grain size relative

distribution (**J**). Raw mineralogy and grain size data are presented in Appendix E, Tables E1 and E2 respectively.

6.4.2 Porewater chemistry

Salinity

At the time of sampling, salinity, presented as total dissolved solids (TDS) in parts per thousand (‰), was lowest for the offshore seawaters (37.9±2.1‰) (Oct. 2017) and ranged from 51-99‰ as the tidal front progresses across the middle ITZ (Jan. 2019). Porewater salinity increases in a broadly linear trend with depth at both sites but was significantly lower at Site 1 (68‰ at 0.5 cm to 108‰ at 33cm) than Site 2 (171‰ at 7.5 cm to 209‰ at 47.5 cm), and all Site 2 porewaters are within the range of groundwater salinities obtained from the three boreholes (170-223‰) (Fig. 6.4.A).

Carbonate chemistry

Porewater *p*H is lower than the mean offshore seawater (8.03 *p*H) and the flood tide surface waters (8.04-8.16 *p*H) and decreases with depth at Site 1 from 0.5 cm (*p*H 7.43) to stabilise from 21.5-33 cm (*p*H 7.03 ±0.03). *p*H at Site 2 decreases in a broadly linear trend with depth from 5.5 cm (7.65 *p*H) to 47.5 cm (6.71 *p*H), which resembles groundwater pH from Borehole 2 (6.68), whilst Boreholes 1 and 3 have lower *p*Hs (6.25 and 6.29 respectively) (Fig. 6.4.A).

Offshore seawater alkalinity was near identical to the mean flood tide surface water alkalinity (~2.51 mmol l^{-1}). Site 1 porewater alkalinity at most depths is higher than the surface waters and increases from 0.5 cm (2.44 mmol l^{-1}) to peak at 9.5 and 12.5 cm (4.20 mmol l^{-1}) before decreasing slightly with depth (Fig. 6.4.A). In contrast Site 2 porewater alkalinity is predominantly lower than surface water alkalinity and displays a slight decreasing trend with depth from 5.5 cm (1.72 mmol l^{-1}) to 15.6 cm (1.38 mmol l^{-1}), before increasing in a broadly linear trend with depth to peak at 43.5 cm (3.05 mmol l^{-1}). The groundwaters have the lowest alkalinities ranging from 2.05-2.48 mmol l^{-1}.

The partial pressure of carbon dioxide (pCO_2) was slightly higher in the offshore seawaters (~0.08%) that the shallow flood tide waters (~0.05%) and was 26 to 68 times higher in the groundwater samples (1.3-3.4%). Porewater pCO_2 at Site 1 increases significantly from 0.5 cm (0.3%) to 12.5 cm (1.2%) and then remains between 0.9-1.2% to the base of the profile. pCO_2 at Site 2 increases more gradually with depth from 5.5 cm (0.09%) to 47.5 cm (1.4%) (Fig. 6.4.B).

Redox potential and methane concentrations

The offshore seawaters, flood tide surface waters, and Site 1 porewaters are oxic. The highest redox potential (Eh) was in the upper 0.5-2.5 cm of Site 1, with the rest of the profile remaining fairly constant at ~100 mV. The upper 5.5 – 15.5 cm at Site 2 is also oxic (Eh ~100 mV) and then decreases in a broadly linear trend, crossing the redox boundary at ~20.5 cm and reaching a minimum of -195 mV at 47.5 cm

(Fig. 6.4.A). Groundwaters appear oxic, though this may be an artefact of aeration whilst pumping the samples out of the boreholes. Methane was low (<0.3 µmol l^{-1}) throughout the majority of Site 1 and 2 porewaters, except at 47.5 cm at Site 2 (0.74 µmol l^{-1}) which was similar to Borehole 1 (0.65 µmol l^{-1}) (Fig. 6.4.A).

Organic chemistry

Dissolved organic carbon (DOC) in offshore seawaters (4.5 mg l^{-1}) is similar to the groundwater DOC (4.8-5.9 mg l^{-1}) whereas flood tide surface waters DOC was variable (2.8-11.5 mg l^{-1}) (Fig. 6.4.C). At 0.5 cm at Site 1 porewater DOC resembles offshore seawater and increases slightly with depth, with a notable peak at 15.5 cm (8.1 mg l^{-1}). DOC was not measured for all porewater samples at Site 2, though appears to peak at 9.5 cm (13.6 mg l^{-1}). Total nitrogen (TN) increases with depth at both Sites 1 and 2 to peak at 15.5 cm (1.45 mg l^{-1}) and 13.5 cm (1.87 1.45 mg l^{-1}) respectively (Fig. 6.4.C). Below 15.5 cm TN decreases at Site 1, and although most analyses are missing from Site 2, the deepest samples have high TN (3.2 mg l^{-1} at 47.5 cm). Groundwater TN varies from 1.2-2.6 1.45 mg l^{-1}.

Saturation indices and ion ratios

Offshore and flood tide surface waters are supersaturated with respect to aragonite, calcite, dolomite and undersaturated with respect to gypsum and halite, whereas groundwaters are dolomite supersaturated and undersaturated with respect to aragonite, calcite, gypsum, and halite (Fig. 6.4.B, C). Site 1 remains predominantly calcite supersaturated and aragonite undersaturated throughout the profile, with a small increase in aragonite saturation to reach equilibrium at 9.5 cm. In contrast Site 2 is aragonite supersaturated from 5.5-9.5 cm and then remains undersaturated from 13.5-47.5 cm, and is calcite supersaturated from 5.5-16.5 cm, undersaturated from 20.5-27.5 cm and around calcite equilibrium from 35-47.5 cm. All porewaters are dolomite supersaturated, (with a notable peak from 5.5.-9.5 cm at Site 2) and undersaturated with respect to gypsum and halite.

Mg/Ca molar ratios are lowest for offshore seawaters (5.3) and flood tide surface waters (range 5.6-5.9). At Site 1, Mg/Ca increases in a broadly linear trend with depth from 0.5 cm (5.8) to peak at 30.5 cm (9.3) which resembles the range of borehole Mg/Ca (5.9-10.2). In contrast Site 2 Mg/Ca ratios are significantly higher than at Site 1 and increase from 5.5 cm (11.9) to peak at 27.5 cm (23.3) before decreasing slightly with depth (Fig. 6.4.C). Using chloride as a tracer for mixing between endmembers (seawater and groundwater) Mg/Cl is slightly lower at Site 2 than Site 1. Site 1 porewaters have Mg/Cl ratios slightly higher than seawater and flood tide surface waters, though remain fairly constant with depth (0.100 ±0.003) (Fig. 6.4.C). Site 2 porewaters remain within range of the offshore sweater and groundwaters and remains fairly constant with depth (0.083 ±0.004). In contrast the porewater Ca/Cl ratios at Site 1 were higher than at Site 2 (Fig. 6.4.C). Site 1 porewater Ca/Cl increases slightly in the upper 2.5 cm to peak at 2.5 which was slightly higher than the mean flood tide surface water Ca/Cl

(0.02). Porewater Ca/Cl then decreases in a broadly linear trend to a minimum of 0.01 at 33 cm (Fig. 6.4.C). In contrast, porewater Ca/Cl ratios at Site 2 were lower, decreasing from 0.007 at 5.5 cm to remain fairly stable from 20.5-47.5 cm (0.004 ±0.0004). Groundwaters Mg/Cl and Ca/Cl ratios ranged from 0.06-0.09 and 0.009-0.010 respectively.

Strontium depletion, using Cl^- as a conservative tracer for mixing (Sr^{2+}/Cl^-) suggests porewaters in the upper half of the profile at Site 1 fall within range of a mixing trend between surface and groundwaters, however porewaters from 15.5-27.5 cm appear slightly Sr^{2+} depleted (Fig. 6.4.D). In contrast at Site 2, porewaters from 5.5-35 cm appear Sr^{2+} depleted, but become less depleted with depth. SO_4^{2-}/Cl^- ratios suggests Site 1 porewaters are enriched in SO_4^{2-} relative to a mixing trend between offshore seawater and groundwater, whereas at Site 2 the upper 5.5-20 cm appear depleted in SO_4^{2-} relative to this mixing trend (Fig. 6.4.D).

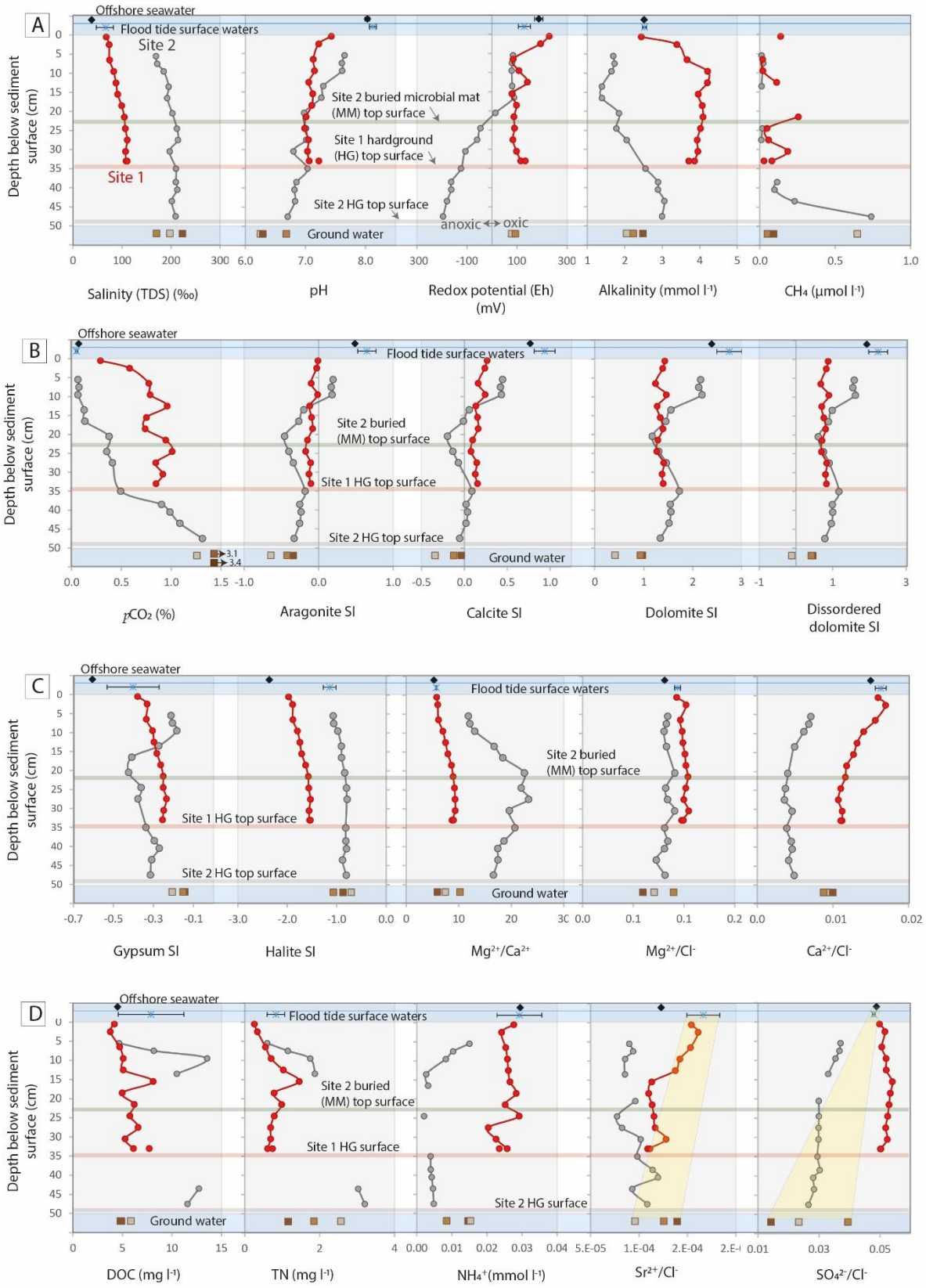

Figure 6.4. Offshore seawater and flood tide surface water (mean ± standard deviation, n=6) (upper panel, blue background), borehole groundwater (lower panel, blue background) and porewaters from Site 1 (red) and 2 (grey). Figure displays; (**A**) salinity (TDS), *p*H, redox potential (Eh), alkalinity and methane (CH_4) concentrations. (**B**) partial pressure of CO_2 (pCO_2), aragonite saturation indices (SI), dolomite SI, and disordered dolomite SI, gypsum SI (calculated using PHREEQC, Pitzer). (**C**) Gypsum and

halite SI (calculated using PHREEQC, Pitzer) and Mg/Ca, Mg/Cl and Ca/Cl molar ratios. (**D**) Dissolved organic carbon (DOC); total nitrogen (TN), ammonium (NH_4^+), strontium depletion as Sr^{2+}/Cl^- and sulphate depletion as SO_4^{2-}/Cl^-, with the yellow section highlighting the range of values expected by mixing between endmembers (seawater and groundwater). Unless displayed, error bars are smaller than the data point. Raw water chemistry data are presented in Appendix E, Table E3.

6.4.3 Sediment *in situ* temperature variability

Throughout the 1.25 years of subsurface temperature logging, sediment *in situ* temperature varied with depth, time, and space. *In situ* temperatures were most variable near the sediment surface and became less variable with depth (Table 6.2, Fig. 6.5). During daytime periods in summer months, sediments at Sites 1 and 2 became cooler with depth, whereas during winter days, the deeper sediments (>39 cm) predominantly remained warmer than the shallower sediments (e.g., Fig. 6.5, 6.6, 6.7, 6.8). Groundwaters from the boreholes had temperatures of 29.9, 30.3 and 32.1 °C at Boreholes 1, 2, and 3 respectively (measured 15th Jan. 2019), which is similar to the mean temperature recorded over the 1.25 years of logging at 45 cm (Site 2) (28.6 °C).

An example winter (20th-28th Jan. 2019) and summer period (24th Jul. – 1st Aug. 2019) were used to assess how *in situ* temperature at Sites 1 (Fig 6.6) and 2 (Fig. 6.7) varies between seasons, and to predict what affect this may have on mineral SI. The winter period was selected as the best approximation for conditions when the porewater and sediment samples were obtained (Fig. 6.2) and spans the transitions from a new moon spring tide (21st Jan.) to a half-moon neap tide (28th Jan.). The summer period covers a half-moon neap tide (25th Jan.) moving towards a full moon spring tide (1st Aug.).

During the winter period, water reached Site 1 at high tide, towards the end of the day on the 20th - 25th January (Fig. 6.6.A), with a peak surface water level of 0.3 m (22nd Jan.), whereas Site 2 remained exposed (Fig. 6.7A). Peak daily air temperature increased during the winter period from 18 °C (20th Jan.) to 29 °C (28th Jan.) (Fig. 6.6.B). Winter *in situ* sediment temperatures at Site 1 were typically cooler than at Site 2 (Fig. 6.6.C; 6.7.C). The sediments at 5 cm (Site 1) and 3 cm (Site 2) varied from 13.3 - 23.7 °C and 12.6 – 32.2 °C respectively. In contrast the deeper sediments had less variable winter temperatures, which ranged from 18.7-19.9 °C (40 cm) at Site 1 and was av.= ~3 °C warmer at Site 2 (range: 21.0-23.5 °C at 39 cm). *In situ* temperatures increased throughout the winter period, particularly at shallower depth (Fig. 6.6B, 6.7.B). During the daytime (5th-6th Jan. 2019) the surface temperature at Site 1 was approximately equal to the air temperature however during the night-time, the surface temperature was up to 7 °C cooler than air temperature (Fig. 6.2). In contrast, during the daytime at Site 2 (6-8th Jan. 2019), surface temperature was up to 16 °C warmer than air temperature and during the night-time surface temperature were up to 8 °C cooler than air temperature (Fig. 6.2).

During the summer period, air temperature was highest between 26th – 31st (peak 43 °C), when the cloud cover was lowest (Fig. 6.6.D). During this period, high tide reached Site 1 every day and was lowest on July 24th (0.14 m) and highest on August 1st (0.65 m) (Fig. 6.6.D). Site 1 was only inundated during the night, meaning the most intense surface warming occurred during this lunar/tidal cycle exemplar period. In contrast, Site 2 was only flooded on July 31st (0.4 m at 01:00) and 1st August (0.10 m at 02:00) in the summer exemplar period (Fig. 6.7.D). From the 24th – 28th July, shallow sediment (3 cm) temperatures at Site 2 increased with increasing air temperature to peak at 54.6 °C (Fig. 6.7.E, F). However, from the 29th July – 1st August, peak *in situ* temperatures at Site 2 of all but the deepest sediments (45 cm) decreases, whilst air temperature remains fairly constant and cloud cover increases to peak at 73% (1st Aug.) (Fig. 6.7.D).

Whilst thermal conductivity of the sediment has not been quantified, we can estimate the rate of heat transfer with depth based on the lag time between peak *in situ* temperatures at shallow depth (5.5 cm Site 1 and 3 cm Site 2), and peak *in situ* temperature throughout the sediment column. This relationship was assessed for a winter day (24th Jan. 2019) and a summer day (29th Jul. 2019). The lag time in peak *in situ* temperatures with depth is almost identical at Site 2 in the winter and summer example days, whereas at Site 1 there a slightly faster heat transfer in summer compared to winter (Fig. 6.9) (likely reflecting variable moisture content). Applying linear regression between points suggests that there is a lag in peak *in situ* sediment temperature at Site 1 of ~3.8 cm per hour from 5.5-28 cm (R^2 0.99), which slows to ~1.6 cm per hour from 28 - 39.5 cm (Fig. 6.9). At Site 2, there is a lag in peak *in situ* sediment temperature of ~2.7 cm per hour from 3-18 cm (R^2 0.96), which slows to ~ 2 cm per hour from 18-45 cm (R^2 0.98) (Fig. 6.9).

Table 6.2. Summary of the range and mean (± standard deviation) temperatures at Site 1 and 2 over one year and during the winter and summer example periods.

	Annual (Jan. 2019 to Jan. 2020)		**Winter period (20th-28th Jan. 2019)**		**Summer period (24th Jul. – 1st Aug. 2019)**	
	Range	Mean	Range	Mean	Range	Mean
Site 1						
5.5 cm	11.0 – 42.0	26.0 ±6.7	13.3-23.7	17.6 ±2.9	28.4-41.4	34.1 ±3.2
20 cm	14.6 – 36.3	26.0 ±5.8	15.8-20.6	18.0 ±1.2	31.1-36.2	33.6 ±1.4
28 cm	16.4 – 34.9	26.1 ±5.4	17.3-19.8	18.5 ±0.6	31.8-34.3	33.1 ±0.7
39.5 cm	17.8 – 33.4	26.1 ±5.0	18.7-19.9	19.2 ±0.3	31.9-33.3	32.6 ±0.4
Site 2						
3 cm	10.4 - 56.7	28.9 ±8.6	12.6-32.3	18.7 ± 4.3	29.3-54.6	38.0 ±6.4
8 cm	15.5 - 48.0	31.1 ±6.8	16.2-28.1	20.2 ±2.6	33.2-47.4	38.6 ±3.6
18 cm	19.1 - 42.0	31.9 ±5.7	19.2-24.7	21.0 ±1.2	35.4-42.0	38.1 ±1.7
25 cm	19.5 -39.3	30.2 ±5.5	21.0-23.5	21.8 ±0.6	35.9-39.3	39.4 ±0.9
39 cm	20.8 - 37.6	30.4 ±4.9	22.6-24.4	23.1 ±0.5	35.0-37.6	36.5 ±0.6
45 cm	20.5- 36.7	30.1 ±4.5	23.4-24.8	23.8 ±0.4	28.5-30.7	35.4 ±0.6

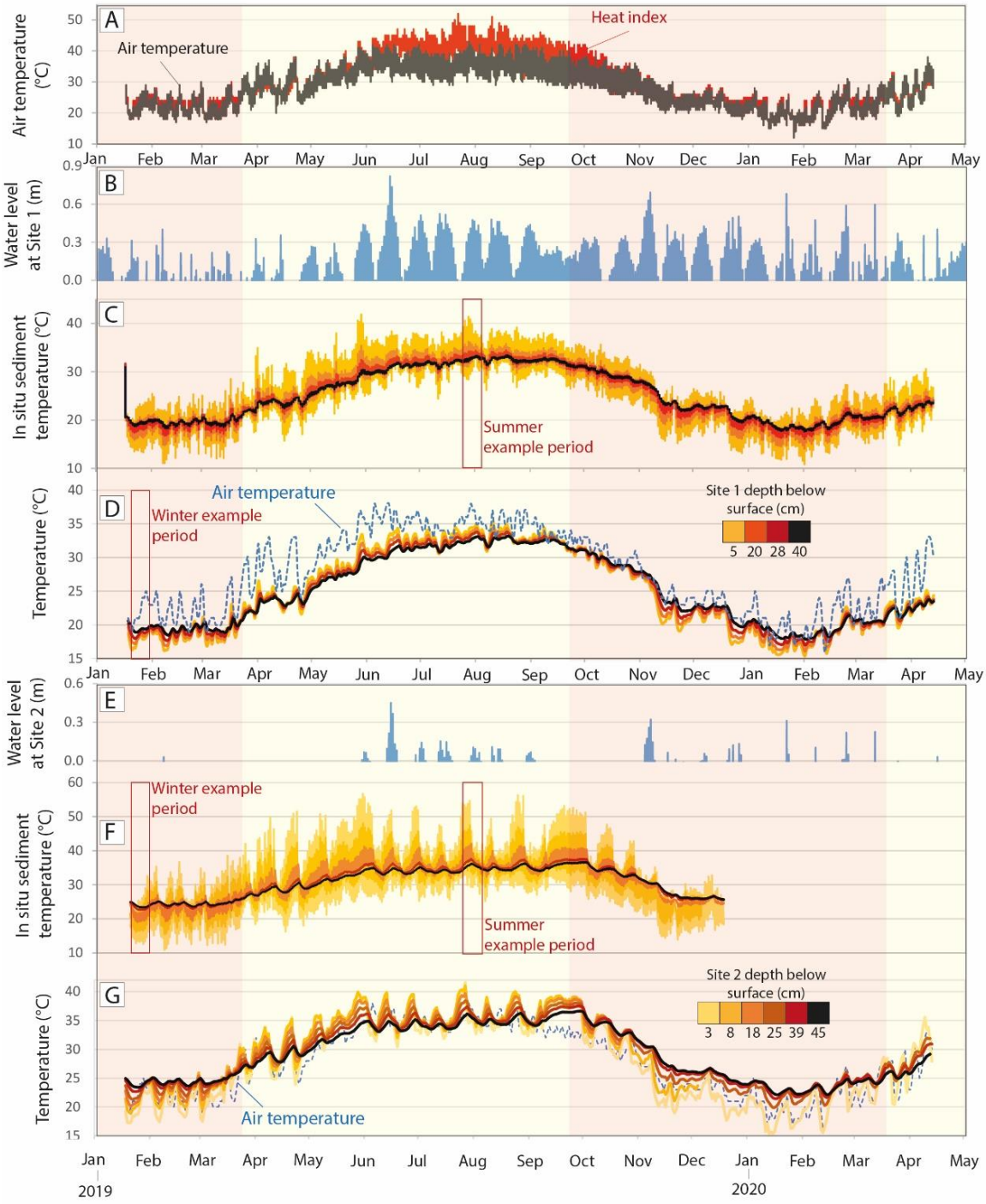

Figure 6.5. (**A**) Air temperature (grey line) and heat index (red line) measured at Abu Dhabi Bateen Airport during logger deployment (18th Jan. 2019 – 14th Apr. 2020); (**B**) Surface water level at Site 1; (**C**) *In situ* sediment temperature at 5, 20, 28, and 40 cm at Site 1 (1-hour intervals), highlighting the winter and summer example periods (red boxes). (**D**) One-day running mean of *in situ* sediment temperature at Site 2 and daily mean air temperature at Abu Dhabi Bateen Airport (blue dashed line). (**E**) Surface water level at Site 2; (**F**) *In situ* sediment temperature at depths of 3, 8, 18, 25, 39, and 45 cm below the sediment surface at Site 2 (1-hour intervals), highlighting the winter and summer example periods (red boxes). (**G**) One-day running mean of *in situ* sediment temperature at Site 2 and daily mean air temperature at Abu Dhabi Bateen Airport (blue dashed line).

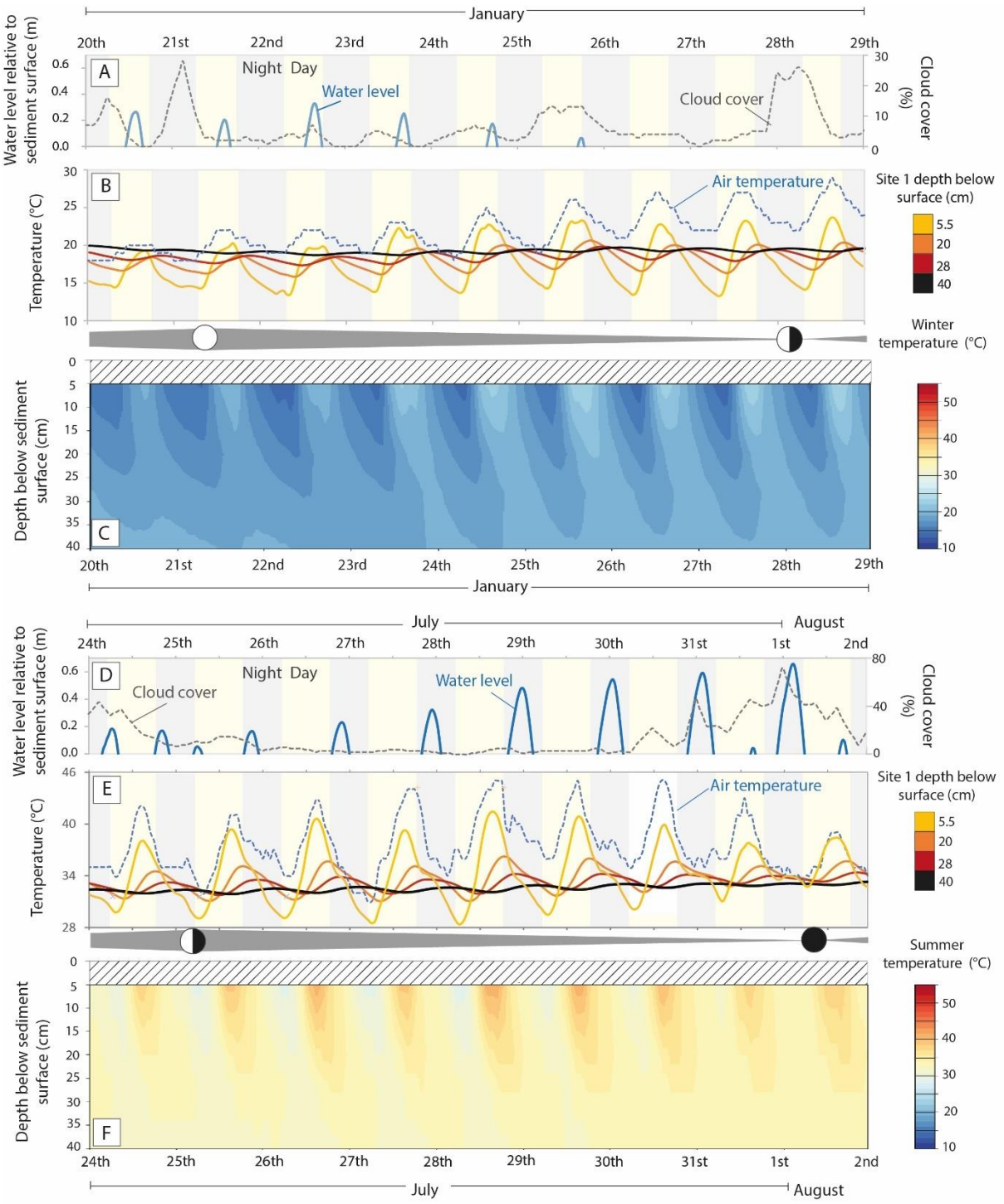

Figure 6.6. Site 1 water level and *in situ* sediment temperature in the winter example period (20th- 29th Jan. 2019) (**A**-**C**) and summer example period (24th Jul. – 1st Aug.) (**D**-**F**). (**A**) Surface water level (blue line) and cloud cover at Abu Dhabi Bateen airport (grey dashed line) in winter; (**B**) winter *In situ* sediment temperature (solid lines) and air temperature at Abu Dhabi Bateen airport (blue dashed line); (**C**) winter *in situ* sediment temperature; no temperature data available above 5 cm (hashed upper panel). (**D**) Surface water level (blue line) and cloud cover at Abu Dhabi Bateen airport (grey dashed line) in summer; (**E**) summer *in situ* sediment temperature (solid lines) and air temperature at Abu Dhabi Bateen airport (blue dashed line); (**F**) summer *in situ* sediment temperature; no temperature data available above 5 cm (hashed upper panel). Note different scales in (**B**) and (**E**).

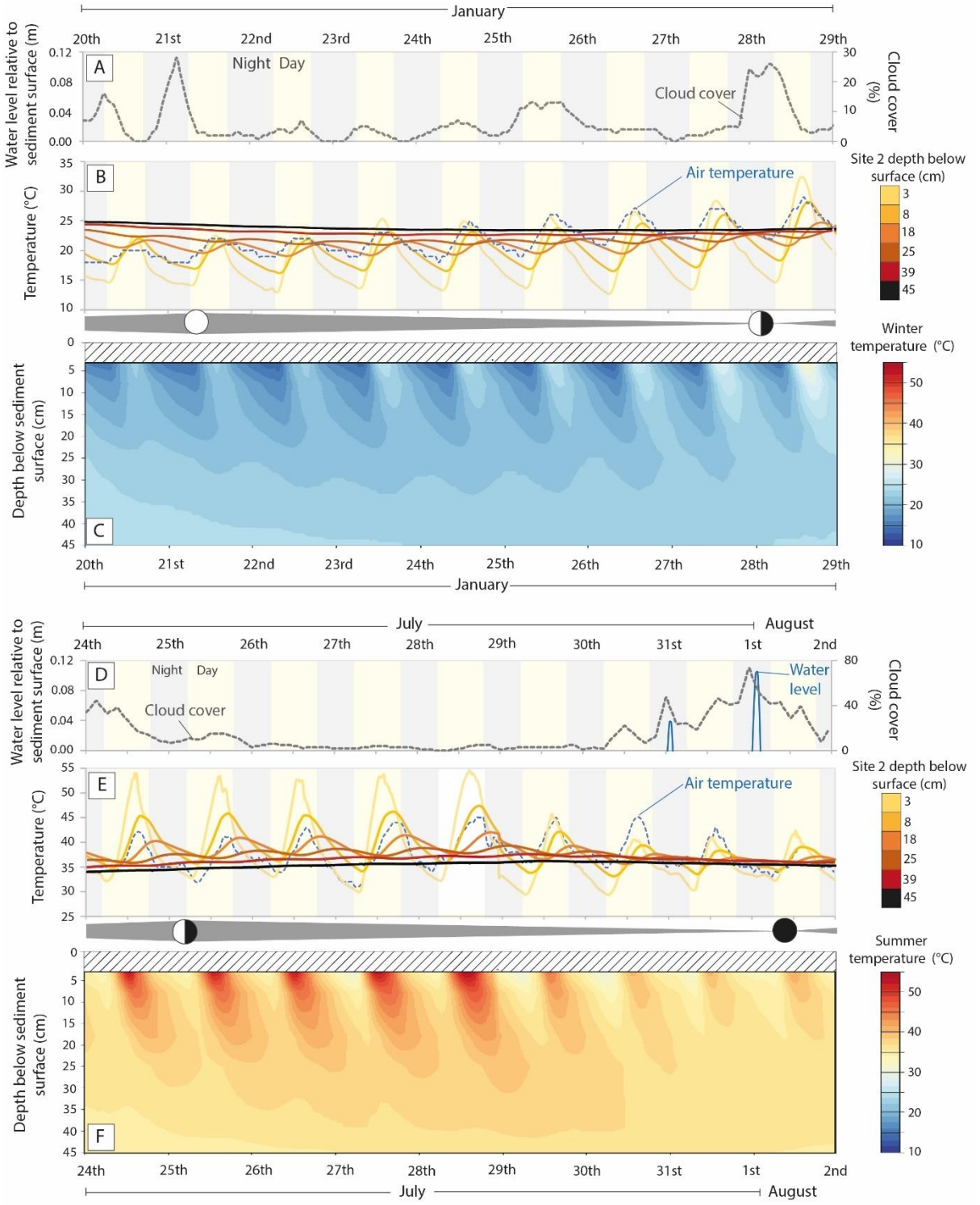

Figure 6.7. Site 2 water level and *in situ* sediment temperature in the winter example period (20th- 29th Jan. 2019) (**A**-**C**) and summer example periods (24th Jul. – 1st Aug. 2019) (**D**-**F**). (**A**) Surface water level (Site B remained exposed during the winter period) and cloud cover at Abu Dhabi Bateen airport (grey dashed line) in winter; (**B**) winter *in situ* sediment temperature (solid lines) and air temperature at Abu Dhabi Bateen airport (blue dashed line); (**C**) winter *in situ* sediment temperature; no temperature data available above 5 cm (hashed upper panel). (**D**) Surface water level (blue line) and cloud cover at Abu Dhabi Bateen airport (grey dashed line) in summer; (**E**) summer *In situ* sediment temperature (solid lines) and air temperature at Abu Dhabi Bateen airport (blue dashed line); (**C**) summer *in situ* sediment

temperature; no temperature data available above 5 cm (hashed upper panel). Note different scales in (**B**) and (**E**).

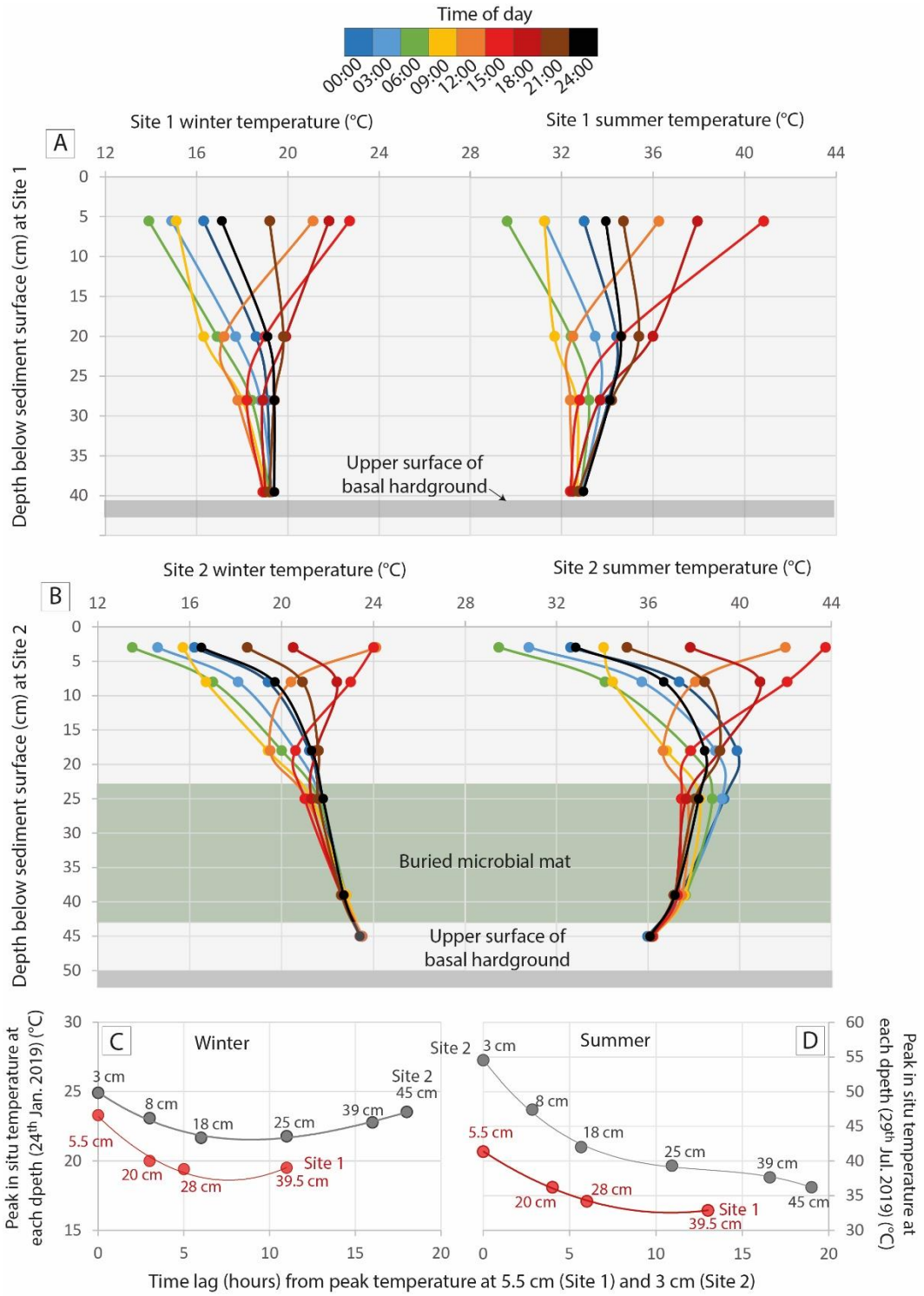

Figure 6.8. *In situ* sediment temperatures during a 24-hour period in winter (24th Jan. 2019) and summer (29th Jul. 2019) at (**A**) Site 1 and (**B**) Site 2. (**C**) Lag time (hours) from peak temperature at 5.5 cm (Site 1) and 3 cm (Site 2) during winter (24th Jan. 2019). (**D**) Lag time (hours) from peak temperature at 5.5 cm (Site 1) and 3 cm (Site 2) during summer (29th Jul. 2019). Note that temperature (y-axis) are on different scales in (**C**) and (**D**).

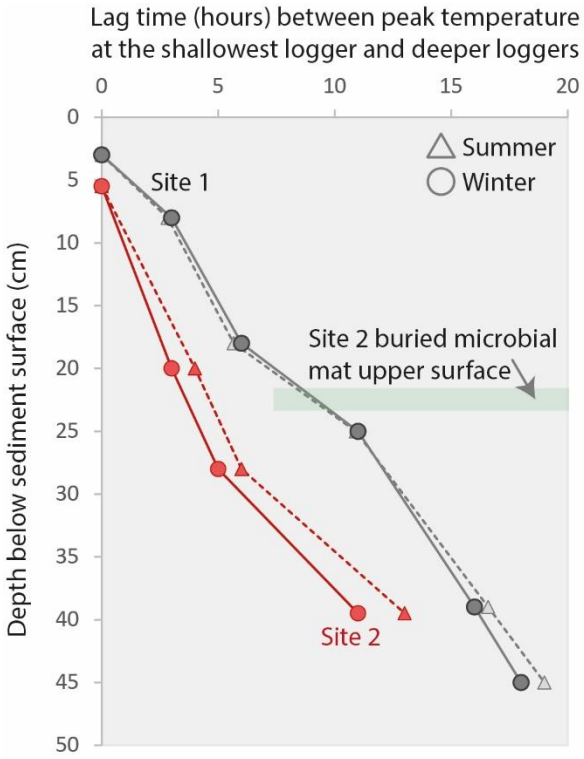

Figure 6.9. The lag time (hours) between peak temperature at the shallowest TidbiT (5.5 cm at Site 1 and 3 cm at Site 2) and peak temperatures at the deeper loggers at Site 1 (red) and Site 2 (grey) during a summer day (29th Jul. 2019) (triangle, dashed line) and winter day (24th Jan. 2019) (circle, solid line).

6.4.4 Variations in modelled saturation indices in winter and summer periods

The thermodynamic model PHREEQC (with the Pitzer database) was used to model porewater chemistries collected in winter at *in situ* winter and summer temperatures to explore the predicted effects of changing *in situ* temperatures on mineral SI (if porewater chemistries remained the same between seasons). Fig. 6.10 illustrates how porewater SI_{arag} at Sites 1 and 2 (collected in winter) would theoretically change at different temperatures and highlights how small changes in temperature have a larger impact on whether porewaters are aragonite under- or over-saturated at Site 1 than Site 2, as the original porewater chemistry at Site 1 was closer to equilibrium (Fig. 6.4). Figures 6.11 and 6.12 demonstrate how the porewater mineral SI may respond to measured summer and winter *in situ* temperatures at Site 1 and 2, respectively.

Porewaters at Sites 1 and 2 remain dolomite supersaturated and gypsum undersaturated throughout the summer and winter example period (Fig. 6.11.G-J, 6.12.G-J). At Site 1, SI_{calc} remains supersaturated in the winter and summer periods whereas at Site 2 SI_{calc} fluctuates from undersaturated to supersaturated with depth (Fig. 6.11.E, F and 6.12.E, F). SI_{arag} fluctuates from undersaturated to supersaturated with depth and time at both sites and is less variable at Site 1 (-0.18 to 0.09) than Site 2 (-0.46 to 0.22) (Fig. 6.11.C, D and 6.12.C, D).

In the winter period at Site 1, porewaters at 9.5 cm are approximately at aragonite equilibrium, whereas above and below 9.5 cm remains aragonite undersaturated (Fig. 6.11.C). However, in summer at Site 1, porewaters at 9.5 cm remain supersaturated throughout the day and night (Fig. 6.11.D). During the summer daytime, porewaters from ~5-19.5 cm are at aragonite equilibrium or supersaturated, with ~6-11 cm appearing aragonite supersaturated, and during the night-time, porewaters at ~6-11 cm and ~17.5-19.5 cm remains around aragonite equilibrium (or higher at 9.5 cm) (Fig. 6.11.D). The same pattern of increased saturation centred at ~9.5 and ~18.5 cm is observed in SI_{calc} at Site 1, though porewaters remain calcite supersaturated during both summer and winter periods (Fig. 6.11.E, F).

At Site 2, differences in SI_{arag} between summer and winter are less stark. In both seasons the upper ~11 cm is supersaturated, at ~11-11.5 cm porewaters are at approximate equilibrium and below 11.5 cm porewaters are aragonite undersaturated (Fig. 6.12.C, D). In winter at Site 2, porewater mineral SI is typically slightly lower than in summer, but the depths at which porewater are oversaturated or supersaturated do not vary markedly. In contrast SI_{calc} at Site 2 does vary a little with depth and time (Fig. 6.12.E, F). During the winter, SI_{calc} decreases from supersaturated at 5.5 cm to reach equilibrium at ~15-17 cm followed by a band of calcite undersaturation from ~17-30 cm (Fig. 6.12.E). From 30-45 cm porewaters fluctuate from slightly calcite supersaturated to equilibrium. During the summer period, calcite remains supersaturated from 5.5-18 cm, become undersaturated from ~20-26 cm, and remains supersaturated from ~28-45 cm (Fig. 6.11.F).

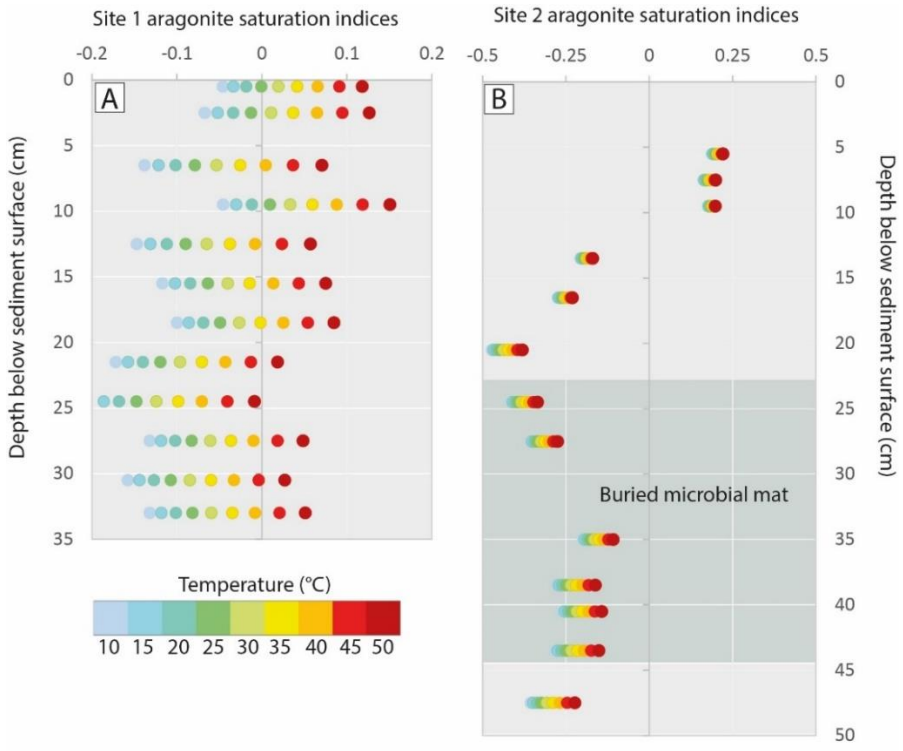

Figure 6.10. Theoretical changes in porewater aragonite SI at (A) Site 1 and (B) Site 2 at a range of theoretical *in situ* temperatures. Note different x-axis scales for Site 1 (A) and Site 2 (B). Site A appears to vary more significantly from under- to over-saturation compared to Site 2 as the original porewater chemistry at Site 1 was closer to equilibrium.

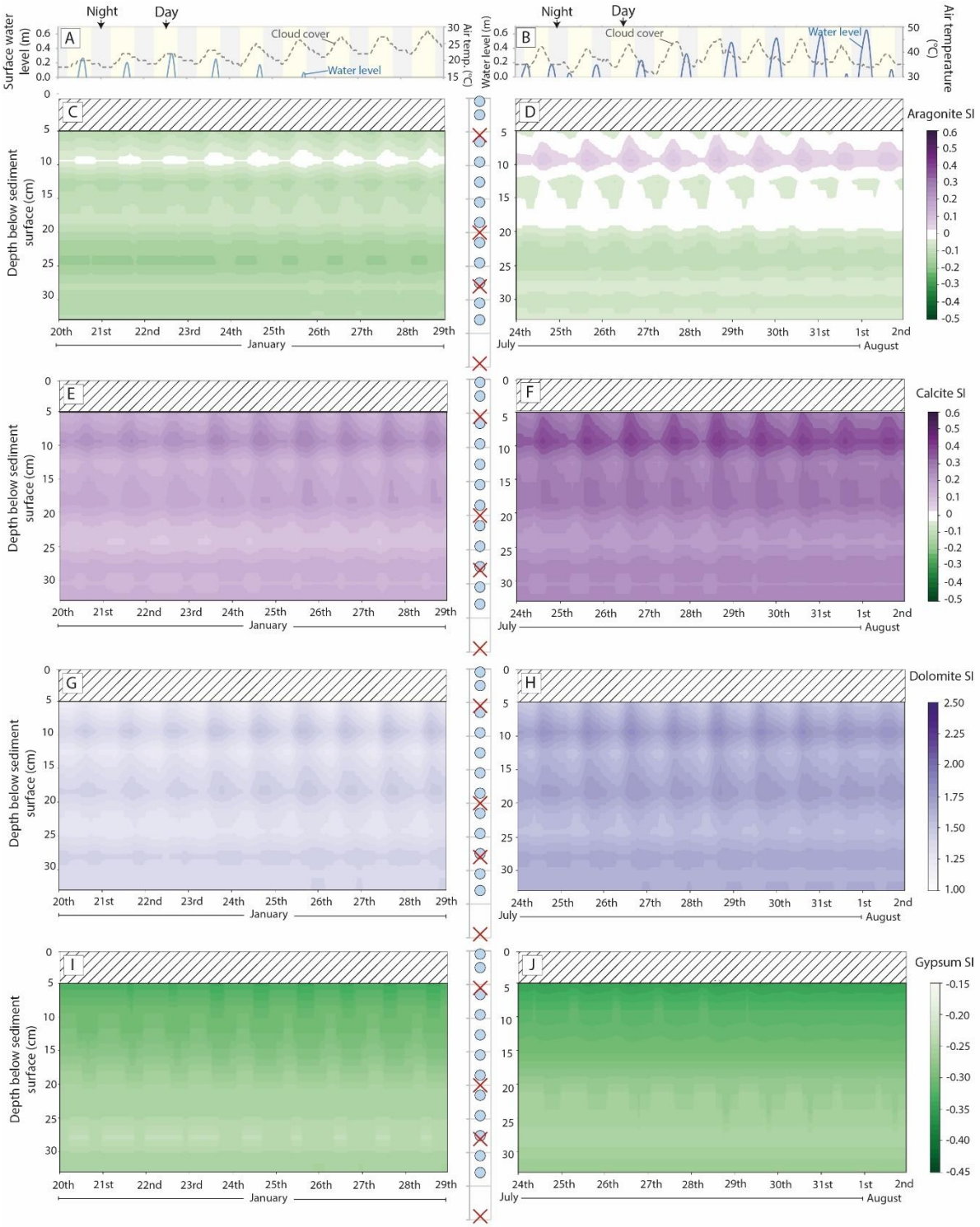

Figure 6.11. Site 1 (lower to middle ITZ) mineral saturation indices (SI) for porewater chemistries (collected 7th Jan. 2019), corrected to *in situ* winter temperatures (20th- 29th Jan. 2019) (left hand column) and *in situ* temperatures during the summer example period (24th Jul. – 1st Aug.) (right-hand column), (temperatures measured with TidbiT temperature loggers). Temperature was interpolated with linear regression between depth with loggers (central panel, red cross) and used to model mineral

saturation state at all depths with porewater samples (central panel, blue circles) using PHREEQC-Pitzer. (**A**) and (**B**) display the surface water level (left y-axis), air temperature (right y-axis), and periods of day/night during the winter and summer periods respectively [note winter and summer air temperatures are on different scales]. Contour figures (**C** – **J**) present aragonite SI during winter (**C**) and summer (**D**); calcite SI during winter (**E**) and summer (**F**); dolomite SI during winter (**G**) and summer (**H**); and gypsum SI during winter (**I**) and summer (**J**). No temperature data is available for the upper 5 cm, and thus mineral SI has not been included from 0-5 cm (hashed upper panel). [Note that dolomite and gypsum SI are not displayed on the same colour scale as aragonite and calcite SI].

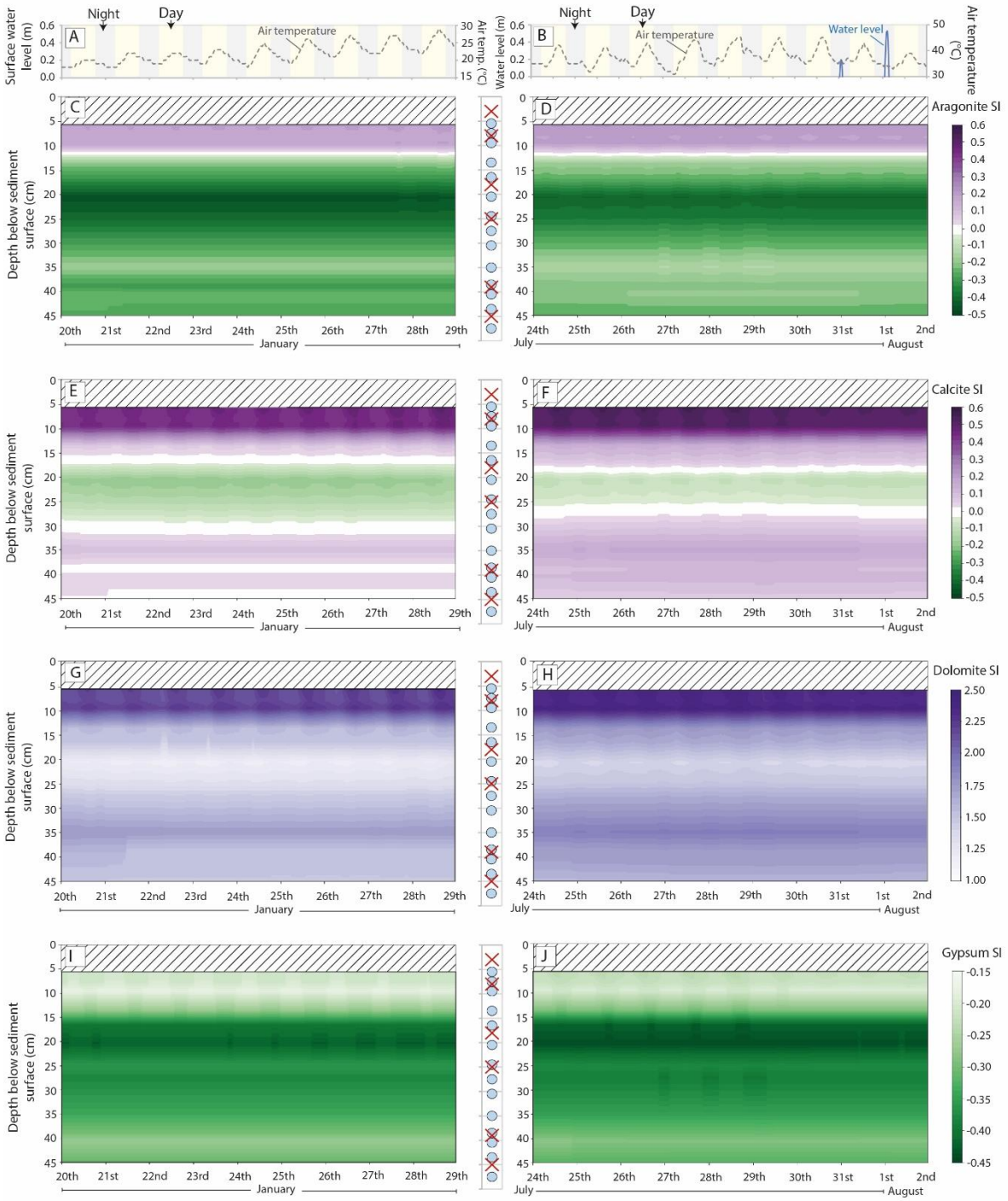

Figure 6.12. Site 2 (upper ITZ) mineral saturation indices (SI) for porewater chemistries (collected 6th Jan. 2019), corrected to *in situ* winter temperatures (20th- 29th Jan. 2019) (left hand column) and *in situ* temperatures during the summer example period (24th Jul. – 1st Aug.) (right-hand column),

(temperatures measured with TidbiT temperature loggers). Temperature was interpolated with linear regression between depth with loggers (central panel, red cross) and used to model mineral saturation state at all depths with porewater samples (central panel, blue circles) using PHREEQC-Pitzer. (**A**) and (**B**) display the surface water level (left y-axis), air temperature (right y-axis), and periods of day/night during the winter and summer periods respectively [note winter and summer air temperatures are on different scales, and water did not reach Site 2 in the winter period]. Contour figures (**C** – **J**) present aragonite SI during winter (**C**) and summer (**D**); calcite SI during winter (**E**) and summer (**F**); dolomite SI during winter (**G**) and summer (**H**); and gypsum SI during winter (**I**) and summer (**J**). No temperature data is available for the upper 5.5 cm, and thus mineral SI has not been included from 0-5 cm (hashed upper panel). [Note that dolomite and gypsum SI are displayed using different colour scale for aragonite and calcite SI].

6.5 Discussion

Temperature impacts the thermodynamics and kinetics of authigenic carbonate precipitation (Higgins *et al*., 2009), however many field studies in sub-tropical carbonate depositional environments are biased towards the cooler months. The potential thermodynamic impact on carbonate diagenesis in summer compared to winter was investigated for two sites in a coastal lagoon in Abu Dhabi by modelling porewaters collected in winter at both winter and summer *in situ* temperatures. Whilst this approach fails to evaluate the role of kinetics in carbonate precipitation/dissolution, or seasonal variations in microbial metabolisms or porewater chemistry (e.g., pH, alkalinity, dissolved organic carbon (DOC)), it simulates the potential role that seasonal temperature variability plays on carbonate diagenesis. Possible issues with the application of PHREEQC for modelling carbonate thermodynamics mean that whilst absolute values may be contentious between different models and databases, the general trends are likely believable (see methods Chapter 2.2).

Site 1 (lower to middle ITZ) and below ~22 cm at Site 2 (upper ITZ), situated in Qantur Lagoon, have a high abundance of aragonitic sediments, in apparently aragonite undersaturated and calcite supersaturated porewaters (Site 1) and porewaters at approximate calcite equilibrium (Site 2). This contradiction between sediment mineralogy and porewater chemistry is observed elsewhere in Qantur Lagoon (e.g., QLTC, Chapter 5), where aragonitic firmgrounds are suggested to be actively forming in some locations (Site A and B, Chapter 5). In other locations (e.g., Sites C and D, Chapter 5) firmgrounds do not appear to be actively forming, though show no evidence of dissolution, whilst also being situated in aragonite undersaturated waters. The predominance of metastable aragonite precipitation over the more-stable calcite phase has been a long-standing observation in marine environments, dubbed the 'calcite-aragonite problem' (Sun *et al*., 2015), however, this only applies to waters that are at aragonite equilibrium or supersaturation.

There are two possible reasons for the discrepancy between the aragonitic sediments and diagenetic cements and the aragonite undersaturated porewaters in coastal Abu Dhabi: (i) the thermodynamic

model (PHREEQC-Pitzer) applied to calculate the mineral SI may be inadequate to represent the true nature of these complex solutions (discussed in Chapter 2.2); or (ii) the porewaters sampled truly are undersaturated with respect to aragonite. In the latter case, this may be due to porewater sampling in winter which does not reflect conditions within the pore system at other times of the year, and/or other kinetic factors relating to the porewater geochemistry may be impacting the shallow sedimentary system. If we assume the porewaters obtained in winter are indeed undersaturated, it is important to understand reasons why this might be. Here we test the hypothesis that seasonal variations in SI_{arag} driven by *in situ* temperature variability could be responsible for the discrepancy between abundant aragonitic sediments and cements and the observation of aragonite undersaturated porewaters collected during the winter.

6.5.1 Diagenesis in the ITZ in winter

There are several discrepancies between sediment mineralogy and the porewater chemistries obtained from Sites 1 and 2 in winter. Firstly, at both sites, dolomite is the most supersaturated mineral (Fig. 6.11.G, H and 6.12.G, H), however Site 1 exhibits negligible amount of dolomite (Fig. 6.3C). Dolomite is commonly supersaturated in modern marine environments, however there are few examples of dolomite formation in natural environments, likely because of kinetic barriers to dolomite formation (Arvidson and Mackenzie, 1999). Site 2 exhibits zones with significant dolomite mineralogy (~10%) (Fig. 6.3H), however it remains unclear if this is detrital, replacive, or forming as a primary precipitate. It is possible that detrital dolomite forms a surface that promotes dolomite precipitation, potentially in response to increases *in situ* temperature as dolomite kinetics are strongly temperature dependent (Gabellone and Whitaker, 2017). Previous work in coast Abu Dhabi suggests authigenic dolomite precipitates within the extra polymeric substances (EPS) associated with microbial mats (Bontognali *et al*., 2010), however there does not appear to be significantly more dolomite in the buried mat at Site 2 compared to the crystalline sediments (Fig. 6.3H). Future work investigating the nature and origin of dolomite at Site 2 may contribute to ongoing debate surrounding the 'dolomite problem' – the contradiction between abundant dolomite in the rock record, and limited examples of formation in modern environments.

Secondly, gypsum is absent from Site 1, and is abundant at Site 2 above ~22 cm (Fig. 6.3H), however the porewaters at both sites are undersaturated with respect to gypsum. This suggests that the gypsum may be residual from more restricted conditions in the lagoon associate with previous low stands (Lokier *et al*., 2015). Whitaker *et al*. (2014) characterised water chemistry throughout the Holocene siliciclastic-dominated sabkha of the upper ITZ and supratidal zone (STZ) in Qatar and found that the precipitation of diagenetic gypsum in the middle sabkha was driven by water table evaporation. However, the Abu Dhabi groundwaters remain gypsum undersaturated at winter near-surface temperatures and gypsum SI decreases with increasing summer temperature owing to Gypsum's

prograde solubility. Alternatively, sulphate reducing bacteria may reduce SO_4^{2-} concentrations, promoting gypsum undersaturation. SO_4^{2-}/Cl^- is significantly lower at Site 2 than Site 1, potentially suggesting SO_4^{2-} consumption by microbial communities, though this warrants further investigation.

Lastly, the sandy sediments at Site 1 are predominantly (>80%) aragonite, however the porewaters appear to be predominantly aragonite undersaturated, though close to equilibrium (Fig. 6.3C, 6.4B). At Site 2, the sediment below 22 cm has significant amounts of aragonite (~50%) and halite (~30%), however porewaters remain aragonite undersaturated below ~11 cm (Fig. 6.3H, 6.4B). The porewater SI_{arag} and SI_{calc} suggest that aragonite dissolution and calcite precipitation should be the dominant diagenetic pathways throughout the profile at Site 1 and below ~22 cm at Site 2, however this is not reflected in the sediment mineralogy (Fig. 6.3C, H).

Modern aragonite has Sr^{2+}/Ca^{2+} ratios approximately five times those of calcite (Joseph *et al*., 2013), and thus the dissolution of aragonite and reprecipitation as calcite would result in an increase in porewater Sr^{2+}. Using Cl^- as a conservative tracer for mixing between seawater and groundwater endmembers, the majority of porewaters in the upper ~12.5 cm at Site 1 appear to lie along the mixing trend between surface seawater and groundwater (Fig. 6.4D). However, porewaters below 12.5 cm at Site 1 appears slightly Sr^{2+} depleted, suggesting this may be an area of aragonite precipitation. Similarly, all but the deepest porewaters at Site 2 appear Sr^{2+} depleted, suggesting aragonite precipitation may be occurring in the upper ~35 cm.

Alkalinity at Site 1 is high relative to the alkalinity of seawaters, groundwaters, and porewaters at Site 2. Increased porewater alkalinity can be generated *via* the dissolution of carbonate minerals but is also a by-product of many microbial respiratory processes that promote carbonate precipitation (e.g., Soetaert *et al*., 2007). pCO_2 is particularly high at Site 1 and is a by-product of microbial respiratory processes that promotes the dissolution of carbonate minerals. Ammonium, another common by-product of many microbial metabolisms, is significantly higher at Site 1, than Site 2, however remains within the range of surface water NH_4^+ concentrations measured in the flood tide surface waters (Fig. 6.4D). Thus, porewaters at Sites 1 and 2 appear predominantly aragonite undersaturated, though show no significant evidence of aragonite dissolution. Future work investigating evidence of dissolution in the sediments and cements would be valuable.

6.5.2 Potential variations in early diagenesis in the ITZ in summer

The range of temperatures experienced in the shallow sediments of coastal Abu Dhabi's ITZ (~10 - 57 °C) may impact both the thermodynamics and kinetics of aragonite and calcite precipitation. Mean *in situ* temperatures were ~15 °C (Site 1) and ~16°C (Site 2) higher in summer than in winter. Such changes may cause seasonal variations in the precipitation and/or dissolution of authigenic carbonate minerals as the degree of carbonate mineral supersaturation and temperature are the two most significant

variables controlling the precipitation and composition of recent marine carbonate cements (Burton and Walter, 1987). If the porewater at 9.5 cm (Site 1) is warmed up from the winter *in situ* winter temperature (~18 °C) to the maximum summer *in situ* temperature (~40 °C), then the water could potentially precipitate ~60 µmol/l of aragonite.

Modelled carbonate system variables at summer *in situ* sediment temperatures suggests there is a marked change in SI_{arag} temporally and spatially at Site 1. The general effect of increased *in situ* temperature is that SI_{arag} increases, which is most pronounced at shallow (<20 cm) depth. In summer, porewaters at ~9.5 cm appear aragonite supersaturated, favouring aragonite precipitation, and possibly also at ~18.5 cm, which reaches aragonite equilibrium. This suggests that if a subsurface firmground were to form at Site 1, lithification may be favoured at two depths, separated by a zone less favourable to precipitation. This is reminiscent of the two layers of very early lithification at QLTC Site A (Chapter 5), potentially actively forming at two depth zones (~6-8 cm and ~9.5-12.5 cm) in association with a gastropod rich layer. Similarly, there are two more well-lithified layers at QLTC Site D (Chapter 5) currently occurring at ~13-16 cm and 17-20 cm, which display no evidence of active precipitation, nor dissolution of cements. This suggests that within the intertidal sediments, two separate (microbially mediated) zones exist that produce chemical by-products that promote carbonate precipitation, though these zones may only enter aragonite supersaturation in summer, driving a seasonal pattern to subsurface cementation. Alternatively, cementation may be favoured at one depth (likely ~9.5 cm) and the deeper firmground represents and older firmground, no longer actively forming.

However, during the summer period at Site 1, the model suggests that porewaters have a higher degree of calcite than aragonite supersaturation in the upper 20 cm. Thus, from a thermodynamic perspective, one would expect the most stable crystalline phase (calcite) to precipitate first from solutions that are supersaturated with respect to both calcite and the metastable aragonite phase. However, in laboratory experiments, Burton and Walter (1978) found that the precipitation rates of aragonite increased more strongly with increasing temperature and were less affected by changes in mineral SI compared to calcite. Experimental evidence found that at temperatures >5 °C, aragonite became increasingly more dominant compared to calcite regardless of the saturation state (if SI_{arag} was > 0), and aragonite precipitation rates were ~4 times faster than calcite at 37 °C, except at very low saturation states (Burton and Walter, 1978). Thus, mineral SI only becomes important when aragonite approaches equilibrium. Furthermore, a high molar ratio of porewater Mg/Ca can lower the rate of/inhibit calcite precipitation in favour of aragonite (Folk, 1974; Zhang and Dawe, 2000), with Mg/Ca ratios >2 favouring aragonite (Sun *et al*., 2015). High sulphate concentrations can lower the Mg/Ca threshold required to destabilise calcite in favour of aragonite, e.g., at 10 mM SO_4^{2-} a Mg/Ca ratio of 0.9 favours aragonite over calcite (Bots *et al*., 2011). Reaction rates can therefore vary

considerably with changes in temperature and brine geochemistry (Crockford *et al*., 2014) meaning that during summer, when $SI_{arag} > 0$, aragonite precipitation should be favoured over calcite at Sites 1 and 2 owing to kinetic factors such as the relatively high mean *in situ* temperatures (>32 °C), high porewater Mg/Ca ratios (5.8-10.2), and high sulphate concentrations (>50 mmol l^{-1}).

Nevertheless, even if aragonite precipitation occurs in summer when $SI_{arag} > 0$, one would expect the aragonite undersaturation to promote dissolution below ~20 cm in summer and throughout the sediment profile in winter. One possibility is that dissolution may become self-limiting as impurities such as aluminosilicate nano-complexes (Eisenlohr *et al*., 1999) or minor ions such as Sr^{2+} (Crockford *et al*., 2014) are released during early stages of mineral dissolution and become adsorbed onto mineral surface, preventing further dissolution. Therefore, if precipitation is favoured in summer, and dissolution prohibited, or limited in winter, this would produce a system that promotes the net production of authigenic aragonite. Another possibility is that the concentrations of H^+, Ca^{2+}, CO_3^{2-}, and HCO_3^- species in the bulk solution (i.e., that sampled by the Rhizons) may not be the same as those at the mineral surface (controlling rates of dissolution/precipitation) (Eisenlohr *et al*., 1999). In future studies, a combined methodology involving extracting porewaters with Rhizons (*in situ*) plus replicate porewater samples obtained *via* whole round squeezing and/or centrifugation of an adjacent core may help determine if preferential sampling from larger pore networks by Rhizons significantly impacts the porewater chemistry. Furthermore, future field campaigns in summer would provide a valuable insight into how the porewater chemistry changes seasonally as there may be significant changes in *p*H, alkalinity, and/or major ion concentrations that are not driven by changing temperature.

6.5.3 The impact of microbial respiration at different spatiotemporal scales

Precipitation of authigenic carbonate is generally attributed to a few metabolic pathways which produce alkalinity (Coleman and Raiswell, 1993) or drive a net increase in *p*H, such as organoclastic sulphate reduction (SR) with pyrite formation (Boudreau and Canfield, 1993; Plet *et al*., 2015), ammonification (Krause *et al*., 2018), Mn and Fe cycling, and AOM (Soetaert *et al*., 2007). Whilst dissolution is associated with aerobic respiration (Hu and Burdige, 2008), Fe and Mn oxidation (Soetaert *et al*. 2007) and SR (in low Fe environments) (Ben-Yaakov, 1973). Thus, precipitation and/or dissolution reactions in the subsurface are intimately linked to the microbial respiratory processes within the sediment column. However, we do not know which microbial communities inhabit the sediments at Site 1 and 2, nor how the community structures vary on seasonal or annual timescales. On a subtropical tidal flat (Taiwan) monthly net primary production (NPP) was highest during summer months during emersion (Lee *et al*., 2011) and some studies suggest metabolic activity increases in a broadly linear trend with increasing temperature (Lee *et al*., 2011; Hubas *et al*., 2006). Lee *et al*., (2011) found that benthic community production during emersion on a sub-tropical tidal flat increased 3.7 times when air temperature increased by 10°C (over range 15-30 °C). Similarly, Lin *et al*. (2020) found

that total respiration increased near linearly from 0-45 °C (East Asia), reaching a maximum at 49.5 °C. However, other workers suggest that each microorganism has an optimum temperature, above which metabolic activity decreases (Robador *et al*., 2016).

Diel temperature and tidal fluctuation influence photosynthetic activity at the surface (e.g., Lee *et al*., 2011), however experimental work on temperate intertidal mudflat sediments (France) suggests diel rhythms do not impact vertical microbial assemblages within the sediment column (Lavergne *et al*., 2018), though this warrants further investigation in sub(tropical) localities. Temporal, and spatial variations in community structure may occur due to gradients in salinity, temperature (Harrison and Phizacklea, 1983; Canion *et al*., 2014), oxygen, redox potential (Bertics and Zeibis, 2009), and OM supply (Kristensen, 2000) that vary with depth and time.

Three sets of controls have been suggested that may affect subsurface microbial community structure that operate on seasonal and/or shorter timescales in temperate locations. (1) seasonal variations in EPS production will not only increase *in situ* OM supply but also reduce permeability in summer months (Zetsche *et al*., 2011). (2) Strong tide/storm/wave action can suspend fine particles/EPS, and increase permeability (Zetsche *et al*., 2011) and reduce microbial diversity *via* physical transport, abrasion, and rapid fluctuations in O_2 and nutrient levels (Böer *et al*. 2009). (3) Temperature is an important control on rates of chemical and biological processes (Kristensen, 2000; Dale, 2006). Whilst simulations from this study suggest there may be a seasonal component to chemical drivers of authigenic carbonate precipitation and firmground formation, further investigation is needed to establish how the microbial communities in the subsurface (and thus the porewater chemical conditions) respond to these temporal controls, and to establish whether subsurface microbial communities in (sub)tropical settings respond to seasonal changes in hydrodynamics, EPS production, and temperature in similar ways to those in temperate locations. This study highlights the importance of capturing field data in multiple seasons.

Physical and biological sedimentary characteristics may also impact diagenesis on a range of scales. Large scale variations arise from differences in local/regional sediment characteristics and overlying seawater chemistry. On smaller scales bioturbation/bioirrigation influences OM supply, the distribution of solutes and dissolved gases (e.g., O_2) and reaction rate geometry (Kristensen, 2000), producing a complex 3D network of oxic/anoxic microenvironments on small (mm to cm scales). Future work investigating the role of burrowers in altering the *in situ* porewater chemistry in the ITZ sediments in Abu Dhabi and how this may be linked to firmground formation would be interesting.

6.5.4 Implications

Carbonate clumped isotopes thermometry is a palaeotemperature proxy based on the ordering of ^{13}C and ^{18}O bonds within the carbonate lattice (Eiler, 2011; Ghosh *et al*., 2006) commonly applied to

reconstruct Earth surface temperatures (Huntington *et al*., 2011; Henkes *et al*., 2018; Bajnai *et al*., 2020). Under thermodynamic equilibrium, the clumped isotopes signature of carbonates (Δ_{47}) is solely dependent on crystallisation temperature and is independent of the $\delta^{13}C$ signature of DIC and the $\delta^{18}O$ signature of the water within which the carbonate formed (Ghosh *et al*., 2006). However, kinetic factors may result in a departure from clumped isotope equilibrium (Loyd *et al*., 2016; Bajnai *et al*., 2020) and recent developments have proposed a dual approach to clumped isotope thermometry that can pinpoint and correct for dominant kinetic processes involved in carbonate (bio)mineralisation (Banjai *et al*., 2020).

Most studies assume that reconstructed temperatures based on carbonate clumped isotopes reflect mean palaeotemperatures (e.g., Ghosh *et al*., 2007). However, if precipitation is seasonal (e.g., favoured in summer as suggested in Qantur Lagoon, or favoured in winter in the case of whitings in the Bahamas (Purkis *et al*., 2017)), then reconstructions may provide significant over- or -under estimations of mean temperature. Similarly, pedogenic carbonates have typically been assumed to form at mean annual temperatures, however recent work suggests that preferential formation of pedogenic carbonates in warm seasons could impact the interpretation of palaeosol carbonate formation temperatures *via* clumped isotope thermometry (Peters *et al*., 2013; Kelson *et al*., 2020).

Δ_{47} reconstructions of carbonates from ancient shallow-water (e.g., shelf) settings often suggest formation temperatures >40 °C (e.g., Stopler and Eiler, 2016). This is typically considered too warm to reflect surface temperatures, and instead is thought to be the product of dissolution-reprecipitation reactions during burial diagenesis (Stopler *et al*., 2018). Stopler *et al*. (2018) applied a model to quantify the effect of dissolution-reprecipitation reactions on Δ_{47} and determined that whilst extensive recrystallization occurs in the upper 1 km of burial, the change in temperature over this distance is likely too small to significantly alter Δ_{47}. In contrast below 1 km, the impact of diagenesis on Δ_{47} is more apparent and may shift predicted temperature by >10 °C (Stopler *et al*., 2018). Results from coastal Abu Dhabi study suggest that subsurface shallow-water carbonate precipitation may be favoured during the summer at temperature ~40 °C, and thus Δ_{47} temperature reconstructions within this range may be possible prior to deeper (> 1km) burial diagenesis.

Whilst a seasonality in growth temperatures has been identified in coral clumped isotope signals (Ghosh *et al*., 2006), to our knowledge, this potential seasonal bias has not been previously identified in non-biogenic marine carbonate clumped isotope records. Thus, it is important to understand how seasonality (specifically temperature) drives carbonate precipitation in the modern environments, and where possible clumped isotope thermometry should consider timing of precipitation (Kelson *et al*., 2020).

6.5.5 Future directions

Future work assessing the diagenetic component of the sediments at Sites 1 and 2 (collected in Jan. 2019), looking for evidence of aragonite dissolution (or lack thereof) would be a logical next step. Rounded crystal edges and/or rough surface textures may suggest dissolution, whereas identification of platy and needle-like cements would suggest no dissolution. Microprobe analysis of diagenetic cements at Sites 1 and 2 would quantitatively determine mineralogy, and the application of secondary ion mass spectrometry (SIMS) to measure the carbon and oxygen isotopic signature of the cements and the allochems could provide valuable information into the origin of carbon. Highly negative $\delta^{13}C$ signatures of cements (~-25‰ to -50‰) may point to the incorporation of organic-derived carbon (by microbial decomposition, e.g., sulphate reduction) (Raiswell and Fisher, 2004), or the incorporation of CH_4 from AOM (Mavromatis *et al*., 2014).

Additionally, a laboratory experiment could be designed for existing core samples obtained from the January 2019 trip to test the heat capacity and transfer/ thermal inertia of the sediment by saturating cores and measuring the temperature difference at the top compared to the bottom. If results differ from those seen in the buried loggers, it suggests there may be more complex porewater circulation at play within the tidal flat environment.

If possible, sampling of sediments and porewater in summer months would provide quantitative evidence of whether the differences in porewater chemistries predicted with PHREEQC are reflected in measured concentrations. Whilst it may be impractical to obtain porewaters *in situ* (due to the increased time it takes in the field), it may be possible to extract cores and return them to the lab for porewater extraction, particularly for the most accessible (landward) sites, though caution and planning would be required when working in such high temperatures. Analysis of the sediments 16 SSU rRNA gene diversity (as a proxy for active microbial communities) at Sites 1 and 2 with depth, in both summer and winter would provide a valuable insight into which communities are involved increasing SI_{arag} and SI_{calc} at ~9.5 and 18.5 cm at Site 1, and whether such communities are temporally stable. Resampling of both sites over multiple years would contribute to the understanding of how temporally stable microbial communities are over multi-annual timescales.

Further development of the PHREEQC model to include aragonite kinetics may also provide valuable insights into temporal patterns of precipitation and/or dissolution. Additionally, further work is needed to test whether PHREEQC-Pitzer is capable of accurately representing this complex carbonate system. Future work combining the Pitzer model for calculating equilibrium constants for brines within the MyAMI model (Hain *et al*., 2015) and applying these constants to calculate carbonate variables within CO2SYS (Pelletier *et al*., 2007) may provide support for (or against) the application of the Pitzer model

in PHREEQC for representing mineral SI at high salinity and may aid in the development of improved methods for modelling brine geochemistry.

Furthermore, the application of deep time models to investigate what the seasonality of carbonate platforms looked like over longer time periods may provide valuable insights into the magnitude of authigenic carbon sequestration in carbonate platforms in the past. In the past, authigenic carbonate deposits played a significant role in the global carbon cycle, particularly during periods of widespread marine anoxia (Higgins *et al*., 2009) when they would have been a substantial carbon sink (Schrag *et al*., 2013). However, we do not know how the development of carbonate platforms at higher latitudes in the geological past (Kiessling *et al*. 2003) may have impacted carbonate sequestration, and what role, if any, seasonality may have played in determining the magnitude this potential carbon sink.

6.6 Conclusions

This preliminary study provides evidence that subsurface aragonite precipitation may be favoured in summer months over winter months, particularly in the upper 20 cm of sediment in the lower-to-middle ITZ. This may result in a seasonality to firmground formation in some locations in coastal Abu Dhabi, such as those detailed at QLTC (Chapter 5). Research in Abu Dhabi and other sub(tropical) carbonate platforms is biased to winter months, and this may result in the sampling of surface and porewater chemistries that are not reflective of the true annual variability. Whilst this study is a vast oversimplification and fails to capture seasonal variability in water chemistry driven by variations in benthic metabolisms (Hubas *et al*., 2006) and hydrodynamic variability (Chapter 4), it highlights the potential variability in mineral saturation driven by temperature alone, with the following conclusions:

1. At Site 1, in the lower-to-middle intertidal zone, aragonite precipitation appears to be favoured in summer months in the upper ~20 cm of sediment, but most significantly at ~9.5 ±3 cm.
2. Lithification appears to be favoured at this depth (9.5 cm) elsewhere within the lower-to-middle intertidal zone of Qantur Lagoon, e.g., evidence of early lithification at Site A (QLTC) and at the upper firmgrounds surface observed at Site B at QLTC (Chapter 5). This may suggest that the combined effect of increased mineral saturation *via* microbial metabolic processes, in conjunction with high *in situ* temperatures promotes firmground formation in summer months at this depth.
3. However, SI_{arag} appears to remain undersaturated below 20 cm throughout the year despite having a predominantly aragonitic sediment mineralogy. This suggests that *in situ* temperature alone cannot account for the discrepancy between modelled porewater chemistry (based on specifications assumed by PHREEQC 's Pitzer database) and sediment mineralogy at Site 1.
4. At Site 2, aragonite was most supersaturated at the sediment surface and decreased with depth to ~11 cm where they reach equilibrium. However, this depth did not correspond with

significant amounts of aragonitic sediment, suggesting the chemistry at Site 2 would not support the development of a subsurface firmground.

7. Conclusions, implications, and future work

7.1 Main conclusions

This study provides the first comprehensive analysis of physical, chemical, and biological drivers of modern firmground formation within shallow intertidal lagoonal sediments. Despite extensive literature on hiatal-hardground and ancient carbonate concretion/nodule formation, investigation into the microbial drivers of biologically influenced carbonate mineralisation of firmgrounds is limited and few studies investigate such processes in areas with a low CH_4 diffusive flux. This study addresses some of these knowledge gaps by interpreting modern firmground formation in relation to biogeochemical processes within the sediment and porewaters of two coastal lagoons in Abu Dhabi with varying degrees of restriction and hydrodynamic complexity.

In Yas lagoon (Chapter 3), the semi-lithified firmground was concluded to be actively forming ~6-11 cm below the sediment surface *via* the precipitation of platy aragonite on the lower firmground surface. Findings point toward the development of a positive feedback system whereby the firmground forms a redox boundary which may act to stabilise the sedimentary environment by limiting fluid exchange and maintaining anoxic conditions below the firmground. This in turn supports the development of slow growing anaerobic microbial communities which create a chemical environment promoting cementation and porosity occlusion, which further limits oxygen exchange. Immediately below the firmground, increased saturation indices (SI) occurred in a narrow (<2 cm) interval of elevated porewater *p*H and low bicarbonate alkalinity. The few cm below the firmground showed evidence of sulphate depletion and an abundance of archaeal Marine Benthic Group D (*Thermoprofundales*) in association with known sulphate-reducing bacteria and rare archaeal taxa. These groups are likely involved in sulphate reduction which, in conjunction with pyrite formation, could drive aragonite supersaturation and firmground formation. Additionally, Fe/Mn-oxide reduction may drive increased *p*H and precipitation of carbonate cements to drive cementation on the upper firmground surface.

Evidence from Yas Lagoon supports the theory of subsurface firmground formation driven primarily by microbial processes within the sediment. However, this study represents only one location, during one period (Oct. 2017), and thus the extent to which microbial processes drive subsurface cementation in the region remains unknown. This theory is also contradictory to the long-standing view that hardgrounds form at the sediment-water interface *via* abiotic processes such as bottom water carbonate supersaturation and seawater circulation (Christ *et al*., 2015); low sedimentation rate or hiatus in sedimentation (Lash and Blood, 2004); and elevated hydrodynamic activity (Dravis, 1979; Lighty, 1985). To test whether firmgrounds were forming in the subsurface by microbial processes elsewhere in Abu Dhabi, firmground formation was investigated at several locations within a second, more hydrodynamically complex coastal lagoon, which links to recent work identifying numerous

concretionary features in the shallow intertidal sediments of coastal Abu Dhabi (Ge *et al*., 2020a, 2020b).

Well-developed firmgrounds (relative to the Yas Lagoon firmground) were observed at several sub-sites within a short distance (<10 m) of a tidal creek in Qantur Lagoon (QLTC), with the upper firmground surfaces located ~8-12.5 cm below the sediment surface. However, the QLTC site was more hydrodynamically complex compared to Yas Lagoon and the nature of cementation was more variable, thus interpretation of firmground formation needed to be set into the wider context of hydrodynamic variability in the intertidal zone (ITZ). Chapter 4 aimed to better constrain the influence of hydrodynamics (changes in seawater and porewater chemistry controlled by tidal-, wave-, and current-driven circulation) on sediment production/accumulation as well as to investigate what impact this may have on diagenesis in the shallow porewaters in the ITZ. Results from Chapter 4 support the finding of Court *et al*. (2017) and concluded that the occurrence of different surface facies across the intertidal-supratidal zone are likely controlled by the duration of tidal flooding and annual tidal ranges. However, unlike Court *et al*. (2017), Chapter 4 applied hydrodynamic monitoring over one year to link the surface facies to the percentage of time flooded annually, and suggested revised boundaries for the lower, middle, and upper ITZ which would have been flooded >20%, 4-20% and 1.5-4% of the time per year, respectively.

Daytime flood tides travelling across the microbial mats of the middle ITZ increase in *p*H due to the consumption of CO_2 by surficial microphytobenthos, which increases carbonate mineral SI potentially promoting the precipitation of carbonate minerals. Daytime ebb tides flowing back down the ITZ from the microbial mats of the middle to upper ITZ and may drive the precipitation of aragonite in the lower ITZ by supplying highly supersaturated water. This may be most significant surrounding tidal creek networks that act as foci for drainage of waters from the upper ITZ to the lower ITZ.

The four QLTC sub-sites (A-D) presented in Chapter 5 were typically more well-lithified and occurred slightly deeper compared to the firmground in Yas Lagoon. Cement crystal morphology of the QLTC firmgrounds included platy aragonite crystals, as seen in the Yas Lagoon firmground, though typically contained more bladed and acicular aragonite crystal morphologies. Site A (~1 m east of the creek) had no visible firmground, however CT-scan analysis suggests there may be two separate horizons at ~6-8 cm and ~9.5-12.5 cm showing signs of early cementation. However, as the carbonate chemistry of porewaters obtained from the core at this site was likely impacted by degassing (see methods summary below), further work is needed to corroborate active precipitation. Site B (within the creek) had a firmground at ~8-13 cm below the surface and like Yas Lagoon, there was a slight decrease in alkalinity and increase in *p*H at ~7 cm, suggesting active carbonate precipitation may be occurring above the firmground, and that precipitation is driven by a process that increases porewater *p*H. The final two QLTC sites (C and D) (~6 m and 10 m east of the creek respectively) exhibited one and two

subsurface firmground respectively, at ~11-15 cm (Site C) and ~12.5-16 cm and ~17-21 cm (Site D). However, unlike the firmgrounds at Site B and in Yas Lagoon, there was no significant increase in saturation indices, alkalinity, or *p*H surrounding the firmground, suggesting they may no longer be actively forming.

If the early signs of cementation at Site A are the precursor to a firmground, this would confirm evidence from Yas that suggests cementation can initiate in the subsurface. Additionally, if the firmground at Site B is actively forming, this may be linked to microbial processes relating to the depth of the redox boundary, as in Yas Lagoon. Analysis of 16 SSU genes diversity at Sites A and B found the upper ~10 cm of sediment host to a range of microbial communities, including abundant sulphate reducing microbes (SRM), and other communities potentially involved in the cycling of nitrogen (N) and metal oxides. This points to the involvement of sulphate reduction and Fe/Mn-oxide reduction in promoting carbonate precipitation at Sites A and B. The formation of pyrite framboids within the firmgrounds provides a pathway for the effective removal of H_2S (by-product of SR), producing a chemical environment favourable to carbonate precipitation. Below ~15 cm there was an increase in microbial communities associated with stressed environments and recalcitrant organic matter. This may be linked to the developing firmground which acts as a permeability baffle, causing porewater chemistries below ~15 cm to be more impacted by the leakage of continental brines than the downward diffusion/advection/bioirrigation of seawater.

Though the limited data presented for Site A and B supports a 'Yas Lagoon' model of firmground formation at QLTC, abiotic processes such as the circulation of supersaturated seawaters cannot be ruled out, though one would expect this to drive cementation at the surface which is not observed. Future work resampling the porewaters *in situ* at Site A and Site B would be valuable to ascertain if firmgrounds are actively forming in the subsurface. The higher degree of lithification of the firmgrounds at Sites B, C, and D suggest these firmgrounds may be older than those in Yas Lagoon and in the case of Site C and D, may no longer be actively forming due to increased sedimentation. However, there is no evidence in the porewater chemistry to suggest a new firmground would begin to form at Sites C and D at shallower depth, though this warrants further investigation. Alternatively, increased lithification may have prevented the flux of water from above or below the firmground, which may be important for providing dissolved species for certain microbial respiratory processes. The observation of two well-developed firmgrounds (Site D) and early evidence of two cemented intervals at Site A, suggest that two separate but synchronous processes may promote cementation at some locations. Alternatively, the deeper cemented layer may represent cementation by the same processes as the shallower layer prior to burial (asynchronous cementation), though this requires further investigation.

One of the most surprising observations at the QLTC sub-sites (and to a lesser degree Yas Lagoon), was that porewaters were predominantly aragonite undersaturated, though sediments and firmgrounds were aragonitic. This suggests that either the thermodynamic model (PHREEQC-Pitzer) employed to calculate carbonate chemistry is inadequate for these complex brines (Chapter 2.1), or that the porewaters sampled in winter truly were aragonite undersaturated. A possible explanation for this contradiction is that field work undertaken in winter may not capture the true variability of porewater chemistry experienced throughout the year. We hypothesised that because of the retrograde solubility of carbonate minerals as well as the positive effect of temperature on biological activity, in warmer months porewaters may become supersaturated with respect to aragonite at certain depths.

One major limitation of the studies presented in Chapter 3 and 5 is that field work was only conducted in winter, as is often the case in (sub)tropical carbonate depositional settings such as Abu Dhabi where summer temperatures can exceed 50 °C. In Chapter 4, we investigated the hydrodynamic variability of the ITZ, and found that whilst astronomical tides (e.g., springs and neaps) are largely responsible for variability in coastal water level, seasonal forcing such as low atmospheric pressure are likely responsible for promoting higher water levels across the ITZ in summer. This accords with the observation of increased salinity in the lagoon channel in summer, likely reflecting the combined effect of the higher summer water levels travelling further inland and dissolving more surface salts, and possibly due to increased evaporation across the ITZ leaving more surface salts and brine pools behind compared to winter months.

Whilst Chapter 4 highlighted how seasonal variability may impact surface water chemistry, it remains unclear what impact changing sediment *in situ* temperatures would have on porewater SI. Chapter 6 aimed to investigate this gap in knowledge by testing the hypothesis that increased *in situ* sediment temperature in summer may promote subsurface carbonate precipitation at specific depths (likely linked to microbial respiratory processes) by thermodynamically increasing carbonate mineral SI. To investigate this, shallow porewater chemistry profiles (~30 cm) (samples collected in winter) were modelled over a range of annual *in situ* temperatures measured with subsurface loggers (*in situ* for 1.25 years), with a focus on comparing a winter and summer period. This method investigated the potential role that seasonal temperature variability plays on the thermodynamics of carbonate diagenesis. Whilst this approach is a vast oversimplification and fails to account for the role of kinetics in carbonate precipitation/dissolution, or seasonal variations in microbial metabolisms or porewater chemistry (e.g., pH, alkalinity, dissolved organic carbon (DOC)), it does highlight the potential thermodynamic implications of increased *in situ* summer temperatures on diagenesis.

Aragonite precipitation appeared to be favoured in the summer months in the upper ~20 cm of sediment, but most significantly at ~9.5 cm at Site 1. The location of Site 1 (Chapter 6) was comparable to the location of QLTC (Chapter 5), as both sites had ~30 cm of sediment overlying the basal

hardground and were situated down-dip of the microbial mats in the lower to middle ITZ. Thus, lithification appeared to be favoured at Site 1 at roughly the same depth as the subsurface firmgrounds were observed at QLTC. This may suggest that the combined effect of increased mineral saturation *via* microbial metabolic processes, in conjunction with high *in situ* temperatures (and the likely effect of kinetic processes inhibiting dissolution in winter) promotes firmground formation in summer months at this depth. We hypothesis that the lack of firmground at Site 1 may reflect increased mobility of the sediments and/or that sediments have accumulated more recently compared to QLTC and thus cementation is yet to imprint a noticeable change on the sediments, though this warrants further investigation.

7.2 Methodological conclusions

This study also highlighted potential issues with current methodologies involving the application of Rhizon porewater samplers by traditional methods (insertion into an extracted core), and with commonly used thermodynamic models for modelling carbonate chemistry across a broad range of salinities (from seawater to brine) (Chapter 2).

Rhizon porewater samplers provide a host of benefits over alternative porewater recovery methods; they allow high resolution porewater sampling that is cost effective, non-destructive, and provides instant filtration. However, Rhizons are associated with two main disadvantages over whole round squeezing and centrifugation; (i) they are likely to preferentially draw water from the largest pore network, which may not be representative of the entire pore-network; and (ii) degassing is likely more pronounced in Rhizons (compared to centrifugation) as minute bubbles of entrained gas to coalesce when passing through the porous tip. Comparison between the traditional methods of porewater extraction from sediment cores and the insertion of Rhizons directly into the sediment (*in situ*) (Chapter 2.1) showed that degassing was minimised when porewaters were extracted *in situ*. This was primarily due to the fact that *in situ* sampling provided larger sample volumes in shorter times, which reduced the amount of time samples spent under vacuum and within plastic syringes and enabled fast analysis of chemical properties sensitive to degassing. Additionally, gradually increasing the size of the wooden stoppers used to create the vacuum in the syringe maintained a low and constant (quasistatic) force exerted by the vacuum as the water was being extracted, reducing bubbling and degassing in the tubes and syringe headspace. This method may provide benefits for porewater extraction from both *in situ* sites and sediment cores. Whilst the *in situ* application of Rhizons appeared to reduce the effects of degassing, it remains unclear how this compares with alternative methods. Further investigation into variations in the carbonate chemistry when comparing whole round squeezing and centrifugation with *in situ* porewater extraction with Rhizon would be valuable.

To investigate drivers of marine carbonate precipitation numerically we must be able to accurately represent the marine carbonate system. However, the seawaters, porewaters, and groundwaters presented in this study span a large salinity range (~35-205‰). Chapter 2.2. compared CO2SYS which is widely used for modelling modern seawater (Naviaux *et al*., 2019) and several PHREEQC databases, including Pitzer which is considered the best model for solutions with high ionic strength (Harvie and Wear, 1980; Clegg and Whitfield, 1991). Chapter 2.2 concluded that CO2SYS was more able to accurately calculate carbonate speciation than PHREEQC for seawater-like solutions, and thus was applied for surface seawaters. However, the K_1 and K_2 constants employed in CO2SYS are not recommended for salinity >43 psu and our results suggest that the benefits of CO2SYS over PHREEQC may only be suitable for salinities ≤56‰. Above this threshold the application of CO2SYS is limited and becomes increasingly erroneous with increasing salinity. Thus, for Abu Dhabi coastal waters with salinity was >56‰, PHREEQC-Pitzer was used. This analysis highlights the limitations of applying the most common thermodynamic models to waters that deviate significantly from modern seawater compositions.

7.3 Research implications

Chapters 4 and 6 highlight the importance of setting porewater, sediment, and microbial data collected in winter in the context of seasonal temperature and salinity variability when interpreting drivers of carbonate diagenesis. Chapters 4 and 6 also highlight the importance of gathering water chemistry data from 'off-seasons' in locations that experience a seasonal bias to field sampling.

Within the geologic record, hardgrounds are often assumed to form at the sediment-water interface and are used to distinguish hiatuses in sedimentation and/or changes in sea level, acting as stratigraphic indicators (Christ *et al*., 2015). However, this study shows that cementation may rely on processes operating beneath the surface, within the shallow sediment column. Further investigation into potential biosignatures of hardgrounds formed by biologically-influenced subsurface precipitation could identify distinguishing features to avoid their erroneous identification as 'classic' hiatal hardgrounds.

Authigenic carbonates have been identified as important indicators of palaeoenvironmental conditions (Plet *et al*., 2016), but direct interpretation of these palaeo-proxies is challenging without a comprehensive understanding of the drivers of precipitation. Results from Chapter 3 and 5 suggest firmgrounds (which may later become hardgrounds) can form in the subsurface *via* microbially mediated processes (e.g., sulphate reduction) which may have implications for interpreting similar features in the geologic record. It is also important to understand how seasonality (specifically temperature) drives carbonate precipitation in the modern environments, and where possible

clumped isotope thermometry should consider timing of precipitation when interpreting palaeotemperatures from similar features (Chapter 6).

Hardgrounds also form barriers or baffles to fluid flow (Manchini *et al*., 2004). Their lateral continuity and spatial variations thus have important implications for platform- and/or basin-wide correlation in sequence stratigraphy and for the effective utilisation of both groundwater and hydrocarbon resources (Agar & Geiger, 2015). Reactive transport models have been increasingly applied to understand and predict changes in depositional properties that result from early diagenesis and infer reservoir properties (Whitaker and Frazer, 2018). However, to confidently apply such process-based models, there is a need for evaluation with reference to hydrological and biogeochemical data from modern environments such as Yas and Qantur Lagoon.

Additionally, the 16 SSU gene diversity presented in Chapters 3 and 5 contributes information on the composition and distribution of bacterial and archaeal communities in an intertidal coastal sub-tropical lagoon alongside porewater and sedimentary chemical profiles. Some communities (e.g., SEEP-SR1) identified in the shallow coastal sediments are typically associated with deep sea settings, and others (e.g., *Aminicenantes*) form a significantly larger relative abundance of the microbial population compared to most studied locations. This highlights the potential benefits of coastal Abu Dhabi sediments for future studies investigating these poorly understood microbial communities. Comparing community composition with porewater and sediment chemistry provides valuable insight into the potential metabolic roles that microbial communities play on biogeochemical cycles within coastal lagoon sedimentary ecosystems. This is important for advancing our understanding on global nutrient cycles, the carbon cycle and specifically carbon sequestration *via* authigenic carbonate precipitation.

7.4 Future work

This study presents evidence for the subsurface formation of marine firmgrounds in relation to microbial metabolic processes (e.g., sulphate reduction, and possibly localised Fe/Mn-oxide reduction and AOM) and highlights the potential role of increased *in situ* temperatures in promoting cementation in summer. However, there are several areas that could be expanded upon and thus the following recommendations are provided as areas for future research:

1. Whilst the cement mineralogy of firmground cements in Yas Lagoon were quantitatively determined to be aragonite *via* electron backscattered diffraction (EBSD), the same was not possible for the QLTC cements. Although QLTC cement morphology appears aragonitic (needle-like crystals), ideally cement mineralogy should be quantitatively determined. This would also help establish if the firmgrounds at Site C and D (QLTC) show evidence of early alteration from aragonite to calcite, as suggested by the porewater chemistry. Early marine

diagenesis can drive changes in porosity and permeability *via* the precipitation, dissolution, or stabilization of authigenic minerals, which provide a template influencing subsequent fluid flow and alteration from early to late burial diagenesis. The morphology, size, and texture of diagenetic calcite crystals affects key petrophysical properties. Recent work suggests that generation of microporosity (derived from the calcite microcrystal texture) is driven not by dissolution-reprecipitation reactions during burial diagenesis but is inherited from the precursor sediment (Deville de Periere, 2011). However, the extent to which early marine dissolution/reprecipitation influences microporosity development requires further attention.

2. The isotopic signature of authigenic carbonates is commonly used to infer metabolic origin (Irwin *et al*., 1977). Whilst $\delta^{13}C$ and $\delta^{18}O$ were determined on bulk sediments from Yas Lagoon, values likely reflect the isotopic signature of the allochems and not the cement, which constitutes only a minor fraction of the bulk sample. Future work targeting the cement crystal rims of firmgrounds from Yas Lagoon and QLTC for isotopic analysis via secondary ion mass spectrometry (SIMS) would provide targeted analysis of cement isotopic signature. This would provide valuable insight into metabolic drivers with mid-range $\delta^{13}C$ (~-25‰) values indicative of organic-derived carbon (e.g., sulphate reduction) (Irwin *et al*., 1977), and lighter values (<-50‰) indicative of AOM (Mavromatis *et al*., 2014).
3. Comparisons between porewater chemistry and microbial community structure (based on 16 SU gene diversity) have been used to infer potential metabolic pathways involved in driving firmground formation. However, a correlation matrix and principal component analysis (PCA) could provide a more robust insight into the strength of these potential correlations. his approach would be most useful with a broader suite of samples and would preferably incorporate a time component should future field campaigns obtain samples in summer.
4. It remains unclear if Fe and/or Mn metabolism are important drivers of the alkalinity engine in Yas Lagoon and surrounding QLTC. Future work investigating sedimentary Mn and Fe in Yas lagoon and porewater Fe and Mn in QLTC would be valuable.
5. Extracellular polymeric substances (EPS) were observed in association with firmground cements in Yas Lagoon, QLTC, and elsewhere in coastal Abu Dhabi by other workers (e.g., Ge *et al*., 2020a). EPS can impact precipitation and dissolution of carbonate minerals in a number of ways; (i) they can act as catalysts or nucleation sites by providing a charged surface onto which ions can bind (Dupraz *et al*., 2009); (ii) aid in physically binding the sediments together; (iii) have the capacity to bind large quantities of Ca^{2+}, which has an inhibitory effect on carbonate precipitation (Braissant *et al*., 2007; Pace *et al*., 2018); and (iv) the heterotrophic degradation of EPS (e.g., by SRM) can release Ca^{2+}, allowing for carbonate nucleation (Dupraz *et al*., 2013). Whilst the role of EPS in driving firmground formation was not the focus of this study, observational evidence suggest that EPS may play an important role in firmground

formation, and warrants a targeted study assessing the role of EPS in driving diagenesis in coastal Abu Dhabi.

6. One of the primary limitations in Chapter 5 was the incompleteness of data sets from the four subsites. Site A and B presented some evidence to support subsurface cementation, however the porewater chemistry from Site A (collected from the core) may have been impacted by degassing, and alkalinity was not measured below the firmground at Site B. Future work targeting these sites would be valuable to ascertain if subsurface cementation is actively occurring around the tidal creek at QLTC.
7. A second key limitation was that sampling was only conducted in winter. Chapter 6 highlighted the potential thermodynamic implications of increased summer *in situ* sediment temperature of mineral SI. However, the methods employed in Chapter 6 only accounted for temperature driven changes, and made many assumptions (e.g., porewater chemistry remaining constant throughout the year) that are unlikely to be true. If possible, a summer field campaign could help validate these predictions and would enable the investigation of how the porewater chemistry may change annually in relation to changing temperature, organic matter supply, and microbial respiratory processes.
8. Future work investigating the application of the MyAMI model (Hain *et al*., 2015) to calculating the equilibrium constants for brines would be a valuable next step, though further amendments (*sensu* Naviaux *et al*., 2019) may need to be implemented to account for the complexity of modelling brine geochemistry. Furthermore, inclusion of kinetics within models could prove valuable for assessing changes in aragonite and calcite SI, particularly given the likely importance of kinetic factors (e.g., high Mg/Ca ration, high sulphate, and high temperature) in promoting aragonite over calcite precipitation in coastal Abu Dhabi.

These future research directions provide examples of the exciting research potential in coastal Abu Dhabi, specifically relating to the chemical, physical, and biological drivers of early diagenesis, and areas where model and methodological development could be beneficial. This study highlights the interplay of spatiotemporal complexities and processes driving early marine carbonate diagenesis in coastal Abu Dhabi.

Reference list

Afshar-Kaveh, N., Nazarali, M. and Pattiaratchi, C. (2020). Relationship between the Persian Gulf Sea-Level Fluctuations and Meteorological Forcing. *Journal of Marine Science and Engineering,* 8(4). DOI: 10.3390/jmse8040285.

Agar, S. M. and Geiger, S. (2015). Fundamental controls on fluid flow in carbonates: current workflows to emerging technologies. *Geological Society, London, Special Publications,* 406(1): 1. DOI: 10.1144/SP406.18.

Aghib, F. S., Bernoulli, D. and Weissert, H. (1991). Hardground formation in the Bannock Basin, Eastern Mediterranean. *Marine Geology,* 100(1): 103-113. DOI: https://doi.org/10.1016/0025-3227(91)90227-U.

Agogué, H., Hugoni, M., Dupuy, C. and Lavergne, C. (2015). C3 group: a rare but active Thaumarchaeal group in intertidal muddy sediment.

Ahm, A.-S. C., Bjerrum, C. J., Blättler, C. L., Swart, P. K. and Higgins, J. A. (2018). Quantifying early marine diagenesis in shallow-water carbonate sediments. *Geochimica et Cosmochimica Acta,* 236: 140-159. DOI: 10.1016/j.gca.2018.02.042.

Akam, S. A., Coffin, R. B., Abdulla, H. A. N. and Lyons, T. W. (2020). Dissolved Inorganic Carbon Pump in Methane-Charged Shallow Marine Sediments: State of the Art and New Model Perspectives. *Frontiers in Marine Science,* 7. DOI: 10.3389/fmars.2020.00206.

Al Disi, Z. A., Zouari, N., Dittrich, M., Jaoua, S., Al-Kuwari, H. A. S. and Bontognali, T. R. R. (2019). Characterization of the extracellular polymeric substances (EPS) of Virgibacillus strains capable of mediating the formation of high Mg-calcite and protodolomite. *Marine Chemistry,* 216: 103693. DOI: https://doi.org/10.1016/j.marchem.2019.103693.

Algeo, T. J. and Li, C. (2020). Redox classification and calibration of redox thresholds in sedimentary systems. *Geochimica et Cosmochimica Acta,* 287: 8-26. DOI: 10.1016/j.gca.2020.01.055.

Almstrand, R., Pinto, A. J., Figueroa, L. A. and Sharp, J. O. (2016). Draft Genome Sequence of a Novel Desulfobacteraceae Member from a Sulfate-Reducing Bioreactor Metagenome. *Genome Announc,* 4(1). DOI: 10.1128/genomeA.01540-15.

Alsharhan, A. S. and Kendall, C. G. S. C. (2003). Holocene coastal carbonates and evaporites of the southern Arabian Gulf and their ancient analogues. *Earth-Science Reviews,* 61(3): 191-243. DOI: https://doi.org/10.1016/S0012-8252(02)00110-1.

Andreote, F. D., Jimenez, D. J., Chaves, D., Dias, A. C., Luvizotto, D. M., Dini-Andreote, F., Fasanella, C. C., Lopez, M. V., Baena, S., Taketani, R. G. and de Melo, I. S. (2012). The microbiome of Brazilian mangrove sediments as revealed by metagenomics. *PLoS One,* 7(6): e38600. DOI: 10.1371/journal.pone.0038600.

Andronico, D., Scollo, S., Cristaldi, A. and Ferrari, F. (2009). Monitoring ash emission episodes at Mt. Etna: The 16 November 2006 case study. *Journal of Volcanology and Geothermal Research,* 180(2): 123-134. DOI: https://doi.org/10.1016/j.jvolgeores.2008.10.019.

Appelo, C. A. J. and Postma, D. (1994). Geochemistry, groundwater, and pollution. Rotterdam, CRC Press.

Arndt, S., Jørgensen, B. B., LaRowe, D. E., Middelburg, J. J., Pancost, R. D. and Regnier, P. (2013). Quantifying the degradation of organic matter in marine sediments: A review and synthesis. *Earth-Science Reviews,* 123: 53-86. DOI: 10.1016/j.earscirev.2013.02.008.

Arvidson, R. and Mackenzie, F. (1999). The dolomite problem: Control of precipitation kinetics by temperature and saturation state. *American Journal of Science,* 299: 257-288. DOI: 10.2475/ajs.299.4.257.

Asaoka, S., Jadoon, W. A., Umehara, A., Takeda, K., Otani, S., Ohno, M., Fujitake, N., Sakugawa, H. and Okamura, H. (2020). Organic matter degradation characteristics of coastal marine sediments collected from the Seto Inland Sea, Japan. *Marine Chemistry,* 225: 103854. DOI: https://doi.org/10.1016/j.marchem.2020.103854.

Bádenas, B. and Aurell, M. (2008). Kimmeridgian epeiric sea deposits of north-eastern Spain: Sedimentary dynamics of a storm-dominated carbonate ramp.

Bajnai, D., Guo, W., Spötl, C., Coplen, T. B., Methner, K., Löffler, N., Krsnik, E., Gischler, E., Hansen, M., Henkel, D., Price, G. D., Raddatz, J., Scholz, D. and Fiebig, J. (2020). Dual clumped isotope thermometry resolves kinetic biases in carbonate formation temperatures. *Nature Communications,* 11(1): 4005. DOI: 10.1038/s41467-020-17501-0.

Banner, J. L. and Hanson, G. N. (1990). Calculation of simultaneous isotopic and trace element variations during water-rock interaction with applications to carbonate diagenesis. *Geochimica et Cosmochimica Acta,* 54(11): 3123-3137. DOI: https://doi.org/10.1016/0016-7037(90)90128-8.

Barker, S. and Ridgwell, A. (2012). Ocean Acidification. *Nature Education Knowledge,* 3: 21.

Bathurst, R. G. C. (1971). Carbonate sediments and their diagenesis. Amsterdam, Elsevier.

Bathurst, R. G. C. (1980). Stromatactis—Origin related to submarine-cemented crusts in Palaeozoic mud mounds. *Geology,* 8(3): 131-134. DOI: 10.1130/0091-7613(1980)8.

Baumgartner, L. K., Reid, R. P., Dupraz, C., Decho, A. W., Buckley, D. H., Spear, J. R., Przekop, K. M. and Visscher, P. T. (2006). Sulfate reducing bacteria in microbial mats: Changing paradigms, new discoveries. *Sedimentary Geology,* 185(3-4): 131-145. DOI: 10.1016/j.sedgeo.2005.12.008.

Bearup, D. and Blasius, B. (2017). Ecotone formation induced by the effects of tidal flooding: A conceptual model of the mud flat-coastal wetland ecosystem. *Ecological Complexity,* 32: 217-227. DOI: https://doi.org/10.1016/j.ecocom.2016.11.005.

Beck, M., Dellwig, O., Holstein, J. M., Grunwald, M., Liebezeit, G., Schnetger, B. and Brumsack, H.-J. (2008). Sulphate, dissolved organic carbon, nutrients and terminal metabolic products in deep pore waters of an intertidal flat. *Biogeochemistry,* 89(2): 221-238. DOI: 10.1007/s10533-008-9215-6.

Beck, M., Köster, J., Engelen, B., Holstein, J. M., Gittel, A., Könneke, M., Riedel, T., Wirtz, K., Cypionka, H., Rullkötter, J. and Brumsack, H.-J. (2009). Deep pore water profiles reflect enhanced microbial activity towards tidal flat margins. *Ocean Dynamics,* 59(2): 371-383. DOI: 10.1007/s10236-008-0176-z.

Beck, M., Reckhardt, A., Amelsberg, J., Bartholomä, A., Brumsack, H.-J., Cypionka, H., Dittmar, T., Engelen, B., Greskowiak, J., Hillebrand, H., Holtappels, M., Neuholz, R., Köster, J., Kuypers, M. M. M., Massmann, G., Meier, D., Niggemann, J., Paffrath, R., Pahnke, K., Rovo, S., Striebel, M., Vandieken, V., Wehrmann, A. and Zielinski, O. (2017). The drivers of biogeochemistry in beach ecosystems: A cross-shore transect from the dunes to the low-water line. *Marine Chemistry,* 190: 35-50. DOI: https://doi.org/10.1016/j.marchem.2017.01.001.

Ben-Yaakov, S. (1973). pH buffering of pore water of recent anoxic marine sediments. *Limnology and Oceanography,* 18(1): 86-94. DOI: 10.4319/lo.1973.18.1.0086.

Bergmann, K. D., Grotzinger, J. P. and Fischer, W. W. (2013). Biological Influences on Seafloor Carbonate Precipitation. *Palaios,* 28(2): 99-115. DOI: 10.2110/palo.2012.p12-088r.

Berner, R. A. (1975). The role of magnesium in the crystal growth of calcite and aragonite from sea water. *Geochemica et Cosmochimica Acta,* 39: 489-504.

Berner, R. A., Scott, M. R. and Thomlinson, C. (1970). Carbonate alkalinity in the pore waters of anoxic marine sediments. *Limnol. Oceanogr.,* 15: 544-549.

Berner, R. A., Westrich, J. T., Graber, R., Smith, J. and Martens, C. S. (1978). Inhibition of aragonite precipitation from supersaturated seawater; a laboratory and field study. *American Journal of Science,* 278(6): 816-837. DOI: 10.2475/ajs.278.6.816.

Bertics, V. J. and Ziebis, W. (2009). Biodiversity of benthic microbial communities in bioturbated coastal sediments is controlled by geochemical microniches. *ISME J,* 3(11): 1269-1285. DOI: 10.1038/ismej.2009.62.

Bertics, V. J. and Ziebis, W. (2010). Bioturbation and the role of microniches for sulfate reduction in coastal marine sediments. *Environmental Microbiology,* 12(11): 3022-3034. DOI: https://doi.org/10.1111/j.1462-2920.2010.02279.x.

Bhupinderpal-Singh, Hedley, M. J. and Saggar, S. (2005). In situ dynamics of recently allocated 14C in pasture soil and soil solution collected with Rhizon Soil Moisture Samplers. *Soil Research,* 43(5): 659-666. DOI: https://doi.org/10.1071/SR04107.

Bianchi, T. S. (2007). Biogeochemistry of Estuaries. New York, NY, USA, Oxford University Press.

Biddle, J. F., Lipp, J. S., Lever, M. A., Lloyd, K. G., Sørensen, K. B., Anderson, R., Fredricks, H. F., Elvert, M., Kelly, T. J., Schrag, D. P., Sogin, M. L., Brenchley, J. E., Teske, A., House, C. H. and Hinrichs, K.-U. (2006). Heterotrophic Archaea dominate sedimentary subsurface ecosystems off Peru. *Proceedings of the National Academy of Sciences of the United States of America,* 103(10): 3846-3851. DOI: 10.1073/pnas.0600035103.

Billerbeck, M., Werner, U., Bosselmann, K., Walpersdorf, E. and Huettel, M. (2006). Nutrient release from an exposed intertidal sand flat. *Marine Ecology Progress Series,* 316: 35-51. DOI: 10.3354/meps316035.

Bischoff, J. L., Greer, R. E. and Luistro, A. O. (1970). Composition of interstitial waters of marine sediments: temperature of squeezing effect. *Science,* 167(3922): 1245-1246. DOI: 10.1126/science.167.3922.1245.

Bishop-Taylor, R., Sagar, S., Lymburner, L. and Beaman, R. J. (2019). Between the tides: Modelling the elevation of Australia's exposed intertidal zone at continental scale. *Estuarine, Coastal and Shelf Science,* 223: 115-128. DOI: 10.1016/j.ecss.2019.03.006.

Böer, S. I., Hedtkamp, S. I., van Beusekom, J. E., Fuhrman, J. A., Boetius, A. and Ramette, A. (2009). Time- and sediment depth-related variations in bacterial diversity and community structure in subtidal sands. *ISME J,* 3(7): 780-791. DOI: 10.1038/ismej.2009.29.

Bolliger, R., Brandl, H., Höhener, P., Hanselmann, K. and Bachofen, R. (1992). Squeeze-Water Analysis for the Determination of Microbial Metabolites in Lake Sediment — Comparison of Methods. *Limnology and Oceanography,* 37: 448-455. DOI: 10.4319/lo.1992.37.2.0448.

Bondoso, J., Godoy-Vitorino, F., Balagué, V., Gasol, J. M., Harder, J. and Lage, O. M. (2017). Epiphytic Planctomycetes communities associated with three main groups of macroalgae. *FEMS Microbiology Ecology,* 93(3). DOI: 10.1093/femsec/fiw255.

Bontognali, T. R. R., Vasconcelos, C., Warthmann, R. J., Bernasconi, S. M., Dupraz, C., Strohmenger, C. J. and Mckenzie, J. A. (2010). Dolomite formation within microbial mats in the coastal

sabkha of Abu Dhabi (United Arab Emirates). *Sedimentology,* 57(3): 824-844. DOI: https://doi.org/10.1111/j.1365-3091.2009.01121.x.

Bontognali, T. R. R., Vasconcelos, C., Warthmann, R. J., Lundberg, R. and McKenzie, J. A. (2012). Dolomite-mediating bacterium isolated from the sabkha of Abu Dhabi (UAE). *Terra Nova,* 24(3): 248-254. DOI: 10.1111/j.1365-3121.2012.01065.x.

Bots, P., Benning, L. G., Rickaby, R. E. M. and Shaw, S. (2011). The role of SO_4 in the switch from calcite to aragonite seas. *Geology,* 39(4): 331-334. DOI: 10.1130/g31619.1.

Bottomley, N. (1996). Recent climate of Abu Dhabi. A review and recent studies. Pisces, Newbury, pp 36–49. Desert ecology of Abu Dhabi. A review and recent studies. O. P. E. Newbury, Pisces**:** 36-39.

Botz, R., Pokojski, H., Schmitt, M. and Thomm, M. (1996). Carbon isotope fractionation during bacterial methanogenesis by CO_2 reduction. *Org. Geochem.,* 25: 255-262.

Boudreau, B. P. and Canfield, D. E. (1993). A comparison between closed and open-system models for porewater pH and calcite-saturation state. *Geochim. Cosmochim. Acta,* 57: 317-334.

Bouillon, S., Middelburg, J. J., Dehairs, F., Borges, A. V., Abril, G., Flindt, M. R., Ulomi, S. and Kristensen, E. (2007). Importance of intertidal sediment processes and porewater exchange on the water column biogeochemistry in a pristine mangrove creek (Ras Dege, Tanzania). *Biogeosciences,* 4(3): 311-322. DOI: 10.5194/bg-4-311-2007.

Bourg, I. C. and Ajo-Franklin, J. B. (2017). Clay, Water, and Salt: Controls on the Permeability of Fine-Grained Sedimentary Rocks. *Accounts of Chemical Research,* 50(9): 2067-2074. DOI: 10.1021/acs.accounts.7b00261.

Bowden, S. and Honsberg, C. (2021). "pveducation." Retrieved 1st June, 2021, from https://www.pveducation.org/pvcdrom/properties-of-sunlight/calculation-of-solar-insolation.

Braissant, O., Decho, A. W., Dupraz, C., Glunk, C., Przekop, K. M. and Visscher, P. T. (2007). Exopolymeric substances of sulfate-reducing bacteria: Interactions with calcium at alkaline pH and implication for formation of carbonate minerals. *Geobiology,* 5(4): 401-411. DOI: 10.1111/j.1472-4669.2007.00117.x.

Bratton, J. F. (2010). The Three Scales of Submarine Groundwater Flow and Discharge across Passive Continental Margins. *The Journal of Geology,* 118(5): 565-575. DOI: 10.1086/655114.

Brochier-Armanet, C., Gribaldo, S. and Forterre, P. (2012). Spotlight on the Thaumarchaeota. *ISME J,* 6(2): 227-230. DOI: 10.1038/ismej.2011.145.

Broecker, W. S. (1970). A boundary condition on the evolution of atmospheric oxygen. *Journal of Geophysical Research,* 75(18): 3553-3557. DOI: 10.1029/JC075i018p03553.

Burdige, D. J. (2006). Geochemistry of Marine Sediments. Oxfordshire, Princeton Univeristy Press.

Burdige, D. J., Zimmerman, R. C. and Hu, X. (2008). Rates of carbonate dissolution in permeable sediments estimated from pore-water profiles: The role of sea grasses. *Limnology and Oceanography,* 53(2): 549-565. DOI: https://doi.org/10.4319/lo.2008.53.2.0549.

Burton, E. A. and Walter, L. M. (1987). Relative precipitation rates of aragonite and Mg calcite from seawater: Temperature or carbonate ion control? *Geology,* 15: 111-114.

Cahoon, L. B. (1999). The role of benthic microalgae in neritic ecosystems. Oceanography and Marine Biology, An Annual Review, CRC Press. 37**:** 47-86.

Caley, T., Riveiros, N. V., Labeyrie, L., Cortijo, E. and Duplessy, J. C. (2021). Climate and the Evolution of the Ocean: The Paleoceanographic Data. Paleoclimatology. G. Ramstein, A.

Landais, N. Bouttes, P. Sepulchre and A. Govin. Cham, Springer International Publishing**:** 225-254.

Camacho, A. (2009). Sulfur Bacteria. Encyclopedia of Inland Waters. G. E. Likens, Academic Press**:** 261-278.

Canion, A., Kostka, J. E., Gihring, T. M., Huettel, M., van Beusekom, J. E. E., Gao, H., Lavik, G. and Kuypers, M. M. M. (2014). Temperature response of denitrification and anammox reveals the adaptation of microbial communities to in situ temperatures in permeable marine sediments that span 50° in latitude. *Biogeosciences,* 11(2): 309-320. DOI: 10.5194/bg-11-309-2014.

Castelle, C. J., Wrighton, K. C., Thomas, B. C., Hug, L. A., Brown, C. T., Wilkins, M. J., Frischkorn, K. R., Tringe, S. G., Singh, A., Markillie, L. M., Taylor, R. C., Williams, K. H. and Banfield, J. F. (2015). Genomic expansion of domain archaea highlights roles for organisms from new phyla in anaerobic carbon cycling. *Curr Biol,* 25(6): 690-701. DOI: 10.1016/j.cub.2015.01.014.

Chafetz, H. S. and Buczynski, C. (1992). Bacterially Induced Lithification of Microbial Mats. *Palaios,* 7(3). DOI: 10.2307/3514973.

Chambers, A., Fitch, R. K. and Haliiday, B. S. (1998). Basic Vacuum Technology, second edition. London, Institute of Physics Publ.

Christ, N., Immenhauser, A., Wood, R. A., Darwich, K. and Niedermayr, A. (2015). Petrography and environmental controls on the formation of Phanerozoic marine carbonate hardgrounds. *Earth-Science Reviews,* 151: 176-226. DOI: 10.1016/j.earscirev.2015.10.002.

Clari, P. A., Dela Pierre, F. and Martire, L. (1995). Discontinuities in carbonate successions: identification, interpretation and classification of some Italian examples. *Sedimentary Geology,* 100(1): 97-121. DOI: https://doi.org/10.1016/0037-0738(95)00113-1.

Claypool, G. E. and Kaplan, I. R. (1974). The origin and distribution of methane in sediments. Natural Gases in Marine Sediments K. I. R. New York, Plenum.

Coffin, R. B., Smith, J. P., Plummer, R. E., Yoza, B., Larsen, R. K., Millholland, L. C. and Montgomery, M. T. (2013). Spatial variation in shallow sediment methane sources and cycling on the Alaskan Beaufort Sea Shelf/Slope. *Marine and Petroleum Geology,* 45: 186-197. DOI: 10.1016/j.marpetgeo.2013.05.002.

Coggon, R. M., Teagle, D. A. H., Smith-Duque, C. E., Alt, J. C. and Cooper, M. J. (2010). Reconstructing Past Seawater Mg/Ca and Sr/Ca from Mid-Ocean Ridge Flank Calcium Carbonate Veins. *Science,* 327(5969): 1114-1117. DOI: 10.1126/science.1182252.

Coleman, M. L. (1993). Microbial processes: Controls on the shape and composition of carbonate concretions. *Marine Geology,* 113: 127 - 140.

Coleman, M. L. and Raiswell, R. (1993). Microbial mineralization of organic matter: mechanisms of self-organization and inferred rates of precipitation of diagenetic minerals. *Phil. Trans. R. Soc. Lond. A,* 344: 69-87.

Consalvey, M., Paterson, D. M. and Underwood, G. J. C. (2004). The ups and downs of life in a benthic biofilm: migration of benthic diatoms. *Diatom Research,* 19(2): 181-202. DOI: 10.1080/0269249X.2004.9705870.

Court, W. M., Paul, A. and Lokier, S. W. (2017). The preservation potential of environmentally diagnostic sedimentary structures from a coastal sabkha. *Marine Geology,* 386: 1-18. DOI: 10.1016/j.margeo.2017.02.003.

Crockford, P., Telmer, K. and Best, M. (2014). Dissolution kinetics of Devonian carbonates at circum-neutral pH, 50bar pCO2, 105°C, and 0.4M: The importance of complex brine

chemistry on reaction rates. *Applied Geochemistry,* 41: 128-134. DOI: 10.1016/j.apgeochem.2013.12.008.

Cubillas, P., Köhler, S., Prieto, M., Causserand, C. and Oelkers, E. H. (2005). How do mineral coatings affect dissolution rates? An experimental study of coupled CaCO3 dissolution—CdCO3 precipitation. *Geochimica et Cosmochimica Acta,* 69(23): 5459-5476. DOI: 10.1016/j.gca.2005.07.016.

Cui, M., Ma, A., Qi, H., Zhuang, X. and Zhuang, G. (2015). Anaerobic oxidation of methane: an "active" microbial process. *Microbiologyopen,* 4(1): 1-11. DOI: 10.1002/mbo3.232.

Dale, A. W., Regnier, P. and Van Cappellen, P. (2006). Bioenergetic Controls on Anaerobic Oxidation of Methane (AOM) in Coastal Marine Sediments: A Theoretical Analysis. *American Journal of Science,* 306(4): 246-294. DOI: 10.2475/ajs.306.4.246.

Davis, K. J., Dove, P. M. and De Yoreo, J. J. (2000). The role of Mg2+ as an impurity in calcite growth. *Science,* 290(5494): 1134-1137. DOI: 10.1126/science.290.5494.1134.

De Choudens-Sanchez, V. and Gonzalez, L. (2009). Calcite and Aragonite Precipitation Under Controlled Instantaneous Supersaturation: Elucidating the Role of CaCO3 Saturation State and Mg/Ca Ratio on Calcium Carbonate Polymorphism. *Journal of Sedimentary Research,* 79: 363-376. DOI: 10.2110/jsr.2009.043.

de Lange, G. J., Cranston, R. E., Hydes, D. H. and Boust, D. (1992). Extraction of pore water from marine sediments: A review of possible artifacts with pertinent examples from the North Atlantic. *Marine Geology,* 109(1): 53-76. DOI: https://doi.org/10.1016/0025-3227(92)90220-C.

Deville de Periere, M., Durlet, C., Vennin, E., Lambert, L., Bourillot, R., Caline, B. and Poli, E. (2011). Morphometry of micrite particles in cretaceous microporous limestones of the Middle East: Influence on reservoir properties. *Marine and Petroleum Geology,* 28(9): 1727-1750. DOI: https://doi.org/10.1016/j.marpetgeo.2011.05.002.

Di Bonito, M., Breward, N., Crout, N., Smith, B. and Young, S. (2008). Overview of selected soil pore water extraction methods for the determination of potentially toxic elements in contaminated soils: operational and technical aspects. Environmental Geochemistry. B. De Vivo, H. E. Belkin and A. Lima. Amsterdam, Elsevier**:** 213-249.

Dickens, G. R., Koelling, M., Smith, D. C., Schneiders, L. and Scientists, t. I. E. (2006). Rhizon Sampling of Pore Waters on Scientific Drilling Expeditions: An Example from the IODP Expedition 302, Arctic Coring Expedition (ACEX). *Scientific Drilling,* 4: 22-25.

Dixon, P. (2003). VEGAN, a package of R functions for community ecology. *Journal of Vegetation Science,* 14(6): 927-930. DOI: https://doi.org/10.1111/j.1654-1103.2003.tb02228.x.

Dravis, J. (1979). Rapid and widespread generation of recent oolitic hardgrounds on a high energy Bahamian platform, Eleuthera Bank, Bahamas. *Journal of sedimentary Petrology,* 49(1): 195-208.

Drupp, P. S., De Carlo, E. H. and Mackenzie, F. T. (2016). Porewater CO_2–carbonic acid system chemistry in permeable carbonate reef sands. *Marine Chemistry,* 185: 48-64. DOI: 10.1016/j.marchem.2016.04.004.

Duarte, C. M., Middelburg, J. J. and Caraco, N. (2005). Major role of marine vegetation on the oceanic carbon cycle. *Biogeosciences,* 2(1): 1-8. DOI: 10.5194/bg-2-1-2005.

Dupraz, C., Fowler, A., Tobias, C. and Visscher, P. T. (2013). Stromatolitic knobs in Storr's Lake (San Salvador, Bahamas): a model system for formation and alteration of laminae. *Geobiology,* 11(6): 527-548. DOI: 10.1111/gbi.12063.

Dupraz, C., Reid, R. P., Braissant, O., Decho, A. W., Norman, R. S. and Visscher, P. T. (2009). Processes of carbonate precipitation in modern microbial mats. *Earth-Science Reviews,* 96(3): 141-162. DOI: 10.1016/j.earscirev.2008.10.005.

Dyksma, S., Pjevac, P., Ovanesov, K. and Mussmann, M. (2018). Evidence for H_2 consumption by uncultured Desulfobacterales in coastal sediments. *Environmental Microbiology,* 20(2): 450-461. DOI: 10.1111/1462-2920.13880.

Edgar, R. C. (2010). Search and clustering orders of magnitude faster than BLAST. *Bioinformatics,* 26(19): 2460-2461. DOI: 10.1093/bioinformatics/btq461.

Edgar, R. C. (2013). UPARSE: highly accurate OTU sequences from microbial amplicon reads. *Nature Methods,* 10(10): 996-998. DOI: 10.1038/nmeth.2604.

Eiler, J. M. (2011). Paleoclimate reconstruction using carbonate clumped isotope thermometry. *Quaternary Science Reviews,* 30(25): 3575-3588. DOI: https://doi.org/10.1016/j.quascirev.2011.09.001.

Eisenlohr, L., Meteva, K., Gabrovšek, F. and Dreybrodt, W. (1999). The inhibiting action of intrinsic impurities in natural calcium carbonate minerals to their dissolution kinetics in aqueous H_2O–CO_2 solutions. *Geochimica et Cosmochimica Acta,* 63(7): 989-1001. DOI: https://doi.org/10.1016/S0016-7037(98)00301-9.

Emerson, S., Jahnke, R., Bender, M., Froelich, P., Klinkhammer, G., Bowser, C. and Setlock, G. (1980). Early diagenesis in sediments from the eastern equatorial Pacific, I. Pore water nutrient and carbonate results. *Earth and Planetary Science Letters,* 49(1): 57-80. DOI: https://doi.org/10.1016/0012-821X(80)90150-8.

Erhardt, A. M., Turchyn, A. V., Dickson, J. A. D., Sadekov, A. Y., Taylor, P. D., Wilson, M. A., Scott, P. and Schrag, D. P. (2020). Chemical Composition of Carbonate Hardground Cements as Reconstructive Tools for Phanerozoic Pore Fluids. *Geochemistry, Geophysics, Geosystems,* 21(3). DOI: 10.1029/2019gc008448.

Evans, G. (1966). The recent sedimentary facies of the Persian Gulf Region. *Phil Trans R Soc*: 291-298.

Evans, G. (2011). An historical review of the Quaternary sedimentology of the Gulf (Arabian/Persian Gulf) and its geological impact. *Quaternary carbonate and evaporite sedimentary facies and their ancient analogues: A tribute to Douglas James Shearman,* 43: 11-44.

Evans, G., Kinsman, D. J. J. and Shearman, D. J. (1964). A Reconnaissance Survey of the Environment of Recent Carbonate Sedimentation Along the Trucial Coast, Persian Gulf. *Developments in Sedimentology,* 1: 129-135. DOI: https://doi.org/10.1016/S0070-4571(08)70477-1.

Evans, G., Schmidt, V., Bush, P. and Nelson, H. (1969). Stratigraphy and Geologic History of the Sabkha, Abu Dhabi, Persian Gulf. *Sedimentology,* 12(1-2): 145-159. DOI: https://doi.org/10.1111/j.1365-3091.1969.tb00167.x.

Evans, P. N., Parks, D. H., Chadwick, G. L., Robbins, S. J., Orphan, V. J., Golding, S. D. and Tyson, G. W. (2015). Methane metabolism in the archaeal phylum Bathyarchaeota revealed by genome-centric metagenomics. *Science,* 350(6259): 434-438. DOI: 10.1126/science.aac7745.

Falcon-Suarez, I., Rammlmair, D., Juncosa-Rivera, R. and Delgado-Martin, J. (2014). Application of Rhizon SMS for the assessment of the hydrodynamic properties of unconsolidated fine-

grained materials. *Engineering Geology,* 172: 69-76. DOI: https://doi.org/10.1016/j.enggeo.2014.02.001.

Falkowski, P. G., Fenchel, T. and Delong, E. F. (2008). The Microbial Engines That Drive Earth's Biogeochemical Cycles. *Science,* 320(5879): 1034-1039. DOI: 10.1126/science.1153213.

Fantle, M. S., Barnes, B. D. and Lau, K. V. (2020). The Role of Diagenesis in Shaping the Geochemistry of the Marine Carbonate Record. *Annual Review of Earth and Planetary Sciences,* 48(1): 549-583. DOI: 10.1146/annurev-earth-073019-060021.

Fantle, M. S. and Ridgwell, A. (2020). Towards an understanding of the Ca isotopic signal related to ocean acidification and alkalinity overshoots in the rock record. *Chemical Geology,* 547. DOI: 10.1016/j.chemgeo.2020.119672.

Farag, I. F., Davis, J. P., Youssef, N. H. and Elshahed, M. S. (2014). Global patterns of abundance, diversity and community structure of the Aminicenantes (candidate phylum OP8). *PLoS One,* 9(3): e92139. DOI: 10.1371/journal.pone.0092139.

Fernandez-Gomez, B., Richter, M., Schuler, M., Pinhassi, J., Acinas, S. G., Gonzalez, J. M. and Pedros-Alio, C. (2013). Ecology of marine Bacteroidetes: a comparative genomics approach. *ISME J,* 7(5): 1026-1037. DOI: 10.1038/ismej.2012.169.

Finneran, D. W. and Morse, J. W. (2009). Calcite dissolution kinetics in saline waters. *Chemical Geology,* 268(1-2): 137-146. DOI: 10.1016/j.chemgeo.2009.08.006.

Flügel, E. (1982). Carbonate Diagenesis. Microfacies Analysis of Limestones. Berlin, Heidelberg, Springer**:** 62-104.

Folk, R. L. (1974). The natural history of crystalline calcium carbonate; effect of magnesium content and salinity. *Journal of Sedimentary Research,* 44(1): 40-53. DOI: 10.1306/74d72973-2b21-11d7-8648000102c1865d.

Forster, S., Bobertz, B. and Bohling, B. (2003). Permeability of Sands in the Coastal Areas of the Southern Baltic Sea: Mapping a Grain-size Related Sediment Property. *Aquatic Geochemistry,* 9: 171-190. DOI: 10.1023/B:AQUA.0000022953.52275.8b.

Frantz, C. M., Petryshyn, V. A. and Corsetti, F. A. (2015). Grain trapping by filamentous cyanobacterial and algal mats: implications for stromatolite microfabrics through time. *Geobiology,* 13(5): 409-423.

Friess, D. A., Krauss, K. W., Horstman, E. M., Balke, T., Bouma, T. J., Galli, D. and Webb, E. L. (2012). Are all intertidal wetlands naturally created equal? Bottlenecks, thresholds and knowledge gaps to mangrove and saltmarsh ecosystems. *Biological Reviews,* 87(2): 346-366. DOI: 10.1111/j.1469-185X.2011.00198.x.

Froelich P. N., Klinkhammer G. P., Bender M. L., Luedtke N. A., Heath G. R., Cullen D., Dauphin P., Hammond D., Hartman B. and V., M. (1979). Early oxidation of organic matter in pelagic sediments of the eastern equatorial Atlantic: Suboxic diagenesis. *Geochim. Cosmochim. Acta,* 43: 1075–1090.

Gabellone, T. and Whitaker, F. (2017). Modelling Stratigraphic Controls on Dolomitisation at the Inter-well Scale: The Assoul Formation Case Study (Central High Atlas, Morocco). AAPG Annual Convention and Exhibition, Houston, United States.

Gaines, R. R., Vorhies, J. S. and Pufahl, P. (2016). Growth mechanisms and geochemistry of carbonate concretions from the Cambrian Wheeler Formation (Utah, USA). *Sedimentology,* 63(3): 662-698. DOI: 10.1111/sed.12234.

Garcia-Pichel, F. (2009). Cyanobacteria. Encyclopedia of Microbiology (Third Edition). M. Schaechter. Oxford, Academic Press**:** 107-124.

Garrels, R. M., Thompson, M. E. and Siever, R. (1961). Control of carbonate solubility by carbonate complexes. *American Journal of Science,* 259(1): 24-45. DOI: 10.2475/ajs.259.1.24.

Ge, Y., Pederson, C. L., Lokier, S. W., Traas, J. P., Nehrke, G., Neuser, R. D., Goetschl, K. E., Immenhauser, A. and Qing, H. (2020a). Late Holocene to Recent aragonite-cemented transgressive lag deposits in the Abu Dhabi lagoon and intertidal sabkha. *Sedimentology*. DOI: 10.1111/sed.12707.

Ge, Y., Lokier, S. W., Hoffmann, R., Pederson, C. L., Neuser, R. D. and Immenhauser, A. (2020b). Composite micrite envelopes in the lagoon of Abu Dhabi and their application for the recognition of ancient firm- to hardgrounds. *Marine Geology,* 423. DOI: 10.1016/j.margeo.2020.106141.

Geske, A., Lokier, S., Dietzel, M., Richter, D. K., Buhl, D. and Immenhauser, A. (2015). Magnesium isotope composition of sabkha porewater and related (Sub-)Recent stoichiometric dolomites, Abu Dhabi (UAE). *Chemical Geology,* 393-394: 112-124. DOI: 10.1016/j.chemgeo.2014.11.020.

Ghosh, P., Adkins, J., Affek, H., Balta, B., Guo, W., Schauble, E. A., Schrag, D. and Eiler, J. M. (2006). $^{13}C–^{18}O$ bonds in carbonate minerals: A new kind of paleothermometer. *Geochimica et Cosmochimica Acta,* 70(6): 1439-1456. DOI: 10.1016/j.gca.2005.11.014.

Ghosh, P., Eiler, J., Campana, S. E. and Feeney, R. F. (2007). Calibration of the carbonate 'clumped isotope' paleothermometer for otoliths. *Geochimica et Cosmochimica Acta,* 71(11): 2736-2744. DOI: https://doi.org/10.1016/j.gca.2007.03.015.

Given, R. K. and Wilkinson, B. H. (1985). Kinetic control of morphology, composition, and mineralogy of abiotic sedimentary carbonates. *Journal of Sedimentary Research,* 55(1): 109-119. DOI: 10.1306/212f862a-2b24-11d7-8648000102c1865d.

Glöckner, J., Kube, M., Shrestha, P. M., Weber, M., Glockner, F. O., Reinhardt, R. and Liesack, W. (2010). Phylogenetic diversity and metagenomics of candidate division OP3. *Environ Microbiol,* 12(5): 1218-1229. DOI: 10.1111/j.1462-2920.2010.02164.x.

Gontharet, S., Pierre, C., Blanc-Valleron, M.-M., Rouchy, J. M., Fouquet, Y., Bayon, G., Foucher, J. P., Woodside, J., Mascle, J. and Party, N. S. (2007). Nature and origin of diagenetic carbonate crusts and concretions from mud volcanoes and pockmarks of the Nile deep-sea fan (eastern Mediterranean Sea). *Deep Sea Research Part II: Topical Studies in Oceanography,* 54: 1292. DOI: 10.1016/j.dsr2.2007.04.007.

Goring, D. G. (1995). Short-term variations in sea level (2–15 days) in the New Zealand region. *New Zealand Journal of Marine and Freshwater Research,* 29(1): 69-82. DOI: 10.1080/00288330.1995.9516641.

Green, M. and Aller, R. (1998). Seasonal patterns of carbonate diagenesis in nearshore terrigenous muds: Relation to spring phytoplankton bloom and temperature. *Journal of Marine Research,* 56. DOI: 10.1357/002224098765173473.

Greene, S. E., Bottjer, D. J., Corsetti, F. A., Berelson, W. M. and Zonneveld, J.-P. (2012). A subseafloor carbonate factory across the Triassic-Jurassic transition. *Geology,* 40(11): 1043-1046. DOI: 10.1130/g33205.1.

Grenthe, I. and Plyasunov, A. (1997). On the use of semiempirical electrolyte theories for modelling of solution chemical data. *Pure and Applied Chemistry,* 69(5): 951-958. DOI: doi:10.1351/pac199769050951.

Grotzinger, J. P. and Knoll, A. H. (1995). Anomalous carbonate precipitates: is the Precambrian the key to the Permian? *Palaios,* 10(6): 578-596.

Hain, M. P., Sigman, D. M., Higgins, J. A. and Haug, G. H. (2015). The effects of secular calcium and magnesium concentration changes on the thermodynamics of seawater acid/base chemistry: Implications for Eocene and Cretaceous Ocean carbon chemistry and buffering. *Global Biogeochemical Cycles,* 29(5): 517-533. DOI: https://doi.org/10.1002/2014GB004986.

Haley, B. A., Klinkhammer, G. P. and McManus, J. (2004). Rare earth elements in pore waters of marine sediments. *Geochimica et Cosmochimica Acta,* 68(6): 1265-1279. DOI: https://doi.org/10.1016/j.gca.2003.09.012.

Harland, S., Wood, R., Curtis, A., van Dijke, M., Stratford, K., Jiang, Z., Kallel, W. and Sorbie, K. (2015). Quantifying flow in variably wet microporous carbonates using object-based geological modelling and both lattice-Boltzmann and pore-network fluid flow simulations. *AAPG Bulletin,* 99: 1827-1860. DOI: 10.1306/04231514122.

Harris, L., Campbell, E. E., Nel, R. and Schoeman, D. (2014). Rich diversity, strong endemism, but poor protection: addressing the neglect of sandy beach ecosystems in coastal conservation planning. *Diversity and Distributions,* 20(10): 1120-1135. DOI: https://doi.org/10.1111/ddi.12226.

Harris, P., Diaz, M. R. and Eberli, G. P. (2019). The Formation and Distribution of Modern Ooids on Great Bahama Bank. *Annual Review of Marine Science,* 11(1): 491-516. DOI: 10.1146/annurev-marine-010318-095251.

Harrison, S. J. and Phizacklea, A. P. (1987). Vertical temperature gradients in muddy intertidal sediments in the Forth estuary, Scotland1. *Limnology and Oceanography,* 32(4): 954-963. DOI: 10.4319/lo.1987.32.4.0954.

Harvie, C. E., Møller, N. and Weare, J. H. (1984). The prediction of mineral solubilities in natural waters: The Na-K-Mg-Ca-H-Cl-SO_4-OH-HCO_3-CO_3^--CO_2-H_2O system to high ionic strengths at 25°C. *Geochimica et Cosmochimica Acta,* 48: 723. DOI: 10.1016/0016-7037(84)90098-x.

Hashim, A. and Hajjaj, M. (2005). Impact of desalination plants fluid effluents on the integrity of seawater, with the Arabian Gulf in perspective. *Desalination,* 182: 373-393.

Haynes, K., Hofmann, T. A., Smith, C. J., Ball, A. S., Underwood, G. J. and Osborn, A. M. (2007). Diatom-derived carbohydrates as factors affecting bacterial community composition in estuarine sediments. *Appl Environ Microbiol,* 73(19): 6112-6124. DOI: 10.1128/AEM.00551-07.

Henkes, G. A., Passey, B. H., Grossman, E. L., Shenton, B. J., Yancey, T. E. and Pérez-Huerta, A. (2018). Temperature evolution and the oxygen isotope composition of Phanerozoic oceans from carbonate clumped isotope thermometry. *Earth and Planetary Science Letters,* 490: 40-50. DOI: 10.1016/j.epsl.2018.02.001.

Hesslein, R. H. (1976). An in situ sampler for close interval pore water studies1. *Limnology and Oceanography,* 21(6): 912-914. DOI: https://doi.org/10.4319/lo.1976.21.6.0912.

Higgins, J. A., Blättler, C. L., Lundstrom, E. A., Santiago-Ramos, D. P., Akhtar, A. A., Crüger Ahm, A. S., Bialik, O., Holmden, C., Bradbury, H., Murray, S. T. and Swart, P. K. (2018). Mineralogy, early marine diagenesis, and the chemistry of shallow-water carbonate sediments. *Geochimica et Cosmochimica Acta,* 220: 512-534. DOI: 10.1016/j.gca.2017.09.046.

Higgins, J. A., Fischer, W. W. and Schrag, D. P. (2009). Oxygenation of the ocean and sediments: Consequences for the seafloor carbonate factory. *Earth and Planetary Science Letters,* 284(1-2): 25-33. DOI: 10.1016/j.epsl.2009.03.039.

Hillgärtner, H. (1998). Discontinuity surfaces on a shallow-marine carbonate platform (Berriasian, Valanginian, France and Switzerland). *Journal of Sedimentary Research,* 68(6): 1093-1108. DOI: 10.2110/jsr.68.1093.

Himmler, T., Bach, W., Bohrmann, G. and Peckmann, J. (2010). Rare earth elements in authigenic methane-seep carbonates as tracers for fluid composition during early diagenesis. *Chemical Geology,* 277(1-2): 126-136. DOI: 10.1016/j.chemgeo.2010.07.015.

Hochard, S., Pinazo, C., Grenz, C., Evans, J. L. B. and Pringault, O. (2010). Impact of microphytobenthos on the sediment biogeochemical cycles: A modelling approach. *Ecological Modelling,* 221(13-14): 1687-1701. DOI: 10.1016/j.ecolmodel.2010.04.002.

Hoehler, T. M., Alperin, M. J., Albert, D. B. and Martens, C. S. (1994). Field and laboratory studies of methane oxidation in an anoxic marine sediment' Evidence for a methanogen-sulfate reducer consortium. *Global Biogechemical Cycles,* 8(4): 451-463.

Hornibrook, E. R. C. and Bowes, H. L. (2007). Trophic status impacts both the magnitude and stable carbon isotope composition of methane flux from peatlands. *Geophysical Research Letters,* 34(21). DOI: 10.1029/2007gl031231.

Hsü, K. J. and Schneider, J. (1973). Progress Report on Dolomitization — Hydrology of Abu Dhabi Sabkhas, Arabian Gulf, Berlin, Heidelberg, Springer Berlin Heidelberg.

Hu, X. and Burdige, D. J. (2007). Enriched stable carbon isotopes in the pore waters of carbonate sediments dominated by seagrasses: Evidence for coupled carbonate dissolution and reprecipitation. *Geochimica et Cosmochimica Acta,* 71(1): 129-144. DOI: 10.1016/j.gca.2006.08.043.

Hu, X. and Burdige, D. J. (2008). Shallow marine carbonate dissolution and early diagenesis; Implications from an incubation study. *Journal of Marine Research,* 66(4): 489-527. DOI: 10.1357/002224008787157449.

Hubas, C., Davoult, D., Cariou, T. and Artigas, L. F. (2006). Factors controlling benthic metabolism during low tide along a granulometric gradient in an intertidal bay (Roscoff Aber Bay, France). *Marine Ecology-Progress Series,* 316: 53–68.

Hubbard, C. R. and Snyder, R. L. (1988). RIR - Measurement and Use in Quantitative XRD. *Powder Diffraction,* 3(2): 74-77. DOI: 10.1017/S0885715600013257.

Huettel, M., Røy, H., Precht, E. and Ehrenhauss, S. (2003). Hydrodynamical impact on biogeochemical processes in aquatic sediments. *Hydrobiol,* 494: 231-236.

Huntington, K. W., Budd, D. A., Wernicke, B. P. and Eiler, J. M. (2011). Use of Clumped-Isotope Thermometry To Constrain the Crystallization Temperature of Diagenetic Calcite. *Journal of Sedimentary Research,* 81(9): 656-669. DOI: 10.2110/jsr.2011.51.

Irwin, H., Curtis, C. and Coleman, M. (1977). Isotopic evidence for source of diagenetic carbonates formed during burial of organic-rich sediments. *Nature,* 269(5625): 209-213. DOI: 10.1038/269209a0.

James, N. P. and Choquette, P. W. (1989). Diagenesis 9. Limestones— The Meteoric Diagenetic Environment. Carbonate Sedimentology and Petrology**:** 45-78.

Jørgensen, N. O. (1992). Methane-derived carbonate cementation of marine sediments from the Kattegat, Denmark: Geochemical and geological evidence. *Marine Geology,* 103(1): 1-13. DOI: https://doi.org/10.1016/0025-3227(92)90006-4.

Jorgensen, S. L., Hannisdal, B., Lanzen, A., Baumberger, T., Flesland, K., Fonseca, R., Ovreas, L., Steen, I. H., Thorseth, I. H., Pedersen, R. B. and Schleper, C. (2012). Correlating microbial community profiles with geochemical data in highly stratified sediments from the Arctic

Mid-Ocean Ridge. *Proc Natl Acad Sci U S A,* 109(42): E2846-2855. DOI: 10.1073/pnas.1207574109.

Joseph, C., Campbell, K. A., Torres, M. E., Martin, R. A., Pohlman, J. W., Riedel, M. and Rose, K. (2013). Methane-derived authigenic carbonates from modern and paleoseeps on the Cascadia margin: Mechanisms of formation and diagenetic signals. *Palaeogeography, Palaeoclimatology, Palaeoecology,* 390: 52-67. DOI: 10.1016/j.palaeo.2013.01.012.

Junkins, E. N. and Stevenson, B. S. (2020). Assessing and Maximizing Cultivated Diversity with Plate-Wash PCR and High Throughput Sequencing. *bioRxiv*: 2020.2011.2019.390864. DOI: 10.1101/2020.11.19.390864.

Kaczmarek, S. E., Fullmer, S. M. and Hasiuk, F. J. (2015). A Universal Classification Scheme For the Microcrystals That Host Limestone Microporosity. *Journal of Sedimentary Research,* 85(10): 1197-1212. DOI: 10.2110/jsr.2015.79.

Kaczmarek, S. E., Hicks, M. K., Fullmer, S. M., Steffen, K. L. and Bachtel, S. L. (2010). Mapping facies distributions on modern carbonate platforms through integration of multispectral Landsat data, statistics-based unsupervised classifications, and surface sediment data. *AAPG Bulletin,* 94(10): 1581-1606. DOI: 10.1306/04061009175.

Kadnikov, V. V., Mardanov, A. V., Beletsky, A. V., Karnachuk, O. V. and Ravin, N. V. (2019). Genome of the candidate phylum Aminicenantes bacterium from a deep subsurface thermal aquifer revealed its fermentative saccharolytic lifestyle. *Extremophiles,* 23(2): 189-200. DOI: 10.1007/s00792-018-01073-5.

Kandianis, M. T., Fouke, B. W., Johnson, R. W., Veysey, J. and Inskeep, W. P. (2008). Microbial biomass: A catalyst for CaCO3 precipitation in advection-dominated transport regimes. *Geological Society of America Bulletin,* 120(3-4): 442-450. DOI: 10.1130/b26188.1.

Kasper, H. and Ronnie, N. G. (2004). Temperature effects on respiration and photosynthesis in three diatom-dominated benthic communities. *Aquatic Microbial Ecology,* 37(3): 265-281.

Kawaichi, S., Ito, N., Kamikawa, R., Sugawara, T., Yoshida, T. and Sako, Y. (2013). Ardenticatena maritima gen. nov., sp. nov., a ferric iron- and nitrate-reducing bacterium of the phylum 'Chloroflexi' isolated from an iron-rich coastal hydrothermal field, and description of Ardenticatenia classis nov. *Int J Syst Evol Microbiol,* 63(Pt 8): 2992-3002. DOI: 10.1099/ijs.0.046532-0.

Kelson, J. R., Huntington, K. W., Breecker, D. O., Burgener, L. K., Gallagher, T. M., Hoke, G. D. and Petersen, S. V. (2020). A proxy for all seasons? A synthesis of clumped isotope data from Holocene soil carbonates. *Quaternary Science Reviews,* 234. DOI: 10.1016/j.quascirev.2020.106259.

Kenig, F., Huc, A. Y., Purser, B. H. and Oudin, J.-L. (1990). Sedimentation, distribution, and diagenesis of organic matter in a recent carbonate environment, Abu Dhabi, U.A.E. *Organic Geochemistry,* 16(4): 735-747. DOI: https://doi.org/10.1016/0146-6380(90)90113-E.

Kennedy, W. J. and Garrison, R. E. (1975). Morphology and genesis of nodular chalks and hardgrounds in the Upper Cretaceous of Southern England. *Sedimentology,* 22: 311-386.

Khalaf, F., Milliman, J. D. and Druffel, E. M. (1987). Submarine limestones in the nearshore environment off Kuwait, northern Arabian Gulf. *Sedimentology,* 34: 67–75.

Kiessling, W., Flügel, E. and Golonka, J. (2003). Patterns of Phanerozoic carbonate platform sedimentation. *Lethaia,* 36(3): 195-225. DOI: https://doi.org/10.1080/00241160310004648.

Kinsman, D. J. J. (1964). Recent carbonate sedimentation near Abu Dhabi, Trucial Coast, Persian Gulf. Department of Geology. London, Imperial College

Kinsman, D. J. J. (1968). Modes of Formation, Sedimentary Associations, and Diagnostic Features of Shallow-Water and Supratidal Evaporites. *AAPG Bulletin,* 52(3): 536-536. DOI: 10.1306/5d25c363-16c1-11d7-8645000102c1865d.

Knight, B. P., Chaudri, A. M., McGrath, S. P. and Giller, K. E. (1998). Determination of chemical availability of cadmium and zinc in soils using inert soil moisture samplers. *Environmental Pollution,* 99(3): 293-298. DOI: https://doi.org/10.1016/S0269-7491(98)00021-9.

Konhauser, K. and Riding, R. (2012). Bacterial Biomineralization. Fundamentals of Geobiology**:** 105-130.

Könneke, M., Bernhard, A. E., de la Torre, J. R., Walker, C. B., Waterbury, J. B. and Stahl, D. A. (2005). Isolation of an autotrophic ammonia-oxidizing marine archaeon. *Nature,* 437(7058): 543-546. DOI: 10.1038/nature03911.

Kraus, E. A., Beeler, S. R., Mors, R. A., Floyd, J. G., GeoBiology, Stamps, B. W., Nunn, H. S., Stevenson, B. S., Johnson, H. A., Shapiro, R. S., Loyd, S. J., Spear, J. R. and Corsetti, F. A. (2018). Microscale Biosignatures and Abiotic Mineral Authigenesis in Little Hot Creek, California. *Frontiers in Microbiology,* 9: 997-997. DOI: 10.3389/fmicb.2018.00997.

Krause, S., Liebetrau, V., Löscher, C., Böhm, F., Gorb, S., Eisenhauer, A. and Treude, T. (2018). Marine ammonification and carbonic anhydrase activity induce rapid calcium carbonate precipitation. *Geochimica et Cosmochimica Acta,* 243. DOI: 10.1016/j.gca.2018.09.018.

Kristensen, E. (2000). Organic matter diagenesis at the oxic/anoxic interface in coastal marine sediments, with emphasis on the role of burrowing animals. *Hydrobiologia,* 426: 1-24.

Kubo, K., Lloyd, K. G., J, F. B., Amann, R., Teske, A. and Knittel, K. (2012). Archaea of the Miscellaneous Crenarchaeotal Group are abundant, diverse and widespread in marine sediments. *ISME J,* 6(10): 1949-1965. DOI: 10.1038/ismej.2012.37.

Kuever, J. (2014). The Family Desulfobulbaceae. The Prokaryotes: Deltaproteobacteria and Epsilonproteobacteria. E. Rosenberg, E. F. DeLong, S. Lory, E. Stackebrandt and F. Thompson. Berlin, Heidelberg, Springer Berlin Heidelberg**:** 75-86.

Lamarche-Gagnon, G., Wadham, J. L., Sherwood Lollar, B., Arndt, S., Fietzek, P., Beaton, A. D., Tedstone, A. J., Telling, J., Bagshaw, E. A., Hawkings, J. R., Kohler, T. J., Zarsky, J. D., Mowlem, M. C., Anesio, A. M. and Stibal, M. (2019). Greenland melt drives continuous export of methane from the ice-sheet bed. *Nature,* 565(7737): 73-77. DOI: 10.1038/s41586-018-0800-0.

Lash, G. G. and Blood, D. (2004). Geochemical and textural evidence for early (shallow) diagenetic growth of stratigraphically confined carbonate concretions, Upper Devonian Rhinestreet black shale, western New York. *Chemical Geology,* 206(3-4): 407-424. DOI: 10.1016/j.chemgeo.2003.12.017.

Lavergne, C., Hugoni, M., Hubas, C., Debroas, D., Dupuy, C. and Agogue, H. (2018). Diel Rhythm Does Not Shape the Vertical Distribution of Bacterial and Archaeal 16S rRNA Transcript Diversity in Intertidal Sediments: a Mesocosm Study. *Microb Ecol,* 75(2): 364-374. DOI: 10.1007/s00248-017-1048-1.

Lazar, C. S., Baker, B. J., Seitz, K. W. and Teske, A. P. (2017). Genomic reconstruction of multiple lineages of uncultured benthic archaea suggests distinct biogeochemical roles and ecological niches. *ISME J,* 11(5): 1118-1129. DOI: 10.1038/ismej.2016.189.

Lee, L. H., Hsieh, L. Y. and Lin, H. J. (2011). In situ production and respiration of the benthic community during emersion on subtropical intertidal sandflats. *Marine Ecology Progress Series,* 441: 33-47. DOI: 10.3354/meps09362.

Lewis, E. L. and Perkin, R. G. (1981). The practical salinity scale 1978: conversion of existing data. *Deep Sea Research Part A. Oceanographic Research Papers,* 28(4): 307-328. DOI: https://doi.org/10.1016/0198-0149(81)90002-9.

Lewis, E. R. and Wallace, D. W. R. (1998). Program Developed for CO2 System Calculations. United States DOI: 10.15485/1464255

Lighty, R. G., Schneidermann, N. and Harris, P. M. (1985). Preservation of Internal Reef Porosity and Diagenetic Sealing of Submerged Early Holocene Barrier Reef, Southeast Florida Shelf. Carbonate Cements: Based on a Symposium Sponsored by the Society of Economic Palaeontologists and Mineralogists, SEPM Society for Sedimentary Geology. 36**:** 0.

Lin, W. J., Wu, J. and Lin, H. J. (2020). Contribution of unvegetated tidal flats to coastal carbon flux. *Glob Chang Biol,* 26(6): 3443-3454. DOI: 10.1111/gcb.15107.

Lloyd, K. G., Schreiber, L., Petersen, D. G., Kjeldsen, K. U., Lever, M. A., Steen, A. D., Stepanauskas, R., Richter, M., Kleindienst, S., Lenk, S., Schramm, A. and Jorgensen, B. B. (2013). Predominant archaea in marine sediments degrade detrital proteins. *Nature,* 496(7444): 215-218. DOI: 10.1038/nature12033.

Lokier, S. and Steuber, T. (2008). Quantification of Carbonate-Ramp Sedimentation and Progradation Rates for the Late Holocene Abu Dhabi Shoreline. *Journal of Sedimentary Research,* 78(7): 423-431. DOI: 10.2110/jsr.2008.049.

Lokier, S. and Steuber, T. (2009). Large-scale intertidal polygonal features of the Abu Dhabi coastline. *Sedimentology,* 56(3): 609-621. DOI: 10.1111/j.1365-3091.2008.00988.x.

Lokier, S. W. (2012). Development and evolution of subaerial halite crust morphologies in a coastal sabkha setting. *Journal of Arid Environments,* 79: 32-47. DOI: 10.1016/j.jaridenv.2011.11.031.

Lokier, S. W. (2013). Coastal Sabkha Preservation in the Arabian Gulf. *Geoheritage,* 5(1): 11-22. DOI: 10.1007/s12371-012-0069-x.

Lokier, S. W., Andrade, L. L., Court, W. M., Dutton, K. E., Head, I. M., van der Land, C., Paul, A. and Sherry, A. (2017). A new model for the formation of microbial polygons in a coastal sabkha setting. *The Depositional Record,* 3(2): 201-208. DOI: 10.1002/dep2.33.

Lokier, S. W., Bateman, M. D., Larkin, N. R., Rye, P. and Stewart, J. R. (2015). Late Quaternary sea-level changes of the Persian Gulf. *Quaternary Research,* 84(1): 69-81. DOI: 10.1016/j.yqres.2015.04.007.

Lokier, S. W., Court, W. M., Onuma, T. and Paul, A. (2018). Implications of sea-level rise in a modern carbonate ramp setting. *Geomorphology,* 304: 64-73. DOI: 10.1016/j.geomorph.2017.12.023.

Lokier, S. W. and Fiorini, F. (2016). Temporal evolution of a carbonate coastal system, Abu Dhabi, United Arab Emirates. *Marine Geology,* 381: 102-113.

Lokier, S. W., Knaf, A. and Kimiagar, S. (2013). A quantitative analysis of Recent arid coastal sedimentary facies from the Arabian Gulf Coastline of Abu Dhabi, United Arab Emirates. *Marine Geology,* 346: 141-152. DOI: 10.1016/j.margeo.2013.09.006.

Lorens, R. B. (1981). Sr, Cd, Mn and Co distribution coefficients in calcite as a function of calcite precipitation rate. *Geochimica et Cosmochimica Acta,* 45(4): 553-561. DOI: https://doi.org/10.1016/0016-7037(81)90188-5.

Loyd, S. J. and Berelson, W. M. (2016). The modern record of "concretionary" carbonate: Reassessing a discrepancy between modern sediments and the geologic record. *Chemical Geology,* 420: 77-87. DOI: 10.1016/j.chemgeo.2015.11.009.

Loyd, S. J., Berelson, W. M., Lyons, T. W., Hammond, D. E. and Corsetti, F. A. (2012). Constraining pathways of microbial mediation for carbonate concretions of the Miocene Monterey Formation using carbonate-associated sulfate. *Geochimica et Cosmochimica Acta,* 78: 77-98. DOI: 10.1016/j.gca.2011.11.028.

Ludwig, R., Al-Horani, F. A., de Beer, D. and Jonkers, H. M. (2005). Photosynthesis-controlled calcification in a hypersaline microbial mat. *Limnology and Oceanography,* 50(6): 1836-1843. DOI: https://doi.org/10.4319/lo.2005.50.6.1836.

Lueker, T. J., Dickson, A. G. and Keeling, C. D. (2000). Ocean pCO_2 calculated from dissolved inorganic carbon, alkalinity, and equations for K1 and K2: validation based on laboratory measurements of CO_2 in gas and seawater at equilibrium. *Marine Chemistry,* 70(1): 105-119. DOI: https://doi.org/10.1016/S0304-4203(00)00022-0.

Lyu, J., Qin, W., Zhang, C. and Li, F. (2020). Nanoparticle Accumulation in Microbial Induced Carbonate Precipitation: The Crucial Role of Extracellular Polymeric Substance. *Geomicrobiology Journal,* 37(9): 837-847. DOI: 10.1080/01490451.2020.1786866.

Ma, K. and Lu, Y. (2011). Regulation of microbial methane production and oxidation by intermittent drainage in rice field soil. *FEMS Microbiol Ecol,* 75(3): 446-456. DOI: 10.1111/j.1574-6941.2010.01018.x.

Mancini, E. A., Llins, J. C., Parcell, W. C., Aurell, A., Badenas, B., Leinfelder, R. R. and Benson, D. J. (2004). Upper Jurassic thrombolite reservoir play, northeastern Gulf of Mexico. *American Association of Petroleum Geologists Bulletin,* 88: 1573-1602.

Mann, S., Didymus, J. M., Sanderson, N. P., Heywood, B. R. and Samper, E. J. A. (1990). Morphological influence of functionalized and non-functionalized α,ω-dicarboxylates on calcite crystallization. *Journal of the Chemical Society, Faraday Transactions,* 86(10): 1873-1880. DOI: 10.1039/FT9908601873.

Markham, A. E. and Kobe, K. A. (1941). The Solubility of Carbon Dioxide and Nitrous Oxide in Aqueous Salt Solutions. *Journal of the American Chemical Society,* 63(2): 449-454. DOI: 10.1021/ja01847a027.

Marshall, J. D. and Pirrie, D. (2013). Carbonate concretions—explained. *Geology Today,* 29(2): 53 - 62.

Mavromatis, V., Botz, R., Schmidt, M., Liebetrau, V. and Hensen, C. (2012). Formation of carbonate concretions in surface sediments of two mud mounds, offshore Costa Rica: a stable isotope study. *International Journal of Earth Sciences,* 103. DOI: 10.1007/s00531-012-0843-7.

Mavromatis, V., Botz, R., Schmidt, M., Liebetrau, V. and Hensen, C. (2014). Formation of carbonate concretions in surface sediments of two mud mounds, offshore Costa Rica: a stable isotope study. *International Journal of Earth Sciences,* 103. DOI: 10.1007/s00531-012-0843-7.

Mayer, L. A. (1991). Extraction of high-resolution carbonate data for paleoclimate reconstruction. *Nature,* 352(6331): 148-150. DOI: 10.1038/352148a0.

McKenzie, J. A. and Bernoulli, D. (1982). Geochemical variations in quarry hardgrounds from the Hellenic Trench region and possible relationship to their tectonic setting." *Tectonophsysics,* 86: 149-157.

McKenzie, J. A., Hsu, K. J. and Schneider, J. F. (1980). Movement of subsurface waters under the sabkha, Abu Dhabi, UAE, and its relation to evaporative dolomite diagenesis. *SEPM Special Publication,* 28: 11-30.

McLaughlin, P., Brett, C. and Wilson, M. (2008). Hierarchy of sedimentary discontinuity surfaces and condensed beds from the middle Paleozoic of eastern North America: Implications for cratonic sequence stratigraphy. *Special Paper - Geological Association of Canada*.

Mcleod, E., Chmura, G. L., Bouillon, S., Salm, R., Björk, M., Duarte, C. M., Lovelock, C. E., Schlesinger, W. H. and Silliman, B. R. (2011). A blueprint for blue carbon: toward an improved understanding of the role of vegetated coastal habitats in sequestering CO_2. *Frontiers in Ecology and the Environment,* 9(10): 552-560. DOI: https://doi.org/10.1890/110004.

McMurdie, P. J. and Holmes, S. (2013). phyloseq: An R Package for Reproducible Interactive Analysis and Graphics of Microbiome Census Data. *PLoS One,* 8(4): e61217. DOI: 10.1371/journal.pone.0061217.

Meijboom, F. and van Noordwijk, M. (1991). Rhizon soil solution samplers as artificial roots. Root ecology and its practical application 3. L. Kutschera, E. Huebl, E. Lichtenegger, H. Persson and M. Sonbotnik. ISRR Symposium., Verein für Wurzelforschung, A-9020 Klagenfurt Austria**:** 793-795.

Meteostat (2021). "Abu Dhabi." Retrieved 1st June, 2021, from https://meteostat.net/en/place/AE-5E9R.

Michael Reynolds, R. (1993). Physical oceanography of the Gulf, Strait of Hormuz, and the Gulf of Oman—Results from the Mt Mitchell expedition. *Marine Pollution Bulletin,* 27: 35-59. DOI: https://doi.org/10.1016/0025-326X(93)90007-7.

Middleton, J. F. (2000). Wind-Forced Upwelling: The Role of the Surface Mixed Layer. *Journal of Physical Oceanography,* 30(5): 745-763. DOI: 10.1175/1520-0485(2000)030.

Milano, S. and Nehrke, G. (2018). Microstructures in relation to temperature-induced aragonite-to-calcite transformation in the marine gastropod Phorcus turbinatus. *PLoS One,* 13(10): e0204577. DOI: 10.1371/journal.pone.0204577.

Miller, M. D., Adkins, J. F. and Hodell, D. A. (2014). Rhizon sampler alteration of deep ocean sediment interstitial water samples, as indicated by chloride concentration and oxygen and hydrogen isotopes. *Geochemistry, Geophysics, Geosystems,* 15(6): 2401-2413. DOI: https://doi.org/10.1002/2014GC005308.

Millero, F. J. and Pierrot, D. (1998). A Chemical Equilibrium Model for Natural Waters. *Aquatic Geochemistry,* 4(1): 153-199. DOI: 10.1023/A:1009656023546.

Molenaar, N. and Zijlstra, J. J. P. (1997). Differential early diagenetic low-Mg calcite cementation and rhythmic hardground development in Campanian-Maastrichtian chalk. *Sedimentary Geology,* 109(3): 261-281. DOI: https://doi.org/10.1016/S0037-0738(96)00064-4.

Monteverde, D. R., Sylvan, J. B., Suffridge, C., Baronas, J. J., Fichot, E., Fuhrman, J., Berelson, W. and Sañudo-Wilhelmy, S. A. (2018). Distribution of Extracellular Flavins in a Coastal Marine Basin and Their Relationship to Redox Gradients and Microbial Community Members. *Environmental Science & Technology,* 52(21): 12265-12274. DOI: 10.1021/acs.est.8b02822.

Moore, C. H. (1989). Carbonate Diagenesis and Porosity, Elsevier Science.

Moore, C. H. and Wade, W. J. (2013). Chapter 7 - Evaporative Marine Diagenetic Environment. Developments in Sedimentology. C. H. Moore and W. J. Wade, Elsevier. 67**:** 133-163.

Moore, T. S., Murray, R. W., Kurtz, A. C. and Schrag, D. P. (2004). Anaerobic methane oxidation and the formation of dolomite. *Earth and Planetary Science Letters,* 229: 141-154.

Morse, J. W. and Mackenzie, F. T. (1990). Geochemistry of Sedimentary Carbonates. Developments in Sedimentology, Elsevier. 48**:** 1-707.

Morse, J. W., Wang, Q. and Tsio, M. Y. (1997). Influences of temperature and Mg:Ca ratio on CaCO3 precipitates from seawater. *Geology,* 25(1): 85-87. DOI: 10.1130/0091-7613(1997)025.

Moshier, S. O. (1989). Microporosity in micritic limestones: a review. *Sedimentary Geology,* 63(3): 191-213. DOI: https://doi.org/10.1016/0037-0738(89)90132-2.

Mozley, P. S. and Burns, S. J. (1993). Oxygen and carbon isotopic composition of marine carbonate concretions; an overview. *Journal of sedimentary Petrology,* 63(1): 73-83.

Murtaza, G., Haynes, R. J., Naidu, R., Belyaeva, O. N., Kim, K.-R., Lamb, D. T. and Bolan, N. S. (2011). Natural Attenuation of Zn, Cu, Pb and Cd in Three Biosolids-Amended Soils of Contrasting pH Measured Using Rhizon Pore Water Samplers. *Water, Air, & Soil Pollution,* 221(1): 351-363. DOI: 10.1007/s11270-011-0795-8.

Naehr, T. H., Eichhubl, P., Orphan, V. J., Hovland, M., Paull, C. K., Ussler, W., Lorenson, T. D. and Greene, H. G. (2007). Authigenic carbonate formation at hydrocarbon seeps in continental margin sediments: A comparative study. *Deep Sea Research Part II: Topical Studies in Oceanography,* 54(11): 1268-1291. DOI: https://doi.org/10.1016/j.dsr2.2007.04.010.

National Centre of Meteorology. (2020). "Climate Yearly Report 2003-2019." 2020, from https://www.ncm.ae/en/climate-reports-yearly.html?id=26.

Naviaux, J. D. (2019). Chemical and Physical Mechanisms of Calcite Dissolution in Seawater, Chapter 3, California Institute of Technology. Dissertation (PhD): 74-96

Naviaux, J. D., Subhas, A. V., Dong, S., Rollins, N. E., Liu, X., Byrne, R. H., Berelson, W. M. and Adkins, J. F. (2019). Calcite dissolution rates in seawater: Lab vs. in-situ measurements and inhibition by organic matter. *Marine Chemistry,* 215. DOI: 10.1016/j.marchem.2019.103684.

Nickerson, N. H. and Thibodeau, F. R. (1985). Association between pore water sulfide concentrations and the distribution of mangroves. *Biogeochemistry,* 1: 183-192.

Niedermayr, A., Köhler, S. J. and Dietzel, M. (2013). Impacts of aqueous carbonate accumulation rate, magnesium and polyaspartic acid on calcium carbonate formation (6–40°C). *Chemical Geology,* 340: 105-120. DOI: 10.1016/j.chemgeo.2012.12.014.

Nordstrom, D. K., Plummer, L. N., Wigley, T. M. L., Wolery, T. J., Ball, J. W., Jenne, E. A., Bassett, R. L., Crerar, D. A., Florence, T. M., Fritz, B., Hoffman, M., Holdren, G. R., Jr., Lafon, G. M., Mattigod, S. V., McDuff, R. E., Morel, F., Reddy, M. M., Sposito, G. and Thrailkill, J. (1979). A comparison of computerized chemical models for equilibrium calculations in aqueous systems. Chemical Modeling in aqueous systems, speciation, sorption, solubility, and kinetics. E. A. Jenne, American Chemical Society**:** 857-892.

Nothdurft, L. D., Webb, G. E. and Kamber, B. S. (2004). Rare earth element geochemistry of Late Devonian reefal carbonates, Canning Basin, Western Australia: confirmation of a seawater REE proxy in ancient limestones. *Geochimica et Cosmochimica Acta,* 68(2): 263-283. DOI: https://doi.org/10.1016/S0016-7037(03)00422-8.

Oni, O. E., Schmidt, F., Miyatake, T., Kasten, S., Witt, M., Hinrichs, K. U. and Friedrich, M. W. (2015). Microbial Communities and Organic Matter Composition in Surface and Subsurface Sediments of the Helgoland Mud Area, North Sea. *Front Microbiol, 6*: 1290. DOI: 10.3389/fmicb.2015.01290.

Orr, J. C., Epitalon, J. M. and Gattuso, J. P. (2015). Comparison of ten packages that compute ocean carbonate chemistry. *Biogeosciences,* 12(5): 1483-1510. DOI: 10.5194/bg-12-1483-2015.

Orsi, W. D., Vuillemin, A., Rodriguez, P., Coskun, O. K., Gomez-Saez, G. V., Lavik, G., Mohrholz, V. and Ferdelman, T. G. (2020). Metabolic activity analyses demonstrate that Lokiarchaeon exhibits homoacetogenesis in sulfidic marine sediments. *Nat Microbiol,* 5(2): 248-255. DOI: 10.1038/s41564-019-0630-3.

Oueslati, W., van de Velde, S., Helali, M. A., Added, A., Aleya, L. and Meysman, F. J. R. (2019). Carbon, iron and sulphur cycling in the sediments of a Mediterranean lagoon (Ghar El Melh, Tunisia). *Estuarine, Coastal and Shelf Science,* 221: 156-169. DOI: 10.1016/j.ecss.2019.03.008.

Pace, A., Bourillot, R., Bouton, A., Vennin, E., Braissant, O., Dupraz, C., Duteil, T., Bundeleva, I., Patrier, P., Galaup, S., Yokoyama, Y., Franceschi, M., Virgone, A. and Visscher, P. T. (2018). Formation of stromatolite lamina at the interface of oxygenic-anoxygenic photosynthesis. *Geobiology,* 16(4): 378-398. DOI: 10.1111/gbi.12281.

Pan, J., Zhou, Z., Beja, O., Cai, M., Yang, Y., Liu, Y., Gu, J. D. and Li, M. (2020). Genomic and transcriptomic evidence of light-sensing, porphyrin biosynthesis, Calvin-Benson-Bassham cycle, and urea production in Bathyarchaeota. *Microbiome,* 8(1): 43. DOI: 10.1186/s40168-020-00820-1.

Parada, A. E., Needham, D. M. and Fuhrman, J. A. (2016). Every base matters: assessing small subunit rRNA primers for marine microbiomes with mock communities, time series and global field samples. *Environmental Microbiology,* 18(5): 1403-1414. DOI: https://doi.org/10.1111/1462-2920.13023.

Parkhurst, D. L. and Appelo, C. A. J. (2013). Description of input and examples for PHREEQC version 3—A computer program for speciation, batch-reaction, one-dimensional transport, and inverse geochemical calculations. *U.S. Geological Survey Techniques and Methods*.

Parsons, T. R., Takahashi, M. and Hargrave, B. (1984). Biological oceanographic processes 3rd edition. London, Pergamon Press.

Patterson, R. J. and Kinsman, D. J. J. (1982). Formation of Diagenetic Dolomite in Coastal Sabkha Along Arabian (Persian) Gulf1. *AAPG Bulletin,* 66(1): 28-43. DOI: 10.1306/03b59a17-16d1-11d7-8645000102c1865d.

Patterson, R. J., Kinsman, D. J. J., Frost, S. H., Weiss, M. P. and Saunders, J. B. (1977). Marine and Continental Groundwater Sources in a Persian Gulf Coastal Sabkha1. Reefs and Related Carbonates—Ecology and Sedimentology, American Association of Petroleum Geologists. 4**:** 0.

Paul, A. and Lokier, S. W. (2017). Holocene marine hardground formation in the Arabian Gulf: Shoreline stabilisation, sea level and early diagenesis in the coastal sabkha of Abu Dhabi. *Sedimentary Geology,* 352: 1-13. DOI: 10.1016/j.sedgeo.2017.02.005.

Paul, A., Lokier, S. W., Sherry, A., Andrade, L. L., Court, W. M., van der Land, C., Dutton, K. E. and Head, I. M. (2021). Erosion-initiated stromatolite and thrombolite formation in a present-day coastal sabkha setting. *Sedimentology,* 68: 382-401. DOI: https://doi.org/10.1111/sed.12783.

Peckmann, J. r., Gischler, E., Oschmann, W. and Reitner, J. (2001). An Early Carboniferous seep community and hydrocarbon-derived carbonates from the Harz Mountains, Germany. *Geology,* 29(3): 271-274. DOI: 10.1130/0091-7613(2001)029.

Pederson, C. L., Klaus, J. S., Swart, P. K. and Mcneill, D. F. (2019). Deposition and early diagenesis of microbial mud in the Florida Everglades. *Sedimentology,* 66(6): 1989-2010. DOI: https://doi.org/10.1111/sed.12569.

Pederson, C. L., Mavromatis, V., Dietzel, M., Rollion-Bard, C., Breitenbach, S. F. M., Yu, D., Nehrke, G. and Immenhauser, A. (2020). Variation in the diagenetic response of aragonite archives to hydrothermal alteration. *Sedimentary Geology,* 406: 105716. DOI: https://doi.org/10.1016/j.sedgeo.2020.105716.

Pederson, C. L., Weiss, L., Mavromatis, V., Rollion-Bard, C., Dietzel, M., Neuser, R. and Immenhauser, A. (2019). Significance of fluid chemistry throughout diagenesis of aragonitic Porites corals – An experimental approach. *The Depositional Record,* 5(3): 592-612. DOI: 10.1002/dep2.82.

Pelletier, G., Lewis, E. and Wallace, D. (2007). CO2SY S.XLS: A calculator for the CO_2 system in seawater for Microsoft Excel/VBA. Wash. State Dept. of Ecology/Brookhaven Nat. Lab., Olympia, WA/Upton, NY, USA.

Perdikouri, C., Piazolo, S., Kasioptas, A., Schmidt, B. and Putnis, A. (2013). Hydrothermal replacement of Aragonite by Calcite: interplay between replacement, fracturing and growth. *European Journal of Mineralogy,* 25: 123-136. DOI: 10.1127/0935-1221/2013/0025-2261.

Perry, C. T. (1999). Biofilm-related calcification, sediment trapping and constructive micrite envelopes: A criterion for the recognition of ancient grass-bed environments? *Sedimentology,* 46(1): 33-45. DOI: 10.1046/j.1365-3091.1999.00201.x.

Peters, N. A., Huntington, K. W. and Hoke, G. D. (2013). Hot or not? Impact of seasonally variable soil carbonate formation on paleotemperature and O-isotope records from clumped isotope thermometry. *Earth and Planetary Science Letters,* 361: 208-218. DOI: 10.1016/j.epsl.2012.10.024.

Petryshyn, V. A., Corsetti, F. A., Berelson, W. M., Beaumont, W. and Lund, S. P. (2012). Stromatolite lamination frequency, Walker Lake, Nevada: Implications for stromatolites as biosignatures. *Geology,* 40(6): 499-502. DOI: 10.1130/g32675.1.

Phelps, R. M., Kerans, C., Da-Gama, R. O. B. P., Jeremiah, J., Hull, D. and Loucks, R. G. (2015). Response and recovery of the Comanche carbonate platform surrounding multiple Cretaceous oceanic anoxic events, northern Gulf of Mexico. *Cretaceous Research,* 54: 117-144. DOI: https://doi.org/10.1016/j.cretres.2014.09.002.

Pitzer, K. S. (1973). Thermodynamics of Electrolytes. I. Theoretical Basis and General Equations. *Molecular Structure and Statistical Thermodynamics*: 386-395. DOI: 10.1142/9789812795960_0057.

Pitzer, K. S. and Mayorga, G. (1973). Thermodynamics of electrolytes. II. Activity and osmotic coefficients for strong electrolytes with one or both ions univalent. *The Journal of Physical Chemistry,* 77(19): 2300-2308. DOI: 10.1021/j100638a009.

Plet, C., Grice, K., Pagès, A., Ruebsam, W., Coolen, M. J. L. and Schwark, L. (2016). Microbially-mediated fossil-bearing carbonate concretions and their significance for palaeoenvironmental reconstructions: A multi-proxy organic and inorganic geochemical appraisal. *Chemical Geology,* 426: 95-108. DOI: 10.1016/j.chemgeo.2016.01.026.

Plummer, L. N., Wigley, T. M. L. and Parkhurst, D. L. (1978). The kinetics of calcite dissolution in CO_2-water systems at 5 degrees to 60 degrees C and 0.0 to 1.0 atm CO_2. *American Journal of Science,* 278(2): 179-216. DOI: 10.2475/ajs.278.2.179.

Pohlman, J. W., Riedel, M., Waite, W. F., Rose, K. and Lapham, L. (2008). Application of RHIZON samplers to obtain high-resolution pore-fluid records during geochemical investigations of gas hydrate systems. *Fire in the Ice: NETL Methane Hydrate Newsletter,* 8(4): 16-17.

Poppe, L. J., Paskevich, V., Hathaway, J. and Blackwood, D. (2001). A Laboratory Manual for X-Ray Powder Diffraction. *US Geological Survey Open File Report,* 1.

Purkis, S., Cavalcante, G., Rohtla, L., Oehlert, A., Harris, P. and Swart, P. (2017). Hydrodynamic control of whitings on Great Bahama Bank. *Geology,* 45. DOI: 10.1130/G39369.1.

Qiao, Y., Liu, J., Zhao, M. and Zhang, X.-H. (2018). Sediment Depth-Dependent Spatial Variations of Bacterial Communities in Mud Deposits of the Eastern China Marginal Seas. *Frontiers in Microbiology,* 9(1128). DOI: 10.3389/fmicb.2018.01128.

Quast, C., Pruesse, E., Yilmaz, P., Gerken, J., Schweer, T., Yarza, P., Peplies, J. and Glöckner, F. O. (2012). The SILVA ribosomal RNA gene database project: improved data processing and web-based tools. *Nucleic Acids Research,* 41(D1): D590-D596. DOI: 10.1093/nar/gks1219.

Raafat, H. (2007). Climate. Physical Geography Sector Paper. A. E. Kumar. Abu Dhabi, Environment Agency Abu Dhabi**:** 72–89.

Raiswell, R. and Fisher, Q. J. (2004). Rates of carbonate cementation associated with sulphate reduction in DSDP/ODP sediments: implications for the formation of concretions. *Chemical Geology,* 211(1-2): 71-85. DOI: 10.1016/j.chemgeo.2004.06.020.

Rankey, E. C. (2002). Spatial Patterns of Sediment Accumulation on a Holocene Carbonate Tidal Flat, Northwest Andros Island, Bahamas. *Journal of Sedimentary Research,* 72(5): 591-601. DOI: 10.1306/020702720591.

Redfield, A. C., Ketchum, B. H. and Richards, F. A. (1963). The Influence of Organisms on the Composition of the Sea Water. The Sea. M. N. Hill. New York, Interscience Publishers. 2.

Reeburgh, W. S. (1967). An improved interstitial water sampler. *Limnology and Oceanography,* 12(1): 163-165. DOI: https://doi.org/10.4319/lo.1967.12.1.0163.

Reid, R. P., Visscher, P. T., Decho, A. W. and al., e. (2000). The role of microbes in accretion, lamination and early lithification of modern marine stromatolites. *Nature,* 406: 989-992.

Reimers, C. E., Alleau, Y., Bauer, J. E., Delaney, J., Girguis, P. R., Schrader, P. S. and Stecher, H. A. (2013). Redox effects on the microbial degradation of refractory organic matter in marine sediments. *Geochimica et Cosmochimica Acta,* 121: 582-598. DOI: https://doi.org/10.1016/j.gca.2013.08.004.

Rich, V. I. and Maier, R. M. (2015). Chapter 6 - Aquatic Environments. Environmental Microbiology (Third Edition). I. L. Pepper, C. P. Gerba and T. J. Gentry. San Diego, Academic Press**:** 111-138.

Rivers, J. M., Varghese, L., Yousif, R., Whitaker, F. F., Skeat, S. L. and Al-Shaikh, I. (2019). The Geochemistry of Qatar Coastal Waters and its Impact on Carbonate Sediment Chemistry and Early Marine Diagenesis. *Journal of Sedimentary Research,* 89(4): 293-309. DOI: 10.2110/jsr.2019.17.

Robador, A., Muller, A. L., Sawicka, J. E., Berry, D., Hubert, C. R., Loy, A., Jorgensen, B. B. and Bruchert, V. (2016). Activity and community structures of sulfate-reducing microorganisms in polar, temperate, and tropical marine sediments. *ISME J,* 10(4): 796-809. DOI: 10.1038/ismej.2015.157.

Rog, S. M. and Cook, C. N. (2017). Strengthening governance for intertidal ecosystems requires a consistent definition of boundaries between land and sea. *J Environ Manage,* 197: 694-705. DOI: 10.1016/j.jenvman.2017.04.052.

Sadooni, F. and Strohmenger, C. (2013). Microbial-Mediated Dolomite from Abu Dhabi Coastal Sabkha Sediments as Analogue to the Mesozoic Dolomite of the Arabian Plate. Microbial Carbonates in Space and Time: Implications for Global Exploration and Production. London

Saffer, D., McNeill, L., Byrne, T., Araki, E., Toczko, S., Eguchi, N., Takahashi, K. and Scientists., T. E. (2010). Proc. IODP, 319: Tokyo (Integrated Ocean Drilling Program Management International, Inc.). DOI: 10.2204/iodp.proc.319.101.2010.

Salhi, N., Douaoui, A., Trolard, F. and Bourrié, G. (2019). Specific interaction theory versus Pitzer's model in groundwaters and brines for checking equilibria/non-equilibria with calcite, gypsum, and halite: application to predict the evolution of solutions concentrated by evaporation in irrigated areas. *Environmental Earth Sciences,* 78(6). DOI: 10.1007/s12665-019-8139-x.

Sanford, W. and Wood, W. (2001). Hydrology of the coastal sabkhas of Abu Dhabi, United Arab Emirates. *Hydrogeology Journal,* 9(4): 358-366. DOI: 10.1007/s100400100137.

Sass, W. and Ben-Yaakov, S. (1977). The carbonate system in hypersaline solutions: dead sea brine. *Marine Chemistry,* 5: 183-199.

Schrag, D. P., DePaolo, D. J. and Richter, F. M. (1995). Reconstructing past sea surface temperatures: Correcting for diagenesis of bulk marine carbonate. *Geochimica et Cosmochimica Acta,* 59(11): 2265-2278. DOI: https://doi.org/10.1016/0016-7037(95)00105-9.

Schrag, D. P., Higgins, J. A., Macdonald, F. A. and Johnston, D. T. (2013). Authigenic Carbonate and the History of the Global Carbon Cycle. *Science,* 339(6119): 540-543.

Schroeder, D. (2000). An Introduction to Thermal Physics. United States: Addison Wesley Longman.

Schrum, H., Murray, R. and Gribsholt, B. (2012). Comparison of Rhizon Sampling and Whole Round Squeezing for Marine Sediment Porewater. *Scientific Drilling,* 13. DOI: 10.5194/sd-13-47-2012.

Schulz, H. D. and Zabel, M. (2006). Marine Geochemistry, Springer-Verlag Berlin Heidelberg.

Seeberg-Elverfeldt, J., Schlüter, M., Feseker, T. and Kölling, M. (2005). Rhizon sampling of porewaters near the sediment-water interface of aquatic systems. *Limnology and Oceanography: Methods,* 3(8): 361-371. DOI: https://doi.org/10.4319/lom.2005.3.361.

Sharp, Z. (2007). Principles of Stable Isotope Geochemistry, Pearson/Prentice Hall.

Sheikholeslami, R. and Ong, H. W. K. (2003). Kinetics and thermodynamics of calcium carbonate and calcium sulfate at salinities up to 1.5 M. *Desalination,* 157: 217-234.

Shinn, E. A. (1969). Submarine lithification of Holocene carbonate sediments in the Persian Gulf. *Sedimentology,* 12: 109-114.

Shiraishi, F., Bissett, A., de Beer, D., Reimer, A. and Arp, G. (2008). Photosynthesis, Respiration and Exopolymer Calcium-Binding in Biofilm Calcification (Westerhöfer and Deinschwanger Creek, Germany). *Geomicrobiology Journal,* 25(2): 83-94. DOI: 10.1080/01490450801934888.

Shiraishi, F., Omori, T., Tomioka, N., Motai, S., Suga, H. and Takahashi, Y. (2020). Characteristics of $CaCO_3$ nucleated around cyanobacteria: Implications for calcification process. *Geochimica et Cosmochimica Acta,* 285: 55-69. DOI: 10.1016/j.gca.2020.06.033.

Shotbolt, L. (2010). Pore water sampling from lake and estuary sediments using Rhizon samplers. *Journal of Paleolimnology,* 44(2): 695-700. DOI: 10.1007/s10933-008-9301-8.

Sigfusson, B., Paton, G. I. and Gislason, S. R. (2006). The impact of sampling techniques on soil pore water carbon measurements of an Icelandic Histic Andosol. *Science of The Total Environment,* 369(1): 203-219. DOI: https://doi.org/10.1016/j.scitotenv.2006.01.012.

Sivan, O., Schrag, D. P. and Murray, R. W. (2007). Rates of methanogenesis and methanotrophy in deep-sea sediments. *Geobiology,* 5(2): 141-151. DOI: 10.1111/j.1472-4669.2007.00098.x.

Słowakiewicz, M., Whitaker, F., Thomas, L., Tucker, M. E., Zheng, Y., Gedl, P. and Pancost, R. D. (2016). Biogeochemistry of intertidal microbial mats from Qatar: New insights from organic matter characterisation. *Organic Geochemistry,* 102: 14-29. DOI: 10.1016/j.orggeochem.2016.09.006.

Soetaert, K., Hofmann, A. F., Middelburg, J. J., Meysman, F. J. R. and Greenwood, J. (2007). Reprint of "The effect of biogeochemical processes on pH". *Marine Chemistry,* 106(1-2): 380-401. DOI: 10.1016/j.marchem.2007.06.008.

Song, J., Luo, Y. M., Zhao, Q. G. and Christie, P. (2003). Novel use of soil moisture samplers for studies on anaerobic ammonium fluxes across lake sediment–water interfaces. *Chemosphere,* 50(6): 711-715. DOI: https://doi.org/10.1016/S0045-6535(02)00210-2.

St. C. Kendall, C. G. and Alsharhan, A. S. (2012). Coastal Holocene carbonates of Abu Dhabi, UAE: depositional setting, sediment distribution, and role of cyanobacteria in micritization. Quaternary carbonate and evaporite sedimentary facies and their ancient analogues**:** 205-219.

Steiner, Z., Lazar, B., Erez, J. and Turchyn, A. V. (2018). Comparing Rhizon samplers and centrifugation for pore-water separation in studies of the marine carbonate system in sediments. *Limnology and Oceanography: Methods,* 16(12): 828-839. DOI: https://doi.org/10.1002/lom3.10286.

Stolper, D. A. and Eiler, J. M. (2016). Constraints on the formation and diagenesis of phosphorites using carbonate clumped isotopes. *Geochimica et Cosmochimica Acta,* 181: 238-259. DOI: https://doi.org/10.1016/j.gca.2016.02.030.

Stolper, D. A., Eiler, J. M. and Higgins, J. A. (2018). Modelling the effects of diagenesis on carbonate clumped-isotope values in deep- and shallow-water settings. *Geochimica et Cosmochimica Acta,* 227: 264-291. DOI: https://doi.org/10.1016/j.gca.2018.01.037.

Strasser, A. (2015). Hiatuses and condensation: an estimation of time lost on a shallow carbonate platform. *The Depositional Record,* 1(2): 91-117. DOI: https://doi.org/10.1002/dep2.9.

Sun, H., Spring, S., Lapidus, A., Davenport, K., Del Rio, T. G., Tice, H., Nolan, M., Copeland, A., Cheng, J.-F., Lucas, S., Tapia, R., Goodwin, L., Pitluck, S., Ivanova, N., Pagani, I., Mavromatis, K., Ovchinnikova, G., Pati, A., Chen, A., Palaniappan, K., Hauser, L., Chang, Y.-J., Jeffries, C. D., Detter, J. C., Han, C., Rohde, M., Brambilla, E., Göker, M., Woyke, T., Bristow, J., Eisen, J. A., Markowitz, V., Hugenholtz, P., Kyrpides, N. C., Klenk, H.-P. and Land, M. (2010). Complete genome sequence of Desulfarculus baarsii type strain (2st14). *Standards in genomic sciences,* 3(3): 276-284. DOI: 10.4056/sigs.1243258.

Sun, W., Jayaraman, S., Chen, W., Persson, K. A. and Ceder, G. (2015). Nucleation of metastable aragonite $CaCO_3$; in seawater. *Proceedings of the National Academy of Sciences,* 112(11): 3199. DOI: 10.1073/pnas.1423898112.

Sun, X. and Turchyn, A. V. (2014). Significant contribution of authigenic carbonate to marine carbon burial. *Nature Geoscience,* 7(3): 201-204. DOI: 10.1038/ngeo2070.

Swart, P. K. (2015). The geochemistry of carbonate diagenesis: The past, present and future. *Sedimentology,* 62(5): 1233-1304. DOI: 10.1111/sed.12205.

Tadier, S., Rokidi, S., Rey, C., Combes, C. and Koutsoukos, P. G. (2017). Crystal growth of aragonite in the presence of phosphate. *Journal of Crystal Growth,* 458: 44-52. DOI: 10.1016/j.jcrysgro.2016.10.046.

Tagliapietra, D., Sigovini, M. and Ghirardini, A. V. (2009). A review of terms and definitions to categorise estuaries, lagoons, and associated environments. *Marine and Freshwater Research,* 60(6): 497-509. DOI: 10.1071/MF08088.

Taylor, J. C. M. and Illing, L. V. (1969). Holocene intertidal calcium carbonate cementation, Qatar, Persian Gulf. *Sedimentology,* 12: 69-107.

Thamdrup, B. and Canfield, D. E. (1996). Pathways of carbon oxidation in continental margin sediments off central Chile. *Limnol. Oceanogr.,* 41(8): 1629-1650.

Tides4Fishing (2021). "Abu Dhabi." Retrieved 1st June, 2021, from https://tides4fishing.com/as/united-arab-emirates/abu-dhabi.

Tiensing, T., Preston, S., Strachan, N. and Paton, G. I. (2001). Soil solution extraction techniques for microbial ecotoxicity testing: a comparative evaluation. *Journal of Environmental Monitoring,* 3(1): 91-96. DOI: 10.1039/B007851O.

Tourney, J. and Ngwenya, B. T. (2009). Bacterial extracellular polymeric substances (EPS) mediate $CaCO_3$ morphology and polymorphism. *Chemical Geology,* 262(3-4): 138-146. DOI: 10.1016/j.chemgeo.2009.01.006.

Tucker, M. E. and Wright, V. P. (1990). Carbonate Sedimentology. London, U.K, Blackwell Scientific Publications.

Tye, A. M., Young, S. D., Crout, N. M. J., Zhang, H., Preston, S., Barbosa-Jefferson, V. L., Davison, W., McGrath, S. P., Paton, G. I., Kilham, K. and Resende, L. (2003). Predicting the activity of Cd^{2+} and Zn^{2+} in soil pore water from the radio-labile metal fraction. *Geochimica et Cosmochimica Acta,* 67(3): 375-385. DOI: https://doi.org/10.1016/S0016-7037(02)01138-9.

Uchupi, E., Swift, S. A. and Ross, D. A. (1996). Gas venting and late Quaternary sedimentation in the Persian (Arabian) Gulf. *Marine Geology,* 129(3): 237-269. DOI: https://doi.org/10.1016/0025-3227(96)83347-0.

Underwood, G. J. C. (2001). Microphytobenthos. Encyclopaedia of Ocean Sciences (Second Edition). J. H. Steele. Oxford, Academic Press**:** 807-814.

van Heuven, S., Pierrot, D., Rae, J., Lewis, E. and Wallace, D. W. R. (2011). CO2SYS v 1.1, MATLAB program developed for CO2 system calculations. *ORNL/CDIAC-105b. Carbon Dioxide Information Analysis Center, Oak Ridge National Laboratory, U.S. DoE, Oak Ridge, TN*.

Veizer, J., Ala, D., Azmy, K., Bruckschen, P., Buhl, D., Bruhn, F., Carden, G. A. F., Diener, A., Ebneth, S., Godderis, Y., Jasper, T., Korte, C., Pawellek, F., Podlaha, O. G. and Strauss, H. (1999). 87Sr/86Sr, δ13C and δ18O evolution of Phanerozoic seawater. *Chemical Geology,* 161(1-3): 59-88. DOI: 10.1016/s0009-2541(99)00081-9.

Veizer, J. and Hoefs, J. (1976). The nature of O18/O16 and C13/C12 secular trends in sedimentary carbonate rocks. *Geochimica et Cosmochimica Acta,* 40(11): 1387-1395. DOI: https://doi.org/10.1016/0016-7037(76)90129-0.

Vinogradov, S. V. and Ponte, R. M. (2010). Annual cycle in coastal sea level from tide gauges and altimetry. *Journal of Geophysical Research,* 115(C4). DOI: 10.1029/2009jc005767.

Visscher, P. T., Reid, P. M., Bebout, B. M., Hoeft, S. E., MacIntyre, I. G. and Thompson, J. A. (1998). Formation of lithified micritic laminae in modern marine stromatolites (Bahamas): The role of sulfur cycling. *American Mineralogist,* 83: 1482-1493.

Wallace, M. W., Hood, A. v., Shuster, A., Greig, A., Planavsky, N. J. and Reed, C. P. (2017). Oxygenation history of the Neoproterozoic to early Phanerozoic and the rise of land plants. *Earth and Planetary Science Letters,* 466: 12-19. DOI: https://doi.org/10.1016/j.epsl.2017.02.046.

Wang, W., Tao, J., Liu, H., Li, P., Chen, S., Wang, P. and Zhang, C. (2020). Contrasting bacterial and archaeal distributions reflecting different geochemical processes in a sediment core from the Pearl River Estuary. *AMB Express,* 10(1): 16. DOI: 10.1186/s13568-020-0950-y.

Warren, J. (2016). Evaporites: A geological Compendium. Second Edition. Springer.

Waska, H., Greskowiak, J., Ahrens, J., Beck, M., Ahmerkamp, S., Böning, P., Brumsack, H. J., Degenhardt, J., Ehlert, C., Engelen, B., Grünenbaum, N., Holtappels, M., Pahnke, K., Marchant, H. K., Massmann, G., Meier, D., Schnetger, B., Schwalfenberg, K., Simon, H., Vandieken, V., Zielinski, O. and Dittmar, T. (2019). Spatial and Temporal Patterns of Pore Water Chemistry in the Inter-Tidal Zone of a High Energy Beach. *Frontiers in Marine Science,* 6(154). DOI: 10.3389/fmars.2019.00154.

Weber, K. A., Achenbach, L. A. and Coates, J. D. (2006). Microorganisms pumping iron: anaerobic microbial iron oxidation and reduction. *Nature Reviews Microbiology,* 4(10): 752-764. DOI: 10.1038/nrmicro1490.

Weigold, P., Ruecker, A., Loesekann-Behrens, T., Kappler, A. and Behrens, S. (2016). Ribosomal Tag Pyrosequencing of DNA and RNA Reveals "Rare" Taxa with High Protein Synthesis Potential in the Sediment of a Hypersaline Lake in Western Australia. *Geomicrobiology Journal,* 33(5): 426-440. DOI: 10.1080/01490451.2015.1049304.

Weiner, S. and Dove, P. M. (2003). An overview of biomineralization and the problem of the vital effect. Biomineralization. P. M. Dove, S. Weiner and J. J. De Yoreo. Washington, D.C, Mineralogical Society of America. Review in Mineralogy and Geochemistry. 54**:** 1-31.

Whitaker, F. and Frazer, M. A. (2018). Process-based Modelling of Syn-depositional Diagenesis. Reactive Transport Modelling: Application to subsurface energy and environmental problems F. W. Y. Xiao, & T. Xu Wiley**:** 107-156.

Whitaker, F. F., Ooi, S. M., Jameson, J. and Strohmenger, C. (2014). Origins of Evaporites in a Holocene Mixed Clastic and Carbonate Coastal Sabkha: Preliminary Hydrological and Geochemical Data from Mesaieed Sabkha, Qatar. *International Petroleum Technology Conference*.

Wilkinson, B. H., Smith, A. L. and Lohmann, K. C. (1985). Sparry calcite marine cement in Upper Jurassic limestones of southeastern Wyoming. Carbonate Cements. N. Schneidermann and P. M. Harris, The society of Economic Paleontologists and Mineralogists, Special Publication,**:** 185–220.

Williams, W. D. (1986). Conductivity and Salinity of Australian Salt Lakes. *Aust. J. Mar. Freshw. Res,* 37: 177-182.

Wilson, A. M., Huettel, M. and Klein, S. (2008). Grain size and depositional environment as predictors of permeability in coastal marine sands. *Estuarine, Coastal and Shelf Science,* 80(1): 193-199. DOI: 10.1016/j.ecss.2008.06.011.

Wong, H. L., Smith, D. L., Visscher, P. T. and Burns, B. P. (2015). Niche differentiation of bacterial communities at a millimeter scale in Shark Bay microbial mats. *Sci Rep,* 5: 15607. DOI: 10.1038/srep15607.

Wood, W. W., Sanford, W. E. and Al Habshi, A. R. S. (2002). Source of solutes to the coastal sabkha of Abu Dhabi. *GSA Bulletin,* 114(3): 259-268.

Woodworth, P. L., Melet, A., Marcos, M., Ray, R. D., Wöppelmann, G., Sasaki, Y. N., Cirano, M., Hibbert, A., Huthnance, J. M., Monserrat, S. and Merrifield, M. A. (2019). Forcing Factors Affecting Sea Level Changes at the Coast. *Surveys in Geophysics,* 40(6): 1351-1397. DOI: 10.1007/s10712-019-09531-1.

WorldWeatherOnline (2021). "Historial Weather Data, Abu Dhabi." Retrieved 1st June, 2021, from https://www.worldweatheronline.com/abu-dhabi-weather-history/abu-dhabi/ae.aspx.

Xiao, Y., Jones, G. D., Whitaker, F., Al-Helal, A. B., Stafford, S., Gomez-Rivas, E. and Guidry, S. (2013). Fundamental approaches to dolomitization and carbonate diagenesis in different hydrogeological systems and the impact on reservoir quality distribution.

Xu, C., Wu, N., Sun, Z., Zhang, X., Geng, W., Cao, H., Wang, L., Zhang, X. and Xu, G. (2018). Methane seepage inferred from pore water geochemistry in shallow sediments in the western slope of the Mid-Okinawa Trough. *Marine and Petroleum Geology,* 98: 306-315. DOI: https://doi.org/10.1016/j.marpetgeo.2018.08.021.

Xyla, A. G., Giannimaras, E. K. and Koutsoukos, P. G. (1991). The precipitation of calcium carbonate in aqueous solutions. *Colloids and Surfaces,* 53(2): 241-255. DOI: https://doi.org/10.1016/0166-6622(91)80140-J.

Yamada, T. and Sekiguchi, Y. (2009). Cultivation of uncultured chloroflexi subphyla: significance and ecophysiology of formerly uncultured chloroflexi 'subphylum i' with natural and biotechnological relevance. *Microbes Environ,* 24(3): 205-216. DOI: 10.1264/jsme2.me09151s.

Yamamuro, M. and Kayanne, H. (1995). Rapid direct determination of organic carbon and nitrogen in carbonate-bearing sediments with a Yanaco MT-5 CHN analyzer. *Limnology and Oceanography,* 40(5): 1001-1005. DOI: https://doi.org/10.4319/lo.1995.40.5.1001.

Yilmaz, P., Parfrey, L. W., Yarza, P., Gerken, J., Pruesse, E., Quast, C., Schweer, T., Peplies, J., Ludwig, W. and Glöckner, F. O. (2014). The SILVA and "All-species Living Tree Project (LTP)" taxonomic frameworks. *Nucleic Acids Res,* 42(Database issue): D643-648. DOI: 10.1093/nar/gkt1209.

Zetsche, E., Paterson, D. M., Lumsdon, D. G. and Witte, U. (2011). Temporal variation in the sediment permeability of an intertidal sandflat. *Marine Ecology Progress Series,* 441: 49-63. DOI: 10.3354/meps09390.

Zhang, J., Kobert, K., Flouri, T. and Stamatakis, A. (2014). PEAR: a fast and accurate Illumina Paired-End reAd mergeR. *Bioinformatics,* 30(5): 614-620. DOI: 10.1093/bioinformatics/btt593.

Zhang, N., Lin, M., Snyder, G. T., Kakizaki, Y., Yamada, K., Yoshida, N. and Matsumoto, R. (2019). Clumped isotope signatures of methane-derived authigenic carbonate presenting equilibrium values of their formation temperatures. *Earth and Planetary Science Letters,* 512: 207-213. DOI: https://doi.org/10.1016/j.epsl.2019.02.005.

Zhang, S. (2020). The relationship between organoclastic sulfate reduction and carbonate precipitation/dissolution in marine sediments. *Marine Geology,* 428. DOI: 10.1016/j.margeo.2020.106284.

Zhang, Y. and Dawe, R. A. (2000). Influence of Mg^{2+} on the kinetics of calcite precipitation and calcite crystal morphology. *Chemical Geology,* 163(1-4): 129-138. DOI: 10.1016/s0009-2541(99)00097-2.

Zhong, S. and Mucci, A. (1989). Calcite and aragonite precipitation from seawater solutions of various salinities: Precipitation rates and overgrowth compositions. *Chemical Geology,* 78(3-4): 283-299. DOI: 10.1016/0009-2541(89)90064-8.

Zhou, Z., Liu, Y., Lloyd, K. G., Pan, J., Yang, Y., Gu, J. D. and Li, M. (2019). Genomic and transcriptomic insights into the ecology and metabolism of benthic archaeal cosmopolitan, Thermoprofundales (MBG-D archaea). *ISME J,* 13(4): 885-901. DOI: 10.1038/s41396-018-0321-8.

Appendices

Appendix A: Chapter 2.2

Table A. Water chemistry for surface seawater (Nordtrom et al., 1979) and for Abu Dhabi (AD) seawaters (SW), groundwaters (GW) and porewaters (PW) of low, medium, and high salinity.

Sample ID	pH	pH temperature (°C)	SEC	Salinity	Alkalinity as HCO_3^- mmol/l	Cl^- mmol/l	SO_4^{2-} mmol/l	Na^+ mmol/l	Mg^{2+} mmol/l	Ca^{2+} mmol/l	K^{2+} mmol/l	Sr^{2+} mmol/l
SSW Nordstrom	8.22	25.00	53.30	35.00	2.30	545.92	28.23	468.38	53.15	10.29	10.21	0.10
AD_SW1	8.15	20.70	53.10	35.11	2.54	676.95	33.00	534.82	54.75	10.11	10.23	0.08
AD_SW2	8.15	20.70	56.20	37.34	2.54	683.75	33.37	537.28	55.35	10.27	10.04	0.08
AD_SW3	8.05	31.00	59.10	39.44	2.49	676.95	33.00	616.67	68.09	13.16	11.45	0.11
AD_SW4	7.97	31.20	59.40	39.66	2.48	683.75	33.37	613.61	66.17	12.97	11.41	0.11
AD_SW5	8.22	19.20	71.80	48.75	2.66	797.08	41.47	675.82	73.96	14.22	13.59	0.13
AD_SW6	8.08	22.30	75.60	51.60	2.62	820.56	38.87	663.51	76.61	13.24	10.47	0.13
AD_SW7	8.21	27.30	80.80	53.52	2.54	859.33	41.90	692.72	80.78	13.80	10.68	0.14
AD_SW8	8.21	23.20	91.00	64.87	2.53	1020.81	49.98	866.79	100.63	17.72	16.02	0.19
PW_Low1	8.10	21.70	100.30	71.99	2.00	1155.03	59.93	919.74	102.45	20.26	17.97	0.17
PW_Low2	7.16	22.80	109.90	79.39	2.27	1293.70	46.89	1074.07	108.71	19.74	18.82	0.17
PW_Low3	7.10	23.10	120.20	86.77	2.30	1417.93	47.72	1185.82	117.96	20.62	20.59	0.19
PW_Med1	7.06	23.10	130.10	96.59	2.30	1556.84	62.98	1315.80	128.92	22.80	22.68	0.21
PW_Med2	7.09	23.20	138.60	108.98	2.97	1718.68	92.58	1426.43	165.96	27.92	25.60	0.26
PW_Med3	6.94	23.10	148.80	117.02	3.21	1897.07	84.58	1533.74	173.83	23.97	24.94	0.25

PW_High1	6.76	23.00	158.60	122.92	2.79	2077.83	47.79	1666.92	154.01	33.74	26.89	0.30
PW_High2	6.69	21.90	164.60	127.77	2.35	2149.38	46.11	1768.79	154.99	34.08	29.83	0.31
PW_High3	6.79	22.20	175.60	134.19	2.12	2214.43	50.17	1909.25	166.60	36.92	32.64	0.34
PW_V-high1	7.65	23.30	192.00	169.09	1.69	2817.77	104.32	2220.60	236.39	19.95	36.97	0.25
PW_V-high2	7.30	24.00	207.80	195.08	1.39	3286.14	108.49	2574.10	271.92	16.25	41.10	0.28
PW_V-high3	6.88	22.50	210.90	191.23	2.13	3184.50	85.45	2666.21	254.42	19.86	43.18	0.31
GW1	6.72	24.10	193.10	170.32	2.22	2745.61	108.36	2344.12	246.44	24.07	39.94	0.34
GW2	6.29	24.20	216.70	197.77	2.05	3320.00	77.64	2767.90	234.46	31.43	47.70	0.32
GW3	6.34	24.00	233.00	222.79	2.48	3759.58	53.59	3256.20	223.25	37.60	60.56	0.52

Biogeochemical drivers of modern carbonate firmground formation: Yas Lagoon, Abu Dhabi: Supplemental

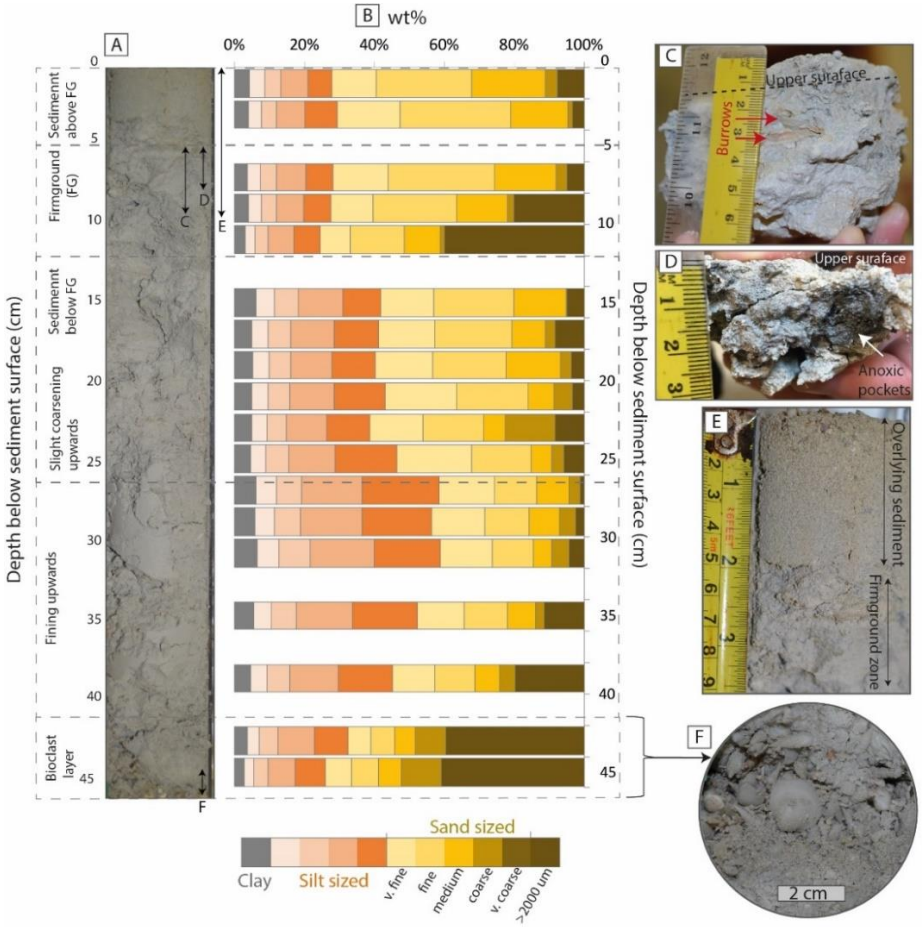

Fig. S1. (**A**) Photograph of Core A; (**B**) Grain size distribution (wt%) (samples from Core A, except at 9, 19 and 27 cm from Core B). (**C**) Hand specimen of full depth of firmground (typically 4 – 6 cm) showing typical variation in lower surface; (**D**) upper 3 cm of firmground from Core A with the lower, most poorly lithified 1-2 cm disaggregated and missing; (**E**) Close up of boundary between overlying sediment and the firmground zone at 5 cm (Core A); (**F**) Coarse bioclast layer at base of core dominated by gastropods and bivalves.

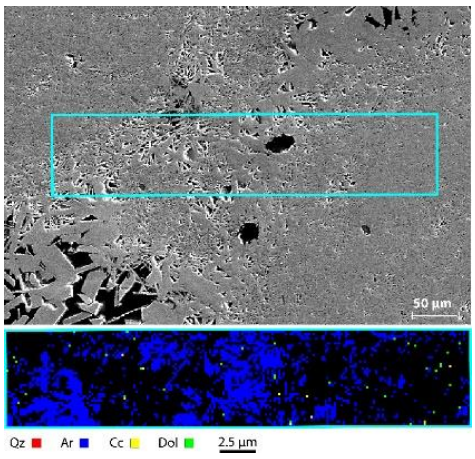

Fig. S2. Close up of EBSD, showing platy cements consisting of aragonite (blue).

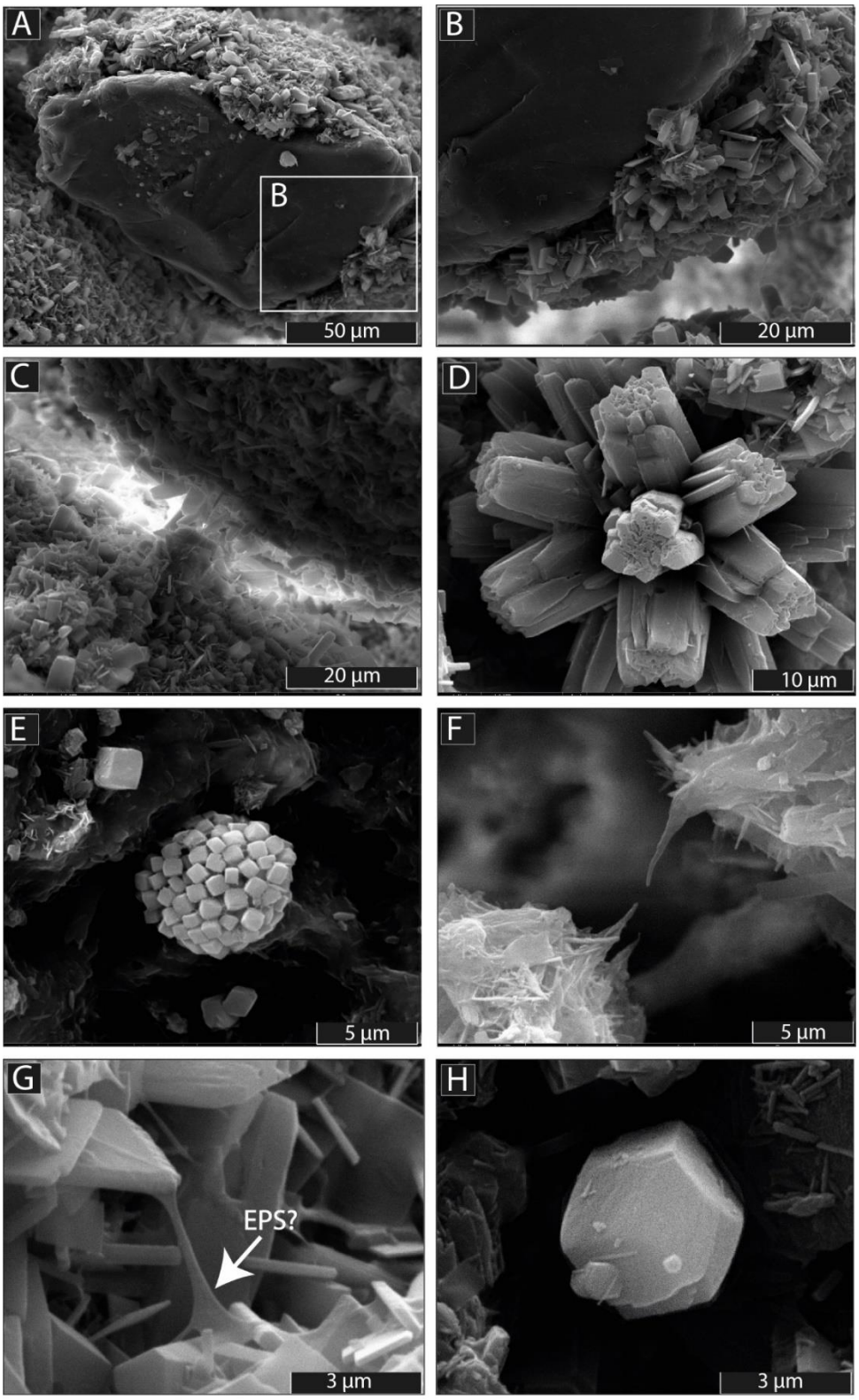

Fig. S3. SEM images of varying crystal morphologies within the firmground hand sample (A, B, C, D and G) and from fragments of firmground removed from core A (E, F, H). **A**, **B** and **C** show cement is dominated by well-defined platy cements with less common fibrous needles occurring at random orientation (with no detectable Mg), (**D**) Crystals forming radial growth bundles; (**E**) pyrite framboid; (**F**) aragonite crystals with pointed terminations converging to bridge the gap between grains. (**G**) potential EPS (white arrow) and (**H**) prismatic/hexagonal high-Mg calcite crystal.

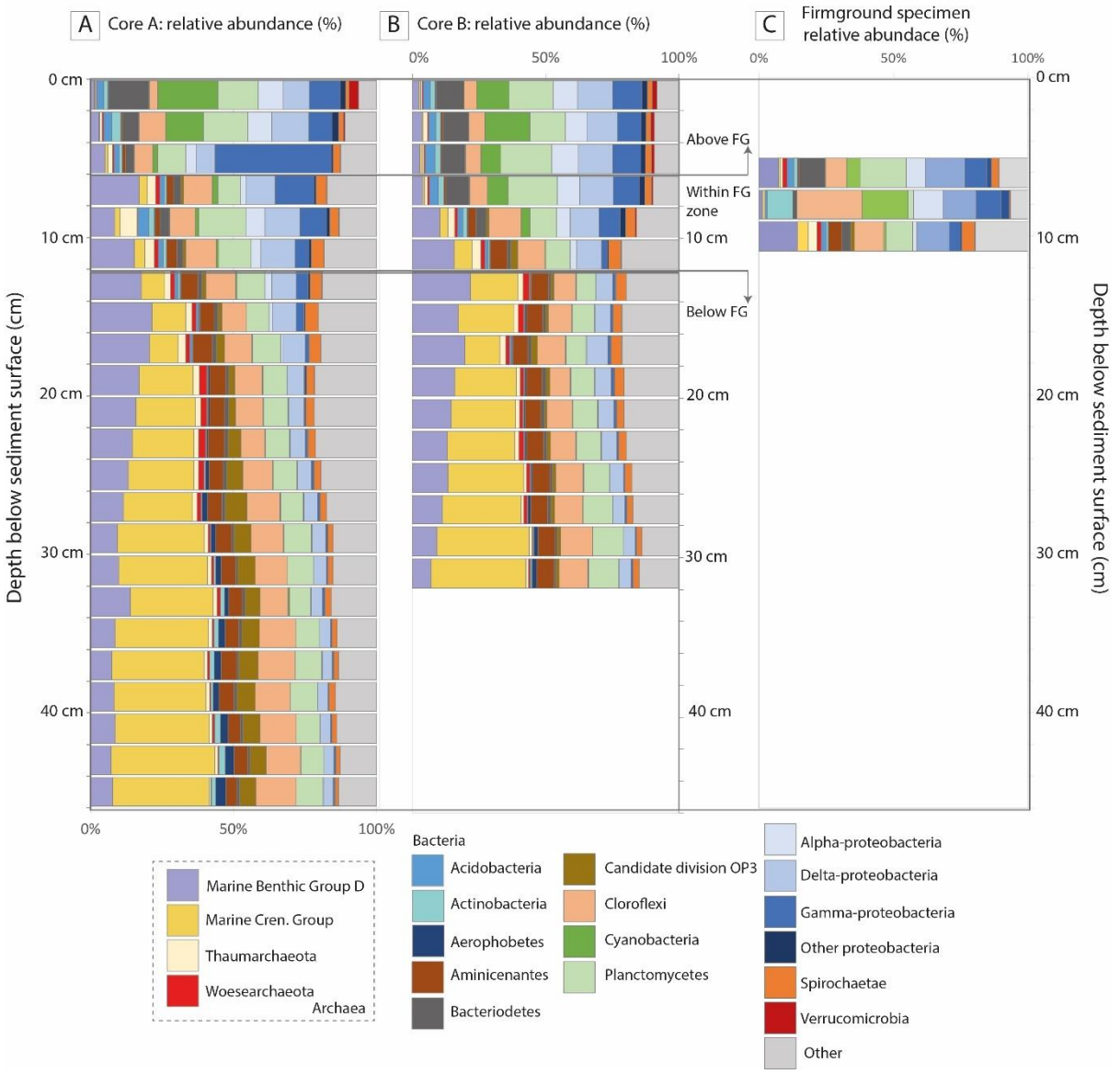

Fig. S4. 16S SSU rRNA genes sequence relative abundance for common communities from (**A**) Core A; (**B**) Core B; and (**C**) firmground specimen.

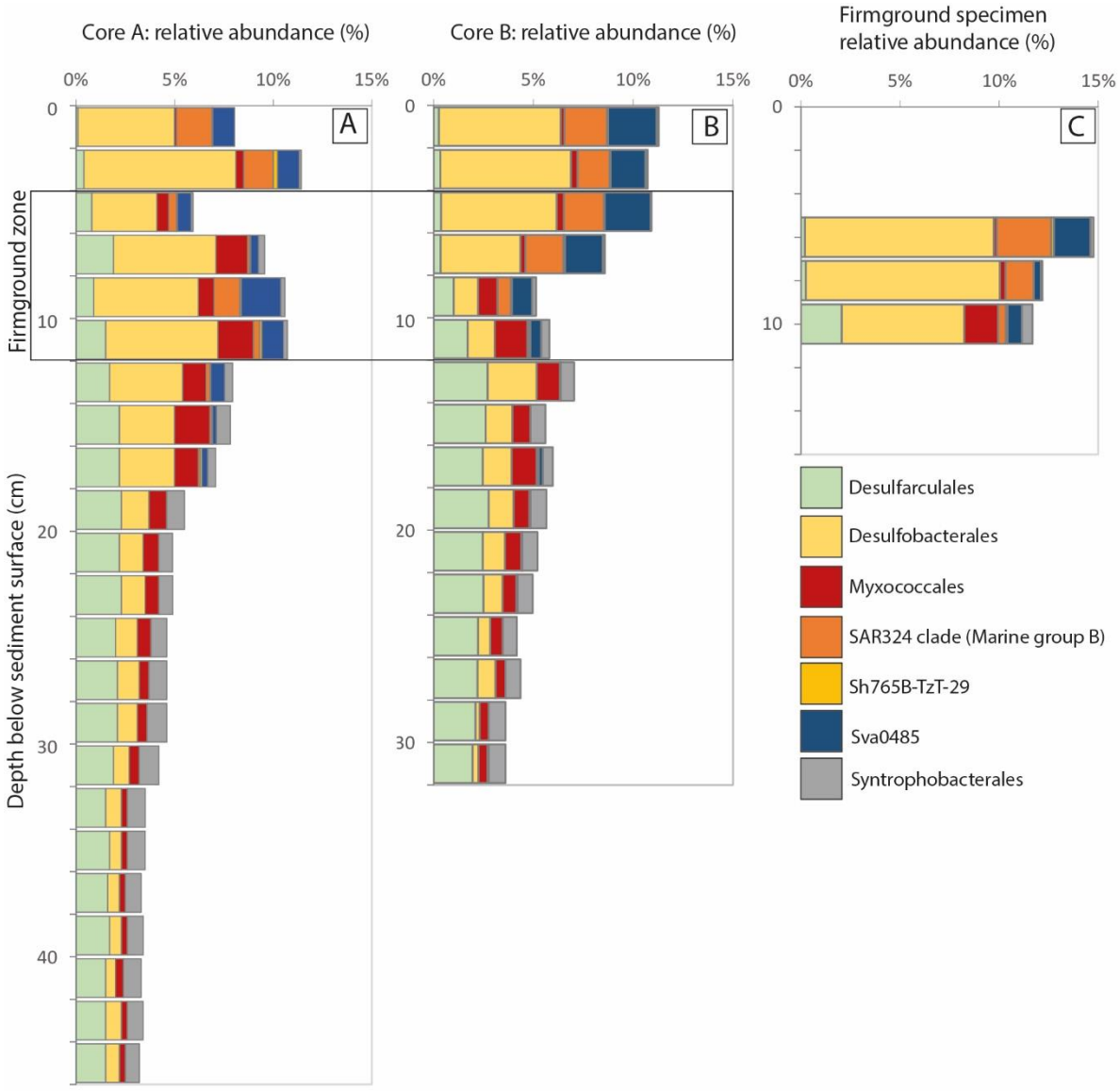

Fig. S5. 16S SSU rRNA genes sequence relative abundance for common *Deltaproteobacteria* communities from (**A**) Core A; (**B**) Core B; and (**C**) firmground specimen.

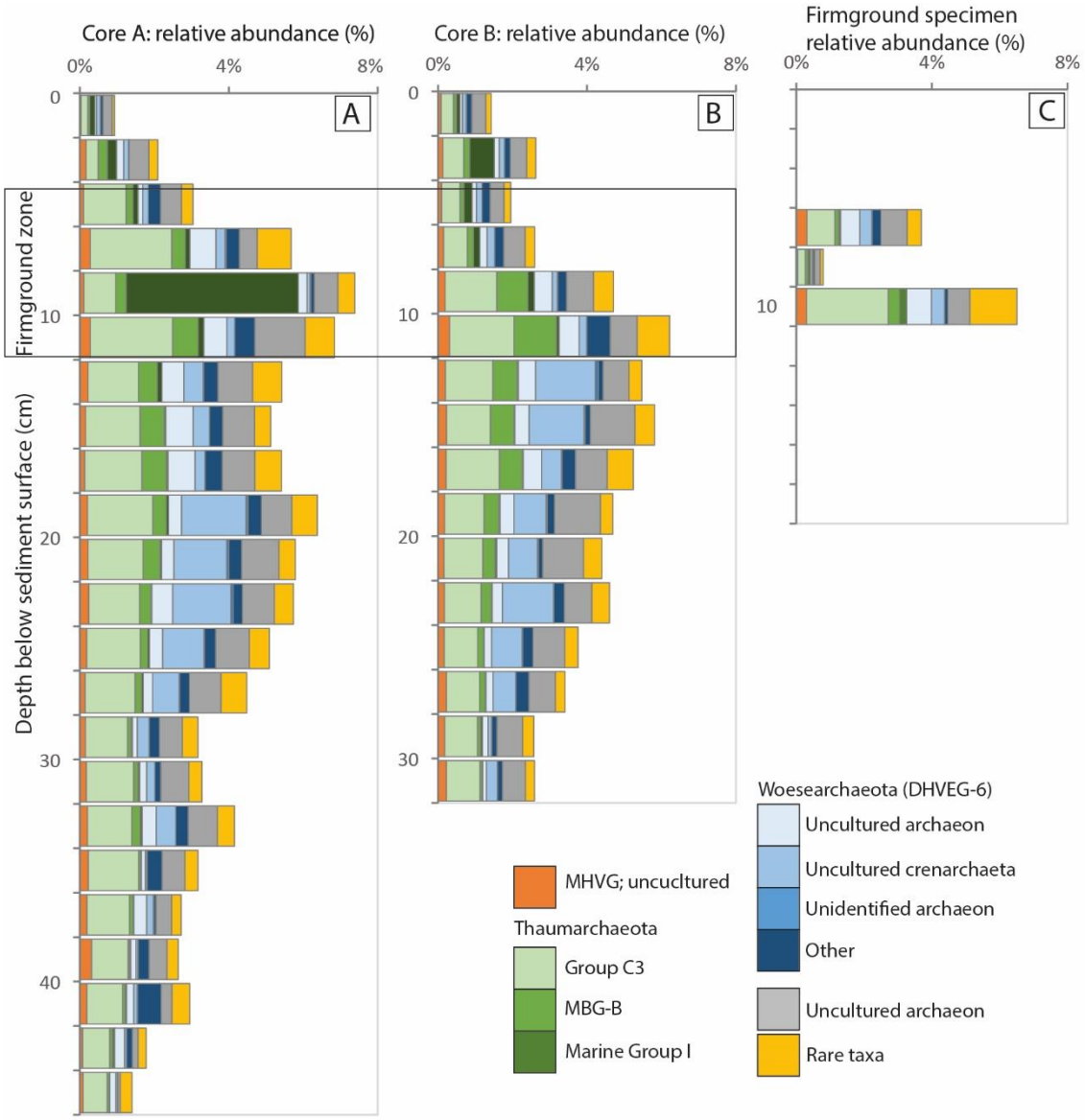

Fig. S6. 16S SSU rRNA genes sequence relative abundance for archaea groups other than MBG-D and *Bathyarchaeota* from (**A**) Core A; (**B**) Core B; and (**C**) firmground specimen. Rare taxa represent the sum of archaeal OTUs with maximum relative abundance <0.5%.

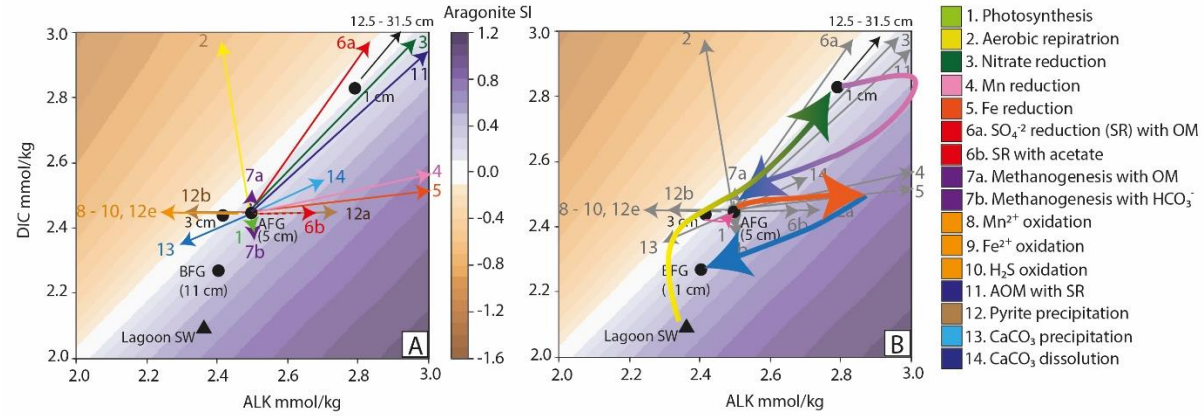

Figure S.7. (**A**) Potential effect of different respiratory metabolisms on alkalinity, DIC and aragonite saturation index (ΔSI_{arag}). Numbers proceeding metabolisms relate to those in Table 1. The porewater sample above the firmground (AFG) is used as a central point to determine which pathways could result in the ΔDIC, ΔALK, and ΔSI_{arag} observed between this point and the porewater sample immediately below the firmground (BFG). Vectors have been scaled relative to the reactants (highlighted in bold in Table 1), though it is not possible to plot them all on the same scale. Eq. 1 has been scaled to 0.1 mol of CO_2, Eq. 2-6a are scaled to 0.005 mol of organic carbon, Eq. 6b is scaled to 0.1 mol of organic carbon, Eq. 7a-b are scaled to 1 mol of organic carbon, Eq. 8-10 and 12-14 are scaled to 0.1 mol of reactant and Eq. 11 is scaled to 0.5 mol of CH_4. (**B**) Coloured arrows indicate potential metabolic pathways involved in altering the porewater chemistry in the upper 11 cm of the profile. SI_{arag} contours were calculated based on varying DIC and ALK for the mean porewater chemistry from 3 cm and 5 cm.

Table B1. Sediment organic chemistry (Core A).

Depth (cm)	TC %	TOC %	CaCO3 %	TN %	C/N
1	11.3	0.56	89.5	0.10	6.4
3	11.3	0.81	87.2	0.09	11.1
5	11.4	0.72	88.9	0.07	11.5
7	11.3	0.63	88.8	0.07	10.9
9	11.3	0.75	88.2	0.07	13.2
11	11.4	0.65	89.4	0.06	12.6
13	11.4	0.74	88.9	0.06	13.9
15	11.3	0.72	88.0	0.06	14.0
21	11.2	0.71	87.8	0.06	13.3
23	11.3	0.66	88.6	0.06	12.1
27	11.2	0.84	86.0	0.07	13.4
31	11.1	0.45	88.9	0.07	7.2
35	10.9	0.84	84.1	0.07	13.2
37	11.0	0.85	84.3	0.07	13.6
39	11.0	0.77	85.1	0.07	12.5
41	11.3	0.45	90.1	0.06	8.3
43	11.4	0.54	90.5	0.06	11.3

Table B2. Sediment isotopic composition (Core B).

Depth (cm)	$d^{13}C^{PDB}$ [‰]	$d^{18}O^{PDB}$ [‰]
1	3.07	2.53
3	2.90	2.36
5	2.99	2.54
7	2.91	2.53
9	3.20	2.47
11	3.20	2.67
13	3.16	2.64
15	3.50	2.55
17	3.16	2.58
19	3.61	2.36
21	3.79	2.06
23	3.80	2.21
25	4.05	1.80
27	3.85	2.13
29	4.01	1.80
31	4.16	1.79

Table B3: Mineralogy (XRD) from Core A

Sample	Aragonite	Calcite	Mg-calcite	Quartz	Halite	Dolomite	Albite	Topaz	Anhydrite	Diaspore	Sylvite	Graphite	Anorthite
0 - 2 cm	69.70	5.40	3.30	11.20	3.50	2.40	4.50						
2 - 4 cm	81.90	5.30	1.40	2.5	1.20	2		5.8					
4 - 6 cm	81.80	6.00	2.50	2.00	1.00	3.70		3.00					
6 - 8 cm	87.30	5.40	1.30	2.00	2.00	2.00							
8 - 10 cm	82.30	5.20	1.40	1.90	1.60	1.10	3.50		0.90	2.20			
10 - 12 cm	88.90	4.70	1.90	1.70	1.90	0.90							
12 - 14 cm	74.60	5.00	1.40	2.10	1.70	0.80					7.3	7.2	
14 - 16 cm	84.80	7.40	1.60	2.80	1.50	1.90							
16 - 18 cm	87.00	5.40	1.90	2.10	2.30	1.20							
18 - 20 cm	75.70	4.40	1.70	9.50	2.00	3.40							3.3
20 - 22 cm	74.30	3.10	1.90	2.70	2.30	4.80							9.8
22 - 24 cm	84.70	3.30	2.20	2.00	2.30	5.50							
26 - 28 cm	69.70	5.40	3.30	11.20	3.50	2.40	4.50						

Table B4. Offshore seawater (Site 1 and 2) at the surface and near the sediment surface (~5.5 m water depth) and lagoon surface water chemistry. [T = temperature, * denotes estimated *in situ* temperature].

Site description	pH	pH T (°C)	*in situ* T (°C)	Eh (mV)	Salinity	Aragonite SI	Calcite SI	pCO_2 (%)	Log CO_3^{2-} activity	Alkalinity as HCO_3^- mmol/l
Site 1 surface water	8.15	20.7	~31*	172.9	35.1	0.65	0.82	0.04	-3.56	2.54
Site 1 bottom water	8.15	20.5	~31*	172.9	37.3	0.66	0.83	0.04	-3.55	2.54
Site 2 surface water	8.05	31.0	31.0	201.4	39.4	0.66	0.84	0.04	-3.53	2.49
Site 2 bottom water	7.97	31.2	31.2	201.9	39.7	0.61	0.78	0.05	-3.59	2.48
Lagoon surface water 1	7.90	32.5	32.5	194.4	47.7	0.60	0.77	0.05	-3.57	2.36
Lagoon surface water 2	7.92	25.2	~32*		48.1	0.49	0.66	0.07	-3.67	2.39
	NH_4^+ mmol/l	DOC mg/l	Cl^- mmol/l	SO_4^{2-} mmol/l	Na^+ mmol/l	Mg^{2+} mmol/l	Ca^{2+} mmol/l	Sr^{2+} mmol/l	Fe µmol/l	Mn µmol/l
Site 1 surface water	0.03	5.87	658	33	535	54.7	10.1	0.08	0.39	0.38
Site 1 bottom water	0.03	3.16	664	33.4	537	55.4	10.3	0.08		
Site 2 surface water	0.03				551	50	9.5	0.09		
Site 2 bottom water	0.03				552	49.5	9.4	0.09		
Lagoon surface water 1	0.04	17.12	779	36.3	605	63.2	12.4	0.1	0.62	0.16
Lagoon surface water 2	0.04	21.62	783	36.1	616	63.9	12.3	0.11		

Table B5. Porewater chemistry (depth presented as cm below the sediment surface) with carbonate chemistry (aragonite and calcite saturation index (SI), pCO_2 and log carbonate activity) calculated with CO2SYS (Pelletier *et al.*, 2007).

Depth (cm)	pH	pH T (°C)	Eh (mV)	Salinity	Aragonite SI	Calcite SI	pCO_2 (%)	Log CO_3^{2-} activity	CH_4 µmol/L	Alkalinity as HCO_3^- mmol/l	NH_4^+ mmol/l

1	7.27	23.6	205	48.6	-0.04	0.14	0.36	-4.18	0.1	2.79	0.05
3	7.29	23.4	196	48.6	-0.10	0.09	0.29	-4.23	0.13	2.42	0.04
5	7.47	24.2	187	48.5	0.09	0.28	0.18	-4.04	0.05	2.5	0.05
11	7.69	23.1	-7	48.3	0.26	0.45	0.10	-3.88	0.15	2.4	0.05
12.5	7.26	22.9	-192	52.1	0.02	0.21	0.44	-4.10	0.56	3.43	0.07
15	7.26	21.9	-212	52.4	0.02	0.21	0.46	-4.09	0.13	3.52	0.07
18	7.26	22.3	-234	53.5	0.00	0.19	0.44	-4.10	0.22	3.35	0.07
19.5	7.28	22.0	-228	52.5	-0.03	0.16	0.38	-4.14	0.17	3.02	0.07
22.5	7.27	22.4	-227	54.6	-0.01	0.19	0.41	-4.11	0.32	3.22	0.06
24.5	7.24	22.4	-240	56.3	-0.01	0.19	0.48	-4.09	0.71	3.46	0.06
26	7.25	22.3	-236	56.2	-0.06	0.14	0.42	-4.14	0.82	3.05	
28.5	7.27	22.5	-248	57.3	-0.04	0.16	0.40	-4.11	0.91	3.06	0.06
31.5	7.3	23.1	-249	60.6	0.03	0.24	0.42	-4.01	0.48	3.45	0.06
Depth (cm)	DOC mg/l	TN mg/l	Cl^- mmol/l	SO_4^{2-} mmol/l	Na^+ mmol/l	Mg^{2+} mmol/l	Ca^{2+} mmol/l	K^+ mmol/l	Sr^{2+} mmol/l	Fe µmol/l	Mn µmol/l
1	20.4	1.51	793	37.1	618	64.8	13	12.6	0.11	7.87	0.65
3	22	3.52	792	37.2	618	64.6	12.4	12.4	0.11	2.72	0.43
5	21	1.93	788	37.2	620	65.6	12.7	12.6	0.11	2.12	0.39
11	18.3	2.31	784	37.3	620	64.8	12.4	12.2	0.11	0.15	0.17
12.5	20.7	3.48	842	40.6	666	71.3	13.6	13.4	0.12	0	0.21
15	16.8	2.91	849	41.3	665	72.3	13.7	13.5	0.12		
18	24.8	4.67	869	42.8	676	72.9	13.8	13.8	0.12		
19.5	20.2	3.18	855	39.5	668	71.6	13.8	13.7	0.12		
22.5	24.3	4.44	889	42.5	693	74.2	14.1	13.8	0.12		
24.5	16	3.32	912	43.4	720	76.8	14.6	14.7	0.13		
26	25.1	3.07	908	43.8	720	77.4	14.7	14.8	0.13		
28.5	26.7	4.94	926	44.9	732	79.3	14.9	15.0	0.13		

31.5	22.2	4.35	1001	48.3	744	81.1	15.3	15.2	0.14		

Appendix C: Chapter 4

Table C1. Surface water chemistries from the flood tide surface waters at Site 3-QL (2019), tidal creek waters at Site 4-QL during the 2017 and 2019 field campaign, offshore seawaters (2017), inland surface waters (2014) and groundwaters (2019).

Sample ID	water depth (cm)	Time sampled	Date sampled	pH	pH temperature	*in situ* temperature (°C)	Eh	DO (%)	SEC	Salinity (TDS)
Site 3-QL flood tide surface waters										
2019_3-QL_1	15	13:38:00	07/01/2019	8.1	22.2		167	100	76	52
2019_3-QL_2	3	13:38:00	07/01/2019	8.2	23.2		135	99	91	65
2019_3-QL_3	40	15:05:00	07/01/2019	8.1	22.3		112	104	76	51
2019_3-QL_4	2	15:05:00	07/01/2019	8.2	22.8		105	99	129	99
2019_3-QL_6	14	15:34:00	07/01/2019	8.2	27.3				81	54
2019_3-QL_7	1	15:40:00	07/01/2019	8.1	29.4				118	89
Site 4-QL tidal creek surface waters 2017										
2017_TC_1		08:55:00	24/10/2017	7.9	30.0	30	149		98	68
2017_TC_2		10:30:00	24/10/2017	8.0	20.3	33*	143		101	71
2017_TC_3		11:27:00	24/10/2017	8.4	21.3	34*	123		109	76
2017_TC_4		11:49:00	24/10/2017	8.1	31.4	34*	126		90	62
2017_TC_5		12:09:00	24/10/2017	8.0	34.5	34	129		78	54
2017_TC_6		12:29:00	24/10/2017	8.0	33.6	34	132		75	51
2017_TC_7		12:48:00	24/10/2017	8.0	33.7	34	132		74	50
2017_TC_8		13:45:00	24/10/2017	8.2	19.6	33*	132		72	49
2017_TC_9		15:00:00	24/10/2017	8.2	19.2	32*	132		72	49
Site 4-QL tidal creek surface waters 2019										
2019_TC_1		11:15:00	16/01/2019	7.9	28.7	21	87	97	74	51
2019_TC_2		12:20:00	16/01/2019	7.9	29.4	23	113	111	74	50

2019_TC_3		13:15:00	16/01/2019	7.9	32.6	28	120	120	74	50
2019_TC_4		14:10:00	16/01/2019	8.0	21.0	27*	63	109	89	61
2019_TC_5		15:20:00	16/01/2019	7.9	23.0	27.5*	105	95	88	61
2019_TC_6		16:20:00	16/01/2019	7.8	22.9	26*	129	95	93	65
2019_TC_7		17:20:00	16/01/2019	7.8	23.4	26*	139	106	111	78
2019_TC_8		17:30:00	16/01/2019	7.9	23.0	26*	136	102	82	57
Site 1-OS and 2-OS: offshore seawaters 2017										
OS1_surface			18/10/2017	8.2	20.7	31*	173		53	35
OS1_bottom			18/10/2017	8.2	20.7	31*	173		56	37
OS2_surface			22/10/2017	8.1	31.0	31	201	98	59	39
OS2_bottom			22/10/2017	8.0	31.2	31	202	107	59	40
Inland surface waters 2014										
2014_4-QL_UI			05/02/2014	8.0	22.0			127	123	99
2014_4-QL_MM2			05/02/2014	8.6	23.0			157	87	66
2014_4-QL_MM1			05/02/2014	8.7	22.6				84	67
Groundwaters from boreholes 2019										
BH1			15/01/2019	6.3	24.2	30	79	44	217	198
BH2			15/01/2019	6.7	24.1	30	94	89	193	170
BH3			15/01/2019	6.3	24.0	32		83	233	223

Table C2: Surface water chemistries (continued) from the flood tide surface waters at Site 3-QL (2019), tidal creek waters at Site 4-QL during the 2017 and 2019 field campaign, offshore seawaters (2017), inland surface waters (2014) and groundwaters (2019).

Sample ID	Alkalinity as HCO_3^- mmol/l	DOC mg/l	TN mg/l	Cl^- mmol/l	SO_4^{2-} mmol/l	Na^+ mmol/l	Mg^{2+} mmol/l	Ca^{2+} mmol/l	K^+ mmol/l	Sr^{2+} mmol/l	NH^{4+} µmol/l
Site 3-QL flood tide surface waters											
2019_3-QL_1	2.53			828.18	40.35	678.90	78.63	13.94	11.67	0.15	35.05
2019_3-QL_2	2.53	9.98	0.81	1020.81	49.98	866.79	100.63	17.72	16.02	0.19	30.87
2019_3-QL_3	2.62			820.56	38.87	663.51	76.61	13.24	10.47	0.13	34.96
2019_3-QL_4	2.48	11.52	1.15	1588.40	70.91	1307.08	140.57	23.85	23.36	0.22	20.15
2019_3-QL_6	2.54	2.79	0.49	859.33	41.90	692.72	80.78	13.80	10.68	0.14	33.66
2019_3-QL_7	2.44	7.24	0.88	1430.23	70.27	1144.91	132.10	23.68	20.68	0.24	20.69
Site 4-QL tidal creek surface waters 2017											
2017_TC_1	2.21			1118.49	56.71	933.52	109.08	18.42	16.79	0.18	23.23
2017_TC_2	2.81			1186.93	60.00	964.98	114.34	18.52	17.15	0.18	23.70
2017_TC_3	1.41			1237.73	57.89	1038.72	109.06	20.33	18.94	0.18	20.25
2017_TC_4	1.92			1015.31	45.11	833.78	88.39	16.48	15.97	0.14	36.14
2017_TC_5	2.34			847.95	42.95	688.54	75.99	14.78	13.25	0.11	34.03
2017_TC_6	2.36			822.41	40.18	658.52	74.67	13.55	12.26	0.14	30.55
2017_TC_7	2.36			797.08	41.47	675.82	73.96	14.22	13.59	0.13	32.80
2017_TC_8	2.27			797.08	41.47	675.82	73.96	14.22	13.59	0.13	32.31
2017_TC_9	2.66			797.08	41.47	675.82	73.96	14.22	13.59	0.13	
Site 4-QL tidal creek surface waters 2019											
2019_TC_1	2.61	3.40	0.27	784.75	40.95	666.44	73.27	14.02	13.28	0.13	34.98
2019_TC_2	2.55	3.03	0.22	797.08	41.47	675.82	73.96	14.22	13.59	0.13	47.10
2019_TC_3	2.35	4.04	0.20	864.11	45.12	726.72	79.93	15.20	14.72	0.14	50.55
2019_TC_4	1.87	6.25	0.34	967.64	48.10	1652.08	175.39	31.42	36.23	0.30	53.70

2019_TC_5	1.89			947.95	46.64	802.83	86.43	16.32	15.44	0.15	41.75
2019_TC_6	1.83	6.12	0.44	1033.53	53.30	869.77	92.89	17.57	16.84	0.16	36.63
2019_TC_7	1.83	6.32	0.36	1237.73	57.89	1038.72	109.06	20.33	18.94	0.18	30.79
2019_TC_8	2.39	4.17	0.25	871.07	41.76	735.81	79.94	15.33	14.27	0.14	29.90
Site 1-OS and 2-OS: offshore seawaters 2017											
OS1_surface	2.54			676.95	33.00	534.82	54.75	10.11	10.23	0.08	30.26
OS1_bottom	2.54			683.75	33.37	537.28	55.35	10.27	10.04	0.08	26.81
OS2_surface	2.49			676.95	33.00	616.67	68.09	13.16	11.45	0.11	28.99
OS2_bottom	2.48			683.75	33.37	613.61	66.17	12.97	11.41	0.11	31.69
Inland surface waters 2014											
2014_4-QL_UI	2.18			1573.00	81.50	1181.00	246.00	28.40	33.00		
2014_4-QL_MM2	2.06			973.00	60.40	907.00	134.00	18.10	13.30		
2014_4-QL_MM1	1.99			1008.00	54.80	891.00	157.00	19.30	21.20		
Groundwaters from boreholes 2019											
BH1	2.05	4.79	2.57	3320.00	77.64	2767.90	234.46	31.43	47.70	0.32	14.60
BH2	2.22	5.85	1.85	2745.61	108.36	2344.12	246.44	24.07	39.94	0.34	15.28
BH3	2.48	4.89	1.16	3759.58	53.59	3256.20	223.25	37.60	60.56	0.52	8.52

Appendix D: Chapter 5

Table D1. Mineralogy (XRD) for Site A, Core A3

Depth (cm)	Aragonite	Calcite	Quart	Mg-calcite ($CaMgCO_3$)	Albite	Dolomite	Amphiobile	Muscovite	Microcline, sodian	Kaolinite
1	81.5	4.3	5.7	1.4	5.3	1.8				
2	79.2	3.9	8.4	1.3	5.4	1.8				
3	75.5	3.6	3.9	2.1	12.9	2				
4	81.9	3.1	8		3.9	1.7				
5	79.7	3.8	8.8	1.6	4.2	1.9				
6	86.9	4.4	9.9	1.6	3	1.6				
7										
8	78.3	3.1	5.9	2.1	9.4	1.3				
9	87.1	2.9	4.1	1.9	2.6	1.4				
10	79.3	4.2	6.9	1.8	2.7	5.1				
11	78.7	4.4	5.4	1.5	2.5	1.6			5.8	
12	80.2	7	7.2	1.8	2.8	1.1				
13	70.2	3.8	11.8	3	6.3	1.8			3.1	
14	60.3	5.9	14.7	3.6	9.2	1.7			3.6	1.1
15	61.8	7.6	11.8	3.9	6.7	2.6		4.8		0.9
16	54.2	6.4	14	3.1	9.6	1.7			9.9	1.2
17	66	11.6	9.5	4.2	5.7	1.5				1.6
18	61.4	7.9	11.9	4.8	6.2	2.2		4.5		1.1
19	59.8	7.2	13.9	5.5	5	5		3.6		
20	62.9	5.8	15.7	8.7	2.3	2.5				2.2
21	49.9	14.4	9.2	4	9.7	1.4			9.9	1.5
22	51.8	5.9	18.1	8	9.1	2.1		5		
23	61.5	12.8	17.2	3.1	2.9	2.6				
24	49.7	5.6	38.6	3.3	1.7	1				
25	51.7	5.9	14	3.7	4.7	4.2	1.8	3.9	10.2	

Table D2. Grain size (µm) at Sites B (Core B2), D (Core D1) and Site 5-TC.

Grain size range (µm):	0.02 - 3.99	4 - 7.99	8 - 14.99	15 - 30.99	31 - 62.99	63 - 87.99	88 - 124.99	125 - 176.99	177 - 249.99	250 - 349.99	350 - 499.99	500 - 709.90	710 - 999.99	1000 - 2000	>20000
Site B															
0 - 2 cm	3.75	4.01	5.71	11.50	13.87	5.71	5.67	5.44	4.79	3.75	2.79	0.89	0.00	12.65	19.44
4 - 6 cm	7.02	6.72	10.08	19.96	18.82	6.03	5.51	5.18	4.64	3.99	3.63	1.63	0.00	1.93	4.81
8 - 9.5 cm	5.01	5.00	7.31	14.53	14.94	5.62	6.02	6.53	6.65	6.40	6.28	3.32	0.00	3.24	9.10
Site D															
0.5 - 1.25 cm	0.09	0.06	0.07	0.08	0.09	0.03	0.07	0.11	0.09	0.05	0.06	0.03	0.01	0.01	0.07
1.5 - 2.5 cm	0.08	0.09	0.11	0.10	0.06	0.01	0.03	0.05	0.04	0.02	0.02	0.01	0.01	0.02	0.34
4 - 5.25 cm	0.17	0.12	0.11	0.09	0.06	0.01	0.04	0.06	0.04	0.02	0.01	0.02	0.01	0.03	0.18
6 - 7 cm	0.18	0.08	0.08	0.07	0.06	0.02	0.05	0.07	0.05	0.02	0.01	0.01	0.01	0.03	0.21
7.5 - 9 cm	0.16	0.09	0.08	0.07	0.05	0.01	0.04	0.06	0.05	0.02	0.02	0.01	0.01	0.03	0.27
9 - 10 cm	0.17	0.10	0.11	0.10	0.08	0.02	0.05	0.09	0.06	0.02	0.02	0.01	0.01	0.03	0.10
10 - 12 cm	0.12	0.08	0.09	0.08	0.07	0.02	0.04	0.06	0.04	0.01	0.01	0.01	0.02	0.06	0.27
21 - 24 cm	0.06	0.05	0.06	0.07	0.09	0.03	0.07	0.10	0.08	0.04	0.04	0.02	0.01	0.12	0.11
22 - 25 cm	0.05	0.05	0.07	0.08	0.10	0.03	0.06	0.09	0.07	0.04	0.04	0.02	0.01	0.08	0.16
24.5 - 27.5 cm	0.06	0.05	0.06	0.07	0.09	0.03	0.06	0.09	0.07	0.04	0.04	0.02	0.00	0.10	0.16
25 - 28 cm	0.08	0.05	0.06	0.06	0.08	0.02	0.06	0.09	0.08	0.04	0.05	0.03	0.01	0.06	0.17
Site 5-TC															
0 - 2.5 cm	0.13	0.11	0.13	0.11	0.07	0.01	0.03	0.06	0.06	0.04	0.04	0.03	0.01	0.05	0.11
3 - 5 cm	0.11	0.12	0.14	0.14	0.09	0.01	0.03	0.06	0.06	0.03	0.03	0.01	0.00	0.03	0.09
5 - 6 cm	0.10	0.11	0.13	0.13	0.09	0.01	0.03	0.06	0.06	0.03	0.03	0.01	0.00	0.03	0.16
6 - 8 cm	0.22	0.13	0.13	0.10	0.07	0.01	0.03	0.06	0.06	0.03	0.02	0.00	0.00	0.03	0.09
8 - 10 cm	0.24	0.14	0.13	0.11	0.07	0.01	0.03	0.05	0.04	0.02	0.03	0.02	0.01	0.02	0.05
10 - 12 cm	0.21	0.12	0.12	0.10	0.07	0.01	0.03	0.05	0.04	0.02	0.03	0.02	0.01	0.04	0.11
12.5 - 14.5 cm	0.10	0.14	0.17	0.16	0.12	0.02	0.04	0.06	0.05	0.02	0.03	0.02	0.01	0.03	0.01
14.5 - 16.5 cm	0.08	0.10	0.13	0.14	0.11	0.02	0.04	0.06	0.05	0.03	0.04	0.04	0.02	0.05	0.05
17 - 19 cm	0.10	0.10	0.11	0.11	0.09	0.02	0.04	0.07	0.06	0.03	0.03	0.00	0.00	0.06	0.15
19.5 - 21.5 cm	0.09	0.08	0.08	0.08	0.07	0.02	0.04	0.06	0.05	0.03	0.04	0.03	0.01	0.09	0.21

Table D3. Water chemistry from Site A-D and Site 5-TC *in situ* porewaters, Site D (Core D1) porewaters, Inland porewater Sites 1 and 2) collected via centrifugation (2014), offshore seawaters and groundwaters.

Depth (cm)	pH	pH T (°C)	Eh	DO (%)	SEC (mS/cm)	Salinity (TDS)	Alkalinity as HCO_3^- mmol/l	DOC mg/l	TN mg/l	Cl^- mmol/l	SO_4^{2-} mmol/l	Na^+ mmol/l	Mg^{2+} mmol/l	Ca^{2+} mmol/l	Sr^{2+} mmol/l	NH^{4+} µmol/l	CH4 µmol/L
Site A *in situ* porewaters																	
0.5	7.50	33.1			80	55	2.45	13.0		1006	49	874	92	17.6	0.09		
2.5	7.41	32.8			81	56	2.34	13.3		1044	51	868	95	17.2	0.09	38.4	0.06
4.5	7.51	32.8			85	58	2.62	14.3		1120	51	849	91	16.6	0.09	39.4	
6.5	7.24	34			91	63	2.57			1231	52					37.7	0.05
8.5	7.39	34.2			93	65	2.60										
10.5	7.26	34.3			100	76	2.56	17.0		1442	56					36.0	
12.5	7.22	35.9			109	82	2.53	15.8		1555	57	1304	136	23.3	0.14	30.3	
14.5	7.24	22.5			116	86	2.44			1638	55	1412	143	26.2	0.16	24.9	0.03
16.5	7.29	27.6			122	91	2.42	23.5		1802	56	1552	154	26.0	0.17	27.5	
18.5	7.23	33.1			124	92	2.28	14.8		1863	57	1566	155	26.0	0.17	26.7	
20.5	7.28	34.8			130	97	2.41	17.3		2039	60	1704	170	28.0	0.19	27.9	
22.5	7.20	37.3			135	102	2.30	14.2		2184	61	1748	171	27.9	0.22	23.5	
24.5	7.18	38.1			137	104	2.25	22.7		2231	61	1862	181	29.2	0.21	24.4	
26.5	7.17	37.3			140	106	2.18			2287	59	1956	188	30.3	0.23		0.23
Site B *in situ* porewaters																	
1	7.15	30.8			97	75	2.50	9.8		1329	54	1083	110	19.9	0.13	32.4	0.11
2	7.21	31.5			90	71	2.53			1334	53	1135	114	20.9	0.14	32.2	
4.5	7.32	32.4			89	71	2.36	11.2		1116	51	994	105	19.1	0.12	37.0	
6	7.33	32.1			73	64	2.20	7.4		1090	52	948	100	17.9	0.11	35.6	
7	7.37	32.3			79	66	1.95	7.2		1017	51	871	95	17.1	0.10	33.0	
15					137	103	2.17	8.3		2298	55	2014	192	34.5	0.27	23.5	0.67
17.5					137	104	2.10	10.8		2144	59	1643	159	28.6	0.20	21.4	0.21
19					163	129	2.24	11.0		2618	49	2414	220	40.2	0.32	30.2	0.38
22					169	136	2.24	18.8		2782	48	2484	227	42.0	0.33	28.0	0.24
27					172	140	2.22	10.9		2933	48	2665	236	43.7	0.35	31.37	0.26

Site C *in situ* porewaters																	
1.5	7.37	22.8	168	64.6	79	54	2.60	7.2	1.0	857	42	709	77	14.8	0.13	34.5	0.02
3	7.36	22.8	158	84.8	80	55	2.71			865	44	727	78	15.0	0.14		0.01
6	7.33	22.8	147	55.7	82	56	2.65	6.4	0.9	889	44	746	80	15.3	0.14	33.9	0.07
10.5	7.17	22.8	-101	49.7	104	73	2.51	10.1	1.1	1171	55	978	100	18.3	0.16	35.1	0.11
16.5	7.10		-145	42.5	120	87	2.30	7.0	1.2	1418	48	1186	118	20.6	0.19	25.1	0.24
18	7.08		-157	47.9	122	89	2.30	5.1	1.4	1459	48	1227	122	21.0	0.19	36.6	0.28
19.5	7.06		-161	39.4	130	97	2.30	5.5	1.4	1557	63	1316	129	22.8	0.21	35.4	0.29
21	7.08		-134	63.8	123	90	2.33	6.0	1.5	1460	62	1213	121	20.6	0.20	41.7	0.19
23	7.06		-160	36.2	127	94	2.31	10.0	1.4	1529	64	1264	125	21.3	0.20	42.3	
24.5	7.02	23.7	-165	35.6	135	99	2.31		1.4	1625	56	1354	132	22.7	0.21	33.6	0.44
28.5	7.02	20.1	-77			107	2.31	7.0	1.2	1780	50	1461	140	24.6	0.22	35.7	0.34
Site D *in situ* porewaters																	
1.5	7.40	23.3	125	59.8	85	60	2.18	6.0	0.5	951	48	783	86	16.1	0.15	39.7	0.02
3	7.37	24.1	124	75.4	82	56	2.44	9.9	1.6	895	44	740	82	15.4	0.14	46.3	0.02
5	7.33	23.1	96	58.6	84	60	2.44	7.9	0.7	958	44	786	84	15.7	0.14	48.2	0.06
7	7.37	22.9	102	75.5	86	60	2.38	6.6	0.6	968	43	796	85	15.7	0.13	45.8	0.02
9	7.28	23.2	-86	54.2	89	63	2.39	3.3	0.5	1015	45	834	88	16.5	0.14	49.7	
11	7.24		-115	60.4		70	2.32	7.1	1.5	1136	45	943	98	17.9	0.16	39.5	0.15
12.5	7.32	24.2	-48			67	2.39			1074	44	887	93	17.2	0.15	43.8	0.03
17	7.23	23.9	-86	63.3	105	75	2.24	6.7	1.5	1222	48	1000	103	18.7	0.16		0.15
21	7.16	22.8	-117	63.1	110	79	2.27	4.9	1.1	1294	47	1074	109	19.7	0.17	33.2	0.23
22.5	7.13	23.5	-145	46.1	117	86	2.27	5.1	1.3	1410	48	1160	117	21.0	0.18	39.3	0.24
24.5	7.13	23.4	-131	46.1	119	87	2.25	7.4	1.3	1429	48	1187	119	21.1	0.19	29.1	0.36
28.5	7.13	23.7	-136	70.9	123	90	2.33	8.6	1.6	1487	48	1222	122	21.6	0.19		0.23
Site D - porewaters from Core D1																	
0.5	7.44	24.1		94.8	85	58	2.64			930	46	754	83	15.6	0.14	43.2	
2.5	7.43		38	91.7	82	56	2.64	3.9	1.4	887	42	731	80	15.0	0.13	51.1	
4.5	7.39		54	90.6	84	58	2.54			913	46	757	84	15.4	0.14	52.8	
6.5	7.37	22.4	60	94.3	88	59	2.53	9.9	1.3	953	46	763	83	15.3	0.13	53.2	

8.5	7.26		66	89.1	94	66	2.43	7.3	1.3	1055	52	876	92	16.9	0.15	45.5	
Site 5-TC *in situ* porewaters																	
3	7.18		16	59.8	97	69	2.49			4771	50	925	99	19.5	0.18	29.5	
6	7.28		39	70.3	88	61	2.71	8.5	1.0	4399	46	806	86	16.9	0.16	28.7	
11	6.80	20.4	-194	31.8	137	102	3.13	4.7	1.5	5738	60	1356	130	27.1	0.25	27.6	
16	6.73	20.9	-193	26.4	145	112	2.99	8.5	1.4	5750	60	1519	141	30.7	0.27	26.4	
23	6.76		-182	42.9	159	123	2.79	6.2	1.8	4591	48	1667	154	33.7	0.30	26.2	
28	6.69	21.9	-122	52.5	165	128	2.35	7.2	1.1	4429	46	1769	155	34.1	0.31	34.5	
34	6.71		19	69.9	175	139	2.11			5042	52	1908	166	37.9	0.33	34.5	
40.5	6.79	22.2	-8		176	134	2.12			4819	50	1909	167	36.9	0.34		
Inland porewaters 1																	
1.5	7.61					187	1.58			2842	117	2643	509	15			
4.5	7.43					193	1.14			2966	115	2749	484	15			
7.5	7.25					191	1.00			2977	100	2679	471	16			
10.5	7.07					188	1.07			2875	95	2748	483	17			
13.5	6.92					194	1.19			3011	97	2791	452	18			
16.5	6.94						1.29			3051	92	290	16	2			
19.5	6.97					193	1.17			3026	95	2722	479	18			
20.5	6.88					196	1.42			3092	93	2782	451	18			
23.5	6.86					196	1.43			3078	86	2812	473	19			
26.5	6.82					194	1.57			3092	87	2702	475	19			
29.5	6.80						1.68			3193	91	241	85	9			
32.5	6.80					198	1.53			3114	84	2845	479	20			
Inland porewaters 2																	
26.5	6.72					203				3225	53	3190	300	18			
27.5						194				3406	51	2629	222	19			
28.5						205				3420	50	3049	265	20			
29.5	6.69					223				3584	48	3377	396	20			
31.5	6.77					227				3702	58	3357	408	19			
32.5						223				3593	54	3375	410	19			
33.5										4810	46	3123	349	19			

35.5	6.56						1.12			3672	58	2490	285	17			
37.5	6.67					221				3564	46	3408	363	20			
38.5	6.72									3015	47	3176	294	21			
40.5	6.74					226				3719	50	3303	383	20			
43.5	6.67					227	1.07			3778	49	3249	377	21			
45.5	6.74					221				3664	46	3212	350	21			
47.5	6.64					224	0.96			3679	45	3269	379	21			
Offshore seawaters																	
OS1 surface	8.15	20.7	173		53	35	2.54			677	33	535	55	10.1	0.08	30.3	
OS1 bottom	8.15	20.7	173		56	37	2.54			684	33	537	55	10.3	0.08	26.8	
OS2 surface	8.05	31.0	201	98.3	59	39	2.49			677	33	617	68	13.2	0.11	29.0	
OS2 bottom	7.97	31.2	202	106.7	59	40	2.48			684	33	614	66	13.0	0.11	31.7	
Groundwaters																	
BH1	6.29	24.2	79	44.0	217	198	2.05	4.8	2.6	3320	78	2768	234	31.4	0.32	14.6	0.65
BH2	6.72	24.1	94	88.9	193	170	2.22	5.9	1.8	2746	108	2344	246	24.1	0.34	15.3	0.05
BH3	6.34	24.0		83.2	233	223	2.48	4.9	1.2	3760	54	3256	223	37.6	0.52	8.5	0.09

Appendix E: Chapter 6

Table E1. Mineralogy (XRD) at Site 1 and Site 2.

Depth (cm)	Aragonite	Calcite	Dolomite	Quartz	Halite	Anhydrite	Gypsum
Site 1							
0	83.9	3.6	0.2	6.1	2.3	3.8	
2	90.5	3.5	0.2	0.0	5.6	0.0	
4	78.8	7.4	0.0	4.6	5.2	3.9	
6	91.0	3.9	1.5	0.6	2.9	0.0	
8	85.5	4.8	0.1	6.4	3.1	0.0	
10							
12	81.3	6.2	2.9	0.1	5.4	4.2	
14	91.0	3.2	0.6	0.7	4.0	0.4	
16	88.8	3.9	0.0	1.0	6.0	0.1	
18	83.6	2.8	0.1	8.7	4.7	0.0	
20	84.9	4.7	0.0	0.1	6.1	4.1	
22	85.1	7.6	0.0	0.3	6.9	0.1	
24	85.0	4.0	0.0	0.2	6.5	4.2	
26	82.3	3.0	0.0	5.4	5.3	4.0	
28	91.2	2.8	0.1	0.0	5.7	0.1	
30	80.0	5.8	0.0	6.8	3.7	3.6	
Site 2							
0	5.2	9.3	5.9	4.4	9.9	0.2	64.9
2	5.5	1.9	0.2	0.5	2.1	0.1	89.8
4	9.4	8.2	3.3	0.8	6.0	0.1	72.2
6	11.3	3.3	3.3	0.6	3.3	0.1	78.1
8	7.6	2.8	2.7	1.0	7.1	0.1	78.7
10	12.3	4.9	3.9	2.1	11.8	0.1	64.9
12	11.5	1.9	2.0	1.2	8.8	0.1	74.5
14	26.4	0.3	4.1	0.8	7.6	0.1	60.8
16	8.1	0.2	4.4	1.9	10.0	0.0	75.4
18	18.8	1.2	8.0	1.0	18.5	0.1	52.0
20	25.0	0.7	11.4	2.8	19.6	0.3	40.0
22	47.2	6.3	10.1	0.2	30.2	0.2	5.8
24	52.2	6.6	6.8	3.8	29.2	0.1	1.2
26	46.7	5.2	3.1	7.1	32.5	4.1	1.3
28	51.6	6.1	0.8	2.4	38.0	0.1	1.0
30	61.0	4.0	0.3	9.0	21.1	4.1	0.7
32	40.5	12.6	2.5	9.3	34.2	0.3	0.5
34	46.0	7.0	10.0	1.3	35.1	0.3	0.8
36	52.5	10.8	5.3	6.1	23.9	0.0	1.4

Table E2. Grain size analysis at Site 1 and Site 2, (classified with the Wentworth (1922) scale).

µm:	0-62	62-125	125-250	250-500	500-1000	1000-2000	2000-4000	>40000
Size class:	silt	v. fine sand	fine sand	medium sand	coarse sand	v. coarse sand	gravel	pebbles
Site 1 depth								
0 - 2 cm	3.3	30.5	32.6	12.3	9.4	6.6	4.4	0.9
2 - 4 cm	1.4	22.7	33.5	13.1	8.7	6.5	7.1	7.0
4 - 6 cm	1.0	17.4	30.1	17.8	11.8	8.3	8.0	5.6
6 - 8 cm	1.0	15.6	34.0	13.1	10.5	8.6	9.3	7.9
8 - 10 cm	0.8	14.1	28.3	15.5	11.7	10.2	10.2	9.2
10 - 12 cm	0.7	14.4	30.9	15.3	10.0	10.5	11.1	7.1
12 - 14 cm	0.7	14.4	30.9	15.3	10.0	10.5	11.1	7.1
14 - 16 cm	0.6	10.0	27.4	16.4	10.3	12.5	12.1	10.7
16 - 18 cm	0.4	8.1	20.0	13.3	13.1	15.0	15.9	14.2
18 - 20 cm	0.3	7.1	22.5	19.7	12.0	14.5	14.2	9.7
20 - 22 cm	0.4	8.3	24.4	18.1	13.2	11.4	11.0	13.2
22 - 24 cm	0.4	7.2	23.5	17.1	12.5	14.0	14.9	10.4
24 - 26 cm	0.4	9.2	24.4	18.0	12.6	12.0	13.2	10.2
26 - 28 cm	0.6	12.1	24.8	13.0	8.8	9.3	13.8	17.6
28 - 32 cm	0.6	12.1	24.8	13.0	8.8	9.3	13.8	17.6
Site 2 depth								
0 - 2 cm	0.1	0.9	4.7	10.0	12.5	14.7	20.0	37.1
2 - 4 cm	0.1	1.4	6.2	10.6	12.0	14.3	18.7	36.7
4 - 6 cm	0.1	1.0	4.2	6.5	9.8	13.8	23.4	41.2
6 - 8 cm	0.1	1.2	4.3	8.2	13.9	18.7	21.5	32.1
8 - 10 cm	0.2	1.7	5.5	7.8	10.7	15.1	20.9	38.1
10 - 12 cm	0.2	1.9	4.4	6.4	9.8	15.6	24.8	36.9
12 - 14 cm	0.3	1.4	3.3	6.8	11.3	17.8	25.1	34.0
14 - 16 cm	0.3	2.2	4.4	7.7	15.1	24.7	31.6	14.0
16 - 18 cm	0.8	3.1	6.6	10.6	13.1	20.7	25.3	19.8
18 - 20 cm	0.9	3.7	6.1	9.3	15.5	22.6	28.3	13.6
20 - 22 cm	0.3	2.0	5.5	7.3	9.6	16.1	24.9	34.3
22 - 24 cm	0.7	3.6	7.0	6.9	7.4	12.4	22.3	39.7
24 - 26 cm	0.5	2.8	6.2	6.0	10.8	18.3	34.2	21.2
26 - 28 cm	0.2	1.4	2.4	3.2	6.0	12.3	27.2	47.3
28 - 30 cm	0.4	3.8	4.1	4.8	8.7	14.2	32.1	31.9
30 - 32 cm	1.1	6.8	7.7	8.3	11.8	16.8	23.0	24.5
32 - 34 cm	0.6	3.7	8.6	10.6	14.1	16.8	19.3	26.3
34 - 36 cm	1.4	8.4	11.0	12.3	15.0	14.8	14.3	22.8

Table E3. Porewater chemistries from Site 1 and Site 2.

Depth (cm)	pH	pH T (°C)	Eh	SEC	Salinity (TDS)	Alkalinity mmol/l	DOC mg/l	TN mg/l	CH_4 µmol/L	Cl^- mmol/l	SO_4^{2-} mmol/l	Na^+ mmol/l	Mg^{2+} mmol/l	Ca^{2+} mmol/l	K^+ mmol/l	Sr^{2+} mmol/l	NH^{4+} µmol/l
Site 1																	
0.5	7.43	23.2	229	97	68	2.44	4.19	0.26	0.14	1086	54	878	101	17.3	16.0	0.17	27.6
2.5	7.22	24.6	195	100	74	3.39	3.77	0.34		1151	59	989	117	19.5	17.6	0.19	24.1
6.5	7.13	24.1	85	103	74	3.66	4.72	0.55	0.02	1187	60	965	114	18.5	17.2	0.18	25.3
9.5	7.15	24.7	108	112	83	4.21	5.08	0.71	0.02	1326	69	1062	130	18.6	18.1	0.19	25.8
12.5	7.06	23.0	142	118	88	4.20	5.08	1.03	0.11	1404	73	1119	139	18.5	18.3	0.19	26.1
15.5	7.12	22.7	80	121	91	3.96	8.11	1.45		1451	78	1168	147	18.5	19.8	0.16	26.5
18.5	7.11	23.0	98	129	99	4.06	4.98	0.78		1585	85	1269	161	18.7	21.1	0.17	28.3
21.5	7.01	23.7	88	136	105	4.08	6.19	0.98	0.25	1666	88	1351	173	19.4	22.4	0.19	25.2
24.5	6.99	23.6	90	138	107	4.02	5.75	0.79	0.05	1713	90	1351	174	18.9	22.0	0.20	29.1
27.5	7.05	23.7	84	140	111	3.93	6.58	0.69	0.06	1792	93	1393	179	19.2	22.2	0.21	20.3
30.5	7.04	22.7	98	138	107	3.95	5.26	0.69	0.18	1718	90	1366	180	19.3	21.5	0.22	22.6
Site 2																	
5.5	7.65	23.3	84	192	169	1.69	4.67	0.60	0.01	2818	104	2221	236	19.9	37.0	0.25	15.0
7.5	7.61	22.7	80	192	171	1.72	8.16	1.15	0.02	2877	106	2228	238	19.6	36.8	0.27	10.3
9.5	7.61	24.1	79	198	185	1.64	13.55	1.75	0.02	3130	111	2384	252	19.3	38.5	0.27	8.2
13.5	7.30	24.0	81	208	195	1.39	10.48	1.87	0.01	3286	108	2574	272	16.3	41.1	0.28	2.7
16.5	7.27	24.6	88	211	69	1.38						2624	278	15.1	42.1	0.28	3.2
20.5	6.98	24.1	14		202	1.84				3319	99	2847	302	13.4	46.0	0.32	
24.5	7.01	23.6	-46		212	1.77			0.02	3567	107	2843	292	13.3	47.0	0.28	2.1
27.5	7.01	24.4	-59		214	2.05			0.01	3593	107	2884	301	12.9	47.1	0.30	
30.5	6.80	23.8	-106		197	0.00				3212	96	2803	291	14.8	47.2	0.33	
35	7.04	23.7	-124		210	2.55				3573	105	2764	289	14.0	44.8	0.35	3.9
38.5	6.85	24.6	-163		210	2.89			0.11	3516	106	2820	295	15.9	47.5	0.40	3.9
40.5	6.82		-163		213	2.88			0.10	3624	102	2806	293	16.8	48.3	0.43	4.2
43.5	6.83		-180		201	3.05	12.72	3.03	0.23	3526	100	2524	256	14.7	43.3	0.33	4.6
47.5	6.71	24.9	-196	218	209	2.99	11.57	3.21	0.74	3519	93	2858	286	17.2	47.7	0.38	4.8